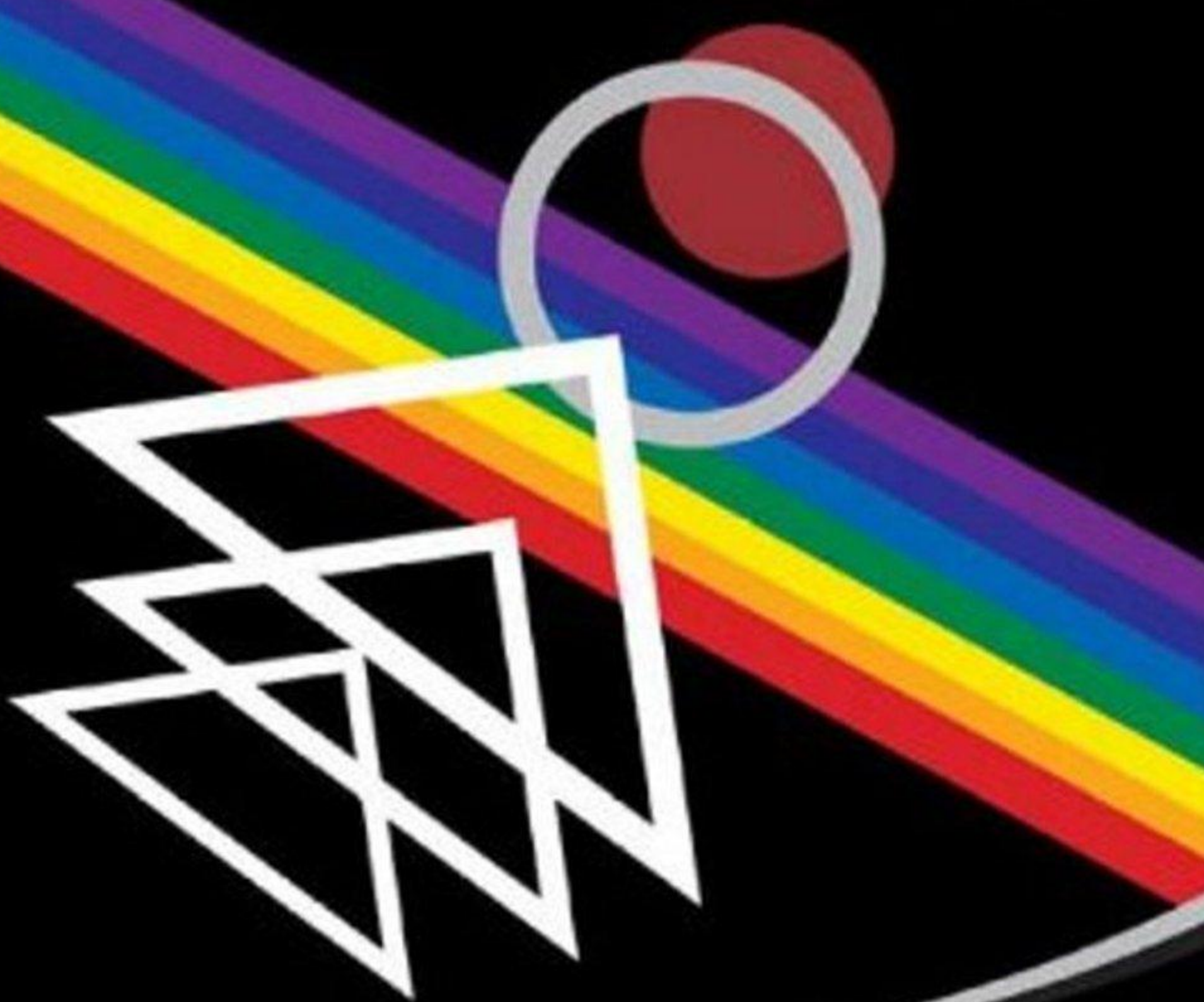


Recent Trends in Radiation Chemistry

James F Wishart • BSM Rao
editors



Recent Trends in Radiation Chemistry

This page intentionally left blank

Recent Trends in Radiation Chemistry

editors

James F Wishart

Brookhaven National Laboratory, USA

B S M Rao

University of Pune, India

 **World Scientific**

NEW JERSEY • LONDON • SINGAPORE • BEIJING • SHANGHAI • HONG KONG • TAIPEI • CHENNAI

Published by

World Scientific Publishing Co. Pte. Ltd.

5 Toh Tuck Link, Singapore 596224

USA office 27 Warren Street, Suite 401-402, Hackensack, NJ 07601

UK office 57 Shelton Street, Covent Garden, London WC2H 9HE

British Library Cataloguing-in-Publication Data

A catalogue record for this book is available from the British Library.

Cover image

The cover image depicts the spirit of pulse radiolysis experiment. The white arrows represent the pulsing of the radiation beam on the target (grey circle) leading to formation of transient species (maroon circle) whose spectrum is exhibited by the colored lines. The picture is redrawn from the mural at the National Centre for Free Radical Research, Department of Chemistry, University of Pune, Pune 411007, India.

RECENT TRENDS IN RADIATION CHEMISTRY

Copyright © 2010 by World Scientific Publishing Co. Pte. Ltd.

All rights reserved. This book, or parts thereof, may not be reproduced in any form or by any means, electronic or mechanical, including photocopying, recording or any information storage and retrieval system now known or to be invented, without written permission from the Publisher.

For photocopying of material in this volume, please pay a copying fee through the Copyright Clearance Center, Inc., 222 Rosewood Drive, Danvers, MA 01923, USA. In this case permission to photocopy is not required from the publisher.

ISBN-13 978-981-4282-07-9

ISBN-10 981-4282-07-3

Typeset by Stallion Press

Email: enquiries@stallionpress.com

Printed in Singapore.

Contents

<i>Foreword</i>	ix
<i>Preface</i>	xiii
<i>About the Editors</i>	xvii
<i>Contributors</i>	xix
Chapter 1 An Incomplete History of Radiation Chemistry <i>Charles D. Jonah</i>	1
Chapter 2 An Overview of Solvated Electrons: Recent Advances <i>Melbran Mostafavi and Isabelle Lampre</i>	21
Chapter 3 The Structure and Dynamics of Solvated Electrons <i>Ilya A. Shkrob</i>	59
Chapter 4 Instrumentation in Pulse Radiolysis <i>Eberhard Janata</i>	97

Chapter 5	Ultrafast Pulse Radiolysis Methods	121
	<i>Jacqueline Belloni, Robert A. Crowell, Yosuke Katsumura, Mingzhang Lin, Jean-Louis Marignier, Mehran Mostafavi, Yusa Muroya, Akinori Saeki, Seiichi Tagawa, Yoichi Yoshida, Vincent De Waele and James F. Wishart</i>	
Chapter 6	A History of Pulse-Radiolysis Time-Resolved Microwave Conductivity (PR-TRMC) Studies	161
	<i>John M. Warman and Matthijs P. de Haas</i>	
Chapter 7	Infrared Spectroscopy and Radiation Chemistry	201
	<i>Sophie Le Caër, Serge Pin, Jean Philippe Renault, Georges Vigneron and Stanislas Pommeret</i>	
Chapter 8	Chemical Processes in Heavy Ion Tracks	231
	<i>Gérard Baldacchino and Yosuke Katsumura</i>	
Chapter 9	Radiolysis of Supercritical Water	255
	<i>Mingzhang Lin, Yusa Muroya, Gérard Baldacchino and Yosuke Katsumura</i>	
Chapter 10	Pulse Radiolysis in Supercritical Krypton and Xenon Fluids	279
	<i>Richard Holroyd</i>	
Chapter 11	Radiation-Induced Processes at Solid–Liquid Interfaces	301
	<i>Mats Jonsson</i>	
Chapter 12	Radiolysis of Water Confined in Nanoporous Materials	325
	<i>Raluca Musat, Mohammad Shahdo Alam and Jean Philippe Renault</i>	

Chapter 13	Metal Clusters and Nanomaterials: Contribution of Radiation Chemistry <i>Hynd Remita and Samy Remita</i>	347
Chapter 14	Radiation-Induced Oxidation of Substituted Benzenes: Structure–Reactivity Relationship <i>B. S. M. Rao</i>	385
Chapter 15	Femtosecond Events in Bimolecular Free Electron Transfer <i>Ortwin Brede and Sergej Naumov</i>	411
Chapter 16	Chemistry of Sulfur-Centered Radicals <i>Krzysztof Bobrowski</i>	433
Chapter 17	Radiolysis of Metalloproteins <i>Diane E. Cabelli</i>	485
Chapter 18	Mechanisms of Radiation-Induced DNA Damage: Direct Effects <i>David Becker, Amitava Adhikary and Michael D. Sevilla</i>	509
Chapter 19	Radiation-Induced DNA Damage: Indirect Effects <i>Clemens von Sonntag</i>	543
Chapter 20	Radiation Chemistry Applied to Antioxidant Research <i>K. Indira Priyadarsini</i>	563
	<i>Index</i>	597

This page intentionally left blank

Foreword

Radiation chemistry, which probes the changes induced in a medium upon absorption of energy, is a mature discipline. Its origins lie in the discovery of ionizing radiations from naturally occurring isotopes in the late 19th Century. It was thrust to importance following the unleashing of atomic energy within the Manhattan Project; the laboratory where I write was founded by Milton Burton at that time. Subsequent advances in instrumentation and techniques for both excitation and detection have provided insight into the detailed nature of the interactions of the deposited radiation within the medium and allowed quantification of the ensuing physical and chemical transformations.

In *Recent Trends in Radiation Chemistry*, *Wishart* and *Rao* have assembled contributions from a number of well-known investigators in the field documenting its growth, highlighting its present-day significance, and offering potential opportunities for its future course.

A historical perspective on these developments is given in the first chapter by *Jonah*. *Janata* offers a detailed account of the key technique of electron pulse radiolysis, then firmly placed on the modern stage of ultrafast techniques in the chapter by *Belloni et al.* By far the most common detection scheme is that of transient optical absorption, however chapters by *Warman* and *de Haas* (on microwave conductivity) and *Le Caër et al.* (on infrared spectroscopy) illustrate alternative approaches. Others, not explicitly addressed, but key to

the identification of transients, include time-resolved resonance Raman and electron paramagnetic resonance spectroscopies to which Tripathi, Schuler and Fessenden from this laboratory, have made signal contributions.

Simply because it is so easily detected, the solvated electron has played and continues to play a central role in the development of the field. *Mostafavi* and *Lampre* provide a fascinating overview of some of the extensive experimental work on this species covering both formation (localization and solvation) and decay (reactivity). Recent theoretical attempts to address its structure and dynamics are reviewed by *Shkrob*, who leaves the reader with a list of significant challenges which must be overcome before a satisfactory understanding of this species can be achieved. We note that even in the most ubiquitous medium, i.e., water, the hydrated electron has not yet, to the best of my knowledge, been accorded a registry number by the Chemical Abstract Service of the American Chemical Society. While the reductive arm of radiolytic decomposition has been extensively investigated and the evolution of the electron spectrum well characterized from early times, much less is known about the initial fundamental processes in the complementary oxidative channels which must also be present.

The radiation chemical yields induced by energetic “heavy ions”, protons, alpha particles and more massive accelerated charged nuclei are significantly different from those due to fast electrons and high-energy photons. Much of the early theoretical work seeking an explanation of these differences is collected in the book of Mozumder on *Fundamentals of Radiation Chemistry*. Key features of the observed track structure of these particles have led to their increasing deployment in radiation therapies. Recent developments and exciting new directions in heavy-ion radiolysis, particularly the introduction of short-time pulse methods, are discussed by *Baldacchino* and *Katsumura*.

It might be expected that after years of study, the radiation chemistry of liquid water and dilute aqueous solutions would have been thoroughly documented. However, many modern day applications take place under conditions far from ambient. In particular, in nuclear

reactors, temperatures and pressures are such that criticality is approached. Indeed future coolants have been proposed in the supercritical regime. *Lin et al.* describe the challenges in obtaining reliable quantification of the processes occurring in sub- and super-critical water and document some of the unusual temperature and pressure dependencies observed in the reaction rates of even fundamental radical species. Other industrial applications in chemical synthesis, extraction, separation processes, and surface cleaning also use supercritical fluids. *Holroyd* reports results from fundamental studies on electron and ion processes in supercritical rare gases in Chapter 10 with an aim to improving the utility of such media.

In real-world applications, the importance of interfaces is hard to overestimate and three chapters are devoted to the effects of radiation at aqueous–solid boundaries. *Jonsson* focuses on applications within the nuclear industry where basic studies on radiation effects at water–metal interfaces have enabled a proposal for safe storage of spent nuclear fuel. Also with implications for the nuclear industry, *Musat et al.* document alterations in the radiation chemistry of liquid water confined on the nanoscale. Such nanoconfined solutions are prevalent in the media proposed and indeed in use for waste storage. In another application, radiation chemistry has successfully been used to produce nanoscale objects such as metallic clusters and nanoparticles, an area summarized by *Remita* and *Remita*.

Fundamental studies on the radiolytic oxidation of aromatics (*Rao*) and radiolytic redox reactions as seen in electron transfers (*Brede* and *Naumov*) are reviewed in Chapters 14 and 15.

The last five chapters illustrate the importance of radiation chemical techniques in building an understanding of biochemical and biological response to the impact of ionizing radiation. *Bobrowski* thoroughly reviews the many aspects of the one-electron oxidation of sulfur-containing species in biosystems. *Cabelli* describes the interaction of radiolytically-generated radicals with amino acids and proteins, while *Priyadarsini* summarizes many of the cellular repair processes involving antioxidants which exist to mitigate such damage to key biomolecules. Radiation damage to that most-important molecular constituent of the cell, DNA, is described in two chapters. *Becker et al.*

discuss direct effects where the consequences of ionization of DNA itself are considered. The interaction of radicals generated by radiolysis of the surrounding medium, such as the electron and hydroxyl, with DNA and its components is the topic of *von Sonntag*.

Recent Trends presents a picture of radiation chemistry as a vibrant field of international venue, still addressing fundamental challenges as it continues to grow into its second century. This image is reinforced, and both broadened and deepened, by a number of edited volumes: *Radiation Chemistry: Present Status and Future Trends* — Jonah and Rao (2001); *Charged Particle and Photon Interactions with Matter* — Mozumder and Hatano (2004); *Radiation Chemistry: From Basics to Applications in Material and Life Sciences* — Belloni *et al.* (2008); which have appeared within the last few years. A clear articulation of prospects for future development was also presented at the recent visionary meeting “Radiation Chemistry in the 21st Century” held at Notre Dame in July, 2009.

Ian Carmichael
Notre Dame Radiation Laboratory

Preface

Radiation chemistry has witnessed an entire gamut of exciting events since its discovery more than a century ago, contributing not only to chemistry but to other branches of science encompassing simple to complex molecules. Today, ionising radiation and its effects are playing a crucial role in a number of technologies such as power generation, advanced materials, the nuclear fuel cycle, radiation therapy, sterilization, and pollution prevention and remediation. The free radical mechanisms of biomolecules relevant to health and medicine, including DNA, are crucial for understanding the origins and treatment of many diseases. Heavy ion radiolysis remains a vital interest of radiation chemists, for example in the areas of fundamental radiolytic processes, nanosynthesis using track structure, highly site-specific radiation therapy, and the effects of heavy ion radiation on astronauts and materials during prolonged space flight.

In this book, we have made an effort to provide an overall view of the emerging trends in radiation chemistry authored by experts in the field. The introductory chapter covers the history of radiation chemistry, underlining its achievements and issues that need to be addressed in future research. By renewing its research directions and capabilities in recent years, radiation chemistry research is poised to thrive because of its critical importance to today's upcoming technologies. Detailed accounts of fast and ultrafast pulse radiolysis instrumentation development and recent advances on ultrafast

dynamics of solvated electrons enabled by the latter form the basis of the chapters immediately following.

In the next two chapters, the coupling of time-resolved microwave conductivity and infrared spectroscopy techniques to pulse radiolysis is discussed. The following review highlights the progress made on water radiolysis with heavy ion beams. The subsequent chapters on the radiolysis of supercritical water, radiation-induced processes at solid–liquid interfaces and radiolysis of water-confined nanoporous materials discuss the essential features that are relevant in the development of new generations of nuclear reactors and waste management. The article on supercritical xenon and krypton fluids focuses on the properties and reactions of charged species, electrons and ions, providing useful information for their utilization in particle detector and industrial applications.

Nanoparticles are rapidly gaining popularity in biomedical, optical and electronic areas. Zapping tumors with multi-walled carbon nanotubes, solar cells to light-attenuators and chip-to-chip optical interconnects in futuristic circuitry are some of the potential applications. Thus finding novel ways for the synthesis of these new age materials is of paramount interest where radiation chemistry is modestly playing a role and the chapter on metal clusters and nanomaterials deals with these aspects.

The fundamental aspects of structure–reactivity relationships in radiation-induced oxidation of substituted benzenes, bimolecular free electron transfer on the femtosecond time scale, the chemistry of sulfur-centered radicals and the radiolysis of metalloproteins are discussed in succeeding chapters. The effects of the direct and indirect mechanisms of radiation-induced DNA damage are discussed individually in two complementary chapters. The last chapter highlights the application of radiation chemical techniques to antioxidant research.

The purpose of the book is to expose graduate students and young scientists working in the field to recent developments in radiation chemistry research and to demonstrate to scientists, engineers and other technologists the utility of radiation chemical techniques in advancing their scientific pursuits. The fact that radiation chemistry is

a vital part of molecular science is more than evident from the diverse topics found within these covers.

The road to completion of this book was long, and we sincerely appreciate the cooperation and understanding of all the individual authors and thank them for their tremendous efforts to painstakingly prepare their chapters to meet the education and outreach goals described above. We enjoyed the job of editing and many people have helped us in this task. We would particularly like to thank Ms. Sook Cheng Lim and Ms. Ling Xiao at World Scientific Publishing who helped us in the planning and execution of the project. Our special thanks go to Ms. Parimal Gaikwad at the University of Pune for doing an excellent job of preparing the near camera-ready copies of the entire book. BSMR thanks the DAE-BRNS for the award of the Raja Ramanna Fellowship enabling the completion of the project. JFW thanks the U.S. DOE for support under contract DE-AC02-98CH10886. Lastly, we would like to thank our wives for their patience and understanding which made our task easier.

James F. Wishart and B. S. M. Rao

This page intentionally left blank

About the Editors

James F. Wishart received a B.S. in Chemistry from the Massachusetts Institute of Technology in 1979 and a Ph.D. in Inorganic Chemistry from Stanford University in 1985 under the direction of Prof. Henry Taube. After a postdoctoral appointment at Rutgers University, in 1987 he joined the Brookhaven National Laboratory Chemistry Department as a Staff Scientist in the Radiation Chemistry Group. He founded and presently supervises the BNL Laser-Electron Accelerator Facility for picosecond electron pulse radiolysis. His research interests include ionic liquids, radiation chemistry, electron transfer, and new technology and techniques for pulse radiolysis. He has authored over 90 papers and chapters, and is the co-editor of *Advances in Chemistry Series* vol. 254, *Photochemistry and Radiation Chemistry*.

B. S. M. Rao presently holds the Raja Ramanna Fellowship of the Department of Atomic Energy at the Department of Chemistry, University of Pune, India where he served as Professor and Head. His research and teaching interests have been in physical chemistry with an emphasis on radiation chemistry and he received training at the Nuclear Research Centre Karlsruhe and the Max Planck Institut für Strahlenchemie at Muelheim, Germany on an Alexander von Humboldt Fellowship. He trained several graduate students and built an active research group at the University of Pune by initiating international collaborations in radiation chemistry. He established the

National Centre for Free Radical Research housing a 7-MeV LINAC facility on the Pune University campus with support from the Department of Atomic Energy. He has published nearly 100 papers and co-edited a book on *Radiation Chemistry: Present Status and Future Trends* in 2001.

Contributors

Dr. Amitava Adhikary

Department of Chemistry
Oakland University
Rochester, MI 48309
USA

Dr. Mohammad S. Alam

CEA, IRAMIS, SIS2M
Laboratoire de Radiolyse
F-91191 Gif-sur-Yvette Cedex
France

Dr. Gérard Baldacchino

CEA, IRAMIS, SIS2M
Laboratoire de Radiolyse
F-91191 Gif-sur-Yvette Cedex
France

Prof. David Becker

Department of Chemistry
Oakland University
Rochester, MI 48309
USA

Prof. Jacqueline Belloni

Laboratoire de Chimie Physique/ELYSE
CNRS/Université Paris-Sud 11
Faculté des Sciences, Bât. 349
91405 Orsay
France

Prof. Ortwin Brede

University of Leipzig
Interdisciplinary Group Time-Resolved Spectroscopy
Permoserstr. 15, 04303 Leipzig
Germany

Prof. Krzysztof Bobrowski

Institute of Nuclear Chemistry and Technology
03-195 Warszawa
Poland

Dr. Diane E. Cabelli

Chemistry Department
Brookhaven National Laboratory
Upton, NY 11973
USA

Dr. Robert A. Crowell

Chemistry Department
Brookhaven National Laboratory
Upton, NY 11973
USA

Dr. Matthijs P. de Haas

Delft University of Technology
Reactor Institute Delft
Mekelweg 15, 2629 JB Delft
The Netherlands

Dr. Richard Holroyd

Chemistry Department
Brookhaven National Laboratory
Upton, NY 11973
USA

Dr. Eberhard Janata

Helmholtz-Zentrum für Materialien und Energie GmbH
Solar Energy Research
Glienicke Str. 100
14109 Berlin
Germany

Dr. Charles D. Jonah

Chemical Sciences and Engineering Division
Argonne National Laboratory
9700 South Cass Avenue
Argonne, IL 60439
USA

Prof. Mats Jonsson

Nuclear Chemistry
Department of Chemistry
Royal Institute of Technology
SE 10044 Stockholm
Sweden

Prof. Yosuke Katsumura

Department of Nuclear Engineering and Management
School of Engineering
The University of Tokyo
Hongo 7-3-1, Bunkyo-ku
Tokyo 113-8656
Japan

Prof. Isabelle Lampre

Laboratoire de Chimie Physique/ELYSE
CNRS/Université Paris-Sud 11
Faculté des Sciences, Bât. 349
91405 Orsay
France

Dr. Sophie Le Caër

CEA/Saclay
DSM/IRAMIS/SIS2M/Laboratoire Claude Fréjacques
URA 331 CNRS
F-91191 Gif-sur-Yvette Cedex
France

Dr. Mingzhang Lin

Advanced Science Research Center
Japan Atomic Energy Agency (JAEA)
2-4 Shirakata Shirane, Tokai, Naka
Ibaraki 319-1195
Japan

Prof. Jean-Louis Marignier

Laboratoire de Chimie Physique/ELYSE
CNRS/Université Paris-Sud 11
Faculté des Sciences, Bât. 349
91405 Orsay
France

Prof. Mehran Mostafavi

Laboratoire de Chimie Physique/ELYSE
CNRS/Université Paris-Sud 11
Faculté des Sciences, Bât. 349
91405 Orsay
France

Dr. Yusa Muroya

Nuclear Professional School
School of Engineering
The University of Tokyo
2-22 Shirakata Shirane, Tokai, Naka
Ibaraki 319-1188
Japan

Dr. Raluca Musat

CEA, IRAMIS, SIS2M
Laboratoire de Radiolyse
F-91191 Gif-sur-Yvette Cedex
France

Dr. Sergej Naumov

Leibniz Institute for Surface Modification
Permoserstr. 15, 04303 Leipzig
Germany

Dr. Serge Pin

CEA/Saclay
DSM/IRAMIS/SIS2M/Laboratoire Claude Fréjacques
URA 331 CNRS
F-91191 Gif-sur-Yvette Cedex
France

Dr. K. Indira Priyadarsini

Radiation and Photochemistry Division
BARC, Mumbai 400085
India

Dr. Stanislas Pommeret

CEA/Saclay
DSM/IRAMIS/SIS2M/Laboratoire de Radiolyse
F-91191 Gif-sur-Yvette Cedex
France

Prof. B. S. M. Rao

National Centre for Free Radical Research
Department of Chemistry
University of Pune
Pune 411007
India

Dr. Hynd Remita

Laboratoire de Chimie Physique/ELYSE
CNRS/Université Paris-Sud 11
Faculté des Sciences, Bât. 349
91405 Orsay
France

Prof. Samy Remita

Laboratoire de Conception des Capteurs Chimiques et Biologiques
LC3B, Chaire de Génie Analytique, EA 4131
Conservatoire National des Arts et Métiers, CNAM
292 rue Saint-Martin
75141 Paris Cedex
France

Dr. Jean Philippe Renault

CEA/Saclay
DSM/IRAMIS/SIS2M/Laboratoire de Radiolyse
F-91191 Gif-sur-Yvette Cedex
France

Dr. Akinori Saeki

CREST, Japan Science and Technology Agency
c/o Osaka University
8-1 Mihogaoka
Ibaraki, Osaka 567-0047
Japan

Prof. Michael D. Sevilla

Department of Chemistry
Oakland University
Rochester, MI 48309
USA

Dr. Ilya A. Shkrob

Chemical Sciences and Engineering Division
Argonne National Laboratory
9700 South Cass Avenue
Argonne, IL 60439
USA

Prof. Clemens von Sonntag

Max-Planck-Institut für Bioanorganische Chemie
Stiftstr. 34-36
45413 Mülheim an der Ruhr
Germany

Prof. Seiichi Tagawa

The Institute of Scientific and Industrial Research
Osaka University
8-1 Mihogaoka
Ibaraki, Osaka 567-0047
Japan

Dr. Georges Vigneron

CEA/Saclay
DSM/IRAMIS/SIS2M/Laboratoire de Radiolyse
F-91191 Gif-sur-Yvette Cedex
France

Dr. Vincent De Waele

Laboratoire de Chimie Physique/ELYSE
CNRS/Université Paris-Sud 11
Faculté des Sciences, Bât. 349
91405 Orsay
France

Dr. John M. Warman

Delft University of Technology
Reactor Institute Delft
Mekelweg 15, 2629 JB Delft
The Netherlands

Dr. James F. Wishart

Chemistry Department
Brookhaven National Laboratory
Upton, NY 11973
USA

Prof. Yoichi Yoshida

The Institute of Scientific and Industrial Research
Osaka University
8-1 Mihogaoka
Ibaraki, Osaka 567-0047
Japan

Chapter 1

An Incomplete History of Radiation Chemistry

*Charles D. Jonah**

1. Introduction

Radiation chemistry, like all fields of science, has been strongly influenced by the techniques that were available to make measurements. As more and more sophisticated techniques become available, more and more sophisticated questions were posed and answered. In this short review of the history of radiation chemistry, I will select the various eras of radiation chemistry, as defined by the techniques available, and discuss the concepts and conclusions of the time. At the end, I will summarize where radiation chemistry is and what are the unanswered questions and new techniques that are needed to answer these questions. Much more on such topics will be found in the rest of the volume.

Radiation chemistry has developed very similarly to photochemistry. Max Matheson, one of the pioneers of radiation chemistry, said, “Radiation chemistry always trails photochemistry in time response.” That trend continues today.

* Chemical Sciences and Engineering Division, Argonne National Laboratory, Argonne, IL 60439, USA. E-mail: CDJonah@anl.gov

The eras of radiation chemistry can be quickly summarized as:

- Experiments done with naturally occurring isotope sources,
- Experiments using high-power X-ray machines,
- Experiments using artificially produced isotope sources,
- Pulse radiolysis experiments,
- Sub-nanosecond pulse radiolysis experiments,
- Picosecond and femtosecond laser experiments,
- Future — true picosecond radiolysis experiments.

This outline, while useful, does not include two important subjects in the evolution of radiation chemistry: the role of theory and the role of modern heavy-ion-radiolysis experiments. One can describe different types of radiation by the rate at which they deposit energy going through a sample. The conventional term is linear energy transfer, abbreviated LET. High-LET radiation deposited energy densely along the path of the ionizing particle while low LET radiation deposited energy discretely along the path of the ionizing particle. Examples of low-LET particles are high-energy X-rays/gamma and electrons. High-LET particles include heavy ions, alpha particles and neutrons.

It is well to remember that much of the early progress was inhibited by the lack of the internet to facilitate transfer of early experimental knowledge. Of course, those experiments were also assisted because there was no internet to act as a massive time sink.

Please also excuse errors in summarizing the earlier experiments. Information about these was obtained by reading the literature and by reading review articles by the relevant authors, as I was not in the field yet. In particular, I will be making use of the information in *Early Developments in Radiation Chemistry* edited by Jerzy Kroh,¹ a book that collected the personal accounts of many of the most prominent radiation chemists of the middle of the 20th century, and *The Chemical Effects of Alpha Particles and Electrons* by Samuel C. Lind,² which discussed much of the radiation chemistry up to 1928.

2. The Period of Natural Isotopic Sources

The discussion in this section is primarily based on Lind's book.² Much of the early work in radiation chemistry was done either with radium sources and/or radon sources. These sources produced primarily alpha rays and weak beta rays. The lack of penetrating power of these particles made early experiments very difficult.

Many of the early experiments measured the effect of radiation on solids, such as the darkening of glass, the change in form of certain minerals, etc. These experiments required a considerable time (often weeks or months) and inherently were very difficult to quantify. No well-established techniques existed for measuring the amount of dose that was deposited in a liquid or solid target, so results varied from laboratory to laboratory.

While there was considerable confusion in the earliest experiments, it appears that most researchers had realized that radiation chemistry depended on the deposition of the energy in the solvent or dominant species and then a redistribution of the energy from the solvent. The exact nature of the early events where energy was deposited in the solvent (or dominant material) and then transferred to the compounds of interest was not known, but the similar products that one would get with different ratios of gases were strong indicators of the role of energy deposition in the solvent.

Early liquid phase experiments determined the formation of hydrogen and oxygen from the radiolysis of water along with the production of H_2O_2 . The yield of hydrogen to oxygen was not two to one, so it was recognized that the third primary product was hydrogen peroxide. Yields were not well established, because one could not easily establish the dose that was deposited in the material.

Quantification of results first came in the radiolysis of gases. Conductivity-type experiments determined the number of ions that would be formed in a particular gas. The yield of products could then be compared with the amount of ionization. This ratio was referred to as M/N , where M was the yield of products and N was the number of ions that were formed by the radiation. It was believed that

when the ratio of products formed to the number of ions formed was much larger than one, that this was a measure of the size of clusters around the ions in the gas phase.

Early experiments in liquids were quite variable for many reasons. The conductivity technique, which was used in the gas phase to measure dose, was not applicable to the liquid phase. Reactions were measured using dissolved radium salts or radon gas as the ionization source. Some thought the chemistry was due to the reactions with radium; however, it was soon recognized that it was the emitted rays that caused the decomposition. Both radium and radon could cause radiation damage. Because the radon would be partitioned between the gas and liquid phase, the amount of energy that was deposited in the liquid depended critically on the experimental conditions such as the pressure and amount of headspace above the liquid. In addition, because the sources were weak, long irradiation times were necessary and products, such as hydrogen peroxide, could decompose.

In summary, in this first era of radiation chemistry it was discovered that the medium absorbs the energy and the result of this energy absorption leads to the initiation of the chemical reactions. The role of radium in these systems was not as a reactant or as a catalyst, but instead as a source of radiation. Most quantitative work was done with gases. It was learned that there was a close correspondence between the amount of ionization measured in a gas and the yield of chemical products. Solid and liquid-phase radiolysis studies were primarily qualitative.

3. X-Ray Generator in Radiation Chemistry

In the late twenties, research started using powerful X-ray generators. With X-rays, it was then possible to use photons that would penetrate vessels and evenly irradiate a reasonable physical volume. With this capability and the development of small ionization chambers to measure X-ray dose, it now became possible to carry out quantitative radiolysis experiments in liquids.

Fricke demonstrated that the yield of Fe^{3+} in the radiolysis of ferrous sulfate was independent of the concentration of the ferrous

salt over a wide range.³ This showed that the energy deposition was to the solvent, and was subsequently passed on to the ferrous ions. He determined the yields in air- and oxygen-saturated systems. This became the Fricke dosimeter, probably the most used dosimeter for the measurement of the amount of radiation. With this advancement, it then became possible to accurately and easily measure the total amount of radiation striking a system and thus to make meaningful quantitative measurements.

At the time, it was known that water could be decomposed by heat or by UV irradiation. However, irradiation by X-rays seemed to show no decomposition of very pure water. This led Hugo Fricke to conclude that radiation created two forms of excited water, which could react with additives in the system or decay back to normal water. Today we certainly know that radiation does decompose water.

It had been hypothesized that the biological effects would arise from the hydrogen peroxide formed in solution. Experimental measurements showed that this was not the case; the results of the ionizing radiation, and in Fricke's picture, the activated water molecules were the important species.

4. Steady-State Radiolysis, the War Years and After

During World War II, the atomic-bomb-development effort in the United States required a sudden increase in the knowledge of radiation chemistry. Water was going to be part of the reactors that were to produce plutonium to make bombs. Materials, including vacuum pumps, hoses, connectors and oils were to be exposed to very high levels of neutron and gamma radiation. Previous work was totally insufficient to understand the effects on these materials.

In the United States, a group under Milton Burton was formed to make these studies⁴ while other research occurred in Canada and elsewhere. These research efforts made use of all radiation sources that were available. It was quickly realized that the experiments had to both be able to predict the effects of radiation on materials, and obtain a basic understanding of the chemistry and physics involved so that intelligent predictions could be made on new systems.

The first efforts were focused on pure water on the assumption that water was an important ingredient in most systems and would be the simplest to understand. Tremendous variability was found in the experimental results and pure water studies were curtailed and efforts were focused on systems closer to those of practical importance, water with ionic solutes. These results were significant in many ways. The experimental results were satisfying both practically and experimentally. The systems were reproducible and of significance to the development of the war effort.⁵

All of these efforts attempted to understand what role radiation played in the generation of the chemistry. In the usual confluence that often occurs in science, the role of radicals, and in particular the H and OH radicals was recognized in many places more or less simultaneously.^{5,6} The first published description of the role of radicals was by Weiss in 1943⁶ as the groups working on bomb production were not allowed to publish their work. These ideas were refined over time.

Allen first described the role of back reactions in the radiation chemistry of water.⁵ This mechanism made clear the reason for the apparent lack of water decomposition in pure water that had been observed by Fricke and which led Fricke to suggest the dominant role of excited water in the radiation chemistry of water. Later on, this understanding of back reactions would be critical in allaying the fears of the “hydrogen bubble” that was suggested that could have occurred in the Three-Mile-Island reactor incident.⁷ Early reports that suggested that there could be a serious consequence from the hydrogen formed by the radiation in the reactor incident were quickly corrected with the known understanding of the importance of back reactions.

Experiments during the war years showed the importance of the different types of radiation, alpha particles, neutrons, and beta particles and gamma rays. These studies also were part of the understanding of the role of back reactions in radiation chemistry.

The rise of reactors after the war led to one of the most important advances in radiation-chemical techniques, the Cobalt-60 and Strontium-90 sources. With a reactor, it is possible to create an

intense radiation source that made possible many of the advances that occurred over the next several decades. One interesting story is that told by Professor Kroh, who took a radiation source back to Poland in a lead pig. He stored it under his bed on the boat back from Canada.⁸ The cobalt-60 source made relatively inexpensive, relatively simple source that could be used in many university environments. The source put out an energetic gamma ray that could easily and uniformly irradiate a liquid target. In the early days of radiation chemistry, the gamma-emitters were too weak to carry out sufficient chemistry for easy study. The alpha- and soft beta-emitters could not be conveniently used with liquids because the range was too short and it was thus difficult to measure radiation doses. The cobalt (and cesium) source solved these problems as Allen has discussed when he enumerated the advantages of isotope sources.⁹

The development of the sources led to studies in polymers, solids, organic systems, which were too numerous to mention. One only needs to look at the chapters by Dole, Willard and others in the book on the history of radiation chemistry to find the wide range of chemical systems that could be studied.¹

Low temperatures that allowed one to trap long-lived species and electrons in glasses could be studied using spin resonance techniques.¹⁰

In the radiation chemistry of water, many steps of the process were clarified. The radical mechanism for the radiation chemistry of water was confirmed and the existence of multiple additional species other than H, OH and H₂O₂, such as HO₂, O and other similar radicals were deduced. One additional complication became clear; there appeared to be two types of H atoms, with different reactivities. Dainton writes of having suggested that one of them might be an electron in solution; however, he was assured by James Franck that that species could not live for chemically significant times.¹¹ After several years, Dainton shook off this pronouncement and both he¹² and Czapski and Schwarz¹³ measured the ionic-strength dependence of the reaction of the “H-atom” and showed that it had a negative charge.

5. A Slight Detour in Our “Tour Through Radiation-Chemistry Techniques”

At this point, I would like to discuss two techniques that do not conveniently fit the technique ordering/timeline for the advances in radiation chemistry. Use of high-LET radiation has been common since the beginning of radiation chemistry. As was mentioned earlier, high-LET radiation studies were common in early experiments because sufficient energy could be deposited to make it possible to observe reaction products. If low-LET sources were used, so little energy was deposited that the yield of products was too low to measure.²

Early on, the differences in the products from radiolysis of water were noticed. It was found, as mentioned above, that the radiolysis of pure water seemed to lead to almost no damage. If there were impurities in the water, radiation damage would occur. However, irradiation by high LET radiation would clearly lead to the formation of hydrogen. Further experiments showed that if one irradiated a sealed sample with high-LET radiation, and then the sample was irradiated with a low-LET source, the gas formed by the radiation would then disappear and it would appear as if there were no long-term decomposition. These data were part of the reason that A. O. Allen proposed the theory of radiation chemistry where back reactions occurred.⁹

The rise of heavy particle accelerators made it possible to study the radiation chemistry as a function of particle LET with machines such as the Lawrence Berkeley Bevatron and others that allowed the expansion of radiolysis to very heavy ions and *very high* LET.

The explanation for the differences of LET radiations arose out of the theoretical development in radiation chemistry. The basic theory is relatively simple; an ionizing particle goes through the solution, creating ions and excited states. These regions of excitation and ionization will be much closer together in high LET particles. In essence, in a simplified framework, high-LET particles make a cylindrical track of ionization, which can be approximated as two-dimensional diffusion. The low-LET particles create ionization regions

that are disjoint and can be approximated by spherical regions. There is a fundamental difference in the solution of these two problems; in cylindrical geometry, eventually everything will recombine, while in spherical geometry, there is a non-zero escape probability. In practice, we know that the escape yield is only a few percent for hydrocarbons, while for water at room temperature, the escape probability is 70%.

The simple description of the probability of energy deposition by high-energy particles is, unfortunately, not sufficient to describe the ultimate chemistry. One must also consider the energy loss from the secondary electrons created by the ionizing radiation, the distance that low energy electrons will travel and what species will be formed. These are not easily simulated using the simple physical principles that describe energy loss from high-energy electrons.

There were two thoughts on the ultimate fate of the electron. Samuels and Magee suggested that the electron would recombine very quickly with the positive ion, potentially leading to the formation of excited states.¹⁴ Platzman suggested the electron would be thermalized and would associate with the water molecules in the solution to form a hydrated electron.¹⁵ He even suggested where the electron would absorb. We know the resolution of this question — a hydrated electron was formed, presumably leading to different distance distributions for the electron. However, Platzman was not omniscient — he had suggested that the electron would have a lifetime of a few nanoseconds or so in water and as we know, with sufficient care, lifetimes into the millisecond range can be obtained.

The diffusion theory of radiation chemistry was developed by many authors in many places. A listing of many of these works is given in the review article by Kuppermann.¹⁶ In the cited articles, the general basis of modern models of radiation chemistry was developed, except that the reactive species were the H atom and the OH radical. Distributions were estimated for the radical species, and even the role of scavengers was considered. With the advent of digital computers, these models could now be calculated in the complexity that might begin to reproduce the actual system. Flanders and Fricke started with integrating the equations (yes the same Fricke of biophysical radiation

chemistry fame).¹⁷ Kuppermann and his collaborators did a large series of calculations, testing the importance of different parameters.¹⁸ The possible parameters became more constrained with the identification of the hydrated electron (experimental work is discussed in the next section). The test for these calculations was to determine the yields of various products in the presence of variable concentrations of scavengers. Probably the seminal paper for this approach was by Schwarz in 1969, who calculated yields for various chemical systems using a form of modified prescribed diffusion.¹⁹ Because of the speed of the calculations, the use of a prescribed diffusion model made it possible to survey a much larger range of parameters.

Models continued to develop including stochastic models and simplifications of the stochastic model, which provided insight into the fact that the systems are not continuous.

This excellent agreement with experimental data only lasted until sub-nanosecond pulse radiolysis experiments became common. We will return to this in Sec. 7.

6. The Development of Pulse Radiolysis

In science, one builds models based on experimental data and one then attempts to verify these models. Experiments using isotope sources provided data that were explained with microscopic models. However, these models could only be indirectly tested because entities that took part in these reactions were too short-lived to be directly observed. Photochemistry had the same problems and to solve it, the techniques of sector photolysis and flash photolysis were developed. The attempts to create sector radiolysis were only marginally successful. The analog of flash photolysis, pulse radiolysis, was developed in three laboratories almost simultaneously and the first publications appeared within a month of each other.²⁰⁻²²

The early studies measured the radicals that occurred in various inorganic and organic systems, including the benzyl radical in cyclohexane, and I_2^- in water using spectrographic techniques. Soon, spectrophotometric techniques made the measurement of kinetics possible and techniques were expanded to include spin resonance

techniques, conductivity, resonance Raman and fluorescent techniques, to list just a few.

The observation and identification of the red spectrum of the hydrated electron was a major advance that occurred using pulse radiolysis. Keene may have first observed this absorption, and Matheson suggested that this observation might be the hydrated electron.²³ This observation was only an aside and, while written before the paper of Hart and Boag, was not published until after their paper. While chemical evidence had strongly suggested that the hydrated electron existed,^{12,13} the publication of Hart and Boag²⁴ was the final confirming experiment that appeared to completely convince the community. The similarity to the electron spectrum in alkali metals, the chemical reactivity and the observation that its reactions were consistent with a negatively charged species certainly confirmed the identification.

The measurement and identification of the hydrated-electron spectrum led to a major increase in activity. It was now possible to directly measure the rate of hydrated-electron reactions with a large variety of inorganic and organic species. With these data, it was then possible to classify reactions in ways that had not been possible previously. It was possible to show that some reactions were diffusion controlled and to suggest that there were some reactions that were even faster than diffusion controlled (at least if one assumed normal reaction radii).²⁵ Conductivity measurements could directly measure the mobility of ions and could provide information that was unavailable in other ways.²⁶

Spectra and kinetics were also determined for many other species. The solvated electron was observed and its spectrum was determined in a wide variety of solvents, from ethers and alcohols to hydrocarbons and even supercritical fluids. Other radicals, including the benzyl radical, the first species studied in pulse radiolysis, were observed. Excited states, both singlet and triplet, anions and cations, were determined for aromatic species. The number and variety of species is large. The importance of these studies was that it was now possible to observe the intermediate states in the radiation-chemical reactions and thus confirm or refute reaction mechanisms that had been proposed based on product yield data.

Radiation chemistry also made it possible to prepare radicals and ions of interest and study their properties. With the advent of pulse radiolysis, it was possible to directly explore the reactivity of such intermediates. In fact, many reactions that were suggested to be of importance in solar energy conversion could be more cleanly studied using radiation chemistry. Similarly, questions about the mobility of actinide species in the biosphere often depended on the reactivity of different oxidation states of materials such as plutonium. Thus, it was possible to show that plutonium oxides were unlikely to move quickly through water in the earth, because the soluble oxides were very reactive and the equilibrium values were far to the side of the insoluble compounds.

One particular example of the use of pulse radiolysis to general chemistry was the work of Miller and co-workers on the rates of electron-transfer reactions. These studies, which were begun using reactants captured in glasses, were able to show the distance dependence of the reaction of the electron with electron acceptors.²⁷ Further work, where molecular frameworks were able to fix the distance between electron donors and acceptors, showed the dependence of electron-transfer rate on the energetics of the reaction.²⁸ These studies were the first experimental confirmation of the electron transfer theory of Marcus.

One of the first experiments on the radiation chemistry of water was the work of the biophysicist, Hugo Fricke. With this background, it is not surprising that the new pulse radiolysis techniques were applied to biological molecules and biological chemistry. The reactions of the hydrated electron with amino acids, proteins, nucleic acids and DNA were studied in great detail. The spectra of the intermediates were also determined. The unfortunate situation is that most biological damage arises out of the reaction of OH radicals rather than the hydrated electron, so while the data on electron reactions are interesting, they are often not of great consequence in understanding biological damage. Rates for hydroxyl radical reactions can be determined by observing the formation of products, or by competition, where one observes the spectrum of the competing product. The direct measurement of the OH kinetics is difficult

because the OH radical is weak and absorbs in the ultraviolet in a region where most species absorb.

Above we talked about the diffusion models that were used to explain the chemical products that occur after irradiation with low-LET radiation. It was pointed out that models, in addition to making specific predictions about the yield of products, also made predictions about the time dependence of products. For low-LET radiation, these models suggested that the primary non-homogeneous reactions would occur in the 30–300-ps-time scale and that there would be continuing decays at longer times. Experimental data, for example by Buxton²⁹ and Thomas³⁰ suggested that the data were not inconsistent with these suggestions.

7. Sub-nanosecond Pulse Radiolysis

To address the questions of non-homogeneous/spur kinetics, John Hunt and his group at Toronto developed a sub-nanosecond pulse-radiolysis system.³¹ In their stroboscopic pulse radiolysis system, they could observe from about 30 to 350 ps after the pulse with a time resolution of about 10 ps. Their results showed no significant decay of the electron between 30 and 350 ps, which was not consistent with the diffusion-kinetic models of spur decay in radiation chemistry.

The foray into sub-nanosecond pulse radiolysis was continued by Matheson and Jonah at Argonne,³² Tabata and co-workers in Tokyo,³³ and Katayama and co-workers in Hokkaido.³⁴ The experiments at Argonne measured the decay of the hydrated electron both from about 100 ps to 4 ns and from 1 ns to 40 ns.³⁵ These results clearly showed that the decay measured was approximately a factor of 10 slower than that predicted by theory. The decay profiles are very similar to those determined using a linac-laser combination about 15 years later.³⁶ The decay of the OH radical was also considerably slower than what theory predicted,³⁷ which is, of course, no surprise that the two should decay at similar rates.

Hamill had suggested that there was a precursor of the hydrated electron that could be scavenged and called this species the dry electron.³⁸ Work by the Hunt group with his stroboscopic pulse radiolysis

system determined a large number of such apparent reactions and found a good correlation between the rate of precursor scavenging and the rate of the reaction of the hydrated electron.³⁹ The only example that they found that did not correlate was the proton — the reaction of the electron with the proton was very fast; however there was no apparent reaction of the electron precursor. The Argonne group, guided by the studies of Miller in “tunneling” reactions, attempted to find species that the rate of the dry electron and the hydrated electron did not correlate. Probably the clearest example was the selenate anion.⁴⁰

Czapski and Peled⁴¹ pointed out that many of these apparent cases of precursor reactions could be equally well explained by the radiation-chemical analog of photochemical “static scavenging”, which in the photochemical case was when an excited state is formed within the reaction radius of a quencher. Such a process would be expected to depend exponentially on concentration, which is indeed what is observed. Most systems in water could be explained that way; however, selenate and electrons in alcohols would not be consistent with such an explanation.

The sub-nanosecond pulse radiolysis techniques have made it possible to study the initial yields of singlets and triplets in the radiolysis of aromatic systems, the decay of electrons in non-polar media, fast electron transfer reactions and solvation experiments.

Other techniques have been used for getting sub-nanosecond time resolution. These include the fast conductivity experiments of the electron in non-polar media.⁴² Streak camera detection has been used for the measurement of fluorescence from scintillators in hydrocarbon solutions. These experiments probe the role of the transfer of energy from solvent excited states to scintillators in comparison with the role of ion-recombination to form the scintillator excited states.⁴³

Recently, laser-driven photocathode accelerators and lasers coupled with compressed pulses have been able to produce electron pulses in the vicinity of 5–10 ps.^{44–46} This has enabled one to improve on the time resolution available from the original Hunt experiments but without the limitations of the multiple pulses. These short times have been used for measuring electron transfer reactions, electrons in

rare gas and supercritical fluids and transport and lifetimes of triplet states. Work at ELYSE has included the measurement of solvation of the electron polyols.

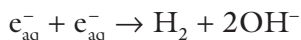
8. Laser-Simulated Radiation Chemistry

Pulse radiolysis was modeled after flash photolysis. The time resolution of laser flash photolysis has always been better than for pulse radiolysis. There are multiple reasons for this effect. (1) Flash photolysis equipment is cheaper than electron accelerators so there have been many more practitioners of the art. (2) Photons do not repel each other so it is possible to focus a larger number of them in a small volume over a short time period than it is possible to do for electrons. (3) The velocity of relativistic electrons in a dense material is much higher than photons in the same material so sample thicknesses must be much thinner for pulse radiolytic experiments than for flash photolytic experiments, thus meaning that signals would be smaller.

Experimenters began applying high-power lasers to creating electrons, the prototypical radiolytically produced species, and studying their structure chemistry, excited states and photochemistry. First, the absorption of the hydrated electron was measured; these results could be interpreted to give an idea of the separation of the electron from its geminate positive ion.⁴⁷⁻⁴⁹ These distances appeared to depend on the energy of the photons used to create the electron.⁵⁰ Much more effort was spent studying the properties of the hydrated electron. Barbara and his co-workers, in particular, studied the role of excited states and structure in the hydrated electron.

Much of the work has been focused on “what is the hydrated electron” and what gives rise to the spectrum. These experiments have suggested that the spectrum of the hydrated electron cannot be clearly shown to be inhomogeneous, i.e. made up of multiple components that do not interconnect on the experimental lifetime. Theoretical studies had suggested that the ground-state spectrum would be made up of three s-p transitions of different energies that would interconvert on the experimental time scale; however, this was not clearly shown by the experimental work.⁵¹

There is clear evidence that the spectrum of the hydrated electron is best described as a charged particle in a cavity in solution, the simplest anion.⁵²⁻⁵⁴ The spectrum and the reactivity are very consistent with such an interpretation. However, there is also clear evidence that this is not the best description of the electron. There is no obvious way to reconcile the reaction



with a cavity model for the electron. Several authors, primarily Tuttle and co-workers⁵⁵ and Robinson and co-workers⁵⁶ have suggested that the electron as a molecular anion is a better or at least a viable alternative. These problems have led to considerable effort to create a model that consistently explains the spectral data and the reaction data; however, in general their solutions have failed to explain the spectra of the electron.

I think it is fair to say that these techniques have given tremendous information about the structure of the species, in particular the hydrated electron, that is generated by ionizing radiation, but little new information on the chemistry that evolves.

9. The Future

Recently, new techniques such as laser-driven photocathode accelerators⁴⁴⁻⁴⁶ have increased the time resolution available for radiation-chemical studies. They have been of great use in studying fast electron-transfer processes, but are not the one-to-two orders of magnitude improvement that would be needed to explore some of the fundamental questions of electron-precursor reactions and initial distribution of radiolytically produced species. Newer techniques, such as the laser-wakefield accelerator, have the potential to answer these sorts of questions; however, they have not reached their maximum potential.^{57,58}

Radiation chemistry has become a mature field of study. Much of the work today makes use of these techniques to study chemical, physical and biological problems rather than studying the fundamental

processes of radiation chemistry. There are still questions that need to be answered such as the identity of electron precursors, the role of spatial distributions, particularly at elevated temperatures. However, much more important are questions of how reactions occur and what the role of temperature and media are on the reactions; questions that are not exclusively, or possibly even primarily radiation chemical but are really more chemical and physical.

References

1. Kroh J. (1989) *Early Developments in Radiation Chemistry*. Royal Society of Chemistry, Cambridge, England.
2. Lind SC. (1928) *The Chemical Effects of Alpha Particles and Electrons*. American Chemical Society Monograph Series, No. 2, The Chemical Catalog Company, New York.
3. Hart EJ. (1989) Radiation chemistry at the biological laboratory, Cold Spring Harbor, Long Island, New York (1928–1938). In: Kroh J (ed.), *Early Developments in Radiation Chemistry*. Royal Society of Chemistry, Cambridge, England, pp. 217–232.
4. Gordon S. (1989) Radiation Chemistry at the Metallurgical Laboratory, Manhattan Project, University of Chicago (1942–1947) and the Argonne National Laboratory, Argonne, IL (1947–1984). In: Kroh J (ed.), *Early Developments in Radiation Chemistry*. Royal Society of Chemistry, Cambridge, England, pp. 163–204.
5. Allen AO. (1989) The story of the radiation chemistry of water. In: Kroh J (ed.), *Early Developments in Radiation Chemistry*. Royal Society of Chemistry, Cambridge, England, pp. 1–6.
6. Weiss J. (1944) Radiochemistry of Aqueous Solutions. *Nature* **153**: 748.
7. Gordon S, Schmidt KH, Honekamp JR. (1983) An analysis of the hydrogen bubble concerns in the Three-Mile Island unit-2 reactor vessel. *Radiat Phys Chem* **21**: 247–258.
8. Kroh J. (1989) Polish contribution to radiation chemistry. In: Kroh J (ed.), *Early Developments in Radiation Chemistry*. Royal Society of Chemistry, Cambridge, England.
9. Allen AO. (1968) Radiation chemistry today. *J Chem Ed* **45**: 290–295.
10. Kevan L. (1989) Solvated electron structure. In: Kroh J (ed.), *Early Developments in Radiation Chemistry*. Royal Society of Chemistry, Cambridge, England, pp. 257–271.
11. Dainton FS. (1989) Recollection of the maturation of radiation chemistry. In: Kroh J (ed.), *Early Developments in Radiation Chemistry*. Royal Society of Chemistry, Cambridge, England, pp. 53–80.

12. Collinson E, Dainton FS, Smith DR, Tazuke S. (1962) Evidence for the unit negative charge on the "Hydrogen Atom" formed by the action of ionising radiation on aqueous systems. *Proc Chem Soc*, p. 140.
13. Czapski G, Schwarz HA. (1962) The nature of the reducing radical in water radiolysis. *J Phys Chem* **66**: 471–474.
14. Samuel AH, Magee JL. (1953) Theory of radiation chemistry. II. Track effects in radiolysis of water. *J Chem Phys* **21**: 1080–1087.
15. Platzman RL. (1953) Energy transfer from secondary electrons to matter. In: Magee JL, Kamen MD, Platzman RL (eds.), *Basic Mechanism. Radiobiology, II, Physical and Chemical Aspects*, Subcommittee on Radiobiology, Committee on Nuclear Science, National Research Council, Washington, DC. Volume 15, pp. 22–50.
16. Kuppermann A. (1959) Theoretical foundations of radiation chemistry. *J Chem Ed* **36**: 279–285.
17. Flanders DA, Fricke H. (1958) Application of a high-speed electronic computer in diffusion kinetics. *J Chem Phys* **28**: 1126.
18. Kuppermann A. (1967) *Diffusion model of the radiation chemistry of aqueous solutions*. In: Silini G. (ed.), *Radiation Research* North-Holland Publishing Company, Amsterdam, pp. 212–234.
19. Schwarz HA. (1969). Applications of the spur diffusion model to the radiation chemistry of aqueous solutions. *J Phys Chem* **73**: 1928–1937.
20. Keene JP. (1960) Kinetics of radiation-induced chemical reactions. *Nature* **188**: 843–844.
21. McCarthy RL, MacLachlan A. (1960) Transient benzyl radical reactions produced by high-energy radiation. *Trans Faraday Soc* **56**: 1187–1200.
22. Matheson MS, Dorfman LM. (1960) Detection of short-lived transients in radiation chemistry. *J Chem Phys* **32**: 1870–1871.
23. Matheson MS. (1962) Radiation chemistry. In: Eyring H, Christensen CJ, Johnston HS. (eds.), *Advances in Physical Chemistry, Annual Reviews*. Palo Alto CA, Vol. 13, pp. 77–106.
24. Boag JW, Hart EJ. (1963) Absorption spectra of 'hydrated' electron. *Nature* **197**: 45–47.
25. Hart EJ, Anbar M. (1970) *The hydrated electron*. Wiley Interscience, New York, p. 188.
26. Schmidt KH, Buck WL. (1966) Mobility of the hydrated electron. *Science* **1151**: 70.
27. Miller JR. (1973) Fast electron transfer reactions in a rigid matrix. Further evidence for quantum mechanical tunneling. *Chem Phys Lett* **22**: 180–182.
28. Closs GL, Calcaterra LT, Green NJ, Penfield KW, Miller JR. (1986) Distance, stereoelectronic effects, and the Marcus inverted region in intramolecular electron transfer in organic radical anions. *J Phys Chem* **90**: 3673–3683.

29. Buxton GV. (1972) Nanosecond pulse radiolysis of aqueous solutions containing proton and hydroxyl radical scavengers. *Proc R Soc London Ser A* **328**: 9–21.
30. Thomas JK, Bensasson RV. (1967) Direct observation of regions of high ion and radical concentration in the radiolysis of water and ethanol. *J Chem Phys* **46**: 4147–4148.
31. Bronskill MJ, Taylor WB, Wolff RK, Hunt JW. (1970) Design and performance of a pulse radiolysis system capable of picosecond time resolution. *Rev Sci Instrum* **41**: 333–340.
32. Jonah CD. (1975) A wide-time range pulse radiolysis system of picosecond time resolution. *Rev Sci Instrum* **46**: 62–66.
33. Tagawa S, Katsumura Y, Tabata Y. (1979) The ultra-fast process of picosecond time-resolved energy transfer in liquid cyclohexane by picosecond single-pulse radiolysis. *Chem Phys Lett* **64**: 258–260.
34. Sumiyoshi T, Katayama M. (1982) The yield of hydrated electrons at 30 picoseconds. *Chem Lett*, 1887–1890.
35. Jonah CD, Matheson MS, Miller JR, Hart EJ. (1976) Yield and decay of the hydrated electron from 100 ps to 3 ns. *J Phys Chem* **80**: 1267–1270.
36. Bartels DM, Cook AR, Mudaliar M, Jonah CD. (2000) Spur decay of the solvated electron in picosecond radiolysis measured with time-correlated absorption spectroscopy. *J Phys Chem A* **104**: 1686–1691.
37. Jonah CD, Miller JR. (1977) Yield and decay of the OH radical from 200 ps to 3 ns. *J Phys Chem* **81**: 1974–1976.
38. Hamill WH. (1969) A model for the radiolysis of water. *J Phys Chem* **73**: 1341–1347.
39. Lam KY, Hunt JW. (1975) Picosecond pulse radiolysis. VI. Fast electron reactions in concentrated solutions of scavengers in water and alcohols. *Int J Radiat Phys Chem* **7**: 317–338.
40. Jonah CD, Miller JR, Matheson MS. (1977) The reaction of the precursor of the hydrated electron with electron scavengers. *J Phys Chem* **81**: 1618–1622.
41. Czapski G, Peled E. (1973) The scavenging of e_{aq}^- and on the possible breakdown of Smoluchowski's equation at high concentrations of solutes. *J Phys Chem* **77**: 893–897.
42. Beck G. (1983) A picosecond pulse-conductivity technique for the study of excess electron reactions. *Radiat Phys Chem* **21**: 7–11.
43. Sauer Jr, MC, Jonah CD, Naleway CA. (1991) Study of the reactions of geminate ions in irradiated scintillator, hydrocarbon solutions using recombination fluorescence and stochastic simulations. *J Phys Chem* **95**: 730–740.
44. Wishart JF, Cook AR, Miller JR. (2004) The LEAF picosecond pulse radiolysis facility at Brookhaven National Laboratory. *Rev Sci Inst* **75**: 4359–4366.
45. Belloni J, Marignier J-L, de Waele V, Gobert F, Larbre J-P, Demarque A, Mostavavi M, Belloni J. (2006) Time-resolved spectroscopy at the picosecond

- laser-triggered electron accelerator ELYSE Source. *Rad Phys Chem* **75**: 1024–1033.
46. Yang J, Kondoh T, Kozawa T, Yoshida H, Tagawa S. (2006) Pulse radiolysis based on a femtosecond electron beam and a femtosecond laser light with double-pulse injection technique. *Rad Phys Chem* **75**: 1034–1040.
 47. Rentzepis PM, Jones RP, Jortner J. (1973) Dynamics of solvation of an excess electron. *J Chem Phys* **59**: 766–773.
 48. Gauduel Y, Migus A, Martin JL, Antonetti A. (1984) Femtosecond and picosecond time-resolved electron solvation in aqueous and reversed micelles. *Chem Phys Lett* **108**: 319–322.
 49. Reid PJ, Silva C, Walhout PK, Barbara PF. (1994) Femtosecond absorption anisotropy of the aqueous solvated electron. *Chem Phys Lett* **228**: 658–664.
 50. Bartels DM, Crowell RA. (2000) Photoionization yield vs energy in H₂O and D₂O. *J Phys Chem A* **104**: 3349–3355.
 51. Cavanagh MC, Martini IB, Schwartz BJ. (2004) Revisiting the pump-probe polarized transient hole-burning of the hydrated electron: Is its absorption spectrum inhomogeneously broadened? *Chem Phys Letts* **396**: 359–366.
 52. Romero C, Jonah CD. (1989) Molecular dynamics simulation of the optical absorption spectrum of the hydrated electron. *J Chem Phys* **90**: 1877–1887.
 53. Wallqvist A, Thirumalai D, Berne BJ. (1987) Path integral Monte Carlo study of the hydrated electron. *J Chem Phys* **86**: 6404–6418.
 54. Schnitker J, Rossky PJ. (1987) Quantum simulation study of the hydrated electron. *J Chem Phys* **86**: 3471–3485.
 55. Golden S, Tuttle Jr, TR. (1982) A new model of solvated-electron systems. Spectral behavior. *J Chem Soc, Faraday Trans 2* **78**: 1581–1594.
 56. Hameka HF, Robinson GW, Marsden CJ. (1987) Structure of the hydrated electron. *J Phys Chem* **91**: 3150–3157.
 57. Oulianov DA, Crowell RA, Gosztola DJ, Shkrob IA, Korovyanko OJ, Rey-de-Castro RC. (2007) Ultrafast pulse radiolysis using a terawatt laser wakefield accelerator. *J Ap Phys* **101**: 053102–053102-9.
 58. Ogata A, Nakajima K, Kozawa T, Yoshida Y. (1996) Femtosecond single-bunched linac for pulse radiolysis based on laser wakefield acceleration. *IEEE Trans Plasma Science* **24**: 453–459.

Chapter 2

An Overview of Solvated Electrons: Recent Advances

Mehran Mostafavi[†] and Isabelle Lampre**

1. Introduction

Since 1962, when it was first characterized by pulse radiolysis transient absorption measurements in water, the solvated electron has been widely studied in numerous solvents. The solvated electron, denoted by e^-_s , is a thermodynamically stable radical, but like most free radicals, it has a short lifetime due to its high chemical reactivity. The solvated electron is a unique chemical moiety whose properties may be compared in many solvents and are not dependent on the method creating the solvated electron. The solvated electron is an important reactive species: as it is the simplest electron donor, its reactions correspond to electron transfer reactions and its reactivity may be used to probe electron transfer properties of acceptors. During the last 40 years, due to its optical absorption properties, the

* Laboratoire de Chimie Physique/ELYSE, UMR 8000 CNRS/Université Paris-Sud 11, Faculté des Sciences, Bât. 349, 91405, Orsay, France.

[†] E-mail: mehran.mostafavi@lcp.u-psud.fr

reactivity of the solvated electron has been widely investigated, mainly by transient absorption measurements using pulse techniques.

EJ Hart and M Anbar have detailed¹ the characteristics and the chemistry of the solvated electron in water, otherwise known as the hydrated electron and denoted by e_{hyd}^- or e_{aq}^- . A number of reviews on the solvated electron are also available.²⁻⁷ In this article, we will recall briefly the main steps of the discovery and the principal properties of the solvated electron. We will then depict its reactivity and focus on recent results concerning the effect of metal cations pairing with the solvated electron. At last, we will present results on the solvation dynamics of electron. Due to the development of ultrashort laser pulses, great strides have been made towards the understanding of the solvation and short-time reactivity of the electron, mainly in water but also in polar solvents. However, due to the vast and still increasing literature on the solvated electron, we do not pretend for this review to be exhaustive.

2. Discovery and Formation of the Solvated Electron

2.1. *Story of the solvated electron*

As early as the nineteenth century, the solvated electron was observed but not identified. In 1808, Sir Humphry Davy⁸ reported for the first time the intense blue coloring obtained by dissolving alkali metals in ammonia (Fig. 1).⁹

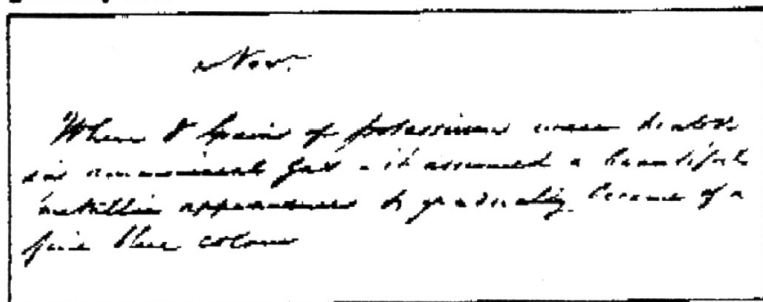
In 1864, W Weyl also observed the blue color of alkali metals solutions in ammonia, methylamine and ethyl amine and found that the resulting solutions had reducing properties, when used in chain synthesis.¹⁰ However, W Weyl did not discover the nature of these blue solutions. Nowadays, it is known that the blue color is due to the solvated electron, as alkali metals dissolved in amine solvents give the metal cation and a solvated electron as in the case of sodium:



In 1908, one century after Davy's discovery, C Kraus showed, by conductivity measurements in liquid ammonia solutions containing

Two entries from the laboratory notebook of Sir Humphry Davy for the period October 1805–October 1812. (Reproduced by courtesy of the Royal Institution, London).

(a) 14 November 1808 'When 8 grains of potassium were heated in ammoniacal gas—it assumed a beautiful metallic appearance and gradually became of a fine blue colour.'



(b) 15 November 1808 'Twelve cubic inches of ammonia were made to act on nine grains of potassium in a green glass retort exposed to the heat of a spirit-lamp, an ebullition of the potassium took place, and its fine silver-colour became blue, which was soon changed to green, it then recovered its original colour but not its splendor'.

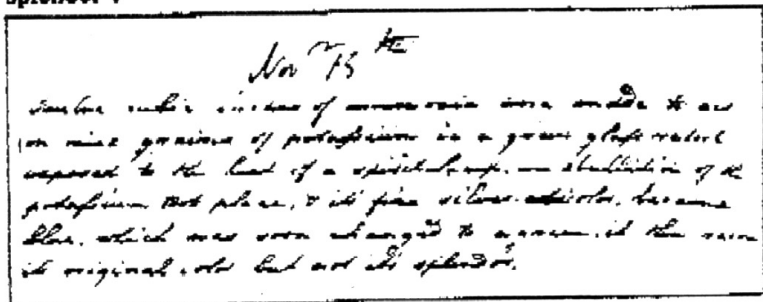


Fig. 1. Manuscripts of Sir Humphry Davy [Royal Institution, London] describing the blue coloring of potassium in contact with ammonia.

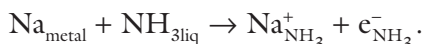
dissolved alkali metals, that the solutions exhibited metallic conductivity and that there was a negatively charged species with a conductivity larger than that of anions, but independent of the counter-ion (Li^+ , Na^+ , K^+). He suggested that this species was an electron surrounded by ammonia molecules behaving like an anion.^{11,12}

With the discovery of radioactivity, radiation chemistry appeared as a new domain in science dealing with changes in matter induced by ionizing radiation. In 1952, to explain the bleaching of aqueous solutions containing methyl blue upon irradiation in the presence of carbon dioxide (CO_2), G Stein proposed the transient formation of a hydrated electron, similar to the solvated electron in ammonia.¹³ From the conductivity measurements performed by R Roberts and AO Allen in 1953, no evidence was obtained for the formation of stabilized electrons during the irradiation of liquid ammonia under those experimental conditions.¹⁴ It was not until 1962 that the existence of the hydrated electron was optically characterized by EJ Hart and JW Boag with pulse radiolysis measurements of aqueous solutions and direct spectroscopic observations of the transient absorption spectrum of the hydrated electron.¹⁵ After these first observations, the solvated electron was soon detected in various solvents through its intense optical absorption band in the visible or near infrared (IR) domain.¹⁶ The solvated electron being an important intermediate in radiation chemistry, its formation and the time required for its solvation were also of some interest as they could have chemical consequences in the effects of ionizing radiation on liquids. The first study of solvation of the electron was done in 1971 by JH Baxendale and P Wardman in liquid alcohols at low temperatures using pulse radiolysis techniques.¹⁷ At low temperature, molecular movements are greatly slowed down and the solvation dynamics of the electron produced by an electron pulsed accelerator may last several nanoseconds. With the development of ultrashort laser pulses in the eighties, studies on the formation and the short-time reactivity of the solvated electron at room temperature started in water.^{18,19} Pump-probe laser experiments performed by A Migus *et al.* showed for the first time that precursors of the hydrated electron exist and absorb in the infra-red spectral domain and that the hydration process is complete within a few hundreds of femto-seconds.¹⁹ Since then, much work has been devoted to the localization and solvation of the electron in liquids.

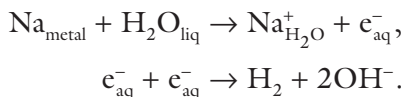
2.2. Production of the solvated electron

Several methods, more or less appropriate according to the medium and the detection systems, may produce solvated electrons and allow their study in different environments.

Historically, the first method was the dissolution of alkali metals in amine solvents; nevertheless, this is useful only in media in which the lifetime of the solvated electron is long enough (at least a few hours in the pure solvent). For example, in liquid ammonia, the solvated electron may be formed from sodium metal:

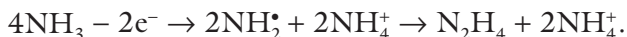


For solvents in which the lifetime of the solvated electron is short, it cannot be observed in this way. For instance in water, the hydrated electron may be formed by dissolving alkali metals. But the metal dissolution timescale is much longer (a hundred of milliseconds) than the lifetime of the electron (a few microseconds) and, as soon as solvated electrons are produced, a very fast reaction occurs between two solvated electrons producing molecular hydrogen, leading to the explosive combustion in air that accounts for the hazardous contact of alkali metal and water.

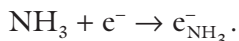


Electrolysis reactions may also be used to produce the solvated electron in similar media; for instance, in liquid ammonia the reactions are:

(1) At the anode:



(2) At the cathode:



Nevertheless, the main method to generate solvated electrons is radiolysis. Under high-energy radiation (γ or X-rays, beams of accelerated electrons or positive ions), electrons may be ejected from the most abundant (solvent) molecules in the medium. These electrons have excess kinetic energy that is lost in collisions with solvent molecules, which may be electronically excited or ionized to produce more electrons in a cascade scheme. When their kinetic energy falls below the ionization/excitation threshold, the electrons are “thermalized” and become “solvated” as solvent molecules get reorganized around them.

Absorption of UV or visible light from a flash lamp or a laser is used to produce the solvated electron, too. Two photolytic processes may occur: (1) the photon energy is sufficient to ionize a solute and produce the electron, for instance, photo-detachment from an anion (Cl^- , $\text{Fe}(\text{CN})_6^{4-}$, $\text{Na}^- \dots$); (2) the laser intensity is high enough to induce ionization of the solvent via multiphoton absorption (e.g. $\text{H}_2\text{O} + nh\nu \rightarrow \text{H}_2\text{O}^+ + e^-$). For water, at least 8 eV is needed to ionize the solvent.

3. Some Physical Properties of the Solvated Electron

The identification and the understanding of the chemical properties of the solvated electron can be made through the knowledge of its physical properties. The properties of the solvated electron depend on several factors such as solvent, temperature and pressure. Compilations of physicochemical properties of solvated electrons in many solvents have already been published.^{20,21}

3.1. *Volume*

In 1921, by dissolving an alkali metal in liquid ammonia, C Kraus and W Lucasse observed a volume expansion of the solution greater than that obtained for the dissolution of ordinary salts.¹² They attributed this volume expansion to the formation of the solvated electron, which is regarded as a particle, since the electron itself has a negligible volume. For example, the dissolution of three moles of sodium in

one liter of liquid ammonia induces an increase in volume of 43 cm^3 of the solution compared to the pure liquid. Assuming that all the metal is dissociated, it may be deduced that in ammonia the electron occupies a spherical volume with a radius of 0.18 nm . In fact, the cavity radius of the solvated electron in ammonia is greater than that value and is about 0.3 nm .

That observed volume expansion accounts for the cavity models developed by theoreticians to describe the solvated electron; that is, the electron occupies a cavity or void in the solvent and is surrounded and solvated by the solvent molecules.

3.2. Charge

Conductivity measurements performed by C Kraus in ammonia solutions of alkali metals gave evidence of a negatively charged species independent of the cation, the solvated electron.¹¹ However, it was to be wondered whether the same species was formed in radiolysis of liquids. In 1962, just before the discovery of the absorption spectrum of the hydrated electron, by studying the rates of reactions of the reducing species produced by γ radiolysis in aqueous solutions containing various solutes, G Czapski and HA Schwarz found that the reaction rate constant of the reducing species is independent of the ionic strength of the solution in the case of neutral solutes, but depends on the ionic strength for ionic solutes. They deduced that the formed reducing species has a unit negative charge and is a hydrated electron.²²

3.3. Mobility

Most methods for determining the electron mobility use pulse radiolysis techniques in which the concentration of electrons is followed during or after the ionizing pulse, either by the time-of-flight method or by measurement of the change in conductivity. However, due to the inherent conductance of polar liquids, direct conductivity measurements of solvated electrons are generally difficult in these media. Therefore, the diffusion coefficient and the mobility of the solvated

electron in various solvents have been indirectly derived through the Smoluchowski and the Nernst–Einstein equations, from the value of the rate constant of a fast reaction thought to be diffusion controlled.²³ In 1969, it was discovered that excess electrons in non-polar solvents are from 100 to 100,000 times more mobile than ions in the same liquids. The electron mobility depends on the solvent and on the structure of the molecules. For example, the mobility in *n*-alkanes decreases with increasing chain length, but it increases with branching; at room temperature, the value is 28.0, 0.15 and 70 cm² V⁻¹ s⁻¹ in ethane, *n*-pentane and 2,2-dimethylpropane, respectively.³ In polar solvents, the electron mobility is generally slightly greater than ionic mobilities, which are about 7×10^{-4} cm² V⁻¹ s⁻¹. In water, the measured mobility of the hydrated electron is 1.9×10^{-3} cm² V⁻¹ s⁻¹. In a viscous solvent as ethane-1,2-diol, the value falls down to 2.8×10^{-4} cm² V⁻¹ s⁻¹. The mobility increases with temperature as the viscosity decreases. The viscosity effect shows that the transport of the solvated electron is mainly due to diffusion and that transport via hopping or tunneling effects is not predominant for that species.

3.4. *Optical absorption*

From the first observations of the blue color of alkali metal solutions in ammonia, the major characteristic of the solvated electron is its optical properties.

The optical absorption spectrum of the solvated electron presents a broad, featureless, but very intense band with a maximum ranging from the visible (500–700 nm for alcohols and aqueous solutions) to the infrared (above 2000 nm for tetrahydrofuran or diethylether, for instance) depending on the medium (Fig. 2).¹⁶ On the whole, the maximum of the absorption band of the solvated electron shifts to higher wavelengths as the dielectric constant of the solvent diminishes. However, the absence of a simple correlation between the maximum and the dielectric constant or the dipolar moment of the solvent suggests that the position of the absorption spectrum is mostly governed by the molecular structure of the liquids.

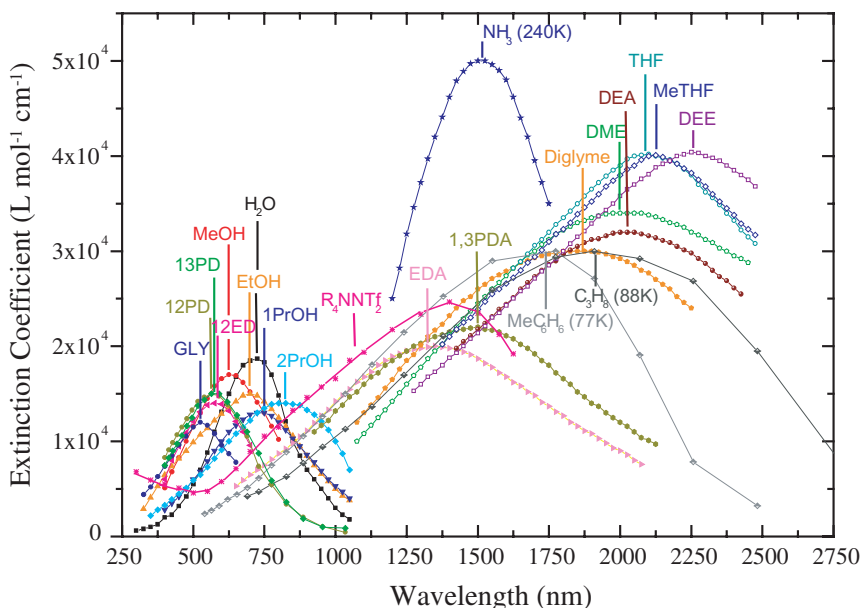


Fig. 2. Optical absorption spectra of the solvated electron in various solvents [from Ref. 16 with additions]. Abbreviations: H₂O: water; MeOH: methanol; EtOH: ethanol; 1PrOH: propan-1-ol; 2PrOH: propan-2-ol; 12ED: ethane-1,2-diol or ethylene glycol; 12PD: propane-1,2-diol; 13PD: propane-1,3-diol; GLY: glycerol or propane-1,2,3-triol; R₄NNTf₂: methyl-tributyl-ammonium bis[trifluoromethyl-sulfonyl]imide; EDA: ethane-1,2-diamine; 1,3PDA: propane-1,3-diamine; NH₃: ammonia; MeC₆H₆: toluene; C₃H₈: propane; DME: dimethylether; DEA: diethanolamine; THF: tetrahydrofuran; MeTHF: methyltetrahydrofuran; DEE: diethylether.

The absorption spectrum of the solvated electron depends not only on the nature of the solvent but also on parameters that modify the structure and properties of the solvent, such as pressure and temperature. The optical absorption band shifts to higher energies (shorter wavelengths) with increasing pressure up to 2000 bar; the shift is larger in primary alcohols than in water and it correlates with the increase in liquid density rather than with the rise in dielectric constant.²⁴ A rise in the temperature induces a red shift of the solvated electron absorption spectrum. Thus, the absorption maximum in water is located around 692 nm at 274 K and 810 nm at 380 K.²⁵

The asymmetric shape of the absorption band of the hydrated electron at temperatures below the critical region is well fitted by Gaussian and Lorentzian functions on the low- and high-energy sides, respectively.²⁵

Lately, quantum-classical molecular-dynamics simulations of an excess electron in water performed for wide ranges of temperature and pressure suggest that the observed red shift of the optical absorption spectrum is a density effect rather than a temperature effect.²⁶ Indeed, by increasing the temperature, the mean volume of the cavity occupied by the solvated electron increases due to weakening of bonds between solvent molecules; the electron is less confined in the cavity, and the potential well becomes less deep.

The temperature dependence of the absorption spectrum of the solvated electron has been recorded not only in water but also in alcohols (Fig. 3).²⁷⁻³⁰ Measurements are performed using nanosecond pulse radiolysis with a specific cell for high temperature and high pressure in a temperature range up to around 600 K depending on the solvent. Indeed, by increasing the temperature, the decay of solvated electrons becomes faster; for example, this decay is much faster in alcohols than in water, so, the data obtained with nanosecond set-up are limited at lower temperatures for alcohols compared with water.

The studies in ethane-1,2-diol (12ED), propane-1,2-diol (12PD) and propane-1,3-diol (13PD) emphasize the influence of the length of the aliphatic chain, and the effect of the distance between the two OH groups on the behavior of the solvated electron.^{27,29,30} At room temperature, the wavelength of the absorption maximum is shorter in 12PD (565 nm) than in 13PD (575 nm), indicating that the two neighboring OH groups in 12PD create deeper electron traps compared to 13PD. However, the traps in 12PD appear less deep than in 12ED since the energy of the absorption maximum of the solvated electron measured at a given temperature is lower in 12PD than in 12ED. That shows an influence of the additional methyl group on the solvent structure, in particular on the created three-dimensional networks of hydrogen-bonded molecules. Moreover, an increase in temperature more greatly affects the electron in 12PD and in 13PD than in 12ED since the temperature coefficient is more negative,

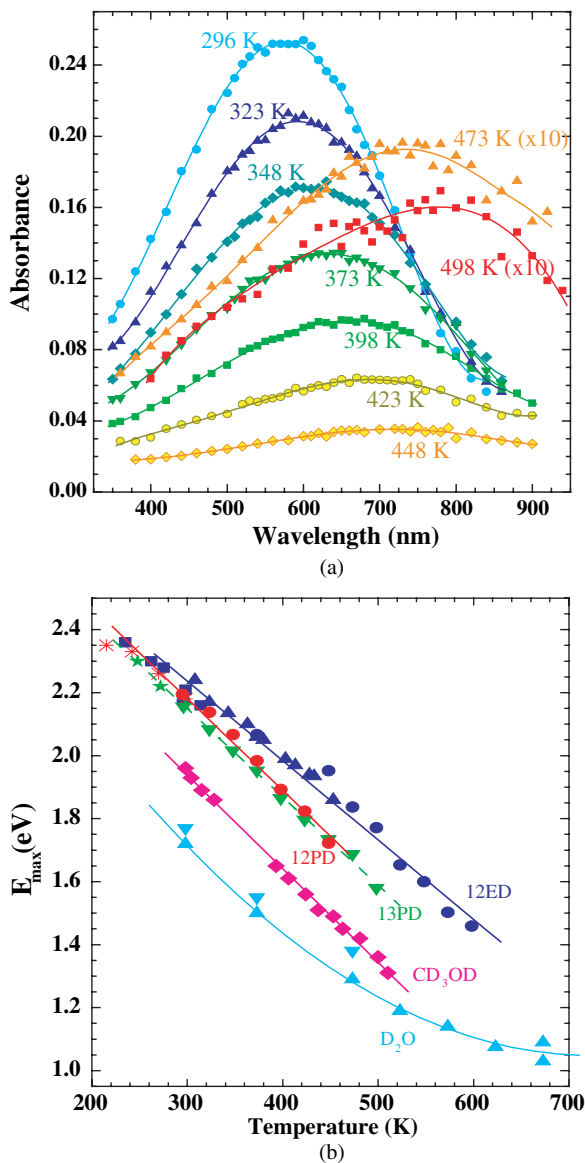


Fig. 3. (a) Absorption spectra of the solvated electron in propane-1,3-diol at different temperatures. (b) Energy of the maximum of the solvated electron absorption band (E_{\max}) as a function of temperature in five different solvents (D_2O : deuterated water; CD_3OD : deuterated methanol; 13PD: propane-1,3-diol; 12PD: propane-1,2-diol; 12ED: ethane-1,2-diol). [Reprinted from Ref. 30, Copyright 2005, with permission from Elsevier.]

i.e. -2.9×10^{-3} , -2.8×10^{-3} and -2.5×10^{-3} eV K⁻¹ for 12PD, 13PD and 12ED, respectively [Fig. 3(b)]. This may be correlated to the decrease in viscosity versus temperature that is larger for 12PD compared to 13PD and 12ED, indicating larger modifications of the solvent structure and molecular interactions. So, the solvated electron may be used as a probe to get information on solvent molecular structure.

Various theoretical and numerical approaches have been dedicated to the study of the solvated electron and its absorption spectrum. The absorption spectrum, i.e. the electronic transition(s), corresponds to the promotion of the solvated electron from its ground state to one or more excited states. Although continuum and semi-continuum models can explain the optical absorption maximum position as a function of temperature or pressure, they cannot account for the optical absorption band shape and width.³¹ Quantum simulations have indicated that, in its ground state, the solvated electron resides in an *s*-like localized state, and that its excited states are three non-degenerate *p*-like states, also bound and localized, followed by a band of delocalized states. Hence, the broad absorption band of the electron corresponds mostly to an *s* → *p* transition with a contribution of the transition from the bound state to the continuum at high energies.^{26,32} The latter contribution accounts for the asymmetry of the spectrum. As the energy levels of the excited states are generally close to the conduction band of the solvent, the position of the absorption maximum gives information on the depth of the potential energy well in which the solvated electron is localized. So, the shorter the wavelength of the absorption maximum is (the higher the transition energy is), the deeper is the well.

3.5. *Structure*

Direct information about the local solvation structure for the solvated electron in condensed media is scarce, although having an accurate picture of, at least, the ground state of the solvated electron, is important to interpret its properties. Steady-state electron paramagnetic resonance (EPR) and electron spin-echo modulation (ESEM) experiments as well

as Resonance Raman (RR) spectra have confirmed the existence of solvated electrons and provided some insight into its structure.

The Electron Spin Resonance (ESR) line for the solvated electron consists of a single, inhomogeneously broadened line at a g value that is very close to that for the free electron. That suggests that the electron is trapped in a potential well surrounded by a number of symmetrically oriented solvent molecules. Geometrical structures of solvated electrons in glassy matrices have been determined from ESEM experiments performed by Kevan's group.³³ From three-pulse electron spin echo experiments in deuterated aqueous matrices³⁴ and ESR line shape analysis on trapped electrons in ¹⁷O enriched 10 M NaOH alkaline ice glass,³⁵ L. Kevan and co-workers deduced that the electrons are solvated by six water molecules, approximately arranged octahedrally, each with one of its OH bonds oriented towards the electron. From 70 GHz ESR spectra of solvated electrons in methanol glass, a geometrical model was proposed based on a solvated electron to OH proton distance determined to be 0.230 ± 0.015 nm and a first solvation shell composed of 4 ± 2 equivalent methanol molecules.³⁶ For ethanol, it was determined that four first-solvation shell molecules were arranged tetrahedrally around the electron with a molecular dipole orientation i.e. with the bisector of the COH bond angle approximately oriented towards the electron.^{37,38} For the solvated electron in ethylene glycol (12ED), L. Kevan and co-workers also suggested a total of four first solvation shell molecules but with only two of these having their OH groups oriented toward the electron.³⁹

Resonance Raman (RR) experiments have also provided valuable data on the structure of the electron. RR spectra of aqueous solvated electrons revealed enhancements of the water inter- and intra-molecular vibrations demonstrating that electronic excitation was significantly coupled to these modes. Frequency downshifts of the resonantly enhanced H₂O bend and stretch were explained by charge donation into solvent frontier orbitals.⁴⁰⁻⁴² RR spectra in primary alcohols (methanol, ethanol, propan-1-ol) revealed strong vibronic coupling of the solvated electron to at least five normal modes of the solvent.⁴³ The spectra showed enhancements of the downshifted OH stretch,

the OH in-plane bend and the OH out-of-plane bend (torsion), which were analogous to the enhanced modes of the aqueous solvated electron. In addition, Franck–Condon coupling of the electronic excitation to methyl/methylene deformations demonstrated that the electronic wave function of the solvated electron extended significantly into the alkyl group of the alcohols.⁴³ Those results corroborate the theory of the absorption spectra of the solvated electron developed by H. Abramczyk and co-workers,^{44–46} in which the coupling between the excess electron and the intramolecular modes of the solvent plays the dominant role and in which the vibrational properties of the electron trap govern the electron dynamics. Those findings indicate that the solvated electron should be regarded as a “quasi-molecule” or a “solvent multimer anion” that consists of both electron and solvating molecules.

To consider the solvated electron as a captured electron in a cavity, as “a particle in a box” may appear too simple. A detailed review about the structure of the solvated electron based on recent experimental and theoretical data is given in the next chapter.

4. Chemical Reactivity of the Solvated Electron

4.1. *Geminate recombinations and spur reactions*

In radiolysis, one of the most important reactions of solvated electrons is recombination with positive ions and radicals that are simultaneously produced in close proximity inside small volumes called spurs. These spurs are formed through further ionization and excitation of the solvent molecules. Thus, in competition with diffusion into the bulk, leading to a homogeneous solution, the solvated electron may react within the spurs. Geminate recombinations and spur reactions have been widely studied in water, both experimentally and theoretically,^{47–50} and also in a few other solvents.^{51–53}

Typically, recombinations occur on a timescale of tens to hundreds of picoseconds. In general, the primary cation undergoes a fast proton transfer reaction with a solvent molecule to produce the stable solvated proton and the free radical. Consequently, the

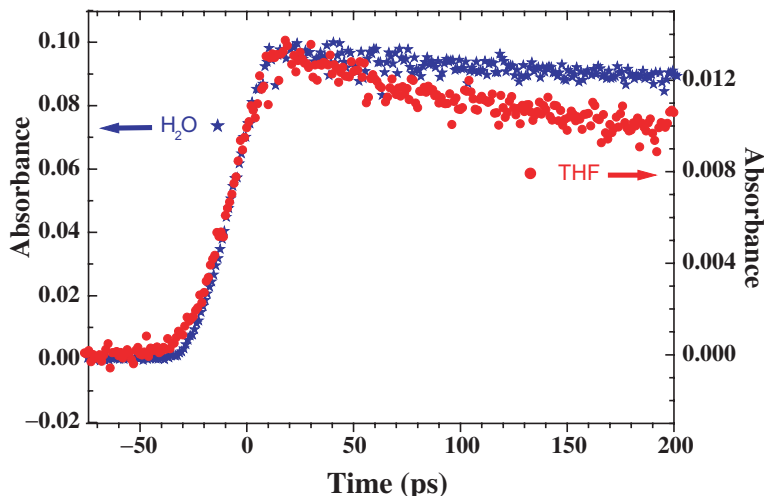
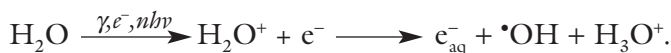


Fig. 4. Decays of the solvated electron in water (H_2O) and in tetrahydrofuran (THF) due to geminate recombination, observed at 790 nm in 5 mm cell with pulse-probe set-up after radiolysis by a picosecond electron pulse. [Reprinted from Ref. 53, Copyright 2006, with permission from Elsevier.]

recombination processes are complex and depend on the solvent (Fig. 4). The central problem in the theory of geminate ion recombination is to describe the relative motion and reaction between the two particles with opposite charges initially separated by a distance r_0 . In water, among the primary products of solvent radiolysis, the main species are the hydrated electron e_{aq}^- , the hydroxyl radical $\bullet\text{OH}$ and the hydronium cation H_3O^+ :



Interestingly, it has been shown that in water the recombination of the solvated electron is greatly dominated by reaction with $\bullet\text{OH}$ radical, because the reaction with H_3O^+ is not diffusion limited despite the Coulombic attraction.⁴⁸ Moreover, the geminate recombination kinetics of the hydrated electron following water multiphoton ionization were measured for photon energies in the range 3.0–5.0 eV; the changes in the kinetics indicate that the

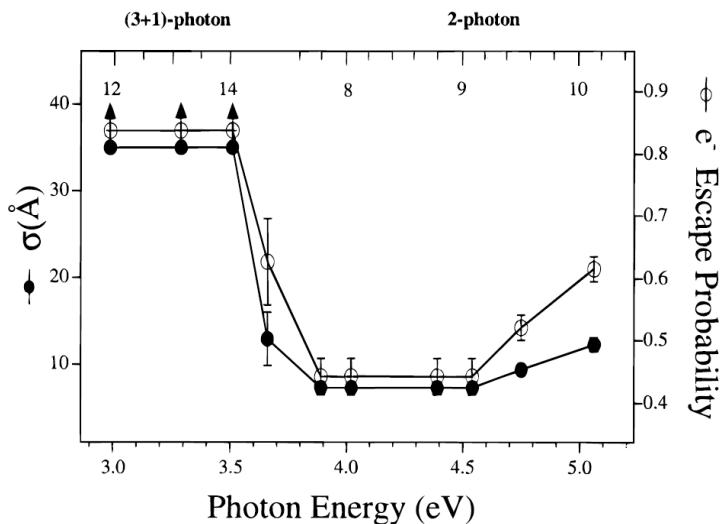


Fig. 5. Fitted electron escape probability and σ (width of the Gaussian distance probability distribution for e^-_{aq}) plotted as a function of the photon energies used to ionize water. The upper x -axis indicates the total excitation energy. Arrows indicate minimum possible values of escape probability or σ . [Reprinted from Ref. 49, Copyright 1996, with permission from American Chemical Society.]

hydrated electron is produced by different mechanisms and that the escape probability and ejection distance depend on the excess energy (Fig. 5).⁴⁹

It is to be noted that, after geminate recombination, when diffusion takes place on the nanosecond and longer time scale, reactions between the radiolytic species still occur and, in the absence of any other solutes, those reactions are responsible of the disappearance of the solvated electron.

4.2. Reaction with a solute

Soon after the discovery of the solvated electron by its absorption spectrum in pulse radiolysis experiments, its reactivity was studied with a wide variety of solutes. Most of the rate constants of reactions between the solvated electron and a solute were measured by decay

kinetics method.^{54,55} Although it is a transient species, the solvated electron is a very strong reducing agent. Indeed, its reduction potential is very low; for the solvated electron in water, the value of $E^\circ(\text{H}_2\text{O}/\text{e}_{\text{aq}}^-)$ is equal to -2.87 V with respect to the standard hydrogen electrode.^{56,57}

Many reactions of the solvated electron with different solutes, such as aliphatic, aromatic or heterocyclic compounds, and also anions and cations, have been studied. The solvated electron has been found to be useful in organic and inorganic chemistry as it may be used to create other reducing agents that are themselves less reactive and thus more selective, such as Zn^+ , Cd^+ , Co^+ , to reduce nitrobenzene, to oxidize organic compounds in the presence of dioxygen.... A wealth of information on the reactions of hydrated electrons has been obtained and a compilation was published in 1988.⁵⁸ The reduction of halogenated hydrocarbons is often used in radiation chemistry to produce well-defined radicals because of the selective cleavage of the carbon-halogen bond by the attack of the solvated electron. This reaction produces the halide ion and a carbon-centered radical, and is of great interest for environmental problems related to the destruction of halogenated organic contaminants in water and soil.^{59,60} Biological systems are also affected by the presence of hydrated electrons, and there is evidence that the hydrated electron plays a role in radiation-induced damage of enzymes and DNA.⁶¹

4.3. Formation of ion pairs

Pulse radiolysis studies of solutions containing alkali or alkaline earth salts have shown that the solvated electron does not reduce these metal ions. The main effect of salts is to produce a blue shift of the solvated electron spectrum.

The first publication on the effect of non-reactive metal cations on the absorption spectrum of the hydrated electron was published in 1965.⁶² A systematic study of the salt concentration effect on the hydrated electron absorption spectrum in very concentrated (up to 15 M) aqueous solutions of LiCl was done by IV Kreitus in 1985,⁶³ then, resumed by P Krebs and co-workers in 1999.⁶⁴ With the development of ultrafast laser pump-probe setup, a few publications noted

a blue shift of the absorption band of the hydrated electron in the presence of high concentration of NaCl and attributed it to a change in the hydration energy of the electron.^{65,66} Recently, molecular dynamics simulations depicted, in the case of sodium cation, the possible formation of a cation–electron pair. The simulated absorption spectrum of the pair showed a blue shift of about 0.3 eV compared to that of the hydrated electron, which is attributed to a destabilization of the p-like state in the close vicinity of the cation.⁶⁷ A general study on the influence of monovalent, divalent and even trivalent non-reactive metal cations on the absorption spectrum of the hydrated electron was recently performed by J Bonin *et al.*^{68,69}

Alkali metal cations and alkaline earth metal cations are not reduced by the hydrated electron as the redox potential of the M^+/M^0 or M^{2+}/M^+ couple is lower than the redox potential of the hydrated electron. Regarding trivalent metal cations, only the lanthanide series presents stable free ions in aqueous solutions. These ions are reduced very slowly by the hydrated electron. Tb^{3+} presents a reaction rate constant with the hydrated electron lower than $10^6 \text{ mol}^{-1} \text{ L s}^{-1}$. Therefore, it is possible to observe the pair formation between Tb^{3+} and hydrated electrons. It was shown that, for the same concentration of metal cation, the shift of the electron absorption spectrum increases with the charge of the metal cation, indicating an electrostatic effect on the energy levels of the solvated electron [Fig. 6(a)]. Moreover, as the salt concentration increases, the spectrum shifts to shorter wavelengths [Fig. 6(b)]. It is also worth noticing that the counter-ion plays a role on the spectral shift of the solvated electron spectrum, since for the same salt concentration (2 mol kg^{-1}), the absorption band maximum is situated at 650 nm for $Mg(ClO_4)_2$ and 685 nm for $MgCl_2$. The blue shift is higher in the case of perchlorate than chloride. As the perchlorate salt is more dissociated in water than the chloride one, the counter-ion effect may be related to the dissociation efficiency of the salts in water. Indeed, if the salt is not fully dissociated, the counter-ion in the proximity of the metal screens the cation charge and diminishes the interaction with the solvated electron.

Several publications have also dealt with the changes that occur in the optical absorption spectra of solvated electrons in liquid amines,

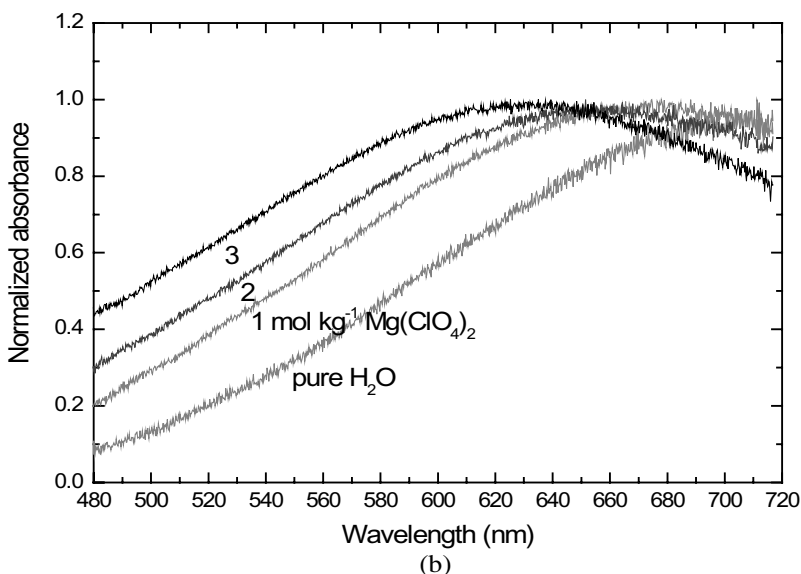
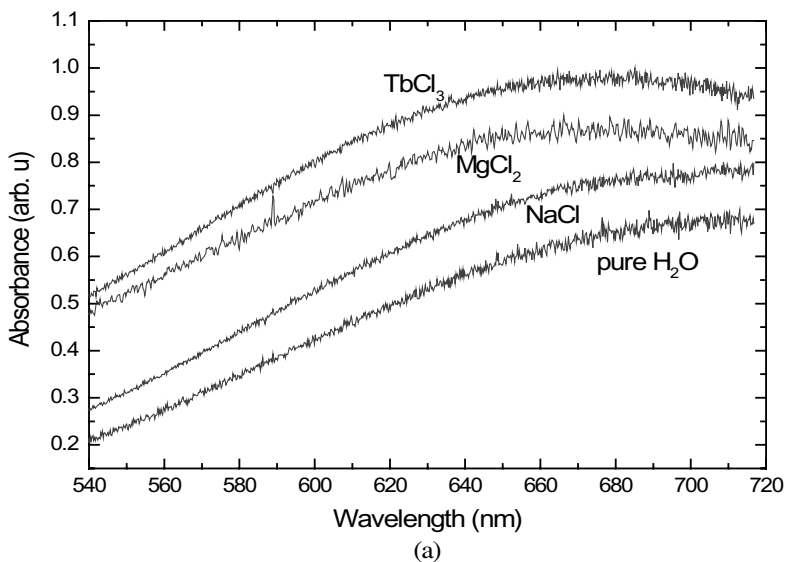


Fig. 6. Optical absorption spectra of solvated electrons at 10°C in pure water and in aqueous solutions containing (a) 2 mol kg⁻¹ of monovalent (Na⁺), divalent (Mg²⁺) and trivalent (Tb³⁺) metal chloride salts, (b) magnesium perchlorate, Mg(ClO₄)₂, with increasing concentration (1, 2 and 3 mol kg⁻¹). [Reprinted from Ref. 68, Copyright 2004, with permission from American Chemical Society.]

ammonia and ethers when alkali metal salts are added.⁷⁰⁻⁷⁵ Pulse radiolysis studies on solutions of alkali metal salts have established the formation of transient optical bands resulting from the reaction of the cation M^+ with the solvated electron. Such bands exhibit a distinct blue-shift from that of the solvated electron in the same solvent and are attributed to the formation of an alkali cation–electron ion pair. The formation of ion pairs between solvated electrons and inert divalent cations was also evoked to explain the decrease in the rate of reduction of Zn^{2+} in ethanol solution in the presence of salts, $Mg(ClO_4)_2$ or $Ca(ClO_4)_2$. Recently, pulse radiolysis experiments done in THF, a low polarity solvent, have demonstrated that the solvated electron reacts with the non-dissociated alkaline earth perchlorate $M(ClO_4)_2$ with $M = Mg^{2+}$, Ca^{2+} or Sr^{2+} and forms a pair (M^{II}, e_s^-) .^{76,77} The structures of the pairs have been determined by *ab initio* calculations.⁷⁶ Surprisingly, while the absorption spectrum of the solvated electron presents a single band located around 2250 nm, the absorption spectra of the pairs are blue-shifted and composed of two bands (Fig. 7).⁷⁷ Those spectra were interpreted as a perturbation of the solvated electron spectrum with the use of an asymptotic model. This model describes the solvated electron as a single electron trapped in a THF solvent cavity and takes into account the effects of electrostatic interaction and polarization due to the solutes that are modeled by their charge distribution. It was shown that the p-like excited states of the solvated electron can be split in the presence of molecules presenting a dipole. So, the model accounts for the results obtained with dissociated alkali and non-dissociated alkaline earth salts in THF since ionic solutes yield absorption spectra with only one absorption band, and dipolar neutral solutes yield absorption spectra with two bands (Fig. 8).⁷⁷

5. Solvation Dynamics of the Electron

Since its spectroscopic discovery, a large number of time-resolved experiments were carried out to clarify the relaxation dynamics of the solvated electron. The first experimental studies of the formation dynamics of electrons in liquids started with electron pulse radiolysis

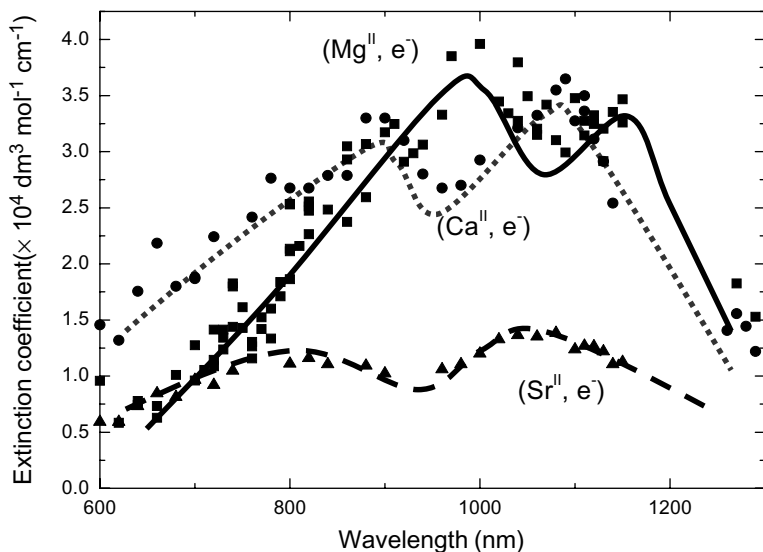


Fig. 7. Optical absorption spectra of the (M^{II}, e^-) pairs formed by the reaction between the solvated electron and $M(\text{ClO}_4)_2$ ($M = \text{Mg}^{2+}, \text{Ca}^{2+}, \text{Sr}^{2+}$) in THF upon pulse radiolysis. [Reprinted from Ref. 77, Copyright 2004, with permission from American Chemical Society.]

experiments in alcohols, first in the nanosecond time range at low temperature,¹⁷ then in the picosecond time range.^{78–80} Picosecond laser studies of electron solvation in alcohols were also done,^{81–83} and with the developments of laser techniques with a better time resolution, the ultrafast dynamics of the solvated electron was studied by femtosecond time-resolved absorption spectroscopy with use of two-^{19,49,51,84–96} or three-pulse sequences.^{66,97–103}

A simplified view of the early processes in electron solvation is given in Fig. 9: (i) the electron is ejected from a molecule upon ionization by radiolysis or photolysis; (ii) in the thermalization step, the ejected electron progressively loses its excess kinetic energy in collisions with solvent molecules; (iii) then, the electron is localized, trapped in a solvent site or cavity and (iv) becomes solvated when the solvent molecules have obtained their equilibrium configuration after relaxation.

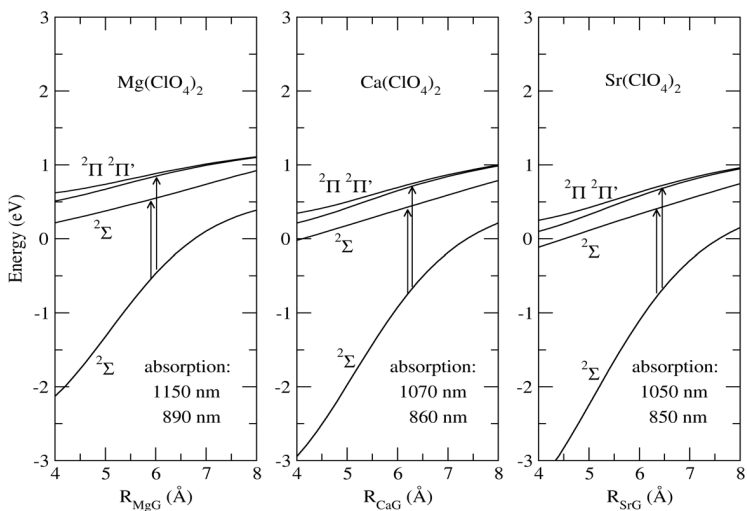
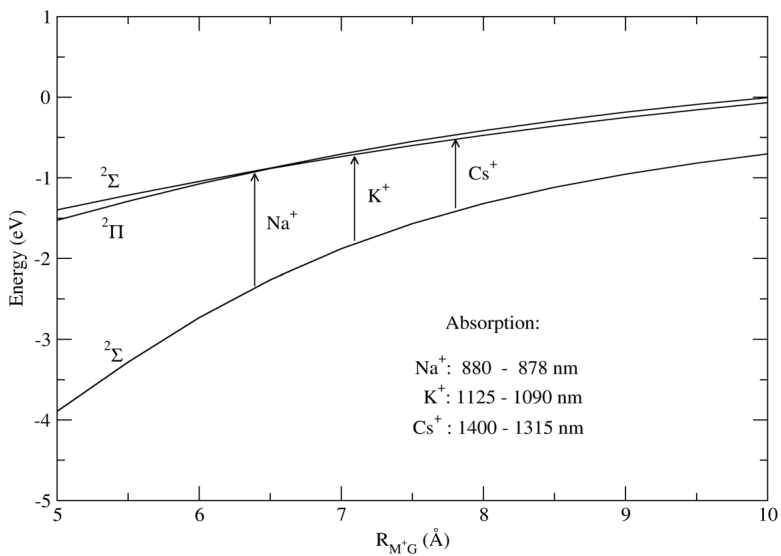


Fig. 8. Potential energy curves of a solvated electron in interaction with (top) an alkali cation, (bottom) an alkaline earth perchlorate in THF. G stands for the center of the Gaussian orbitals of the electron. The values of the two transitions indicated by the arrows at the same distance are given on the figure. [Reprinted from Ref. 77, Copyright 2004, with permission from American Chemical Society.]

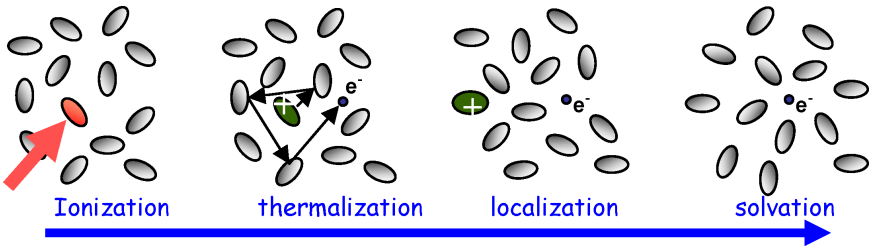


Fig. 9. Cartoon showing the formation of the solvated electron upon solvent ionization.

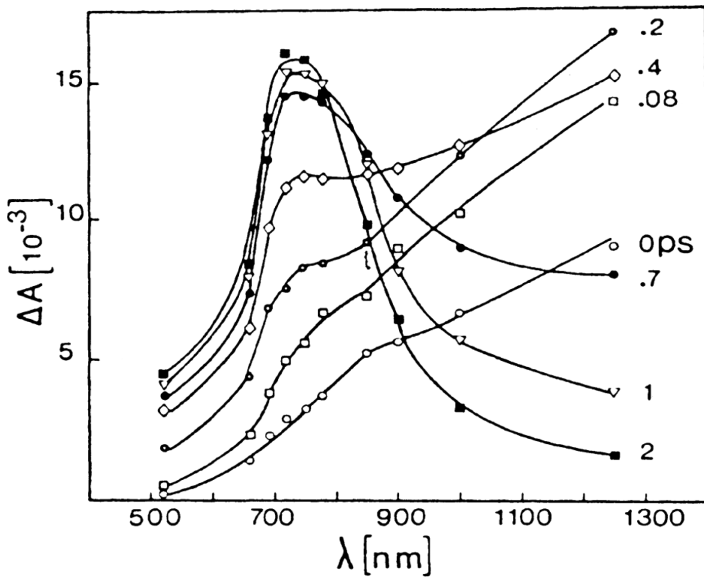


Fig. 10. Absorption spectra of the electron at different delays after photo-ionization of liquid water at 21°C by two photon excitation with pulses of 100 fs duration at 310 nm. [Reprinted from Ref. 19, Copyright 1987, with permission from The American Physical Society.]

The pioneering work of A. Migus *et al.*¹⁹ in water showed that the solvation process is complete in a few hundreds of femtoseconds and hinted at the existence of short-lived precursors of the solvated electron, absorbing in the infrared spectral domain (Fig. 10). Such precursors had already been suggested from picosecond experiments

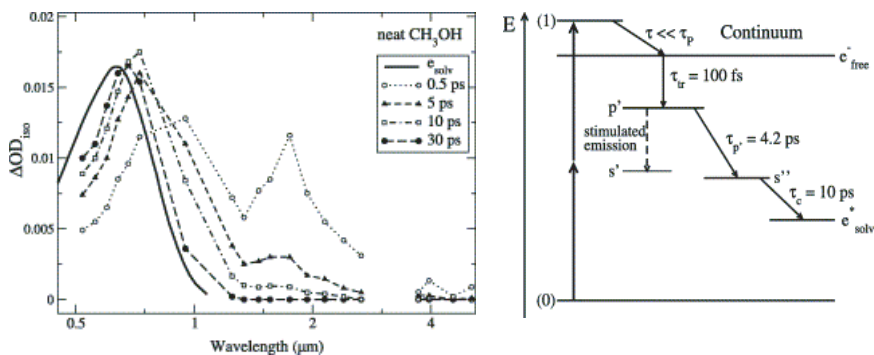


Fig. 11. Time-resolved absorption spectra in neat methanol after two-photon absorption at 273 nm and energy level scheme used to account for the measured dynamics during the generation of solvated electrons. [Reprinted from Ref. 94, Copyright 2003, with permission from Elsevier.]

in alcohols.⁷⁸ So, subsequent studies often depicted the electron solvation process by stepwise mechanisms with several electron precursors (Fig. 11), each precursor having a fixed, individual spectrum (Fig. 12).^{83–85,87,88,94,101–104} The assignments of those precursors were various: excited p state, “hot” ground state, partially solvated electron....

However, other works on electron solvation after photoionization of water favored the so-called “continuous shift” model in which the existence of these IR-absorbing species is not strictly required.^{51,92,93} In the latter model, only one localized electron is considered but its spectrum, as a whole, undergoes a continuous evolution shifting to the blue (short wavelengths) during the solvation, without changing its shape. This continuous shift of the absorption spectrum of the solvated electron has been interpreted by two ways. First, this shift would be governed by solvent molecular reorientation around the electron (solvation), which has been suggested by a correlation between the formation time of the solvated electron and the dielectric relaxation time of the solvent.^{78,83} Second, as proposed by D Madsen *et al.*⁹³ the shift could be due to a “cooling” of the solvated electron i.e. a “cooling” of water around the solvation cavity since the spectrum of the solvated electron is known to shift to higher

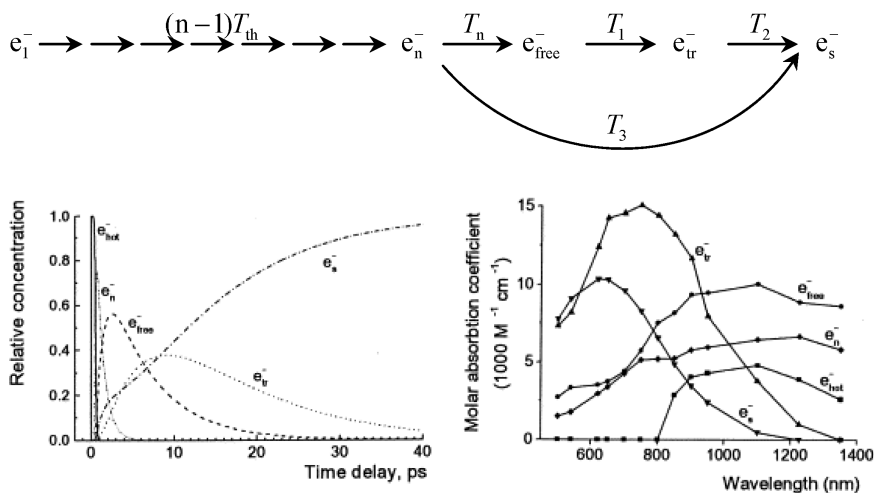


Fig. 12. Temporal evolution of the relative concentrations and spectra of the five electronic species including in the given mechanism for electron solvation in neat methanol at room temperature; the spectrum labeled e_{hot}^- is an average assigned to all thermalizing species from e_1^- to e_{n-1}^- . [Reprinted from Ref. 104, Copyright 1999, with permission from Elsevier.]

wavelengths at higher temperatures. That means that the absorption spectrum of the electron at any time during that thermal process is identical to the spectrum of the solvated electron in the state of equilibrium with the solvent at some higher temperature. In this approach, the electron solvation is viewed as a succession of quasi-equilibrium states that are fully characterized by the time evolution of the local temperature. The necessity to include both the stepwise mechanism and continuous relaxation to successfully interpret experiments has also been suggested.^{86,89-91}

In alcohols, the formation of the solvated electron is slower than in water; the duration increases with the size of the n -alcohol molecule^{78,80,87,91} but also depends on the number of OH groups.⁷⁸ Lately, the formation of the solvated electron in ethane-1,2-diol,⁹⁶ propanediols¹⁰⁵ and propane-1,2,3-triol¹⁰⁶ was studied by photoionization of the solvent at 263 nm with 200 fs pulses. The results showed that, in the three diol solvents, the excess electron presents a wide absorption band in the visible and near-IR domains at short

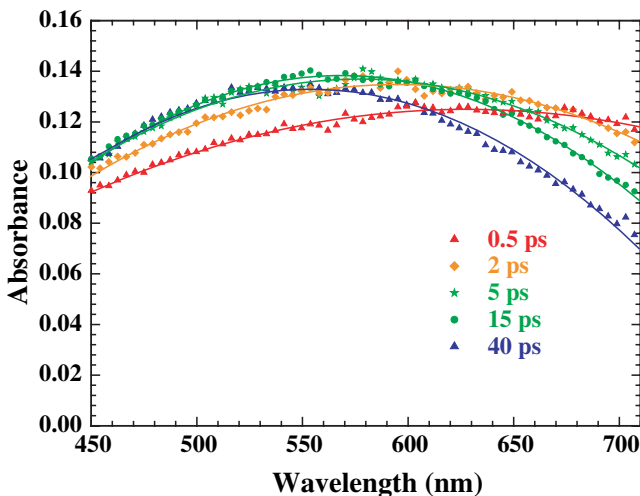


Fig. 13. Transient absorption spectra of excess electrons in liquid ethane-1,2-diol for five time delays after two-photon ionization of the solvent by 200 fs pulses at 263 nm.

delay times after the pump pulse, and that the red part of the absorption band drops in the first few picoseconds while the blue part increases slightly (Fig. 13). In contrast to diols, in the case of propanetriol, even at very short time after the pump pulse, no significant absorption was observed in the near-IR domain and in the first tens of picoseconds, only the red part of the spectrum decreases without change in the blue side. The time evolution of the peak position of the electron absorption band in the four polyols revealed that the solvation dynamics is faster in propanetriol compared to the diols, despite the higher viscosity of propanetriol (Fig. 14). These results indicate that the solvation dynamics depends on the molecular structure of the solvent, in particular on the OH groups. The time resolved spectra were also fitted using different solvation models and at least, two models are able to reproduce correctly the data: a two-step mechanism (Fig. 15) and a continuous relaxation model including a change in the shape of the electron spectrum during the solvation. However, the fact that the time-evolution of the absorption spectrum of the solvated electron can be accurately described by the temperature-dependent absorption

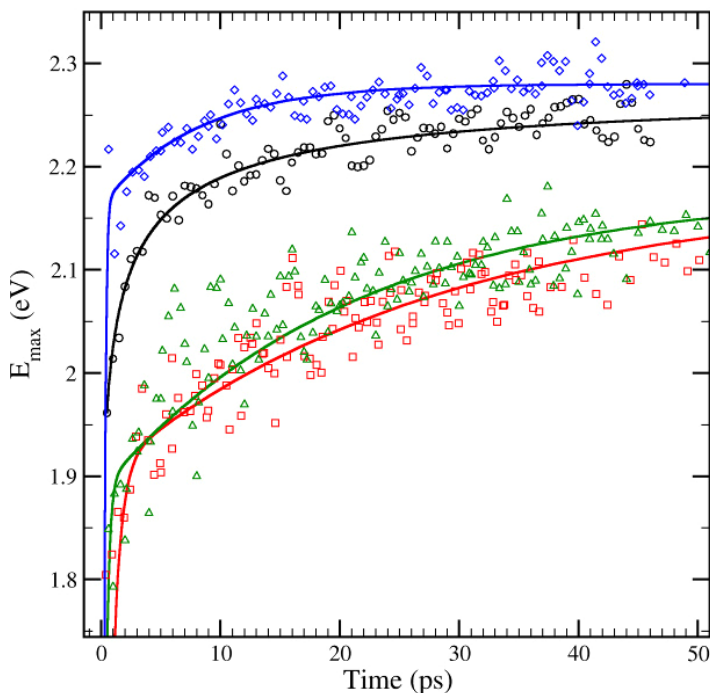


Fig. 14. Time evolution of the peak position E_{\max} of the absorption band of the electron photogenerated in four polyols: \diamond propane-1,2,3-triol, \circ ethane-1,2-diol, \square propane-1,3-diol and Δ propane-1,2-diol [Reprinted from Ref. 106, Copyright 2008, with permission from American Chemical Society].

spectrum of the ground state solvated electron (Fig. 16) suggests that the spectral blue shift would be mostly caused by a continuous relaxation or “cooling” of the electron trapped in a solvent cavity. The constancy of the spectral profile used in the initial “continuous shift” model was rather postulated than observed and is contradicted by the time-evolution of the spectral shape monitored for the electron produced in D_2O by multiphoton ionization,⁹⁰ and lately, for the electron generated by two-photon ionization of liquid H_2O and D_2O .⁹⁵ In both studies, a Gaussian–Lorentzian analysis of the transient spectra was performed and gave evidence for a decrease in the Gaussian width with time. In the work of Lian *et al.*,⁹⁵ two distinct regimes of the spectral evolution of the electron were observed. In the first picosecond after

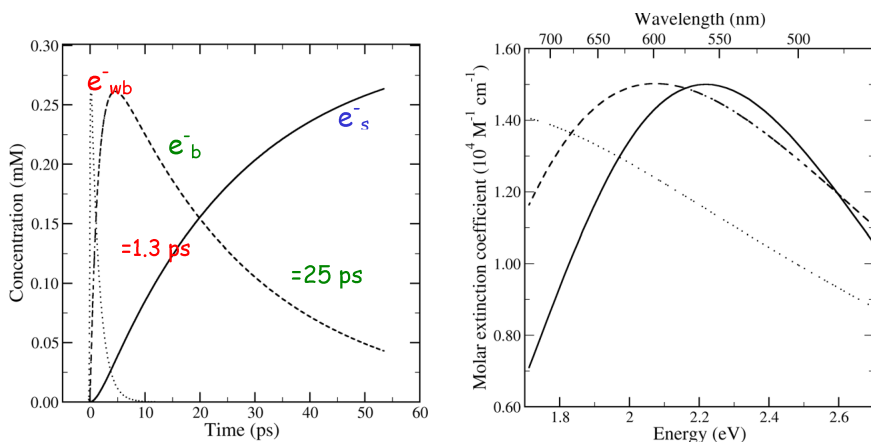


Fig. 15. Time evolution of the concentrations and absorption spectra of the three electron species involved in the two-stepwise mechanism $e_{wb}^- \rightarrow e_b^- \rightarrow e_s^-$ used to fit the experimental data (Fig. 13) obtained in ethane-1,2-diol: (. . .) e_{wb}^- , (- - -) e_b^- , (—) e_s^- [Reprinted from Ref. 96, Copyright 2006, with permission from American Chemical Society].

photoionization, while the main absorption band of the electron progressively shifts to the blue (from 820 to 720 nm), a new peak at 1.15 μm and a shoulder at 1.4 μm are observed, which fully decayed in one picosecond.

Lately, time-resolved Resonance Raman with 250 fs time resolution carried out in water showed that the rise time of Raman bands was faster than the appearance of the equilibrated hydrated electron, indicating that the electron precursor also gives enhanced Raman signals.¹⁰⁷ Since the intensity enhancement arises from the resonance with the $s \rightarrow p$ transition, it was concluded that the precursor is a non-equilibrium s -state electron and that the femtosecond relaxation process of the hydrated electron is the conformational change of the solvation structure around the ground s -state electron. Moreover, using Auger electron decay spectra, D. Nordlund *et al.* recently probed the electron delocalization in liquid water and ice at attosecond time scales.¹⁰⁸ They reported that the hydrogen-bonded network delocalizes the electron in less than 500 as, but that broken or weak hydrogen bonds provide traps where the electron remains

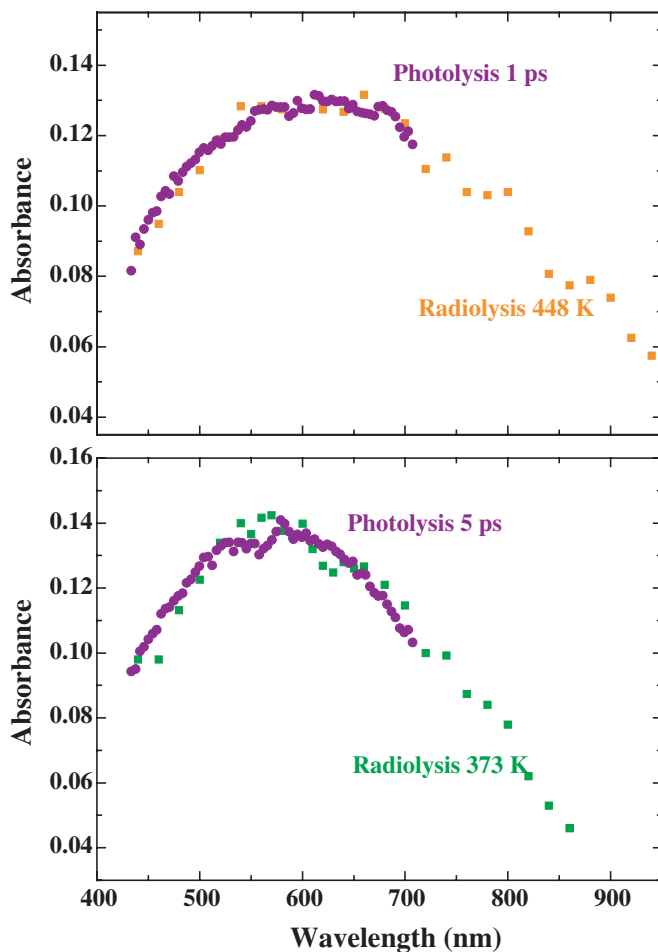


Fig. 16. Comparison between the absorption spectra recorded in liquid ethane-1,2-diol at early time after two-photon ionisation (Fig. 13) at 295 K and the absorption spectra of the solvated electron obtained at high temperature by pulse radiolysis.

localized longer than 20 fs, time scale long enough for libration response of the water molecules and then solvation dynamics to occur leading to the hydrated electron.¹⁰⁸

In the last couple of years, ionic liquids have attracted much interest in their potential applications as solvents for chemical reactions, in

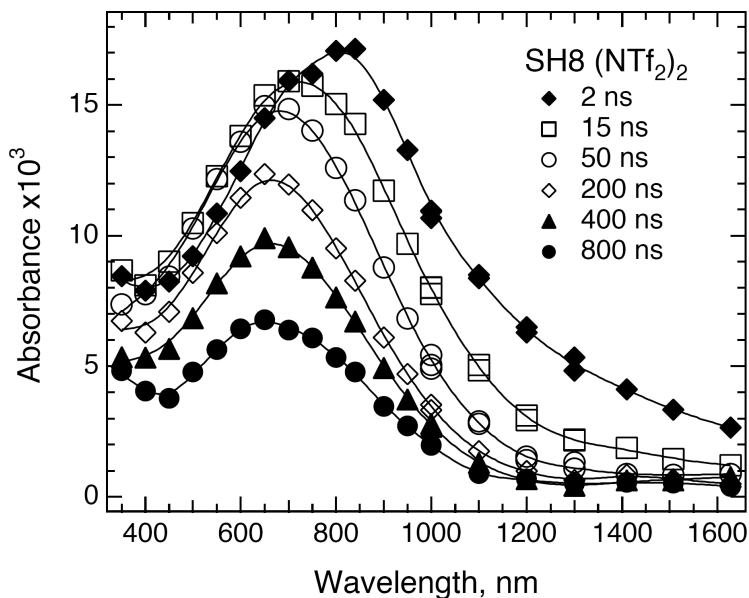


Fig. 17. Pulse radiolysis transient absorption spectra of excess electrons in the alcohol-functionalized ionic liquid $(\text{CH}_3)_2(\text{CH}_2)_3\text{OH})\text{N}^+(\text{CH}_2)_8\text{N}^+((\text{CH}_2)_3\text{OH})-(\text{CH}_3)_2(\text{NTf}_2^-)_2$; NTf_2^- stands for bis(trifluoromethylsulfonylimide); dose: 23 Gy [Reprinted from Ref. 112, Copyright 2005, with permission from Elsevier].

particular within the nuclear fuel cycle.¹⁰⁹ Consequently, pulse radiolysis studies have explored fast reactions occurring in these media.^{110,111} Pulse radiolysis transient absorption spectra on nanosecond timescales revealed that solvation of the excess electron is particularly slow in the case of alcohol-functionalized ionic liquids, the blue shift of the electron spectrum to the customary 650 nm peak lasting 25–40 ns at 21°C (Fig. 17).¹¹² By comparison with the relaxation dynamics observed in viscous 1,2,6-trihydroxyhexane, this slow relaxation process was not correlated with bulk viscosity but was attributed to the hindering effect on the ionic liquid lattice on the hydroxypropyl side chain reorientation. The existence of a slow solvation step in the ionic liquid alcohols presents an opportunity to probe this process with more detail and to get a better insight on the intermediate solvation states of the electron.

6. Conclusion

The solvated electron is a transient chemical species which exists in many solvents. The domain of existence of the solvated electron starts with the solvation time of the precursor and ends with the time required to complete reactions with other molecules or ions present in the medium. Due to the importance of water in physics, chemistry and biochemistry, the solvated electron in water has attracted much interest in order to determine its structure and excited states. The solvated electrons in other solvents are less quantitatively known, and much remains to be done, particularly with the theory. Likewise, although ultrafast dynamics of the excess electron in liquid water and in a few alcohols have been extensively studied over the past two decades, many questions concerning the mechanisms of localization, thermalization, and solvation of the electron still remain. Indeed, most interpretations of those dynamics correspond to phenomenological and macroscopic approaches leading to many kinetic schemes but providing little insight into microscopic and structural aspects of the electron dynamics. Such information can only be obtained by comparisons between experiments and theoretical models. For that, developments of quantum and molecular dynamics simulations are necessary to get a more detailed picture of the electron solvation process and to unravel the structure of the solvated electron in many solvents.

References

1. Hart EJ, Anbar M. (1970) *The Hydrated Electron*. Wiley-Interscience, New-York.
2. Feng D-F, Kevan L. (1980) Theoretical models for solvated electrons. *Chem Rev* **80**: 1–20.
3. Holroyd RA. (1987) In *Radiation Chemistry, Principles and Applications*, (eds.) Farhaziz, Rodgers MAJ, VCH, pp. 201–235.
4. Kestner NR. (1987) In *Radiation Chemistry, Principles and Applications*, (eds.) Farhaziz, Rodgers MAJ, VCH, pp. 237–262.
5. Bernas A, Ferradini C, Jay-Gerin J-P. (1996) Electrons en excès dans les milieux polaires homogènes et hétérogènes. *Can J Chem* **74**: 1–23.
6. Shkrob IA, Sauer MC. (2005) Photostimulated electron detrapping and two-state model for electron transport in nonpolar liquids. *J Chem Phys* **122**: 134503.

7. Shkrob IA. (2006) Ammoniated electron as a solvent stabilized multimer radical anion. *J Phys Chem A* **110**: 3967–3976.
8. Thomas JM, Edwards PP, Kuznetsov VL. (2008) Sir Humphry Davy: Boundless chemist, physicist, poet and man of action. *Chem Phys Chem* **9**: 59–66.
9. Davy SH. (1808) *Laboratory Notebook*, Royal Institution, London.
10. Weyl W. (1864). *Ann Phys Chem (Poggendorff)* **121**: 601.
11. Kraus CA. (1908) Solutions of metals in non-metallic solvents; IV. Material effects accompanying the passage of an electrical current through solutions of metals in liquid ammonia. Migration experiments. *J Am Chem Soc* **30**: 1323–1344.
12. Kraus CA, Lucasse WW. (1921) The conductance of concentrated solutions of sodium and potassium in liquid ammonia. *J Am Chem Soc* **43**: 2529–2539.
13. Stein G. (1952) Some aspects of the radiation chemistry of organic solutes. *Discuss Faraday Soc* **12**: 227–234.
14. Roberts R, Allen AO. (1953) Irradiation of liquid ammonia. *J Am Chem Soc* **75**: 1256–1257.
15. Hart EJ, Boag JW. (1962) Absorption spectrum of the hydrated electron in water and in aqueous solutions. *J Am Chem Soc* **84**: 4090–4095.
16. Dorfman LM, Jou FY. (1973) In *Electrons in Fluids*, (eds.) Jortner J, Kestner NR, Springer, New York, p. 447.
17. Baxendale JH, Wardman P. (1971) Direct observation of solvation of the electron in liquid alcohols by pulse radiolysis. *Nature* **230**: 449–450.
18. Nikogosyan DN, Oraevsky AA, Rupasov VI. (1983) Two-photon ionization and dissociation of liquid water by powerful laser UV radiation. *Chem Phys* **77**: 131–143.
19. Migus A, Gauduel Y, Martin JL, Antonetti A. (1987) Excess electrons in liquid water: First evidence of a prehydrated state with femtosecond lifetime. *Phys Rev Lett* **58**: 1559–1562.
20. Belloni J, Marignier J-L. (1989) Electron-solvent interaction: Attachment solvation competition. *Radiat Phys Chem* **34**: 157–171.
21. Jay-Gerin J-P, Ferradini C. (1994) Compilation of physicochemical properties of solvated electrons in polar liquids. *J Chim Phys* **91**: 173–187.
22. Czapski G, Schwarz HA. (1962) The nature of the reducing radical in water radiolysis. *J Phys Chem* **66**: 471–474.
23. Delaire JA, Delcourt M-O, Belloni J. (1980) Mobilities of solvated electrons in polar solvents from scavenging rate constants. *J Phys Chem* **84**: 1186–1189.
24. Jou FY, Freeman GR. (1977) Shapes of optical spectra of solvated electrons. Effect of pressure. *J Phys Chem* **81**: 909–915.
25. Jou FY, Freeman GR. (1979) Temperature and isotope effects on the shape of the optical absorption spectrum of solvated electron in water. *J Phys Chem* **83**: 2383–2387.
26. Nicolas C, Boutin A, Levy B, Borgis D. (2003) Molecular simulation of a hydrated electron at different thermodynamic state points. *J Chem Phys* **118**: 9689–9696.

27. Okazaki K, Idriss-Ali KM, Freeman GR. (1984) Temperature and molecular structure dependences of optical spectra of electrons in liquid diols. *Can J Chem* **62**: 2223–2230.
28. Herrmann V, Krebs P. (1995) Temperature dependence of optical absorption spectra of solvated electrons in CD₃OD for $T \leq T_c$. *J Phys Chem* **99**: 6794–6800.
29. Mostafavi M, Lin M, He H, Muroya Y, Katsumura Y. (2004) Temperature-dependent absorption spectra of the solvated electron in ethylene glycol at 100 atm studied by pulse radiolysis from 296 to 598 K. *Chem Phys Lett* **384**: 52–55.
30. Lampre I, Lin M, He H, Han Z, Mostafavi M, Katsumura Y. (2005) Temperature dependence of the solvated electron absorption spectra in propanediols. *Chem Phys Lett* **402**: 192–196.
31. Fueki K, Feng D-F, Kevan L. (1974) Application of the semi-continuum model to temperature effects on solvated electron spectra and relaxation rates of dipole orientation around an excess electron in liquid alcohols. *J Phys Chem* **78**: 393–398.
32. Rossky PJ, Schnitker J. (1988) The hydrated electron: Quantum simulation of structure, spectroscopy, and dynamics. *J Phys Chem* **92**: 4277–4285.
33. Kevan L. (1981) Solvated electron structure in glassy matrices. *Acc Chem Res* **14**: 138–145.
34. Narayana PA, Bowman MK, Kevan L. (1975) Electron spin echo envelope modulation of trapped radicals in disordered glassy systems: Application to the molecular structure around excess electrons in γ -irradiated 10M sodium hydroxide alkaline ice glass. *J Chem Phys* **63**: 3365–3371.
35. Schlick S, Narayana PA, Kevan L. (1976) ESR line shape studies of trapped electrons in γ -irradiated ¹⁷O enriched 10M NaOH alkaline ice glass: Model for the geometrical structure of the trapped electron. *J Chem Phys* **64**: 3153–3160.
36. Kevan L. (1979) Forbidden matrix proton spin flip satellites in 70 GHz ESP spectra of solvated electrons; A geometrical model for the solvated electron in methanol glass. *Chem Phys Lett* **66**: 578–580.
37. Narayana M, Kevan L. (1980) Electron spin echo modulation study of the geometry of solvated electrons in ethanol glass: An example of a molecular dipole oriented solvation shell. *J Chem Phys* **72**: 2891–2892.
38. Narayana M, Kevan L. (1981) Geometrical structure of solvated electrons in ethanol glass determined from electron spin echo modulation analyses. *J Am Chem Soc* **103**: 1618–1622.
39. Narayana M, Kevan L, Samskog PO, Lund A, Kispert LD. (1984) Electron spin echo modulation studies of the structure of solvated electrons in ethylene glycol glass. *J Chem Phys* **81**: 2297–2299.
40. Tauber MJ, Mathies RA. (2002) Resonance Raman spectra and vibronic analysis of the aqueous solvated electron. *Chem Phys Lett* **354**: 518–526.

41. Tauber MJ, Mathies RA. (2003) Structure of the aqueous solvated electron from Resonance Raman spectroscopy: Lessons from isotopic mixtures. *J Am Chem Soc* **125**: 1394–1402.
42. Mizuno M, Tahara T. (2003) Picosecond time-resolved resonance raman study of the solvated electron in water. *J Phys Chem A* **107**: 2411–2421.
43. Tauber MJ, Stuart CM, Mathies RA. (2004) Resonance Raman spectra of electrons solvated in liquid alcohols. *J Am Chem Soc* **126**: 3414–3415.
44. Abramczyk H. (1991) Absorption spectrum of the solvated electron. 1. Theory. *J Phys Chem* **95**: 6149–6155.
45. Abramczyk H, Kroh J. (1992) Near-IR absorption spectrum of the solvated electron in alcohols and deuterated water. *Radiat Phys Chem* **39**: 99–104.
46. Abramczyk H, Kroh J. (1994) Spectroscopic properties of the solvated electron in water, alcohols, amines, ethers and alkanes. *Radiat Phys Chem* **43**: 291–297.
47. Green NJB, Pilling MJ, Pimblott SM, Clifford P. (1990) Stochastic modeling of fast kinetics in a radiation track. *J Phys Chem* **94**: 251–258.
48. Goulet T, Jay-Gerin J-P. (1992) On the reactions of hydrated electrons with OH and H_3O^+ . Analysis of photoionization experiments. *J Chem Phys* **96**: 5076–5087.
49. Crowell RA, Bartels DM. (1996) Multiphoton ionization of liquid water with 3.0–5.0 eV photons. *J Phys Chem* **100**: 17940–17949.
50. Thomsen CL, Madsen D, Keiding SR, Thogersen J, Christiansen O. (1999) Two-photon dissociation and ionization of liquid water studied by femtosecond transient absorption spectroscopy. *J Chem Phys* **110**: 3453–3462.
51. Kloefer JA, Vilchiz VH, Lenchenkov VA, Germaine AC, Bradforth SE. (2000) The ejection distribution of solvated electrons generated by the one-photon photodetachment of aqueous I^- and two-photon ionization of the solvent. *J Chem Phys* **113**: 6288–6307.
52. Soroushian B, Lampre I, Pernot P, De Waele V, Pommeret S, Mostafavi M. (2004) Formation and geminate recombination of solvated electron upon two-photon ionisation of ethylene glycol. *Chem Phys Lett* **394**: 313–317.
53. De Waele V, Sorgues S, Pernot P, Marignier J-L, Monard H, Larbre J-P, Mostafavi M. (2006) Geminate recombination measurements of solvated electron in THF using laser-synchronized picosecond electron pulse. *Chem Phys Lett* **423**: 30–34.
54. Hart EJ, Gordon S, Thomas JK. (1964) Rate constants of hydrated electrons reactions with organic compounds. *J Phys Chem* **68**: 1271–1274.
55. Thomas JK, Gordon S, Hart EJ. (1964) The rates of reaction of the hydrated electron in aqueous inorganic solutions. *J Phys Chem* **68**: 1524–1527.
56. Schwartz HA. (1981) Free radicals generated by radiolysis of aqueous solutions. *J Chem Educ* **58**: 101–105.
57. Hickel B. (1992) *Biological and Chemical Actions of Ionizing Radiations*, (ed.) Tilquin B. Academia Erasme, Louvain-la-Neuve.

58. Buxton GV, Greenstock CL. (1988) Critical review of rate constants for reactions of hydrated electrons, hydrogen atoms and hydroxyl radicals in aqueous solution. *J Phys Chem Ref Data* **17**: 513–886.
59. Mackenzie K, Kopinke F-D, Remmler M. (1996) Reductive destruction of halogenated hydrocarbons in liquids and solids with solvated electrons. *Chemosphere* **33**: 1495–1513.
60. Sun G-R, He J-B, Pittman Jr CU. (2000) Destruction of halogenated hydrocarbons with solvated electrons in the presence of water. *Chemosphere* **41**: 907–916.
61. Schüssler H, Navaratnam S, Distel L. (2005) Rate constants for the reactions of DNA with hydrated electrons and with OH radicals. *Radiat Phys Chem* **73**: 163–168.
62. Anbar M, Hart EJ. (1965) The effect of solvent and solutes on the absorption spectrum of solvated electrons. *J Phys Chem* **69**: 1244–1247.
63. Kreitus IV. (1985) Effect of solution microstructure on the hydrated electron absorption spectrum. *J Phys Chem* **89**: 1987–1990.
64. Asaad AN, Chandrasekhar N, Nashed AW, Krebs P. (1999) Is there any effect of solution microstructure on the solvated electron absorption spectrum in LiCl/H₂O solutions? *J Phys Chem A* **103**: 6339–6343.
65. Gelabert H, Gauduel Y. (1996) Short-time electron transfer processes in ionic aqueous solution: Counterion and H/D isotope effects on electron-atom pairs relaxation. *J Phys Chem* **100**: 13993–14004.
66. Assel M, Laenen R, Laubereau A. (1998) Dynamics of excited solvated electrons in aqueous solution monitored with femtosecond-time and polarization resolution. *J Phys Chem A* **102**: 2256–2262.
67. Spezia R, Nicolas C, Archirel P, Boutin A. (2004) Molecular dynamics simulations of the Ag⁺ or Na⁺ cation with an excess electron in bulk water. *J Chem Phys* **120**: 5261–5268.
68. Bonin J, Lampre I, Soroushian B, Mostafavi M. (2004) First observation of electron paired with divalent and trivalent nonreactive metal cations in water. *J Phys Chem A* **108**: 6817–6819.
69. Bonin J, Lampre I, Mostafavi M. (2005) Absorption spectrum of the hydrated electron paired with nonreactive metal cations. *Radiat Phys Chem* **74**: 288–296.
70. Fisher M, Ramme G, Claesson S, Szwarc M. (1971) Collapse of e⁻, Na⁺ pairs into sodium atoms and the reactions of solvated electrons and of e⁻, Na⁺ pairs. *Chem Phys Lett* **9**: 309–312.
71. Salmon GA, Seddon WA. (1974) Production of solvated electrons, ion-pairs and alkali metals anions in tetrahydrofura studied by pulse radiolysis. *Chem Phys Lett* **24**: 366–368.
72. Fletcher JW, Seddon WA. (1975) Alkali metal species in liquid amines, ammonia and ethers. Formation by pulse radiolysis. *J Phys Chem* **79**: 3055–3064.

73. Bockrath B, Gavlas JF, Dorfman LM. (1975) Spectra of the solvated electron coupled with metal cations. Lithium in tetrahydrofuran. *J Phys Chem* **79**: 3064–3064.
74. Seddon WA, Fletcher JW, Catterall R, Sopchyshyn FC. (1977) The effect of coordination on the optical spectra of alkali metal cation-electron pairs in ethers. *Chem Phys Lett* **48**: 584–586.
75. Golden S, Tuttle TR, M, LS. (1987) Effect of added salt on the optical absorption spectra of solvated electrons in liquid ammonia. *J Phys Chem* **91**: 1360–1365.
76. Renou F, Mostafavi M, Archirel P, Bonazzola L, Pernot P. (2003) Solvated electron pairing with earth alkaline metals in THF. 1. Formation and structure of the pair with divalent magnesium. *J Phys Chem A* **107**: 1506–1516.
77. Renou F, Archirel P, Pernot P, Levy B, Mostafavi M. (2004) Pulse radiolysis study of solvated electron pairing with alkaline earth metals in Tetrahydrofuran. 3. Splitting of p-like excited states of solvated electron perturbed by metal cations. *J Phys Chem A* **108**: 987–995.
78. Chase WJ, Hunt JW. (1975) Solvation time of the electron in polar liquids. Water and alcohols. *J Phys Chem* **79**: 2835–2845.
79. Kenney-Wallace GA. (1977) Picosecond molecular relaxations: The role of the fluid in electron solvation. *Can J Chem* **55**: 2009–2016.
80. Kenney-Wallace GA, Jonah CD. (1982) Picosecond spectroscopy and solvation clusters. The dynamics of localizing electrons in polar fluids. *J Phys Chem* **86**: 2572–2586.
81. Wang Y, Crawford MK, McAuliffe MJ, Eienthal KB. (1980) Picosecond laser studies of electron solvation in alcohols. *Chem Phys Lett* **74**: 160–165.
82. Miyasaka H, Masuhara H, Mataga N. (1987) Picosecond 266-nm multiphoton laser photolysis studies on the solvated electron formation process in water and liquid alcohols. *Laser Chem* **7**: 119–128.
83. Hirata Y, Mataga N. (1990) Solvation dynamics of electrons ejected by picosecond dye laser pulse excitation of p-phenylenediamine in several alcoholic solutions. *J Phys Chem* **94**: 8503–8505.
84. Long FH, Lu H, Eienthal KB (1990) Femtosecond studies of the presolvated electron: An excited state of the solvated electron? *Phys Rev Lett* **64**: 1469–1472.
85. Sander M, Brummund U, Luther K, Troe J. (1992) Fast processes in UV-two-photon excitation of pure liquids. *Ber Bunsenges Phys Chem* **96**: 1486–1490.
86. Pépin C, Goulet T, Houde D, Jay-Gerin J-P. (1994) Femtosecond kinetic measurements of excess electrons in methanol: Substantiation for a hybrid solvation mechanism. *J Phys Chem* **98**: 7009–7013.
87. Shi X, Long FH, Lu H, Eienthal KB. (1995) Electron solvation in neat alcohols. *J Phys Chem* **99**: 6917–6922.

88. Reuther A, Laubereau A, Nikogosyan DN. (1996) Primary photochemical processes in water. *J Phys Chem* **100**: 16794–16800.
89. Turi L, Holpar P, Keszei E. (1997) Alternative mechanisms for solvation dynamics of laser-induced electrons in methanol. *J Phys Chem A* **101**: 5469–5476.
90. Pépin C, Goulet T, Houde D, Jay-Gerin J-P. (1997) Observation of a continuous spectral shift in the solvation kinetics of electrons in neat liquid deuterated water. *J Phys Chem A* **101**: 4351–4360.
91. Goulet T, Pépin C, Houde D, Jay-Gerin J-P. (1999) On the relaxation kinetics following the absorption of light by solvated electrons in polar liquids: Roles of the continuous spectral shifts and of the stepwise transition. *Radiat Phys Chem* **54**: 441–448.
92. Hertwig A, Hippler H, Unterreiner A-N. (1999) Transient spectra, formation, and geminate recombination of solvated electrons in pure water UV-photolysis: An alternative view. *Phys Chem Chem Phys* **1**: 5633–5642.
93. Madsen D, Thomsen CL, Thogersen J, Keiding SR. (2000) Temperature dependent relaxation and recombination dynamics of the hydrated electron. *J Chem Phys* **113**: 1126–1134.
94. Scheidt T, Laenen R. (2003) Ionization of methanol: Monitoring the trapping of electrons on the fs time scale. *Chem Phys Lett* **371**: 445–450.
95. Lian R, Crowell RA, Shkrob IA. (2005) Solvation and thermalization of electrons generated by above-the-gap (12.4 eV) two-photon ionization of liquid H₂O and D₂O. *J Phys Chem A* **109**: 1510–1520.
96. Soroushian B, Lampre I, Bonin J, Pernot P, Pommeret S, Mostafavi M. (2006) Solvation dynamics of the electron produced by two-photon ionization of liquids polyols. I. Ethylene glycol. *J Phys Chem A* **110**: 1705–1717.
97. Walhout PK, Alfano JC, Kimura Y, Silva C, Reid PJ, Barbara PF. (1995) Direct pump/probe spectroscopy of the near-IR band of the solvated electron. *Chem Phys Lett* **232**: 135–140.
98. Silva C, Walhout PK, Reid PJ, Barbara PF. (1998) Detailed investigations of the pump-probe spectroscopy of the equilibrated solvated electron in alcohols. *J Phys Chem A* **102**: 5701–5707.
99. Silva C, Walhout PK, Yokoyama K, Barbara PF. (1998) Femtosecond solvation dynamics of the hydrated electron. *Phys Rev Lett* **80**: 1086–1089.
100. Emde MF, Baltuska A, Kummrow A, Pshenichnikov MS, Wiersma DA. (1998) Ultrafast librational dynamics of the hydrated electron. *Phys Rev Lett* **80**: 4645–4648.
101. Assel M, Laenen R, Laubereau A. (1999) Retrapping and solvation dynamics after femtosecond UV excitation of the solvated electron in water. *J Chem Phys* **111**: 6869–6874.
102. Kambhampati P, Son DH, Kee TW, Barbara PF. (2002) Solvation dynamics of the hydrated electron depends on its initial degree of electron delocalization. *J Phys Chem A* **106**: 2374–2378.

103. Thaller A, Laenen R, Laubereau A. (2006) The precursors of the solvated electron in methanol studied by femtosecond pump-repump-probe spectroscopy. *J Chem Phys* **124**: 024515.
104. Holpar P, Megyes T, Keszei E. (1999) Electron solvation in methanol revisited. *Radiat Phys Chem* **55**: 573–577.
105. Bonin J, Lampre I, Pernot P, Mostafavi M. (2007) Solvation dynamics of electron produced by two-photon ionization of liquid polyols. II. Propanediols. *J Phys Chem A* **111**: 4902–4913.
106. Bonin J, Lampre I, Pernot P, Mostafavi M. (2008) Solvation dynamics of electron produced by two-photon ionization of liquid polyols. III. Glycerol. *J Phys Chem A* **112**: 1880–1886.
107. Mizuno M, Yamaguchi S, Tahara T. (2005) Relaxation dynamics of the hydrated electron: Femtosecond time-resolved resonance raman and luminescence study. *J Phys Chem A* **109**: 5257–5265.
108. Nordlund D, Ogasawara H, Bluhm H, Takahashi O, Odelius M, Nagasono M, Pettersson LGM, Nilsson A. (2007) Probing the electron delocalization in liquid water and ice at attosecond time scales. *Phys Rev Lett* **99**: 217406.
109. Allen D, Baston G, Bradley AE, Gornam T, Haile A, Hamblett I, Hatter JE, Healey MJF, Hodgson B, Lewin R, Lovell KV, Newton B, Pitner WR, Rooney DW, Sanders D, Seddon KR, Sims HE, Thied RC. (2002) An investigation of the radiochemical stability of ionic liquids. *Green Chem* **4**: 152–158.
110. Behar D, Neta P, Schultheisz C. (2002) Reaction kinetics in ionic liquids as studied by pulse radiolysis: Redox reactions in the solvents methyltributylammonium bis(trifluoromethylsulfonyl)imide and N-butylpyridium tetrafluoroborate. *J Phys Chem A* **106**: 3139–3147.
111. Wishart JF, Neta P. (2003) Spectrum and reactivity of the solvated electron in the ionic liquid methyltributylammonium bis(trifluoromethylsulfonyl)imide. *J Phys Chem B* **107**: 7261–7267.
112. Wishart JF, Lall-Ramnarine SI, Raju R, Scumpia A, Bellevue S, Ragbir R, Engel R. (2005) Effects of functional group substitution on electron spectra and solvation dynamics in a family of ionic liquids. *Radiat Phys Chem* **72**: 99–104.

Chapter 3

The Structure and Dynamics of Solvated Electrons

*Ilya A. Shkrob**

1. Introduction

In this chapter, the recent progress in the understanding of the nature and dynamics of excess (solvated) electrons in molecular fluids composed of polar molecules with no electron affinity (EA), such as liquid water (hydrated electron, e_{hyd}^-) and aliphatic alcohols, is examined. Our group has recently reviewed the literature on solvated electron in liquefied ammonia¹ and saturated hydrocarbons² and we refer the reader to these publications for an introduction to the excess electron states in such liquids. We narrowed this review to bulk neat liquids and (to a much lesser degree) large water anion clusters in the gas phase that serve as useful reference systems for solvated electrons in the bulk. The excess electrons trapped by supramolecular structures (including single macrocycle molecules^{3,4}), such as clusters of polar molecules^{5,6} and water pools of reverse micelles^{7,8} in nonpolar liquids and complexes of the electrons with cations⁹ in concentrated salt solutions, are examined elsewhere.

*Chemical Sciences and Engineering Division, Argonne National Laboratory, 9700 South Cass Avenue, Argonne, Illinois 60439, USA. E-mail: shkrob@anl.gov

This narrative echoes the themes addressed in our recent review on the properties of uncommon solvent anions.¹⁰ We do not pretend to be comprehensive or inclusive, as the literature on electron solvation is vast and rapidly expanding. This increase is currently driven by ultrafast laser spectroscopy studies of electron injection and relaxation dynamics (see Chap. 2), and by gas phase studies of anion clusters by photoelectron and IR spectroscopy. Despite the great importance of the solvated/hydrated electron for radiation chemistry (as this species is a common reducing agent in radiolysis of liquids and solids), pulse radiolysis studies of solvated electrons are becoming less frequent perhaps due to the insufficient time resolution of the method (picoseconds) as compared to state-of-the-art laser studies (time resolution to 5 fs¹¹). The welcome exceptions are the recent spectroscopic and kinetic studies of hydrated electrons in supercritical^{12,13} and supercooled water.¹⁴ As the theoretical models¹² for high-temperature hydrated electrons and the reaction mechanisms for these species are still under debate, we will exclude such extreme conditions from this review.

Over the last 15 years, there was rapid progress in understanding the properties of solvated/hydrated electron. The advances were made simultaneously in many areas. First, it became possible to study the energetics and IR spectra of relatively large ammonia and water (and now methanol¹⁵) anion clusters in the gas phase. Very recently, pump-probe studies of such clusters have begun.^{16,17} Second, resonance Raman spectra of solvated electrons in water and alcohols were obtained; these spectra provide direct insight into their structure.^{18–22} Only magnetic resonance [electron paramagnetic resonance (EPR) and electron spin echo envelope modulation (ESEEM)] studies carried out in the 1970s and the 1980s have provided comparably detailed structural insight into electron localization.²³ Third, there were multiple studies of ultrafast electron localization in water, alcohols, ethers, and ionic liquids following either photo-^{24–28} or radio-lytic²⁹ ionization of the solvent or electron detachment from a solvated anion (e.g. Ref. 30). Numerous pump-probe studies of ϵ_{hyd}^- ^{11,31–35} and solvated electron in alcohols³⁶ and ethers, such as tetrahydrofuran (THF),³⁷ have been carried out. These studies addressed the initial stages of electron localization that are still not

fully understood. Fourth, theoretical (dynamic) models of electron solvation rapidly grew in sophistication and realism. In addition to one-electron models, both adiabatic and nonadiabatic approaches, such as path integral,^{38–40} mixed quantum-classical (MQC) molecular dynamics (MD),^{41–43} mobile basis sets,^{44–46} *ab initio* and density functional (DFT) approaches have been developed, chiefly for small- and medium-size water anion clusters.^{47–49} Recently, these many-electron approaches began to be applied to solvated electrons in bulk liquids, using Car–Parrinello (CP)⁵⁰ or Born–Oppenheimer MD and hybrid MQC/MD:DFT calculations.⁵¹ Meanwhile, the one-electron MQC MD methods are advancing towards more accurate representation of nonadiabatic transitions, decoherence effects⁵² and quantum effects involving solvent degrees of freedom.⁵³ Fifth, these methods are presently applied to solvents of medium and low polarity, such as THF⁵⁴ and the alkanes,^{2,4} where the electron dynamics and energetics are qualitatively different from those in water, and to dielectrons in water.⁵⁵

While the dynamics studies of electron solvation are very important for understanding its chemistry, interpreting these dynamics is conditional on having the accurate picture of the ground state of the solvated electron. The point that is made in this review is that the current paradigm of the solvated electron as “a particle in a box” that informed the studies of the solvated electron for over 60 years^{56–60} needs to be reassessed, despite its many successes. In place of this paradigm we suggest another conceptual picture, which is nearly as old as the “particle in a box” view of the electron (see Ref. 1), suggesting that the solvated electron is a solvent-stabilized multimer anion in which the excess electron density occupies voids and cavities between the molecules in addition to frontier (antibonding) p-orbitals in the heteroatoms in the solvating groups. We argue that such a view does not contradict the experimental observations for the ground state electron and, in fact, accounts for several observations that have not been rationalized yet using one-electron models, including the dynamic behavior of the excess electron. The emerging picture of the solvated electron as such an anion is complementary to the familiar one-electron models, retaining and rationalizing the desirable features

of the “particle in a box” paradigm and adding new features that are lacking in the one-electron models. In this respect, the multimer anion picture is minimalist and conservative: it is quite different from more radical suggestions⁶¹ that postulate a different atomic structure for the “solvated electron.”

2. The Cavity Electron

In the standard picture of electron solvation in polar liquids, the *s*-like excess electron occupies a (on average, nearly isotropic) solvent cavity that is stabilized through (i) Pauli exclusion of the solvent molecules (repulsive interaction) by the electron filling the cavity and (ii) point-dipole attractive interactions with the polar groups (such as HO groups in water) of 4–8 solvent molecules that collectively localize and trap the electron inside the cavity. Only the species in which some electron density is located inside this cavity (or the interstitial voids between the solvent molecules) can be rightfully called the “solvated electron.” All such species exhibit a characteristic broad, asymmetric absorption band in the VIS (visible) or NIR (near infrared) region, most of which is from *s* → *p* excitation of the *s*-like ground state electron to three nodal *p*-like (bound) excited states (for electrons in deep traps in polar solvents) or free *p*-waves in the conduction band (CB), in less polar and nonpolar solvents. Since the cavity is slightly anisotropic, these *p*-like states are nondegenerate, and the VIS-NIR band is a superposition of three homogeneously broadened *p*-subbands. The more anisotropic the cavity is, the greater is the energy splitting between the centroids of these three subbands. To the blue of this composite *s*–*p* band, there is usually a Lorentzian “tail” extending towards the UV, due to the transitions from the ground state directly into the CB of the liquid. Some other excitations (*s*–*d*) might also contribute to this “tail” absorbance.^{44–46,62} So characteristic is this “a bell and a tail” spectrum that most of the “solvated electrons” in liquids have been identified by this feature alone. Another distinguishing property of the solvated electron is the pronounced temperature dependence of this spectrum,^{13,14} with systematic red shift of the absorption peak and broadening of the absorption line with the

increasing temperature (see Chap. 2). Solvated electron is, in fact, one of the best molecular “thermometers” in chemistry. These trends are commonly rationalized as an increase in the volume occupied by the electron as the cavity expands due to weakening of bonds between the solvent molecules, although there are experimental observations (such as the lack of spectral shift for $\bar{\epsilon}_{\text{hyd}}$ in supercritical water as the density changes from 0.1 to 0.6 g/cm³,¹³ and much greater sensitivity of the absorption maximum to the changes of density that are induced by pressure rather than temperature decrease) that hint at the complex nature of the change observed that is not captured by the existing models. In particular, the recent suggestion that the energetics of solvation is solely a function of water density¹² does not appear to be supported experimentally.^{13,14}

Negative EA is not a sufficient condition for the formation of the cavity electron¹⁰: the dimers and multimers of the solvent molecules should also have negative EA, lacking a way of accommodating the electron through the formation of bonded or stacked multimer anions. The depth of the potential well in which the electron resides broadly correlates with the solvent polarity. For such solvents as liquid, water and ammonia, the trap is more than 1 eV below the CB of the liquid, and thermal excitation of the electron into the CB is impossible. Solvated electrons in such liquids move adiabatically, following fast molecular motions in the liquid. In low-temperature solids, such electrons undergo trap-to-trap tunneling in competition with deepening of the traps due to the relaxation of the cavity, which may take as long as micro- and milli-seconds at 20–100 K. In nonpolar liquids, some of which (e.g. alkanes) also yield solvated electrons; the traps are just 0.1–0.2 eV below the CB, and thermal excitation of the electrons localized in such traps is sufficient to promote the electron into the CB. Such electrons perpetually oscillate between the bottom of the CB and the solvent traps. Only recently has it been shown how fast these electron equilibria are in the alkanes²: the typical residence time of the electron in a trapped state is under 10 ps (at 300 K) and the typical trapping time of the quasifree CB electron is just 15–30 fs, which is shorter than the relaxation of its momentum. Note that the p-like electrons in polar solvents are also very close to the mobility

edge of the liquid^{41–43} and might be spontaneously emitted into the CB as a result of solvent fluctuations.⁶³ There is also a class of solvated/trapped electrons that coexist either in two distinct forms (such as electrons in low-temperature hexagonal ice^{64,65} and cation-bound electrons in concentrated ionic solutions and glasses)^{9,64,65} or in a dynamic equilibrium with a molecular anion (a monomer or a bound multimer), which occurs in some liquids (benzene,⁶⁶ acetonitrile⁶⁷) or in dilute solutions of polar molecules in nonpolar liquids (e.g. for clustered hydroxylic molecules in dilute alkane solutions⁵). Many modes of electron localization are known and perhaps even more are still unknown.

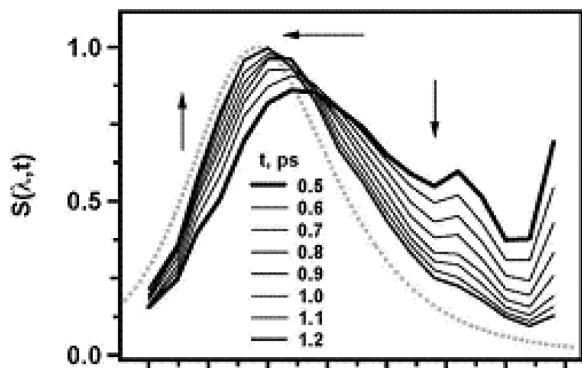
For molecules lacking permanent polar groups (e.g. alkanes) or having the dipole oriented in such a way that the positively charged end of the dipole is looking outwards (e.g. ethers, amides, esters, and nitriles), the electron is solvated by the alkyl groups, and the trapping potential originates chiefly through the polarization of C–C and C–H bonds.² The exact origin of this potential is poorly understood; it appears that polarizability of these bonds, in the absence of percolation of the electron density onto the aliphatic chains, is insufficient to account for the energetics observed. The likely mechanism for electron trapping in such liquids, in the framework of multi-electron approach, is examined in Refs. 2 and 4.

3. Excited States, Precursors, and Dynamics

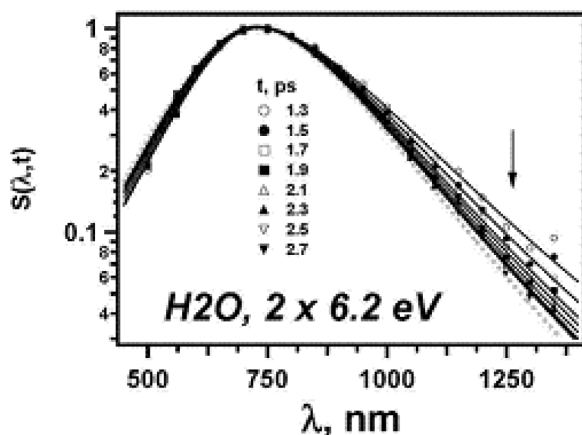
3.1. “Hot” *s*- and *p*-like states

For polar molecules with X–H groups (X=N, O), the origin of the trapping potential is well understood: it is electrostatic interaction of the *s*-like electron residing inside the cavity and dangling (or “non-hydrogen-bonding”) X–H groups at the wall of the cavity; the wavefunction of the electron “washes” the protons in such groups and instantly responds to their rapid motion. The migration of the electron occurs either as the result of such molecular motions (in liquids),⁶⁸ tunneling to neighboring voids appearing as the result of solvent fluctuations, or repeated thermal emission to CB and

relocalization. This relocalization can be induced directly by 1-⁶³ or 2-photon^{31,32} excitation of the electron into the CB, or even by photo excitation of the s-like electron into the p-like excited state, as the manifold of these p-states is close to the CB.⁶³ As for the existence of other than (1)s- and (1)p-like cavity states (such as 2s- and d-states), while these states are periodically invoked in the literature (e.g. for vitreous ethers), there seem to be no recent corroborations of their existence, except for the electron bubbles in liquid ⁴He. Importantly, these are all virtual states: once the electron is excited into one of these states, many new states appear as the solvent accommodates to the excitation. These occupied states are classed into p- and s-state manifolds, although such a classification is somewhat misleading, as the wavefunction of the lowest (“s-like”) state in an anisotropic, fluctuating cavity has substantial p- and d-characters.^{44–46} The best understood of these excited states of the cavity electron are the so-called “hot” s-like states that relax adiabatically to the fully thermalized, fully solvated s-like state by damping their excess energy into the solvent. These are, basically, s-like states that are structurally and electronically very similar to the ground state of the electron but reside in a slightly modified cavity. Such states are produced in all situations when the electron is excited or ejected into the liquid preceding the formation of a fully thermalized s-like electron on the picosecond time scale. The spectral manifestation of the relaxation for these “hot” states is the so-called “continuous blue shift” of the s–p band that occurs on the time scale of 300–1000 fs in water^{24–29,69,70} and even slower in alcohols and diols (a few picoseconds^{25,71,72} or even a few tens of picoseconds,²⁹ in cold liquids). Only this type of dynamics was observed in photoionization of liquid water and electron photodetachment in the course of charge transfer to solvent (CTTS).³⁰ We have recently shown²⁸ (Fig. 1) that this process is bimodal: there is a rapid blue shift of the entire spectrum on the sub-picosecond time scale [that is not conserving the shape of the spectrum, contrary to the frequently made assumption^{24–27,69–72}; Fig. 1(a)] and a slower narrowing of the spectral envelope to the red of the maximum that looks similar to vibrational relaxation in photoexcited molecules. During this delayed narrowing, the position of



(a)



(b)

Fig. 1. Spectral evolution of the “hot” s-like state of hydrated electron generated in two 6.2 eV photon ionization of light water. The arrows indicate the trends observed in the direction of longer delay times of the probe pulses. Panel (a) demonstrates the evolution between 500 fs and 1.2 ps, showing considerable blue shift and fast decay of the IR features. Panel (b) shows the slow relaxation regime that is observed after 1.2 ps (note the logarithmic scale). In this regime, the band maximum is “locked” within 20 meV and the spectral evolution is due to relatively slow, isotope sensitive narrowing of the spectral envelope on the red side of the spectrum. This narrowing is likely to be caused by vibrational relaxation of the “hot” s-like state. See Ref. 28 for more detail.

the absorption maximum is “locked” within 20 meV from the equilibrium position [Fig. 1(b)]. The time constants for this narrowing are 560 fs for H₂O and 640 fs for D₂O, whereas the time constant for the initial blue shift is < 300 fs. Inability to distinguish between these two regimes, due to sparse spectral sampling and reliance on prescribed spectral evolution, might explain considerable scatter of time constants for “continuous blue shift” in the literature. Typically, such a shift (with the conserved envelope of the spectrum plotted as a function of excitation energy) is postulated rather than observed directly, as there are interfering absorbances and side processes occurring on the same time scale. Interestingly, the “hot” s-like electrons generated by 2×6.2 eV photoionization exhibit a short lived (< 100 fs) absorbance in the region where H₂O has the third overtone of the O–H stretch mode [the 1.2 μm band in Fig. 1(a) that is not seen for heavy water] indicative of a strong vibronic coupling between the short-lived, energetic “hot” s-like state and the solvent.²⁸

Apart from these “hot” s-like states, other light-absorbing states were identified using decomposition analysis of transient absorption spectra. There are as many such analyses as there are authors, and relatively few common, agreed upon features have emerged from such analyses. The most likely culprit is the core assumption that a small number of states with well-defined, time independent spectra (or a species with prescribed “continuous blue shift” spectral evolution) suffices to account for the observed dynamics. The validity of such an assumption is unobvious for a species like solvated electron that is a statistical average over many solvent configurations. Only few general remarks are thus possible. There appears to be no evidence that p-like states are generated as detectable intermediates in the course of ionization or electron photodetachment, though such states may be generated by s–p and s–CB excitation of solvated electrons and large water anion clusters. The most likely reason for that is the extremely short lifetime of these p-like states (see below). In bulk liquids, these p-like states are predicted to exhibit diffuse p–CB absorption bands centered at < 1 eV.⁷³ The initial relaxation of these p-like states in bulk water is expected to occur very rapidly (10–30 fs); the inertial component of this relaxation is very pronounced and it is expected to

exhibit a large isotope effect. For medium size water anion clusters in the gas phase, such p-like states are readily identified using angle-resolved photoelectron spectroscopy, as the photoelectrons generated from these states carry orbital momentum.^{16,17}

Two general schemes were put forward for the subsequent dynamics of the “relaxed” p-like states: (i) relatively slow adiabatic internal conversion (IC) and (ii) very fast nonadiabatic IC. In both of these scenarios the p-like states convert to a “hot” s-like state that subsequently undergoes adiabatic relaxation. In the adiabatic IC scenario, the lifetime of the relaxed p-like states is 100–300 fs^{31–34}; this time increases to ca. 2 ps for methanol.³⁶ In the rapid, nonadiabatic IC scenario, this lifetime is on the order of 50 fs, and the 300–400 fs component is interpreted as the initial stage in the thermalization of the “hot” s-like state.¹¹ For $n = 25$ –50 water anion clusters, $(\text{H}_2\text{O})_n^-$, the time constant for IC scales as n^{-1} decreasing with the increased cluster size n from 180 to 130 fs for H_2O and 400 to 225 fs for D_2O .¹⁶ Extrapolating these estimates to water bulk ($n \rightarrow \infty$) suggests that the time constant for IC is < 50 fs. While the validity of such extrapolation may be questioned,^{16,17,74} as it has not been firmly established that such clusters trap the electrons internally, the recent measurements of emission lifetime of the p-like states in liquid water give an estimate of 30 fs.¹⁸ Photon echo and transient grating measurements¹¹ using 5 fs pulses suggested 50–70 fs time scale for the IC. These ultrafast measurements indicate the involvement of 850 cm^{-1} libration mode in the solvent dynamics of photogenerated p-like states; the same modes show the largest resonance Raman enhancements. A large isotope effect of 1.4 on the lifetime of the fast (35 fs) component in the kinetics observed after s–p excitation^{31,32} also implicates the involvement of these libration modes in the relaxation or IC of the p-like electron. The short lifetime of these p-like states readily accounts for the absence of the expected p–CB absorbances in various photoionization and photodetachment experiments and the fact that the same photoinduced absorbances are generated in the s–p and the s–CB photoexcitations: regardless of the excitation energy, transient absorption spectra are always dominated by the “hot” s-like states.³⁴

Nonadiabatic MQC MD calculations of Schwartz and Rossky⁷³ for the e_{hyd}^- are consistent only with the slow adiabatic IC scenario, and only approximately, predicting much longer adiabatic relaxation of the p-like states (300 fs) and IC of relaxed p-like states (1 ps) and yielding unrealistically rapid relaxation of the “hot” s-states (< 100 fs). There is still no satisfactory formulation of a dynamic MQC theory rationalizing rapid, nonadiabatic IC suggested by the experimental observations. There is much current activity in developing the next generation of MQC MD models (e.g. Ref. 52) that might be capable of addressing this issue. Very recently, Borgis, Rossky, and Turi,⁵³ re-estimated nonadiabatic IC rates using a kinetic model based on modified Fermi golden rule with either classical or standard quantized version of the correlation functions and obtained IC lifetimes of 30–60 fs for water and 80–160 fs for methanol. For harmonic quantization, even shorter p-like state lifetimes (a few fs) were computed. The authors caution, though, that their results are very sensitive to the choice of model potentials; nevertheless, it appears that the time constant for IC would be short in these models with more realistic treatment of electron-solvent interaction and quantized vibrations. The semicontinuum solvation model of Fischer and Zharikov⁷⁵ also favors short IC times (ca. 130 fs for water). For internally trapping “octahedral” S_6 ($n = 6$) water anion cluster, Scherer *et al.*⁶² estimated an IC time of ca. 100 fs. It seems that the case for rapid, nonadiabatic IC for e_{hyd}^- is growing stronger, whereas no new models or credible experiments favoring the slow, adiabatic IC scenario are appearing. If the former scenario is correct, transient absorbances attributed to p–CB bands (with the life times of a few 100s of ps) in Refs. 31–34 should be reinterpreted as those originating from the s–p bands of “hot” s-like states undergoing the first stage of their bimodal relaxation dynamics.

3.2. “Weakly bound” and “dry” electrons, relocation, and attachment

Apart from these s- and p-like states, other short-lived, excited states were postulated by various authors. Such states go under the vague

name of “weakly bound” (wb) electrons, meaning a state that is localized yet not completely solvated.^{24,25,72} It is assumed that such wb electrons in some (vague) way are structurally different from the strongly bound (sb) electrons observed at a later stage of the solvation process (the “hot” and the relaxed s-like states). In laser photoionization of water, some of these intermediate wb states (with lifetime of ca. 110 fs) were claimed to be the electrons coupled to the OH radical (yielding large transient absorbances near the O–H stretch of the water),²⁷ though no such states have been observed in electron photodetachment from hydroxide anion.⁷⁶ For water, there is no evidence that these wb electrons are more than artifacts of multiexponential kinetic analyses.^{28,a} What is certain, however, is that the localization of the electron is preceded by the formation of short-lived *delocalized* states capable of extremely fast scavenging reactions with certain solutes (such as Cd²⁺ and selenate and nitrate anions)^{79–81} that are also known as scavengers of “dry” electrons generated in radiolysis of water. The evidence for such states is indirect (as there is no spectroscopic signature); nevertheless, the existence of these states can be deduced from the occurrence of long-range scavenging (electron attachment) that occurs on the time scale < 50 fs. The typical static scavenging radii for s-like and p-like electrons by such solutes are 0.5 and 0.8–1 nm, respectively; whereas the CB electrons generated via s–CB excitation have radii of 3–5 nm.^{63,79–81} Beyond these estimates, little is known about the nature of “dry” or CB electrons in polar liquids. The recent ultrafast photoemission studies of amorphous ice on metals suggest extremely short lifetime (< 20–50 fs) and rapid scattering for these CB states.^{82,83} By contrast, CB electrons in low temperature ice-Ih are readily observed using dc and GHz conductivity, over many nanoseconds.⁸⁴

^a It should be stressed that multiphoton pump-probe studies are frequently carried out at high excitation density; this may result in a bulk thermal spike that considerably changes both the electron thermalization and geminate recombination dynamics.^{77,78} It seems likely that irreproducible reports of unusual spectral features and exotic short-lived intermediates are traced to the effects of such thermal spikes.

In liquid ethers, such as THF, Schwartz and co-workers^{37,54,85} observed theoretically, using nonadiabatic MQC MD model, a relocalization of photoexcited s-like electrons that proceeds via the formation of disjoint and multicavity states. Relatively large cavities occur naturally in these poorly packed liquids as the result of solvent fluctuations. The interaction of the solvent molecules with the electron is so weak that these nascent cavities have comparable binding energies to the relaxed cavities that are already occupied by the excess electron.⁵⁴ The “tail” in the absorption spectrum originates from weak transitions from the ground state to such disjoint and multicavity states rather than s–CB transitions. The classification of such states into s- and p- is not particularly useful due to the great anisotropy of the solvation cavity and numerous crossings between the excited states. Even the excited states that remain localized in their parent cavity after their relaxation may fleetingly occupy the neighboring cavities. Experiments on relocalization of solvated electrons in THF³⁷ are consistent with the picture of population transfer into these disjoint cavities that occurs bypassing the CB of the liquid; both the experiment and the theory indicate that $\approx 30\%$ of photoexcited s-like electrons relocalize into such states (in the experiment, this process competes with geminate recombination).^{37,85} It is not known whether such a mechanism can operate in H-bonded, well-packed solvents such as liquid water and alcohols, but one cannot entirely exclude such a possibility, especially at high temperature.

Packing of the solvent molecules in an organic liquid has another important effect on the dynamics of electron localization: there could be more than one type of electron-trapping cavity and the interconversion between such cavities could be relatively slow, especially in viscous liquids. In aliphatic alcohols, the relaxation of “hot” s-like states is much slower than in water (e.g. 12 ps for methanol^{24,25}), and the wb electrons can be observed directly on the sub-ps time scale (recombining or converting to a “hot” s-like state on the picosecond time scale). Spectrally distinguishable IR-absorbing wb state is observed most clearly in ethylene glycol at 300 K; the spectral evolution is consistent with 2.5 ps decay of this wb state without relaxation to a “hot” s-like state.⁷² Mostafavi and co-workers⁷² suggested that

wb electrons in the diols are trapped electron species that are partially solvated by methylene groups; the wb electrons are observed before the conformational dynamics allow the OH groups to arrange properly around the solvation cavity (see Chap. 2). Such a picture is also suggested by *ab initio* calculations for methanol clusters⁸⁶ indicating possible participation of methyl groups. This rationale implies that there should be no “wb electrons” in liquid water (indeed, no such species in liquid water is suggested by the existing theoretical models or reliably observed experimentally). The situation is different in low-temperature hexagonal ice where rotations of water molecules are hindered; the wb electrons with lifetime of several milliseconds are readily observed in the D₂O ice below 20 K.^{64,65} The most likely trapping site for these wb electrons is a water vacancy at the wall of an ice cage (with two dangling OH groups interacting with the electron), as argued in Ref. 23.

In polar solids, the existence of wb electrons is beyond doubt, being richly documented in pulse radiolysis studies of vitreous alcohols, water–alcohol glasses, and salt glasses at low temperature.^{64,65} Arrested molecular motions in such solids, long-range tunneling, and trap-to-trap downhill hopping of the electron readily explain the dynamics of wb electrons observed in these low-temperature glasses.⁶⁵ That the IR-absorbing wb electrons are partially or entirely trapped by the alkyl groups have been suggested by Shida *et al.* 35 years ago,⁸⁷ and this hypothesis is supported by the observed correlation of the position of the IR absorption peak with the length of the aliphatic chains and the similarity of this band to the absorption band of trapped electrons in vitreous alkanes^{65,66} and small clusters of alcohol molecules in alkane liquids.^{5,6} Ultrafast laser studies of liquid alcohols and diols thus recreate the familiar features of electron dynamics in low-temperature glasses, albeit on a much shorter time scale. It seems, therefore, that obtaining detailed structural data on these long-lived (> 1 ms in *n*-propanol at 77 K⁶⁵) wb states in such solids would be preferable to the more involved studies of essentially the same wb states on the picosecond time scale, in room temperature liquids.

The relatively unaddressed issue is the dissociative electron attachment (DEA) involving photoexcited solvated electrons. DEA

(presumably, involving protonated phosphate groups in the sugars) involving low-energy electrons (a few eV) has been implemented in inducing irreversible DNA damage⁸⁸; DEA in water (involving a short-lived electron precursor, such as subexcitation electron) has been suggested as the main source of prompt H₂ in radiolysis of aqueous solutions.⁸⁹ DEA involving photoexcited solvated electron was observed in solid and liquid alcohols³⁶ and reverse micelles⁸⁷ but not in neat water, where the H⁻ + HO[•] resonances are relatively high in energy. Given that DEA involving “precursor” states has been postulated for many radiolytic systems in order to account for the prompt bond breaking observed in such systems, more studies of the DEA involving energetic electron states are merited, as presently there is no other way of accessing such states in bulk solvents.

Concluding this section, we note that though the main intermediates of electron solvation have been identified, many controversies remain. Phenomenological approaches in interpreting these dynamics resulted in proliferation of mutually exclusive kinetic schemes providing limited or no insight into the physics and structural aspects of the electron dynamics. In our opinion, subsequent advance in understanding these dynamics can only be made by direct comparison of the experimental dynamics with theoretical models. Unfortunately, the current state of these models does not allow such a comparison. In the following, we will focus on the ground state of the solvated electron, as better understanding of this ground state is the likely key to developing theoretical models that can make this direct comparison possible.

4. The Cavity Electron Revisited

Studies of electron solvation are popular with chemical physicists largely due to the perceived simplicity of the problem. The latter notion rests upon the mental picture of the solvated electron as a single quantum mechanical particle confined in a classical potential well: *a particle in a box*. This picture was first suggested by Ogg in 1946 and subsequently elaborated by Cohen, Rice, Platzmann, Jortner, Castner, and many others. First such models were static, but

in the mid-1980s it became possible to treat the (classical) dynamics of the solvent molecules explicitly using computer models and MQC MD and path integral approaches flourished. The current state-of-the-art dynamic models are the direct descendants of these one-electron models. Despite their great sophistication, such models still rest on the initial *ad hoc* assumption that the cavity electron and the valence electrons in the solvent molecules may be treated wholly separate. Yet this basic assumption is unobvious, and as such, it has been the subject of much debate in the late 1960s and the early 1970s (that was eventually resolved in favor of the one-electron approximation). Indeed, there are multiple experimental observations that are not accounted for by these one-electron models and, which is more troubling, obviously contradict these models.

For example, the one-electron models incorrectly predict (even at a qualitative level) the Knight shifts in ^1H and ^{14}N NMR spectra of ammoniated electron, e_{am}^- ,¹ and solvated electrons in amines (Sec. 4.1). The same problem arises in the explanation of magnetic (hyperfine) parameters obtained from ^2H ESEEM spectra of trapped (hydrated) electrons in low-temperature alkaline ices.²³ The recent resonance Raman spectra of e_{hyd}^- ^{18–20} also appear to be incompatible with the one-electron models, as all vibrational bands (including the HOH bend) undergo substantial downshift that indicates weakening of the bonds (Sec. 4.2). Surprisingly, *the experimental methods that provide the most direct insight in the structure of the solvation cavity appear to be the least compatible with the one-electron models.* The latter models, however, do capture the essential physics of electron solvation, given their historical success in explaining the absorption properties, the energetics, the dynamics, and the spectral evolution of the electrons. These two lines of reasoning suggest that the one-electron models adequately describe the electron wavefunction inside the cavity (“the particle”) but err in their description of the electron wavefunction extending beyond the cavity (“the box”). Both the hyperfine constants (that is, the spin density in the solvent molecules) and the vibrational frequencies of the solvent molecules are the properties of “the box.” The “dissenting” experimental results, therefore, indicate that electron solvation significantly modifies the properties of these solvent

molecules, and this salient feature is not included in the current MQC models.

4.1. Magnetic resonance

The way in which this solvent modification occurs is suggested by the pattern of hyperfine constants for e_{am}^- (which is one of the few solvated electron species sufficiently stable to obtain its NMR spectrum). The Knight shift K_X of NMR lines is due to the contact Fermi (isotropic) hyperfine interaction of the excess electron with the magnetic nuclei (X) in the solvent molecules; it is the measure of spin density $|\phi_s(0)|_X^2$ in the s -type atomic orbitals centered on a given nucleus X : $K_X \propto \sum_X |\phi_s(0)|_X^2$. This shift can be converted into the sum $\sum_X a$ of isotropic hyperfine coupling constants (hfcc's) for all nuclei of type X . In ammonia, this calculation gives +110 G for ^{14}N nuclei and -5.7 G for ^1H nuclei. Given that the atomic hfcc for the electron in the N 2s orbital is +550 G, ca. 20% of the total spin density of the excess electron is transferred into these N 2s orbitals.¹ Even more is expected to be transferred to N 2p orbitals, and this accounts for the negative sign of proton coupling constants: the spin density in the hybridized H 1s orbital is negative due to the spin bond polarization involving the filled N 2p orbital; this inversion is typical of p-radicals. The negative sign of the isotropic hfcc for protons was demonstrated by dynamic nuclear polarization experiments and then confirmed by direct NMR measurements. Note that only positively valued constants are obtained in the one-electron models for the s -like state, as such models do not include spin bond polarization effects.

A similar situation exists for the electron trapped in low temperature alkaline ice. It was ^2H ESEEM studies of this species that prompted Kevan⁹⁰ to suggest the textbook octahedral model of hydrated electron (the so-called "Kevan's model") in which the electron is stabilized through dipolar interactions with six O-H groups pointing to a common center. Following the original interpretation of these ESEEM spectra by Kevan *et al.*⁹⁰ (which gave positively valued isotropic hfcc's for the protons), it was subsequently demonstrated that isotropic hfcc's of the protons at the cavity wall (roughly 0.2 nm

from the center) are, in fact, negative: $a \approx -0.92$ G.⁹¹ These negative hfcc's hint at nonzero spin density in the O 2p orbitals of water molecules. Tight-binding *ab initio* models of small anion water and ammonia clusters suggested the same.⁹² However, given the many approximations made in these models, these dissenting results were not given due consideration at a time when the conceptual picture of the solvated electron was still evolving. The consensual picture that emerged in the mid-1970s was that the solvated electron is indeed a "particle in a box," to a very good approximation. The competing view that the solvated electron is a multimer anion was suggested for e_{am}^- by Symons,⁹³ who estimated that the spin density is divided between six ammonia molecules in the first solvation shell (with hfcc of 12 G) and 12 molecules in the second solvation shell (ca. 3 G). A more detailed account of magnetic resonance studies of ammoniated and hydrated electron given in Refs. 1 and 23, respectively. In retrospect, the main reason for rejection of the multimer anion picture of electron solvation (that has been around since 1953)⁹⁴ was the resolute and erroneous insistence of the proponents of this picture that *all* of the excess electron density resides *all* on the solvent molecules, their inability to explain the observed energetics and absorption properties of the solvated electron, and their denial of cavity formation.

The latter was especially damaging for the multielectron view, as there is abundant evidence that such cavity electrons do exist in molecular fluids.⁹⁵ Furthermore, the existence of the cavity logically follows from the occurrence of charge sharing between several solvent molecules: although only a small fraction of the negative charge resides on each solvent molecule forming the cavity, Coulomb repulsion between these partially charged molecules assists in opening of the cavity. The latter can be formed through this mechanism even when the occupancy of the cavity is relatively small (as may be the case for the alkanes⁴). The conflict with these incontrovertible experimental observations is resolved by making the assumption that only a fraction of the total negative charge is localized on the solvent molecules; the rest is localized inside the solvation cavity. This view, first suggested by Symons⁹³ and Kevan,⁹⁶ partakes of the best features of the cavity and the multimer anion models.

4.2. Vibrational spectroscopy

Magnetic resonance is not the only piece of evidence indicative of the excess electron density in the antibonding orbitals of the solvent molecules. The hydrated electron exhibits a second absorption band at 190 nm⁹⁷ that originates through the perturbation of O 2p orbitals in the solvating water molecules; obviously, such a feature cannot be treated using the standard one-electron models.

Further evidence is suggested by the recent resonance Raman (RR) observations.¹⁸⁻²² The vibrational peaks of e_{hyd}^- (which demonstrate resonant enhancements over 10^5) all exhibit significant downshifts relative to these Raman peaks in neat water. In RR spectroscopy, only those vibrational modes that are significantly displaced upon electronic excitation show resonance enhancement; thus, this spectroscopy provides a probe of the water molecules in the immediate vicinity of e_{hyd}^- . The RR peak position for the e_{hyd}^- in H₂O (vs. those for bulk water), in cm⁻¹, are: librations at 410 (vs. 425-450), 530 (vs. 530-590), 698 (vs. 715-766); the H-O-H bend at 1610 (vs. 1640); and the H-O stretches at 3100 (vs. 3420).^{18,19} Thus, the downshift of the bend mode, which exhibits a narrow, symmetric line, is ca. 30 cm⁻¹, and the downshift of the stretch mode is 200-300 cm⁻¹. Similar RR downshifts were observed for solvated electrons in alcohols, with the downshift of the O-H stretching mode increasing with the solvent polarity.²¹ For methanol, the O-H torsion peak is downshifted by 180 cm⁻¹ and the O-H stretch is downshifted by 340 cm⁻¹, which is greater than the downshift of the O-H stretch in liquid water. This large downshift is readily explained by the reduction in the number of solvation O-H groups (from 4 to 6) in methanol, as suggested by ESEEM spectroscopy²³ which results in greater penetration of the electron density into the O 2p orbitals (see below). Normal mode analysis of enhancement factors for RR peaks indicates that all enhanced modes are predominantly O-H in character; the C-H stretching bands that have no O-H character are not observed and the largest enhancements are for libration modes. So far, all RR observations are consistent with the notion that the electron in water and alcohols is solvated by dangling O-H groups, and the

electron–solvent coupling is mediated primarily by these O–H groups; there is no evidence that *sb* electrons are solvated by C–H groups of the alcohols. A more speculative idea suggested by Stuart *et al.* is that the alignment of these O–H groups changes from pointing straight towards the center of mass (*X*) of the electron to dipole coupling to the alcohol molecule, as the carbon number increases from 1 to 4 (with the X–O–H angle increasing by 30°, respectively).²¹

These downshifts are such a general feature of the RR spectra that there must be a common mechanism for these downshifts in all solvents. Observe that the disruption of the H-bond structure cannot account for these RR results: weakening of the H-bonds results in O–H band upshifts, and the H–O–H bending mode in water does not change even when this liquid is heated to 600 K or saturated with salts (in fact, halide anion solvation in alcohols upshifts the O–H stretch by 50 cm⁻¹).²¹ It has been concluded^{18,19} that the only way of explaining these substantial downshifts is by assuming partial occupancy of solvent antibonding orbitals.

Most recently, Mizuno *et al.* presented a femtosecond version (250 fs time resolution, 160 cm⁻¹ spectral resolution) of the RR experiment to probe the O–H band of the electron as it hydrates following 2×4.66 eV photon excitation. Mizuno *et al.*²² conclude that the precursor of the hydrated electron that undergoes “continuous blue shift” on the time scale of 1–2 ps also yields a downshifted O–H stretch signal whose resonance enhancement follows the efficiency of Raman excitation as the absorption spectrum of the *s*-like state shifts to the blue (thus indirectly confirming its identity as a “hot” *s*-like state). The comparison of anti-Stokes and Stokes Raman intensities indicates that the local temperature rise is < 100 K at 250 fs. This estimate agrees with the estimates based on the evolution of the spectral envelope during the thermalization, using the dependence of the absorption maximum of thermalized electron on the bath temperature.^{26,69}

4.3. Substructure of the *s*–*p* absorption band

The *s*–*p* absorption band of the solvated electron can be thought of as three overlapping, homogeneously broadened *s*–*p* transitions.

Variation of the Raman depolarization ratio across the O–H stretch band and significant deviation of this ratio from $\frac{1}{3}$ for the O–H stretch and libration bands indicate that the p-like states are nondegenerate (which does not exclude considerable homogeneous broadening of the lines).¹⁸ The analyses of the spectral envelopes using RR data also suggest that inhomogeneous broadening is much stronger than homogeneous broadening, both for the water and the alcohols.^{18,21} These observations are inconsistent with the recent suggestions¹¹ that the electron spectrum is a single inhomogeneously broadened line (which is also in striking disagreement with all existing dynamic models of electron solvation). Still, at the present there is no further experimental evidence other than the RR results that distinct p-subbands do exist.

Ultrafast laser experiments^{34,35,98} that were specifically designed to demonstrate this subband structure using polarized transient hole burning (PTHB) yielded no conclusive evidence for this structure. PTHB spectroscopy is a form of pump-probe spectroscopy that examines the ground-state dynamics of a system by first exciting a subset of members of an ensemble with polarized light and then probing at a later time the dynamics of the remaining, unexcited members with light polarized parallel or perpendicular to the original excitation polarization.^{35,99} If the three p-like states interchange roles slowly (as the solvation cavity deforms in response to solvent motion), then PTHB should show different dynamics for these two probe polarizations. When the lowest-energy transition along the long axis of the cavity is excited with polarized light, until the cavity reorients, there would be less absorption by the remaining electrons when probing with light of the same polarization at the excitation energy, but the remaining electrons would continue to absorb at higher energies. The parallelly and perpendicularly-polarized THB signals should become identical once solvent motions have scrambled the three p-like states and memory of which transition dipole moment pointed which direction in space is lost. MQC MD simulations of Schwartz and Rossky⁹⁹ predicted that pumping the lowest-lying transition and probing either the same or the higher-lying transitions should give an anisotropy that persists for 1 ps, as it takes this long for the water molecules to

rearrange enough so that the cavity changes shape and thus scrambles memory of the transition dipole directions. Reid *et al.*⁹⁸ reported this persistent anisotropy, but subsequent studies^{34,35} did not confirm the presence of a long-lived anisotropy. Explaining this striking inability of the PTHB experiment to demonstrate the predicted effect remains an open problem, and solving this problem requires reexamination of the origin of the absorption spectrum and the dynamics of the e_{hyd}^- . The discrepancy may be due to strong homogeneous broadening of the absorption spectrum of the e_{hyd}^- or extremely fast interchange of the p-like orbitals.³⁵ We suggest, however, that the failure might be, in part, with the very concept of the excess electron as “a particle in a box.”¹⁰⁰

5. The Heterodoxy: Solvent Stabilized Multimer Radical Anion

In a series of recent publications on the excess electrons in ammonia¹ and water,^{23,51,100} we addressed these issues by developing multi-electron models of electron solvation and demonstrating how such models account for the known properties of the solvated electrons. Our models are inspired by *ab initio* and DFT studies of large, internally trapping water anion clusters.^{47–49} What follows from these latter studies is that the electron is localized by several dangling O–H groups; in the medium size water clusters ($n = 17–24$), the cavity is typically tetrahedral. Examination of the highest occupied molecular orbitals (HOMOs) of these clusters suggests that part of the electron density is contained in the frontal orbitals of the dangling O–H groups. Computations of Kim *et al.*⁴⁷ and Domcke *et al.*⁶¹ and the others suggest that small internally trapping clusters ($n < 10$) have some of their vibrational bands downshifted with respect to neutral water clusters. Recent calculations of vibrational properties of water anion clusters that trap the electron externally, by dipole binding to the so-called AA (double acceptor) water molecule at the surface of the cluster,^{101,102} suggest that the main cause for these red shifts is donor-acceptor stabilization between the unpaired electron and O–H σ^* orbitals.¹⁰¹ This is, basically, another way to describe the

mechanism suggested by Tauber and Mathies for e_{hyd}^- ¹⁸ and Symons for e_{am}^- .⁹³ It thus appears that most of the physics that is necessary to address the problems discussed in Sec. 4 is already contained in such *ab initio* and DFT models. The problem with this inference is that the small and the medium size water anion clusters in the gas-phase have quite different structure from the e_{hyd}^- in the bulk water, and this makes direct comparison impossible. Furthermore, it is well understood that e_{hyd}^- is a dynamic entity, a statistical average over many solvent configurations that cannot be adequately represented by any given structure; a quantitative description of the e_{hyd}^- within the multielectron approach has to address this inherent variability.

One path to this goal is by using Car–Parrinello molecular dynamics (CPMD), and such a calculation for the e_{hyd}^- in the room temperature and supercritical water has been implemented by Boero *et al.*⁵⁰ Unfortunately, CPMD is a computationally demanding approach, and this requires the use of small solvent cells of a few tens of water molecules; the solvated electron fills the substantial part of these cells. Since the solvent cell also has net negative charge, diffuse positive charge has to be spread on the neighboring cells, further reducing the fidelity of the model. To speed up the computation, CPMD calculations involve pseudopotentials; the use of such pseudopotentials has to be justified. For these and other reasons, the results of the CPMD calculation⁵⁰ look quite different from both MQC MD calculations for electron in liquid water and *ab initio* and DFT calculations for gas-phase water anion clusters. To further complicate the assessment of these CPMD results, the computation of magnetic resonance parameters, distribution of charge, absorption spectra, and PTHB dynamics requires high-quality local expansion of the wavefunction which is difficult to achieve using plane wave basis that is used for the CPMD calculations.

Hence we suggested a different approach that is less computationally demanding but appears to successfully capture the essential physics of the problem.⁵¹ Our approach capitalizes on the remarkable success of MQC models to account for the solvated electron properties.^{38–46} MQC MD was used to generate a dynamical trajectory of the s-like e_{hyd}^- , and then temporally well-separated snapshots from this

trajectory (100 fs per frame) were extracted and became the input for DFT and single-excitation configuration interaction (CIS) calculations. In these calculations, only one or two complete solvation shells for the excess electron were considered explicitly; the remaining atoms in the simulated solvent were replaced by point charges, a procedure that is referred to as matrix embedding (this approach has been used to study neutral water¹⁰³ and hydrated radicals¹⁰⁴). Significant sharing of spin and charge of the excess electron by O 2p orbitals in the first-shell water molecules was observed (ca. 20%). This hybrid MQC MD:DFT(CIS) approach can account for (i) the energetics and the equilibrium optical spectrum of the e_{hyd}^- in the visible and the UV; (ii) the EPR and ESEEM spectra, (iii) the vibrational (resonance Raman) spectrum of the e_{hyd}^- ,^{23,51} and (iv) rapid PTHB dynamics.¹⁰⁰ Although the multielectron picture of the e_{hyd}^- is complex, on average, the radial density of the HOMO and the three lowest unoccupied molecular orbitals (LUMO) resemble the s-like and p-like orbitals predicted by the one-electron models. For some observables (e.g. the optical spectrum), the fine details of this orbital structure do not matter. For other observables (e.g. the spin density maps provided by EPR and ESEEM spectroscopies and the resonance Raman spectrum), this level of approximation is inadequate.

The typical HOMO of the hydrated electron is shown in Fig. 2 (to the left) next to the average radial wavefunction (to the right). While there is considerable density in the O 2p orbitals (with the negative frontal lobes accounting for 12% of the total density), the ensemble average wavefunction is hydrogenic. The most probable position of the electron is at 0.175 nm, which is within the cavity radius of ca. 0.226 nm (the mean distance between the center of mass X of the electron and the nearest protons in dangling O–H groups). The mean X–O–H angle is close to 16%, so the O–H groups are oriented towards the cavity center. Ca. 50–60% of the density is contained within the cavity, with only 5% contained beyond the first solvation shell. Mulliken population analysis indicates that the excess charge and spin densities are localized mainly on the H and O atoms in the dangling O–H groups. The radius of gyration of the electron is estimated as 0.275 nm (vs. 0.204 nm in the MQC MD model and

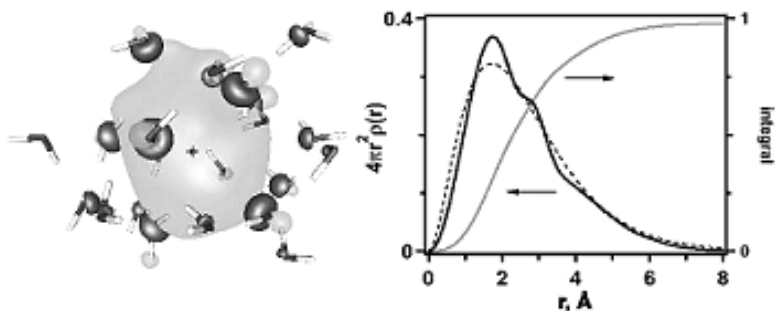
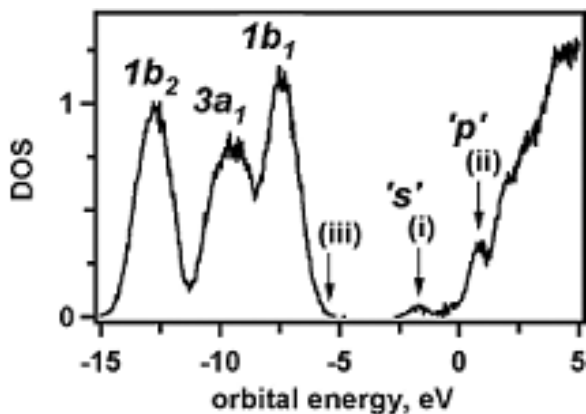


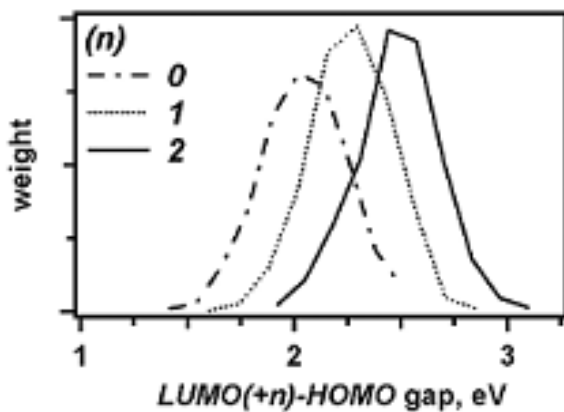
Fig. 2. (On the left) Isodensity map for s-like HOMO of hydrated electron given by MQC MD–DFT calculation; a single snapshot is shown (only two solvation shells are shown, the embedding matrix of water molecules is removed for clarity). The central s-like orbital (grey) has the opposite sign to frontier O 2p orbitals in water molecules “solvating” the electron. Ca. 20% of the electron density is in these O 2p orbitals. Despite that, the ensemble average radial component of the HOMO (on the right, solid line) closely resembles hydrogenic wavefunction (broken line). On average, ca. 60% of the electron density is contained inside the cavity and 90–95% within the first solvation shell. See Ref. 51 for more detail.

experimental estimate of 0.25–0.26 nm) and the semiaxes of the gyration ellipsoid (the measure of cavity anisotropy) are 0.15 nm × 0.16 nm × 0.17 nm. This anisotropy splits the energies of the lowest unoccupied orbitals.

The computed DOS function [Fig. 3(a)] exhibits two features near the bottom of the CB. Feature (i) results from the HOMO (the s-like orbital) that is located ca. -1.69 eV below the vacuum energy (the DOS maximum is at -1.8 eV vs. -1.75 eV given by the CPMD calculation).⁵⁰ Feature (ii) derives from the three lowest unoccupied molecular orbitals, which have centroids at 0.42, 0.65, and 0.86 eV, respectively, that correspond to the three nondegenerate p-like states observed in one-electron models. The histograms of the corresponding transition energies show three distinctive p-subbands with centroids at 2.11, 2.34, and 2.55 eV [Fig. 3(b)]. For comparison, path integral calculations^{38–40} using the same pseudopotential as for our MQC MD calculations gave peak positions at 2.1, 2.5, and 2.9 eV. The absorption spectra calculated using the CIS method are very similar to those calculated using the MQC MD method.



(a)



(b)

Fig. 3. (a) Kohn–Sham density of states (DOS) function for “hydrated electron” (embedded water anion clusters). The three core orbitals of water are shifted by 1 eV towards the midgap as a result of Stark shift. Features (i) and (ii) originate from s-like HOMO and p-like LUMO(0, +1, +2) orbitals. (b) The histogram of energy gaps between the s- and p-like states.

The three p-subbands correspond to the three lowest excited states that have nearly orthogonal transition dipole moments. Each one of these subbands carries an integral oscillator strength of ca. 0.3.

In Fig. 4, isodensity contour plots of the Kohn–Sham LUMO are shown. The familiar dumbbell shape of the “p-like orbital” is not

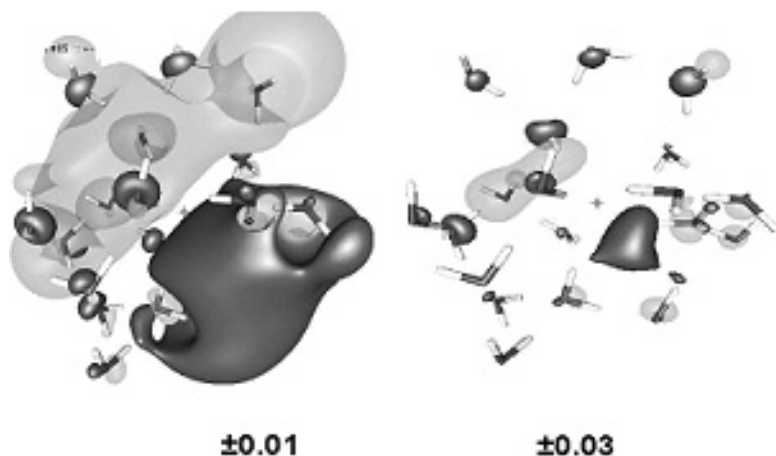


Fig. 4. The anatomy of a “p-like state”. Two isodensity contour maps (± 0.01 and ± 0.03 a.u.⁻³) of the same LUMO orbital are shown side by side. Unlike the p-like orbitals in one-electron models, LUMO states in MQC MD–DFT and CIS models have the lobes pushed outwards between the first and the second solvation shells, with < 20% of the spin density residing inside the cavity. This results in considerable fragmentation of the diffuse part of the wavefunction. The O 2p orbitals are strongly polarized, with opposite signs of the orbitals attained by water molecules on the opposite sides of the cavity in the direction of transition dipole moment.

readily recognizable, although the three lower unoccupied states do exhibit p-like polarization, each orthogonal to the others. Only a fraction of the total “p-like state” density (ca. 20%) is contained inside the cavity and the p-character of these electronic states is achieved through the polarization of the frontal O 2p orbitals in the O–H groups forming the cavity: the phase of the electron in these orbitals on one side of the cavity assumes a positive sign, while the phase of the electron in the O 2p orbitals straight across the cavity in the direction of the transition dipole moment assumes a negative sign (Fig. 4). There is also both positive and negative excess electron density in the interstitial cavities between the water molecules of the first and the second solvation shells. The gyration ellipsoid for these p-like orbitals is 0.18 nm \times 0.22 nm \times 0.33 nm, making them nearly twice the size of the gyration ellipsoid for the HOMO, so the “p-like” states extend

further out of the cavity than the “s-like” ground state. This readily accounts for the experimental observation that s–p excitation of the electron causes relocalization, albeit with a low probability.⁶³ The complex orbital structure of the p-like orbitals may also be important for understanding the mechanism for rapid, nonadiabatic IC involving these orbitals (Sec. 3.1). Indeed, the orbital momentum carried by the polarized cavity should be rapidly lost via small-amplitude motions of the water molecules.

A novel feature that is not captured by one-electron models is a band of HOMO-1 orbitals that are composed of $1b_1$ orbitals (O 2np orbitals) of the water molecules in the first solvation shell [Fig. 3(a)]. Our calculations suggest that the onset of this band starts 5.75 eV below the vacuum level. The presence of this peak suggests that there should be an electronic transition from the occupied O 2p orbitals into the HOMO at ca. 210 nm. The experimentally observed UV band of the \bar{e}_{hyd}^- peaks at 190 nm with an onset around 220 nm. By placing the unit negative charge at the center of the cavity, one can demonstrate that this feature originates through a Stark shift of the eigenvalues towards the midgap, by ca. 1.1 eV.

Using DFT calculations, it is possible to calculate hyperfine constants and then simulate ^1H EPR and ^2H ESEEM spectra of the \bar{e}_{hyd}^- . The correspondence between such simulated and experimental⁹¹ spectra is very good, with all of the salient features discussed above reproduced. The residual discrepancy is for ^{17}O nuclei: the calculated second moment (M_2) of the EPR for the 37% oxygen-17 enriched sample studied by Schlick *et al.*¹⁰⁵ is 2250 G² vs. the reported experimental estimate of 134 G². This is not a failure of the particular DFT model: all *ab initio* and DFT models of the \bar{e}_{hyd}^- give large estimates for isotropic hfcc’s on oxygen atoms. The estimate of Schlick *et al.*¹⁰⁵ is compromised by their subsequent observation¹⁰⁶ of a strong spectral overlap between one of the resonance lines of the $^{17}\text{O}^-$ radical and the narrow EPR signal from the “electron,” which had a peak-to-peak width (ΔB_{pp}) of 18 ± 1 G. In ^{16}O glasses, the two narrow EPR signals from \bar{e}_{hyd}^- and $^{16}\text{O}^-$ are spectrally well separated, but because the signals overlap in ^{17}O enriched samples, the EPR spectrum in such ^{17}O enriched samples is very complex. We used our calculated hfc tensors

to simulate the EPR spectrum of an oxygen-17 enriched sample. The EPR line decomposed into two distinct spectral contributions, a narrow one with $\Delta B_{pp} \approx 23$ G and $M_2 \approx 135$ G² (in good agreement with the estimates of Schlick *et al.*¹⁰⁵) and a very broad line with $\Delta B_{pp} \approx 89$ G and $M_2 \approx 1980$ G². For a sample with 37% ¹⁷O enrichment, there is a ca. 10% probability that the first solvation shell would have no ¹⁷O nuclei. The narrow line arises from such isotopic configurations, so that the electron is only weakly coupled to the ¹⁷O nuclei in the second solvation shell. The isotope configurations that include at least one ¹⁷O nucleus in the first solvation shell, on the other hand, are responsible for the broad line. Small-amplitude movements of water molecules in the frozen samples would cause efficient spin relaxation for this line. The narrow EPR line was recognized as a signal originating from $\bar{\epsilon}_{\text{hyd}}$ from its long relaxation time, using microwave saturation of the resonance signals. Broad resonance lines were attributed to the ¹⁷O⁻ radical; this criterion eliminates strongly coupled water anion configurations. Thus, the EPR results for oxygen-17 enriched samples do not contradict the MQC MD-DFT model.

To examine the vibrational spectra of the $\bar{\epsilon}_{\text{hyd}}$, IR and Raman spectra of the embedded clusters were calculated⁵¹ retaining only the first solvation shell, as such calculations do not include resonant enhancement. Although the absolute positions of the vibrational features calculated using the embedded neutral water and water anion clusters do not match experiment, the downshifts of these bands in the presence of the excess electron are well described by the hybrid calculation: there are downshifts of the librational, the H–O–H bending and the O–H stretch modes. The calculated downshift for the H–O–H bending mode is ca. 50–60 cm⁻¹ (as compared to the experimental estimate of 30 cm⁻¹¹⁸) and the calculated downshift for the O–H stretching modes is 80–180 cm⁻¹ (vs. 200–300 cm⁻¹ for the band center).¹⁸ Electrostatic interactions alone cannot account for these downshifts, as placing the unit negative charge at the center of the cavity does not cause such large shifts.

Interestingly, the multielectron model also accounts for the “failure” of the PTHB experiment: since part of the transition dipole moment is carried out by O 2p orbitals in water molecules, their rapid

reorientation quickly destroys the correlation. The slow reorientation of the cavity is still observed, but it is predicted to have little weight in the corresponding correlation functions. Direct calculation of PTHB dynamics using the method used by Schwartz and Rossky⁹⁹ and the transition dipole moments calculated using the CIS model indicates that (i) the anisotropic PTHB signal is very small (less than 2–5% of the isotropic contribution) and (ii) this signal fully decays in 250 fs. As the earliest delay time at which the PTHB signal is observed is ca. 200 fs,³⁵ the lack of the signal is readily rationalized.

For ammonia,¹ the DFT calculations suggest that small clusters that exhibit internal trapping of the electron automatically yield large positive Knight shifts on ¹⁴N nuclei and small negative Knight shifts on ¹H nuclei. In a typical $n = 18$ cluster, the spin density was mainly contained between three dangling NH bonds, but the diffuse s-like orbital enveloped the entire cluster, with 50% of the density contained within the radius of gyration (0.4 nm). The isotropic hfcc's for ¹⁴N nuclei of the three nearest molecules are 16–20 G. The “second solvation shell” molecules have hfcc's ranging from +1.9 to +6.6 G, depending on the proximity to the central cavity. The sum totals of isotropic hfcc's for ¹⁴N and ¹H nuclei are $\sum_N a \approx +117$ G and $\sum_H a \approx -4.1$ G, respectively, in good agreement with the experiment. These calculations strengthen the case for extensive sharing of spin density by N 2p orbitals by ammonia molecules in the first and the second solvation shells. Just the *negative* lobes of N 2p functions of the HOMO account for 7% of the total spin density.

Even more extensive delocalization onto the solvent might occur for solvated electrons in alkane liquids. In one-electron models, the degree of the delocalization is determined by the binding energy of the electron. In alkanes, where the binding energy is 50–200 meV, the s-like electron (even in the one-electron models) spreads well beyond the hard core radius of the cavity.^{2,4} This is in contrast to the electron in water that is still largely confined inside the solvation cavity. Thus, the problem of adequate description of the interaction of the electron and the solvent molecules is even more important for the alkanes. In our recent study, we demonstrated that the most likely way in which the nitriles and the alkanes “solvate” the electron is through

the formation of a cavity in which the electron is mainly contained in the C 2p orbitals of the methyl (methylene) groups forming the solvation cavity.⁴ For alkanes, the spin density spreads along the aliphatic chain, with alternating occupancy of C 2p orbitals receding towards the ends of the chains removed from the cavity. Such a structure for the excess electron in the alkanes further erases the distinction between the solvent stabilized multimer radical anion and the cavity electron.

One can ask a question: does such a distinction exist at all in the solvents of low polarity? The same question can be brought to a focus by the following thought experiment (“electron encapsulation”).^{3,4} Suppose that the entire first solvation shell of the solvated electron is replaced by a single supramolecular structure (the “cage”) that has the internal cavity lined by polar groups. The cage is suspended in a liquid with low binding energy for the excess electron. Assuming that the cage traps the excess electron, what is the result of this capture? Should one regard the resulting species as a “solvated electron” or as a molecular anion? We have recently addressed this problem experimentally⁴ and theoretically,^{3,4} for hydrogenated calixarene and polynitrile rings, and the answer appears to be that no firm criteria exist for classification of such borderline species. Multimer solvent anions (electron residing on the molecules) and cavity electrons (electrons residing in the voids between the molecules) are two realizations of the same structural motif; the real “solvated/encapsulated” electron is always in between these two extreme cases.

6. Concluding Remarks

To conclude this review, despite rapid progress, many outstanding questions about the solvated electron remain unanswered. The structure and the behavior of these unusual species turned out to be much more complex than originally believed. Further advances will require greater focus on the quantum-chemical character of the “solvated electron” explicitly treating the valence electrons in the solvent, and more realistic dynamic models of the solvent degrees of freedom and electron–solvent interactions. Developing a many-electron, dynamic

picture of the “solvated electron” presents formidable difficulty, yet this is a task that can no longer be avoided, as the potential of one-electron models to address the unsolved problems is inherently limited. The simplicity of the solvated electron (that is its major attraction to chemical physicists) is imaginary; the solvated electron is a complex, nanoscale multimer anion. The ideal object imagined by Ogg nearly 60 years ago, a chemical implementation of “the particle in a box,” has distant relation to the species that is observed experimentally.

Below I provide a short list of the important problems concerning the solvated electron in polar media (author’s choice, no particular order):

- Why is the lifetime of p-like states of hydrated electrons so short? What is the structure of these p-like states? Are there other cavity states in water? Disjoint states? Multicavity states? How to prove their (non)existence experimentally?
- Can the electron be “simplified” by restriction/removal of the solvent degrees of freedom? Can it be encapsulated?
- How does the nature of the solvated electron change from one liquid to another? Does it become more of a multimer anion as the polarity decreases? How does one describe the dynamic behavior of such a multimer anion species?
- What is the nature of wb (“weakly bound”) electrons observed on the short time scale and in solids? Does such a species exist in liquid water? Are the wb electrons in alcohols partially solvated by their alkyl groups? Are these solvent vacancy trapped electrons, as suggested for ice-Ih? Are these the same species that are observed in low-temperature solids?
- How do photoinduced relocalization and photoejection of the electron occur? Is there indeed a “conduction band” in polar liquids? Does the light-induced relocalization of the electron involve this “conduction band?” What kind of species is the “dry” electron? Is there actually such a species? Can it be an excitonic state of the solvent?
- How does water vibrate around the hydrated electron? What is the effect of these vibrations on the absorption, electronic, and

dynamic properties of the solvated electron? What is the mechanism for relaxation of “hot” s-like electron on the sub-picosecond and picosecond time scales?

- How do water anion clusters in the gas phase relate to the solvated electrons observed in the bulk? How does 2D electron localization in layers of polar molecules on metal and metal oxide surfaces⁸³ relate to 3D localization in the bulk?
- What is the structure and the dynamics of hydrated/solvated electron in hot/supercritical water? In dispersed clusters of polar liquids in nonpolar liquids? In microheterogeneous media (e.g. water clusters in zeolite cavities)? In mixed and complex solvents of practical importance (e.g. Ref. 107)? on surfaces?
- Can the solvated/trapped/encapsulated electron³ be used for molecular electronics and quantum computing? It is the tiniest capacitor known in chemistry and the electron degrees of freedom are largely decoupled from the nuclear ones. Can the solvated electron be the organic chemistry substitute for quantum dots?

I hope that this review will foster interest in these problems. This work was performed under the auspices of the Office of Basic Energy Sciences, Division of Chemical Science, US-DOE under contract number DE-AC-02-06CH11357. I would like to thank M. C. Sauer, Jr. for technical assistance and B. J. Schwartz, R. Mathies and D. M. Bartels for useful discussions and for communicating prepublication versions of their recent papers.

References

1. Shkrob IA. (2006) *J Phys Chem A* **110**: 3967.
2. Shkrob IA, Sauer Jr MC. (2005) *J Chem Phys* **122**: 134503.
3. Shkrob IA, Schlueter JA (2006) *Chem Phys Lett* **431**: 364.
4. Shkrob IA, Sauer Jr MC. (2006) *J Phys Chem A* **110**: 8126.
5. Shkrob IA, Sauer Jr MC. (2005) *J Phys Chem A* **109**: 5754.
6. Kenney-Wallace GA, Jonah CD. (1982) *J Phys Chem* **86**: 2572.
7. Bernas A *et al.* (1990) In *Excess Electrons in Dielectric Media*, (eds.) Ferradini C, Jay-Gerin J-P. CRC Press, Boca Raton, p. 368; Bernas A *et al.* (1996) *Can J Chem* **74**: 1 and references therein.

8. Lee YJ *et al.* (2004) *J Phys Chem B* **108**: 3474; Laria D, Kapral R. (2002) *J Chem Phys* **117**: 7712.
9. Spezia R *et al.* (2003) *Phys Rev Lett* **91**: 208304; *J Chem Phys* **120**: 5261 and references therein.
10. Shkrob IA, Sauer Jr MC. (2004) In *Charged Particle and Photon Interactions with Matter*, (eds.) Hatano Y, Mozumder A. Marcel Dekker, New York, p. 301.
11. Pshenichnikov MS *et al.* (2004) *Chem Phys Lett* **389**: 171; Kummrow A *et al.* (1999) *Z. Phys. Chem.* **212**: 153; (1998) *J Phys Chem A* **102**: 4172; Emde MF *et al.* (1998) *Phys Rev Lett* **80**: 4645.
12. Nicolas C *et al.* (2003) *J Chem Phys* **118**: 9698; Boutin A *et al.* (2005) *Chem Phys Lett* **409**: 219.
13. Bartels DM *et al.* (2005) *J Phys Chem A* **109**: 1299 and references therein.
14. Du Y *et al.* (2007) *Chem Phys Lett* **438**: 234.
15. Kammrath A *et al.* (2006) *J Chem Phys* **125**: 171102.
16. Verlet RJR *et al.* (2005) *Science* **307**: 93; Kammrath A. (2006) *J Chem Phys* **125**: 076101.
17. Bragg AE *et al.* (2004) *Science* **306**: 669; (2005) *J Am Chem Soc* **127**: 15283.
18. Tauber MJ, Mathies RA. (2003) *J Am Chem Soc* **125**: 1394; (2002) *Chem Phys Lett* **354**: 518; (2001) *J Phys Chem A* **105**: 10952.
19. Mizuno M, Tahara T. (2003) *J Phys Chem A* **107**: 2411.
20. Tauber MJ, Mathies RA. (2002) *Chem Phys Lett* **354**: 518.
21. Stuart CM *et al.* (2007) *J Phys Chem A* **111**: 8390; (2004) *J Am Chem Soc* **124**: 3414.
22. Mizuno M *et al.* (2005) *J Phys Chem A* **109**: 5257.
23. Shkrob IA. (2006) *J Phys Chem A* **111**: 5223; (2007) *Chem Phys Lett* **443**: 289.
24. Pepin C *et al.* (1997) *J Phys Chem A* **101**: 4351.
25. Jay-Gerin J-P. (1997) *Can J Chem* **75**: 1310.
26. Hertwig A *et al.* (2000) *J Phys: Cond Mat* **12**: A165; (1999) *Phys Chem Chem Phys* **1**: 5663; (2002) *Phys Chem Chem Phys* **4**: 4412.
27. Laenen R *et al.* (2000) *Phys Rev Lett* **85**: 50; (2001) *J Mol Str* **598**: 37; Thaller A *et al.* (2004) *Chem Phys Lett* **398**: 459.
28. Lian R *et al.* (2005) *J Phys Chem A*. **109**: 1510.
29. Lewis MA, Jonah CD. (1986) *J Chem Phys* **90**: 5367.
30. Lenchenkov V *et al.* (2001) *J Phys Chem A* **105**: 1711.
31. Silva C. (1998) *Phys Rev Lett* **80**: 1086.
32. Yokoyama K. (1998) *J Phys Chem A* **102**: 6957.
33. Kimura Y *et al.* (1994) *J Phys Chem* **98**: 3450; Alfano JC. (1993) *J Chem Phys* **98**: 5996.
34. Assel M *et al.* (1999) *J Chem Phys* **111**: 6869; (1998) *J Phys Chem A* **102**: 2256.
35. Cavanagh MC *et al.* (2004) *Chem Phys Lett* **396**: 359.

36. Silva C *et al.* (1998) *J Phys Chem A* **102**: 5701; Walhout PK. (1995) *Chem Phys Lett* **232**: 135.
37. Martini IB *et al.* (2002) *Chem Phys Lett* **360**: 22, *J Am Chem Soc* **124**: 7622; (2001) *J Phys Chem B* **105**: 12230.
38. Schnitker J, Rossky PJ. (1986) *J Chem Phys* **86**: 3471; (1988) *Phys Rev Lett* **60**: 456.
39. Wallqvist A *et al.* (1986) *J Chem Phys* **86**: 6404.
40. Martyna G, Berne BJ. (1988) *J Phys Chem* **92**: 1721.
41. Rossky PJ, Schnitker J. (1988) *J Phys Chem* **92**: 4277.
42. Webster F *et al.* (1991) *Comp Phys Comm* **63**: 494; (1991) *Phys Rev Lett* **66**: 3172.
43. Schwartz BJ, Rossky PJ. (1995) *J Mol Liq* **65/66**: 23; Murphrey TH, Rossky PJ. (1993) *J Chem Phys* **99**: 515; Neri E *et al.* (1991) *Phys Rev Lett* **67**: 1011.
44. Borgis D, Staib A. (1994) *Chem Phys Lett* **230**: 405; (1996) *J Chim Phys* **93**: 1628.
45. Staib A, Borgis D. (1995) *J Chem Phys* **103**: 2642; (1996) *J Chem Phys* **104**: 9027; (1996) *J Phys: Cond Mat* **8**: 9389.
46. Borgis D, Staib A. (1996) *J Chem Phys* **104**: 4776.
47. Kim KS *et al.* (1996) *Phys Rev Lett* **76**: 956; (1997) *J Am Chem Soc* **119**: 9329; Lee HM, Kim KS. (2002) *J Chem Phys* **117**: 706; Lee HM *et al.* (2003) *J Chem Phys* **118**: 9981; (2003) *J Chem Phys* **119**: 187.
48. Khan A. (2006) *J Chem Phys* **125**: 024307; (2005) *Chem Phys Lett* **401**: 85; (2003) *J Chem Phys* **118**: 1684; (2003) *J Chem Phys* **121**: 280.
49. Herbert JM, Head-Gordon M. (2006) *J Am Chem Soc* **128**: 13293; (2005) *J Phys Chem A* **109**: 5217; (2006) *Phys Chem Chem Phys* **8**: 68.
50. Boero M *et al.* (2003) *Phys Rev Lett* **90**: 226403.
51. Shkrob IA *et al.* (2006) *J Phys Chem A* **111**: 5232.
52. Larsen RE *et al.* (2006) *J Phys Chem B* **110**: 20055 and (2005) *J Chem Phys* **123**: 234106; Prezhdo OV, Rossky PJ. (1996) *J Phys Chem* **100**: 17094.
53. Borgis D *et al.* (2006) *J Chem Phys* **125**: 064501.
54. Bedard-Hearn MJ *et al.* (2006) *J Chem Phys* **125**: 194509; (2005) *J Chem Phys* **122**: 134506; (2004) *J Chem Phys* **121**: 374.
55. Larsen RE, Schwartz BJ. (2003) *J Chem Phys* **119**: 7672; (2004) *J Phys Chem B* **108**: 11760; (2005) *J Phys Chem B* **110**: 1006 and 9692.
56. Helbert J *et al.* (1972) *J Chem Phys* **57**: 723; Yoshida H *et al.* (1973) *J Chem Phys* **58**: 3411; Bales BL *et al.* (1974) *J Phys Chem* **78**: 221; (1975) *J Chem Phys* **63**: 3008.
57. Jortner, J. (1959) *J Chem Phys* **30**: 839; Kestner NR. (1973) In *Electrons in Fluids*, (eds.) Jortner J, Kestner NR. Springer-Verlag, New York.

58. Sprik M *et al.* (1985) *J Chem Phys* **83**: 5802; (1986) *Phys Rev Lett* **56**: 2326; (1989) *J Chem Phys* **91**: 5665; (1988) *J Chem Phys* **89**: 1592; Marchi M *et al.* (1990) *J Phys Chem* **94**: 431.
59. Romero C, Jonah CD. (1988) *J Chem Phys* **90**: 1877; Miura S, Hirata F. (1994) *J Phys Chem* **98**: 9649.
60. Ogg RA. (1946) *J Chem Phys* **14**: 114 and 295; (1946) *Phys Rev* **69**: 243 and 668.
61. Ermoshin VA *et al.* (2002) *Chem Phys Lett* **356**: 556; Sobolewski AL, Domcke W. (2002) *J Phys Chem A* **106**: 4158; (2003) *Phys Chem Chem Phys* **5**: 1130; Neumann S *et al.* (2004) *Phys Chem Chem Phys* **6**: 5297; see also Symons RMC. (1988) *J Phys Chem* **92**: 7260; Hamelka HF *et al.* (1987) *J Phys Chem* **91**: 3150; Robinson GW *et al.* (1986) *J Phys Chem* **90**: 4224.
62. Scherer JPO, Fischer SF. (2006) *Chem Phys Lett* **421**: 427.
63. Son DH *et al.* (2001) *Chem Phys Lett* **342**: 571; (2001) *J Phys Chem A* **105**: 8269.
64. Gillis HA, Quickenden TI. (2001) *Can J Chem* **89**: 80.
65. Kroh J. (1991) In *Pulse Radiolysis*, (ed.) Tabata Y. CRC Press, Boca Raton, p. 358.
66. Holroyd RA. (2004) In *Charged Particle and Photon Interactions with Matter*, (eds.) Mozumder A, Hatano Y. New York, pp. 175.
67. Shkrob IA, Sauer Jr MC. (2002) *J Phys Chem A* **106**: 9120; Shkrob IA *et al.* (2002) *J Phys Chem A* **106**: 9132.
68. Barnett RB *et al.* (1988) *J Chem Phys* **93**: 8187.
69. Thomsen CL. (1999) *J Chem Phys* **110**: 3453; Madsen D *et al.* (2000) *J Chem Phys* **113**: 1126.
70. Keszei E *et al.* (1995) *J Phys Chem* **99**: 22.
71. Pepin C *et al.* (1994) *J Phys Chem* **98**: 7009.
72. Soroushian B. (2006) *J Phys Chem A* **110**: 1705; (2004) *Chem Phys Lett* **394**: 313.
73. Schwartz BJ, Rosicky PJ. (1994) *J Chem Phys* **101**: 6902 and 6917; Murphrey TH, Rosicky PJ. (1993) *J Chem Phys* **99**: 515.
74. Paik DH *et al.* (2004) *Science* **306**: 672; Turi L *et al.* (2006) *J Chem Phys* **125**: 014308 and references therein.
75. Zharikov AA, Fischer SF. (2006) *J Chem Phys* **124**: 054506.
76. Lian R *et al.* (2004) *J Chem Phys* **120**: 11712.
77. Crowell R *et al.* (2004) *J Phys Chem A* **108**: 9105.
78. Lindenberg AM *et al.* (2005) *J Chem Phys* **122**: 204507.
79. Kambhampati P *et al.* (2002) *J Phys Chem A* **106**: 2374.
80. Kee TW *et al.* (2001) *J Phys Chem A* **105**: 8434.
81. Gauduel Y *et al.* (1998) *J Phys Chem* **102**: 7795.
82. Andrianov I *et al.* (2005) *J Chem Phys* **122**: 234710; Gahl C. (2003) *Surf Sci* **532-535**: 108; and (2002) *Phys Rev Lett* **89**: 107402; Bowensiepen U. (2003) *J Phys Chem B* **107**: 8706.

83. Zhao J *et al.* (2006) *Chem Rev* **106**: 4402 and references therein.
84. Vebern JB *et al.* (1978) *Nature* **272**: 343; Warman JM *et al.* (1980) *J Phys Chem* **84**: 1240, (1983) *J Phys Chem* **87**: 4089 and 4096.
85. Barthel ER *et al.* (2003) *J Chem Phys* **118**: 5916; Shoshana O *et al.* (2006) *Phys. Chem. Chem. Phys.* **8**: 2599.
86. Turi L. (1999) *J Chem Phys* **110**: 10364.
87. Shida T *et al.* (1972) *J Phys Chem* **76**: 3683.
88. Pan X, Sanche L. (2005) *Phys Rev Lett* **94**: 198104; Pan X *et al.* (2003) *Phys Rev Lett* **90**: 208102; Zheng Y *et al.* (2006) *Phys Rev Lett* **96**: 208101.
89. Pastina B *et al.* (1999) *J Phys Chem A* **103**: 5841.
90. Narayana PA *et al.* (1975) *J Chem Phys* **63**: 3365.
91. Astashkin AV *et al.* (1988) *Chem Phys Lett* **144**: 258; Dikanov SA, Tsvetkov YD. (1992) *Electron Spin Echo Envelope Modulation (ESEEM) Spectroscopy*, CRC Press, Boca Raton, pp. 244–251.
92. Newton MD. (1975) *J Phys Chem* **79**: 2795; Clark T, Illing G. (1987) *J Am Chem Soc* **109**: 1013.
93. Symons RMC (1976) *Chem Soc Rev* **5**: 337.
94. Kaplan J, Kittel C. (1953) *J Chem Phys* **21**: 1429.
95. Hart EJ, Anbar M. (1970) *The Hydrated Electron*. Wiley-Interscience, New York.
96. Kevan L. (1978) *J Phys Chem* **82**: 1144.
97. Nielsen SO *et al.* (1976) *J Phys Chem* **80**: 2482.
98. Reid PJ *et al.* (1994) *Chem Phys Lett* **228**: 658.
99. Schwartz BJ, Rossky PJ. (1994) *Phys Rev Lett* **72**: 3282; Motakabbir KA *et al.* (1989) *J Chem Phys* **90**: 6916.
100. Shkrob IA. (2008) *Chem Phys Lett* **467**: 84.
101. Herbert JM, Head-Gordon M. (2006) *J Am Chem Soc* **128**: 13293.
102. Jordan KD, Wang F. (2003) *Annu Rev Phys Chem* **54**: 367; Hammer NI *et al.* (2006) *J Phys Chem* **109**: 11526; (2005) *J Phys Chem A* **190**: 7896; (2004) *Science* **306**: 675; Ayotte P *et al.* (1998) *J Chem Phys* **108**: 444.
103. Cabral do Couto P. (2005) *J Chem Phys* **123**: 054510.
104. Bradforth SE, Jungwirth P. (2002) *J Phys Chem A* **106**: 1286.
105. Schlick S *et al.* (1976) *J Chem Phys* **64**: 3153.
106. Schlick S, Kevan L. (1977) *J Phys Chem* **81**: 1083.
107. Shkrob IA, Marin TW. (2008) *Chem Phys Lett* **465**: 234.

Chapter 4

Instrumentation in Pulse Radiolysis

*Eberhard Janata**

1. Introduction

Pulse radiolysis has proven to be a powerful instrument in studying chemical processes of various kinds. It is one of the kinetic methods used in physical chemistry along with flash photolysis (Porter, Norrish), relaxation spectroscopy (Eigen), and stopped-flow/rapid-mixing. Because the chemical processes in pulse radiolysis normally occur at times much faster than the time resolution of the human eye, sophisticated instrumentation and equipment are required (i) to start the chemical process under observation, and (ii) to make a record of the chemical process. In pulse radiolysis, basically it is only the solvent that is altered by high-energy irradiation, not the chemicals under investigation. The solvent most often used is water, for which the yields and characteristics of the irradiation products are already well known. Irradiation is performed in most cases by high-energy electrons which are able to penetrate several centimeters of water.

* Helmholtz Zentrum Berlin für Materialien und Energie GmbH, Bereich Materialien für die Solarenergietechnik, Glienicker Str. 100, 14109 Berlin, Germany. E-mail: janata@helmholtz-berlin.de

Instrumentation has undergone drastic changes since the first successful performance of pulse radiolysis experiments some 50 years ago.¹ In keeping with the purpose of this book, recent trends in the instrumentational realization of detection methods, in accelerators, and in the application of computers are discussed in this chapter.

2. Instrumentation

2.1. General

To start the chemical processes under investigation, irradiation produces chemically highly reactive species at intervals generally much shorter than the observation period. In most cases irradiation is performed by high-energy electrons produced by suitable accelerators. Figure 1 depicts the basic arrangement of a pulse radiolysis facility. The measuring cell, which contains the solvent and the chemicals

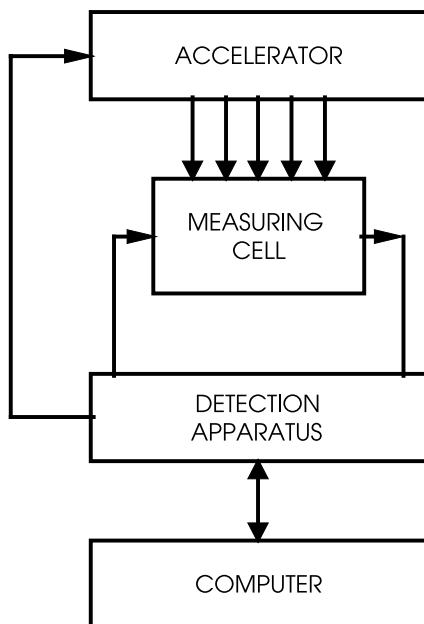


Fig. 1. Schematic of a pulse radiolysis apparatus.

under investigation, is irradiated homogeneously. The detection apparatus consists of appropriate devices depending on the physical properties being studied, i.e. an analyzing light source and a photodetector for optical detection, or, a voltage generator and an electrical detection circuit for conductometric studies. A device for recording the kinetic voltage vs. time curves is also necessary. A computer may be used to store the transient curves for later analysis or may even be used to control the entire experiment.

2.2. Accelerators

Accelerators supply high-energy particles, such as electrons, in most cases in the form of short pulses which are utilized to produce chemical changes in the solvent, such as splitting water into highly reactive species. The energy of the particles is high enough to produce reactive species but is low enough to prevent collisions with atomic nuclei and thus avoids generation of radioactive species. The usual energy lies in the order of some MeV, thus the speed of high-energy electrons is more than 99% of the speed of light in vacuum and the penetration depth in water is in the range of a few centimeters. These electron pulses should exhibit reproducible energy, timing, and charge per pulse.

The methods for accelerating electrons commonly in use in pulse radiolysis are (i) Febetrons, which use the principle of a Marx generator to produce high energy pulses of up to 2 MeV, (ii) electrostatic accelerators, such as Van de Graaff accelerators or Peletrons, by which a high DC-voltage of several million volts is utilized to accelerate the electrons, and (iii) linear accelerators, which use high-power, high-frequency electrical waves. Recent linear accelerator installations can be found at the Radiation Laboratory of the University of Notre Dame, at CEA/Saclay, and at the Pune University Linac Facility (PULAF). These linear accelerators use either magnetrons or klystrons as a source of high-power r.f.-energy, up to 10 MW during the pulse, in the Gigahertz frequency range, i.e. S-band (2998 MHz). They provide high-energy electrons in the 7–10 MeV range. The PULAF accelerator, for example, generates single and repetitive pulses with

pre-settable durations between 10 ns and 3 μs .² Febetrans produce very high peak currents of some thousand amperes, the peak current needs to be attenuated in order to achieve doses suitable for pulse radiolysis experiments. In order to overcome problems in pulse timing, some Van de Graaff accelerators have been modernized to generate either pulses with sub-nanosecond duration and an 80 ns pre-trigger signal³ or to deliver pulses from 2 ns to 1 μs duration, selectable in 1 ns steps, with time uncertainties as low as 10 ps.⁴ The latter version can also produce trains of pulses with intervals between the pulses as short as 150 ns. High doses per pulse corresponding to about 1×10^{-6} mol dm⁻³ of hydrated electrons per 1 ns of pulse duration are also achieved. Automatic conditioning of a Van de Graaff accelerator as a procedure performed each day has also been reported.⁵

2.3. *Detection apparatus*

The interaction of high-energy irradiation with the solvent in the measuring cell creates short-lived species of various kinds which are to be detected and the changes in their concentrations to be recorded. In pulse radiolysis, two methods of detection are common: (i) optical detection, which is widely used because every species exhibits a specific "color," i.e. an absorption spectrum of its own, and (ii) conductometric methods for the detection of charged species. The time scale during which the transients are recorded depends on the needs of the laboratory. Here, we will concentrate on "real time" experiments with time scales ranging from a few tens of nanoseconds to hours. Methods utilizing sampling techniques for time scales well below a nanosecond will be covered in Chap. 5 of this book.

In general, optical experiments can be done by either observing absorption at a certain wavelength and by recording one absorption vs. time curve per irradiation or by recording one complete spectrum at a given time per irradiation. In "real time" experiments, recording kinetic traces at a given wavelength is the method most commonly practiced. For recordings slower than a few milliseconds the recording of complete spectra at given times has been achieved.

The intensity of the analyzing light and the absorbed dose per pulse need to be both known and documented for reproducible recordings.

2.3.1. *Measuring cell*

The measuring cell contains a solution of the chemical system under investigation. The cell can be constructed as a flow cell allowing the easy exchange of solution in between irradiation pulses. The optical windows should be planar and parallel. Where optical absorption measurements are to be taken at normal pressures and temperatures, the cell is made of fused silica in order to minimize radiation damage. High-purity fused silica, such as SUPRASIL II, seems practically unaffected by irradiation and the inherent radiation-induced absorption can be neglected.⁶ In experiments utilizing high pressure and/or high temperature, cells need to be specially constructed and sapphire is used for the optical windows.⁷ The measuring cells for conductivity or for combined optical and conductometric experiments contain electrodes of appropriate form and material; they are discussed later in the paragraph describing conductometric techniques.

2.3.2. *Optical detection*

To be detected optically, species must absorb light. The basis for optical detection is the law of Lambert–Beer:

$$J = J_0 - \Delta J(t) = J_0 \cdot 10^{-OD}, \quad (1)$$

with J_0 the light intensity in front of the cell, J the intensity behind the cell and $\Delta J(t)$ the — usually transient — change in light intensity. The apparatus for optical detection basically utilizes the analyzing light source, a lamp, the measuring cell, and the detector, a photo-detector, as depicted in Fig. 2. The photo-detector converts the intensity of the analyzing light into an electrical signal, under ideal condition both signals are linearly related. A photo-detector regardless of the type, is in electrical terms, a current source; its output is always an electrical current. A load resistor R_L is required to transform the current signal into a voltage signal. The current, or the change in

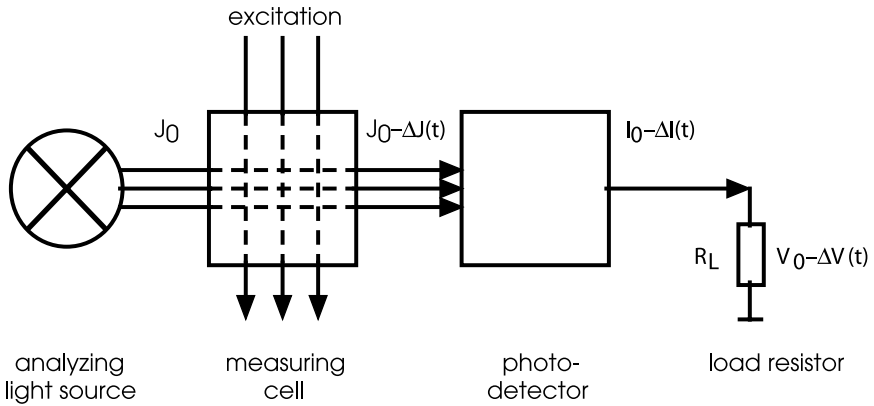


Fig. 2. Basic optical detection.

current, is independent of the value of the load resistor. Subsequently, the electrical voltage signal can be recorded. In some cases, the steady state current of the photomultiplier is compensated for and measured so that only the transient signal is recorded.

As the sources of analyzing light, xenon arc lamps are in common use because they emit a continuous spectrum from 200 nm up to several μm without strong lines, i.e. white light. They consume electrical power between 150 W and 450 W and are available without reflector, such as XBO 150 or XBO 450 lamps, or with a built-in reflector, such as a 175-W Cermax lamp. For short time measurements, light intensity can be enhanced for a few milliseconds by increasing the electrical power. The lamp housing also contains lenses for focusing the light. A monochromator is necessary for selecting the wavelength at which the kinetic trace should be recorded. Such a monochromator is mounted close to the photo-detector. Monochromators use prisms or gratings to diverge the light, double-prism or double-grating monochromators are used in order to avoid stray light especially in the near-UV range but also exhibit high attenuation. High-transmission bandpass UV filters (Schott UV-R series) are also in use. On the other hand, light sources, such as LEDs and lasers, which only emit at a particular wavelength can also be used as the analyzing light source thus eliminating the need for a monochromator and its inherent loss

in light intensity. An electrically actuated shutter is normally mounted between the light source and the measuring cell so that the analyzing light only penetrates the cell during measurements in order to minimize potential photolysis in the solution under investigation.

Two kinds of photo-detectors are in use, a photomultiplier tube and a semiconductor photodiode. They exhibit various features such as gain, time or frequency response, and response to the light spectrum. Photomultipliers exhibit gains ranging from 10^2 to 10^6 and cover the spectral range from below 200 nm to about 900 nm. Side-window types, such as the 1P28, R928 or R955, are in common use. Their output current is linear with light intensity, depending on the external circuitry, up to about 0.5 mA for constant light operation and up to 5 mA and more when the analyzing light intensity is intensified for a few milliseconds. Transition times of photomultiplier tubes are in the order of a few nanoseconds due to long internal connections. They can be reduced to the sub-nanosecond time domain simply by shortening the internal connections.⁸ More recently, compact-sized photomultipliers, such as the R7400U series, have become available which cover the same optical range but exhibit, due to their small size, superior time response.⁹ Figure 3 shows a side-window type photomultiplier tube next to a compact-sized one.



Fig. 3. Side-window PMT (bottom) and compact size PMT (top).

Semiconductor photo-detectors exhibit low sensitivity in the near-UV range but find usage in the near-IR range. The useful spectral range depends on the semiconductor material, up to 1100 nm for silicon photodiodes, up to 1700 nm for germanium or InGaAs photodiodes, and, up to 3.6 μm for InAs photodiodes. The capacity of the junction determines the time response, i.e. the larger the active area of the photodiode, the slower the time response. Germanium, Si and InGaAs avalanche photodiodes are also available exhibiting internal gains between 10 and 100; the gain depends strongly on temperature. Transition times in the order of one nanosecond or less can easily be achieved.

The use of a commercially available diode array multichannel detector is also described.¹⁰ The advantage of using such a detector is the ability to immediately record a complete spectrum from near UV to IR with one measurement. The detector is a linear photodiode array consisting of 1024 diodes. It takes 25 ms to record the full spectrum, making the apparatus suitable for applications which start in the millisecond time domain. The experiment, i.e. the arbitrary recording of the spectra as well as the irradiation of the sample, is controlled by a computer program according to a timetable which is preset individually.

Optical fibers can be used to convey light from one point to another, for example, from the lamp to the cell or from the cell to the photo-detector. While plastic fibers exhibit fairly high losses, silica fibers have lower losses. Losses in silica fibers depend on the way they are manufactured, i.e. on the kind and amount of dopants. Attenuation varies with wavelength and ranges from 1000 dB/Km at 200 nm to about 1 dB/Km at between 1000 nm and 1600 nm and increases again at longer wavelengths. The losses at wavelengths below 1000 nm are mainly determined by Rayleigh scattering and are inversely proportional to wavelength taken to the fourth power.¹¹

2.3.3. *Conductometric detection techniques*

Charged species generated during an experiment can be detected using conductometric methods. Such measurements often provide

additional information on the reaction mechanism, especially if species of high molar conductance, such as protons, hydrated electrons or hydroxide ions are involved.¹² The apparatus for measuring the transient conductance basically consists of a suitable measuring cell, a load resistor, both forming a voltage divider string, and the voltage source applied to the divider string. The measuring cell contains electrodes which are in contact with the solution under investigation; the measuring cell could also be regarded as a current source. The principle is depicted in Fig. 4(a) with G_C representing the intrinsic conductance of the measuring cell, G_L the conductance of the load resistor, and $\Delta G_C(t)$ the additional transient conductance. As the current through the cell changes due to transient charged species being generated in the cell, the voltage $\Delta V_S(t)$ across the load resistor changes simultaneously.

Either AC-voltages or DC-voltages can be used for the supply voltage V . For constant sensitivity, the voltage across the measuring cell should be nearly equal to the supply voltage V ; this is obtained when the conductance of the load resistor is much greater than that of the measuring cell. A bridge configuration, as depicted in Fig. 4(b), could be used to compensate for the steady state current through the cell. An AC-bridge configuration with a synchronous detector and powered by a 10-MHz voltage source allows to distinguish between

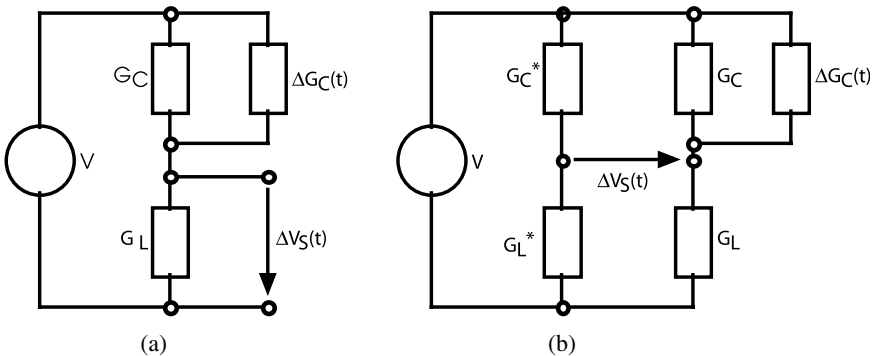


Fig. 4. Schematic of conductometric detection. (a) The voltage divider string. (b) The bridge configuration.

an increase or a decrease in the concentration of charged species and permits measurements with a time resolution of some microseconds.¹³ For experiments involving larger molecules, where the measuring frequency may influence conductance, a bridge configuration with a synchronous detector and a supply voltage of variable frequency has been utilized.¹⁴

Measurements on a shorter time scale use a simple voltage divider string configuration to which a DC-voltage pulse is applied. Several physical effects need to be considered when conductometric measurements with nanosecond or microsecond time resolution are required to supplement optical measurements. There is a spurious negative signal superimposed on the transient conductance signal which makes it difficult to record. This spurious signal results from beam electrons striking the electrodes of the measuring cell and can be several orders of magnitude larger than the conductance signal. The time which elapses after the pulse before meaningful measurements can be made depends on how fast the detection system recovers from the overload caused by this spurious signal. A balanced-to-unbalanced transformer and a symmetrical cell arrangement is suitable to minimize the spurious signal.¹⁵ A limiting amplifier has also been reported which limits the beam induced signal to values that allow the oscilloscope amplifier to recover from overload during some tens of nanoseconds; the conductivity signal is not affected by this amplifier.¹⁶ Both of these approaches allow measurements to be taken about 100 ns after the beginning of the electron pulse. Furthermore, the use of a conventional cell made of quartz with platinum electrodes results in two spurious signals in addition to that of the negative beam induced signal.¹⁷ Both differ in decay time: one is only present for about 100 ns after irradiation, the second occurs for several microseconds. Both amplitude and polarity depend on the voltage across the cell. The first signal apparently results from ionization of the air surrounding the cell. The observed half-life for the decay of this component of about 15 ns agrees with that reported for thermal electron attachment in O₂-N₂ mixtures under atmospheric conditions.¹⁸ The second signal is probably caused by a build-up of charge in the quartz walls of the cell during irradiation.¹⁹ In addition, it was found

that when platinum electrodes were used, poisoning of them frequently occurred resulting in distortions of the baseline in the microsecond range. Glassy carbon, which conducts and is apparently inert, has proven to be a far better material for electrodes in all kinds of conductometric cells. A unique cylindrical cell has been constructed using glassy carbon material for both the electrodes and the outer tube. A suitable cell housing provides a 50- Ω connection for the signal line. This allows measurements to be taken over a pH range of 3 to 11.5, beginning about 7 ns after a fast electron pulse.¹⁷

2.3.4. *Other detection methods*

In some laboratories, other methods for detecting chemical changes are connected to pulse radiolysis and thus contribute additional information. For example, kinetic line-broadening techniques, such as NMR and the related EPR techniques are ideal for monitoring proton or hydrogen atom reactions²⁰⁻²³; time-resolved resonance Raman spectroscopy is used to study the reactions of aqueous protons with zwitterions.²⁴ Time-resolved circular dichroism is coupled to pulse radiolysis for studying the reduction of ferricytochrome c in neutral aqueous solutions.²⁵ The polarographic method is also combined with pulse radiolysis. The radicals are produced by a pulse of high-energy electrons in the vicinity of a dropping mercury electrode. The polarogram is obtained by recording the current versus time curves at various potentials of the electrode.²⁶⁻²⁸

2.4. *Auxiliary circuits*

The output signals of the photo-detector or the conductometric detector must somehow be recorded versus time. Basically, the detector can be connected directly to the vertical input of an oscilloscope where a trigger signal starts the horizontal sweep of the time base. The trigger signal needs to be synchronized with the excitation pulse. For linear accelerators, the trigger signal for the experiment is derived from the accelerator timing system; the trigger signal may be synchronous with the accelerating r.f.-field.²⁹ Van de Graaff type

accelerators are not bound to such limitations. If measurements in the millisecond time regime are required, the synchronization of the experiment to the mains is feasible, especially if baseline subtraction is realized in order to eliminate signals induced by the mains being superimposed on the detector signal.

As mentioned above, optical or conductometric detectors are themselves current sources. The intensity of the voltage at the detector output therefore depends on the value of the load resistor, as does time response. The time constant is represented by the product of load resistance and capacity, which along with the capacity of the detector and the input capacity of the oscilloscope, is primarily derived from the capacity of the connecting coaxial cable, 68 pF/m for the commonly used RG58/U type. Terminated coaxial cables do not exhibit this capacity, but an upper frequency limit depending on cable length and due to cable losses and cable dispersion also needs to be taken into account. Cable losses vary from 0.05 dB/m at 10 MHz to about 0.6 dB/m at 1000 MHz for RG58/U cables. A terminated 50- Ω system is the choice for measurements from the nanosecond time scale onwards. Broadband amplifiers in 50 Ω technology may be employed to increase the sensitivity of the recorder where necessary, as for example when using a semiconductor photo-detector. Such amplifiers should cover a broad frequency range and should exhibit low input noise and, ideally, no input bias current, because the latter will superimpose on the detector steady-state current. Such an amplifier has recently been described.³⁰ Coaxial switches are needed to insert the amplifier into the signal line.

Displaying optical data in units of optical density requires the knowledge of the steady-state detector current before excitation. This could be done simply by recording the full signal, i.e. $V_0 - \Delta V(t)$ in Fig. 1, and making a software compensation for the steady state component V_0 . In this case, detection sensitivity is determined by the vertical resolution of the digital recording scope. More sophisticated systems use a baseline compensation circuit in order to compensate for and measure the background current I_0 .^{31,32} In this case, only the transient current creates a voltage drop across the load resistor, thus allowing the use of a pre-amplifier. This way, optical densities as small

as 1×10^{-4} could be recorded.³³ With the introduction of digital storage for the compensation current, the length of the usable time range is no longer limited.³² Usage in the picosecond time domain is also possible.³⁴

The knowledge of the exact value of the excitation, i.e. the charge of the electron pulse, in each single experiment is essential in pulse radiolysis for precise normalization during signal averaging, for calculation of optical and conductometric curves as well as for a general understanding of the experiment. A monitoring device should be able to provide an electrical signal, normally a voltage, which is precisely proportional to the area under the curve of the excitation pulse intensity over time. One basic method is the measurement of secondary electrons generated in a thin metal foil through which the electron beam passes, i.e. a secondary emission foil.^{1,35,36} Another method is the measurement of a signal which is induced by the beam when passing through a coil, i.e. a current transformer.³⁷⁻⁴² A third method involves stopping the beam in a solid metal block, i.e. a Faraday cup. The secondary emission foil and the Faraday cup deliver signals which can be interpreted directly. The beam is slightly distorted, however, in passing the secondary emission foil. The Faraday cup is mounted behind the measuring cell; any changes in density of the medium under investigation will influence the calibration. The use of a current transformer allows measurement without distorting the beam, but has the drawback of generating an oscillating response signal, which is sometimes difficult to interpret. Another method, and the newest development, is the use of Cherenkov emission created in a "foil" of optical fibers as an indicator of the excitation.⁴³ The use of Cherenkov emission in single optical fibers as a beam loss monitor for the surveillance of accelerators of long length has also been described recently.¹¹ The dimensions of the fiber foil are larger than the diameter of the beam in order to monitor the whole beam. High sensitivity and accuracy are achieved in the measurement with only slight distortion of the beam. Because the Cherenkov emission coincides with the beam profile, this method can ideally be applied to the measurement of excitation pulses of various duration, and especially to those having durations in the picosecond to nanosecond time domain

where other methods begin to reach their limits in time resolution. The integration circuit is basically the same for all detectors and should allow automatic zeroing.⁴⁴

In the near UV region, the intensity of the Cherenkov light, which is inevitably emitted as the beam electrons pass the measuring cell, becomes more and more disturbing. The intensity of the Cherenkov emission is proportional to the inverse of the wavelength to the second power. Also, the intensity of xenon lamps decreases considerably in the UV region. One solution is to intensify the analyzing light by pulsing the electrical power consumed by the lamp to a much higher value for a few milliseconds.⁴⁵⁻⁵⁰ This way, usable time is reduced to some hundred microseconds while the gain in light intensity is 60-fold at 700 nm and more than 400-fold at 240 nm.⁵⁰

Today, digital recording devices are in common use in pulse radiolysis experiments for recording the transient voltage vs. time. A variety of such recorders is offered by various manufacturers with eight to twelve bit vertical resolution, analog bandwidths up to a few GHz and sensitivities down to 1 mV/div, sampling rates of up to 20 Giga samples/s and recording lengths of as long as several million samples per run. The high sample rate and extensive recording length allow "horizontal" averaging by which several channels are averaged into one thus improving the signal-to-noise ratio noticeably.

2.5. Computer aided experiments

It has been a long way from the early pulse radiolysis experiments where pictures were taken from the oscilloscope screen,¹ via the first application of a computer to record experimental curves,⁵¹ to today's computer-aided kinetic experiments. Such a computer-aided experiment should feature easy performance, precision in calculating data, and, most importantly, should eliminate human error. However, a certain standard in data acquisition hardware is also required, such as depicted in Fig. 5 for the simultaneous recording of two channels.⁵² The hardware for processing the electrical signals is the same for both channels allowing various detectors, such as photomultipliers, semiconductor photodiodes, or circuits for detecting conductometric

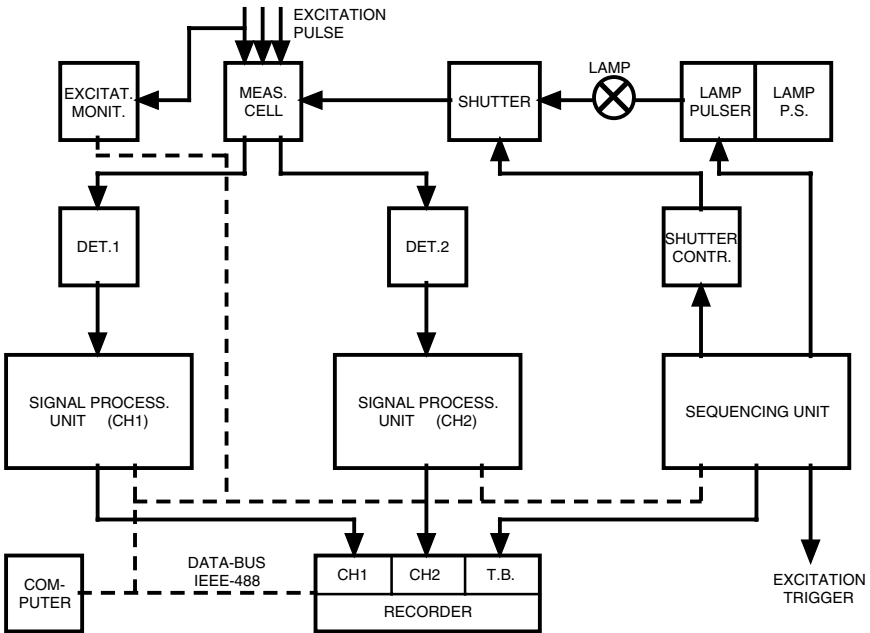


Fig. 5. Schematic of a computer-aided pulse radiolysis detection apparatus.

changes, to be employed. The sequencing unit controls the timing for the whole experiment, for the optical shutter and for the lamp pulser, as well as for the digital recorder and for the excitation pulse in such a way that a short but fixed portion of the sweep always occurs before the pulse, independent of the recording time. Computer-aided kinetic experiments allow several features to be performed such as (i) entering and storing the experimental parameters and setting the respective devices accordingly, (ii) controlling the run of the experiment as well as data capturing and processing, (iii) storage, retrieval and analysis of data, and, (iv) special functions. For example, the experimental parameters determine the conditions under which an experiment is carried out. They separate basically into three categories: (1) parameters for controlling the experiment, such as number of averages, time interval between recordings, deciding whether baseline recoding and the lamp pulser are initiated; (2) individual parameters for controlling

the recording of each channel when simultaneous multi-channel recording is activated, such as, recording time, sensitivity, offset, bandwidth, pre-amplification, wavelength, etc.; and (3) parameters for the calculation of data, such as recording mode, G-value, length of the optical path of the measuring cell.

In running the experiment, averaging data in order to improve signal-to-noise ratio is one of the most important features of computer-aided experiments. During the last few years several results have only become possible by extensive signal averaging. One has to keep in mind that most pulse radiolysis experiments utilize concentrations of a few micromol and that absorptivity is already very low, so low that it extends beyond the limits of commercially available steady-state photospectrometer. In some cases quite a few of averages need to be performed because noise reduction is proportional to the square root of the number of experiments.

Data curves together with all associated parameters are stored on mass storage media. At retrieval, the stored curves and the related parameter are loaded and can be modified. After retrieval, (1) data can be plotted as multiple kinetic curves, and each individual curve, can be the average of several stored experiments, (2) spectra can be constructed at selected times from a file of kinetic curves recorded at various wavelengths, (3) computer simulation can be carried out and compared immediately with the kinetic data, as discussed below.

One special function would be dosimetry which establishes a relationship between the voltage provided by the beam monitor and the absorbed irradiation dose. For convenience, in several experimental set-ups dose is expressed as the initial radical concentration in the measuring cell. From optical measurements, the concentration can be calculated for a known molar absorptivity. The plot of concentration vs. the electrical value should result in a straight line. The slope and, possibly, a small intercept, are stored as the dosimetry data. If in a second channel the conductance is measured simultaneously, the cell constant can be determined for a known change in conductance.

Last, but not least, computer simulation of experimental kinetic curves should be discussed. Computer modeling of the kinetics of a

reaction mechanism is often essential for the quantitative understanding of the results obtained in kinetic spectroscopy including the evaluation of rate constants, as well as for the careful design of complex kinetic experiments. An isothermal multi-component chemical reaction system can be described by a set of kinetic equations which are solved numerically, see for example Ref. 53 and the publications cited therein. Although using a simple integration method, this version benefits from the ability to superimpose the results of the simulation onto the experimental data for direct comparison. This comparison enables the rate constants to be determined with high accuracy. Furthermore, data for the reaction mechanism can be conveniently entered. For documentation purposes, the experimental curve and the calculated ones can be plotted, the parameters of the reaction mechanism can be printed, or the simulation and the experimental curve can be stored on disk. An exclusive feature of this program is the facility to simulate a train of pulses which can be used to examine multiple pulse experiments or the kinetics during long pulse durations. In general, one has to keep in mind that even a well-working simulation model does not necessarily represent the only possible explanation for experimental data. If the results of the simulation are interpreted most cautiously and carefully, however, simulation can turn out to be most helpful.

3. Summary

This discourse tries to give an overview of the current state-of-the-art instrumentation in real-time pulse radiolysis experiments utilizing optical, conductometric and other methods. Pump-and-probe techniques for the sub-nanosecond time domain are believed to be beyond the scope of this discussion.

4. Appendix

4.1. *Calculation of optical properties*

First a voltage vs. time curve is calculated from the raw data obtained from the recorder. The time scale is calculated by multiplying the

number of each point with the x -increment (time/point). The voltage value is calculated by multiplying the raw data with the y -increment (volt/bit) and considering the gain of a possible pre-amplifier, as

$$\Delta V = \text{DATA}_{\text{raw}} \cdot \Upsilon_{\text{incr}}/A_{\text{preamp}}, \quad (\text{A1})$$

or, if the baseline is subtracted, as

$$\Delta V = \{\text{DATA}_{\text{raw}}(E) - \text{DATA}_{\text{raw}}(Z)\} \cdot \Upsilon_{\text{incr}}/A_{\text{preamp}}, \quad (\text{A2})$$

where $\text{DATA}_{\text{raw}}(E)$ is the raw data recorded with excitation and $\text{DATA}_{\text{raw}}(Z)$ the data without excitation. In the case of optical entities, $\Delta V/I_0$ is first calculated as

$$\Delta V/I_0 = \{\text{DATA}_{\text{raw}}(E)/I_0(E) - \text{DATA}_{\text{raw}}(Z)/I_0(Z)\} \cdot \Upsilon_{\text{incr}}/A_{\text{pre}} \quad (\text{A3})$$

where the raw data are divided by the respective light levels.

For the calculation of the $\Delta I/I_0$ curve, the $\Delta V/I_0$ data are simply divided by the load resistor R_{load} :

$$\Delta I/I_0 = (\Delta V/I_0)/R_{\text{load}}. \quad (\text{A4})$$

The change in absorbance, i.e. in optical density ΔOD , is calculated and normalized to a cell length of 1 cm, according to

$$\Delta OD = -\log(1 - \Delta I/I_0)/L_{\text{cell}}. \quad (\text{A5})$$

Dividing ΔOD by the respective initial radical concentration c_{init} and the density of the solution ρ results in the presentation of the kinetic data in units of molar absorptivity

$$\Delta \Theta = \Delta OD/(c_{\text{init}} \cdot \rho) [\text{dm}^3 \text{ mol}^{-1} \text{ cm}^{-1}], \quad (\text{A6})$$

which allows easy comparison of kinetic curves taken for various excitation doses or with published ε values. The initial radical concentration is determined from electrical measurements of the charge of the beam pulse (see dosimetry).

4.2. *Calculation of conductometric properties*

For the voltage divider string arrangement of Fig. 4(a), the signal voltage is written as

$$\begin{aligned}\Delta V_s(t) &= V_{s0} + \Delta V_s(t) \\ &= \{G_C + \Delta G_C(t)\} \cdot V / \{G_L + G_C + \Delta G_C(t)\}.\end{aligned}\quad (\text{A7})$$

For $G_L \gg \Delta G_C(t)$ and $G_L \gg G_C$, it follows that

$$\Delta V_s(t) = \{G_C + \Delta G_C(t)\} \cdot V / G_L. \quad (\text{A8})$$

Similarly, for the bridge configuration of Fig. 4(b),

$$\Delta V_s(t) = \Delta G_C(t) \cdot V / G_L. \quad (\text{A9})$$

Clearly, the signal voltage obtained for the voltage divider string contains a constant value representing the conductance of the intrinsic ion concentration in the cell, whereby this term is omitted in the bridge configuration. The signal voltage is linearly dependent on the supply voltage V ; the higher V is the more sensitive is the measurement. The change in molar conductance is calculated as

$$\Delta \Lambda(t) = (\Delta V_s(t) \cdot C_{\text{cell}} \cdot 1000) / (V_{\text{cell}} \cdot R_{\text{load}} \cdot c_{\text{init}}), \quad (\text{A10})$$

where C_{cell} is the cell constant, V_{cell} the voltage applied to the cell and R_{load} the load resistor.

4.3. Dosimetry

In dosimetry, the initial radical concentration c_{init} is calculated for a known value of molar absorptivity (ϵ_{known}) as

$$c_{\text{init}} = OD / (\epsilon_{\text{known}} \cdot \rho) \quad (\text{A11})$$

and can readily be used for the calculation of a relation between radical concentration and an electrical value related to the beam charge. The optical density OD is here already normalized to a cell length of 1 cm and ρ is the density of the solution. If in another channel the conductance is measured simultaneously, the cell constant C_{cell} of the measuring cell is determined for a known change in conductance and the initial radical concentration by

$$C_{\text{cell}} = (\Delta \Lambda_{\text{known}} \cdot V_{\text{cell}} \cdot R_{\text{load}} \cdot c_{\text{init}}) / (\Delta V_s(t) \cdot 1000). \quad (\text{A12})$$

4.4. Noise and signal-to-noise ratio

For electronic equipment, two different sources of noise are important: firstly, thermal or Johnson noise, caused by charged particles undergoing continuous random motion, and secondly, “shot noise,” because the passage of current through electronic devices is accomplished by the movement of discrete charges. For the voltage generated by thermal noise, it follows that

$$V_{\text{tn}} = (4 \cdot R \cdot k \cdot T \cdot Bw)^{1/2}, \quad (\text{A13})$$

with R the resistance of the electronic element, k the Boltzmann constant ($1.38 \times 10^{-23} \text{ J K}^{-1}$), T the temperature in Kelvin, and Bw the bandwidth of the circuit.

The voltage generated by “shot” noise is

$$V_{\text{sn}} = R \cdot (2 \cdot q \cdot I \cdot Bw)^{1/2}, \quad (\text{A14})$$

with q the charge of each charge carrier and I the total current through the device.

The total noise is the sum of both. If noise is random, it increases under summation as the square root of the number of experiments averaged, while the signal increases linearly. The signal-to-noise ratio improves with the square root of the number of experiments n

$$S/N = \text{const} \cdot \sqrt{n}. \quad (\text{A15})$$

Signal-to-noise ratio is improved similarly by “horizontal” averaging as long as the data in the channels to be averaged are not governed by the time constant of the detection system, i.e. they contain white noise.

References

1. Keene JP. (1964) Pulse radiolysis apparatus. *J Sci Instrum* **41**: 493–496.
2. Yadav P, Kulkarni MS, Shirdhonkar MB, Rao BSM. (2007) Pulse radiolysis: Pune University LINAC facility. *Current Science* **92**: 599–605.
3. Luthjens LH, Vermeulen MJW, Hom ML, Loos MJ, de Geer SB van der. (2005) Revision of (sub)nanosecond pulser for IRI Van de Graaff electron accelerator aided by field propagation calculations. *Rev Sci Instrum* **76**: 024702.

4. Janata E, Gutsch W. (1998) Instrumentation of kinetic spectroscopy-15. Injector pulse generators for electron accelerators, Part 3. *Radiat Phys Chem* **51**: 65–71.
5. Janata E. (1992) Instrumentation of kinetic spectroscopy-9. Use of a computer for automatic performance of start-up procedures on a 4 MeV van de Graaff electron accelerator. *Radiat Phys Chem* **40**: 217–223.
6. Janata E. (2006) Transient absorption in fused silica by trains of high-energy electron pulses. *Chem Phys Lett* **417**: 170–172.
7. Takahashi K, Cline JA, Bartels DM, Jonah CD. (2000) Design of an optical cell for pulse radiolysis of supercritical water. *Rev Sci Instrum* **71**: 3345–3350.
8. Beck G. (1976) Operation of a 1P28 photomultiplier with subnanosecond response time. *Rev Sci Instrum* **47**: 537–541.
9. Janata E. (2007) Instrumentation of kinetic spectroscopy-21. The use of a compact size photomultiplier tube in kinetic spectroscopy. *Radiat Phys Chem* **76**: 1156–1159.
10. Janata E. (2003) Instrumentation of kinetic spectroscopy-17. The use of a diode array multichannel detector in kinetic experiments. *Radiat Phys Chem* **66**: 145–148.
11. Janata E. (2002) Determination of location and intensity of radiation through detection of Cherenkov emission in optical fibers. Part 1. Method and experimental. *Nucl Instr and Meth A* **493**: 1–7.
12. Asmus K-D, Janata E. (1982) Conductivity monitoring techniques. In: Baxendale JH, Busi F (eds.), *The Study of Fast Processes and Transient Species by Electron Pulse Radiolysis*, pp. 91–113. D Reidel Publishing Company.
13. Janata E, Lilie J, Martin M. (1994) Instrumentation of kinetic spectroscopy-11. An apparatus for a.c.-conductivity measurements in laser flash photolysis and pulse radiolysis experiments. *Radiat Phys Chem* **43**: 353–356.
14. Bothe E, Janata E. (1994) Instrumentation of kinetic spectroscopy-13. A.C.-conductivity measurements at different frequencies in kinetic experiments. *Radiat Phys Chem* **44**: 455–458.
15. Maughan RL, Michael BD, Anderson RF. (1978) The application of wide band transformers to the study of transient conductivity in pulse irradiated aqueous solutions by the d.c. method. *Radiat Phys Chem* **11**: 229–238.
16. Janata E. (1980) Submicrosecond pulse radiolysis conductivity measurements in aqueous solutions-I. Experimental section. *Radiat Phys Chem* **16**: 37–41.
17. Janata E. (1982) Pulse radiolysis conductivity measurements in aqueous solutions with nanosecond time resolution. *Radiat Phys Chem* **19**: 17–21.
18. Shimamori H, Hatano Y. (1976) Mechanism of the thermal electron attachment in O₂-N₂ mixtures. *Chem Phys* **12**: 439–445.
19. Balkas TI, Fendler JH, Schuler RH. (1970) Radiolysis of aqueous solutions of methyl chloride. The concentration dependence for scavenging electrons within Spurs. *J Phys Chem* **74**: 4497.

20. Eiben K, Fessenden RW. (1971) Electron spin resonance studies of transient radicals in aqueous solutions. *J Phys Chem* **76**: 1186–1201.
21. Beckert D, Mehler K. (1983) Investigations of hydrogen atom addition to vinyl monomers by time resolved ESR spectroscopy. *Ber Bunsenges Phys Chem* **87**: 587–591.
22. Mezyk S, Bartels DM. (1997) Rate of hydrogen atom reaction with ethanol, ethanol-d₅, 2-propanol, and 2-propanol-d₇ in aqueous solution. *J Phys Chem A* **101**: 1329–1333.
23. Shkrob IA, Tadjikov BM, Trifunac AD. (2000) Magnetic resonance studies on radiation-induced point defects in mixed oxide glasses. I. Spin centers in B₂O₃ and alkali borate glasses. *J Non-Cryst Solids* **262**: 6–34.
24. Tripathi GNR. (2005) Time resolved resonance Raman observation of the extreme protonation forms of a radical zwitterions in water. *J Chem Phys* **122**: 071102.
25. O'Connor DB. (1994) Pulse radiolysis with circular dichroism detection. *Radiat Phys Chem* **44**: 371–376.
26. Lilie J, Beck G, Henglein A. (1971) Pulseradiolyse und Polarographie: Halb-stufenpotentiale für die Oxydation und Reduktion von kurzlebigen organischen Radikalen an der Hg-Elektrode. *Ber Bunsenges Phys Chem* **75**: 458–465.
27. Henglein A. (1976) Pulse radiolysis and polarography. Electrode reactions of short-lived free radicals. In: Bard AJ (ed.), *Electroanalytical Chemistry — A Series of Advances*, Vol. 9, pp. 163–244. Marcel Dekker Inc, New York.
28. Asmus K-D, Janata E. (1982) Polarography monitoring techniques. In: Baxendale JH, Busi F (eds.), *The Study of Fast Processes and Transient Species by Electron Pulse Radiolysis*, pp. 115–128. D Reidel Publishing Company.
29. Janata E. (1986) On the generation of trigger pulses synchronous with the accelerating r.f.-field of a linear L-band accelerator. *Radiat Phys Chem* **28**: 403–406.
30. Janata E. (2003) Instrumentation of kinetic spectroscopy-18. A wideband dc-coupled amplifier. *Radiat Phys Chem* **66**: 215–218.
31. Keene JP, Bell C. (1973) Automatic circuits for backing off the photodetector signal in kinetic spectroscopy. *Int J Radiat Phys Chem* **5**: 463–477.
32. Janata E. (1986) A baseline compensation circuit for measurement of transient signals. *Rev Sci Instrum* **57**: 273–275.
33. Sarkar A, Janata E. (2007) Formation of the silver hydride ion AgH⁺ upon the reduction of silver ions by H[•] in aqueous solution. A pulse radiolysis study. *Z Phys Chem* **221**: 403–413.
34. Janata E. (1992) Instrumentation of kinetic spectroscopy-8. The use of baseline compensation in the subnanosecond time domain. *Radiat Phys Chem* **39**: 319–320.
35. Taimuty SI, Deaver Jr BS. (1961) Transmission current monitor for high energy electron beams. *Rev Sci Instrum* **32**: 1098–1100.

36. Okabe S, Tabata T, Ito R. (1961) Nonobstructive low energy electron beam monitor. *Rev Sci Instrum* **32**: 1347–1348.
37. Bess L, Ovidia J, Valassis J. (1959) External beam current monitor for linear accelerators. *Rev Sci Instrum* **30**: 985–988.
38. Jansen JA, Veenhof GJ, De Vries C. (1969) High precision electron current monitoring system. *Nucl Instr and Meth* **74**: 20–26.
39. Feist H, Koep M, Reich H. (1971) A current transformer and gated integrator for measurement of weak currents from pulsed accelerators. *Nucl Instr and Meth* **97**: 319–321.
40. Steiner R, Merle K, Andresen HG. (1975) A high-precision ferrite-induction beam-monitor system. *Nucl Instr and Meth* **127**: 11–15.
41. Zimek Z. (1978) A single-pulse toroidal coil beam-charge monitor. *Radiat Phys Chem* **11**: 179–181.
42. Vojnovic B. (1985) A sensitive single-pulse beam charge monitor for use with charged particle accelerators. *Radiat Phys Chem* **24**: 517–522.
43. Janata E. (2004) Instrumentation of kinetic spectroscopy-20. Cherenkov emission in a ‘foil’ of optical fibers to measure the excitation in pulse radiolysis. *Radiat Phys Chem* **69**: 199–203.
44. Janata E. (1992) Instrumentation of kinetic spectroscopy-7. A precision integrator for measuring the excitation in laser flash photolysis and pulse radiolysis experiments. *Radiat Phys Chem* **39**: 315–317.
45. Hodgson BW, Keene JK. (1972) Some characteristics of a pulsed xenon lamp for use as a light source in kinetic spectroscopy. *Rev Sci Instrum* **43**: 493–496.
46. Hviid T, Nielsen SO. (1972) 35 volt, 180 ampere pulse generator with droop control for pulsing xenon arcs. *Rev Sci Instrum* **43**: 11928–1199.
47. Taylor WB, LeBlanc JC, Whillams DW, Herbert MA, Johns HE. (1972) Intensified ultraviolet analyzing lamp for flash photolysis. *Rev Sci Instrum* **43**: 1797–1799.
48. Luthjens LH. (1973) High intensity pulsed analyzing light sources for nano- and micro- second absorption spectroscopy. *Rev Sci Instrum* **44**: 1661–1665.
49. Beck G. (1974) Simple pulse generator for pulsing xenon arcs with high repetition rate. *Rev Sci Instrum* **45**: 318–319.
50. Janata E. (2002) Instrumentation of kinetic spectroscopy-16. A pulse generator for Xenon lamps. *Radiat Phys Chem* **65**: 255–258.
51. Patterson LK, Lilie J. (1974) A computer-controlled pulse radiolysis system. *Int J Radiat Phys Chem* **6**: 129–141.
52. Janata E. (1992) Instrumentation of kinetic spectroscopy-10. A modular data acquisition system for laser flash photolysis and pulse radiolysis experiments. *Radiat Phys Chem* **40**: 437–443.
53. Janata E. (2003) Instrumentation of kinetic spectroscopy-19. A method for the simulation of kinetics of reaction mechanisms. *Radiat Phys Chem* **66**: 219–222.

Chapter 5

Ultrafast Pulse Radiolysis Methods

*Jacqueline Belloni**, *Robert A. Crowell†*, *Yosuke Katsumura‡,§*,
Mingzhang Lin‡, *Jean-Louis Marignier**, *Mehran Mostafavi**,
Yusa Muroya¶, *Akinori Saeki||,***, *Seiichi Tagawa||,***,
Yoichi Yoshida||, *Vincent De Waele** and *James F. Wishart†,††*

1. Introduction

The pulse radiolysis technique is a very powerful method for studying short-lived chemical species. Time-resolved observation gives access

* Laboratoire de Chimie Physique-ELYSE, UMR CNRS-UPS, Bât. 349, Université Paris-Sud, 91405 Orsay, France.

† Chemistry Department, Brookhaven National Laboratory, Upton, NY 11973, USA.

‡ Advanced Science Research Center, Japan Atomic Energy Agency, 2-4 Shirakata-shirane, Tokai, Naka, Ibaraki 319-1195, Japan.

§ Department of Nuclear Engineering and Management, School of Engineering, The University of Tokyo, Hongo 7-3-1, Bunkyo-ku, Tokyo 113-8656, Japan.

¶ Nuclear Professional School, School of Engineering, The University of Tokyo, 2-22 Shirakata Shirane, Tokai, Naka, Ibaraki 319-1188, Japan.

|| The Institute of Scientific and Industrial Research, Osaka University, 8-1 Mihogaoka, Ibaraki, Osaka 567-0047, Japan.

** CREST, Japan Science and Technology Agency, c/o Osaka University, 8-1 Mihogaoka, Ibaraki, Osaka 567-0047, Japan.

†† E-mail: wishart@bnl.gov

to properties of these transients such as optical absorption and emission, conductivity, structure, chemical rate constants, oxido-reduction potential, and so forth. Hence, various chemical mechanisms and the role played by the short-lived intermediates can be elucidated, not only in the elementary steps occurring in radiation chemistry after the absorption of high energy radiation by a system, but much more generally in any type of chemical or biochemical process.

The principle is to generate the short-lived species using a pulse of radiation that should be much shorter than the time constants of the subsequent reactions that create or destroy transient species and to detect these species by various time-resolved techniques. Since the early pulse radiolysis experiments of the 1960s, continued refinements and the wholesale development of new technologies have led to the installation of facilities with increasingly faster time-resolution, with shorter pulses and advanced detection techniques.

It is particularly worth noting that pulse radiolysis with a time resolution of microseconds was used by Hart and Boag in 1962 to discover the hydrated electron,¹ which was studied by Keene² as the first short-lived homolog of the well-known metastable electron solvated in ammonia. As early as the 1970s, nanosecond electron pulses were delivered by machines such as Van de Graaff accelerators or direct current impulse generators.³ Since then, much effort has been devoted to attaining a time-resolution better than nanoseconds. Indeed, most elementary chemical processes occur in the picosecond, or even sub-picosecond time range, such as solvation processes of electrons, cations and anions, geminate ion recombination, formation and decay of excited states in liquids, nucleation-growth processes of nanoparticles, electron transfer and reactions in radiolytic spurs or highly confined systems, to name a few.

2. Picosecond Accelerator Technology

2.1. *The first generation of picosecond accelerators for radiolysis*

The construction of the first picosecond pulse radiolysis facilities enabled pioneering investigations of the elementary processes mentioned

above. The first picosecond pulse radiolysis system to be based on the stroboscopic method (pulse-and-probe method) was constructed by Hunt *et al.* in 1968.^{4,5} Picosecond electron pulse trains at 350 ps intervals and optically-delayed Čerenkov light, simultaneously emitted in air from the same pulse train, were used for irradiation and analyzing probe light, respectively. A similar system was also developed at Hokkaido University.^{6,7} At that time it was possible to trace the kinetic behavior of chemical species from 30 up to 350 ps, the latter being the time interval between electron pulses within the train.

In 1971 the generation of a single 20-picosecond electron pulse was introduced to pulse radiolysis, enabling the upper time limit of the kinetics studied to extend up to a few nanoseconds by 1975 at Argonne National Laboratory, USA.^{8,9} In 1979, a streak camera was synchronized with the single, 10-picosecond pulse from the S-band linear accelerator (linac) at the University of Tokyo Nuclear Engineering Research Laboratory (NERL, now Nuclear Professional School),¹⁰ making picosecond optical emission pulse radiolysis possible for the first time.^{10,11} By 1984, improvements of intensity fluctuation and time jitter between the electron pulse and the streak camera trigger^{12,13} led to the ability to record a picosecond transient absorption trace in a single shot, using a gated streak camera to extend the time window to several hundred nanoseconds¹⁴ (see further in Sec. 3.4). In the 1980s, a “Twin Linac” pulse radiolysis system, where one linac was used for irradiation and the other as a Čerenkov light source, was constructed at the NERL.¹³ Contemporaneously, linacs for picosecond pulse radiolysis were installed at Osaka University¹⁵ and the Institute of Chemical Kinetics, Novosibirsk.¹⁶ Subsequently, a “Laser-Linac Twin Linac” system was installed at the NERL, using a synchronized picosecond diode laser for delayed optical probe detection instead of Čerenkov light,¹⁷ and a femtosecond laser was for the first time synchronized to the electron pulse of the Osaka accelerator.^{18,19} Some of the scientific advances made with this first generation of accelerators for picosecond pulse radiolysis are mentioned in Chap. 1.

These single-pulse, picosecond electron linacs employed a method called “sub-harmonic pre-bunching” (Fig. 1) to create a

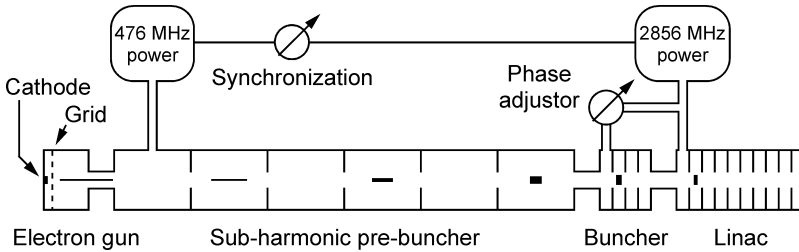


Fig. 1. Schematic representation of a pre-bunched picosecond linear accelerator.

short electron pulse that could be accelerated at microwave frequencies (1–3 GHz). This was necessary because it is not technically feasible to electrically gate on and off a thermionic cathode assembly fast enough to inject an electron bunch into the accelerating phase of one microwave cycle having a period of 350–1000 ps. Instead, a fast-gating electron gun was used to inject electrons into a pre-bunching section operating at a lower microwave frequency sub-harmonic to the main accelerator frequency. As the electron bunch is accelerated through the pre-buncher, it becomes compressed in pulse width to the point that it can be injected into a single microwave cycle of the main accelerator. The technically stringent aspects of this technique involve adjustment of the phase relationships between the accelerator sections and regulation of their drift with time.

2.2. *Magnetic pulse compression*

During the last decade, there has been remarkable progress in shortening the electron pulse width of traditional linear accelerators by using magnetic pulse compression (Fig. 2).^{20–22}

Starting in the late 1980s, picosecond and sub-picosecond electron pulses have been available for the experiments through implementation of the magnetic compression technique. A typical “chicane”-type system used at the Nuclear Professional School, University of Tokyo is presented in Fig. 2.²³ An electron pulse with a duration of seven picoseconds is generated by an S-band linac and compressed down to less than two picoseconds by the chicane.

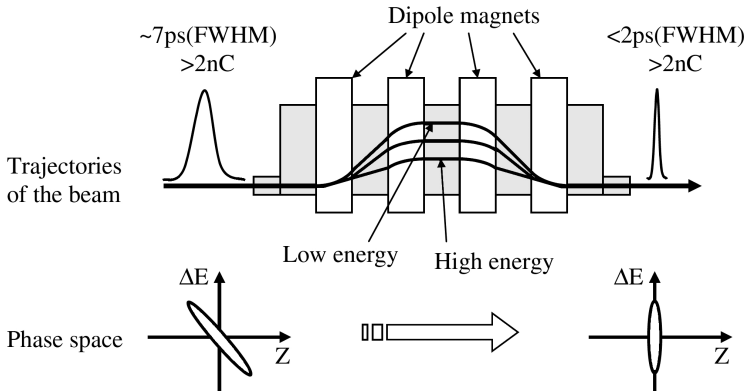


Fig. 2. Chicane-type magnetic compression of electron beam pulse duration. (Reproduced with permission from Ref. 38.)

It works by the deflection of the electrons within the pulse on the basis of their kinetic energy as shown in Fig. 2. Electrons in the early part of the pulse have lower energy and take the longer trajectory through the chicane while the trailing electrons with higher energy take a shorter path, causing compression by compensation of the arrival times. This method can be used to compress the pulse shorter than 0.1 ps but the actual duration is controlled by space charge effects due to repulsive interactions between the electrons. The technique depends on having a strong correlation between the energies of the electrons and their position within the bunch, which physicists describe as having a “low emittance.” If the charge of the pulse becomes large, space-charge repulsion interferes with the correlation, resulting poorer compression and longer pulses. However, experiments using large bunch charges are often preferable in order to obtain an intense and detectable signal, since light absorbance by radiolytic transients is proportional to the irradiation dose or the charge quantity of the electron pulse (for a given beam cross section). Therefore, from a viewpoint of practical applications, both per-pulse charge and pulse duration have a trade-off relation and real-world experiments necessitate a compromise.

2.3. *Laser photocathode electron gun accelerators*

Although the first-generation picosecond radiolysis facilities markedly increased our knowledge of short-lived species in numerous domains, their construction and maintenance costs and their complexity of operation seriously restricted their number actually installed. A new generation of accelerators, which issued from the technology of injectors for high-energy physics instruments adapted to the requirements of pulse radiolysis, was developed. These more compact and affordable instruments have generated an increasing amount of activity using pulse radiolysis for the study of ultra-short time scale chemical mechanisms.

The only way for achieving simultaneously both a short pulse and a large charge-per-pulse is to generate a very low-emittance beam. Since the qualities of the electron beam, charge, pulse width, and emittance greatly depend on the performance and properties of the electron source, the source is the key to ultrafast pulse radiolysis. Currently, laser-excited photocathodes are considered to be the leading source for low-emittance electron beams. Instead of being produced over the course of one to several nanoseconds by thermionic cathodes as used in traditional sources for linacs, the electrons are extracted from the cathode by the photoelectric effect using a short femtosecond or picosecond laser pulse. Due to their method of creation, it is possible to get a very strong energy-position correlation and a very low-emittance beam from laser photocathode electron guns. Unlike the thermionic-cathode based picosecond linacs described above, there is no need for a sub-harmonic pre-bunching system and the entire accelerator can be much more compact (Fig. 3),^{24,25} making the shielding of the facility much easier and less costly.

Because tenfold-lower emittance beams can be generated from photocathodes compared with those from conventional thermionic guns, photocathode systems have significant advantages in efficient transportation of the charge from the gun to the radiolysis target and in magnetic pulse compression effectiveness.

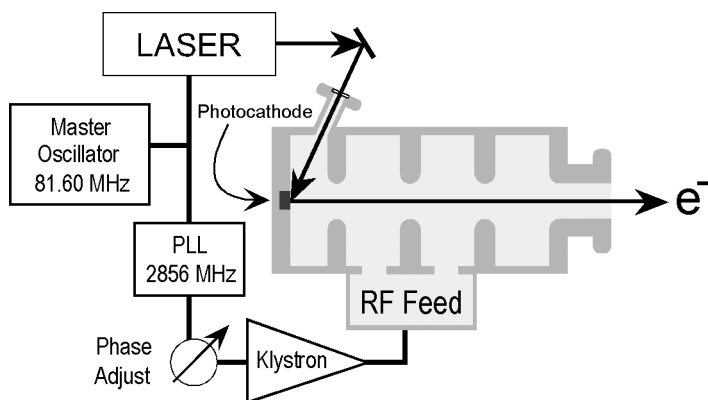


Fig. 3. Scheme of a laser photocathode electron gun, showing the relationship between laser and microwave synchronization. The example resembles the BNL LEAF facility. The length of the electron gun is approximately 30 cm.

In addition, since the pulses of the ultrafast lasers used for photoelectron generation are necessarily synchronized with the electron pulses, parts of them can be used as the probe light for analyzing the short-lived chemical species by the pulse-probe time-resolved spectrophotometry method. The reproducibility and the stability of the repetitive pulses permit the accumulation of signals and the detection of transients with weak absorbance changes. That is why several projects for the construction of these short time-resolved pulse radiolysis systems of the new generation, composed of a femtosecond laser system and a photocathode RF gun have been realized worldwide, namely the LEAF facility at Brookhaven National Laboratory (BNL),^{25,26} the ELYSE facility at the University of Paris-Sud,^{24,27,28} Osaka University,^{29–31} Sumitomo Heavy Industries (SHI, Tokyo),^{32,33} Waseda University (Tokyo),³⁴ and the NERL, University of Tokyo.^{35–38} Other facilities are under construction at the Technical University of Delft and at the Bhabha Atomic Research Center in Mumbai. The facility of Waseda University is also able to generate soft X-rays by inverse Compton scattering.³⁹ The characteristics of these facilities are given in Table 1.

Table 1. Comparison of specifications of photocathode electron gun accelerators for picosecond pulse radiolysis.

Facility [Ref.]	LEAF BNL [26]	ELYSE U. Paris-Sud [40]	NERL U. Tokyo [38]	Osaka U. [31]	Waseda U. ^a [34]
Laser	Ti:Sapphire	Ti:Sapphire	Ti:Sapphire	Nd:YLF	Nd:YLF
Laser pulse on cathode	266 nm	263 nm	265 nm	262 nm	262 nm
	1–3 ps	200 fs	100 fs	5.3 ps	10 ps
	400 μ J	15 μ J	30 μ J	1.4 mJ	36 μ J
Photocathode	Mg	Cs ₂ Te	Cs ₂ Te, NaKSb	Cu	Cs ₂ Te
Laser Beam incidence angle ν s. electron beam (degrees)	65	2	70	2	70
Electron energy (MeV)	8.7	4–9	20–22	32	4.6
Charge per pulse (nC)	5–10	2–8	2–2.8	2.5	4
Repetition rate (Hz)	10	1–25	10	10	5
Pulse duration FWHM (ps)	7	5–15	1–3	0.1	10
Emittance (mm mrad)		<60	20	3	

^aSome of the figures in this column are more recent than Ref. 34 (M. Washio, private communication).

2.3.1. *Laser and electron gun synchronization*

In photocathode electron guns, the timing between the microwaves used for acceleration and the photocurrent-generating laser pulse is of critical importance. Precise synchronization between the laser and electron beams is obtained by using a MHz quartz master oscillator to control the cathode pump laser repetition rate and the microwave amplifier system seed frequency (Fig. 3).

The entire technology is enabled by the commercial availability of laser oscillator systems that regulate their cavity length to match external clock periods to within fractions of a picosecond. However, larger timing jitter and drift at the photocathode can occur due to thermal expansion of microwave system components, shifts in the laser amplifier, and fluctuations in the air that some laser beams traverse (longer installations use evacuated transport tubes). Timing jitter where the electron and laser probe beams coincide in the radiolysis target can be caused by fluctuations of microwave power (which transform to beam energy, position and timing fluctuations) and laser beam transport issues. Therefore, stabilization of the microwave and laser systems is very important. Ideally the whole facility should be thermally stabilized, especially the temperature of the laser and accelerator rooms, and that of the cooling water for the accelerator and the microwave amplifier system.

The maximum photosensitivities of the various photocathode materials used generally lie in the UV region. As shown in Table 1, at the various accelerator facilities the photocathodes are triggered by 263–266 nm laser pulses obtained from frequency-tripled, amplified Ti-sapphire lasers or by the fourth harmonic of amplified Nd:YLF lasers. The energy per pulse is selected according to the choice of the photocathode material. Frequently using a shutter for beam chopping, the photocathode excitation laser beam is delivered at frequencies of 1–25 Hz, or on a single-shot basis, depending on the type of experiment.

2.3.2. *Photocathodes*

The quantum yield η of electrons extracted by the laser pulse in the UV highly depends on the material of the photocathode used (Table 1),

from $\eta = 0.01\%$ electron per photon for metals, such as Cu or Mg, up to $\eta = 0.25\%$ electron per 263 nm photon for semiconductors such as Cs_2Te .⁴¹ However, the use of highly oxygen-sensitive cathodes such as Cs_2Te requires their preparation and transfer to the electron gun accelerator under extreme vacuum. They are prepared either *in situ* in a special preparation chamber attached to the gun, as in ELYSE,⁴⁰ or in a separate chamber and then transferred to the accelerator via a vacuum transport system, as in the NERL Tokyo facility³⁸ and at Waseda University.³⁹ The higher quantum yield of semiconductor cathodes can be worth the added effort, since electron pulses containing several nanocoulombs (the amount required for the effective optical detection of transient species) can be obtained from laser pulses on the order of microjoules to tens of microjoules, much lower than the 0.3–1 mJ required for obtaining similar charges from metal photocathodes (Table 1). Provided that the accelerator vacuum is strictly maintained, the Cs_2Te photocathodes can be robust and not damaged for years.⁴⁰

The diameter of the laser spot on the cathode ranges from 1–6 mm depending on the facility. In order to produce photoelectrons with a time structure as short as possible and as close as possible to that of the laser, it is preferable either that the laser beam impinges onto the photo-cathode with a normal incidence (as for example in ELYSE facility, Table 1) or that the diameter of the laser spot is limited to less than two millimeters for high angles of incidence. At ELYSE, the laser pulse energy delivered to the photo-cathode is measured at the exit of the frequency-tripling crystal by using a switchable mirror to deflect it onto a virtual cathode equipped with a joulemeter.⁴⁰

2.3.3. *Energy dependence of electron beam characteristics*

The energy of the electron beam is also an important factor for the time resolution because of the scattering of the electron beam in irradiated samples (usually condensed media). Figure 4 shows the electron penetration into liquid water and trajectories calculated by a Monte Carlo calculation code (EGS5⁴²) for electron penetration into

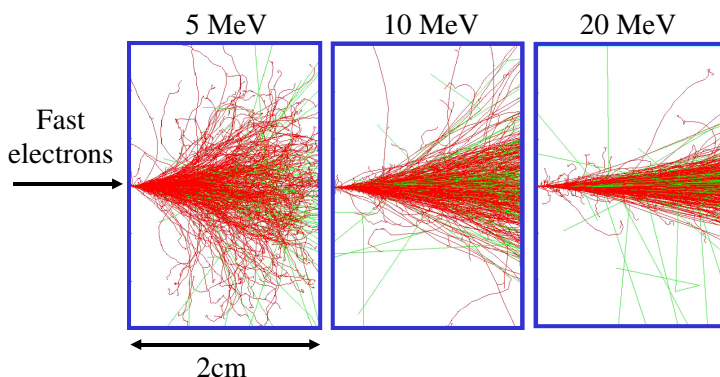


Fig. 4. Penetration of 5, 10 and 20 MeV electron beams through a 2 cm water cell calculated by the EGS5 code; red and green lines show the trajectories of electrons and secondary X-ray photons, respectively. (Reproduced with permission from Ref. 38.)

liquid water at three beam energies. The higher the energy, the more collimated the beam remains with distance.

If the energy of the electron beam is 5 MeV, scattering of the beam over a 1-cm path length or greater is significant and the radiolytic dose is spread over a larger cross section the deeper the beam penetrates into the sample cell. Moreover, scattered electrons take zigzag trajectories, which make the apparent time duration of the pulse in the medium longer. Hence, time resolution as well as signal intensity become worse with deeper penetration at lower beam energies. However, electron beams with energies over 10 MeV begin to cause some photonuclear radioactivation of the sample and accelerator and experimental system components. Therefore, although the electron beam can be more easily manipulated and focused, higher electron energies in the range 10–30 MeV require precautions suitable only for specially equipped laboratories, such as at the universities of Tokyo and Osaka (Table 1). For other facilities, a maximum energy of 9 MeV is the best compromise. It enables sufficient penetration, in particular, to achieve studies under conditions of high pressure or high temperature that require specific cells with thick, strong windows.^{43,44}

2.3.4. Typical picosecond electron gun accelerator systems

Figure 5 presents the scheme of the 18 MeV S-band linac at the University of Tokyo NERL, with a 0.3 TW femtosecond Ti:Sapphire laser beam providing 795 nm, 100 fs (FWHM), 30 mJ/shot pulses, which are split to provide photocathode illumination through third harmonic generation into a 265-nm pulse with 4 to 6 ps (FWHM) duration, as well as probe laser beams.

The electron beam is accelerated in two stages, initially up to 4 MeV through the 1.6-cell accelerating cavity of the electron gun, and finally up to 18–22 MeV in the standard linac accelerating section. The resulting electron pulse has a duration of ~ 5 ps (FWHM), a charge of more than 2 nC, and an energy spread of around 1% (FWHM) (Table 1). Here, if the energy spread across the electron bunch is modulated by adjusting the phases of the two accelerating sections, the bunch can be compressed to shorter than 1 ps (FWHM) in the chicane-type magnetic compressor.

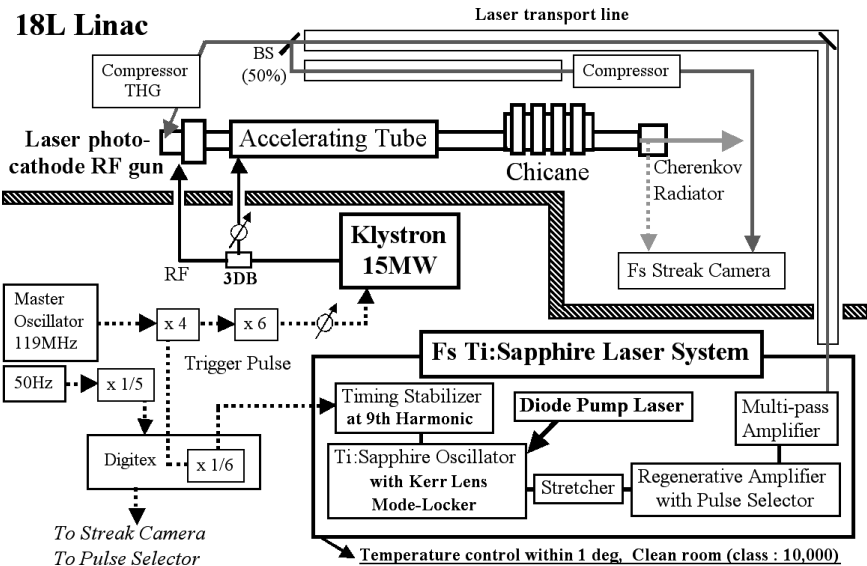


Fig. 5. Ultrafast pulse radiolysis system at NERL, University of Tokyo.

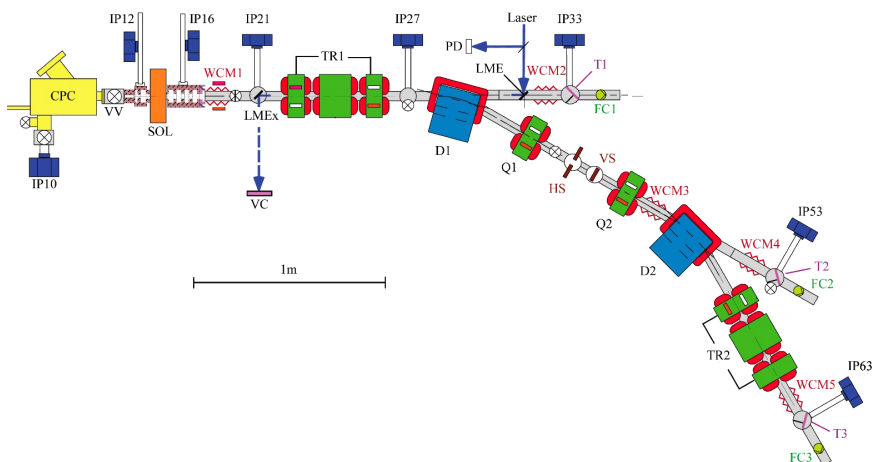


Fig. 6. Scheme of the laser-driven RF electron accelerator of pulse radiolysis facility ELYSE. IP: ion vacuum pump, CPC: cathode preparation chamber, VV: vacuum valve, SOL: solenoid, D: dipole, TR1 and 2: triplets, Q: quadrupole, WCM: wall current monitor, FC: Faraday cup, T: translator for Čerenkov light emitter and visualization screen; LME: laser entrance mirror, LMEx: laser exit mirror, VC: virtual cathode; HS: horizontal slit, VS: vertical slit. (Reproduced with permission from Ref. 28.)

Several installations, such as those at BNL, Université Paris-Sud, Osaka University and Waseda University, work at energies of 4–9 MeV. Among this group, only the ELYSE accelerator at Université Paris-Sud (Fig. 6) uses a booster accelerating section, for the rest the electron gun provides all the acceleration. In the LEAF, ELYSE and Waseda facilities, the electron beam may be alternatively bent by magnets to different beam lines, output windows and experimental areas equipped with various detection systems.

At ELYSE, the intensity and position of the electron beam is observed upstream of each experimental area by wall current monitors. Ceramic screens are used to indicate the transverse beam profile. The charge per pulse is measured by a moveable Faraday cup. The charge extracted from the Cs_2Te photo-cathode is 1–8 nC, with a linear slope of $\eta = 0.25\%$ electron per 263 nm photon absorbed at laser pulse energies up to 4 μJ . At higher laser pulse energies, the current

still increases but the quantum efficiency decreases due to the loss of part of the charge by recombination, up to a saturation level. Moreover, the electron repulsion increases with the charge per pulse and the pulse width becomes longer.

2.4. Laser wakefield accelerators for ultrafast pulse radiolysis

More recently a radically different approach that capitalizes on advances in laser wakefield acceleration has been pursued. Significant advances have been made in ultrafast ultrahigh-power femtosecond laser technology. Ti:sapphire-based table-top terawatt (T^3) laser systems are now routinely capable of generating peak powers in excess of 10 TW.⁴⁵ It has been shown that by focusing terawatt laser pulses to irradiances exceeding 10^{18} W/cm² in a pulsed supersonic gas jet, it becomes possible to generate subpicosecond electron pulses with a charge of a few nanocoulombs and to accelerate these electrons to energies in the mega-electron-volt range.⁴⁶

It has also been demonstrated that laser wakefield accelerators can produce sufficient charge-per-pulse for detection of radiolysis products using transient absorption laser spectroscopy. Using the laser wakefield accelerator (LWA) at the University of Michigan Center for Ultrafast Optical Studies, subpicosecond electron pulses were generated by focusing terawatt laser pulses into a supersonic helium jet and subsequently used to ionize liquid water. Using the Michigan LWA, hydrated electron concentrations as high as 20 μ M were generated and the attachment of e_{aq}^- to traces of O₂ in water was followed on the nano- to microsecond time scale.⁴⁷ More recently Brozek-Plushka *et al.*⁴⁸ have demonstrated approximately 20 ps resolution using a LWA for pulse radiolysis of liquid water, and Oulianov and Crowell *et al.*⁴⁹ were able to achieve a time resolution of better than two picoseconds.

In a LWA, the electron and laser pulses are inherently synchronized, so the time jitter sources associated with photocathode accelerators are not an issue. The ultimate time resolution should depend only upon the cross correlation between the laser and electron pulses and the physics of the electron beam interaction with the

sample. For an LWA this should be on the order of 50 fs. There are three main constraints that limit the current time resolution to about two picoseconds. One of the major time resolution limitations for ultrafast radiolysis measurements, as described in Sec. 3.1, is the time-of-flight difference between the light and electron pulses. Another fundamental constraint is that the present LWAs do not reliably produce monoenergetic electron beams, although recent work^{50–55} indicates that this will change in the near future. The typical LWA has an electron spectrum that has an energy spread that is more than 100%, relative to the mean. This dispersion in energy results in the dispersion of arrival times at the sample as the electron pulse travels through space; to a much larger degree than in laser transient absorption experiments, time resolution is limited by the nature and the physical dimensions of the sample, and the dispersion of the electron beam. Improvements in time resolution will require thin samples and the development of more sensitive detection techniques.

2.5. *Electron pulse width determination*

The electron pulse length can be measured through the generation of Čerenkov light by causing the beam to strike a sapphire plate, or if the beam energy is high enough, through air.^{56,57} This light pulse is transferred for temporal analysis to the slit of a high-speed streak camera. Another method uses the fact that the moving electron bunch generates a broadband emission of electromagnetic radiation whose spectrum depends on the temporal width of the pulse. Measuring the ratio of emitted radiation at two microwave frequencies permits determination of the pulse length⁵⁸ in real time without intercepting the pulse, enabling measurements to be made during experimental data collection. Real-time, non-destructive beam monitoring capability vastly improves the ability to maintain high performance of the accelerator and beam quality during long acquisitions, as in pulse-probe measurements, and across a series of experiments for cross-comparisons or spectral reconstruction.

Recently, a new single shot electro-optic sampling technique (Fig. 7) has been developed for the non-invasive characterization of the

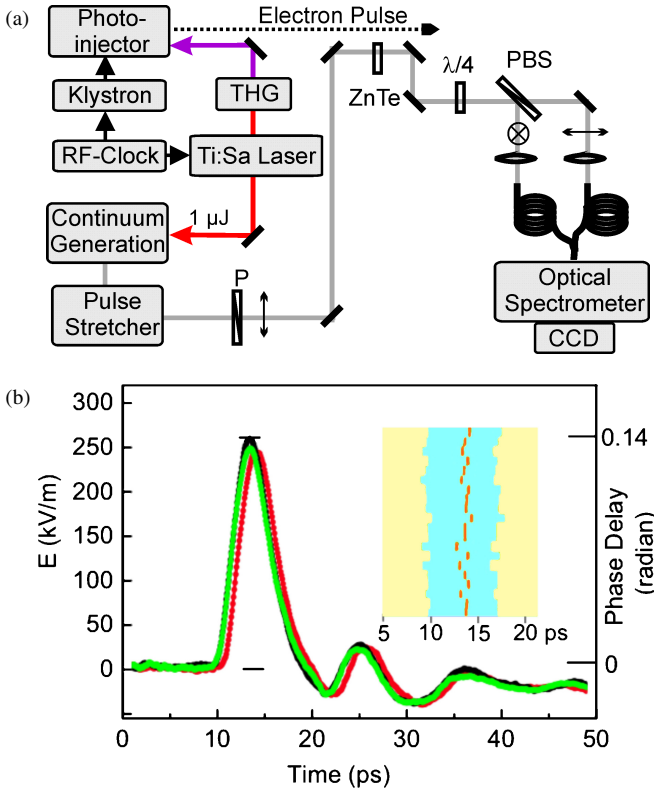


Fig. 7. (a) Scheme of the electro-optic single shot diagnostic based on supercontinuum encoding with balanced detection implemented at ELYSE. The perpendicular polarization states of the optical probe are denoted by an arrow and a circle. THG: third harmonic generation, P: polarizer, $\lambda/4$: achromatic quarter wave plate, PBS: polarizing beam splitter. (b) Three consecutive single shot measurements for low bunch charge and energy; the oscillations are due to free space THz radiation generated by the transition of the bunch through the exit window and reflected inside the ZnTe crystal. The arrival time (red) and FWHM duration (blue) of a series of 20 bunches are shown in the inset.

longitudinal electron bunch distribution at the ELYSE facility.^{59,60} The transverse electric field of the electron bunch is encoded to the temporally dispersed spectrum of a supercontinuum by the transient birefringence induced in a ZnTe crystal that is located close to the

electron beam. The wavelength-dependent polarization state of the optical probe is then analyzed in balanced detection with linear response.

The high sensitivity and stability of the set-up allow monitoring of the single bunches next to the sample position. Therefore, bunch parameters such as the shot-to-shot stability, the charge and the duration can be optimized for specific picosecond radiolysis experiments.

3. Optical Detection Systems for Ultrafast Pulse Radiolysis

As described above, recent advances in accelerator technology have enabled the production of very short electron pulses for the study of radiation-induced reaction kinetics. Typically, digitizer-based optical absorbance or conductivity methods are used to follow reactions by pulse radiolysis (Chap. 4). However, the time resolution afforded by picosecond accelerators exceeds the capability of real-time detection systems based on photodetectors (photomultiplier tubes, photodiodes, biplanar phototubes, etc.) and high-bandwidth oscilloscopes (Fig. 8). Faster experiments use streak cameras or various methods that use optical delay to encode high temporal resolution, taking advantage of the picosecond-synchronized laser beams that are available in photocathode accelerator installations.

3.1. *Temporal resolution considerations for fast optical detection*

The overall time resolution δt_T of a picosecond pulse radiolysis detection system is approximately expressed as:

$$\delta t_T \approx \delta t_F + \sqrt{\delta t_E^2 + \delta t_L^2 + \delta t_{\text{Sync}}^2}, \quad (1)$$

where δt_F represents the flight time difference between the electron and probe light beams through the sample, δt_E and δt_L the durations of the electron and laser pulses, and δt_{Sync} the synchronization jitter between the electron and probe pulses.

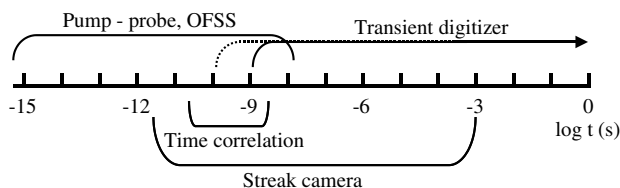


Fig. 8. Time ranges of various optical detection systems. The dotted line for transient digitizer indicates the highest-performance configurations, the solid line routine ones.

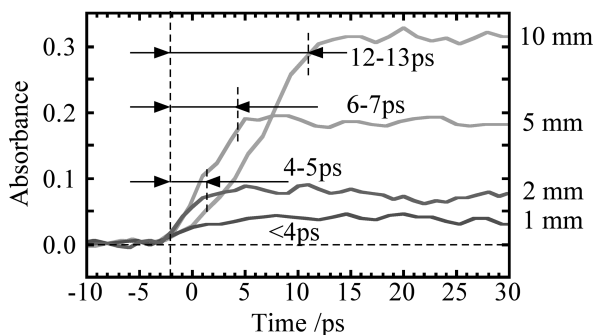


Fig. 9. Rise times of the hydrated electron signal at 700 nm, with path lengths indicated on the right (NERL, University of Tokyo).

The flight time difference is due to the velocity difference between the electron and light pulses passing through the sample. The relativistic electron beam travels through the sample at nearly c , the speed of light in vacuum, while due to the refractive index n , the probe light pulse travels at c/n . For example, in the case of co-propagating electron and light beams passing through a water sample, the light is slowed down by a factor of 1.33 and the flight time difference δt_F is about one picosecond per mm of optical path, or ten picoseconds total in a standard 1-cm cuvette.⁶¹ One way to reduce this difference is to shorten the optical path length. In doing so, it is essential to irradiate with a high charge and tightly focused electron beam to generate a higher concentration of transient species to compensate for the shorter optical path. Figure 9 shows the effect of path length on signal intensity and temporal resolution for the rise time of the aqueous electron (whose solvation time is 0.2 ps).⁶² The rise time of e_{solv}^- absorbance is

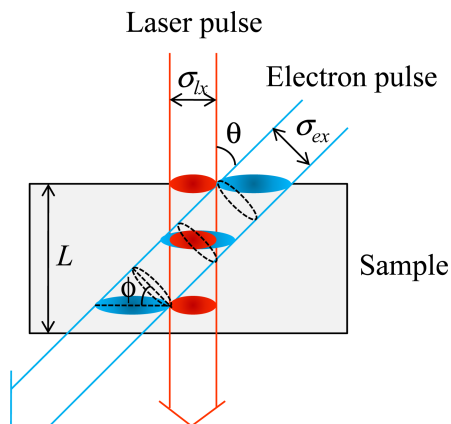


Fig. 10. Concept of EVS for pulse radiolysis by using a rotated electron pulse.

broadened according to Eq. (1) both by the electron pulse length δt_E and the flight time difference δt_F .

The technique of equivalent velocity spectroscopy (EVS)⁶³ has been implemented at Osaka University to improve the time resolution of the pulse radiolysis by overcoming the effect of group velocity mismatch between the electrons and the light in the sample. As shown in Fig. 10, the electron beam and the laser light are injected into the sample at an angle θ , which is determined by the refractive index (n) of the sample as $\cos\theta = 1/n$. In this case, the electrons pass through the sample along the longer path. By rotating the electron pulse at the same angle of θ , both the electron and the light pulses coincide at every point and throughout the propagation time. The resolution limitation due to the velocity mismatch is thus fully removed.

3.2. Pulse-probe detection systems

Three different approaches have been employed to observe radiation-induced kinetics on the picosecond timescale. The first, pulse-probe detection, is covered in this section. Section 3.3 discusses a related technique that uses temporally-dispersed probe beams to record a kinetic trace in a single shot. Finally, Sec. 3.4

describes the use of streak cameras for temporally and spectrally dispersed measurements.

The stroboscopic pulse-probe detection method is analogous to laser pump-probe experiments that have been commonplace for decades. Indeed, electron pulse — Čerenkov light probe measurements were the first picosecond radiolysis experiments to be performed, as mentioned earlier in this chapter.^{4,8,13} The major difference between the early pulse-probe systems and those of today is the availability of picosecond-synchronized ultrafast laser systems that provide highly collimated probe beams over a wavelength range from the UV to the near-infrared. In addition to the quality of the laser probe beams, their low divergence allows the probe pulses to be transported a reasonable distance after passing through the sample before collection into a detector, which helps with rejection of the divergent Čerenkov radiation generated in the sample by the electron pulse. The pulse-probe detection system at the University of Tokyo NERL is depicted in Fig. 11 as an example. Table 2 summarizes comparable systems at other laboratories.

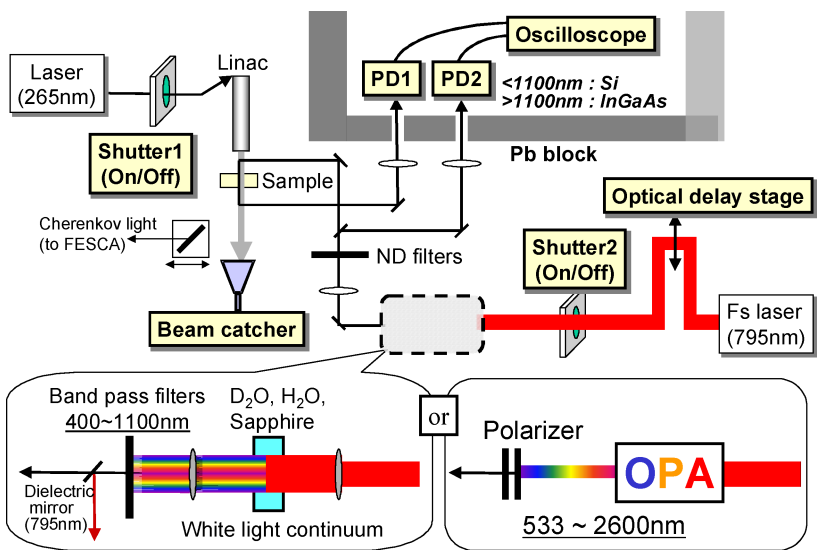


Fig. 11. Schematic of the picosecond pulse-probe detection system at NERL, University of Tokyo.

Table 2. Comparison between time-resolved spectrophotometric detection set-ups of several laser-photocathode electron accelerator facilities for picosecond pulse radiolysis.

Facility [Ref.]	LEAF BNL [26]	ELYSE U. Paris-Sud [40]		NERL U. Tokyo [38]	U. Osaka [30, 31] 2 systems	Waseda U. [34]
Detection system	Pulse-probe & OFSS	Pulse-probe	High dynamic range streak camera	Pulse-probe	Pulse-probe [30] Pulse-probe [31]	Pulse-probe
Probe light	Laser 400, 800 nm & OPA 100 fs	Laser 790 nm & NOPA 100 fs	Xe flash lamp 25 Hz 60 mJ/cm ² /flash	Laser 795 nm, continuum & OPA 30–100 fs	Laser OPO, continuum 523, 800, 1047 nm	Laser 523, 1047 nm, continuum
Frequency (Hz)	P-P: 10 OFSS <1	1–25	5	10	<10 10	5
Wavelength range (nm)	240–1600 (–2600)	240–1600	250–850	290–2600	300–1600 523,800,1047	680–880
Time range	7 ps–15 ns	5 ps–4 ns	5 ps–1 ms	5 ps–6 ns	0.8 ps–2 ns 0.2 ps–1 ns	16–250 ps

Essentially, a small part of the laser pulse train that is ultimately used to trigger the photocathode is split off to create a synchronized laser probe pulse train. The probe line is equipped with different non-linear optical devices that permit the tunability of the probe beam from the near UV to the NIR. Available probe sources include the laser fundamental (790 nm) and second harmonic (395 nm), a white-light continuum (470–750 nm) generated in a sapphire plate, and a continuously tunable Optical Parametric Amplifier (470–750 nm, 1000–1600 nm, and 240–375 nm by SHG), able to deliver light pulses shorter than 30 fs after compression.

The various probe beams can be coupled into the same single-wavelength, dual-channel pulse-probe transient optical absorption set-up. A one-meter-long optical delay line is used to control the variable time delay between the electron and the probe pulses. Approximately half of the probe beam is deflected onto a reference photodiode while the other half of the beam is slightly focused into the sample, which is placed in front of the output window of the accelerator. Subsequently, the probe beam is then transported to the sample photodiode. (Alternatively, in some laboratories the probe and reference beams are transported into the detection room by long, low-OH silica optical fibers in order to reduce electronic noise pickup on the detector signal cables.)

The intensities of the sample and reference beams are measured with photodiodes by an analog data acquisition card and/or digital oscilloscopes to calculate the absorbance of the sample. The time resolution of the photodiodes is not important for this application but it is essential that their photoresponse is strictly linear to the light pulse intensity. Each absorbance measurement can be corrected for the absorbed radiolytic dose by measuring the charge in the electron bunch using a Faraday cup or some other detector. At each pulse-probe delay, it is necessary to measure the sample absorbance in the presence and absence of the electron beam, the latter measurement serving as the baseline. In practice, since the probe beam transport distances in these facilities may be several meters or more, optical transport fluctuations due to vibration and air turbulence in the 40–100 ms interval between the sample and baseline measurements

can be an appreciable source of noise in the experiment at facilities that use low repetition rate laser amplifiers. For facilities that use kilohertz laser amplifiers, such as at Osaka University³⁰ and ELYSE, the baseline measurement can be as little as one or two milliseconds apart from the electron beam shot, significantly reducing the effects of fluctuations on the data.

At Osaka University, the probe beam is a white-light continuum generated in a sapphire crystal³⁰ used in a single-beam configuration (no reference arm). Two consecutive probe pulses one millisecond apart, with the second one being synchronized to the electron pulse, pass through the sample and are dispersed through a monochromator onto a CCD camera that is set to continually shift charges. In this way the reference and signal probe spectral intensities can be independently measured and an absorbance spectrum obtained in one accelerator shot (Fig. 12). The 1-ms interval between the reference and signal pulses reduces the noise level to half or less than that observed with longer delays between probe pulses that are more susceptible to the low frequency fluctuations mentioned above. For single-wavelength measurements, the double probe technique can be applied to use consecutive pulses from a Ti:Sapphire laser oscillator (ca. 80 MHz) using a single photodetector, where it is even more effective due to the shorter delay interval and the stability of the oscillator compared to an amplified system.^{64,65}

On the Osaka University thermionic cathode L-band linac, a time resolution of two picoseconds was achieved using magnetic pulse compression and time jitter compensation systems (Fig. 13).⁶⁶ The time jitter between the Čerenkov light from the electron beam and the laser pulse was measured shot-by-shot with a femtosecond streak camera to accurately determine the relative time of each measurement in the kinetic trace. In this way, the time jitter that would otherwise degrade the time resolution was corrected, and the remaining factor dominating the rise time was the electron-light velocity difference over the 2-mm sample depth.

At ELYSE, two consecutive laser pulses ($\Delta t = 2$ ns) are picked from the 1 kHz probe laser pulse train in a single-wavelength, dual beam configuration. The first pulse is synchronized with the acceler-

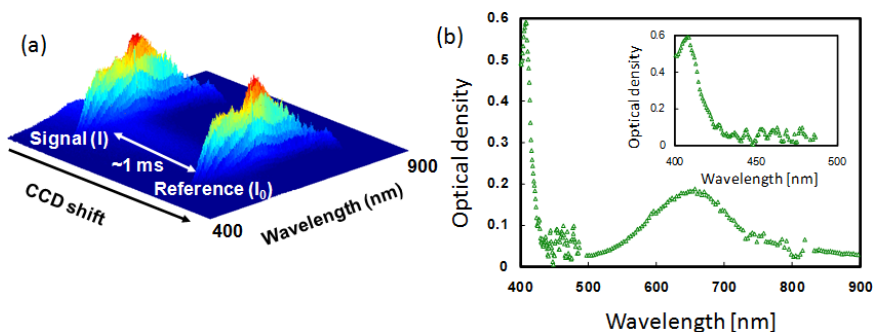


Fig. 12. Transient photoabsorption spectrum acquisition at ISIR, Osaka University. (a) Two consecutive femtosecond pulses of white light continuum collected by single scan of CCD camera. (b) Transient absorption spectrum of 100 mM biphenyl in Ar-bubbled tetrahydrofuran solution at 200 ps after the end of pulse. The peaks are attributed to biphenyl radical anion. Each point in near-UV region (ca. from 400 to 500 nm) and visible-NIR region (ca. from 500 to 900 nm) was measured by averaging over 10 and 2 beam-probe shots, respectively. The inset is a magnification in 400–500 nm.

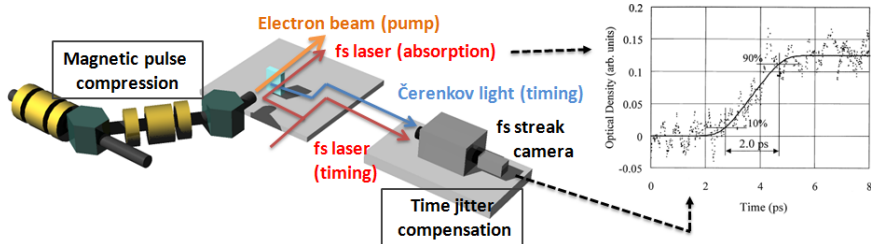


Fig. 13. Schematic of high time-resolution pulse radiolysis equipped with a magnetic pulse compression and time jitter compensation system at ISIR, Osaka University. An example of the rise time of the hydrated electron signal at 780 nm is shown.

ator microwave system and gives the measurement with the electron pulse (I^{probe} and I^{ref}), while the second pulse gives the signal without excitation (I_0^{probe} and I_0^{ref}). As an example, signals are shown in Fig. 14. An absorbance increase is observed at 345 nm in solutions of 2 M NaCl and 1 M NaCl plus 1 M HCl, respectively.⁶⁷ In both

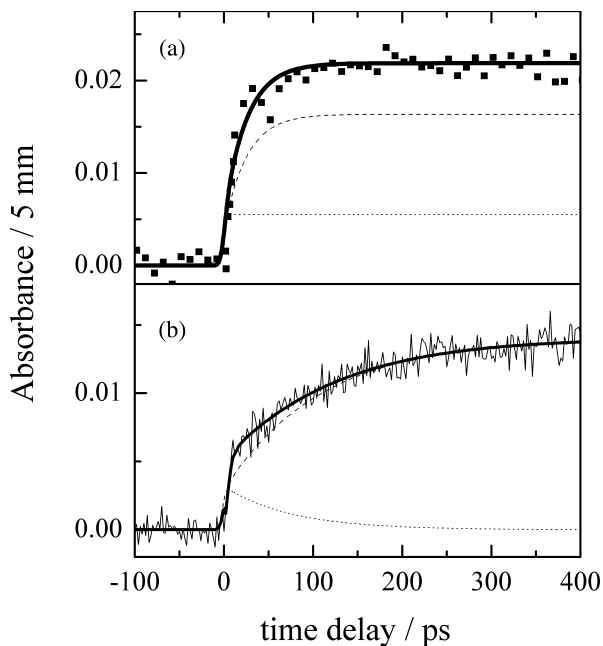


Fig. 14. Transient optical absorption at 345 nm recorded at the ELYSE facility using the pulse-probe method. (a) Neutral aqueous 2 M NaCl solution, dose per pulse 16.7 Gy. Dotted line: hydrated electron component, dashed line: ClOH^- absorbance. (b) Acidic aqueous solution 1 M NaCl and 1 M HCl, dose per pulse 5.5 Gy. Dotted line: hydrated electron component, dashed line: Cl_2^- absorbance.

cases the signals contain a component due to the hydrated electron. The complementary absorbance is assigned in neutral medium (16.7 Gy per pulse) to the radical ClOH^- (extinction coefficient $\epsilon = 4060 \text{ l mol}^{-1} \text{ cm}^{-1}$) that is formed within 50 ps by the scavenging of OH^\bullet radicals by Cl^- . Under acidic conditions (5.5 Gy per pulse), the differential absorbance is assigned to the Cl_2^- radical, which is formed within 250 ps by the formation of Cl^\bullet followed by the complexation with Cl^- .

Thanks to the advent of sophisticated accelerators and detection systems, pulse-probe pulse radiolysis experiments have become widely used to explore very fast chemical events and to answer questions about the inhomogeneous chemistry that occurs at early times following

radiolysis. For example, it was used^{68,69} to re-evaluate the initial yield of the hydrated electron, which had been an issue for over 30 years. Reported values of $G(e_{\text{aq}}^-)$ varied from 0.41 to 0.49 $\mu\text{mol J}^{-1}$ (4.0–4.8 molecules/100 eV). The re-evaluation was done by a combination of stroboscopic and conventional kinetic methods, using the same accelerator, to estimate $G(e_{\text{aq}}^-)$ at 20 ps to be $0.42 \pm 0.02 \mu\text{mol J}^{-1}$. This value was supported by Monte Carlo calculations.⁷⁰ The same methods were carried forward to make systematic studies on alcohols, from simple alcohols to polyols, to elucidate the initial yields and solvation processes.⁷¹ Wavelength-dependent measurements of solvated electrons in diols in the NIR show rather different behavior as compared to water or simple alcohols, suggesting that a large portion of electrons might be “solvated” directly by pre-existing trap sites without pre-solvation processes.⁴³

Picosecond pulse-probe radiolysis has been used to investigate the reactions of solvated and pre-solvated electrons in tetrahydrofuran.⁷² It has also led to surprising insights into the mechanism of dissociative electron attachment to aryl halides. The high time resolution of pulse-probe detection provided key data that led to the deduction that the pathway for halide ion dissociation from the aryl halide anion radical involves bending of the halide–carbon bond out of the aryl ring plane instead of direct in-plane bond cleavage.⁷³ Pulse-probe radiolysis also was used to observe the formation of Xe_2^* excimers by electron-ion recombination in irradiated supercritical xenon.⁷⁴ The studies showed that the excimers, which absorb broadly throughout the visible, can be quenched by adding small amounts of ethane, facilitating the detection of other transients by absorption spectroscopy. Pulse-probe measurements of geminate recombination in alkanes³¹ and in aromatic hydrocarbons⁷⁵ have been combined with theoretical calculations to investigate electron-hole pair distance distributions.

3.3. Single-shot radiolysis using a temporally-dispersed probe beam

Pulse-probe pulse radiolysis detection techniques are very powerful, however to obtain kinetic profiles of fast reactions they all rely to

some extent on repetitive measurements taken at numerous points in time (optical delay), often amounting to hundreds or thousands of shots. The result is that a large radiolytic dose can accumulate in the sample, requiring it to be changed frequently or circulated in moderate volumes to dilute the cumulative radiation damage so that it does not interfere with the measurement. This can be a fatal drawback for many interesting experiments involving samples that are too viscous to flow (such as some ionic liquids), samples made of precious materials that cannot be used practically in large volumes, and samples that may be too air or moisture sensitive to tolerate exposure to even a well-designed circulating system.

To help solve these problems, the “Optical Fiber Single Shot” (OFSS) method was developed at the BNL LEAF. OFSS uses a bundle of optical fibers to temporally disperse a single optical probe pulse to measure absorption over a range of discrete delay times using a single shot.⁷⁶ It starts with a monochromatic laser probe pulse that is directed into a bundle of 100 optical fibers, where each fiber has a unique length selected to create a specific optical delay in relation to the complete set of fibers. In the first iteration of the fiber bundle, the 100 fibers were trimmed to generate approximate delay intervals of 15 ps, creating a total time window of 1.5 ns. The image of the light exiting the fiber bundle is split so that one image of the bundle is relayed onto the reference channel CCD camera, while the other image is focused into the sample cell to coincide with the area irradiated by the electron beam, then relayed to the sample channel CCD. An absorbance corresponding to each delay time is calculated by integrating the image intensity for each individual fiber on the reference and sample cameras. In this way, 100 absorbance measurements at different delay times are made in a single shot. Typically, 25 accelerator shots are enough to obtain very good signal-to-noise for the transient kinetics. Kinetic traces over longer time windows can be constructed by increasing the optical delay before the probe pulse enters the fiber bundle to collect temporally overlapping sets of absorbance data. An example is shown in Fig. 15.

The kinetic traces in Fig. 15 were measured on static ionic liquid samples in ordinary spectrophotometer cuvettes, using approximately

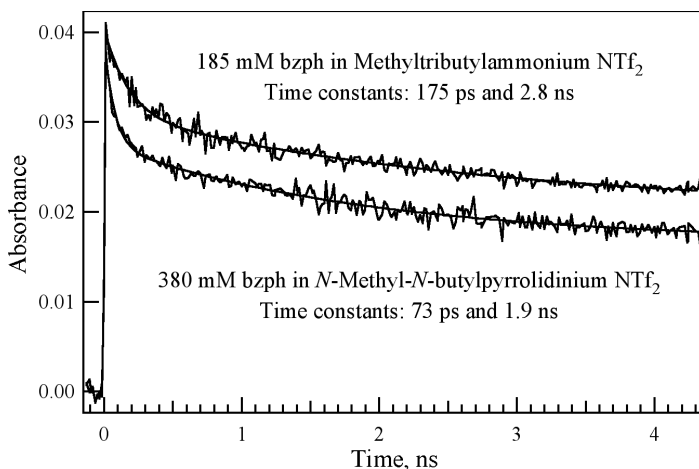


Fig. 15. Benzophenone anion solvation observed at 800 nm in two ionic liquids by OFSS pulse radiolysis spectroscopy. The traces consist of three 1.5-ns OFSS segments.

75 shots total for each sample. The relatively low cumulative dose required to obtain good data indicates that the OFSS technique is appropriate for precious or hard-to-handle samples. While the OFSS method is robust, there are many technical details that needed to be addressed to make it work, including calibration of optical fiber delays as functions of wavelength, compensation for various sample refractive indices, automated fiber bundle image analysis software, and compensation for dose variation across the bundle image within the sample. Presently, OFSS detection is available only over the wavelength range covered by silicon CCD cameras (<1100 nm); NIR area detectors will extend the range to longer wavelengths in the future. This capability would be particularly useful for studies of solvated electrons in non-polar solvents and ionic liquids.

3.4. Streak camera absorbance detection

Another approach for picosecond optical absorption detection is to use a light source with an intensity stable for a time period much longer and an optical detector with a response time much shorter

than the absorbance variation to be studied. For this purpose, an original setup was developed at ELYSE based on a high-repetition Xe flash lamp⁷⁸ coupled with a high dynamic range streak camera used in absorbance mode, both being synchronized with the electron pulses.

The time-resolved UV-Vis absorbance detection system consists of a Hamamatsu C7700-01 high dynamic range streak camera connected to a Chromex 250 IS flat field spectrograph.⁷⁷ The role of the spectrograph is to spectrally disperse the white-light probe pulse across the entrance slit of the streak camera. Schematically, in order to time-resolve the signals, light is converted via a semiconductor photocathode into a corresponding extended photoelectron beam that is rapidly swept in the streak tube in the direction transverse to the entrance slit. The photoelectrons are then amplified by a microchannel plate before exciting a phosphor screen which is recorded by a CCD camera in the form of a 2D image digitalized into 1024×1344 points along the time and wavelength axes, respectively. This system is suitable for high-intensity pulsed light with a dynamic range up to $10^4:1$. The absorbance data result from a series of four measurements: the background of the streak camera, the analyzing light only, the analyzing light with the electron beam and the Čerenkov light. Data are collected as the average of at least 20 pulses, but are generally acquired by averaging 400 pulses. Because of the rather long transfer distance from the light source to the streak camera, a time of flight difference between the blue and the red parts of the spectrum can be observed on records at the 500 ps time scale. This is easily seen on streak images of the Čerenkov light (measurements for subtraction of the Čerenkov light from the absorbance signal or for the estimation of the duration of the electron pulse). At least for the highest time resolution, the time origin is therefore taken from the ultra-short Čerenkov emission signal at the corresponding wavelength. From a single shot of the accelerator, the transient spectrum at any time (sweep time/full screen 500 ps to 1 μ s) and the time evolution of the short-lived species at each wavelength (from 250 to 850 nm in 360 nm sections) can be simultaneously obtained. However, when the 360 nm spectral range is recorded at 500 ps full sweep, a fogging

effect appears due to the high light intensity required to get an image. This is why the highest resolution is only obtained by recording a restricted wavelength domain (± 5 nm) so that the fogging effect is negligible. Work is in progress to evaluate this effect using known reference systems, and thus to obtain the highest time resolution over the entire spectral range.

The light source consists of a home-made pulse generator driving a commercial xenon lamp having a high and constant maximum intensity for a period of about 500 ns, with a rise time of 2 μ s and a repetition rate up to 25 Hz.⁷⁸ The cross section of the analyzing light beam is smaller (0.2 cm) than that of the electron beam and both are collinear. Alignment of the electron beam relative to the probe light beam is optimized by adjusting the magnets to maximize the reference absorbance signal (generally of the hydrated electron) recorded by a control photomultiplier equipped with filters selecting the wavelength range. The photomultiplier is located in the detection room at the arrival of the probe beam and systematically used to control the optimization of the absorbance before reflecting the beam to the spectrograph-streak camera set-up.

The major advantage of using such a device is to obtain in a single pulse the information both on kinetics and on the transient absorption spectrum. The method is particularly well adapted to the spectral identification of the transients and to an overview of the chemical mechanism. This set-up can be used to observe transients from the end of the pulse up to rather long time, in the range of 500 ns, or with an adequate light source, up to 1 ms full scale for longer-lived species.

Figure 16(a) presents an image of the time evolution of the transient spectrum of the solvated electron in ethylene glycol recorded with the streak camera between 360 and 720 nm with a full time range of 3700 ps (charge 3.5 nC per pulse, optical path 1 cm). In Figs. 16(b) and 16(c) the spectrum at 65 ps and the kinetics at 570 nm are given, respectively, both extracted from the image of Fig. 16(a). In Fig. 17 the kinetics at 700 nm of the hydrated electron absorbance is shown on a full time scale of 500 ps and a resolution time of four picoseconds.

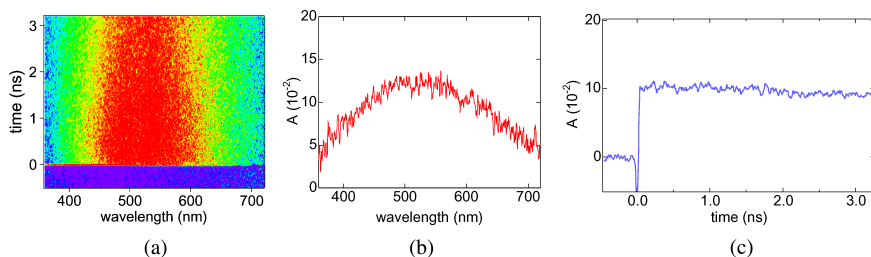


Fig. 16. Signals obtained using a streak camera. (a) Image obtained from the streak camera measurements (1024×1344 pixels) where each pixel indicates the value of the optical density at the corresponding time and wavelength (in false colors, increasing absorbance from blue to red). (b) Spectrum measured 65 ps after the electron pulse. (c) Kinetic profile at 570 ± 5 nm.

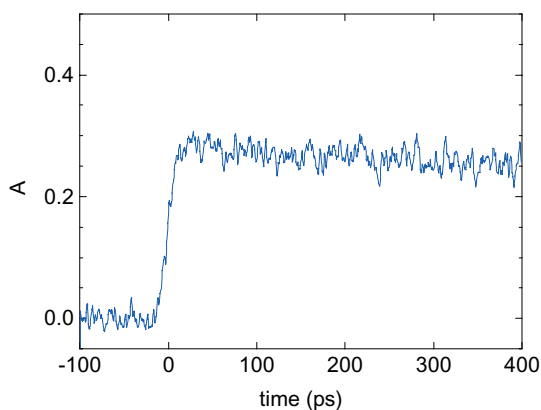


Fig. 17. Kinetic profile of hydrated electron at 700 nm recorded with the streak camera after subtraction of the Čerenkov light (average of 400 pulses).

4. Future Trends

During the last decade, the technology of laser-driven picosecond accelerators has been successfully applied to pulse radiolysis experiments in diverse areas of chemistry. The reliability of the accelerators and their beam characteristics, and the development of real-time, non-destructive beam diagnostics to monitor them, have provided a

high level of performance for pulse radiolysis experimentation. The availability of synchronized laser beams for ultrafast detection schemes and of reliable picosecond-scale streak camera and oscilloscope trigger signals have made the measurement of early radiolytic phenomena easily accessible to researchers. Yet, the new generation of picosecond accelerator facilities is still in its adolescence and many technical advances are still to be expected.

For example, continuing technological improvements in quantum yield and durability of photocathodes will increase the available bunch charge and radiolytic dose for experiments. The use of more quantum-efficient semiconductor photocathodes, in place of metal ones, is now well mastered and offers the possibility to considerably increase the charge-per-pulse of the electron beam for a given level of UV illumination, thus reducing performance demands on the laser systems. The development of cathodes covered with thin diamond films for secondary electron emission presently underway promises large charge emission from very durable cathodes.⁷⁹ Nonetheless, the cathode improvements will be complemented by increases in laser stability and laser beam mode quality, which will allow optimum extraction of charge from the photocathode without risk of exceeding plasma breakdown thresholds.

Access to subpicosecond electron pulses has already been achieved at Osaka University by a new double-decker accelerator concept.⁸⁰ In order to reduce the time jitter for the detection of the optical absorption signals in pulse radiolysis studies, the light pulse used for the pump-probe system is Čerenkov emission which is produced in the same cell by a synchronized second electron beam and is concomitant with the electron path. The distance between the axes of the two beams is 1.6 mm. The pulse durations of these electron pulses, which are both produced by delayed beams issued from the same laser, are 430 ± 25 fs and 510 ± 20 fs, respectively, and the charge per pulse is 0.65 nC. An electron bunch of 100 fs and 0.17 nC has already been generated.

Detection methods will also continue to advance and diversify. In addition to general improvements of the techniques described above, new detection systems are being developed.

Pulse-pump-probe radiolysis is an extension of pulse-probe radiolysis where a strong laser pulse is used to excite a radiation-induced transient species to investigate its photophysics or photochemistry. In this mode, the laser pump and probe pulses may occur at some relatively long time after the electron radiolysis pulse, to allow time for the desired transient species to be formed. In theory, because the pump and laser pulses are short and travel at practically the same velocity through the sample, it would be possible to look at processes on the femtosecond time scale. As a practical matter, the signal averaging required to obtain such kinetics on the excited states of radiolytic transients is quite tedious and such experiments have not yet been reported. It should be possible to adapt streak camera transient absorption and OFSS detection methods to this purpose. In addition, photo-induced reactions of radiolytic species are not confined to the ultrafast regime and it is quite practical to use digitizer-based transient absorption techniques to observe the reactivity of excited states. This method has been used at BNL to study forbidden transitions in radical anion excited states and electron transport in molecular wires.

Because the yield of observable excited states for pulse-pump-probe radiolysis depends on the concentration of the radiolytic transient species available to be photolysed, it is often necessary to deliver a very large radiolytic dose. This can be achieved at photocathode accelerator facilities by using a several-nanosecond-long, frequency-quadrupled Nd:YAG or Nd:YLF laser pulse to generate the photoelectrons instead of the normal picosecond pulse. The resulting electron “macropulse” consists of a train of picosecond pulses separated by the microwave period, typically 350 ps. The macropulse may contain 10–20 times more charge than the typical single bunch, however transport of the electrons to the region of the sample being probed is less efficient because of the large spread in electron energies.

Despite the lower transport efficiency, the macropulse method is very effective at delivering large doses, which will be essential for the addition of vibrational spectroscopies to ultrafast pulse radiolysis. Vibrational spectroscopy is very useful for identifying transient species because of its sensitivity to molecular structure and the ability to

calculate predicted IR and Raman spectra of various candidate structures for identification purposes. Precedents exist for the successful use of IR⁸¹ and Raman⁸² spectroscopies for pulse radiolysis detection. Efforts are underway to integrate these methods into ultrafast pulse radiolysis facilities and improve their time resolution.

References

1. Boag JW, Hart EJ. (1963) Absorption spectra in irradiated water and some solutions — Absorption spectra of hydrated electron. *Nature* **197**: 45–47.
2. Keene JP. (1963) Absorption spectra in irradiated water and some solutions — Optical absorptions in irradiated water. *Nature* **197**: 47.
3. Wishart JF. (2008) Tools for radiolysis studies. In *Radiation Chemistry, From Basics to Applications in Material and Life Sciences*, (eds). Spothem-Maurizot M, Mostafavi M, Douki T, Belloni J. Chapter 2, pp. 17–33, EDP Sciences.
4. Bronskill MJ, Taylor WB, Wolff RK, Hunt JW. (1970) Design and performance of a pulse radiolysis system capable of picosecond time resolution. *Rev Sci Instrum* **41**: 333.
5. Hunt JW (1976) Early events in radiation chemistry. In *Advances in Radiation Chemistry*, (eds.), Burton M, Magee JL. Vol. 5, pp. 185–315. John Wiley & Sons, Inc., New York.
6. Sumiyoshi T, Katayama M. (1982). The yield of hydrated electrons at 30 picoseconds. *Chem Lett* 1887–1890.
7. Sumiyoshi T, Tsugaru K, Yamada T, Katayama M. (1985) Yields of solvated electrons at 30 picoseconds in water and alcohols. *Chem Soc Jpn B* **58**: 3073–3075.
8. Jonah CD. (1975) Wide-time range pulse-radiolysis system of picosecond time resolution. *Rev Sci Instrum* **46**: 62–66.
9. Jonah CD, Matheson MS, Miller JR, Hart EJ. (1976) Yield and decay of hydrated electron from 100 ps to 3 ns. *J Phys Chem* **80**: 1267–1270.
10. Tagawa S, Katsumura Y, Ueda T, Tabata Y. (1980) Evidence for two fast formation processes of solute excited states in liquid toluene solutions studied by picosecond single pulse radiolysis. *Radiat Phys Chem* **15**: 287–291.
11. Tagawa S, Katsumura Y, Tabata Y. (1979) The ultra-fast process of picosecond time-resolved energy transfer in liquid cyclohexane by picosecond single-pulse radiolysis. *Chem Phys Lett* **64**: 258–260.
12. Kobayashi H, Ueda T, Kobayashi T, Tagawa S, Tabata Y. (1981) Performance and improvements of an electron accelerator producing a picosecond single electron pulse. *Nucl Instrum Meth* **179**: 223–228.
13. Tabata Y, Kobayashi H, Washio M, Tagawa S, Yoshida Y. (1985) Pulse-radiolysis with picosecond time resolution. *Radiat Phys Chem* **26**: 473–479.

14. Kobayashi H, Ueda T, Kobayashi T, Tagawa S, Yoshida Y, Tabata Y. (1984) Absorption spectroscopy system based on picosecond single electron beams and streak camera. *Radiat Phys Chem* **23**: 393–395.
15. Kobayashi H, Ueda T, Kobayashi T, Washio M, Tabata Y, Tagawa S. (1983) Picosecond single electron pulse for pulse radiolysis studies. *Radiat Phys Chem* **21**: 13–19.
16. Grigoryants VM, Lozovoy VV, Chemousov YuD, Shebolaev IV, Arutyunov AV, Anisimov OA, Molin YuN. (1989) Pulse radiolysis system with picosecond time resolution referred to Cherenkov radiation. *Radiat Phys Chem* **34**: 349–352.
17. Yoshida Y, Ueda T, Kobayashi T, Shibata H, Tagawa S. (1993) Studies of geminate ion recombination and formation of excited states in liquid *n*-dodecane by means of a new picosecond pulse radiolysis system. *Nucl Instrum Meth A* **327**: 41–43.
18. Kozawa T, Nagahara S, Yoshida Y, Tagawa S, Watanabe T, Yamashita Y. (1997) Radiation-induced reactions of chemically amplified X-ray and electron beam resists based on deprotection of *t*-butoxycarbonyl groups. *J Vac Sci Tech B* **15**: 2582–2586.
19. Yoshida Y, Mizutani Y, Kozawa T, Saeki A, Seki S, Tagawa S, Ushida K. (2001) Development of laser-synchronized picosecond pulse radiolysis system. *Radiat Phys Chem* **60**: 313–318.
20. Uesaka M, Tauchi K, Kozawa T, Kobayashi T, Ueda T, Miya K. (1994) Generation of a subpicosecond relativistic electron single bunch at the S-band linear-accelerator. *Phys Rev E* **50**: 3068–3076.
21. Uesaka M, Kinoshita K, Watanabe T *et al.* (1998) Femtosecond electron beam generation and measurement for laser synchrotron radiation. *Nucl Instrum Meth A* **410**: 424–430.
22. Yang J, Kondoh T, Kan K, Kozawa T, Yoshida Y, Tagawa S. (2006) Femtosecond single electron bunch generation by rotating longitudinal bunch phase space in magnetic field. *Nucl Instrum Meth A* **556**: 52–56.
23. Uesaka M, Kinoshita K. (2005) Magnetic bunch compression. In *Femtosecond Beam Science*, (ed.) Uesaka M. pp. 40–52. Imperial College Press.
24. Belloni J, Marignier JL, Gaillard M. (1998) ELYSE: Une nouvelle infrastructure pour la Chimie Physique d'Orsay. *Cahiers de Radiobiologie* **8**: 25–28.
25. Wishart JF. (1998) Accelerators and other sources for the study of radiation chemistry. In *Photochemistry and Radiation Chemistry*, Wishart JF, Nocera DG (eds.) *Adv Chem Ser*, Vol. 254, pp. 35–50. American Chemical Society, Washington, DC.
26. Wishart JF., Cook AR, Miller JR. (2004) The LEAF picosecond pulse radiolysis facility at Brookhaven National Laboratory. *Rev. Sci. Instrum.* **75**: 4359–4366.
27. Monard H, Bourdon J-C, Le Duff J, Garvey T, Mouton B, Rodier J, Thiery Y, Gaillard M. (1999) *Proc of the 1999 Part Acc Conf*, New York, p. 2012.

28. Belloni J, Monard H, Gobert F, Larbre JP, Demarque A, De Waele V, Lampre I, Marignier JL, Mostafavi M, Bourdon JC, Bernard M, Borie H, Garvey T, Jacquemard B, Leblond B, Lepercq P, Omeich M, Roch M, Rodier J, Roux R. (2005) ELYSE — A picosecond electron accelerator for pulse radiolysis research. *Nucl Instrum Meth A* **539**: 527–539.
29. Kozawa T, Mizutani Y, Yokoyama K, Okuda S, Yoshida Y, Tagawa S. (1999) Measurement of far-infrared subpicosecond coherent radiation for pulse radiolysis. *Nucl Instrum Meth A* **429**: 471–475.
30. Saeki A, Kozawa T, Tagawa S. (2006) Picosecond pulse radiolysis using femtosecond white light with a high S/N spectrum acquisition system in one beam shot. *Nucl Instrum Meth A* **556**: 391–396.
31. Yang J, Kondoh T, Norizawa K, Nagaishi R, Tagushi M, Takahashi K, Katoh R, Anishchik SV, Yoshida Y, Tagawa S. (2008) Picosecond pulse radiolysis: Dynamics of solvated electrons in ionic liquid and geminate ion recombination in liquid alkanes. *Radiat Phys Chem* **77**: 1233–1238.
32. Aoki Y, Nakajyo T, Tsunemi A, Yang JF, Okada Y, Yorozu M, Hirose M, Sakai F, Endo A. (2001) Performance of compact pulse radiolysis system using a photocathode RF gun. *Res Chem Intermediat* **27**: 689–697.
33. Aoki Y, Yang JF, Hirose M, Sakai F, Tsunemi A, Yorozu M, Okada Y, Endo A, Wang XJ, Ben-Zvi I. (2000) A new chemical analysis system using a photocathode-RF gun. *Nucl Instrum Meth A* **455**: 99–103.
34. Nagai H, Kawaguchi M, Sakaue K, Komiya K, Nomoto T, Kamiya Y, Hama Y, Washio M, Ushida K, Kashiwagi S, Kuroda R. (2007) Improvements in time resolution and signal-to-noise ratio in a compact pico-second pulse radiolysis system. *Nucl Instrum Meth B* **265**: 82–86.
35. Muroya Y, Watanabe T, Wu G, Li X, Kobayashi T, Sugahara J, Ueda T, Yoshii K, Uesaka M, Katsumura Y. (2001) Design and development of a subpicosecond pulse radiolysis system. *Radiat Phys Chem* **60**: 307–312.
36. Muroya Y, Lin M, Watanabe T, Wu G, Kobayashi T, Yoshii K, Ueda T, Uesaka M, Katsumura Y. (2002) Ultra-fast pulse radiolysis system combined with a laser photocathode RF gun and a femtosecond laser. *Nucl Instrum Meth A* **489**: 554–562.
37. Muroya Y, Lin M, Iijima H, Ueda T, Katsumura Y. (2005) Current status of the ultra-fast pulse radiolysis system at NERL, the University of Tokyo. *Res Chem Intermediat* **31**: 261–272.
38. Muroya Y, Lin M, Han Z, Kumagai Y, Sakumi A, Ueda T, Katsumura Y. (2008) Ultra-fast pulse radiolysis: A review of the recent system progress and its application to study on initial yields and solvation processes of solvated electrons in various kinds of alcohols. *Radiat Phys Chem* **77**: 1176–1182.
39. Sakaue K, Gowa T, Hayano H, Kamiya Y, Kashiwagi S, Kuroda R, Masuda A, Moriyama R, Urakawa J, Ushida K, Wang X, Washio M. (2008) Recent progress of a soft X-ray generation system based on inverse Compton scattering at Waseda University. *Radiat Phys Chem* **77**: 1136–1141.

40. Marignier J-L, De Waele V, Monard H, Gobert F, Larbre J-P, Demarque A, Mostafavi M, Belloni J. (2006) Time-resolved spectroscopy at the picosecond laser-triggered electron accelerator ELYSE. *Radiat Phys Chem* **75**: 1024–1033.
41. Chevally E, Durand J, Hutchins S, Suberlucq G, Wurgel M. (1994) Photocathodes tested in the dc gun of the CERN photoemission laboratory. *Nucl Instr Meth A* **340**: 146–156.
42. Karawkow I, Rogers DWO. (2003) The EGSnrc code system: Monte Carlo simulation of electron and photon transport. NRC Report PIRS-701 (fourth printing).
43. Mostafavi M, Lin M, He H, Muroya Y, Katsumura Y. (2004) Temperature-dependent absorption spectra of the solvated electron in ethylene glycol at 100 atm studied by pulse radiolysis from 296 to 598 K. *Chem Phys Lett* **384**: 52–55.
44. Baldacchino G, De Waele V, Monard H, Sorgues S, Gobert F, Larbre J-P, Vigneron G, Marignier J-L, Pommeret S, Mostafavi M. (2006) Hydrated electron decay measurements with picosecond pulse radiolysis at elevated temperature up to 350°C. *Chem Phys Lett* **424**: 77–81.
45. Backus S, Dufree CG, Murnane MM, Kapteyn HC. (1998) High power ultrafast lasers. *Rev Sci Instrum* **69**: 1207–1223.
46. Bingham R. (2006) Basic concepts in plasma accelerators. *Phil Trans R Soc A* **364**: 559–575.
47. Saleh N, Flippo K, Nemoto K, Umstadter D, Crowell RA, Jonah CD, Trifunac AD. (2000) Pulse radiolysis of liquid water using picosecond electron pulses produced by a table-top terawatt laser system. *Rev Sci Instrum* **71**: 2305–2308.
48. Brozek-Pluska B, Gligier D, Hallou A, Malka V, Gauduel YA. (2005) Direct observation of elementary radical events: Low- and high-energy radiation femtochemistry in solutions. *Radiat Phys Chem* **72**: 149–157.
49. Oulianov DA, Crowell RA, Gosztola DJ, Shkrob IA, Korovyanko OJ, Rey-de-Castro RC. (2007) Ultrafast pulse radiolysis using a terawatt laser wakefield accelerator. *J Appl Phys* **101**: 053102.
50. Miura E, Koyama K, Kato S, Saito N, Adachi M, Kawada Y, Nakamura T, Tanimoto M. (2005) Demonstration of quasi-monoenergetic electron-beam generation in laser-driven plasma acceleration. *Appl Phys Lett* **86**: 251501.
51. Hidding B, Amthor K-U, Liesfeld B *et al.* (2006) Generation of quasimonoenergetic electron bunches with 80-fs laser pulses. *Phys Rev Lett* **96**: 105004.
52. Hosokai T, Kinoshita K, Ohkubo T, Mackawa A, Uesaka M. (2006) Observation of strong correlation between quasimonoenergetic electron beam generation by laser wakefield and laser guiding inside a preplasma cavity. *Phys Rev E* **73**: 036407.
53. Mangles SPD, Murphy CD, Najmudin Z *et al.* (2004) Monoenergetic beams of relativistic electrons from intense laser-plasma interactions. *Nature* **431**: 535–538.

54. Geddes CGR, Toth CS, Van Tilborg J, Esarey E, Schroeder CB, Bruhwiler D, Cary J, Leemans WP. (2004) High-quality electron beams from a laser wakefield accelerator using plasma-channel guiding. *Nature* **431**: 538–541.
55. Faure J, Glinec Y, Pukhov A, Kiselev S, Gordienko S, Lefebvre E, Rousseau J-P, Burgy F, Malka V. (2004) A laser-plasma accelerator producing monoenergetic electron beams. *Nature* **431**: 541–544.
56. Mavrogenes GS, Jonah C, Schmidt KH, Gordon S, Tripp GR, Coleman LW. (1976) Optimization of isolated electron pulses in the picosecond range from a linear accelerator using a streak camera-TV diagnostic system. *Rev Sci Instrum* **47**: 187–189.
57. Watanabe T, Sugahara J, Yoshimatsu T, Sasaki S, Sugiyama Y, Ishi K, Shibata Y, Kondo Y, Yoshii K, Ueda T, Uesaka M. (2002) Overall comparison of subpicosecond electron beam diagnostics by the polychromator, the interferometer and the femtosecond streak camera. *Nucl Inst Meth A* **480**: 315–327.
58. Kuroda R, Kashiwagi S, Sakaue K, Washio M, Hayano H, Urakawa J. (2004) Bunch length monitor using two-frequency analysis for RF gun system. *Jpn J Appl Phys* **43**: 7747–7752.
59. Schmidhammer U, De Waele V, Marquès J-R, Bourgeois N, Mostafavi M. (2009) Single shot linear detection of 0.01-10 THz electromagnetic fields. *Appl Phys B* **94**: 95–101.
60. Schmidhammer U, De Waele V. (2007) Procédé et dispositif de mesure monocoupe de la biréfringence transitoire induite par une perturbation appartenant au domaine des fréquences THz. Dépôt le 21-12-07. No. 0760269.
61. Magee JL, Chatterjee A. (1987) Theoretical aspects of radiation chemistry. In *Radiation Chemistry. Principles and Applications*, (eds.) Farhatziz A, Rodgers AJ. VCH, pp. 137–199.
62. Migus A, Gauduel Y, Martin JI, Antonetti A. (1987) Excess electrons in liquid water; first evidence of a prehydrated state with femtosecond lifetime. *Phys Rev Lett* **58**: 1559–1562.
63. Yang J, Kondoh T, Norizawa K, Yoshida Y, Tagawa S. (2009) Breaking time-resolution limits in pulse radiolysis. *Radiat Phys Chem* **78**: 1164–1168.
64. Kozawa T, Saeki A, Yoshida Y, Tagawa S. (2002) Study on radiation-induced reaction in microscopic region for basic understanding of electron beam patterning in lithographic process (I) development of subpicosecond pulse radiolysis and relation between space resolution and radiation-induced reactions of onium salt. *Jpn J Appl Phys* **41**: 4208–4212.
65. Saeki A, Kozawa T, Yoshida Y, Tagawa S. (2002) Study on radiation-induced reaction in microscopic region for basic understanding of electron beam patterning in lithographic process (II) D relation between resist space resolution and space distribution of ionic species. *Jpn J Appl Phys* **41**: 4213–4216.

66. Kozawa T, Mizutani Y, Miki M, Yamamoto T, Suemine S, Yoshida Y, Tagawa S. (2000) Development of subpicosecond pulse radiolysis system. *Nucl Inst Meth A* **440**: 251–253.
67. Atinault E, De Waele V, Schmidhammer U, Fattahi M, Mostafavi M. (2008) Scavenging of e_s^- and OH^\bullet Radicals in concentrated HCl and NaCl aqueous solutions. *Chem Phys Lett* **460**: 461–465.
68. Bartels DM, Cook AR, Mudaliar M, Jonah CD. (2000) Spur decay of the solvated electron in picosecond radiolysis measured with time-correlated absorption spectroscopy. *J Phys Chem A* **104**: 1686–1691.
69. Muroya M, Lin M, Wu G, Iijima H, Yoshii K, Ueda T, Kudo H, Katsumura Y. (2005) A re-evaluation of the initial yield of the hydrated electron in the picosecond time range. *Radiat Phys Chem* **72**: 169–172.
70. Muroya Y, Meesungnoen J, Jay-Gerin J-P, Filali-Mouhim A, Goulet T, Katsumura Y, Mankhetkorn S. (2001) Radiolysis of liquid water: An attempt to reconcile Monte-Carlo calculations with new experimental hydrated electron yield data at early times. *Can J Chem* **80**: 1367–1374.
71. Lin M, Mostafavi M, Muroya Y, Han Z, Lampre I, Katsumura Y. (2006) Time-dependent radiolytic yields of the solvated electrons in 1,2-ethanediol, 1,2-propanediol, and 1,3-propanediol from picosecond to microsecond. *J Phys Chem A* **110**: 11404–11410.
72. Saeki A, Kozawa T, Ohnishi Y, Tagawa S. (2007) Reactivity between biphenyl and precursor of solvated electrons in tetrahydrofuran measured by picosecond pulse radiolysis in near-ultraviolet, visible, and infrared. *J Phys Chem A* **111**: 1229–1235.
73. Takeda N, Poliakov PV, Cook AR, Miller, JR. (2004) Faster dissociation: Measured rates and computed effects on barriers in aryl halide radical anions. *J Am Chem Soc* **126**: 4301–4309.
74. Holroyd RA, Wishart JF, Nishikawa M, Itoh K. (2004) Reactions of charged species in supercritical xenon as studied by pulse radiolysis. *J Phys Chem B* **107**: 7281–7287.
75. Okamoto K, Kozawa T, Saeki A, Yoshida Y, Tagawa S. (2007) Subpicosecond pulse radiolysis in liquid methyl-substituted benzene derivatives. *Radiat Phys Chem* **76**: 818–826.
76. Shen Y, Cook AR. (2009) Optical fiber-based single-shot picosecond absorption spectroscopy. *Rev Sci Instrum* **80**: 073106.
77. Marignier J-L. (2009) to be published.
78. Herren R, Bazouin J-R, Marignier J-L. (2008) Générateur de flashes lumineux, spectromètre d'absorption utilisant un tel générateur et procédé de génération de flashes lumineux. Université Paris-Sud. *French patent No.* 0850457, 24 January.
79. Ben-Zvi I, Rao T, Burrill A, Chang X, Grimes J, Rank J, Segalov Z, Smedley J. (2007) Diamond secondary emitter. *Int J Modern Phys A* **22**: 3759–3775.

80. Yang J, Kondoh T, Yoshida A, Yoshida Y. (2006) Double-decker femtosecond electron beam accelerator for pulse radiolysis. *Rev Sci Instrum* **77**: 043302.
81. Le Caër S, Vigneron G, Renault J-P, Pommeret S. (2006) First coupling between a LINAC and FT-IR spectroscopy: The aqueous ferrocyanide system. *Chem Phys Lett* **426**: 71–76.
82. Tripathi GNR, Su YL. (2004) The origin of base catalysis in the $\bullet\text{OH}$ oxidation of phenols in water. *J Phys Chem A* **108**: 3478–3484.

Chapter 6

A History of Pulse-Radiolysis Time-Resolved Microwave Conductivity (PR-TRMC) Studies

John M. Warman^{,†} and Matthijs P. de Haas^{*}*

1. Introduction

A large fraction of the energy transferred to a material on exposure to high-energy electromagnetic or particulate radiation results in the ejection of orbitally bound electrons. The chemical changes that result from radiolysis are therefore, to a large extent, determined by the physico-chemical processes occurring subsequent to *ionization*. Because of this, the attention of academic radiation chemists has focused on the nature and reactions of electrons and their geminate radical cations. To this end, a variety of investigative methods have been applied, including mass spectrometric, spin resonance, optical absorption, and DC conductivity techniques.

In the mid 1960s one of the present authors (JMW) together with Richard Fessenden began applying microwaves to the study of

* Delft University of Technology, Reactor Institute Delft, Mekelweg 15, 2629 JB Delft, The Netherlands.

† E-mail: j.m.warman@tudelft.nl

ionization in pulse-irradiated gases.¹ This was based on the microwave technique first proposed by Biondi² and successfully used to monitor electrons in gaseous discharges.

In the early 1970s the present authors modified the technique to allow the investigation of ionization in nanosecond pulse-irradiated dielectric liquids.^{3,4} This was subsequently extended to solid materials, including ice and hydrated biopolymers, inorganic semiconductors, conjugated polymers and discotic liquid crystals. In addition to the fundamental scientific interest of the authors, the direction of the research was driven by technological developments (for example the changing interest from gaseous to solid-state to molecular electronics), and the availability at any given time of interesting (and pure) chemical compounds. It is the purpose of this review to give a brief report of the salient results obtained within this historical perspective over the last 40 years.

A separate development of the TRMC techniques was their application to the study of dipolar and excitonic species formed on *flash-photolysis* of dilute solutions^{5,6} and, more recently, to charge transport and charge separation in thin (aligned) solid films.^{7,8} In the present review we restrict ourselves to results that we have obtained on *pulse-irradiated* materials, for which the method has become known as the pulse-radiolysis time-resolved microwave conductivity or PR-TRMC technique.

2. The Technique

Experimental details of the PR-TRMC technique and the methods of data analysis have been presented in previous papers and the interested reader is referred to these publications.^{1,4,9-12} In brief, the method makes use of the fact that microwaves propagating in a weakly pulse-ionized medium can undergo a phase-shift due to a change in the imaginary component of the conductivity, or attenuation due to a change in the real component. The former effect is dominant for highly mobile, “free” charge carriers and was used for the initial studies of electrons in gases. For later measurements on the

much lower mobility charge carriers in condensed phases of molecular materials, it was decided to change to a method that monitored only changes in the real, absorptive component. This was used for all measurements (even those on gaseous media) reported by the present authors after 1970. Because of the increasing cost and often only small quantities of solid materials available in solid-state studies, it was decided to change from the original X-band system (8.2–12.4 GHz) to the smaller dimension Ka band (26–42 GHz) in the mid-1980s.

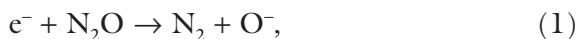
3. Materials and Mechanisms Investigated

In what follows the results obtained using the PR-TRMC technique are presented in a quasi-historic manner beginning with the first gas phase studies of electron attachment and thermalization, extending to electronic processes in dielectric liquids, and finishing with more recent investigations of charge carriers in conjugated polymers and discotic liquid crystals. Of necessity, only the most salient conclusions are given here. Detailed accounts, including more general references to the areas of interest, are to be found in the papers referred to in the text.

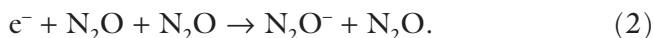
3.1. Gases

3.1.1. Electron attachment

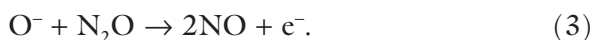
Nitrous Oxide, N₂O, was the ubiquitous electron scavenger used by radiation chemists in the 1960s, and an understanding of the process of electron attachment and the subsequent reactions leading to the formation of nitrogen was of primary concern. Hence, one of the first applications of PR-TRMC, by one of the present authors (JMW), was to the study of electron attachment in pure N₂O gas.¹³ The results indicated that direct dissociative attachment leading to O⁻ formation,



was unimportant for pressures in excess of a few tens of torr, where three-body attachment leading, most probably, to the formation of N_2O^- was predominant.

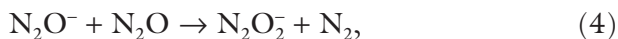


The low effective value for the direct dissociative attachment process was later shown to be due, in part, to the regeneration of electrons via the associative detachment reaction,¹⁴



The predicted formation of N_2 and NO via a chain reaction involving Eqs. (1) and (3) at low N_2O pressures was verified by chemical analysis.¹⁴

At high pressures and in condensed media however, the results indicated that the primary product of electron attachment to N_2O should be N_2O^- . In order to explain the common finding in such systems that more than one N_2 molecule was formed per attached electron, it is necessary to propose a subsequent reaction of N_2O^- , e.g.



with N_2O_2^- eventually undergoing dissociation to form an additional molecule of nitrogen.

Also of interest to radiation chemists at the time were the rate coefficients for attachment of thermal electrons to SF_6 and CCl_4 that were known to be extremely efficient electron scavengers in the gas (and liquid) phase. This property was responsible for the widespread use of SF_6 in the insulating gas mixtures in high-voltage transformers and particle accelerators. The values determined were $2.2 \times 10^{-7} \text{ cm}^3\text{s}^{-1}$,¹⁵ and $4.1 \times 10^{-7} \text{ cm}^3\text{s}^{-1}$,¹⁶ respectively. The latter value was of particular interest since it was very close to the de Broglie wavelength limit for the attachment of thermal electrons at room temperature of $5.0 \times 10^{-7} (300/T)^{0.5} \text{ cm}^3\text{s}^{-1}$.¹⁶ PR-TRMC studies of electron attachment to other halogen-containing molecules demonstrated the large

variation in the thermal attachment coefficients and their activation energies.^{15,16}

3.1.2. *Electron thermalization*

Of importance in the above studies were the ultra-high frequency and relatively low field strength of the microwaves used since these resulted in a minimal perturbation of the (thermal) energy distribution of the electrons. Ionization, however, invariably results in the formation of electrons with excess kinetic energy and a frequently asked question was: “how long does it take for this excess energy to be degraded yielding a thermally equilibrated Maxwellian distribution?” A method of estimating this thermalization time was presented by PR-TRMC measurements on gases containing a small concentration of CCl_4 .^{17,18} This method was based on the pronounced decrease in the attachment coefficient of CCl_4 for energies above thermal that resulted in a non-exponential decay of electrons during post-pulse energy relaxation. From an analysis of the decay kinetics, the time required for the average electron kinetic energy to relax to within 10% of kT was estimated for a variety of atomic and molecular gases.¹⁸ These, admittedly rather rough, estimates of $\tau_{\text{th}}P$ (with the pressure P in torr) demonstrated the extremely large variation in thermalization efficiency, from *ca* 1 millisecond for argon, to 0.2 microseconds for methane, and 10 nanoseconds for acetone, all at 1 torr pressure.

In later PR-TRMC measurements, the after-pulse relaxation of the microwave conductivity itself in pure gases was monitored with nanosecond time-resolution and this provided a more detailed, quantitative method of monitoring electron thermalization.^{19–22} Of particular importance was a detailed study of thermalization in helium, which could be used to test the predictions of different theoretical treatments for this well-characterized gas.²¹ Detailed thermalization data were also obtained for oxygen, for which the concurrent three-body attachment process provides an interesting complication.²² The dramatic influence of small concentrations of water vapor on the thermalization process was also demonstrated for samples of dry and humid air.²⁰ The (unexpectedly) high thermalization

efficiency of CO_2 , which because of this is used in insulating gas mixtures together with SF_6 , was confirmed with a τ_{th} value of only *ca* 50 ns at 1 torr.²³

An important and unique study using PR-TRMC was reported by Shimamori *et al.* in 1992.¹⁵ In this work they made use of the extremely low thermalization efficiency of xenon which is caused by the “Ramsauer minimum” effect. This allowed them to increase the average equilibrium electron energy by applying even relatively low microwave power levels. In this way, detailed information was obtained on the energy dependence of the attachment coefficient for a variety of halogen-containing compounds.

3.1.3. *Recombination*

The ultimate process of charge recombination in pulse-ionized gases is considerably more complex than it might seem at first sight. This is due to the fact that the majority of the orbits experienced by an electron approaching a positive ion are open if there is no mechanism available for the electron to lose the kinetic energy gained in the attractive coulomb field. Because of this, the low-pressure, two-body recombination rate coefficients, α_2 , even for molecular gases are many orders of magnitude lower than the value of *ca* $1 \times 10^{-3} \text{ cm}^3\text{s}^{-1}$ which is calculated for the reaction of a thermal electron with a velocity of *ca* $1 \times 10^7 \text{ cms}^{-1}$ and a reaction radius equal to the Onsager escape distance of *ca* 600 Å. Thus, values within the range $(5 \pm 2) \times 10^{-6} \text{ cm}^3\text{s}^{-1}$ have been measured by PR-TRMC for a variety of molecular gases.^{24,25}

In all cases, however, a pronounced increase in the rate of recombination occurs with increasing pressure, corresponding to a three-body process of rate coefficient α_3 . As opposed to the close similarity of the α_2 values, the values of α_3 were found to increase by two orders of magnitude in going from iso-pentane to water vapor.²⁴ The magnitude of α_3 could in fact be directly related to the efficiency of the different molecules at exchanging energy with electrons while within the coulomb well, which results in closed rather than open orbits.

On increasing the pressure for NH_3 the three-body effect was eventually found to saturate and ultimately, at the highest pressures, a decrease in the recombination rate with increasing pressure was found.²⁶ This overall pressure dependence was explained by the change from free-flight to diffusional recombination at high gas densities.

3.2. Dielectric liquids

In the 1960s great strides were made in the understanding of the primary processes and species formed in ionized dielectric liquids.²⁷ Of particular importance were the findings of very large and strongly molecular-structure-dependent mobilities and yields of the excess electrons formed. For these measurements, time-resolved methods using constant voltage (DC) conductivity cells were used. In 1971 the present authors decided to attempt to make conductivity measurements in pulse-irradiated dielectric liquids using the contact-less PR-TRMC technique. As mentioned previously, for these measurements it was decided to monitor the change in the real (absorptive) component rather than the phase shift which had been previously applied to the study of the much higher mobility electrons in gases.

3.2.1. Electron mobility and reaction kinetics

The initial success of the method was first reported in 1973 with results on excess electrons in liquid iso-octane.³ Using previously measured free-ion yields, electron mobilities were determined from the end-of-pulse conductivity for several hydrocarbon liquids.^{27,28} Where measurements by others using DC techniques were available, the agreement was found to be good with values varying from a low of $0.013 \text{ cm}^2/\text{Vs}$ for trans-decalin to a high of $5.3 \text{ cm}^2/\text{Vs}$ for iso-octane. Of particular interest was the finding that the electron mobility in *cis*-decalin was almost an order of magnitude larger than for the *trans* isomer. This further demonstrated the strong dependence of the electron mobility on quite subtle changes in molecular structure (or shape). The large difference in electron

mobility for the decalins was also reflected in the rate coefficients for electron scavenging by SF_6 or CH_3Br , with an average value of $1.4 \times 10^{12} \text{ M}^{-1}\text{s}^{-1}$ for the *cis* and $0.16 \times 10^{12} \text{ M}^{-1}\text{s}^{-1}$ for the *trans* isomer.²⁷

A liquid which proved to be of particular interest was perfluorobenzene, C_6F_6 , for which the electrons would be expected to be highly localized on the individual molecules because of their high electron affinity. The electron mobility of $1.1 \times 10^{-2} \text{ cm}^2/\text{Vs}$ found was however 40 times larger than expected for transport via molecular ion diffusion.^{29,30} The “electrons” in C_6F_6 also displayed high values for reactions with the highly electron affinic solutes CBr_4 and tetracyanoethylene (TCNE).³⁰ Clearly, electron transport via intermolecular electron transfer was playing a dominant role in this liquid resulting effectively in a large increase in the rate of diffusion of the negative charge.

3.2.2. Radical cation (“hole”) mobility and reaction kinetics

One of the driving forces behind the development of the PR-TRMC technique for the study of liquid media was the hope of being able to conclusively demonstrate the high mobility of the primary radical cation (or “hole”) in cyclohexane which had been predicted on the basis of steady-state and optical pulse-radiolysis results. After rigorous attention to purity, this effort was rewarded with success and the first direct determination of the hole mobility in cyclohexane of $9.5 \times 10^{-3} \text{ cm}^2/\text{Vs}$ could be made.³¹ A similar high mobility was subsequently found for the hole in *trans*-decalin.³² These values were more than an order of magnitude larger than expected for charge transport based on molecular diffusion and it was concluded that diffusion of the radical cation in cyclohexane and *trans*-decalin must occur via an electron transfer mechanism.

In agreement with the high mobility, the rate constants for scavenging of the radical cation in cyclohexane were found to be more than an order of magnitude larger than expected for reactions controlled by molecular diffusion, i.e. ranging from 1 to $3 \times 10^{11} \text{ M}^{-1}\text{s}^{-1}$.³³ While large rate coefficients for hole scavenging were also found for

trans-decalin,^{27,34} the values were much more sensitive to the nature of the solute than in cyclohexane, presumably because of the considerably lower ionization potential of the former solvent.

While the mobilities of electrons were invariably found to be thermally activated in hydrocarbon solvents, those for the holes in cyclohexane and *trans* decalin were found, if anything, to have a slightly negative activation energy.^{27,32} This had the interesting consequence that for sub-ambient temperatures in *trans*-decalin, the hole was found to be even *more* mobile than the electron.³²

Despite what appeared to be conclusive evidence that the mobile positive ion in cyclohexane was the radical cation diffusing via an electron transfer mechanism, Trifunac *et al.* disputed this for many years, proposing alternative mechanisms of proton and hydride ion transfer.³⁵ These mechanisms were however eventually retracted in the mid 1990s³⁶ and the hole mechanism could then be considered to be universally accepted.

As an aside, it is worth mentioning that the study of primary radical cations in saturated hydrocarbon liquids presents a much greater “purity” problem than for excess electrons since many potential impurities and products of irradiation tend to have ionization potentials lower than that of the saturated hydrocarbon solvent. Rigid purification from unsaturated and even isomeric impurities, and very low accumulated doses are therefore imperative in such studies.³⁷

3.2.3. (*Geminate*) charge recombination

One of the distinct advantages of the use of microwave, as opposed to DC techniques, is that the charge carriers are not separated or drifted over macroscopic distances during the course of the measurements. This allows the decay kinetics to be followed in a non-perturbative way for long times. This capability was applied to the study of the ultimate (*geminate*) recombination in solutions for which both the electron and hole had been scavenged on a timescale shorter than the pulse length.³⁸ In this way it was possible to test the predicted dependence of the *geminate* decay on the inverse square root of time

at long-times. In fact a $t^{-0.6}$ dependence was found to provide a better fit to the data, in agreement with the long-time behavior predicted by a full numerical simulation of geminate decay kinetics.^{39,40}

In addition to the scavenged hydrocarbon systems, geminate decay kinetics were also studied in pure CCl_4 for which a comparison was made between the decay kinetics observed using the TRMC technique with that found using a DC method.^{41,42} This comparison further substantiated the potential of the PR-TRMC technique for carrying out non-perturbative studies of short-lived, “dipolar” states. This potential would be extensively applied in later studies of molecular excited states using the flash-photolysis TRMC technique.

As a byproduct of the measurements in the fully scavenged systems the sum of the mobilities of the molecular ions was determined for 10 hydrocarbon liquids varying in viscosity from 0.3 to 3 cP. As expected the values were close to linearly dependent on the viscosity of the solvent with an average value for $\eta[\mu(\text{S}^+) + \mu(\text{S}^-)]$ of $0.75 \pm 0.25 \times 10^{-3} \text{ cm}^2/\text{Vs}$ with η the viscosity in centipoise.²⁷

3.2.4. *Electron thermalization*

Using a microwave cavity capable of sustaining high pressures, it proved possible to monitor the relaxation of the mobility of electrons as they thermalized in the heavy rare gas liquids Ar, Kr and Xe.^{43,44} The thermalization times at close to the triple points were 0.9, 4.4 and 6.5 ns respectively with shorter values of 0.5, 2.2 and 4.4 ns found in the solid phase.⁴⁴ A full density dependence showed that a maximum in the thermalization time occurred at a density of *ca* 1.2×10^{22} atoms per cm^3 for all three compounds.⁴³ For liquid methane thermalization was found to occur within the *ca* 200 ps response time of detection.⁴⁴

3.3. *Frozen aqueous media*

By its nature the TRMC technique is not applicable to polar liquids for which the dipole relaxation times usually lie in the picosecond time regime, i.e. the same regime as the oscillation period of microwaves.

The relaxation times of frozen aqueous media are however sufficiently far removed from the microwave region that application of the PR-TRMC technique to low temperature aqueous systems is possible.

3.3.1. *Ice*

The initial studies, were carried out on pure, macroscopic crystals of hexagonal ice. This was considered to be a model system for studying “dry” electrons and the results were therefore thought to be of possible relevance to direct effects in the radiolysis of biological systems.

The initial measurements demonstrated immediately the high mobility of excess electrons in the ice matrix of $25 \text{ cm}^2/\text{Vs}$,⁴⁵ approximately four orders of magnitude larger than the mobility of the solvated electron in water. While the mobility was found to have only a small, negative activation energy, the rate of trapping was found to be highly thermally activated above a temperature of -70°C with an activation energy of 0.55 eV .^{46,47} As a result the lifetime of the mobile electrons decreased by close to three orders of magnitude in going from -70°C (*ca* 100 ns) to -10°C (*ca* 100 ps). Based on the effects of the classic ice dopants HF, NH_3 and NH_4F ,⁴⁸ it was concluded that the primary trapping site for the mobile electrons was a compound point defect consisting of a vacancy dressed with a D defect i.e. a cavity with three rather than two OH protons oriented towards the center. Below approximately -80°C the electron lifetime was close to a microsecond and almost independent of temperature, presumably due to “freezing-in” of the defect concentration.

At elevated temperatures, where the electron lifetime was much shorter than the pulse lengths of a few nanoseconds used, a second mobile species could be observed as a slowly decaying after-pulse conductivity component for large pulses.⁴⁹ This was attributed to proton conduction with a proton mobility of $6.4 \times 10^{-3} \text{ cm}^2/\text{Vs}$ in H_2O ice and a somewhat lower value in D_2O ice.⁵⁰ In the case of the proton, the mobility was found to have an appreciable negative activation energy of 0.22 eV . The motion and trapping of protons was tentatively explained in terms of an equilibrium between “free” protons and a proton complexed with an orientational L-defect.⁵⁰

3.3.2. Hydrated biopolymers

As mentioned in the previous section, the experiments on charge carriers in pure ice were considered to be possibly relevant to the reactions of the primary, “dry” electrons produced in irradiated biological systems. In subsequent studies, first reported in 1983,⁵¹ an attempt was made to monitor the behavior of primary charge carriers in actual biologically relevant molecular media. Of particular interest was the influence of water of hydration on molecules such as DNA, collagen and gelling polymers such as gelatin itself and κ -carrageenan.⁵²⁻⁵⁴ Because of the high dielectric loss for temperatures even somewhat lower than 0°C, these experiments were necessarily carried out on samples cooled to -20°C and below.

In their “dry”, dehydrated form, none of these polymers displayed a measurable radiation-induced conductivity using the PR-TRMC technique. At a given hydration level however, readily measurable conductivity transients became apparent. In the early experiments this “critical” water weight fraction was found to be 0.27, 0.30, 0.32 and 0.45 for κ -carrageenan, *tropo*-collagen, gelatin and (calf thymus) DNA, respectively. Above these weight fractions (corresponding to *ca* 20 water molecules per nucleotide for DNA) the conductivity was found to increase close to linearly with increasing water content.⁵⁴ The similarity of the extrapolated values of the radiation-induced conductivity to the value found for pure ice, suggested that the transients were arising from excess electrons in “ice-like” regions within the hydrated matrix rather than from charge carriers intimately associated with the biopolymer backbone. Interestingly, the after-pulse lifetime of these mobile electrons was in general much longer than in pure ice. This was taken to indicate that incorporation of the biopolymer into the ice matrix results in depletion of vacancy- and/or D-defects within the vicinal ice-like regions.

The results for DNA were of particular relevance, since suggestions have been made over the years that the stacked base-pairs within DNA could function as a “molecular wire” supporting rapid charge transport. Because of this a subsequent series of measurements was carried out in which wet-spun, aligned samples of hydrated DNA were

subjected to extremely careful examination using a cell construction in which the polymer backbone could be aligned parallel or perpendicular to the microwave electric field vector.^{55,56} These experiments provided no evidence of the anisotropy in the radiation-induced conductivity that would have been expected if it resulted from rapid charge transport within the stacked base-pair core of the DNA.

What could be observed in the later experiments was a radiation-induced conductivity at water contents considerably lower than observed in the initial measurements. Thus, in the region of 12 to 22 water molecules per nucleotide (corresponding to the A DNA structure) a water-concentration-independent conductivity was observed.⁵⁶ It was concluded that this does not arise from ice-like regions but from a layer of water molecules that is more intimately connected with the structure of the bio-molecule. The nature of the mechanism underlying this conduction remains to this day a mystery.

It is perhaps relevant to remark that the many experimental and theoretical studies that have been carried out on the “DNA conductivity problem” in the last three or more decades, have resulted in the generally accepted conclusion that charge transfer and electron tunneling between the stacked base pairs can occur and can play an important role in radiation damage and its repair. To our knowledge, however, there is still no experimental evidence for naturally-occurring DNA functioning as a highly conductive, “copper-like” molecular wire, as has been proposed by some.

3.4. *Inorganic semiconductors*

The majority of studies using PR-TRMC in recent years have involved complex organic materials such as conjugated polymers or discotic liquid crystals. Inorganic semiconductor materials have however also received attention over the years. The first of these was a study of the radiation-induced conductivity in a powder sample of the “high-T_c” superconductor DyBa₂Cu₃O_{7-x}.⁵⁷ The superconductivity transition at 88 K on cooling was found to be accompanied by a dramatic, sudden increase in the radiation-induced conductivity; an effect which

remains, as yet, unexplained. Results on other inorganic materials investigated are presented below.

3.4.1. *Cadmium sulfide*

Prior to its demise, because of carcinogenicity problems, cadmium sulfide was one of the “great hopes” of photovoltaic solar energy conversion. A PR-TRMC study of this material was initially carried out on a high-resistivity, macroscopic single crystal.⁵⁸ The value of the electron mobility was determined to be $280 \text{ cm}^2/\text{Vs}$ in agreement with values determined by DC methods. The decay of the conductivity was unexpectedly found to display an inverse accumulated dose effect with the lifetime *increasing* with increasing radiation dose. This effect was attributed to the saturation of electron trapping sites and a full kinetic analysis allowed the rate coefficients for trapping and de-trapping to be evaluated.

In subsequent studies, five commercially-available powder samples of nominally “ultra-pure” CdS were investigated with dramatically different experimental results.⁵⁹ Both the end-of-pulse conductivity and the decay time were found to vary by many orders of magnitude from sample to sample. The largest PR-TRMC transient was obtained for Fluka purissima CdS which had an end-of-pulse conductivity close to that for a crushed powder sample of the previously mentioned single crystal and a decay half-life of two milliseconds. This is to be compared with the smallest transient observed, for Johnson Matthey Puratronic CdS, with an end-of-pulse conductivity a factor of 250 lower and a half-life of only 11 nanoseconds. These large differences are presumably due to a combination of differing particle sizes and concentrations of trapping defects resulting from non-stoichiometric composition.

An experimental innovation introduced for these measurements was the use of a pseudo-logarithmic time-base that allowed transients to be monitored from nanoseconds to seconds using a single accelerator pulse. This proved to be of general use in studies of the disperse decay kinetics found in the majority of solid inorganic and organic materials.

3.4.2. *Metal oxides*

Metal oxides, in particular titanium dioxide, are of particular interest because of their proposed applications in photocatalysis and photovoltaic devices for solar energy conversion. Several commercially-available samples of TiO_2 were investigated by PR-TRMC and, as for the previous CdS materials, large differences in both the end-of-pulse conductivity and the decay kinetics were found.⁶⁰ The differences in this case could, in part, be ascribed to different morphological forms of the material. Thus, the largest mobility values, in the range 2 to 5 cm^2/Vs , were found for pure anatase samples and the lowest, close to 0.04 cm^2/Vs , for pure rutile. The mixed morphology material Degussa P25 was found to have an intermediate mobility of *ca* 0.2 cm^2/Vs . This relatively low value for a mainly anatase morphology could, at least in part, be explained by the small particle size (average radius *ca* 15 nm) of the P25 material. To test this hypothesis, the size dependence was investigated for samples of “flame reactor” TiO_2 prepared with radii varying from 5 to 47 nm and the corresponding mobility values were found to increase from 0.05 to 1.4 cm^2/Vs .⁶⁰

The important influence of the surface on the electronic properties of Degussa P25 particles was illustrated by the dramatic effect of a layer of isopropanol on the decay kinetics of electrons.⁶¹ This resulted in an increase in the mobile electron lifetime from a few hundred nanoseconds to seconds. In addition, on repetitive pulsing the end of pulse conductivity increased to a value corresponding to a mobility of *ca* 1 cm^2/Vs . These effects were attributed to the retardation of surface recombination with holes which are removed from the surface as protons by reaction with the alcohol.

3.4.3. *Amorphous silicon*

The possible application of the PR-TRMC technique to the study of thin semiconductor films was illustrated by results obtained on 0.9 micron thick layers of amorphous silicon on glass.⁵⁹ These results yielded an electron mobility of 1.5 cm^2/Vs in good agreement with values determined

using DC techniques. In addition, the second order recombination of charge carriers in this material could be studied in detail.

3.4.4. *C60*

The (semi)conductive properties of fullerene derivatives and carbon nanotubes have been a topics of intense recent interest. Unfortunately, at the time of writing it is still not possible to obtain well-defined samples of nano-tubes in sufficient amounts to carry out PR-TRMC measurements. Relatively pure, powder samples of C60 were however available in the mid-1990s and large, if short-lived, PR-TRMC transients could be observed.⁶² More recently attention has focused on the methyl ester of phenyl-C61-butyric acid (PCBM) which is a soluble C60 derivative that has found applications as the electron accepting component in hetero-junction materials for solar energy conversion.

A PR-TRMC study of a microcrystalline powder sample of PCBM was recently carried out and showed mobile charge carriers to be produced with lifetimes extending to many milliseconds.⁶³ This is orders of magnitude longer than expected for homogeneous diffusional charge recombination. PCBM appears therefore to be an indirect-gap organic semiconductor. The charge mobility, in the range 0.04 to 0.3 cm²/Vs, was however an order of magnitude lower than that found for unsubstituted C60. The much longer lifetime of the conductivity in PCBM than in C60 can, most probably, be ascribed to the high solubility and hence more rigorous purification of the former compound. Surprisingly, it was found that the lifetime of the mobile charge carriers in PCBM decreased substantially on annealing above approximately 100°C.⁶⁴ This could have practical consequences since high-temperature annealing is a common practice in the production of PCBM-containing films for solar energy devices.

3.5. *Polymers*

3.5.1. *Polyethylene*

The high mobilities of charge carriers found in saturated hydrocarbon liquids suggested that mobile species should also be prevalent in

ionized solid hydrocarbons such as polyethylene (PE). Because of this, several attempts were made in the 1980s to observe mobile carriers in polyethylene samples using the PR-TRMC technique, without success. It was only with the advent of highly crystalline, ultra-high molecular weight polyethylene (UHMW-PE) that it proved possible to obtain radiation-induced conductivity transients with lifetimes longer than the nanosecond pulses used.⁶⁵ From the end-of-pulse conductivity, a charge carrier mobility sum of *ca* $1 \text{ cm}^2/\text{Vs}$ was estimated, based on a free ion yield of $0.1 (100 \text{ eV})^{-1}$. Even in this highly crystalline material however the lifetime of the mobile carriers was only *ca* 10 ns. This was attributed to rapid migration to trapping sites, probably consisting of less well organized, amorphous regions. It is worth mentioning in this regard that completely amorphous polymers, such as polymethylmethacrylate (PMMA), display no radiation-induced conductivity. This is taken advantage of in its use for the design of “inert” sample holders for studying solid samples for which only small amounts (tens of milligrams) of material are available.

An interesting aspect of the work on UHMW polyethylene was the possibility of studying the anisotropy of the conductivity since aligned samples of stretch-oriented fibers could be produced and the effect of fiber orientation investigated. These experiments showed charge transport to be favored by a factor of approximately 20 along the direction of the oriented fibers compared with perpendicular to the fibers.⁶⁶ This represented the first measurement of anisotropic conduction using the PR-TRMC technique.

3.5.2. *Polydiacetylenes*

Polydiacetylenes (PDAs) were the first class of conjugated polymer that could be produced in pure, single crystal form by the polymerization of the corresponding crystals of the monomeric dialkyne derivatives. DC measurements had demonstrated large electron mobilities in such PDA crystals. Because of this they were considered at the time to be of potential application as an organic semiconductor layer in electronic devices. While these hopes were unfulfilled, these

materials remained of considerable fundamental interest because of their unique, well-defined crystal structures.

The first PR-TRMC study of a PDA derivative was reported in 1994.⁶⁷ In this work the initial monomeric crystals (of 4BCMU) were radiation-polymerized using the same accelerator as for the transient measurements and the PR-TRMC transients were measured at increasing monomer conversion. These measurements confirmed the high charge mobility within the polymerized regions with a lower limit of $5 \text{ cm}^2/\text{Vs}$ being estimated. They also demonstrated however, the negative effect of increasing accumulated radiation dose on both the mobility and the lifetime of the mobile carriers.⁶⁷ These effects were found to be particularly pronounced for the doses, in excess of 100 Gy, that had been typically used to produce “fully polymeric” crystal samples.

Subsequent PR-TRMC studies on a variety of PDAs have recently been reviewed⁶⁸ and references to the individual papers are to be found in that report. In general the results confirmed those of the initial study with high mobilities, up to *ca* $40 \text{ cm}^2/\text{Vs}$, being measured. As expected, the values for the low-dose polymerized samples were in good agreement with values for samples which had been thermally polymerized.

An extensive series of measurements was also carried out on the anisotropy of the radiation-induced conductivity by carefully orientating single PDA crystals within the microwave cavity.⁶⁹ Charge transport was found to be favored by up to two orders of magnitude along, as opposed to perpendicular to, the directors of the polymer chains.

3.5.3. *π -bond conjugated polymers*

The synthesis of other conjugated polymers in pure form suffered for many years from their lack of solubility in organic solvents. By functionalizing the conjugated backbone with solubilizing hydrocarbon chains a large variety of pure conjugated polymers did however eventually become available in the 1990s. An important driving force behind this development was the discovery, reported in 1990,⁷⁰ of the

electroluminescence of polyphenylenevinylene. By the early 1990s pure materials were being produced at several laboratories in sufficient (tens of milligram) quantities to allow the first PR-TRMC experiments on bulk solid samples to be made.^{71,72} Examples of some of the substituted conjugated backbone structures that have been studied in recent years are shown in Fig. 1. The results obtained on

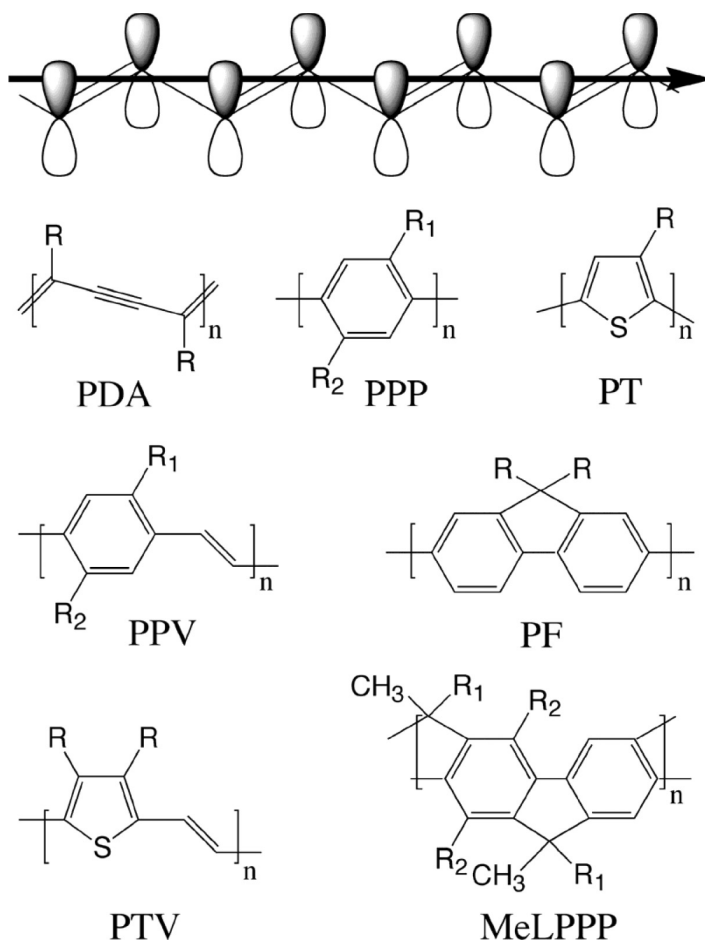


Fig. 1. Backbone structures of some of the conjugated polymers investigated as bulk solids and in dilute solution using the PR-TRMC technique. The position of the solubilizing hydrocarbon substituents is indicated by R.

polyphenylenevinylene (PPV) derivatives¹¹ and other conjugated polymers have recently been reviewed.⁶⁸

Despite the acknowledged high purity, consistent results on the mobility of charge carriers in bulk conjugated polymeric materials have proven to be difficult to achieve. This is undoubtedly due to the complex and varied morphology of these materials which is controlled to a greater or lesser extent by the nature of the solubilizing substituents. For example, the mobility determined by PR-TRMC for a freshly precipitated sample of methoxy, 2-ethylhexoxy substituted PPV of $3.6 \times 10^{-3} \text{ cm}^2/\text{Vs}$ was more than an order of magnitude lower than that of $60 \times 10^{-3} \text{ cm}^2/\text{Vs}$ determined for the di-octadecyloxy derivative.^{11,68} The mobility values have furthermore been found to increase after high temperature annealing,¹¹ which is attributed to thermally-induced structural relaxation resulting in a better organized morphology. In this regard it is worth pointing out that the two polymers found to have the highest mobilities ($> 0.1 \text{ cm}^2/\text{Vs}$) both display liquid crystalline behaviour,⁶⁸ a reflection of their tendency towards self-organization. In all cases, the temperature dependence of the mobility (after annealing) has been found to be only slightly thermally activated with activation energies of, at most, on the order of 0.1 eV.

In addition to the mobilities, which are determined from the end-of-pulse values of the conductivity, the after-pulse decay kinetics have been found to vary dramatically even within a given backbone family.¹¹ In all cases studied so far the decay of the transient conductivity has been found to be highly disperse, obeying neither first order nor second order homogeneous decay kinetics. It is worth mentioning again that the TRMC detection method is non-perturbative and does not influence the natural decay pathways by separating or macroscopically displacing the charge carriers, as can occur in DC methods.

In a study of the decay kinetics for annealed dimethyloctyloxy, methoxy-PPV (dMOM-PPV),⁷² the form of the decay was found to gradually change from stretched-exponential ($\Delta\sigma = \Delta\sigma(0)\exp[-(t/\tau)^\beta]$) at 150°C to an inverse power-dependence ($\Delta\sigma = \Delta\sigma(0)[1 - (\tau/t)^\alpha]$) at -50°C . A similar effect has been found in a more thorough analysis of the decay kinetics for regio-regular

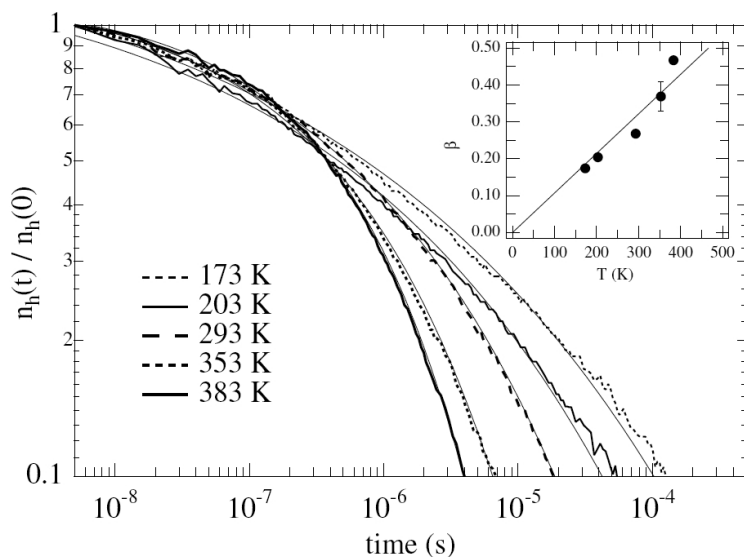


Fig. 2. The decay of the conductivity (mobile hole concentration) in bulk regioregular-poly-3-hexylthiophene (Merck) at different temperatures. The full smooth curves are least-square fits using a stretched-exponential time dependence with the temperature dependence of the fit parameter β shown in the inset. [Reprinted from Ref. 74, Copyright 2005, with permission from Elsevier.]

poly-3-hexylthiophene.⁷³ For this material, the β parameter in the stretched exponential dependence was found to decrease from 0.47 at -110°C to 0.17 at -100°C ; see Fig. 2. The degree of dispersivity, in other words, increases dramatically on decreasing the temperature. Possible explanations for this have been discussed.⁷⁴

Only for dMOM-PPV has an effect of accumulated radiation dose been studied in detail.⁷² Even up to a total dose in excess of one megaGray the end-of-pulse conductivity (proportional to the mobility) remained constant. The after-pulse decay of the conductivity did however become appreciably more rapid for accumulated doses in excess of a few tens of kiloGray. Interestingly, this latter effect could be changed reversibly by thermal annealing at 150°C . The trapping centres produced by irradiation appeared therefore to be charged defect sites which could be removed by detrapping and charge recombination on annealing.

The di-octadecoxy-PPV derivative ((OD)₂-PPV) is of particular interest since it undergoes a transition to a fluid medium at close to 200°C. Even in the fluid phase however, the PR-TRMC transients remain large with an estimated mobility of 0.17 cm²/Vs.¹¹

3.5.4. σ -bond conjugated polymers

Because of its extremely large band-gap, in excess of 6 eV, polyethylene has never been seriously considered to be a semi-conductive material, although, as we have shown, the mobility of charge carriers in UHMW-PE is possibly as high or even higher than in the *conjugated* polymers discussed in the previous section. In the case of the heavier group IV elements, the much stronger electronic intra-chain interactions result in a considerable decrease in the band-gap energy. In addition, due to the larger inter-atomic backbone bond distance, the elements can be di-substituted with functional groups which can lead to a further reduction in the band gap and to polymers with unique electronic and material properties. We were fortunate in the early 1990s to come into contact with Holger Frey who was synthesizing a series of di-alkyl substituted poly-silanes that displayed interesting mesomorphic behavior. This led to an extensive study of the optical and the conductive properties of these materials.⁷⁵⁻⁸⁰

In the initial PR-TRMC study,⁷⁶ results for the amorphous methyl,phenyl derivative (PMPSi) were compared with those for the mesomorphic di-hexyl derivative (PD6Si). The latter compound displayed a radiation-induced conductivity in its crystalline solid phase that was two orders of magnitude larger than for PMPSi, corresponding to a mobility of at least 0.1 cm²/Vs. On entering the liquid crystalline phase of PD6Si at *ca* 40°C, the conductivity decreased by a factor of 20 but was still larger than in PMPSi.

Subsequent studies illustrated the complexity of the phase transitions in di-alkyl polysilanes and the dramatic effects these have on the optical and conductive properties.^{75,78,80} A general conclusion that could be reached was that the mobility of charge invariably decreases in going from the crystal to the liquid crystal phase, and if subsequent higher temperature liquid crystal phase transitions occur, these result

in a further decrease in the mobility. This effect can be explained by the negative influence of thermally induced structural fluctuations on the transport of charge along the polymer backbone. The fact that transport does in fact occur along the backbone was demonstrated by the anisotropy of PR-TRMC transients for a sample of PD6Si that was aligned by stretch-orientation of a solid solution in UHMW-PE above the meso-phase transition temperature of PD6Si.⁷⁷

In addition to polysilanes, a di-*n*-hexyl derivative of polygermane (PD6Ge)⁷⁹ and, more recently, a di-*n*-butyl derivative of polystannane (PD4Sn)⁸¹ have been investigated by PR-TRMC. Both of these compounds also display mesomorphic behavior with a decrease in the charge mobility occurring at the transition from the crystal to the liquid-crystal phase. The results for the poly-stannane compound are shown in Fig. 3. Of interest is that the liquid crystalline phase of PD4Sn is the stable phase even at room temperature. A comparison of the mobility values in the crystalline phase and meso-phase of the PDnM compounds showed, perhaps surprisingly, that the mesophase

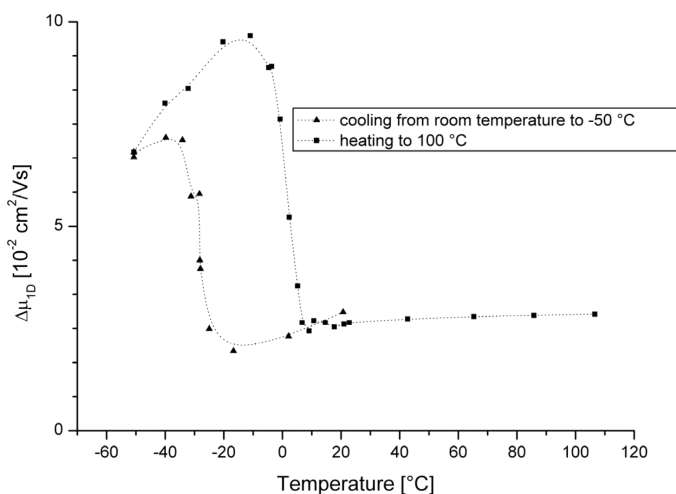


Fig. 3. The temperature dependence of the intra-chain charge mobility in poly-di-*n*-butylstannane (PD4Sn). The data illustrate the sudden change (with large hysteresis) at the solid/liquid-crystal phase transition on cooling and heating; from Ref. 81. [Copyright Wiley-VCH Verlag GmbH & Co. KGaA. Reproduced with permission.]

mobilities differ by less than a factor of two, with no apparent systematic dependence on the nature of the backbone element.⁸¹

3.6. *Liquid solutions of conjugated polymers*

In a previous section (Sec. 3.2 Dielectric liquids), results were presented of PR-TRMC studies of dilute solutions of small molecules in hydrocarbon solvents. In that case, mobile primary charge carriers become localized on the (small) solute molecules and the charge mobility reverts to that for an ion undergoing diffusive molecular motion, i.e. $ca\ 0.4 \times 10^{-3}\ \text{cm}^2/\text{Vs}$ for a liquid of viscosity 1 cP.²⁷ For a conjugated polymer as solute, however, the result of charge scavenging can be quite different. Thus, while the charged polymer chain as a whole will undoubtedly have a low mobility, the charge may be able to migrate rapidly along the polymer backbone. Such an intra-chain mobility could even exceed that of the primary solvent charge carrier. This can result in the observation of an actual *increase* in the microwave conductivity after pulsed irradiation as charge is transferred to the polymer. This effect was first observed for a solution of a phenylene-vinylene polymer (MEH-PPV) in benzene.⁸² By using additional competitive electron or hole scavengers, it was possible to draw the important conclusion that both the hole *and* the electron were highly mobile on a PPV chain, with effective 1D mobilities in excess of $0.1\ \text{cm}^2/\text{Vs}$. Up to that time no conclusive evidence had been found for highly mobile electrons for this type of conjugated polymer. The similarity in mobility of electrons and holes has also been demonstrated recently by PR-TRMC for a poly(thienylenevinylene) derivative with values of 0.23 and $0.38\ \text{cm}^2/\text{Vs}$ respectively.⁸³

In Fig. 4 the after-pulse growth of the PR-TRMC transients due to positive ion scavenging by different π -bond conjugated polymers in oxygen saturated benzene is illustrated.⁸⁴ From kinetic fits to the transients,¹² using the known free-ion yield in benzene, the intra-chain hole mobility could be determined and the values were found to vary from a low of $0.02\ \text{cm}^2/\text{Vs}$ for the polythiophene to a high of $0.74\ \text{cm}^2/\text{Vs}$ for the polyfluorene derivative.⁸⁴ Mobility values in the

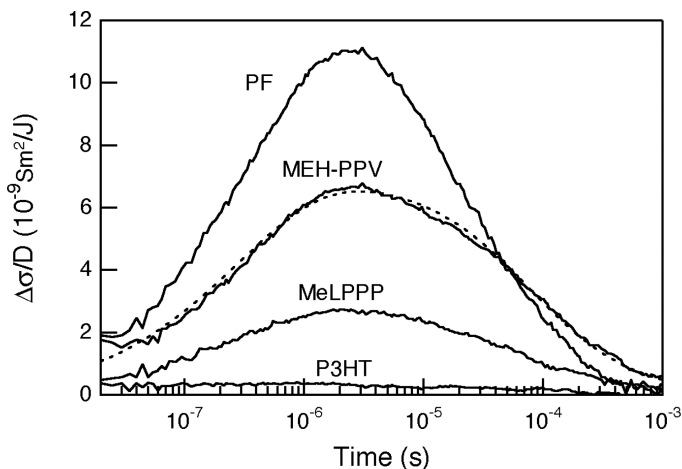


Fig. 4. The temporal dependence of the (microwave) conductivity of dilute solutions of different conjugated polymers in oxygen-saturated benzene following 5 ns pulse ionization; from Ref. 84. The data illustrate the after-pulse increase in conductivity accompanying the reaction of the relatively low-mobility, initially-formed solvent cations with the polymer leading to high-mobility holes on the conjugated polymer backbone. The eventual decay of the conductivity occurs via recombination of the polymer radical cations with the O_2 counterions in the solution. The smooth, dashed curve drawn through the MEH-PPV transient is a calculated best fit. The polymer pseudonyms shown in the figure can be related to the backbone structures shown in Fig. 1. [Copyright Wiley-VCH Verlag GmbH & Co. KGaA. Reproduced with permission.]

same range were also found for isolated σ -bond conjugated chains of some substituted poly-silanes dissolved in benzene.⁸⁴

In addition to the mobility values which can be derived from the magnitude of transients such as those shown in Fig. 4, information can be obtained from the temporal form on the kinetics of the reaction of the polymer with the primary hole (or electron) and the rate constant for the ultimate charge recombination reaction which controls the decay of the conductivity at long times.^{12,84} Recent studies have looked into the influence of broken conjugation⁸⁵ and polymer chain length^{86–88} on the intra-chain mobility.

It is worth emphasizing here that in the case of the bulk solid polymers, it is not possible to differentiate between the positive and negative charge carrier mobilities and only a mobility sum can be

derived from the PR-TRMC transients. In addition, in the solid phase the actual yield of charge carrier pairs is unknown and the mobility values given are minimum values based on the assumption that all of the ionization events lead to long-lived charge carriers. Alternatively, in the dilute solutions the yield and hence mobilities of the charge carriers are accurately known and, by preferential competitive scavenging, the individual electron and hole mobilities can be determined.

3.7. *Discotic liquid crystals*

The most extensive series of experiments using the PR-TRMC technique in recent years has been directed towards an understanding of the charge transport properties of discotic materials. In these materials the individual molecules, consisting of an aromatic core with several peripherally substituted alkyl chains, columnarly stack with the columns packed in a well-organized, two-dimensional lattice. The types of aromatic cores investigated are illustrated in Fig. 5.

In addition to their novel mode of self-organization, these compounds are of interest because they display mesomorphic behavior with many of them having extensive liquid crystalline phases. Because of the close (*ca* 3.5 Å) intra-columnar stacking distance and resulting π - π overlap within the aromatic core of the columns, it was thought that they should be capable of supporting rapid one-dimensional charge transport. This was shown to be the case by the initial PR-TRMC measurements on discotic phthalocyanine and porphyrin derivatives.^{89,90} The measurements furthermore provided information on the process of inter-columnar electron tunneling through the intervening saturated hydrocarbon mantle.^{89,91} The results have been extensively reported in recent review articles⁹²⁻⁹⁴ and only a brief presentation of the more salient aspects and conclusions will be given here.

The majority of the early experiments were carried out on a variety of alkoxy-substituted phthalocyanines on the basis of which the following qualitative conclusions could be drawn: (a) the intra-columnar mobility was relatively insensitive to the nature of the peripheral alkyl chain substituents which did however influence the mesomorphic properties; (b) the mobility invariably decreased on

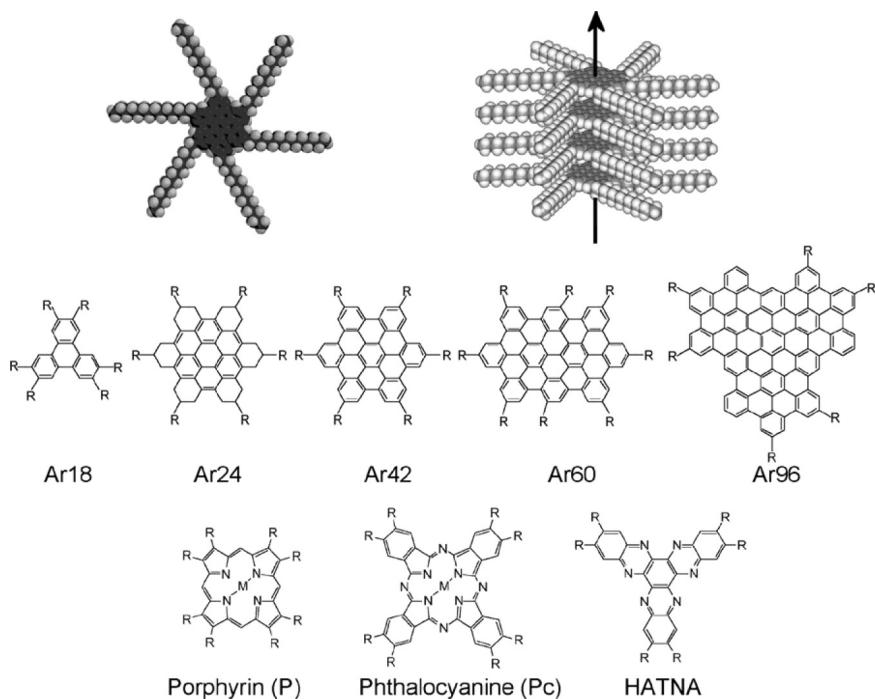


Fig. 5. The molecular structures of discotic cores investigated using the PR-TRMC technique with the position of peripheral hydrocarbon substituents indicated by R.

going from the solid crystalline phase to the liquid crystalline phase; (c) within a given phase the mobility was only weakly dependent on temperature; (d) as opposed to the intra-columnar mobility, the decay of the radiation-induced conductivity was strongly dependent on the structure of the peripheral hydrocarbon chains.

Conclusion (b) was of particular importance since it had been predicted by some that horizontal stacking of the cores, and hence better π - π overlap, in the mesophase should result in a substantial *increase* in the charge mobility. The negative effect actually observed, which is now generally accepted, can be attributed to the structural fluctuations within the core that result on melting of the hydrocarbon side chains. Important in the general acceptance of this effect was a comparative study of PR-TRMC results with DC time-of-flight results on

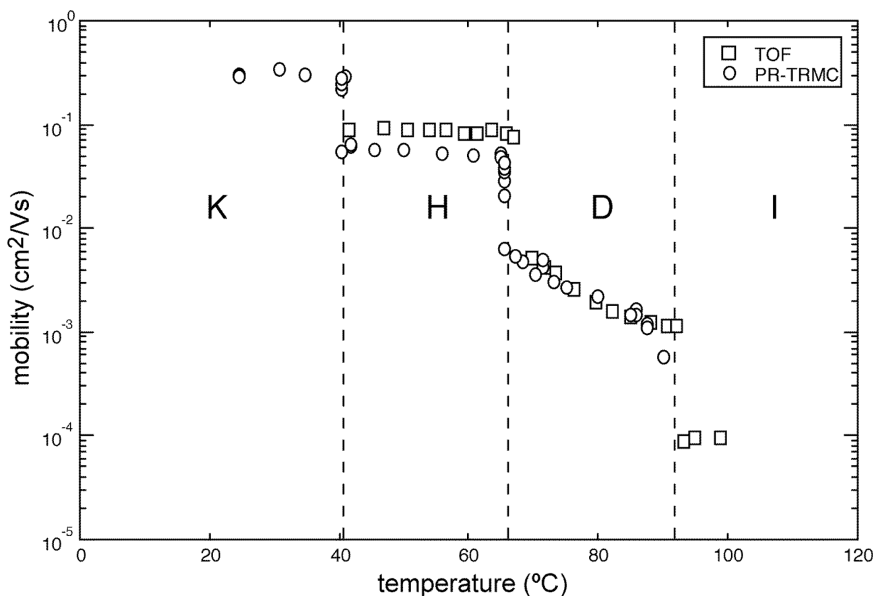


Fig. 6. The temperature dependence on heating of the one-dimensional hole mobility in *hexa*-hexylthiotriphenylene (HHTT) determined by PR-TRMC (circles) or time-of flight (TOF) (squares) methods; from Ref. 95. [Copyright Wiley-VCH Verlag GmbH & Co. KGaA. Reproduced with permission.]

the compound *hexa*-hexylthiotriphenylene (HHTT).⁹⁵ Not only did both measurement techniques show a decrease in mobility on entering a higher temperature mesophase, but even the absolute values of the mobilities derived were almost identical, as shown in Fig. 6. This latter point furthermore provided support for the method of deriving mobility values from the PR-TRMC data. This was particularly important since the *electrodeless* PR-TRMC method could be generally applied to all microcrystalline materials, most of which were not readily amenable to investigation by the time-of-flight method.

A point of theoretical interest was the dependence of the intracolumnar charge mobility on the size (i.e. the number of π electrons) of the aromatic core. On the basis of an admittedly limited number of different cores, an exponentially increasing relationship between mobility and core size was initially proposed.⁹⁶ This had to be reconsidered however when the series of large aromatic cores shown

in Fig. 5 were more recently investigated.⁹⁷ These results showed that the mobility, in fact, tended to attain a plateau value of *ca* 0.3 cm²/Vs for aromatic cores larger than approximately 40 carbon atoms. The lower mobility values found for the smaller triphenylene and porphyrin derivatives could possibly be due more to the lower cohesion of these small aromatic cores, and hence greater sensitivity to thermal fluctuations, rather than a π - π overlap effect.

Next to the phthalocyanines, the group of compounds most studied in recent years has been hexa-alkyl derivatives of hexa-*peri*-hexabenzocoronene (“HBC” or “Ar42” in Fig. 5).^{92,94} The results obtained have substantiated the general conclusions given above based on the early phthalocyanine measurements. Substantially larger charge mobilities, of close to 1.0 and 0.3 cm²/Vs in the solid and liquid crystalline phases respectively, are however found for the HBCs. Interestingly, the mobilities found for these non-covalently bonded discotic materials are at least as large as for the π -bond conjugated polymers.⁹⁴

Because of the fascination of synthetic organic chemists and molecular electronics device designers with ever-increasing charge mobilities, attention was focussed mainly on the magnitude of the end-of-pulse conductivity of PR-TRMC transients. Because of this, the after-pulse decay kinetics in discotic materials received only scant attention. The dramatic influence of the nature of the peripheral chains on the lifetime of the PR-TRMC conductivity transients, was in fact demonstrated early-on for octa-alkoxy phthalocyanine derivatives⁹¹ as mentioned previously in this section. This effect is illustrated with more recent data for some hexa-alkyl HBC derivatives in Fig. 7.

In Fig. 8 is shown a semi-logarithmic plot of the $1/e$ decay time of the conductivity transients, τ_e , against the disc diameter for several discotic phthalocyanine and HBC derivatives.⁹⁸ The good agreement with the straight line drawn through the data illustrates the exponential dependence of the decay of the conductivity on the inter-columnar distance, i.e. $\tau_e = \tau_e(0)\exp\{\beta R\}$. The process responsible is therefore concluded to be charge recombination via electron tunneling through the saturated hydrocarbon mantle separating the columns.

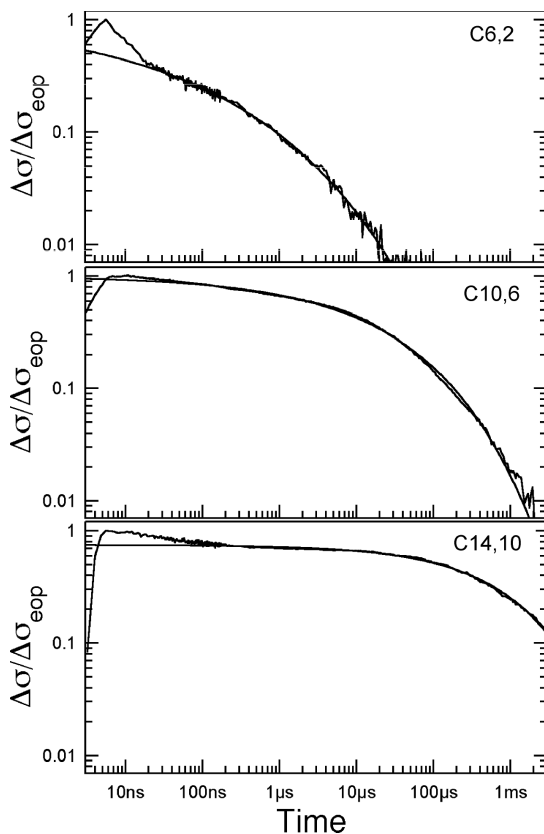


Fig. 7. The temporal dependence of the conductivity decay, normalized to the end-of-pulse value, on 5 ns pulsed ionization of hexa-alkyl derivatives of hexa-*peri*-hexabenzocoronene (HBC) with ethyl-hexyl (C6,2), hexyl-decyl (C10,6), and decyl-tetradecyl (C14,10) branched alkyl chains; illustrating the dramatic increase in lifetime of the charge carriers with increasing length of the peripheral chains. [Reprinted WPh permission from Ref. 98. Copyright 2005 American Chemical Society.]

Interestingly, even the absolute values of τ_e are closely similar for the phthalocyanine and HBC derivatives, indicating this to be a universal property of the hydrocarbon chains alone. From the results the exponential β parameter for electron tunneling was estimated to be *ca* 0.8 \AA^{-1} with a pre-exponential (zero-distance) electron transfer time of *ca* 50 ps.⁹⁸ These parameters are of considerable practical interest since

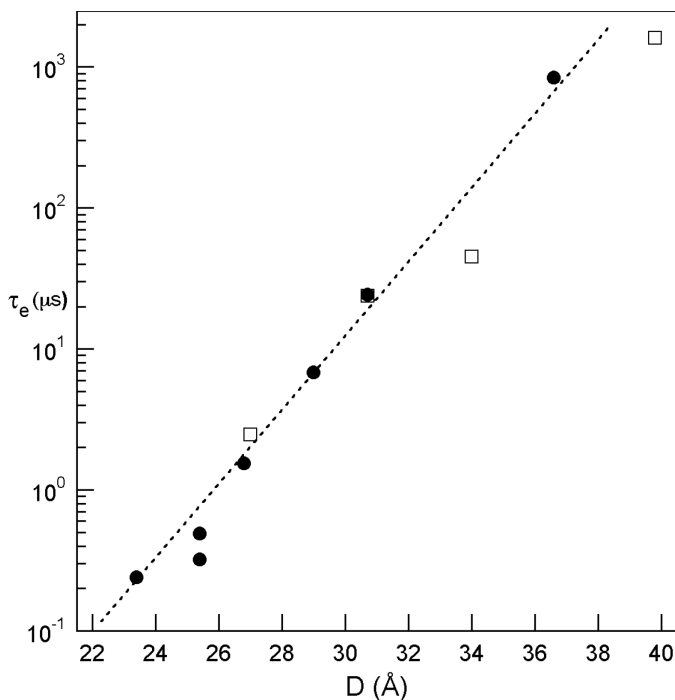


Fig. 8. A semi-logarithmic plot of the $1/e$ decay time of the conductivity, τ_e , versus the calculated disk diameter, D , for hexa-alkyl derivatives of hexa-*peri*-hexabenzocoronene (filled circles) and octa-alkoxy derivatives of phthalocyanine (open squares). The straight line drawn through the points corresponds to an exponential dependence of τ_e on D . [Reprinted WPh permission from Ref. 98. Copyright 2005 American Chemical Society.]

they define the distance between organic molecular circuit components at which cross-talk will become an important problem; for example a nanosecond, microsecond and millisecond correspond to tunneling distances of 12 Å, 21 Å and 30 Å respectively. The last is close to the thickness of the hydrocarbon region in biological cell membranes.

4. Future Perspectives

In the above we have illustrated the wide range of materials and physico-chemical processes to which the PR-TRMC technique has

been applied in the past. Most of these areas are by no means exhausted in terms of their fundamental scientific interest and the insights that the PR-TRMC technique can provide. Certain areas, such as the kinetics of electron capture and recombination in gases, the electronic and protonic properties of ice, and the nature and reactions of primary charge carriers in ultra-high-purity dielectric liquids, will probably receive little future attention because of their lack of direct relevance to fashionable areas of technology. The application of the technique to probe the properties of charge carriers in complex materials such as powders, liquid crystals and “conducting” polymers should however continue to provide fundamental information of relevance to practical areas involving molecular electronics, such as photovoltaic cells, light-emitting diodes, and field-effect transistors.

As mentioned in the introduction, we have deliberately limited the present review to results obtained using “*pulse-radiolysis*” as the method of formation of the charged species capable of being detected by the “time-resolved microwave conductivity” technique. The pulse-radiolysis approach has the advantage over other excitation methods that bulk (micro-heterogeneous) samples, of multi-millimeter dimensions, can be ionized with close-to-uniform and well-defined energy deposition per unit volume. However, the diminishing availability of laboratories with pulsed-beam electron accelerators suitable for PR-TRMC measurements bodes ill for the future of this investigative method.

In the 1980s *FP*-TRMC techniques were introduced in which “*flash-photolysis*” was the method of formation of intermediates capable of detection using the time-resolved microwave conductivity approach. This resulted in pioneering studies of charge-separated excited states of single molecules in dilute solution,^{5,6,99,100} semiconductor-particle suspensions,¹⁰¹ and more recently in studies of charge separation in aligned thin layers of discotic materials,⁸ and multi-layers of organic and inorganic materials.⁷ Such studies should ensure a lively future for the TRMC approach to the study of charge transport and electronic processes in complex molecular materials which will undoubtedly provide unique information, unobtainable using other techniques.

References

1. Fessenden RW, Warman JM. (1968) The study of electron decay in pulse-irradiated gases by a microwave technique. *Adv Chem Ser* **82**: 222–230.
2. Biondi MA. (1950) Measurements of the electron density in ionized gases by microwave techniques. *Rev Sci Instrum* **22**: 500–502.
3. Warman JM, de Haas MP, Hummel A. (1973) The detection of electrons in pulse irradiated liquid hydrocarbons by microwave absorption. *Chem Phys Lett* **22**: 480–483.
4. Infelta PP, de Haas MP, Warman JM. (1977) The study of the transient conductivity of pulse irradiated dielectric liquids on a nanosecond timescale using microwaves. *Radiat Phys Chem* **10**: 353–365.
5. de Haas MP, Warman JM. (1982) Photon-induced molecular charge separation studied by nanosecond time-resolved microwave conductivity. *Chem Phys* **73**: 35–53.
6. Fessenden RW, Carton PM, Shimamori H, Scaiano JC. (1982) Measurement of the dipole moments of excited states and photochemical transients by microwave dielectric absorption. *J Phys Chem* **86**: 3803–3811.
7. Kroeze JE, Savenije TJ, Vermeulen MJW, Warman JM. (2003) Contactless determination of the photoconductivity action spectrum, exciton diffusion length and charge separation efficiency in polythiophene-sensitized TiO₂ bilayers. *J Phys Chem B* **107**: 7696–7705.
8. Piriš J, Debije MG, Stutzmann N, Laursen BW, Pisula W, Watson MD, Bjornholm T, Müllen K, Warman JM. (2004) Aligned thin films of discotic hexabenzocoronenes: Anisotropy in the optical and charge transport properties. *Adv Funct Mater* **14**: 1053–1061.
9. Warman JM. (1982) The microwave absorption technique for studying ions and ionic processes. In: Baxendale JH, Busi F. (eds.), *The Study of Fast Processes and Transient Species by Electron Pulse Radiolysis*, pp. 129–161. Reidel, Dordrecht.
10. Warman JM, de Haas MP. (1991) Time-resolved conductivity techniques, DC to microwave. In: Tabata Y (ed.), *Pulse Radiolysis*, pp. 101–133. CRC Press, Boca Raton.
11. Warman JM, Gelinck GH, de Haas MP. (2002) The mobility and relaxation kinetics of charge carriers in molecular materials studied by means of pulse-radiolysis time-resolved microwave conductivity: Dialkoxy-substituted phenylene-vinylene polymers. *J Phys Condensed Matter* **14**: 9935–9954.
12. Grozema FC, Hoofman RJOM, Candeias LP, de Haas MP, Warman JM, Siebbeles LDA. (2003) The formation and recombination kinetics of positively charged poly(phenylene vinylene) chains in pulse-irradiated dilute solutions. *J Phys Chem A* **107**: 5976–5986.
13. Warman JM, Fessenden RW. (1968) Three body electron capture by nitrous oxide. *J Chem Phys* **49**: 4718–4719.

14. Warman JM, Fessenden RW, Bakale G. (1972) Dissociative attachment of thermal electrons to N_2O and subsequent electron detachment. *J Chem Phys* **57**: 2702–2711.
15. Shimamori H, Tatsumi Y, Ogawa Y, Sunagawa T. (1992) Low-energy electron attachment to molecules studied by pulse-radiolysis microwave-cavity technique combined with microwave heating. *J Chem Phys* **97**: 6335–6347.
16. Warman JM, Sauer MC. (1971) The temperature dependence of electron attachment to CCl_4 , $CHCl_3$ and $C_6H_5CH_2Cl$. *Int J Radiat Phys Chem* **3**: 273–282.
17. Warman JM, Sauer MC. (1970) Determination of electron thermalization times in irradiated gases. *J Chem Phys* **52**: 6428–6429.
18. Warman JM, Sauer MC. (1975) An investigation of electron thermalization in irradiated gases using CCl_4 as an electron energy probe. *J Chem Phys* **62**: 1971–1981.
19. Warman JM, de Haas MP. (1975) The delayed absorption of microwaves due to electron thermalization in nanosecond pulse irradiated N_2 , He and Ar at atmospheric pressure. *J Chem Phys* **63**: 2094–2100.
20. Warman JM, Mei Z-L, van Lith D. (1984) Electron thermalization in nanosecond pulse-ionized dry and humid air. *J Chem Phys* **81**: 3908–3914.
21. Scales MJ, Cooper R, Warman JM, de Haas MP. (1987) Electron thermalization in helium at atmospheric pressure. *Radiat Phys Chem* **29**: 365–367.
22. Warman JM, Cooper R. (1990) Electron thermalization and attachment in pulse-irradiated oxygen studied by time-resolved microwave conductivity. *Radiat Phys Chem* **36**: 517–521.
23. Warman JM, de Haas MP. (1988) The use of CO_2 gas as an *in-situ* dosimeter for DC and microwave pulse-radiolysis conductivity experiments. *Radiat Phys Chem* **32**: 31–36.
24. Warman JM, Sennhauser ES, Armstrong DA. (1979) Three-body electron-ion recombination in molecular gases. *J Chem Phys* **70**: 995–999.
25. Sennhauser ES, Armstrong DA, Warman JM. (1980) The temperature dependence of three-body electron-ion recombination in gaseous H_2O , NH_3 and CO_2 . *Radiat Phys Chem* **15**: 479–483.
26. Armstrong DA, Sennhauser ES, Warman JM, Sowada U. (1982) The electron-ion recombination coefficients in CO_2 and NH_3 . Deviations from a linear density dependence at elevated pressures. *Chem Phys Lett* **86**: 281–284.
27. Warman JM. (1982) The dynamics of electrons and ions in non-polar liquids. In: Baxendale JH, Busi F (eds.), *The Study of Fast Processes and Transient Species by Electron Pulse Radiolysis*, pp. 433–533. Reidel, Dordrecht.
28. de Haas MP, Warman JM, Hummel A. (1975) Hole conductivity in liquid hydrocarbons. *Proc 5th Int Conf on Conduction and Breakdown in Dielectric Liquids*, Delft University Press, pp. 15–18.
29. Nyikos L, van den Ende CAM, Warman JM, Hummel A. (1980) High mobility excess electrons in the electron-attaching liquid hexafluorobenzene. *J Phys Chem* **84**: 1154–1155.

30. van den Ende CAM, Nyikos L, Warman JM, Hummel A. (1982) Mobility, reaction kinetics and optical absorption spectrum of the excess electron in pure C_6F_6 and admixtures with non polar liquids. *Radiat Phys Chem* **19**: 297–308.
31. de Haas MP, Warman JM, Infelta PP, Hummel A. (1975) The direct observation of a highly mobile positive ion in nanosecond pulse irradiated liquid cyclohexane. *Chem Phys Lett* **31**: 382–386.
32. de Haas MP, Hummel A, Infelta PP, Warman JM. (1976) The measurement of a positive charge mobility larger than that of the excess electron in irradiated liquid trans-decalin. *J Chem Phys* **65**: 5019–5020.
33. Warman JM, Infelta PP, de Haas MP, Hummel A. (1976) Rate constants for the reaction of positive ions with solutes in irradiated liquid cyclohexane. *Chem Phys Lett* **43**: 321–325.
34. Warman JM, de Leng HC, de Haas MP, Anisimov OA. (1990) Positive ion scavenging by olefins in trans-decalin: TRMC and product analysis studies. *Radiat Phys Chem* **36**: 185–190.
35. Trifunac AD, Sauer MC, Jonah CF. (1985) Pulse-radiolysis of cyclohexane: The identity of the high-mobility positive ion. *Chem Phys Lett* **113**: 316–319.
36. Shkrob IA, Sauer MC, Schmidt KH, Liu AD, Yan J, Trifunac AD. (1997) Electron transfer from cyclohexane to photoexcited aromatic ions. Generation and kinetics of high-mobility solvent holes. *J Phys Chem* **101**: 2120–2123.
37. Anisimov OA, Warman JM, de Haas MP, de Leng HC. (1987) The effect of accumulated dose on the lifetime of the highly mobile positive charge carriers formed in irradiated cyclohexane and trans-decalin. *Chem Phys Lett* **137**: 365–368.
38. Warman JM, Infelta PP, de Haas MP, Hummel A. (1977) The study of primary and secondary charge carriers in nanosecond pulse irradiated liquid dielectrics using a resonant microwave cavity. *Can J Chem* **55**: 2249–2257.
39. van den Ende CAM, Nyikos L, Warman JM, Hummel A. (1980) Geminate ion decay kinetics in nanosecond pulse irradiated cyclohexane solutions studied by optical and microwave absorption. *Radiat Phys Chem* **15**: 273–281.
40. van den Ende CAM, Warman JM, Hummel A. (1984) Geminate recombination and scavenging of charged species in irradiated liquid *n*-hexane, cyclohexane and isooctane. *Radiat Phys Chem* **23**: 55–59.
41. van den Ende CAM, Luthjens LH, Warman JM, Hummel A. (1982) Geminate ion recombination in irradiated liquid CCl_4 as observed by means of microwave and optical absorption pulse radiolysis and compared with calculations based on a single ion pair model. *Radiat Phys Chem* **19**: 455–466.
42. de Haas MP, Warman JM, Vojnovic B. (1984) Geminate ions in nanosecond pulse irradiated CCl_4 detected by DC conductivity. *Radiat Phys Chem* **23**: 61–65.
43. Sowada U, Warman JM, de Haas MP. (1982) The density dependence of hot-electron thermalization in liquid argon, krypton and xenon. *Chem Phys Lett* **90**: 239–241.

44. Sowada U, Warman JM, de Haas MP. (1982) Hot-electron thermalization in solid and liquid argon, krypton and xenon. *Phys Rev B* **25**: 3434–3437.
45. Verberne JB, Loman H, Warman JM, de Haas MP, Hummel A, Prinsen L. (1978) Excess electrons in ice. *Nature* **272**: 343–344.
46. Warman JM, de Haas MP, Verberne JB. (1980) Decay kinetics of excess electrons in crystalline ice. *J Phys Chem* **84**: 1240–1248.
47. de Haas MP, Kunst M, Warman JM, Verberne JB. (1983) Nanosecond Time-Resolved Conductivity Studies of Pulse-Ionized Ice: 1. The mobility and trapping of conduction-band electrons in H₂O and D₂O ice. *J Phys Chem* **87**: 4089–4092.
48. Kunst M, Warman JM, de Haas MP, Verberne JB. (1983) Nanosecond time-resolved conductivity studies of pulse-ionized ice: 3. The electron as a probe for defects in doped ice. *J Phys Chem* **87**: 4096–4098.
49. Kunst M, Warman JM. (1980) Proton mobility in ice. *Nature* **288**: 465–467.
50. Kunst M, Warman JM. (1983) Nanosecond time-resolved conductivity studies of pulse-ionized ice: 2. The mobility and trapping of protons. *J Phys Chem* **87**: 4093–4095.
51. van Lith D, de Haas MP, Warman JM, Hummel A. (1983) Highly mobile charge carriers in hydrated DNA and collagen formed by pulsed ionization. *Biopolymers* **22**: 807–810.
52. van Lith D, Warman JM, de Haas MP, Hummel A. (1986) Electron migration in hydrated DNA and collagen at low temperatures: 1. Effect of water concentration. *J Chem Soc Faraday Trans 1* **82**: 2933–2943.
53. Eden J, van Lith D, Warman JM, Hummel A. (1987) The effect of water content on the dark and radiation induced microwave conductivity of frozen gelatin gels. *Radiat Phys Chem* **29**: 51–56.
54. Eden J, van Lith D, Warman JM, Hummel A. (1989) The dark and radiation-induced microwave conductivity of frozen aqueous gels. *J Chem Soc Faraday Trans 1* **85**: 991–998.
55. Warman JM, de Haas MP, Rupprecht A. (1995) Radiation-induced conductivity in oriented DNA. In: Hagen U, Harder D, Jung H, Streffer C (eds.), *Radiation Research 1895–1995*, vol 2. pp. 212–215. Universitätsdruckerei H. Stürtz, Würzburg, Germany.
56. Warman JM, de Haas MP, Rupprecht A. (1996) DNA: A molecular wire? *Chem Phys Lett* **249**: 319–322.
57. de Haas MP, Warman JM. (1988) Radiation-induced microwave dielectric loss in small particles of a high-T_c superconductor. *Radiat Phys Chem* **32**: 751–752.
58. Warman JM, de Haas MP, van Hövell tot Westerflier SWFM, Binsma JJM, Kolar. ZI. (1989) Electronic processes in semiconductor materials studied by nanosecond time-resolved microwave conductivity I. Cadmium sulfide macroscopic crystal. *J Phys Chem* **93**: 5895–5899.

59. Warman JM, de Haas MP, Wentinck HM. (1989) The study of radiation induced conductivity changes in microheterogeneous materials using microwaves. *Radiat Phys Chem* **34**: 581–586.
60. Warman JM, de Haas MP, Pichat P, Koster TPM, van der Zouwen-Assink EA, Mackor A, Cooper R. (1991) Electronic processes in semiconductor materials studied by nanosecond time-resolved microwave conductivity-III. Al₂O₃, MgO and TiO₂ powders. *Radiat Phys Chem* **37**: 433–442.
61. Warman JM, de Haas MP, Pichat P, Serpone N. (1991) Effect of isopropyl alcohol on the surface localization and recombination of conduction-band electrons in Degussa P25 TiO₂. A pulse-radiolysis time-resolved microwave conductivity study. *J Phys Chem* **95**: 8858–8861.
62. Hoofman RJOM, van der Laan GP, de Haas MP, Tanigaki K. (1997) Charge migration in pulse-irradiated undoped C60 powder studied with the time-resolved microwave conductivity technique. *Synth Met* **86**: 2355–2356.
63. de Haas MP, Warman JM, Anthopoulos TD, de Leeuw DM. (2006) The mobility and decay kinetics of charge carriers in pulse-ionized microcrystalline PCBM powder. *Adv Funct Mater* **16**: 2274–2280.
64. Warman JM, de Haas MP, Anthopoulos TD, de Leeuw DM. (2006) The negative effect of high-temperature annealing on charge-carrier lifetimes in microcrystalline PCBM. *Adv Mater* **18**: 2294–2298.
65. de Haas MP, Hummel A. (1989). Charge migration in irradiated polyethylene. *IEEE Trans Electrical Insulation* **24**: 349–351.
66. de Haas MP, Hummel A, Warman JM. (1991) Anisotropic transient conductivity in stretch-oriented ultra-high molecular weight (UHMW) polyethylene. *Synth Met* **41/3**: 1255–1258.
67. van der Laan GP, de Haas MP, Warman JM, de Leeuw DM, Tsibouklis J. (1994) Charge carrier generation and migration in a polydiacetylene compound, studied by pulse radiolysis time-resolved microwave conductivity. In: Ito H, Tagawa S, Horie K. (eds.), *Polymeric Materials for Microelectronic Applications*, pp. 316–327. ACS Symposium series 579.
68. Warman JM, de Haas MP, Dicker G, Grozema FC, Piris J, Debije MG. (2004) Charge mobilities in organic semiconducting materials determined by pulse-radiolysis time-resolved microwave conductivity: Pi-bond-conjugated polymers versus pi-pi-stacked discotics. *Chem Mater* **16**: 4600–4609.
69. Hoofman RJOM, Siebbeles LDA, de Haas MP, Hummel A, Bloor D. (1998) Anisotropy of charge-carrier mobility in polydiacetylene crystals. *J Chem Phys* **109**: 1885–1893.
70. Burroughes JH, Bradley DDC, Brown AR, Marks RN, Mackay K, Friend RH, Burns PL, Holmes AB. (1990) Light-emitting diodes based on conjugated polymers. *Nature* **347**: 539–541.

71. Remmers M, Neher D, Gruener J, Friend RH, Gelinck GH, Warman JM, Quattrocchi C, dos Santos DA, Brédas J-L. (1996) The optical, electronic, and electroluminescent properties of novel poly(p-phenylene)-related polymers. *Macromol* **29**: 7432–7445.
72. Gelinck GH, Warman JM. (1996) Charge carrier dynamics in pulse-irradiated polyphenylenevinylenes: Effects of broken conjugation, temperature and accumulated dose. *J Phys Chem* **100**: 20035–20042.
73. Dicker G, de Haas MP, Warman JM, de Leeuw DM, Siebbeles LDA. (2004) The disperse charge-carrier kinetics in regioregular poly(3-hexylthiophene). *J Phys Chem B* **108**: 17818–17824.
74. Dicker G, de Haas MP, de Leeuw DM, Siebbeles LDA. (2005) Origin of the stretched-exponential hole relaxation in regioregular poly(3-hexylthiophene). *Chem Phys Lett.* **402**: 370–374.
75. van der Laan GP, de Haas MP, Warman JM, Frey H, Möller M. (1993) Highly mobile charge carriers in poly(di-*n*-alkyl)silanes in the solid and in the mesophase. *Mol Cryst Liq Cryst* **236**: 165–172.
76. Frey H, Möller M, de Haas MP, Zenden NJP, Schouten PG, van der Laan GP, Warman JM. (1993) Radiation-induced conductivity in poly(methylphenylsilylene) and poly(di-*n*-hexylsilylene) studied by time-resolved microwave conductivity. *Macromol* **26**: 89–93.
77. van der Laan GP, de Haas MP, Hummel A, Frey H, Sheiko S, Möller M. (1994) Anisotropic radiation-induced conductivity in oriented poly(di-*n*-hexyl-silylene) in the solid phase and in the mesophase. *Macromol* **27**: 1897–1904.
78. van der Laan GP, de Haas MP, Frey H, Möller M. (1995) Charge carrier mobilities in liquid crystalline mesomorphic poly(di-*n*-alkyl)-silylenes; Influence of backbone conformation. *Macromol Symp* **96**: 219–228.
79. van der Laan GP, de Haas MP, van Walree CA, van Slageren J, Jenneskens LW, Frey H. (1996) Optical and charge transport properties of di-*n*-hexyl substituted polysilylene and polygermylene. *Macromol Symp* **102**: 355–362.
80. van der Laan GP, de Haas MP, Hummel A, Frey H, Möller M. (1996) Charge carrier mobilities in substituted polysilylenes; influence of backbone conformation. *J Phys Chem* **100**: 5470–5480.
81. de Haas MP, Choffat F, Caseri WR, Smith P, Warman JM. (2006) Charge mobility in the room-temperature liquid-crystalline semiconductor poly(di-*n*-butylstannane). *Adv Mater* **18**: 44–47.
82. Hoofman RJOM, de Haas MP, Siebbeles LDA, Warman JM. (1998) Highly mobile electrons and holes on isolated chains of the semiconducting polymer poly(phenylene vinylene). *Nature* **392**: 54–56.
83. Prins P, Candeias LP, van Breemen AJJM, Sweelssen J, Herwig JPT, Schoo HFM, Siebbeles LDA. (2005) Electron and hole dynamics on isolated chains of a solution-processable poly(thienylene vinylene) derivative in dilute solution. *Adv Mater* **17**: 718–723.

84. Grozema FC, Siebbeles LDA, Warman JM, Seki S, Tagawa S, Scherf U. (2002) Hole conduction along molecular wires: Sigma-bonded silicon versus pi-bond-conjugated carbon. *Adv Mater* **14**: 228–231.
85. Candeias LP, Grozema FC, Padmanaban G, Ramakrishnan S, Siebbeles LDA, Warman JM. (2003) Positive charge carriers on isolated chains of MEH-PPV with broken conjugation: Optical absorption and mobility. *J Phys Chem B* **107**: 1554–1558.
86. Prins P, Grozema FC, Schins JM, Patil S, Scherf U, Siebbeles LDA. (2006) High intrachain hole mobility on molecular wires of ladder-type poly(p-phenylenes). *Phys Rev Lett* **96**: 146601.
87. Prins P, Grozema FC, Schins JM, Savenije TJ, Patil S, Scherf U, Siebbeles LDA. (2006) Effect of intermolecular disorder on the intrachain charge transport in ladder-type poly(p-phenylenes). *Phys Rev B* **73**: 045204.
88. Prins P, Grozema FC, Siebbeles LDA. (2006) Efficient charge transport along phenylene-vinylene molecular wires. *J Phys Chem B* **110**: 14659–14666.
89. Warman JM, de Haas MP, van der Pol JF, Drenth W. (1989) Charge separation and recombination in pulse-irradiated columnar aggregates of peripherally octa-*n*-alkoxy-substituted phthalocyanines. *Chem Phys Lett* **164**: 581–586.
90. Schouten PG, Warman JM, de Haas MP, Fox MA, Pan H-L. (1991) Charge migration in supramolecular stacks of peripherally substituted porphyrins. *Nature* **353**: 736–737.
91. Schouten PG, Warman JM, Gelinck GH, Copyn MJ. (1995) Charge recombination via long-distance electron transfer through frozen and molten *n*-alkyl chains in pulse-irradiated mesomorphic phthalocyanines. *J Phys Chem* **99**: 11780–11793.
92. Warman JM, van de Craats AM. (2003) Charge mobility in discotic liquid crystals studied by PR-TRMC. *Mol Cryst Liq Cryst* **396**: 41–72.
93. Warman JM, Kroeze JE, Schouten PG, van de Craats AM. (2003) Charge mobility in discotic liquid crystalline porphyrins and phthalocyanines measured by PR-TRMC. *J Porphyrins and Phthalocyanines* **7**: 341–349.
94. Warman JM, de Haas MP, Dicker G, Grozema FC, Piris J, Debije MG. (2004) Charge mobilities in organic semiconducting materials determined by pulse-radiolysis time-resolved microwave conductivity: Pi-bond-conjugated polymers versus pi-pi-stacked discotics. *Chem Mater* **16**: 4600–4609.
95. van de Craats AM, Warman JM, de Haas MP, Adam D, Simmerer J, Haarer D, Schuhmacher P. (1996) The mobility of charge carriers in all four phases of the columnar discotic material hexakis(hexylthio)triphenylene: Combined TOF and PR-TRMC results. *Adv Mater* **8**: 823–826.
96. van de Craats AM, Warman JM. (2001) The core-size effect on the mobility of charge in discotic liquid crystalline materials. (2001) *Adv Mater* **13**: 130–133.

97. Debije MG, Piris J, de Haas MP, Warman JM, Tomovi  Z, Simpson CD, Watson MD, M llen K. (2004) The optical and charge transport properties of discotic materials with large aromatic hydrocarbon cores. *J Am Chem Soc* **126**: 4641–4645.
98. Warman JM, Piris J, Pisula W, Kastler M, Wasserfallen D, M llen K. (2005) Charge recombination via intercolumnar electron tunneling through the lipid-like mantle of discotic hexa-alkyl-hexa-peri-hexabenzocoronenes. *J Am Chem Soc* **127**: 14257–14262.
99. Warman JM, de Haas MP, Paddon-Row MN, Cotsaris E, Hush NS, Oevering H, Verhoeven JW. (1986) Light-induced giant dipoles in simple model compounds for photosynthesis. *Nature* **320**: 615–616.
100. Schuddeboom W, Jonker SA, Warman JM, Leinhos U, Kuhnle W, Zachariasse KA. (1992) Excited state dipole moments of dual fluorescent 4-(dialkylamino)benzonnitriles. Influence of alkyl chain length and effective solvent polarity. *J Phys Chem* **96**: 10808–10819.
101. Warman JM, de Haas MP, Graetzel M, Infeltes PP. (1984) Microwave probing of electronic processes in small particle suspensions. *Nature* **310**: 305–306.

Chapter 7

Infrared Spectroscopy and Radiation Chemistry

Sophie Le Caër^{,†}, Serge Pin^{*}, Jean Philippe Renault[†],
Georges Vigneron[†] and Stanislas Pommeret[†]*

1. Introduction

The present chapter deals with the use of infrared spectroscopy in radiation chemistry. After an historical introduction and the presentation of the basic knowledge needed in infrared spectroscopy, we describe the major milestones of its implementation within that field. Section 3 describes the use of infrared spectroscopy in astrophysics. Starting in the 1980s, such studies aim at characterizing the sample's modifications after irradiation. Section 4 describes the implementation of infrared reflection-absorption spectroscopy (IR-RAS) and its use in understanding the radiation-induced surface chemistry. Section 5 is focused on the chemistry induced by swift heavy ions in polymers. Section 6 presents recent developments that enable us to perform

* CEA/Saclay, DSM/IRAMIS/SIS2M/Laboratoire Claude Fréjacques, URA 331 CNRS, F-91191 Gif-sur-Yvette Cedex, France

† CEA/Saclay, DSM/IRAMIS/SIS2M/Laboratoire de Radiolyse, F-91191 Gif-Yvette Cedex, France

‡ Email: sophie.le-caer@cea.fr

in situ time-resolved infrared spectroscopy coupled to a linear accelerator. Such a technique has already been applied to various systems including organometallic chemistry, nanosciences, and biology.

2. Infrared Spectroscopy

2.1. Some definitions

The infrared (IR) absorption spectrum of a compound is probably one of its most unique properties: it has often been called its “fingerprint”. As a matter of fact, except for optical isomers, two compounds having different structures have different infrared spectra. In some cases, such as with polymers differing only slightly in molecular weight, the differences may be very small but they do exist.

Infrared is very useful in the elucidation of unknown structures due to the presence of “group wavenumbers”: certain chemical groups (carbonyl, methyl...) give characteristic absorption bands which are detected in a certain energy range and which exhibit a typical intensity. Indeed, molecules are in constant motion, and produce vibrations (Fig. 1). The frequency of these vibrations depends on the mass of the concerned atoms, as well as the strength of the bonds. When the frequency of the incoming infrared radiation matches the frequency of the vibration, energy is absorbed by the vibrating bonds. This change in amplitude is detected in the infrared spectrum as a peak at the frequency of the bond which absorbed the energy. Because particular types of vibration always occur at similar frequencies, it is possible to build up a table of characteristic absorption wavenumbers. Thus, the 4000–2500 cm^{-1} region corresponds in general to the stretching mode of single bonds to hydrogen (C–H, O–H, N–H). In the 2500–2000 cm^{-1} region, triple bonds stretching modes are detected (C \equiv C, C \equiv N). Another famous example: stretching modes of double bonds (C=C, C=O) are detected in the 2000–1500 cm^{-1} region. Infrared spectroscopy is thus able to provide rich structural information. Together with *ab initio* calculations, it allows, for instance, researchers to determine the structure of organometallic complexes.^{1,2} In other systems such as water, the

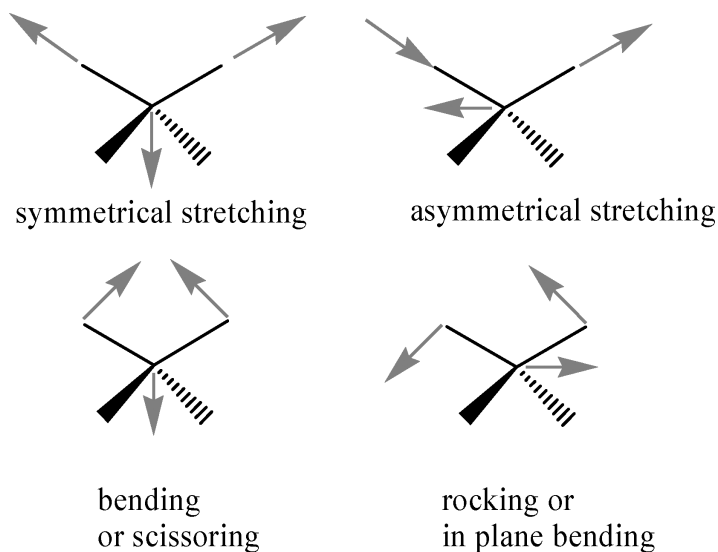


Fig. 1. Few examples of typical vibrations for a tetragonal carbon.

OH stretching frequency is directly linked to the H-bond length.³ Infrared spectroscopy makes it possible to characterize phase transitions, for example ultrafast superheating and melting of bulk ice.⁴

Besides, infrared spectroscopy allows the performance of quantitative measurements: according to Beer's law, the absorbance of a species at a given wavelength is proportional to its concentration.

Another advantage of infrared spectroscopy is directly linked to the wavelength of the light. Indeed the light diffusion ($I_D \propto \lambda^{-4}$) is proportional to the inverse of the wavelength to the power of four. This property of the light diffusion makes it possible to probe systems with IR light, even if they diffuse light in the visible range, spectrum range (400–800 nm). As a consequence it is then “easy” to implement IR spectroscopy for samples diffusing light in the visible range, such as nanomaterials and biological samples. Let us point out that the infrared technique is universal: samples can be liquids, solids or gases; they can be organic or inorganic.

Nevertheless, only vibrations resulting from a change of the molecular dipole and having absorption frequencies in the infrared

region of the spectrum absorb infrared radiation. Thus, homopolar molecules such as O_2 and N_2 are transparent under ordinary conditions to infrared radiations. In this ideal landscape, a limitation may be due to the strong absorption of water when handling aqueous solutions. Another drawback is that infrared spectroscopy is usually not very sensitive to impurities in a sample at levels below 1%.

A term often encountered in infrared spectroscopy is the wavenumber ($\bar{\nu}$) whose relationship to the wavelength (λ) is $\bar{\nu}(\text{cm}^{-1}) = 10^4/\lambda$, λ being expressed in micrometers. The IR region of the spectrum is usually considered to start near the red end of the visible spectrum, which is about 12800 cm^{-1} (or $0.780 \mu\text{m}$). The “near” IR region lies between 12800 and 4000 cm^{-1} ($2.5 \mu\text{m}$). The mostly-used IR region (also called “middle” IR region) extends from 4000 cm^{-1} to 200 cm^{-1} (or $50 \mu\text{m}$). It contains strong diagnosis infrared absorptions of molecules, making it the prime region for identification of species, as opposed to the near-IR region, which contains weaker overtone absorption bands. Lastly, the “far” IR region covers the 200 cm^{-1} to 10 cm^{-1} span. Radiations at frequencies lower than 10 cm^{-1} ($1000 \mu\text{m}$) are classified as being in the microwave or radiowave region.

2.2. *Principle of an infrared spectrometer*

All infrared spectrometers consist of a source of infrared light, a system to analyze the infrared light and a detector.⁵ The source of infrared light is usually a solid heated to incandescence by an electric current. In the $100\text{--}4000 \text{ cm}^{-1}$ region, one of the most popular sources is the Globar one which consists of a silicon carbide rod. The infrared detector measures the infrared energy of the source which has passed through the spectrometer. There are two types: thermal detectors which measure the heating effect of light and respond equally to all wavelengths (for example, the deuterated triglycine sulphate DTGS pyroelectric detector consisting of a thin pyroelectric crystal) and selective detectors whose response depends on the wavelength (for example, the mercury cadmium telluride MCT detector which is a photoconductive cell having a very rapid response and a high sensitivity).

Between the source and the detector is put either monochromators used in dispersive instruments or interferometers used in Fourier transform infrared (FT-IR) instruments. In a dispersive instrument the intensity at each wavenumber is measured one by one in sequence and only a small spectral range falls on the detector at any one time. In a FT-IR instrument the intensities of all the wavenumbers are measured simultaneously by the detector. Fourier transform infrared spectroscopy offers some advantages compared to dispersive instruments, namely (i) higher signal-to-noise ratios for spectra obtained under conditions of equal measurement time, and (ii) higher accuracy in frequency for spectra recorded over a wide range of frequencies. Therefore we will give below a brief picture of the principle of FT-IR spectroscopy, based on a Michelson interferometer (Fig. 2).

The interferometer consists of two plane mirrors, one fixed and the other moving, and a beam splitter. The light comes parallel from the source, strikes the beam splitter at 45° . The beam splitter then transmits half of the light and reflects the other half. The transmitted and reflected beams strike the two mirrors oriented perpendicular to

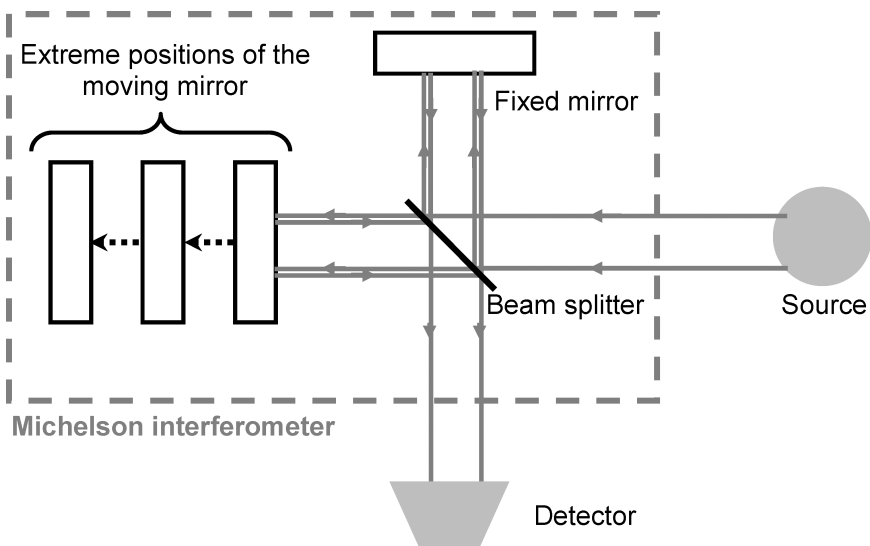


Fig. 2. Simplified picture of the optics of an infrared spectrometer.

each beam and are reflected back to the beam splitter. Please note that the moving mirror travels a very short distance (typically a few millimeters) away from the beam splitter. Interferences, depending on the position of the moving mirror, occur at the beam splitter where the light coming from the two mirrors combines. The beam is then directed through the sample (transmitted through or reflected off the sample surface) and focused onto the detector. A laser beam, undergoing the same change of optical path as the infrared beam, references the position of the mirror during the scan and initiates the collection of data points from the signal of the infrared detector at uniform intervals of mirror travel. The data points are digitized by an analog-to-digital converter and stored in a computer memory. The result is an interferogram, i.e. a record of the signal of the infrared detector as a function of the difference in path (retardation) for the two beams in the interferometer. The Fourier transform converts the signal as a function of retardation to a signal as a function of frequency.

The large number of infrared set-ups around the world (especially FT-IR spectrometers) together with the possibility to perform infrared time-resolved experiments on a huge number of systems makes infrared spectroscopy a very powerful tool. Indeed, infrared detection is widely used in photolysis. For instance, FT-IR detection coupled to photolysis allowed to study systems as various as compounds of astrophysical interest in matrix,⁶ vinyl halides,⁷ intermediates in organic chemistry,⁸ organometallic chemistry,⁹ biology,¹⁰ femtosecond pump-probe spectroscopy¹¹.... Other types of IR detection can also be used, such as diode laser¹².... Surprisingly, infrared detection is scarcely used in radiolysis experiments. The aim of the present chapter is to get an insight into what has been done so far in the coupling of radiation chemistry with infrared spectroscopy, and then to give some prospects for the future.

3. First Coupling of Radiation Chemistry and Infrared Spectroscopy: The Astrophysical Studies on Ice

Interestingly, the first *in situ* coupling of infrared detection with accelerated particles comes from astrophysics/astrochemistry: studies

were undertaken in the 1980s in order to understand the differences between new and evolved comets.¹³ Impinging particles are used to mimic cosmic-ray exposure, and the system under study is ice. Indeed, ice is found in various astronomical environments (carbon dust surfaces in dense interstellar clouds, on comets, on planetary surfaces...). A large number of ice and mixtures of ice have thus been irradiated in different laboratories in order to study their chemical and/or structural evolution. Samples are made at low temperatures (10–20 K) and their infrared spectra are recorded before, during and after ion irradiation. As H₂O is the major species in ice in the interstellar medium, also with contributions from CO, CO₂, CH₃OH and traces of molecules such as CH₄ and NH₃, these icy mixtures were the first to be studied, always under physical conditions (temperature, pressure...) as similar as possible to the astrophysical ones. For instance, Moore *et al.*¹³ showed that the irradiation of (H₂O + NH₃ + CH₄) icy mixtures by 1 MeV protons at 20 K leads to the formation of CO₂, C₂H₆, CO, and N₃. Under irradiation, new molecular species are thus synthesized, and these results may account for the differences observed between new and more evolved comets.¹³ Another group¹⁴ also studied using *in situ* infrared spectroscopy irradiation of ice by keV light ions: CH₄ films at 35 K were irradiated with 40 keV H₂⁺ ions. The results obtained in this work demonstrated that the relative abundance of the new species created under irradiation was very sensitive to the composition of the initial ice as well as to the fluence of the irradiating beam.

Since these first studies in the 1980s, many icy mixtures have been studied using *in situ* high-energy particles irradiation and infrared detection. The experimental set-up used by Moore *et al.* is depicted in Fig. 3.

Far infrared spectroscopy has also revealed to be an efficient tool to study phase transitions. Low-frequency vibrations are different depending on whether water is crystalline (absorptions at 229 and 162 cm⁻¹) or amorphous (broad absorption at 220 cm⁻¹).¹⁵ The authors have shown that crystalline water ice is converted into an amorphous phase under proton irradiation: infrared spectroscopy enables quantifications of the rate of radiation-induced amorphization. The conversion

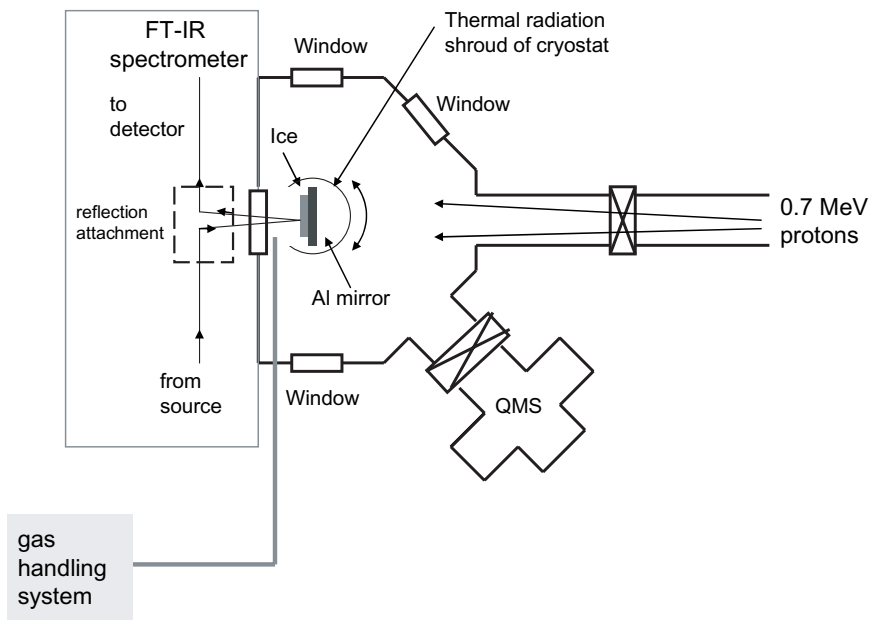


Fig. 3. Experimental set-up used by Moore *et al.* in order to study *in situ* the effect of radiations on ice. This figure is inspired from Refs. 15–17. Solid samples are prepared by slow condensation with a thickness of a few micrometers from the vapor phase at $T \sim 295$ K onto an aluminium substrate kept at a very low temperature (~ 10 K) in a vacuum chamber. An infrared spectrum can then be recorded. After that, the sample is rotated 180° to face the high-energy protons coming from a Van de Graaff accelerator. The sample is irradiated and then rotated again for the IR spectrum to be recorded. The sample temperature is adjustable. Note that the beam of the infrared spectrometer passes through the ice before and after reflection at the ice–mirror interface. The spectra are thus transmission–reflection–transmission spectra. Moreover, species released from the ice during warming can be detected using the quadrupole mass spectrometer (QMS). In another configuration of the experimental set-up,¹⁷ a window has been replaced by a UV lamp. This enables the authors to perform UV photolysis and proton irradiation using the same experimental set-up, under the same experimental conditions and then to evidence the differences of reactivity using these two types of excitation.

rate depends on the temperature and increases when the temperature decreases from 77 to 13 K. The results are in agreement with other results obtained in the mid-IR (in the $3000\text{--}3600\text{ cm}^{-1}$ wavenumber range)¹⁸ performed from 10 to 100 K under 3 keV He^+ irradiation

showing that crystalline H_2O is more resistant to radiation damage at the higher temperatures.

All these studies provide evidence for a rich radiation chemistry. For example, in N_2 -dominated ice (modeling the surfaces of Pluto and Triton, a moon of Neptune),¹⁹ the authors have proven by infrared spectroscopy the formation of HCN as well as HNC starting from N_2/CH_4 and $\text{N}_2/\text{CH}_4/\text{CO}$ mixtures. Other species such as HNCO, NH_3 , NH_4^+ , OCN^- , CN^- and N_3^- were also detected. As many of these species are involved in reactions producing biomolecules (amino acids, polypeptides), these results suggest the possibility of an interesting prebiotic chemistry on Triton and Pluto.

Recently, the production of hydrogen peroxide (H_2O_2) has been determined using its infrared feature centered around 2850 cm^{-1} . Experiments on thin water ice and mixtures irradiated with 800 keV H^+ ,²⁰ prove that H_2O_2 is produced after irradiation of water at 16 K, and that the presence of O_2 and CO_2 in the icy mixture enhances the production of H_2O_2 by radiolysis. Other irradiations using 200 keV H^+ and He^+ and 400 keV Ar^{2+} were performed by another group.²¹ They evaluated the formation of hydrogen peroxide using these three different ions at 16 and 77 K using an experimental set-up described in Ref. 22. In fact, the authors have two experimental set-ups dedicated to the studies of ion-irradiated samples: *in situ* Raman spectroscopy, and *in situ* infrared spectroscopy. These two techniques give complementary information to characterize ion-induced chemistry.

Lastly, in this field, it is worth citing the work of Kaiser *et al.*²³ who performed five keV electron irradiations coupled to an *in situ* FT-IR spectrometer and a quadrupole mass spectrometer. This allows detections of the molecules released during the heating phase, once irradiation is finished. The experiments are combined with electronic structure calculations. All these techniques together enable the authors to propose potential energy surfaces of the systems under study.

4. Advances in the Understanding of Radiation-Induced Surface Chemistry: The IR-RAS Technique

Infrared reflection-absorption spectroscopy (IR-RAS) is a technique which enables us to study the vibrational spectra of species adsorbed

on metal surfaces, the infrared light being reflected off a reflective surface. This experimental method can be extended by introducing the polarization modulation (PM) to the IRRAS experiment, which has the advantages of high surface sensitivity and the surface selection rule. This rule is used to study molecular orientation on thin films or monolayers deposited on metal or dielectric substrates. With IR-RAS or PM-IRRAS techniques, it is possible to extract detailed structural information on the chemistry of surfaces/interfaces with a high spectral resolution and using a non-destructive method. More details of PM-IRRAS measurements can be found in Ref. 24.

A few authors have used IR-RAS coupled to low-energy electron beams to study the effects of irradiation on thin films of polymers²⁵ or on monolayers adsorbed on gold substrates.²⁶ Bermudez²⁵ has shown that using the PM-IRRAS technique coupled to 10–50 eV electron beam irradiation, low-energy electrons seem to damage thin films of poly(methyl-methacrylate) in the same manner as more energetic radiations do such as high-energy electrons, γ -rays.... Olsen and Rowntree²⁶ have quantified the dissociative processes occurring in alkanethiol/Au monolayers during 0–20 eV electron irradiation. Moreover, they have pointed out a drawback of the IR-RAS method: as a matter of fact, large sample sizes are required for accurate surface studies, which means that an extended irradiation is also necessary.²⁶

5. Infrared Spectroscopy: A Tool to Characterize the Specificities of Swift Heavy Ions (SHI) Irradiations

Radiolysis using swift heavy ions (SHI) is very different from radiolysis using γ -rays or accelerated electrons. This is due to strong differences of the energy deposition in the medium and in particular due to the strong modification of the linear energy transfer ($LET = (dE/dx)_{\text{elec}}$): in the first case (SHI), it has a high value (up to tens of keV/nm), whereas in the latter (γ and e^-) it has a small value (for instance 1 MeV electrons have a LET of 1.6×10^{-3} keV/nm). This leads to very different particles–matter interactions. For high LET values, the dose distribution is very inhomogeneous and it is mainly high in the vicinity of the ion path (SHI inducing a huge density of

excitations and ionizations along the ion path); moreover, the deposited energy is highly localized and is transferred from the excited target electrons to the atoms by processes which could be very different from those using γ -rays or accelerated electrons. The high LET values are then able to change the radiation response of radiolysis-sensitive materials and may induce, above a LET threshold value, damage in radiolysis-insensitive materials.

In the Grand Accélérateur National d'Ions Lourds (GANIL, Caen, France) facility, ion beams are delivered in order to understand the specific characteristics of SHI-matter interactions. In particular, polymers are investigated. Infrared spectroscopy is a very powerful tool to characterize organic species in general and polymers in particular. FT-IR spectra have been recorded in GANIL since 1994 in order to understand the specificities of SHI-polymers behavior. The first studies were *ex situ* measurements. Since 2003, SHI irradiations have been analyzed by means of *in situ* FT-IR spectroscopy.

In the first studies, the *ex situ* FT-IR measurements were performed in a specific cell used for irradiations.^{27,28} This cell allowed recording of the transmission FT-IR spectra without removing the sample. Moreover the gaseous atmosphere in the cell could be controlled accurately; for instance air contact could be avoided in order to prevent oxidation reactions. By comparing the behavior of poly(vinylidene difluoride) (PVDF, $-(\text{CH}_2-\text{CF}_2)_n$) films²⁷ using 5 MeV/amu Kr ion (LET ~ 8.3 keV/nm) or 1 MeV electron (LET $\sim 1.6 \cdot 10^{-3}$ keV/nm) irradiations, the authors concluded that the high LET value induces a very significant increase of main chain bond scissions ($-\text{C}\equiv\text{CH}$ and $-\text{CH}=\text{CF}_2$). Due to the high density of simultaneous ionizations, Kr ion irradiations induce specifically alkyne formation (as compared to electron irradiations). This has been evidenced by the CH stretching vibration in $\text{H}-\text{C}\equiv\text{C}-\text{CH}_2-\text{R}$ detected at 3304 cm^{-1} . These results can be generalized by studying other polymers (polystyrene $-(\text{CH}_2-\text{CH}(\text{C}_6\text{H}_5))_n$ and polyethylene $-(\text{CH}_2-\text{CH}_2)_n$) irradiated by other ions.²⁸

In GANIL, another FT-IR set-up in the absorption mode dedicated to gases has been developed.²⁹ The gas mixture released from the polymer film is measured after irradiation of the sample: gases

emitted from the film go to the IR cell. During the ion irradiation (30–60 min), the gases have enough time to diffuse from the irradiation chamber to the infrared cell. The results obtained by infrared spectroscopy were compared to those obtained by mass spectrometry.²⁹ The conclusion is that infrared spectroscopy gives a very accurate determination of the species and of the yields of the emitted gases. However, H₂ or, more generally speaking, symmetric molecules cannot be measured by this technique. Therefore the two techniques provide complementary information.

Lastly, *in situ* FT-IR spectroscopy was performed.^{30,31} A specific cell that allows researchers to perform the irradiations and to record the infrared spectra without removing the sample (FT-IR analysis during the beam stops) was placed on the medium energy line facility of the GANIL accelerator. Thus, modifications of SHI-irradiated polyethylene³¹ could be studied *in situ*.

6. Towards Time-Resolved Experiments: Coupling a LINAC with Infrared Spectroscopy

The experiments described above do not allow us to perform time-resolved measurements and to track the kinetics initiated by irradiation. While the time-resolved infrared spectroscopy was intensively and successfully developed with flash laser photolysis, time-resolved infrared spectroscopy was surprisingly not implemented in radiation chemistry until recently.

6.1. Kinetics of radiation-induced polymerization

The first coupling of a LINAC with infrared spectroscopy has been performed by Palmese *et al.* in order to study *in situ* kinetics of radiation-induced cationic polymerization of epoxy systems.³² The aim of the study is to understand the curing behavior of polymers under irradiation. A UV light source and an electron beam (10 MeV; pulse width of the beam from 2.5 to 10 μm) are coupled to a portable near infrared (NIR) instrument. Briefly, a portable NIR spectrometer (Control Development Incorporated, South Bend, IN, USA) is used,

the spectral range being 4440–8620 cm^{-1} . The infrared light is collimated, goes through the sample and is collected by a lens before going to the spectrometer through a fibre optic. Thus, the IR instrument is not exposed to radiations which would damage it. UV or electron beam radiations go to the sample perpendicular to the infrared light. This set-up is used to track the disappearance of epoxy groups (at 4530 cm^{-1}) as a function of the irradiation time, on a time scale of hundreds of seconds (the spectral collection rate being one in 0.166 s). Moreover, the temperature of the sample can be controlled, which allows recording infrared spectra under irradiation as a function of temperature and investigating the effect of temperature on the extent of reaction achieved using electron beam (or UV) to initiate cationic polymerization. This new set-up was then used to characterize *in situ* the cationic cure kinetics of epoxy systems induced by accelerated electrons. Such experiments were possible because the near infrared light can be guided through a fiber optic. This technique cannot be extended to mid-infrared light because one cannot use fiber optics anymore. That is the reason why mid-infrared spectroscopy coupled to a linear accelerator was not developed until recently (see below).

6.2. Organometallic chemistry

In the Laboratoire de Radiolyse (CEA/Saclay, France), recently we have coupled our 10 MeV electrons accelerator with FT-IR spectroscopy. The experimental set-up is briefly described below.

The FT-IR spectrometer (Bruker Vertex 70) and the MCT (mercury cadmium telluride) detector are moved out of the accelerator room to be protected against radiation (Fig. 4). The infrared beam is guided on a distance of six meters by dried air or N_2 -purged gold coated optical conduits and mirrors. The spectra are obtained from 100 scans with a 4 cm^{-1} resolution. Under our conditions, 24 seconds are required to record a spectrum. It is thus possible to follow the evolution of the spectra after irradiation by recording spectra every 30 seconds, for example. In all cases, spectra of irradiated samples are recorded with reference to the same sample just before irradiation, which allows detecting the effects of irradiation by measuring its

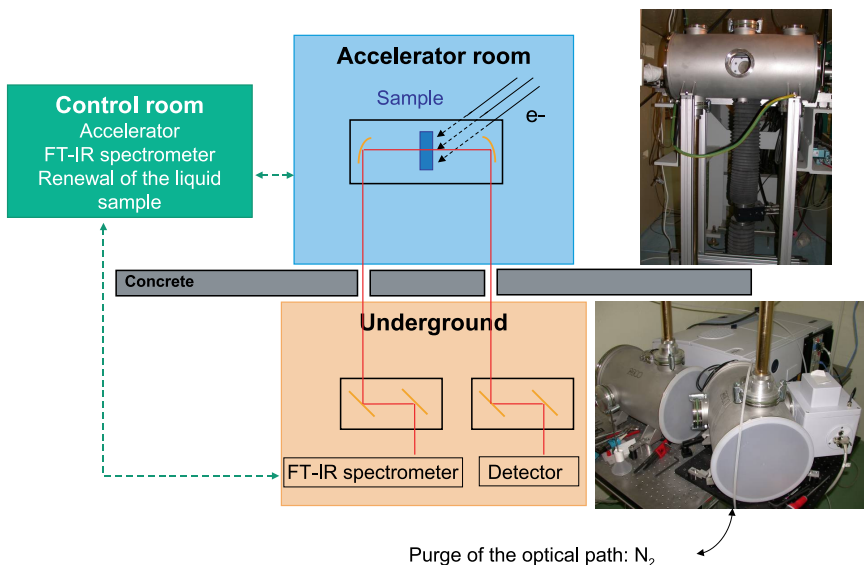


Fig. 4. Experimental set-up developed in Laboratoire de Radiolyse/CEA Saclay for the coupling of the 10 MeV electrons accelerator and the FT-IR spectrometer. The FT-IR spectrometer (Bruker Vertex 70) and the MCT (mercury cadmium telluride) detector are moved out of the accelerator room to be protected against radiation. The infrared beam is guided on a distance of six meters by dried air or N_2 -purged gold coated optical conduits and mirrors.

differential absorption. Our first studies were performed with aqueous solutions of ferrocyanide^{33,34} and the main results are summarized below.

The FT-IR spectra of a 10^{-2} mol.dm⁻³ ferrocyanide solution (at neutral pH) recorded just after irradiation are represented in Fig. 5(a) for different doses; Fig. 5(b) highlights the 2090–2140 cm⁻¹ region of those differential spectra. The negative-going band at 2037 cm⁻¹ represents the loss of ferrocyanide. Just after irradiation, Fig. 5(b) shows that two peaks are observed: the first one, located at 2115 cm⁻¹, is attributed to $Fe(CN)_6^{3-}$ whereas the second one is located around 2102 cm⁻¹. This band was attributed to the $Fe(CN)_5(OH)^{3-}$ ion.³³ Let us point out that the wavenumbers of the infrared bands can be relatively easily modeled using *ab initio* calculations and that these

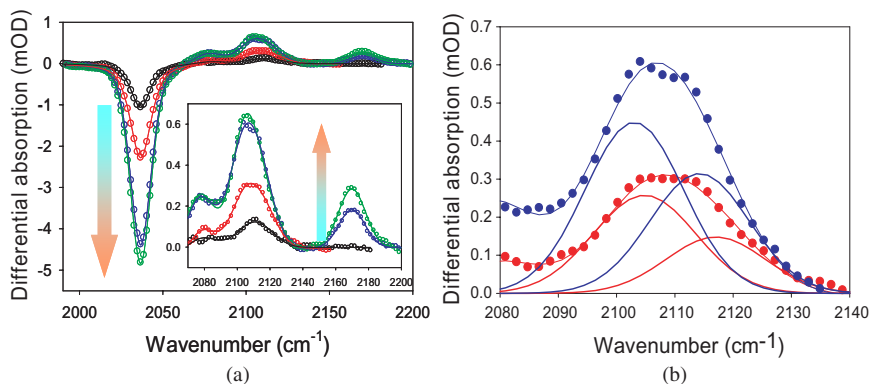


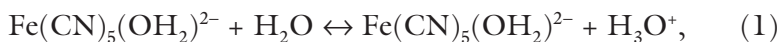
Fig. 5. Evolution of the differential absorbance (after/before irradiation) of a 10^{-2} mol. dm^{-3} potassium ferrocyanide solution as a function of the dose: 275 Gy (black circles); 1275 Gy (red circles); 4000 Gy (blue circles); 5000 Gy (green circles). The spectra have been recorded just after irradiation; the recording time is 24 s.

(a) Spectra recorded in the 1980–2200 cm^{-1} spectral domain. The data are represented with the symbols and the fitted curves are the corresponding thin lines. It is worth noting that the fitted curves correspond nicely to the experimental ones. The arrows indicate the evolution of the bands as a function of the dose.

(b) Focus on the 2090–2140 cm^{-1} spectral domain and on the experimental 1275 Gy (red circles) and 4000 Gy (blue circles) curves; the decomposition into the two bands centered at 2102 and 2115 cm^{-1} is presented in red for the 1275 Gy irradiation, and in blue in the second case. The thin lines are the fitted curves.

wavenumbers are a fingerprint of the present species. These two reasons together account for the great advantage of infrared spectroscopy as compared to UV-visible spectroscopy and constitute a strong motivation for implementing it and developing time-resolved experiments.

The acid–base equilibrium constant for reaction,



is reported as $\text{pK} = 8.4$.³⁵ The pH has been measured just after irradiation: it increases from 9.0 after a 200 Gy irradiation to 10.4 after a 5000 Gy irradiation. These pH values are in good agreement with

the presence of the $\text{Fe}(\text{CN})_5(\text{OH})^{3-}$ ion. The pH increase is attributed to the release of cyanide ions in the solution during irradiation.

The shoulder observed in Fig. 5(a) at 2078 cm^{-1} is assigned to the free CN^- ejected. The CN^- anion is only seen as a shoulder, as its extinction coefficient is much weaker than when it is bound within a complex. We determined an integrated absorption coefficient of $840\text{ mol}^{-1}\text{dm}^3\text{cm}^{-2}$ for the CN^- band at 2080 cm^{-1} and an integrated absorption coefficient for $\text{Fe}(\text{CN})_6^{4-}$ of $97,000\text{ mol}^{-1}\text{dm}^3\text{cm}^{-2}$. The integrated absorption coefficient for $\text{Fe}(\text{CN})_6^{3-}$ was determined as $15,800\text{ mol}^{-1}\text{dm}^3\text{cm}^{-2}$. These determinations of integrated absorption coefficients enable us, after deconvolution of the peaks observed thanks to a fitting procedure, to know exactly the concentrations of the different species detected.

With increasing doses, we notice a peak appearing at 2170 cm^{-1} [Fig. 5(a)]. This peak was assigned to the formation of iron(III) hexacyanoferrate(III) or Berlin green $\text{Fe}^{\text{III}}[\text{Fe}^{\text{III}}(\text{CN})_6]$.

The evolution of the different bands after irradiation at 1500 Gy can be followed as a function of time. Thirty spectra were recorded, one every 30 seconds. Knowing the integrated absorption coefficients and assuming that the integrated absorption coefficients for the $\text{Fe}(\text{CN})_5(\text{OH})^{3-}$ ions and for the $\text{Fe}(\text{CN})_6^{3-}$ ions are the same, we get the evolution of the different concentrations as a function of time after irradiation (Fig. 6).

We can then draw the following conclusions:

- The $\text{Fe}(\text{CN})_6^{4-}$ ions are oxidized after irradiation (bleaching at 2037 cm^{-1}), leading to the formation of $\text{Fe}(\text{CN})_5(\text{OH})^{3-}$ and CN^- ions. The primary product of oxidation is the $\text{Fe}(\text{CN})_6^{3-}$ ion which can then undergo a substitution reaction. First, it should replace a CN^- ligand by a H_2O ligand, H_2O being the solvent. Then, considering the pH of the irradiated solution, the formation of hydroxocyanoferrate(III) complexes is observed.
- When the irradiation is cut off, the cyanide absorption band disappears, showing that recombination of CN^- takes place: the $\text{Fe}(\text{CN})_5(\text{OH})^{3-}$ ions are slowly converted back to $\text{Fe}(\text{CN})_6^{3-}$ ions. The kinetics related to the absorption band of the $\text{Fe}(\text{CN})_5(\text{OH})^{3-}$

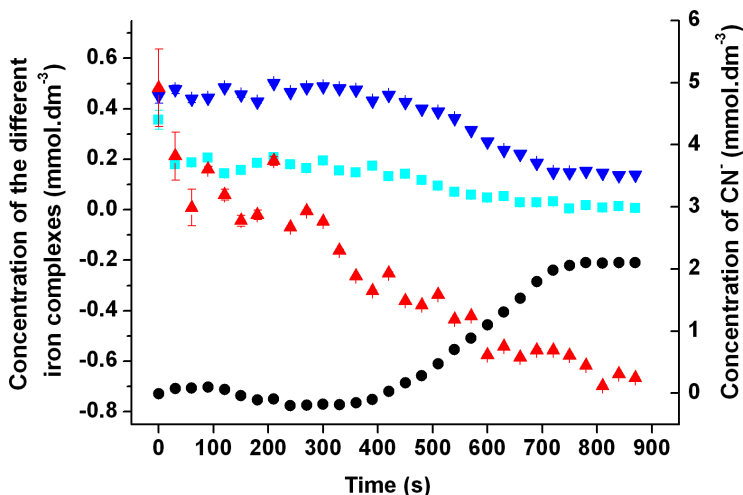
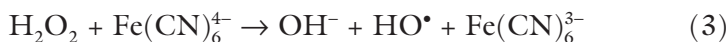


Fig. 6. Evolution of the concentration of the different species expressed in $\text{mmol}\cdot\text{dm}^{-3}$ produced after a 1500 Gy irradiation. Time zero corresponds to the end of irradiation. The spectra are recorded every 30 seconds, on a 15-minutes time scale. The different colors correspond to the absorptions of the following species: $\text{Fe}(\text{CN})_6^{4-}$ (●); CN^- (▲); $\text{Fe}(\text{CN})_5(\text{OH})^{3-}$ (■) and $\text{Fe}(\text{CN})_6^{3-}$ (▼). The cyanide ions are represented using the right scale. The uncertainties obtained during the fitting procedure are represented. The negative concentration of the ferrocyanide is indeed the differential concentration of the ferrocyanide before and after irradiation.

and CN^- ions are well correlated and well fitted with an exponential law with a time constant $\tau = 410 \pm 30$ s [Eq. (2)]:



- Although the weak absorption of the cyanide leads to important uncertainties on the cyanide concentration, more than one cyanide ligand is ejected from one iron complex.
- At longer times, $\text{Fe}(\text{CN})_6^{3-}$ ions are then reduced back to $\text{Fe}(\text{CN})_6^{4-}$ [Eq. (3)]: this can be attributed to hydrogen peroxide in basic media:



At the pH attained here (around 10), the reduction of ferricyanide to ferrocyanide is supposed to be complete and fast, and the value of the related rate constant could be estimated³³: $k \sim 3 \text{ mol}^{-1} \text{ dm}^3 \text{ s}^{-1}$.

Lastly, we have characterized the behavior of the system at different pH and under different gaseous atmospheres.³⁴ We have shown that at pH = 12, more $\text{Fe}(\text{CN})_5(\text{OH})^{3-}$ ions are formed together with a larger release of CN^- anions than when starting from a neutral solution. The formation of Berlin green under extended irradiation is also favored as compared to neat solutions. Working under different gaseous atmospheres (air, O_2 , N_2O), we have proven that dioxygen plays a very important role in the redox chemistry of ferrocyanide through the formation and reactivity of the superoxide radical anion, and that it displaces the ferro/ferricyanide equilibrium towards the ferrocyanide.

In standard laser flash photolysis, improved time-resolved techniques such as rapid scan and step scan have been implemented.³⁶ The rapid scan technique enables us to record kinetics on the millisecond time range, depending on the speed of the moving mirror. In this case, the moving mirror's velocity is chosen so that on the time scale of the dynamic event, each scan is effectively instantaneous. The step-scan technique enables us to record kinetics with a time resolution which can be as low as the nanosecond: the mirror retardation is achieved in discrete "steps", the moving mirror being kept fixed while data are collected. Thus, time-resolved data at each position in the interferogram can be recorded following an excitation event. We are currently implementing those techniques with ionizing radiation excitation. They will lead to experiments giving information not only on reaction mechanisms but also, as mentioned in the introduction, on the structure of the involved species.

6.3. Towards the characterization of nanomaterials under irradiation

The behavior of nanomaterials under irradiation is a hot topic nowadays (see Chap. 12 "Radiolysis of water confined in nanoporous

materials”). One reason is that water radiolysis in nanomaterials has to be understood in order to improve the predictions on the storage and disposal of nuclear wastes. Therefore we have been working on H₂ production in silica at low³⁷ and high dose rate.³⁸ In order to better understand the system, we have performed infrared spectroscopy on irradiated silica pellets.

FT-IR spectra are obtained from mesoporous silica (MCM-41) dispersed in potassium bromide (KBr) pellets (the mass ratio of MCM-41 over KBr is in the 10⁻² range). MCM-41 is obtained by a sol-gel process. It is an ordered mesoporous silica with a hexagonal array of one-dimensional pores and a narrow pore-size distribution of about four nanometers. The glass was baked at 140°C for one hour and then at 400°C for another hour to remove any carbon contaminates.

FT-IR spectra of dried MCM-41 in the 3000–4000 cm⁻¹ region are attributed to O–H stretching vibrations,³⁹ namely (quoting the most striking features observed under our conditions):

- O–H stretching of adsorbed water molecule for the 3200–3500 cm⁻¹ energy range;
- SiO–H stretching of adjacent pairs of SiOH groups with hydrogens bonded to each other for the 3540–3550 cm⁻¹ region;
- SiO–H stretching of isolated pairs of adjacent SiOH groups (vicinal) mutual hydrogen bonded for the 3650–3660 cm⁻¹ energy range.

After irradiation (Fig. 7), the negative-going band exhibits a broad feature with a minimum near 3450 cm⁻¹. This represents the loss of adsorbed water, while the components at 3500–3800 cm⁻¹ represent the consumption of H-bonded silanols. This consumption can be attributed to condensation processes, leading to the formation of Si–O–Si, namely siloxane-bridge sites. Irradiation corresponds mainly to a dehydration of the system, essentially of water adsorbed on silica. This dehydration increases with the dose. Water adsorbed on silica is consumed, leading to the formation of H₂ and H₂O₂. These observations are consistent with our previous results obtained with Controlled Pore Glasses.^{38,40}

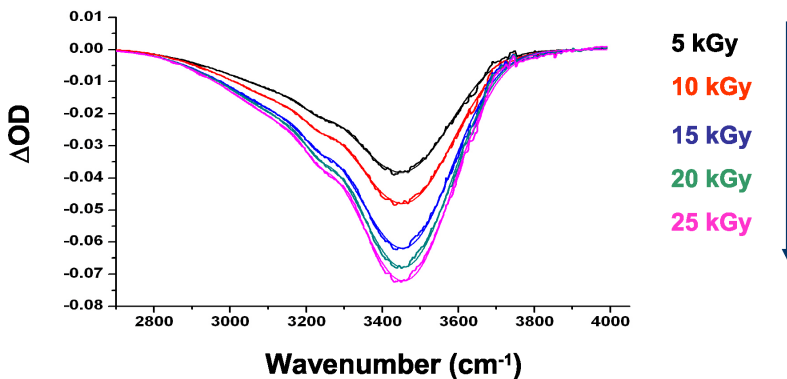


Fig. 7. Evolution of the differential optical density in the O–H stretching region for MCM-41 irradiated with increasing doses: 5 kGy (black), 10 kGy (red), 15 kGy (blue), 20 kGy (green), and 25 kGy (purple).

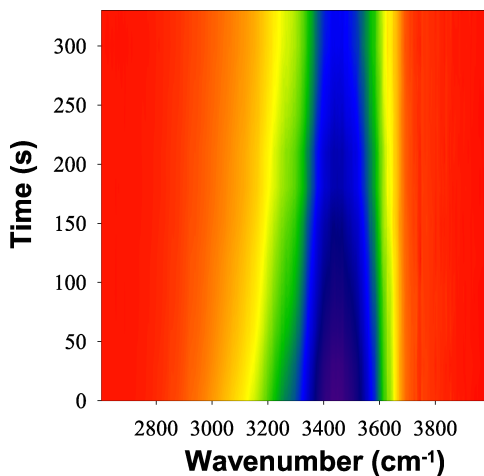


Fig. 8. Evolution of the frequency in the OH stretching region as a function of time after a 25 kGy irradiation. Color code: red (differential Optical Density = 0); violet (differential Optical Density = 0.075).

After irradiation at 25 kGy, the O–H stretching region was observed for a few minutes (Fig. 8) and slow rehydration of the surface at ambient atmosphere was evidenced. Water present in the atmosphere adsorbs on the silica and the damages created by irradiation on

the surface are slowly repaired, at a time scale between a few minutes and a few hours.

6.4. *Infrared spectroscopy and radiation biochemistry*

Radical species are produced by normal metabolic processes. When cellular protections (enzymes, antioxidants) against radicals are insufficient, under the sensitizing effect of oxygen, there is an uncontrolled production of these radicals and especially the reactive oxygen species.⁴¹ In biological systems, oxygen radicals cause subcellular and cellular damage by reacting with macromolecules such as DNA, proteins, polysaccharides and lipids. These damages can be implicated in the phenomena of aging and in a number of diseases (Refs. 42–45 and articles therein). Radical species can also be produced by exogenous chemicals (drugs, alcohols, smoking, metals, toxic compounds) and both UV and ionizing radiations (γ , X, electron) (Ref. 46 and articles therein Refs. 47 and 48). In particular, the radicals are produced by ionizing radiations during drugs or food sterilization and during therapeutic or accidental exposures. The radicals toxicity is thus involved in pathologic metabolic processes. For all these reasons, it is essential to know the effects of the radical species on the biological macromolecules and molecules of biological interest. Their structural changes can explain the well-known mutagenic, cytotoxic and carcinogenic effects of the ionizing radiations.

The DNA is a major target, and during the last two decades, efforts have been made to develop sensitive and specific assays to detect and quantify DNA lesions in cells. A powerful approach requires DNA extraction and digestion to nucleosides and involves the use of liquid chromatography coupled to tandem mass spectrometry (HPLC-MS/MS).^{49,50} Fourier transform infrared microscopy (FTIRM) was also used to study radiation-induced cellular damages at the molecular level in cells.^{51,52} This technique allows the simultaneous detection of the biochemical changes in the various subcellular compartments. Position and absorbance variations of nucleic acids and proteins infrared bands are characteristic of global conformational changes. Even by using such methods to determine the formation of

radiation-induced DNA and proteins lesions in cells, the study of the mechanisms remains, however, difficult within the integrated framework of the cell.

To study the molecular effects induced by the radicals on the biomolecules, we are using water radiolysis that is the powerful technique to generate selectively and quantitatively only one radical species (e_{aq}^- , H^\bullet , OH^\bullet or HO_2^\bullet).⁵³ It is thus possible to describe the involved mechanisms and also to identify the formed products of their reactions with biological molecules.⁵⁴ To determine the reaction rates implicating radicals generated by radiolysis, the classical time-resolved radiolysis set-ups are coupling the ionizing radiation source with a UV-visible spectrophotometer. However, whereas the characterization of products is difficult with the UV-visible spectroscopy, infrared spectroscopy is a method of choice to study the structural modifications in (bio)molecules.

Besides the chemical studies, the Laboratoire de Radiolyse (CEA/Saclay, France) has carried out the new set-up coupling its ionizing radiation source (an electron linear accelerator) with a Fourier-transformed infrared spectrometer (see Fig. 4) in order to analyze the structural modifications induced by radicals on (bio)molecules. As the sample is localized at the electron-beam exit and is crossed by the infrared beam, this LINAC-FTIR coupling makes it possible to obtain the molecule infrared spectrum directly *in situ* in the cell before and after the electron pulse. In these conditions, it is possible to reach the sensibility to measure differential infrared signals of about 10^{-3} – 10^{-4} units of absorbance. The differential infrared spectroscopy allows us to attribute the chemical functions of the macromolecule involved in its structural changes. Here we present results obtained by studying the effects of ionizing radiation on the myoglobin⁵⁵ which was a model in many physico-chemical studies (for studies with pulse radiolysis, see Refs. 56 and 57 and articles therein). The irradiation experiments were performed in two different conditions: (i) in aqueous solution to study the indirect effects of irradiation (radiations ionize water producing the radicals which will react with the protein) and (ii) in KBr pellets to study the direct effect of radiations (KBr being inert to the ionizing radiations which thus interact directly with the protein).

6.4.1. *Study of aquometmyoglobin modifications in buffered solution*

Infrared spectra of 3×10^{-3} mol.dm⁻³ myoglobin solutions were recorded just before irradiation as a reference and after the irradiation. In this study, the 10-MeV electron pulse duration was 10 ns with a repetition rate of 10 Hz and a dose rate of 4.5 Gy/pulse. Each spectrum was averaged from 2790 scans in 4 min at a resolution of 4 cm⁻¹. The flow cell allowed us to renew the myoglobin solution. Horse heart aquometmyoglobin solution was prepared.^{56,57} The differential infrared spectra of the protein (3×10^{-3} mol.dm⁻³ aquometmyoglobin in a 5×10^{-3} mol.dm⁻³ sodium phosphate– 1×10^{-1} mol.dm⁻³ sodium formiate buffer, pH 7) collected after increasing electron radiations (up to 9200 Gy) show, in particular, a negative band at 1102 cm⁻¹ and a weak positive band at 1112 cm⁻¹ (data not shown). From FT-IR difference spectroscopy studies on molecular changes following oxidoreduction of cytochrome *b559*,^{58,59} the signals at 1102 and 1112 cm⁻¹ are assigned to side-chain modes from histidine ligand of the heme-iron (F8 proximal histidine residue). The variations of intensity of infrared modes account for the presence of the neutral derivative of the imidazole group. This structural structural change could be an effect of the reduction of heme-Fe(III) of the aquometmyoglobin by the hydrated electrons.⁵⁷

6.4.2. *Study of metmyoglobin modifications in KBr pellet*

The aquometmyoglobin solution (in water without buffer) was lyophilized and the pellets were prepared by mixing 1 mg of lyophilized metmyoglobin with 99 mg of KBr powder (1% myoglobin mass/pellet mass). Figure 9 shows the differential infrared spectra of pellets collected after increasing electron radiations (up to 147,200 Gy). Contrary to the experiments performed in solution, the absence of water infrared signal permits the measurement of signals beyond 2500 cm⁻¹. Moreover, the intensity of the negative and positive bands which appear increases when the dose increases. Without discussing all spectral features, the negative bands around 3270, 2920–2850 and

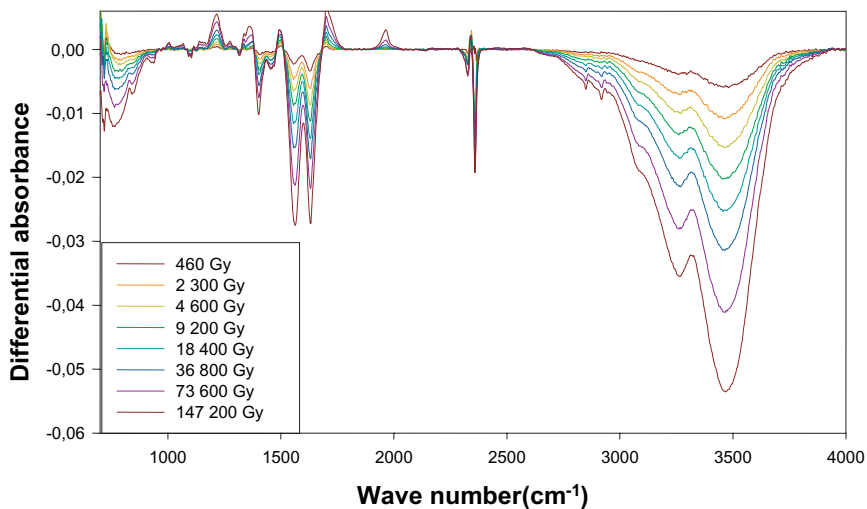


Fig. 9. Differential IR spectra of a 1% metmyoglobin-99% KBr pellet. The reference spectrum was measured with the non-irradiated pellet.

1630 cm^{-1} can be assigned to the disappearance of -NH- , CH_2 and C=O (from amide) groups, respectively; the positive bands around 3320 and 1700 cm^{-1} can correspond to the appearance of N-H (from amine) groups and C=O (from carboxylic acid), respectively. Two direct effects of ionizing radiation on myoglobin in solid-state are the breakage of C-H bonds and the fragmentation of the polypeptide chain (see Ref. 60 and articles therein) between the carbonyl carbon atom and the nitrogen atom of the amide functional group of peptide bonds.

7. Conclusion and Perspectives

Radiation chemistry has been coupled to infrared spectroscopy since more than 20 years ago. Nevertheless, most studies are done in a static manner. Infrared spectroscopy has many advantages to study the molecular effects induced by radicals on molecules. This technique permits the determination of the modifications in the structure of molecules and the variations in the interactions within the molecules.

The experiments can be carried out in solution or in solid state (for example in KBr pellet) in order to study both direct and indirect effects of ionizing radiations. The experiments can also be carried out with samples in crystal, layer or gel. The experiments require only limited amounts of sample, a condition which is often restrictive to study the biological molecules for instance. The size of the studied molecules is not limited: small molecules as well as macromolecules, such as the nucleic acids or polymers, can be studied, allowing the identification of radiation-induced effects.

The challenge now is to perform time-resolved experiments and thus, to benefit from the huge potentialities of infrared spectroscopy to identify reaction mechanisms induced by irradiation. For example, in the LINAC–FTIR coupling, the Rapid Scan system of the spectrometer can be used with a resolution of 100 to 10 ms, and for reactions much faster it could be possible to use the Step Scan system.

References

1. Lemaire J, Boissel P, Heninger M, Mauclaire GB, G, Mestdagh H, Simon A, Le Caër S, Ortega JM, Glotin F, Maître P. (2002) Gas phase infrared spectroscopy of selectively prepared ions. *Phys Rev Lett* **89**: 273002/1–273002/4.
2. Le Caër S, Heninger M, Lemaire J, Boissel P, Maître P, Mestdagh H. (2004) Structural characterization of selectively prepared cationic iron complexes bearing monodentate and bidentate ether ligands using infrared photodissociation spectroscopy. *Chem Phys Lett* **385**: 273–279.
3. Gale GM, Gallot G, Hache F, Lascoux N, Bratos S, Leicknam JC. (1999) Femtosecond dynamics of hydrogen bonds in liquid water: A real time study. *Phys Rev Lett* **82**: 1068–1071.
4. Iglev H, Schmeisser M, Simeonidis K, Thaller A, Laubereau A. (2006) Ultrafast superheating and melting of bulk ice. *Nature* **439**: 183–186.
5. Colthup NB, Daly LH, Wiberley SE. (1990) *Introduction to Infrared and Raman Spectroscopy*, 3rd ed. Academic Press, San Diego.
6. Guennoun Z, Piétri N, Couturier-Tamburelli I, Aycard J-P. (2004) Photolysis of water/dicyanoacetylene complexes: An infrared matrix isolation and theoretical study. *Chem Phys* **300**: 23–31.
7. Carvalho A, Hancock G, Saunders M. (2006) The reaction products of the 193 nm photolysis of vinyl bromide and vinyl chloride studied by time-resolved Fourier transform infrared emission spectroscopy. *Phys Chem Chem Phys* **8**: 4337–4346.

8. Cohen AD, Zeng B-B, King SB, Toscano JP. (2003) Direct observation of an acyl nitroso species in solution by time-resolved IR spectroscopy. *J Am Chem Soc* **125**: 1444–1445.
9. Zhang J, Grills DC, Huang K-W, Fujita E, Bullock RM. (2005) Carbon-to-metal hydrogen atom transfer: Direct observation using time-resolved infrared spectroscopy. *J Am Chem Soc* **127**: 15684–15685.
10. Martin CB, Shi X, Tsao M-L, Karweik D, Brooke J, Hadad CM, Platz MS. (2002) The photochemistry of riboflavin tetraacetate and nucleosides. A study using density functional theory, laser flash photolysis, fluorescence, UV-Vis and time resolved infrared spectroscopy. *J Phys Chem B* **106**: 10263–10271.
11. Nibbering ETJ, Elsaesser T. (2004) Ultrafast vibrational dynamics of hydrogen bonds in the condensed phase. *Chem Rev* **104**: 1887–1914.
12. Bengali AA, Grunbeck AR. (2005) Investigating the reactivity of the (η^6 -C₆H₅R)Cr(CO)₂-(η^2 -C₆H₅R) [R=H, CH₃, CF₃] bond: A laser flash photolysis study with infrared detection. *Organometallics* **24**: 5919–5924.
13. Moore MH, Donn B, Khanna R, A'Hearn MF. (1983) Studies of proton-irradiated cometary-type ice mixtures. *Icarus* **54**: 388–405.
14. Benit J, Bibring J-P, Rocard F. (1988) Chemical irradiation effects in ice. *Nucl Instr and Meth in Phys Res B* **32**: 349–353.
15. Hudson RL, Moore MH. (1995) Far-IR spectral changes accompanying proton irradiation of solids of astrochemical interest. *Radiat Phys Chem* **45**: 779–789.
16. Moore MH, Hudson RL. (1992) Far-infrared spectral studies of phase changes in water ice induced by proton irradiation. *Astrophys J* **401**: 353–360.
17. Gerakines PA, Moore MH, Hudson RL. (2000) Carbonic acid production in H₂O:CO₂ ice. UV photolysis vs. proton bombardment. *Astronom Astroph* **357**: 793–800.
18. Strazzulla G, Baratta GA, Leto G, Foti G. (1992) Ion-beam-induced amorphization of crystalline water ice. *Europhys Lett* **18**: 517–522.
19. Moore MH, Hudson RL. (2003) Infrared study of ion-irradiated N₂-dominated ice relevant to Triton and Pluto: Formation of HCN and HNC. *Icarus* **161**: 486–500.
20. Moore MH, Hudson RL. (2000) IR detection of H₂O₂ at 80 K in ion-laboratory ice relevant to Europa *Icarus* **145**: 282–288.
21. Gomis O, Leto G, Strazzulla G. (2004) Hydrogen peroxide production by ion irradiation on thin water ice films. *Astronom Astroph* **420**: 405–410.
22. Strazzulla G, Baratta GA, Palumbo ME. (2001) Vibrational spectroscopy of ion-irradiated ice. *Spectrochimica Acta Part A* **57**: 825–842.
23. Bennett CJ, Jamieson CS, Osamura Y, Kaiser RI. (2005) A combined experimental and computational investigation on the synthesis of acetaldehyde CH₃CHO (X¹A') in interstellar ice. *Astrophys J* **624**: 1097–1115.

24. Golden WG. (1985) *Fourier Transform Infrared Reflection-Absorption Spectroscopy*. Academic Press, Orlando.
25. Bermudez VM. (1999) Low-energy electron beam effects on poly(methyl methacrylate) resist films. *J Vac Sci Technol B* **17**: 2512–2518.
26. Olsen C, Rowntree PA. (1998) Bond-selective dissociation of alkanethiol based self-assembled monolayers adsorbed on gold substrates, using low-energy electron beams. *J Chem Phys* **108**: 3750–3764.
27. Betz N, Le Moël A, Balanzat E, Ramillon JM, Lamotte J, Gallas JP, Jaskierowicz G. (1994) A FTIR study of PVDF irradiated by means of swift heavy ions. *J Polym Sci Polym Phys Ed B* **32**: 1493–1502.
28. Balanzat E, Betz N, Bouffard S. (1995) Swift heavy ion modification of polymers. *Nucl Instr and Meth in Phys Res B* **105**: 46–54.
29. Picq V, Balanzat E. (1999) ion-induced molecular emission of polymers: Analytical potentialities of FT-IR and mass spectroscopy. *Nucl Instr and Meth in Phys Res B* **151**: 76–83.
30. Dehaye F, Balanzat E, Ferain E, Legras R. (2003) Chemical modifications induced in bisphenol A polycarbonate by swift heavy ions. *Nucl Instr and Meth in Phys Res B* **209**: 103–112.
31. Mélot M, Ngono-Ravache Y, Balanzat E. (2003) Role of the irradiation temperature on the modifications of swift-heavy-ion irradiated polyethylene. *Nucl Instr and Meth in Phys Res B* **209**: 205–211.
32. Mascioni M, Sands JM, Palmese GR. (2003) Real time *in situ* spectroscopic characterization of radiation induced cationic polymerization of glycidyl ethers. *Nucl Instr and Meth in Phys Res B* **208**: 353–357.
33. Le Caër S, Vigneron G, Renault JP, Pommeret S. (2006) First coupling between a LINAC and FT-IR spectroscopy: The aqueous ferrocyanide system. *Chem Phys Lett* **426**: 71–76.
34. Le Caër S, Vigneron G, Renault JP, Pommeret S. (2007) Radiolysis of ferrocyanide solutions studied by infrared spectroscopy. *Rad Phys Chem* **76**: 1280–1284.
35. Espenson JH, Wolenuk SGJ. (1972) Kinetics and mechanisms of some substitution reactions of pentacyanoferrate(III) complexes. *Inorg Chem* **11**: 2034–2041.
36. Smith GD, Palmer RA. (2002) *Fast Time-Resolved Mid-Infrared Spectroscopy Using an Interferometer*. John Wiley & Sons Ltd.
37. Rotureau P, Renault JP, Lebeau B, Patarin J, Mialocq J-C. (2005) Radiolysis of confined water: Molecular hydrogen formation. *Chem Phys Chem* **6**: 1316–1323.
38. Le Caër S, Rotureau P, Brunet FC, T, Blain G, Renault JP, Mialocq J-C. (2005) Radiolysis of confined water: Hydrogen production at a high dose rate. *Chem Phys Chem* **6**: 2585–2596.
39. Legrand AP, Hommel H, Tuel A, Vidal A, Balard H, Papirer E, Levitz PC, M, Erre R, Van Damme H, Gallas JP, Hemidy JF, Lavalley JC, Barres O, Burneau A, Grillet Y. (1990) Hydroxyls of silica powders. *Adv Colloid Interface Sci* **33**: 91–329.

40. Le Caër S, Rotureau P, Vigneron G, Blain G, Renault JP, Mialocq J-C. (2005) Irradiation of controlled pore glasses with 10 MeV electrons. *Rev Adv Mater Sci* **10**: 161–165.
41. Rice-Evans CA, Burdon RH. (1994) *Free Radical Damage and Its Control*, Elsevier Science B.V., Amsterdam.
42. Packer L. (1983) Oxygen radicals in biological systems. *Methods Enzymol* **105**: 3–600.
43. Packer L, Glazer AN. (1990) Oxygen radicals in biological systems. Part B: Oxygen radicals and antioxidants. *Methods Enzymol.* **186**: 1–855.
44. Packer L. (1994) Oxygen radicals in biological systems. Part C. *Methods Enzymol* **233**: 3–711.
45. Packer L. (1994) Oxygen radicals in biological systems. Part D. *Methods Enzymol* **234**: 3–704.
46. Packer L, Sies H. (2000) Singlet oxygen, UV-A, and ozone. *Methods Enzymol* **319**: 3–682.
47. Cadet J, Douki T, Gasparutto D, Ravanat J-L. (2005) Radiation-induced damage to cellular DNA: Measurement and biological role. *Rad Phys Chem* **72**: 293–299.
48. Audette-Stuart M, Houée-Levin C, Potier M. (2005) Radiation-induced protein fragmentation and inactivation in liquid and solid aqueous solutions. Role of OH and electrons. *Rad Phys Chem* **72**: 301–306.
49. Frelon S, Douki T, Ravanat J-L, Pouget J-P, Tornabene C, Cadet J. (2000) High performance liquid chromatography–tandem mass spectrometry for the measurement of radiation-induced base damage to isolated and cellular DNA. *Chem Res Toxicol* **13**: 1002–1010.
50. Pouget J-P, Frelon S, Ravanat J-L, Testard I, Odin F, Cadet J. (2002) Formation of modified DNA bases in cells exposed either to gamma radiation or to high-LET particles. *Radiat Res* **157**: 589–595.
51. Gault N, Lefaix J-L. (2003) Infrared microspectroscopic characteristics of radiation-induced apoptosis in human lymphocytes. *Radiat Res* **160**: 238–250.
52. Gault N, Rigaud O, Poncy J-L, Lefaix J-L. (2005) Infrared microspectroscopy study of γ -irradiated and H₂O₂-treated human cells. *Int J Radiat Biol* **81**: 767–779.
53. von Sonntag C, Schuchmann H-P. (1994) Pulse radiolysis. *Methods Enzymol* **233**: 3–20.
54. Buxton GV, Greenstock CL, Helman WP, Ross AB (1988) Critical review of rate constants for reactions of hydrated electrons, hydrogen atoms and hydroxyl radicals ($\cdot\text{OH}/\cdot\text{O}^-$) in aqueous solution. *J Phys Chem Ref Data* **17**: 513–882.
55. de Renty M. (2005) Etude par spectroscopie infrarouge des effets d'irradiation sur la structure des protéines. [Radiation effects on protein structure studied by FT-IR spectroscopy] *Microthèse de l'Ecole Nationale Supérieure de Chimie de Paris*.

56. Pin S, Hickel B, Alpert B, Ferradini C. (1989) Parameters controlling the kinetics of ferric and ferrous heme proteins reduction by hydrated electrons. *Biochim Biophys Acta* **994**: 47–51.
57. Le Tilly V, Pin S, Hickel B, Alpert B. (1997) Pulse radiolysis reduction of myoglobin. Hydrated electrons diffusion inside the protein matrix. *J Am Chem Soc* **119**: 10810–10814.
58. Berthomieu C, Boussac A, Mäntele W, Breton J, Navedryk E. (1992) Molecular changes following oxidoreduction of cytochrome *b*559 characterized by Fourier transform infrared difference spectroscopy and electron paramagnetic resonance: Photooxidation in photosystem II and electrochemistry of isolated cytochrome *b*559 and iron protoporphyrin IX-bisimidazole model compounds. *Biochemistry* **31**: 11460–11471.
59. Hienerwadel R, Berthomieu C. (1995) Bicarbonate binding to the non-heme iron of photosystem II investigated by Fourier transform infrared difference spectroscopy and ¹³C-labeled bicarbonate. *Biochemistry* **34**: 16288–16297.
60. Stadtman ER. (1993) Oxydation of free amino acids and amino acid residues in proteins by radiolysis and by metal-catalysed reactions. *Annu Rev Biochem* **62**: 797–821.

Chapter 8

Chemical Processes in Heavy Ion Tracks

Gérard Baldacchino and Yosuke Katsumura†*

1. Introduction

In radiation chemistry, “heavy ion” is usually the name given to particles different from electrons and γ -rays. There is no relationship with the mass or the charge of ions as they can be protons or uranium nuclei. The chemistry as a consequence of irradiation with heavy ions has been studied for a long time in several ways, for example, by using solution of radio-elements or by external irradiation of pure solution. All these aspects have been summarized in recent reviews for a large range of particles.¹⁻⁴ During these last 10 years, heavy ion irradiation researches have concerned many materials and applications from the nuclear fuel cycle^{5,6} to the life science^{7,8} and more recently the cancer-therapy.^{9,10} Recently new fields and new objects using the specific characteristic of the interaction of heavy ions in matter have emerged such as the synthesis of nano-wires¹¹

* CEA, IRAMIS, SIS2M, Laboratoire de Radiolyse, F-91191 Gif-sur-Yvette Cedex, France. E-mail: gerard.baldacchino@cea.fr

† Department of Nuclear Engineering and Management, School of Engineering, The University of Tokyo, Hongo 7-3-1, Bunkyo-ku, Tokyo 113-8656, Japan.

and nano-clusters,¹² or by using the sputtering effect, the production of membranes¹³ for filtering and analysis, or the interest of understanding the processes in organic materials like benzene,¹⁴ polymers¹⁵ or scintillators.¹⁶

Even if irradiation with heavy ions concerns evidently many materials such as solids or liquids and gases, this chapter will deal with the effect of high-energy heavy particles in liquid water. Actually, chemical mechanisms in pure water have been depicted a few decades ago and this medium is undoubtedly the one in the nature, more generally in the living systems, and also in the industry to be extensively used. Therefore this chapter tries to give the new trends of the research on water radiolysis with heavy ion beams, the methods developed with their associated problems and the facilities used for these studies.

As radiolytic yields remain the main parameter to quantify the evolution of the chemistry after the ionization step, we attempt to depict the evolution of the localization of the reactions during the diffusion stage. It is simply a description of time- and spatially-resolved events with various initial track structures which gives sensitively various results in terms of yield.

At the same time, a critical approach of problems such as the dosimetry for high-energy particles, the fragmentation of water molecules and the determination of radiolytical yields will be attempted. As it is not fully satisfactory to have only experimental data, a few words will be written about the modelization and particularly the recent Monte Carlo simulations. Even if many studies have been developed during these last decades, finally this field of radiation chemistry is probably at the beginning and one can imagine that part of the conventional radiation chemistry studies (i.e. γ and electron beam radiolysis) will be partly transferred to ion beams. Unfortunately, the difficulties of access to cyclotrons will remain for a long time and the experiments as interesting they are, cannot be quickly achieved. That is why a brief future map of this discipline will be depicted along with the current facilities used for ion beam irradiations and some known future projects.

2. Summary of the Specific Interaction of High Energy Ions with Water

The interaction of an accelerated heavy nucleus, which has a charge Z and an energy E between a few MeV to a few GeV, and a liquid-state water molecule is mainly a Coulombic interaction. The energy exchange is then purely electronic and no nuclear effect is observed in water. The theory describing this interaction is a few decades old. In most cases the Bethe equation allows the calculation of the fraction of energy deposited dE along a segment dx of the propagation axis of the particle. The electronic linear energy transfer (LET) is then given by,

$$-\frac{dE}{dx} = \frac{4\pi e^4 Z^2 N}{mV^2} \ln\left(\frac{2mV^2}{I}\right) \quad (1)$$

where e and m are the charge and mass of the electron, Z and V the charge and velocity of the projectile, and N and I the electron density and mean excitation potential of the medium.² At higher energy level, one can expect a fragmentation process of both the swift nucleus and the water molecule. It can cause some difficulties of interpretation in the experiments with the highest energy ions, particularly in the evaluation of the deposited dose. We try to explain how to understand the effect of this process in the next few paragraphs. For intermediate values of energy, LET and ranges can then be calculated for many projectiles and homogeneous targets (see the example of Carbon ions in water presented in Fig. 1).

If the number of positive charges brought by the nucleus of the projectile is elevated, the electric field in the surrounding of its propagation axis becomes huge. The water molecules in this region are affected by ionizations and electronic excitations. The excess of energy deposited in these molecules in a few attoseconds is the start point of a long story depicted in Fig. 2.

The first 10^{-15} – 10^{-12} s are not accessible to time-resolved heavy ion experiments but they are available from laser femtochemistry.¹⁸ In the

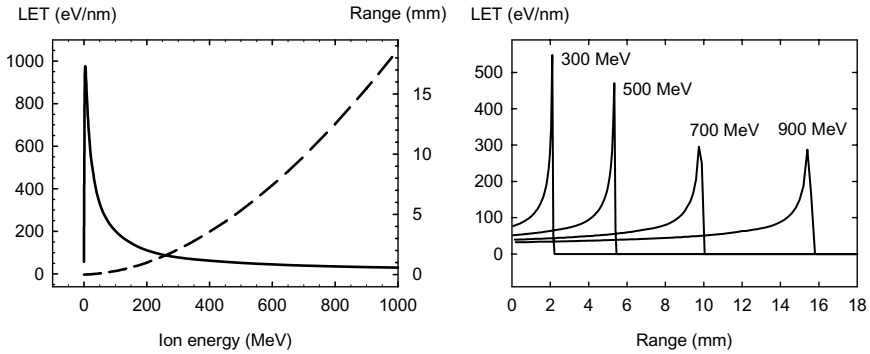


Fig. 1. Carbon ions in water. Ranges and LET as a function of its energy (determined from SRIM2006, Ref. 17).

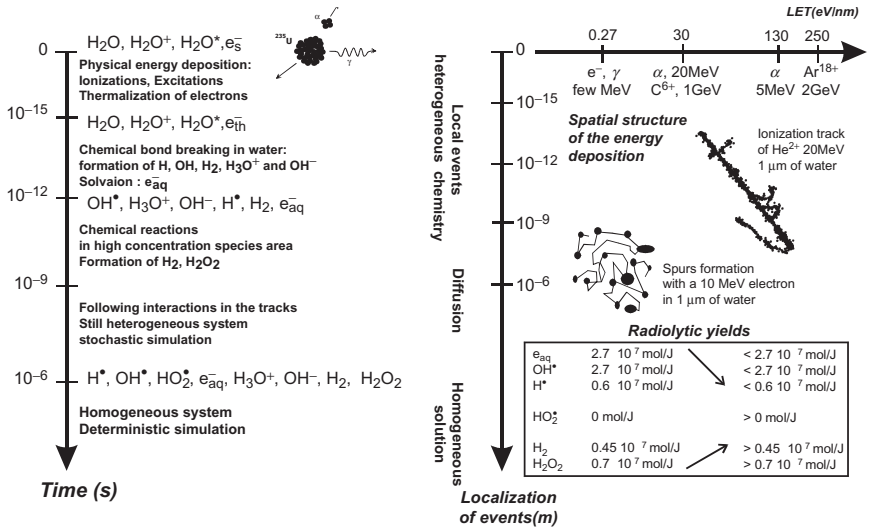


Fig. 2. Description of events after the ionization step due to radiation on water molecules. 3D presentation with time, space and LET.

case of heavy ion irradiation, this step is the most important because high local concentrations (localized in space due to the value of LET) of species make the chemistry very efficient in this range of time.

The radicals and molecules that escaped from the track recombination can diffuse in the bulk by making the chemical system homogeneous where the slowest reactions can take place. At the

microsecond scale the distribution of chemical species is given by the radiolytic yields. From this time onwards the evolution of the species concentrations is determined by the resolution of the same differential equations system that is used for γ or high-energy electron radiolysis. In other terms, the chemical system reactivity becomes independent from the LET value. If one takes a picture at this moment, the distribution of the species is different from the case of heavy ion irradiation from a γ radiolysis. The radicals have been massively recombined in the earliest steps to produce stable molecules i.e. the molecular hydrogen and the hydrogen peroxide. As a consequence, the yield of the latter increases dramatically. That is the main reason why the high LET radiolysis of water is a key research area for the safety in nuclear industry (power plant and waste storage).

3. Determination of Doses, Concentrations and Yields

3.1. *Some comments concerning the G-value and track segment G-value*

The radiolytic yield, named *G-value*, is essential to predict the long term chemistry. For example, a deterministic program which solves a set of differential equations uses it to quickly obtain the amount of molecular hydrogen produced during the exploitation of a water cooling system. The yield determination needs the measurement of the *concentration* of the concerned chemical species produced or consumed during irradiation and also the *dose* delivered to the solution. Both of them are difficult to obtain in the case of heavy ion irradiation.

3.2. *Concentration measurement methods*

Actually the concentrations of interesting radicals in water radiolysis are about 10^{-8} – 10^{-9} M and it is necessary that they are measured using sensitive methods. The direct absorption spectroscopy is limited by the saturation and the linearity of the detector that must receive a high flux of light to detect a small amount of absorbed light. The emission spectroscopy is more convenient and more sensitive but

often the chemical system response is not easy to deconvolute.^{14,18} This is also often a relative measure needing a calibration. The scavenging method is also limited by the highest concentrations necessary to measure the earliest *G*-values in the track-core. Chemical systems used must be checked for their possible interference of “high local-concentration” reactions.

3.3. *Dose evaluation*

Dosimetry with high-energy particles is a sensitive point because there are not enough experimental data for each type and energy of ion beams and the calculated yields depend strongly on the dose. The evaluation of the dose cannot be as accurate as for γ or high energy electron beams for which a few secondary dosimeters have been determined such as Fricke dosimeter, thiocyanate and ceric systems, for example.

Nevertheless, the physical approach consisting in counting the number of ion seems to be currently the best method because it is based on the wide-range data base and Monte Carlo program developed by IBM, SRIM.¹⁷ But the accuracy of this program of about 10% will never give an absolute value of the dose. As an example of a chemical system extensively used for the dosimetry in liquid, a compilation of the radiolytic yields of the common Fricke dosimeter for various and large range of ions is presented in Fig. 3. Other presentations exist by considering MZ^2/E instead of LET.¹⁹ As it is shown, the radiolytic yield of the Fricke dosimeter changes too much with the type and the energy of the particle to be reliable enough and used in experiments. It remains a good topic of experimental research and calculations.^{19,21} Unfortunately the structure dependence of the energy deposition, the change of energy in the experiment with low energy particles (moreover sometimes integrating the Bragg peak) then consequently cannot give a stable and trusty radiolytical yield for dose determination. The chemical dosimetry is rather difficult because it needs also a primary *G*-value deduced from a primary dosimeter (calorimeter for example). So the accuracy of the measure becomes uncertain. Some attempts were also made with the thiocyanate system

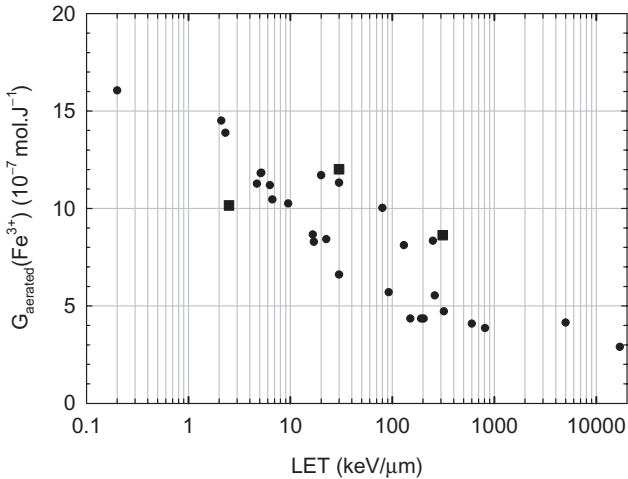


Fig. 3. Compilation of radiolytic yields of the Fricke dosimeter in aerated conditions for various ions and energy. The squares are unpublished results obtained from 34 MeV protons, 1 GeV carbon ions and 2 GeV argon ions.

which is a well-known dosimeter in pulse radiolysis with high energy electrons.²² This system requires a pulse beam and currently the lack of knowledge of the OH “story” with ion irradiation cannot make it a good dosimeter yet.

As one can notice in the Fig. 4 the signal obtained from a microsecond pulse of 1-GeV carbon ions has a rather good signal-to-noise ratio and could be useful as it is in the electron pulse radiolysis.²³ However, this newly developed method for ion currently suffers from a lack of data and it is not yet so easy-to-use to be widely exploited.

Then the current determinations of the dose in high LET experiments are mainly performed by counting the number of ions delivered to the sample. This is a physical determination using the X-ray emission or secondary-electron emission in thin metallic materials. This method is indirect and needs a calibration with a direct counting method using a Faraday cup. For very low dose (for example by using the short-duration pulses), the sensitivity of the detector is the limiting factor, unlike at higher dose or very high LET particles the linearity of the detectors is also limiting. In the future, great effort is

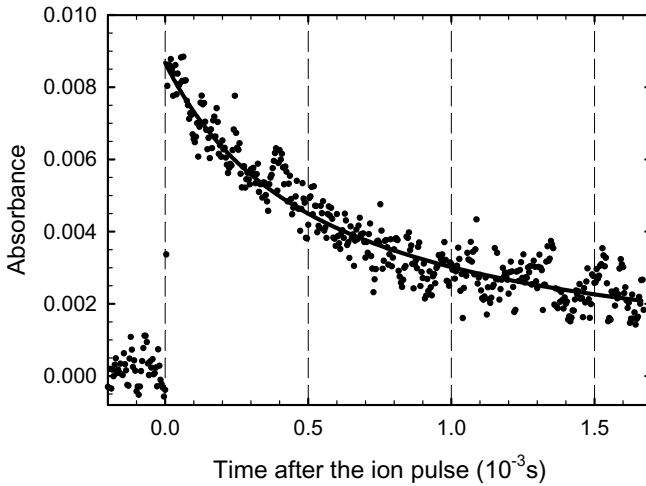


Fig. 4. Absorption kinetics over the time range of 1.7 ms of $(\text{SCN})_2^{*-}$ at 515 nm in an aqueous solution of 10^{-3} M of thiocyanate saturated with nitrous oxide after a 5- μs pulse of $^{12}\text{C}^{6+}$. The dose was 4 Gy/pulse and the number of accumulations was 3899 with a repetition rate of 20 Hz.²³

expected in the dosimetry of high LET particle because the accuracy of G -value simply depends on the dose measurement.

3.4. Fragmentation for very high energy particles

Nuclear fragmentation of the projectile is expected for very high energy ($E > \text{GeV}$) of particles because nuclear interaction cross section becomes no more negligible between atom-nuclei of water and the projectile.^{24–29} The nuclear physics can provide information for each projectile and target.¹⁷ Nevertheless what is the chemical consequence of fragmentation? As the energy deposition depends mainly on the charge and velocity of the projectile and as the charge and velocity can only decrease during this physical processes, the value of LET for each fragment should be lower and lower. The ranges of the new projectiles are also reduced. As a result the radiolysis along the track can change dramatically from a mixture of high and low LET radiolysis to

a high LET radiolysis. Then a part of the energy deposition can influence the fate of the subsequent chemistry in the proportion of the final molecules. This effect could explain some possible abnormal values of yields in some peculiar cases. A clear experimental determination of the chemical effects should be very useful.

4. Time Dependence, Comments About the Homogeneous Distribution and the Scavenging Time

G-values are mandatory for deterministic simulations of long-term effects of radiation. But these values must correspond to a homogeneous distribution of chemical species in the solution. The highly-structured ionization track, unlike the spurs in γ -irradiation, makes the diffusion of chemical species very long. Which time after ionization to choose, 1 μ s or more? Sometimes a criterion of homogeneity is essential. On the other hand, in fundamental studies, the scavenging effect can occur at very different time-ranges and by this way the *G*-value can change a lot. Attention must be paid to the scavenging method because several reactions in the tracks occur at the same time.

4.1. Track average yields

Many experimental data come from low-energy ion beams and consequently the range of the ions is very short (less than 1 mm). The yield determinations in this case are the result of the integration of the energy deposited along the track (from the penetration of the ion in the solution to the end of the Bragg peak). A model is needed to obtain the differential yield relevant from a segment of the track then to a given track structure.

4.2. Track segment yields

The track segment yield (also named differential yield) describes the chemistry within a track segment in which heavy ion characteristics

such as energy and LET remain constant (as far as possible and easily achievable with high energy particles). This quantity is directly calculated by the Monte Carlo simulations, but some experiments especially those which were performed with high energy ions can also produce this kind of yield. In the other cases, the product $G \times E$ is relevant to the evolution of the yield with the energy of the incident particle and many determinations as a function of energy are necessary. Generally, track segment and track average yields must give the same value when the ion energy approaches zero (in the Bragg peak) and when the yield becomes independent of energy (this state is expected at very short time, $t < \text{ns}$, in the track core).

4.3. *G-value dependence of LET and MZ^2/E*

The radiolytic yields do not seem to be uniquely determined by the LET value. That means many attempts have been made to find an empirical relationship between the G -values and LET. If it was right for one type of ion, it does not fit with others with other energies and charges, even with the same LET because two types of heavy ions of different velocities can have the same LET. Significant differences in the track structure, due essentially to the spatial distributions of the ejected secondary electrons, are the origin of this behavior. It has been suggested that the parameter MZ^2/E is a better indicator than LET (see Table 1 for some values) for describing the long time yields in heavy ion radiolysis, where M , Z , and E are the mass, charge, and energy of the incident ion, respectively.³⁰⁻³²

Table 1. A collection of radiolytic yields in molecule/100 eV for four orders of magnitude of LET and at various time ranges.

Type of radiation	LET (eV/nm)	$\text{O}_2^{\bullet -}$		OH^{\bullet}		H_2O_2		e_{aq}^-	
		μs – ms	ns	μs	μs	ns	μs		
γ /fast electrons	0.27	0.02	3.2	2.7	0.72	3.8	2.7		
$^{12}\text{C}^{6+}$	30	0.02	1.5	<1	0.96	3.5–4.5	1		
$^{36}\text{S}^{16+}$, $^{40}\text{Ar}^{18+}$	250–280	0.06–0.05	0.4	<0.4	0.9	0.06	—		

5. Experimental Results with High LET Particles

Many of the results from the last decade were obtained by scavenging method but some of them were from direct detection with pulsed beam. We summarize here a selection of important papers concerning the hydrated electron, the hydroxyl radical, the superoxide radical, the molecular product, the hydrogen peroxide, and molecular hydrogen.

5.1. *The hydrated electron*

The hydrated electron is commonly detected by pulse radiolysis with electron beams. In the case of highly-structured track, this very reducing species reacts easily with oxidant like OH^\bullet radical in its vicinity at earliest time after the ionization track is formed. That is the reason why it is a real challenge to detect this species yet with heavy ion irradiation. Giving a G -value remains delicate because the concentrations are lower than 10^{-7} M and dose must be measured with a high accuracy. As it is shown in Fig. 5, the time dependence of hydrated electron is typical of a track structure in space and time: in the first 100 ns the concentration of initial hydrated electron is at least divided

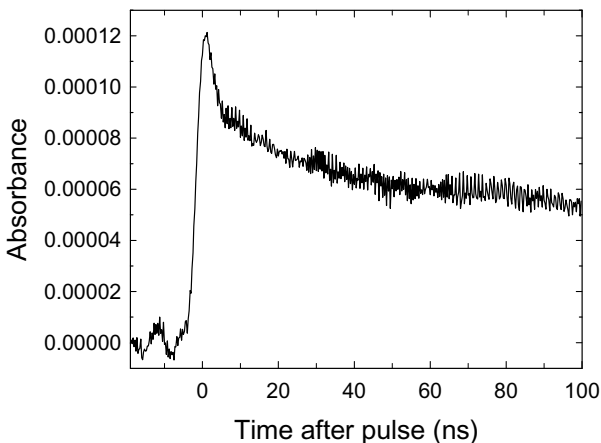


Fig. 5. Absorbance kinetics of the hydrated electron after a 1-ns pulse of $^{12}\text{C}^{6+}$ of 1 GeV in water [result published in Ref. 34].

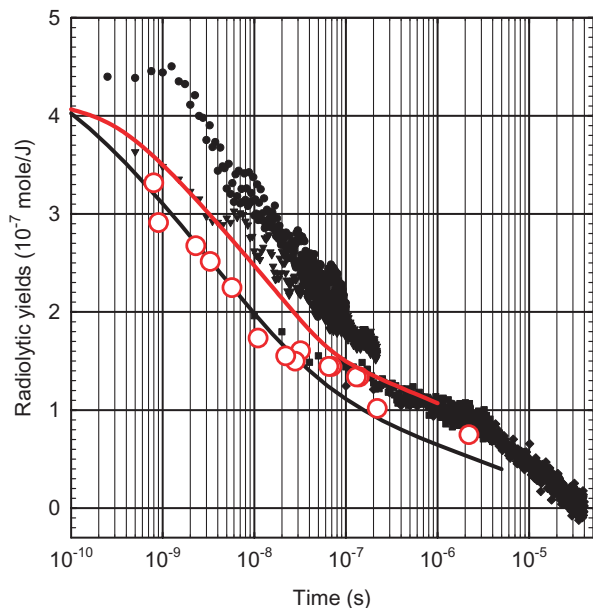


Fig. 6. Measured and calculated time-dependence of the hydrated electron decay. Dark small symbols are from experiment with 1-ns pulses of $^{12}\text{C}^{6+}$ of 1 GeV in water, red open circles are from experiments with 2-MeV ns-pulse of protons and line with corresponding color are simulations of track-segment yields.^{30,34,35}

by a factor of two. Afterward the concentration seems to begin a slower decay. This evolution is well depicted in Fig. 6 where, in a log-representation, the Monte Carlo simulation reproduces the time dependence. The comparison of G -value is not reliable but is not so bad. To detect very low concentrations at short time with the absorption spectroscopy, one needs to optimize all elements in the acquisition chain: the light source, the irradiation cell and the optics for transmission, the detector and the signal acquisition. The improvement of the first and the last one has contributed to detecting almost 1 nM of hydrated electron. The acquisition system allowed an averaging of about one million of kinetics with 1 kHz of repetition rate during the flow of the solution.³³⁻³⁵

LaVerne *et al.* has discussed recently the results of Baldacchino *et al.* by pointing out the high value of yield at earliest times.³⁰ This

value is actually greater than 4 molecule/100 eV which is a common admitted value deduced from the ionization potential of water. As discussed before, many reasons can be reported for explaining this experimental yield: the dosimetry needing also high stability of the pulse, the detection accuracy for very low level of absorbance, and so on. This result is also the first result for this kind of ion and for a track segment as well. Therefore one cannot exclude other unknown effects in the core-tracks. Other track-average yields were reported in the 1980s with low-energy protons (2 MeV) including the Bragg peak energy deposition.

But the comparison is still not easy because there are not enough comparable results that are obtained with the same method (pulse radiolysis) and similar conditions (track segment). Most of the other studies on hydrated electron under heavy ion irradiation were performed by the scavenging method by using the glycyglycin species³⁰ or $S_2O_8^{2-}$.^{36,37}

The plots of G -value as a function of the scavenging capacity (product of the rate constant and the concentration of scavenger) must be discussed in several factors by considering the energy and the range of the ions in order to compare with high energy track segment results. In every case, the tendency of higher yields at earliest times is respected. Discussing the absolute G -value needs much more results.

5.2. *The hydroxyl radical*

The hydroxyl radical is visible only in the deep UV with a low absorption coefficient. It is almost only detected by using scavengers. Recently Taguchi and co-workers have used the phenol molecule and detected the stable products of the reaction by using a powerful HPLC method in order to distinguish the different adducts formed in the track of low energy carbon ions.^{38,39} Other methods using pulse radiolysis have given interesting results by detecting transient species. They showed that the scavenger molecule can be subject to multiple possible reactions in the track of heavy ions. Nevertheless other results tend to show that the increase of OH^\bullet -yield, with the increase of the scavenging capacity, can saturate or even decrease after a maximum

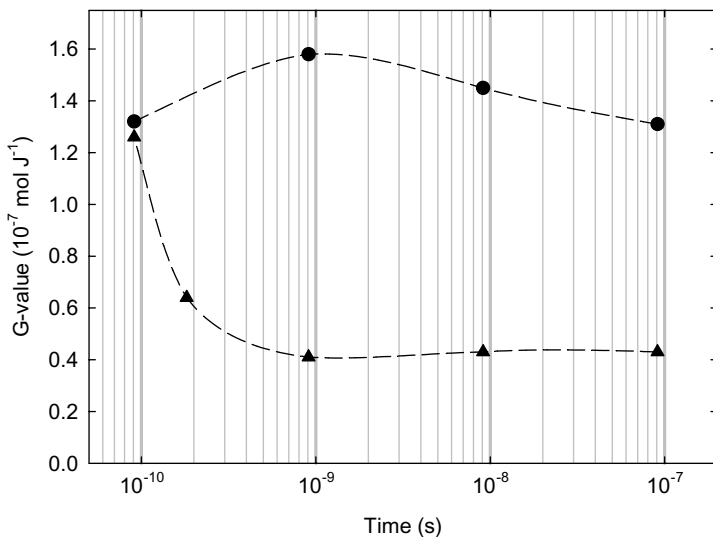


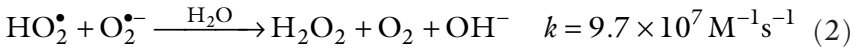
Fig. 7. Measured OH yields by using the thiocyanate solutions as scavenger and μ s-pulses of $^{12}\text{C}^{6+}$ of 1 GeV (circles) and $^{36}\text{Ar}^{18+}$ of 2 GeV (triangles) in water [from Ref. 23].

value of the yield. This effect has been noticed in two papers concerning the same scavenger species, SCN^- and similar ions (carbon and helium ions).^{23,40} Non-linear effect due to interfering reactions at high concentration can become efficient with some track structures. The size of the track core can actually play an important role in the shape of the scavenging plot as we can see in Fig. 7 with carbon and argon ions.

5.3. The superoxide radical

The superoxide radical ($\text{HO}_2^\bullet/\text{O}_2^{\bullet-}$) is a peculiar case in water radiolysis. Its yield of production increases with LET which is completely contrary to the recombination rule in dense ionization tracks. Actually, the general trend is that these radical recombinations increase the production of molecular species (H_2 and H_2O_2). The low reactivity of this radical in pure water essentially due to its

disproportionation (reaction 1) allows it to escape the track in the diffusion step.



This has several potential consequences in biology and medicine. Actually the hadrontherapy uses heavy ion beam for the local energy deposition in the Bragg peak region.

Nevertheless, even if the main therapeutic gain is brought by the precise localization of the energy deposition, the generation of molecular oxygen in hypoxic tumors is known to enhance the sensitization of the cells. But the production of molecular oxygen in the track is still questionable. Some studies have showed the possible direct detection by the pulse radiolysis method and have tried to explain how superoxide radical is formed in the tracks of heavy ions and many mechanisms have been suggested in the past.⁴¹

Multiple-ionizations model is one of the most probable models because the huge energy deposited in the medium is considerably greater than the total energy needed to ionize the total number of water molecules along the ion track.⁴² This has been recently exploited in Monte Carlo simulations (see Fig. 8).^{43,44} This model seems to be in good agreement with the few experimental results concerning $\text{HO}_2^\bullet/\text{O}_2^{\bullet-}$ and H_2O_2 obtained for low LET.

With a low-energy ion beam, the ions generally stop in the volume of the analyzed solution and the whole energy beam is deposited including the Bragg region which is characterized by a huge energy deposition. Effects and ionization structures in the Bragg peak cannot be currently taken into account separately due to the lack of knowledge and the unavailable simulation about this part of the track. Determination of track segment yields of $\text{HO}_2^\bullet/\text{O}_2^{\bullet-}$ and O_2 is expected in the near future in order to clarify the situation.

5.4. *Molecular species: H₂O₂ and H₂*

Molecular and stable species like molecular hydrogen and hydrogen peroxide are the result and consequence of the short story of the

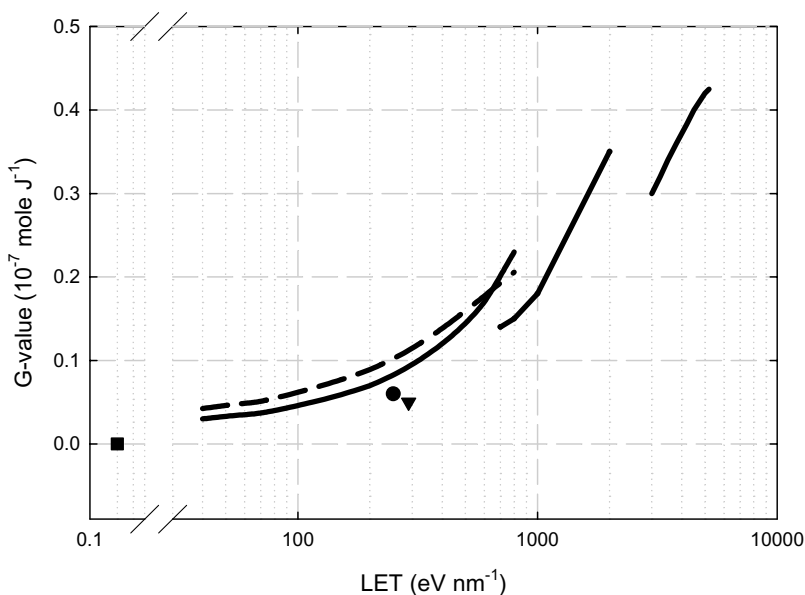


Fig. 8. Superoxide radical G -values as a function of LET. The square symbol is the common yield accepted with γ -rays and high energy electron beam irradiation. Plain lines are from scavenging experiments with C, Ne and Ni ion beam by Laverne and Schuler [Cited in Refs. 41 and 42]. The circle and triangle symbols are from track-segment pulse radiolysis experiments.⁴¹ Dash line is from Monte Carlo simulation.⁴³

track reactions. They are less reactive but are the source of main problems in nuclear industry such as corrosion (H_2O_2) and safety (H_2). As their yield is increased due to the intra-track recombination, they become a serious potential danger (see for instance the variation of H_2O_2 -yield as a function of LET in Fig. 9).

From a fundamental point of view the origins of H_2O_2 and H_2 take place at the earliest step after ionization: basically the recombination of OH forms H_2O_2 ,⁴⁵ and the recombination of hydrated electron forms H_2 and a “non-scavengable” part of H_2 directly originates from the ionization of water molecule⁴⁶ and then enters the reaction mechanism of water radiolysis very early.

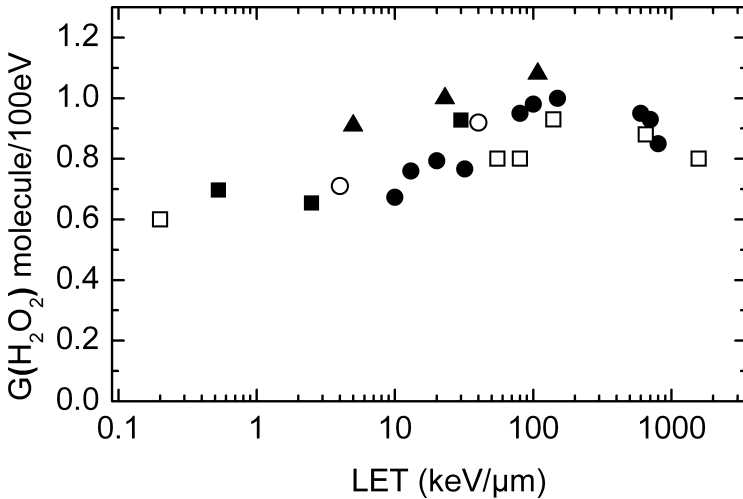


Fig. 9. Hydrogen peroxide yield compilation as a function of LET: (dark squares) ^{137}Cs γ -rays, 30 MeV protons, 1140 MeV carbon ions, (open squares) ^{60}Co γ -rays; 10 MeV protons; 35, 18.5, 6.4 MeV helium ions; 46 MeV nitrogen ions; 30 MeV neon ions, (triangles) ^{60}Co γ -rays; 18 MeV deuterons; 32, 18 MeV helium ions, (dark circles) 15, 10, 5, 2 MeV proton; 15, 10, 5 MeV helium ions; 30, 20, 10 MeV carbon ions, (open circles) rapid neutron; 26 MeV deuterons. [Data from Ref. 45]

6. Simulation

Several methods have been published to simulate the time-evolution of an ionization track in water. Monte Carlo (with the IRT method or step-by-step) and deterministic programs including spur diffusion are the main approaches. With the large memory and powerful computer now available, simulation has become more efficient. The modeling of a track structure and reactivity is more and more precise and concepts can now be embedded in complex simulation programs. Therefore corrections of rate constants with high concentrations of solutes in the tracks and the concept of multiple ionizations have improved the calculation of G -values and their dependence on time.

The range of energy and LET value to consider through the simulation is also wider because the large number of ionizations at elevated LET is directly related to the memory space in the computer.

A virtual limit of 1 keV/nm seems to be reached but it depends on the distance of the selected track segment.⁴⁷⁻⁵⁰ Because simulations are generally performed with a segment of track where the energy of the particle does not change too much, they do not take into account the end of the track where the Bragg peak energy deposition is. This should be a large field of investigation for future simulations and experiments.

Simulations can be used to calculate the radiolytical yields of any existing species in water radiolysis, at any time after an ion crosses the bulk of water, but only a few can represent the experimental results. In these cases the comparison is possible in order to adjust some parameters, e.g. all the earliest processes like the distance of thermalization of electrons or the branching ratio for the multiple-ionization model.

7. Future

7.1. Heavy ion picosecond pulse radiolysis

In the near future, the ion-beam radiation-chemist community will probably understand earlier processes in the track of heavy ions. This supposes two things: accelerators must deliver shorter pulses than those used currently and the detection must be more sensitive and highly time-resolved. That means a picosecond pulse radiolysis research with heavy ions. That is not a foolish project because new designs of accelerators for proton and heavier ions have already started.^{51,52} Physics of plasma has made recent progress^{51,52} and probably in the next year will appear the first results in radiation chemistry with protons with at least a picosecond time resolution. A few intentions have already been published.⁵³

7.2. Influence of chemical and thermodynamic parameters

The need of basic research in the field of nuclear industry and the fundamental interest to understand the reactivity in the tracks will

partly motivate the next experiments in this field. The coupled influence of LET and high temperature or high pressure should bring new approaches to the understanding of the track structures. After solving the technical challenges the expected studies could be done by the scavenging method as well as the pulse radiolysis. Moreover, as it was investigated in the picosecond time-range, the effect of temperature in the tracks should be coupled to the new generation of particle accelerators which will deliver picosecond high energy heavy ions. Here also the energy of available particle bunches is only about a few MeV and is still incompatible with high-pressure and high-temperature cells. High values of pH or solute concentrations are also a large domain of investigation that can bring new interesting behaviors in the intense chemical-competition in the track cores.

8. A Non-exhaustive List of Facilities Devoted to Radiation Chemistry with Heavy Ion

Europe

- GANIL/Caen/France
- CERI/Orléans/France
- GSI/Darmstadt/Germany

Japan

- HIMAC/NIRS/Chiba/Japan
- TIARA/JAEA/Takasaki/Japan

United States

- FN Tandem Van de Graff of Notre Dame Nuclear Structure Laboratory
- ATLAS/Linear Accelerator of Argonne National Laboratory
- K1200 cyclotron of the Michigan State University/National Superconductor Cyclotron Laboratory (NSCL).

Acknowledgment

The authors would like to thank the staff of GANIL and HIMAC cyclotrons used for the radiation chemistry experiments related in this

chapter. All participants of these difficult experiments are greatly acknowledged: G. Vigneron, S. Pin, E. Ballanzat, JC Mialocq, JP Renault, S. Le Caer, S. Pommeret, M. Taguchi and S. Yamashita. Special thanks go to the instigators of the pulse radiolysis with high energy ions: B. Hickel, M. Gardes-Albert and S. Bouffard. We have also appreciated the fruitful discussions and help of B. Gervais and JP Jay-Gerin.

References

1. LaVerne JA. (2004) Radiation chemical effects of heavy ions. In: Mozumder A, Hatano Y. (eds.), *Charged Particle and Photon Interactions with Matter. Chemical, Physicochemical, and Biological Consequences with Applications*, pp. 403–429. Marcel Dekker, New York.
2. Mozumder A. (1999) *Fundamentals of Radiation Chemistry*. Academic Press, San Diego.
3. LaVerne JA. (2000) Track effects of heavy ions in liquid water. *Radiat Res* **153**: 487–496.
4. Kudo H, Katsumura Y. (2002) Ion-beam radiation chemistry. In: Jonah CD, Rao BSM. (eds.), *Radiation Chemistry: Present Status and Future Trends*, pp. 37. Elsevier, London.
5. Corbel C, Sattonnay G, Guilbert S, Garrido F, Barthe MF, Jegou C. (2006) Addition versus radiolytic production effects of hydrogen peroxide on aqueous corrosion of UO₂. *J Nucl Mat* **348**(1–2): 1–17.
6. Corbel C, Sattonnay G, Lucchini JF, Ardois C, Barthe MF, Huet F, Dehaut P, Hickel B, Jegou C. (2001) Increase of the uranium release at an UO₂/H₂O interface under He²⁺ ion beam irradiation. *Nuclear Instruments and Methods in Physics Research* **B179**(2): 225–229.
7. Kraft G. (2000) Tumor therapy with heavy charged particles. *Progress in Particle and Nuclear Physics* **45**(Suppl. 2): 473–544.
8. Shinoda H, Kanai T, Kohno T. (2006) Application of heavy-ion CT. *Phys Med Biol* **51**(16): 4073–4081.
9. Bowman MK, David B, Michael DS, Zimbrick JD. (2005) Track structure in DNA irradiated with heavy ions. *Radiat Res* **163**(4): 447–454.
10. Giustranti C, Rousset S, Balanzat E, Sage E. (2000) Heavy ion-induced plasmid DNA damage in aerated or deaerated conditions. *Biochimie* **82**(1): 79–83.
11. Tsukuda S, Seki S, Tagawa S, Sugimoto M, Idesaki A, Tanaka S, Oshima A. (2004) Fabrication of nanowires using high-energy ion beams. *J Phys Chem* **B108**(11): 3407–3409.
12. Remita H, Lampre I, Mostafavi M, Balanzat E, Bouffard S. (2005) Comparative study of metal clusters induced in aqueous solutions by gamma-rays, electron or C6+ ion beam irradiation. *Rad Phys Chem* **72**(5): 575–586.

13. Chennamsetty R, Escobar I, Xu XL. (2006) Characterization of commercial water treatment membranes modified via ion beam irradiation. *Desalination* **188**(1–3): 203–212.
14. LaVerne JA, Araos MS. (2002) Heavy ion radiolysis of liquid benzene. *J Phys Chem* **A106**(46): 11408–11413.
15. LaVerne JA, Chang Z, Araos MS. (2001) Heavy ion radiolysis of organic materials. *Rad Phys Chem* **60**(4–5): 253–257.
16. Broggio D, Barillon R, Jung JM, Yasuda N, Yamauchi T, Kitamura H, Bischoff P. (2007) Polyvinyltoluene scintillators for relative ion dosimetry: An investigation with Helium, Carbon and Neon beams. *Nucl Instr and Meth in Phys Res* **B254**: 3–9.
17. Ziegler JF, Biersack JP, Littmark U. (1985) *The Stopping Power and Range of Ions in Matter*, vol. 1. Pergamon Press, New York. <http://www.srim.org>
18. Wasselin-Trupin V, Baldacchino G, Bouffard S, Balanzat E, Gardès-Albert M, Abedinzadeh Z, Jore D, Deycard S, Hickel B. (2000) A new method for the measurement of low concentrations of OH/O₂-radical species in water by high-LET pulse radiolysis. A time-resolved chemiluminescence study. *J Phys Chem* **A104**: 8709–8714.
19. Pimblott SM, LaVerne JA. (2002) Effects of track structure on the ion radiolysis of the Fricke dosimeter. *J Phys Chem* **A106**(41): 9420–9427.
20. Calcul-Ohno S, Furukawa K, Taguchi M, Namba H, Watanabe H. (1999) Predicted radiolysis yield in a Fricke solution irradiated with various heavy ions. *Rad Phys Chem* **55**(5–6): 503–506.
21. LaVerne JA, Schuler RH. (1996) Radiolysis of the Fricke dosimeter with ⁵⁸Ni and ²³⁸U ions: Response for particles of high linear energy transfer. *J Phys Chem* **100**: 16034–16040.
22. Milosavljevic BH, LaVerne JA. (2005) Pulse radiolysis of aqueous thiocyanate solutions. *J Phys Chem A* **109**: 165–168.
23. Baldacchino G, Vigneron G, Renault JP, Le Caër S, Pin S, Mialocq JC, Balanzat E, Bouffard S. (2006) Hydroxyl radical yields in the tracks of high energy ¹³C⁶⁺ and ³⁶Ar¹⁸⁺ ions in liquid water. *Nucl Instrum and Methods in Phys Res* **B245**: 288–291.
24. Matsufuji N, Komori M, Sasaki H, Akiu K, Ogawa M, Fukumura A, Urakabe E, Inaniwa T, Nishio T, Kohno T, Kanai T. (2005) Spatial fragment distribution from a therapeutic pencil-like carbon beam in water. *Phys in Med and Biol* **50**(14): 3393–3403.
25. Gunzert-Marx K, Schardt D, Simon RS. (2004) Fast neutrons produced by nuclear fragmentation in treatment irradiations with C-12 beam. *Radiation Protection Dosimetry* **110**(1–4): 595–600.
26. Matsufuji N, Fukumura A, Komori M, Kanai T, Kohno T. (2003) Influence of fragment reaction of relativistic heavy charged particles on heavy-ion radiotherapy. *Phys in Med and Biol* **48**(11): 1605–1623.

27. Brede HJ, Greif KD, Hecker O, Heeg P, Heese J, Jones DTL, Kluge H, Schardt D. (2006) Absorbed dose to water determination with ionization chamber dosimetry and calorimetry in restricted neutron, photon, proton and heavy-ion radiation fields. *Phys in Med and Biol* **51**(15): 3667–3682.
28. Brede HJ, Hecker O, Hollnagel R. (2000) An absorbed dose to water calorimeter for collimated radiation fields. *Nuclear Instruments and Methods in Physics Research* **A455**(3): 721–732.
29. Aso T, Kimura A, Tanaka S, Yoshida H, Kanematsu N, Sasaki T, Akagi T. (2005) Verification of the dose distributions with GEANT4 simulation for proton therapy. *IEEE Trans on Nuclear Science* **52**(4): 896–901.
30. LaVerne JA, Stefanic I, Pimblott SM. (2005) Hydrated electron yields in the heavy ion radiolysis of water. *J Phys Chem* **A109**(42): 9393–9401.
31. LaVerne JA, Tandon L, Knippel BC, Montoya VN. (2005) Heavy ion radiolysis of methylene blue. *Rad Phys Chem* **72**(2–3): 143–147.
32. LaVerne JA, Tandon L. (2003) H₂ production in the radiolysis of water on UO₂ and other oxides. *J Phys Chem* **B107**(49): 13623–13628.
33. Baldacchino G, Bouffard S, Balanzat E, Gardès-Albert M, Abedinzadeh Z, Jore D, Deycard S, Hickel B. (1998) Direct time resolved measurement of radical species formed in water by heavy ions irradiation. *Nucl Instrum and Meth in Phys Res* **B146**: 528–532.
34. Baldacchino G, Vigneron G, Renault JP, Pin S, Abedinzadeh Z, Deycard S, Balanzat E, Bouffard S, Gardès-Albert M, Hickel B, Mialocq JC. (2004) A nanosecond pulse radiolysis study of the hydrated electron with high energy ions with a narrow velocity distribution. *Chem Phys Lett* **385**: 66–71.
35. Baldacchino G, Vigneron G, Renault JP, Pin S, Remita S, Abedinzadeh Z, Deycard S, Balanzat E, Bouffard S, Gardes-Albert M, Hickel B, Mialocq JC. (2003) A nanosecond pulse radiolysis study of the hydrated electron with high energy carbon ions. *Nucl Instruments and Methods in Phys Res* **B209**: 219–223.
36. Katsumura Y. (2001) Ion beam pulse radiolysis study on intra-track reactions in aqueous solutions. *Res Chem Intermediates* **27**(4–5): 333–341.
37. Chitose N, Katsumura Y, Domae M, Zuo Z, Murakami T. (1999) Radiolysis of aqueous solutions with pulsed helium ion beams — 2. Yield of SO₄⁻ formed by scavenging hydrated electron as a function of S2O8²⁻-concentration. *Rad Phys Chem* **54**(4): 385–391.
38. Taguchi M, Matsumoto Y, Moriyama M, Namba H, Aoki Y, Hiratsuka H. (2000) Effect of specific energy of heavy ions for 1,2,4,5-tetracyanobenzene radical anion formation. *Rad Phys Chem* **58**(2): 123–129.
39. Taguchi M, Kojima T. (2005) Yield of OH radicals in water under high-density energy deposition by heavy-ion irradiation. *Radiat Res* **163**(4): 455–461.
40. Chitose N, Katsumura Y, Domae M, Cai ZL, Muroya Y, Murakami T, LaVerne JA. (2001) Radiolysis of aqueous solutions with pulsed ion beams. 4. Product

- yields for proton beams in solutions of thiocyanate and methyl viologen/formate. *J Phys Chem* **A105**(20): 4902–4907.
41. Baldacchino G, Le Parc D, Hickel B, Gardès-Albert M, Abedinzadeh Z, Jore D, Deycard S, Bouffard S, Mouton V, Balanzat E. (1998) Direct observation of HO₂/O₂⁻ free radicals generated in water by high LET pulsed heavy ion beam. *Radiat Res* **149**: 128–133.
 42. Ferradini C, Jay-Gerin J-P. (1998) Does multiple ionization intervene for the production of HO₂ radicals in high-LET liquid water radiolysis? *Radiat Phys Chem* **51**: 263–267.
 43. Gervais B, Beuve M, Olivera GH, Galassi ME, Rivarola RD. (2005) Production of HO₂ and O₂⁻ by multiple ionization in water radiolysis by swift carbon ions. *Chem Phys Lett* **410**: 330–334.
 44. Meesungnoen J, Jay-Gérin JP. (2005) High-LET Radiolysis of liquid water with H-1(+), He-4(2+), C-12(6+), and Ne-20(9+) ions: Effects of multiple ionization. *J Phys Chem* **A109**: 6406–6419.
 45. Wasselin-Trupin V, Baldacchino G, Bouffard S, Hickel B. (2002) Hydrogen peroxide yields in water radiolysis by high-energy ion beams at constant LET. *Rad Phys Chem* **65**: 53–61.
 46. Pastina B, LaVerne JA. (2001) Effect of molecular hydrogen on hydrogen peroxide in water radiolysis. *J Phys Chem* **A105**(40): 9316–9322.
 47. Calcul-Ohno S, Furukawa K, Taguchi M, Kojima T, Watanabe H. (2001) An ion-track structure model based on experimental measurements and its application to calculate radiolysis yields. *Rad Phys Chem* **60**(4–5): 259–262.
 48. Muroya Y, Plante I, Azzam EI, Meesungnoen J, Katsumura Y, Jay-Gerin JP. (2006) High-LET ion radiolysis of water: Visualization of the formation and evolution of ion tracks and relevance to the radiation-induced bystander effect. *Radiat Res* **165**: 485–491.
 49. Cobut V, Corbel C, Patau JP. (2005) Influence of the pH on molecular hydrogen primary yields in He²⁺ ion tracks in liquid water. A Monte Carlo study. *Rad Phys Chem* **72**(2–3): 207–215.
 50. Champion C, L'Hoir A, Politis MF, Fainstein PD, Rivarola RD, Chetioui A. (2005) A Monte Carlo code for the simulation of heavy-ion tracks in water. *Radiat Res* **163**(2): 222–231.
 51. Umstadter D. (2001) Review of physics and applications of relativistic plasmas driven by ultra-intense lasers. *Physics Plasmas* **8**(5): 1774–1785.
 52. Malka V. (2002) Charged particle source produced by laser-plasma interaction in the relativistic regime. *Laser and Part Beams* **20**(2): 217–221.
 53. Crowell RA, Shkrob IA, Oulianov DA, Korovyanko O, Gosztola DJ, Li YL, Rey-de-Castro R. (2005) Motivation and development of ultrafast laser-based accelerator techniques for chemical physics research. *Nucl Instrum and Meth in Phys Res* **B241**(1–4): 9–13.

Chapter 9

Radiolysis of Supercritical Water

Mingzhang Lin[†], Yusa Muroya[‡], Gérard Baldacchino[§]
and Yosuke Katsumura[¶]*

1. Introduction

Due to their peculiar solvent properties, supercritical fluids offer a range of unusual chemical possibilities such as in environmentally benign separation and destruction of hazardous waste, as well as for new materials synthesis.¹⁻⁶ These intriguing reaction media make it possible to sensitively control reaction rate and selectivity with changes in temperature and pressure. The thermophysical properties of water as well as more than 70 other fluid systems have been formulated and/or compiled by IAPWS⁷ and NIST.⁸

* Corresponding author.

[†] Advanced Science Research Center, Japan Atomic Energy Agency, 2-4 Shirakata Shirane, Tokaimura, Nakagun, Ibaraki 319-1195, Japan.

[‡] Nuclear Professional School, School of Engineering, The University of Tokyo, 2-22 Shirakata Shirane, Tokaimura, Nakagun, Ibaraki 319-1188, Japan.

[§] Laboratoire de Radiolyse, CEA/Saclay, DSM/DRECAM/SCM 331, 91191 Gif-Sur-Yvette Cedex, France.

[¶] Department of Nuclear Engineering and Management, School of Engineering, The University of Tokyo, Hongo 7-3-1, Bunkyo-ku, Tokyo 113-8656, Japan.

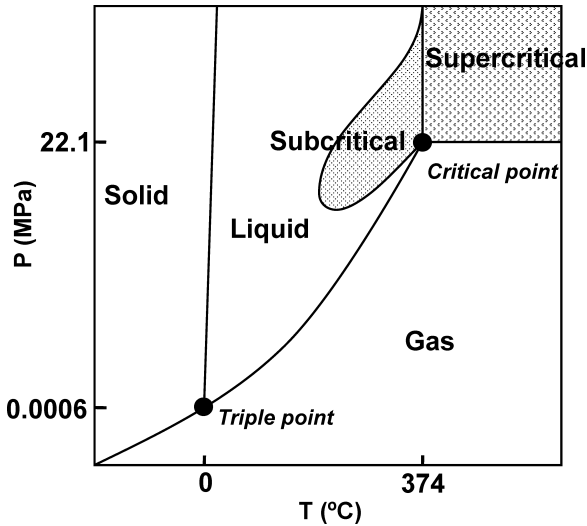


Fig. 1. Schematic representation of the phase diagram of H₂O.

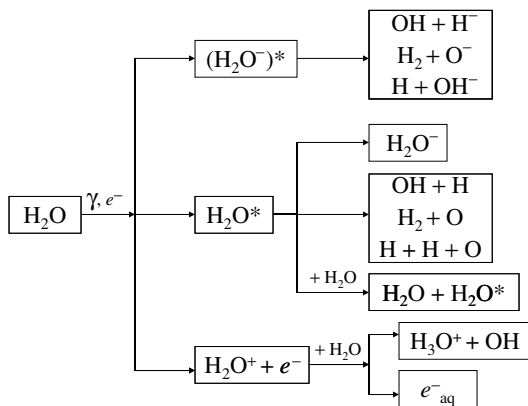
The studies on the radiolysis of supercritical water ($T_c = 374^\circ\text{C}$, $P_c = 22.1$ MPa, Fig. 1) was motivated by the development of one of the next generation (GenIV) nuclear reactors — supercritical water-cooled reactor (SCWR).^{9–11} This new concept reactor has advantages of higher thermal conversion efficiency, simplicity in structure, and safety, etc. In these reactors, the same as in boiling water reactor (BWR) and pressurized water reactor (PWR), light water or heavy water is used not only as a coolant but also as a moderator. The water is exposed to a strong radiation field composed of γ -rays and 2 MeV fast neutrons, etc. As is well known in the BWR and PWR, two radiolysis products of water, O₂ and H₂O₂, strongly affect the corrosion of structural materials in the reactors. Proper water chemistry control, in particular, the injection of H₂ into the coolant to convert O₂ and H₂O₂ into H₂O by radiolytic processes, may represent the key to keep the integrity of the reactors. Computer simulations are usually required to help predict the concentrations of water decomposition products. These simulations require the knowledge of the temperature dependent G -values (denoting the experimentally measured radiolytic yields, with unit molecules/100eV in this context)

as well as rate constants of a set of about 50 reactions. The rate constants and G-values of the radiolysis of light and heavy water over the range 0–300°C have been compiled by Elliot^{12,13} and reviewed by Buxton.¹⁴ It is thought that a similar simulation of water radiolysis in SCWR would be required. As is known, BWRs or PWRs are operated at constant temperature (280–325°C) and pressure (15–20 MPa). However, according to the current conceptual design of SCWR, the inlet temperature is 280°C and the outlet temperature is >500°C, with a fixed pressure of 25 MPa.^{10,11} Thus it is necessary to accumulate the basic data on water radiolysis above 325°C.

In supercritical water, due to the breaking of hydrogen bond network, the dielectric constant dramatically decreases from 78 at room temperature to 2.6 at 400°C/25 MPa, which is similar to that of benzene or toluene. Thus many organic compounds can be easily dissolved in SCW while they have rather low solubility at room temperature. Contrarily, the inorganic salts are difficult to dissolve in SCW due to extremely small ion products. It has also been reported that the water structure exhibits remarkable change in SCW,^{15,16} besides the breaking of hydrogen bond network. The compact tetrahedral-like water structure is decomposed and long-distance water–water interactions increase, and thus water consists of small clusters, much smaller aggregates such as oligomers, and even monomeric gas-like water molecules under supercritical conditions.¹⁵ It is expected that the changes of these properties would reflect on *G* values, rate constants, and spectral properties of the transient species by water radiolysis. In this review, we attempt to summarize the most recent results obtained in the studies of radiation chemistry on SCW, especially the estimation of *G* values, briefly classifying the data on rate constants because they have been reviewed recently.¹⁷

2. General Concepts of Water Radiolysis

Irradiation with electron beam, γ -rays or high-energy charged particles leads to the decomposition of water molecules through excitation and ionization, and the initial processes of water radiolysis can be summarized as shown in Scheme 1.¹⁸



Scheme 1. Initial processes in the water radiolysis.

Electrons are stabilized by the surrounding water molecules to form hydrated electrons in less than 1 ps. The yields at this stage are defined as initial yields. The resulting transient species such as e_{aq}^- , $\cdot\text{H}$, $\cdot\text{OH}$ are distributed locally along the track where the energy deposits, called spur. The spatial distribution greatly depends on the LET of the incident beam. Then these products diffuse randomly and either react together or escape into the bulk solution. After the completion of spur processes, which take place within 10^{-7} – 10^{-6} s, the products homogeneously distribute in the solution, and the yields at this time are known as primary yields. Since the increase of temperature as well as the changes in water properties and water structure would strongly affect the spur reactions, some interesting changes of the radiolytic yields under supercritical conditions are thus expected.

3. Experimental System and Technical Difficulties

By now most of the studies were carried out using nanosecond pulse radiolysis techniques coupled with spectroscopic detection method, only a few were reported to use muonium reactions,^{19,20} steady state (γ -)radiolysis,^{21,22} laser photolysis,²³ and picosecond pulse radiolysis.²⁴ Since conventional pulse radiolysis techniques are well known, here we just briefly introduce the high temperature high pressure (HTHP)

system for pulse radiolysis²⁵⁻²⁷ and point out the technical difficulties in the experiments.

The size, the structure and the sealing mechanism of the optical windows may have some difference from group to group, but the HTHP system is usually composed of a preheating system and an optical cell made of high strength and corrosion-resistant alloy such as Hastelloy or SUS316 and sapphire windows. At least one thermocouple should be available for the direct monitoring of the solution temperature, that is, its tip contacts to or is immersed in the solution. Some special consideration and sometimes compromise are necessary for obtaining a system with good S/N ratio, less dead volume, quick temperature equilibration, and faster flushing of the cell, etc. Figure 2 shows the HTHP cell used at the University of Tokyo.

Like many other experiments, there are some problems or difficulties to overcome in the pulse radiolysis studies on SCW.

- (a) *Corrosion and damage of the sapphire windows*: SCW is corrosive, especially in acidic or alkaline condition, and in the presence of some additives, such as O₂.
- (b) *Thermal stability of chemical reagents*: most chemical reagents are thermally unstable at elevated temperatures.

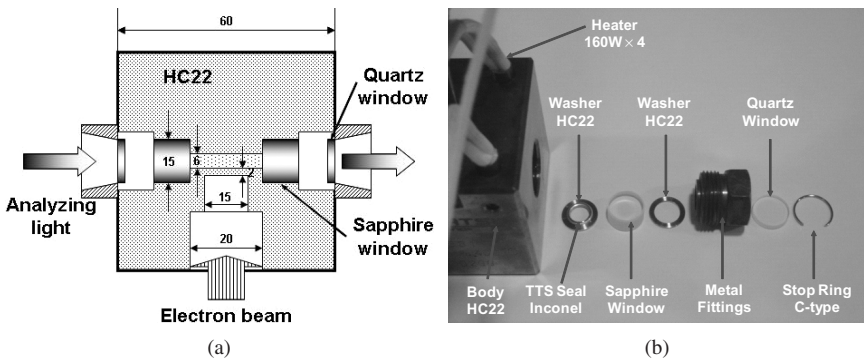


Fig. 2. High temperature high pressure optical cell used at the University of Tokyo. (a) Schematic diagram of the optical cell; (b) Sealing mechanism of a Sapphire window.

- (c) *Solubility of inorganic compounds*: the dissociation constant is very small for salts under supercritical conditions.
- (d) *Limitation of detection techniques*: signal intensity dramatically decreases for low density SCW; and many reactions become much faster than at room temperature — this requires higher time resolution pulse radiolysis system for more precise measurements.

4. Measurement of the Yields of Water Decomposition Products

As is known, the estimation of G values of water decomposition products can be done by pulse radiolysis techniques or steady state radiolysis with product analysis methods. For pulse radiolysis, although a direct measurement of these transient species is desirable, it is difficult to be effectuated by nanosecond pulse radiolysis because of the acceleration of spur reactions and/or the limitation of detection techniques (e.g. the absorption of OH radical is in deep UV with a rather small absorption coefficient). One is forced to adopt the scavenging method, that is, to use a chemical additive to react with the transient species and form another easy-to-detect and relatively stable product. In this section, we mainly introduce the estimation of G values by pulse radiolysis, with the support by γ -radiolysis of some aromatic compounds.

4.1. $G(e_{aq}^-)$

One suitable scavenging system is the use of 0.5 mM methyl viologen (MV^{2+}) in the presence of *tert*-butanol as OH radical scavenger, under neutral pH condition.²⁸ Another is the use of 0.5 mM 4,4'-bipyridyl (4,4'-bpy) together with *tert*-butanol in alkaline solution (pH > 11).²⁹ In both cases, ideally only e_{aq}^- reacts MV^{2+} or 4,4'-bpy to form radical cation MV^{*+} or radical 4,4'-bpyH $^{\bullet}$, with fairly strong absorption at 605 and ~540 nm, respectively. The temperature-dependent $G(e_{aq}^-)$ from 25 to 400°C at a fixed pressure of 25 MPa is shown in Fig. 3(a). $G(e_{aq}^-)$ increases with temperature up to 300°C, which agrees well with the previous reports, then it decreases to a minimum

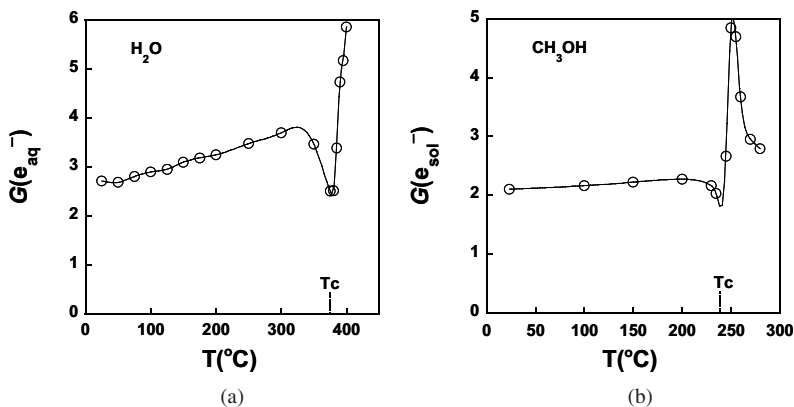


Fig. 3. G value of solvated electrons in water and methanol as a function of temperature at constant pressure: (a) 25.0 MPa for H₂O and (b) 9.0 MPa for CH₃OH.³⁰

near T_c before jumping to a rather high value at 400°C. An independent measurement of $G(e_{\text{sol}}^-)$ in methanol shows a similar tendency [Fig. 3(b)].³⁰

The big change of $G(e_{\text{sol}}^-)$ at constant pressure is due to density effects. As displayed in Fig. 4, under supercritical conditions, at a fixed density $G(e_{\text{sol}}^-)$ decreases with increasing temperature while at a fixed temperature $G(e_{\text{sol}}^-)$ decreases with increasing density. From the viewpoint of W -value and the initial yield of hydrated electron (recent values are 4.0–4.2 molec./100 eV),^{31,32} $G(e_{\text{aq}}^-)$ in low density SCW seems to be over-estimated. This could be due to the use of extrapolating absorption coefficient of MV^{2+} or incomplete scavenging of H atom by *tert*-butanol.²⁸

4.2. $\{G(e_{\text{aq}}^-) + G(\text{H}) + G(\text{OH})\}$

Two scavenging systems have been used to evaluate $\{G(e_{\text{aq}}^-) + G(\text{H}) + G(\text{OH})\}$ (denoted as G_{sum} hereafter). One is 0.5 mM MV^{2+} with 0.2 M ethanol, another is 0.5 mM 4,4'-bpy in the presence of 10 mM HCOONa.²⁸ The solutions are deaerated by Ar gas. Ethanol MV^{2+} and HCOO⁻ are used to convert $\cdot\text{OH}$ radical and $\cdot\text{H}$ atom to ethanol

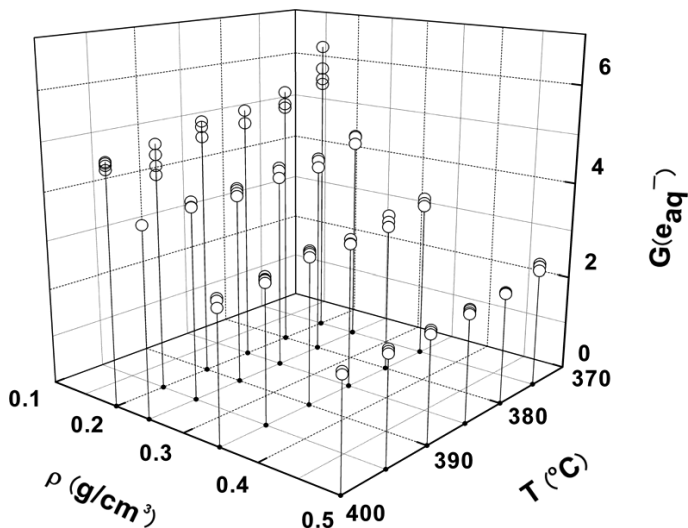


Fig. 4. Three-dimensional plots of $G(e_{\text{aq}}^-)$ as a function of temperature and water density in SCW.²⁸

radical and $\text{COO}^{\bullet-}$, which will subsequently reduce MV^{2+} and 4,4'-bpy to form $\text{MV}^{\bullet+}$ and 4,4'-bpyH, the same as those produced by (e_{aq}^-) , that is, the total yields of $\text{MV}^{\bullet+}$ or 4,4'-bpyH should be equal to the total yield G_{sum} . Figure 5(a) shows the temperature dependence of G_{sum} at 25 MPa and Fig. 5(b) displays the 3D plots of G_{sum} as a function of temperature and water density. Their tendency is very similar to that of $G(e_{\text{aq}}^-)$.

Figure 6 shows the experimental results of γ radiolysis of benzophenone from room temperature to 400°C, in deaerated solutions or N_2O saturated solutions.²¹ Apparently, the tendency of the temperature-dependent yields of benzophenone decomposition and various products formation [Fig. 6(a)], as well as the water density effects on the yields at 400°C [Fig. 6(b)], are also similar to those of $G(e_{\text{aq}}^-)$ and G_{sum} . The studies on other aromatic compounds such as phenol and benzene gave also similar results.²² All these strongly imply that the decomposition of the aromatic compounds reflects the yields of water decomposition under irradiation. However, it should

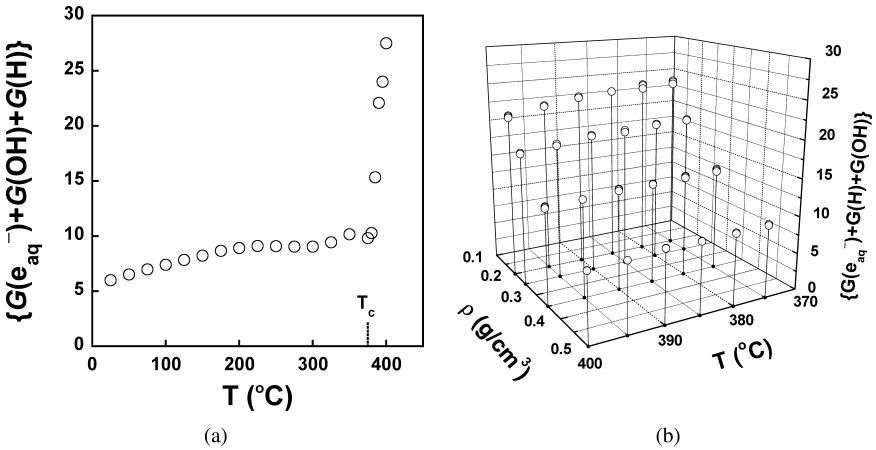


Fig. 5. (a) G_{sum} as a function of temperature at 25 Mpa. (b) 3D plots of G_{sum} as a function of temperature and water density.

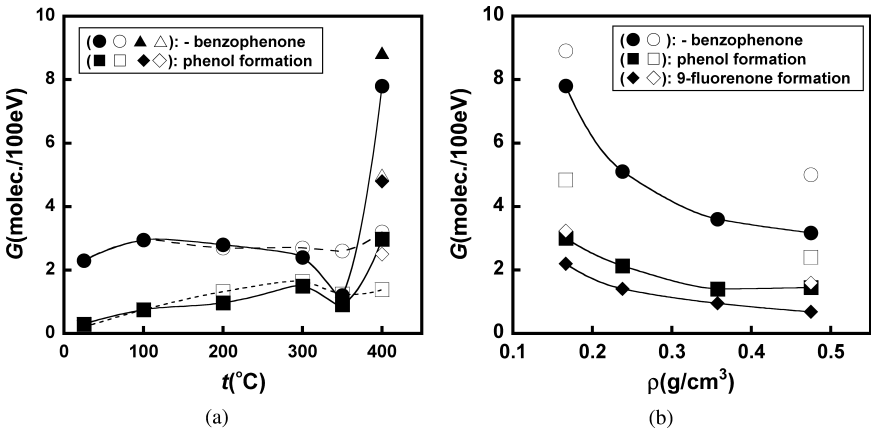


Fig. 6. g -Radiolysis of benzophenone.²¹ (a) G -values of benzophenone consumption and phenol formation at various temperatures and pressures. (b) Density dependence at 400°C of total G -values of benzophenone consumption and products formation.

be pointed out that the reactions for steady state radiolysis are much more complicated and some reverse reactions could even give back the reactant, thus the yields of decomposition are generally much lower than those of water decomposition.^{21,22}

4.3. $G(\text{OH})^{33}$

The estimation of $G(\text{OH})$ has been carried out using an aerated solution of 100 mM NaHCO_3 or a deaerated solution of 100 mM NaHCO_3 in the presence of 1 mM NaNO_3 . In these systems, hydrated electrons are scavenged by O_2 or NO_3^- while the reaction between H atoms and HCO_3^- is rather slow. Consequently, the yield of $\text{CO}_3^{\cdot-}$ would correspond to $G(\text{OH})$. Figure 7 shows $G(\text{OH})$ as a function of temperature. From room temperature to 380°C , the pressure is 25 MPa while at 400°C it is 35 MPa because the solubility of NaHCO_3 at $400^\circ\text{C}/25$ MPa is too small to do the measurements.

4.4. *About $G(\text{H})$*

$G(\text{H})$ has not been measured directly, but it can be calculated by a subtraction of G_{sum} with $G(\text{e}_{\text{aq}}^-)$ and $G(\text{OH})$. The tendency is that it slightly increases as temperature increases up to 200°C and drops to a minimum around T_c , and then increases sharply. At $400^\circ\text{C}/25$ MPa ($\rho = 0.167$ g/cm³), it reaches a value of 7.5 molec./100 eV. If this

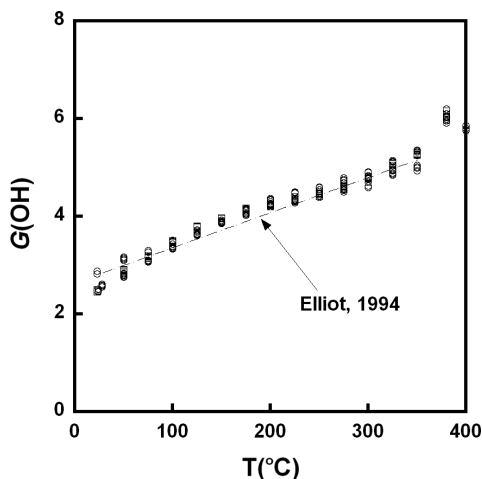


Fig. 7. $G(\text{OH})$ as a function of temperature at 25 MPa (35 MPa at 400°C). The line is based on the equation given by Elliot.¹²

value is divided by $G(e_{aq}^-)$, then we have a ratio of $G(H)/G(e_{aq}^-) \approx 1.3$. Considering that $G(e_{aq}^-)$ might be overestimated, the ratio $G(H)/G(e_{aq}^-)$ could be higher than 1.3. As is known, at room temperature, $G(H)/G(e_{aq}^-)$ is about 0.16. This qualitatively agrees with the result reported by Cline *et al.*, who derived the ratio $G(H)/G(e_{aq}^-)$ from the fittings of the decay kinetics of hydrated electrons scavenged by SF_6 under alkaline solutions.³⁴ They found that at 380°C, the ratio is greater than unity and becomes larger as density decreases. In low-density supercritical water, the initial yield of H atoms seems to be roughly five to six times the yield of hydrated electrons, as shown in Fig. 8. Considering the uncertainty of the fittings, these two results seem to be consistent.

As for the yield of molecular products, especially $G(H_2)$ and $G(H_2O_2)$, it is difficult to evaluate by pulse radiolysis techniques. This should be clarified by experiments, although H_2O_2 might be thermally unstable under supercritical conditions. At least one of these two molecular products should be measured by product analysis, then another component could be calculated by the material balance equation:

$$G(-H_2O) = G(e_{aq}^-) + G(H) + 2G(H_2) = G(OH) + 2G(H_2O_2)$$

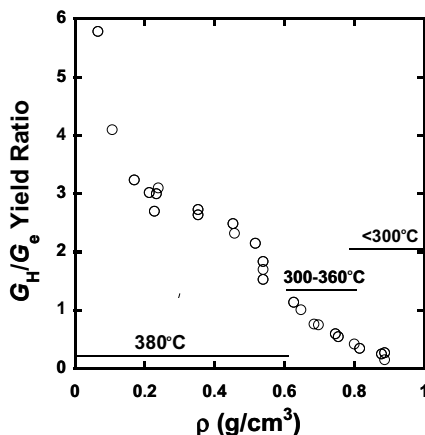


Fig. 8. G_H/G_e as a function of density.³⁴

5. Radiation-Induced Reactions and Rate Constants

In this section, we do not attempt to describe in details all the reactions that have been studied, but only focus on the common features of the radiation-induced reactions with the two most important species of water radiolysis, hydrated electron and hydroxyl radical, although some other reactions such as the reaction of H atoms with hydroxide ions have also been reported.³⁵

5.1. Reactions with e_{aq}^-

5.1.1. Ionic reactants

The temperature-dependent reaction rates of e_{aq}^- with H^+ , NO_3^- , and NO_2^- have been reported.^{34,36,37} As mentioned above, around the supercritical point, the dielectric constant of water is similar to non-polar organic solvents, and the dissociation constants of inorganic salts are extremely small. It is thought that these properties would affect those ionic reactions which are Coulombic-force related. As shown in Fig. 9, for the reaction with H^+ , the rates strongly increase

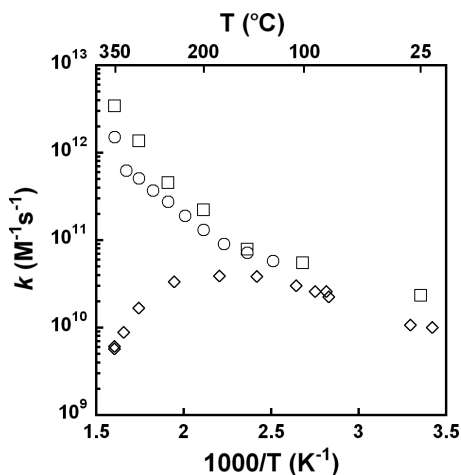


Fig. 9. Temperature-dependent rate constants for the reactions of e_{aq}^- with nitrate ion (\diamond , 25.7 MPa from Ref. 36) and proton (\circ , 25.7 Mpa from Ref. 36; \square , 25 MPa from Ref. 37).

between 250 and 350°C. For NO_3^- , the rate constant increases as the temperature increases, reaches a maximum around 125–200°C and then decreases.

As is known, rate constants for diffusion-controlled reactions can be described by the Debye–Smoluchowski equation:

$$k_{\text{diff}} = 4\pi R D F_D,$$

$$F_D = (r_c/R)/(\exp(r_c/R) - 1),$$

where F_D is the Debye factor, R is the reaction distance, and $r_c \equiv e^2/\epsilon k_B T$ (e : electronic charge, ϵ : dielectric constant, k_B : Boltzmann constant) represents the critical distance at which the electron–positive-ion potential energy equals numerically to $k_B T$. Because the dielectric constant of water decreases as temperature increases, the Coulomb potential between reactants will change significantly. Thus the rate of the proton–electron reaction is accelerated further by attraction, while the nitrate–electron reaction is retarded due to repulsion between the two anions.³⁶

For a non-diffusion controlled reaction, it was explained using the Noyes equation³⁶:

$$1/k_{\text{obs}} = 1/k_{\text{diff}} + \exp(r_c/R)/k_{\text{act}},$$

where k_{act} is the activated rate constant. There are two limiting cases: when $k_{\text{act}} \gg k_{\text{diff}}$, the reaction will occur on every encounter, so that $k_{\text{obs}} \approx k_{\text{diff}}$; when $k_{\text{act}} \ll k_{\text{diff}}$, the reaction rate will be given by $k_{\text{obs}} \approx k_{\text{act}}$.

5.1.2. Hydrophobic or neutral species

Reaction rates of e_{aq}^- with O_2 , SF_6 , N_2O , and nitrobenzene have been investigated.^{34,38,39} As shown in Fig. 10(a), for temperatures < 300°C, the rate constants for scavenging by O_2 or SF_6 follow Arrhenius behavior but become increasingly dependent on water density (pressure) at higher temperatures. At a fixed temperature 380°C ($T/T_c = 1.01$), rate constants for these reactions reach a distinct

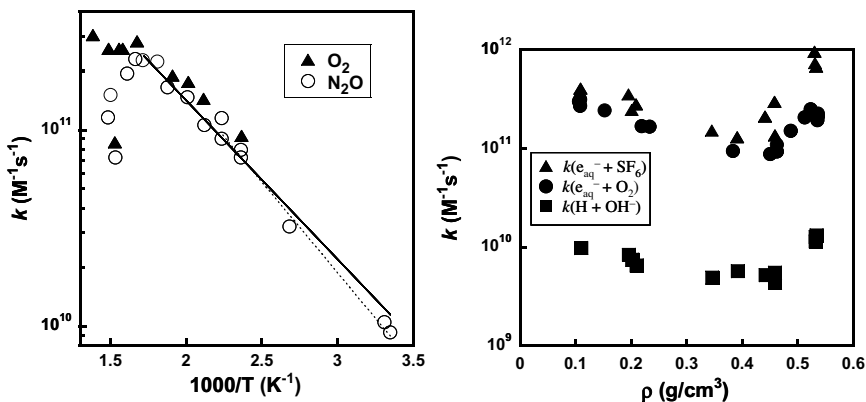


Fig. 10 (a) Temperature-dependent rates of the reactions of e_{aq}^- with N_2O ³⁹ and O_2 .³⁴ (b) Density effect on the rate of the reactions of e_{aq}^- with O_2 .³⁴

minimum near $0.45 \text{ g}/\text{cm}^3$ [Fig. 10(b)]. This behavior has been interpreted in terms of the potential of mean force separating an ion (OH^- or e_{aq}^-) from a hydrophobic species (H , O_2 , or SF_6) in the compressible fluid. As is well known, around the supercritical point, the inhomogeneity of water density or the clustering effect of water molecules becomes a very important feature, which would affect the distribution of hydrophobic reactant and hydrated electron. For example, the hydrophobic molecules such as O_2 might exist in the lower density region with higher probability. This kind of inhomogeneous distribution will hinder the encounter of hydrophobic molecules with hydrated electrons, thus the reaction rates decrease dramatically.

5.2. Reactions with $\cdot\text{OH}$ radical

$\cdot\text{OH}$ radical could be the most important oxidizing species that is assumed to be closely related to the corrosion of the structural materials in nuclear reactors. The studies of the reactions of $\cdot\text{OH}$ radical at elevated temperatures or supercritical water are thus essential.

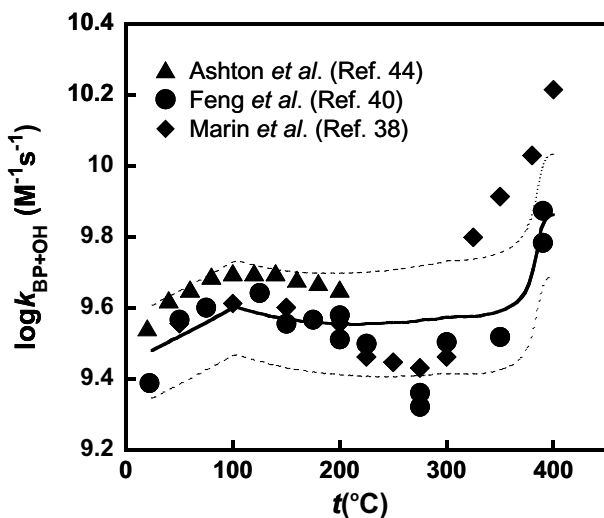


Fig. 11. Comparison between the experimental and modeled bimolecular rate constants, k_{bi} , with 95% confidence intervals (the two dashed lines), for the reaction between OH radical and nitrobenzene at 25 MPa and temperatures between 25°C and 390°C.⁴⁰

Most of the studies were carried out with aromatic compounds, or simple molecules such as CO_3^{2-} or HCO_3^- , partly due to their excellent thermal stability.^{25,38,40-43}

Figure 11 shows a typical example of the temperature-dependent behavior for the reactions of $\bullet\text{OH}$ radical with aromatic compounds.⁴⁰ The measured bimolecular rate constants of $\bullet\text{OH}$ radical with nitrobenzene showed distinctly non-Arrhenius behavior below 350°C, but increased in the slightly subcritical and supercritical region. Feng *et al.*⁴⁰ succeeded in modeling these data with a three-step reaction mechanism originally proposed by Ashton *et al.*,⁴⁴ while Ghandi *et al.* claimed to have developed a so-called multiple collisions model to predict the rates for the reactions of $\bullet\text{OH}$ radical in sub- and super-critical water.⁴²

It is worth mentioning that the rate constant for the reaction of $\cdot\text{OH}$ radical with H_2 , which is one of the most important reactions in water chemistry, has also been studied up to 350°C by competition kinetics using nitrobenzene as a competing $\cdot\text{OH}$ scavenger.⁴⁵ At higher temperatures, the rate constant undershoots an extrapolation of the Arrhenius plot and actually decreases in value above 275°C . At 350°C , the measured rate constant is more than a factor of five below the Arrhenius extrapolation.⁴⁵ This implies that the amount of hydrogen injection calculated by the current model of water radiolysis in nuclear reactor should be reconsidered.

6. Spectral Properties of Transient Species

6.1. Hydrated electron

Whilst temperature-dependent spectral properties of the solvated electron have been of great interest in many studies, only a few reports have been related to supercritical fluids.^{27,46–48} A general tendency is that the spectra of the solvated electrons shift strongly to the red (to longer wavelength) as temperature is raised [Fig. 12(a)]. At supercritical temperatures, the spectra of hydrated electrons shift slightly to the red as density decreases, as shown in Fig. 12(b). With the application of spectral moment theory, Bartels *et al.* estimated the average size of the electron wave function and of its kinetic energy.⁴⁶

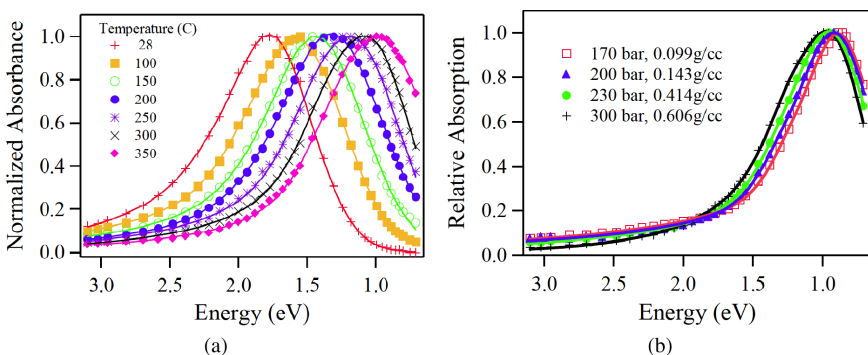


Fig. 12. Temperature- and density-dependent spectra of hydrated electrons.⁴⁶

It appears that for water densities below about 0.6 g/cc, and down to below 0.1 g/cc, the average radius of gyration for the electron remains constant at around 3.4 Å, and its absorption maximum is near 0.9 eV. For higher densities, the electron is squeezed into a smaller cavity and the spectrum is shifted to the blue.⁴⁶

Meanwhile, some computer simulations have contributed to the temperature-dependent behavior of the absorption spectrum of solvated electron.⁴⁹⁻⁵² Boero *et al.* carried a first principles study of a hydrated electron in water at ordinary and supercritical conditions.⁴⁹ According to their study, for normal water, the hydrogen bond (H bond) network needs about 1.6 ps to accommodate the additional e⁻. Then the delocalized state becomes localized, the H bonds of the system rearrange, and water molecules reorient in such a way that a cavity forms in the system. Six water molecules reorient in such a way that all of them point at least one H toward the electronic cloud, thus forming a solvation shell and the electron distribution is assumed to be in an ellipsoidal shape. Those cavities survive for a period ranging from ~50 fs to a maximum of about 90 fs. At supercritical conditions, instead, the H-bond network is not continuous and the electron localizes in preexisting cavities in a more isotropic way. Four water molecules form the solvation shell but the localization time shortens significantly. Boutin and co-workers have performed quantum-classical molecular-dynamics (QCMD) simulations to study the temperature and density dependence of absorption spectra of hydrated electron at elevated temperatures and supercritical conditions.^{50,51} Their simulation results could quantitatively explain the experimental data. It was also suggested that the observed shift could be a density rather than a temperature effect. Moreover, when extending these simulations to very low densities corresponding to supercritical conditions, the results display a progressive “desolvation” of the hydrated electron.

6.2. Other transient species

Table I lists the spectral shifts of some of the intermediate radicals at room temperature and elevated temperatures (in most cases, above T_c). Generally, the anion or cation radicals show a red-shift

Table 1. Spectral shifts of various intermediate radicals.

Chemical	Radical form	λ_{\max} at RT	λ_{\max} in SCW*	References
Benzophenone	$\phi_2^{\bullet}\text{COH}$	545 nm	525 nm (400°C)	37
	$\phi_2^{\bullet}\text{CO}^-$	610 nm	650 nm (300°C)	37
Thiocyanate	$(\text{SCN})_2^{\bullet-}$	470 nm	510 nm (400°C)	53
Carbonate	$\text{CO}_3^{\bullet-}$	600 nm	600 nm (400°C)	43
Silver	Ag°	355 nm	370 nm (200°C)	54
	Ag_2^+	310 nm	380 nm (380°C)	54
Methyl viologen	$\text{MV}^{\bullet+}$	605 nm	605 nm (400°C)	28
4,4'-bipyridyl	44BpyH^{\bullet}	540 nm	525 nm (400°C)	29

* λ_{\max} is density dependent in SCW; here we choose a typical value.

while the neutral radicals of aromatic compounds show a blue-shift, except that $\text{CO}_3^{\bullet-}$ and $\text{MV}^{\bullet+}$ exhibit no change with increasing temperature, probably due to their fairly good symmetric molecular structure and the delocalization of the electric charge. The spectral shift reflects a change in the energy difference between the ground state and the excited state with the changes of solvent environment. These energies reflect the differences in solvation where the solvent responds to a solute by means of lowering the energy of the system. Recently, Wu *et al.*³⁷ have qualitatively interpreted the red-shift of benzophenone anion and the blue-shift of the neutral ketyl radical in terms of electrostatic forces and hydrogen bonding of water. Boutin *et al.*⁵⁰ have quantitatively explained the red-shifts of Ag° and Ag_2^+ using QCMD simulations. Nevertheless, a more general and precise model is remained to be developed, taking into account the hydrogen bonding network, the dielectric constant, the electrostatic forces and polarity of solute, and the clustering effects of water molecules under supercritical conditions, etc.

7. Conclusions

Under sub- or super-critical conditions, the radiolytic yields of water decomposition products (and their ratios), the reaction rate constants and the spectral properties of transient species are significantly

different from those of water at ambient condition or even at elevated temperatures below 300°C. These properties are not only dependent on temperature but also greatly affected by water density in SCW, or in other words, they exhibit non-linear behavior or even non-monotonic function with temperature at a fixed pressure. This would strongly suggest a re-consideration of current model of aqueous radiation chemistry in nuclear reactors and a more complicated model for the future SCW reactors. On the other hand, these unusual behaviors are certainly related to the peculiar properties of supercritical water such as dielectric constant, hydrogen bonding network, and density inhomogeneity, etc. Thus it is expected to stimulate the fundamental studies on the primary chemical processes, the direct measurement of radiolytic yields, the spur reaction processes and other more general chemical interests in these intriguing reaction media. To achieve these goals, more sophisticated equipments such as picosecond or sub-picosecond pulse radiolysis systems as well as the involvement of theoretical calculations are essential.

Acknowledgments

The authors are grateful to Mr. T. Ueda and Prof. M. Uesaka for their technical assistance in pulse radiolysis experiments and encouragement. We are also thankful to Prof. M. Mostafavi, Dr. G. Wu, Dr. T. Miyazaki, Dr. H. He, and Dr. Z. Han for their significant contribution to research on pulse radiolysis of supercritical fluids. Our work described in this chapter was partly entrusted by the Ministry of Education, Culture, Sports, Science and Technology (MEXT), Japanese Government, as a “Fundamental R&D program on water chemistry of supercritical pressure water under radiation field”, and was also partly supported by “Reimei Research Promotion Project of JAEA (Japan Atomic Energy Agency)”.

References

1. Akiya N, Savage PE. (2002) Roles of water for chemical reactions in high-temperature water. *Chem Rev* **102**: 2725–2750.

2. Darr JA, Poliakoff M. (1999) New directions in inorganic and metal-organic coordination chemistry in supercritical fluids. *Chem Rev* **99**: 495–541.
3. Eckert CA, Knutson BL, Debenedetti PG. (1996) Supercritical fluids as solvents for chemical and materials processing. *Nature* **383**: 313–318.
4. Jessop PG, Ikariya T, Noyori R. (1994) Homogeneous catalytic-hydrogenation of supercritical carbon-dioxide. *Nature* **368**: 231–233.
5. Savage PE. (1999) Organic chemical reactions in supercritical water. *Chem Rev* **99**: 603–621.
6. Savage PE, Gopalan S, Mizan TI, Martino CJ, Brock EE. (1995) Reactions at supercritical conditions — Applications and fundamentals. *Aiche J* **41**: 1723–1778.
7. <http://www.iapws.org/> (The International Association for the Properties of Water and Steam).
8. <http://webbook.nist.gov/chemistry/fluid/> (Thermophysical Properties of Fluid Systems).
9. Oka Y, Kataoka K. (1992) Conceptual design of a fast breeder reactor cooled by supercritical steam. *Ann Nucl Energy* **19**: 243–247.
10. Oka Y, Koshizuka S. (1998) Conceptual design study of advanced power reactors. *Prog Nucl Energy* **32**: 163–177.
11. Squarer D, Schulenberg T, Struwe D, Oka Y, Bittermann D, Aksan N, Maraczy C, Kyrki-Rajamaki R, Souyri A, Dumaz P. (2003) High performance light water reactor. *Nucl Eng Des* **221**: 167–180.
12. Elliot AJ. (1994) *Rate Constants and G-Values for the Simulation of the Radiolysis of Light Water over the Range 0–300°C*. AECL-11073, COG-94-167.
13. Elliot AJ, Ouellette DC, Stuart CR. (1996) *The Temperature Dependence of the Rate Constants and Yields for the Simulation of the Radiolysis of Heavy Water*. AECL-11658, COG-96-390-1.
14. Buxton GV. (2001) High temperature water radiolysis. In: Jonah CD, Rao BSM (eds.), *Radiation Chemistry — Present Status and Future Trends*, pp. 145–162. Elsevier, Tokyo.
15. Ohtaki H, Radnai T, Yamaguchi T. (1997) Structure of water under subcritical and supercritical conditions studied by solution X-ray diffraction. *Chem Soc Rev* **26**: 41–51.
16. Tucker SC, Maddox MW. (1998) The effect of solvent density inhomogeneities on solute dynamics in supercritical fluids: A theoretical perspective. *J Phys Chem B* **102**: 2437–2453.
17. Garrett BC, Dixon DA, Camaioni DM *et al.* (2005) Role of water in electron-initiated processes and radical chemistry: Issues and scientific advances. *Chem Rev* **105**: 355–389.
18. Draganic IG, Draganic ZD. (1971) *The Radiation Chemistry of Water*. Academic Press, New York.

19. Percival PW, Brodovitch JC, Ghandi K, Addison-Jones B, Schuth J, Bartels DM. (1999) Muonium in sub- and supercritical water. *Phys Chem Chem Phys* **1**: 4999–5004.
20. Percival PW, Ghandi K, Brodovitch JC, Addison-Jones B, McKenzie I. (2000) Detection of muoniated organic free radicals in supercritical water. *Phys Chem Chem Phys* **2**: 4717–4720.
21. Miyazaki T, Katsumura Y, Lin M, Muroya Y, Kudo H, Asano M, Yoshida M. (2006) γ -Radiolysis of benzophenone aqueous solution at elevated temperatures up to supercritical condition. *Radiat Phys Chem* **75**: 218–228.
22. Miyazaki T, Katsumura Y, Lin M, Muroya Y, Kudo H, Taguchi M, Asano M, Yoshida M. (2006) Radiolysis of phenol in aqueous solution at elevated temperatures. *Radiat Phys Chem* **75**: 408–415.
23. Lin M, Katsumura Y, Muroya Y, He H. (2006) A high temperature/pressure optical cell for absorption studies of supercritical fluids by laser photolysis. *Indian J Radiat Res* **3**: 69–77.
24. Baldacchino G, De Waele V, Monard H, Sorgues S, Gobert F, Larbre JP, Vigneron G, Marignier JL, Pommeret S, Mostafavi M. (2006) Hydrated electron decay measurements with picosecond pulse radiolysis at elevated temperatures up to 350°C. *Chem Phys Lett* **424**: 77–81.
25. Ferry JL, Fox MA. (1998) Effect of temperature on the reaction of HO center dot with benzene and pentahalogenated phenolate anions in subcritical and supercritical water. *J Phys Chem A* **102**: 3705–3710.
26. Takahashi K, Cline JA, Bartels DM, Jonah CD. (2000) Design of an optical cell for pulse radiolysis of supercritical water. *Rev Sci Instrum* **71**: 3345–3350.
27. Wu G, Katsumura Y, Muroya Y, Li X, Terada Y. (2000) Hydrated electron in subcritical and supercritical water: A pulse radiolysis study. *Chem Phys Lett* **325**: 531–536.
28. Lin M, Katsumura Y, Muroya Y, He H, Wu G, Han Z, Miyazaki T, Kudo H. (2004) Pulse radiolysis study on the estimation of radiolytic yields of water decomposition products in high-temperature and supercritical water: Use of methyl viologen as a scavenger. *J Phys Chem A* **108**: 8287–8295.
29. Lin M, Katsumura Y, He H, Muroya Y, Han Z, Miyazaki T, Kudo H. (2005) Pulse radiolysis of 4,4'-bipyridyl aqueous solutions at elevated temperatures: Spectral changes and reaction kinetics up to 400°C. *J Phys Chem A* **109**: 2847–2854.
30. Han H, Katsumura Y, Lin M *et al.* unpublished.
31. Bartels DM, Cook AR, Mudaliar M, Jonah CD. (2000) Spur decay of the solvated electron in picosecond radiolysis measured with time-correlated absorption spectroscopy. *J Phys Chem A* **104**: 1686–1691.
32. Muroya Y, Meesungnoen J, Jay-Gerin JP, Filali-Mouhim A, Goulet T, Katsumura Y, Mankhetkorn S. (2002) Radiolysis of liquid water: An attempt to

- reconcile Monte-Carlo calculations with new experimental hydrated electron yield data at early times. *Can J Chem* **80**: 1367–1374.
33. Lin M, Katsumura Y, Muroya Y *et al.* *unpublished*.
 34. Cline J, Takahashi K, Marin TW, Jonah CD, Bartels DM. (2002) Pulse radiolysis of supercritical water. 1. Reactions between hydrophobic and anionic species. *J Phys Chem A* **106**: 12260–12269.
 35. Marin TW, Jonah CD, Bartels DM. (2005) Reaction of hydrogen atoms with hydroxide ions in high-temperature and high-pressure water. *J Phys Chem A* **109**: 1843–1848.
 36. Takahashi K, Bartels DM, Cline JA, Jonah CD. (2002) Reaction rates of the hydrated electron with NO_2^- , NO_3^- , and hydronium ions as a function of temperature from 125 to 380°C. *Chem Phys Lett* **357**: 358–364.
 37. Wu G, Katsumura Y, Lin M, Morioka T, Muroya Y. (2002) Temperature dependence of ketyl radical in aqueous benzophenone solutions up to 400°C: A pulse radiolysis study. *Phys Chem Chem Phys* **4**: 3980–3988.
 38. Marin TW, Cline JA, Takahashi K, Bartels DM, Jonah CD. (2002) Pulse radiolysis of supercritical water. 2. Reaction of nitrobenzene with hydrated electrons and hydroxyl radicals. *J Phys Chem A* **106**: 12270–12279.
 39. Takahashi K, Ohgami S, Koyama Y, Sawamura S, Marin TW, Bartels DM, Jonah CD. (2004) Reaction rates of the hydrated electron with N_2O in high temperature water and potential surface of the N_2O^- anion. *Chem Phys Lett* **383**: 445–450.
 40. Feng J, Aki SNVK, Chateauneuf JE, Brennecke JF. (2002) Hydroxyl radical reactivity with nitrobenzene in subcritical and supercritical water. *J Am Chem Soc* **124**: 6304–6311.
 41. Ferry JL, Fox MA. (1999) Temperature effects on the kinetics of carbonate radical reactions in near-critical and supercritical water. *J Phys Chem A* **103**: 3438–3441.
 42. Ghandi K, Percival PW. (2003) Prediction of rate constants for reactions of the hydroxyl radical in water at high temperatures and pressures. *J Phys Chem A* **107**: 3005–3008.
 43. Wu G, Katsumura Y, Muroya Y, Lin M, Morioka T. (2002) Temperature dependence of carbonate radical in NaHCO_3 and Na_2CO_3 solutions: Is the radical a single anion? *J Phys Chem A* **106**: 2430–2437.
 44. Ashton L, Buxton GV, Stuart CR. (1995) Temperature-dependence of the rate of reaction of Oh with some aromatic-compounds in aqueous-solution — Evidence for the formation of a pi-complex intermediate. *J Chem Soc Faraday T* **91**: 1631–1633.
 45. Marin TW, Jonah CD, Bartels DM. (2003) Reaction of $\cdot\text{OH}$ radicals with H_2 in sub-critical water. *Chem Phys Lett* **371**: 144–149.
 46. Bartels DM, Takahashi K, Cline JA, Marin TW, Jonah CD. (2005) Pulse radiolysis of supercritical water. 3. Spectrum and thermodynamics of the hydrated electron. *J Phys Chem A* **109**: 1299–1307.

47. Han Z, Katsumura Y, Lin M, He H, Muroya Y, Kudo H. (2005) Temperature and pressure dependence of the absorption spectra and decay kinetics of solvated electrons in ethanol from 22 to 250°C studied by pulse radiolysis. *Chem Phys Lett* **404**: 267–271.
48. Wu G, Katsumura Y, Muroya Y, Li X, Terada Y. (2001) Pulse radiolysis of high temperature and supercritical water: Experimental setup and e_{aq}^- observation. *Radiat Phys Chem* **60**: 395–398.
49. Boero M, Parrinello M, Terakura K, Ikeshoji T, Liew CC. (2003) First-principles molecular-dynamics simulations of a hydrated electron in normal and supercritical water. *Phys Rev Lett* **90**: 226403-1 to 226403-4.
50. Boutin A, Spezia R, Coudert FX, Mostafavi M. (2005) Molecular dynamics simulations of the temperature and density dependence of the absorption spectra of hydrated electron and solvated silver atom in water. *Chem Phys Lett* **409**: 219–223.
51. Nicolas C, Boutin A, Levy B, Borgis D. (2003) Molecular simulation of a hydrated electron at different thermodynamic state points. *J Chem Phys* **118**: 9689–9696.
52. Rodriguez J, Skaf MS, Laria D. (2003) Solvation of excess electrons in supercritical ammonia. *J Chem Phys* **119**: 6044–6052.
53. Wu G, Katsumura Y, Muroya Y, Lin M, Morioka T. (2001) Temperature dependence of $(SCN)_2^{\bullet-}$ in water at 25–400°C: Absorption spectrum, equilibrium constant, and decay. *J Phys Chem A* **105**: 4933–4939.
54. Mostafavi M, Lin M, Wu G, Katsumura Y, Muroya Y. (2002) Pulse radiolysis study of absorption spectra of Ag° and Ag_2^+ in water from room temperature up to 380°C. *J Phys Chem A* **106**: 3123–3127.

Chapter 10

Pulse Radiolysis in Supercritical Krypton and Xenon Fluids

*Richard Holroyd**

1. Introduction

Recently, supercritical fluids have become quite popular in chemical and semiconductor industries for applications in chemical synthesis, extraction, separation processes, and surface cleaning.¹⁻³ These applications are based on: the high dissolving power due to density build-up around solute molecules, and the ability to tune the conditions of a supercritical fluid, such as density and temperature, that are most suitable for a particular reaction. The rare gases also possess these properties and have the added advantage of being supercritical at room temperature. Information about the density build-up around both charged and neutral species can be obtained from fundamental studies of volume changes in the reactions of charged species in supercritical fluids. Volume changes are much larger in supercritical fluids than in ordinary solvents because of their higher compressibility. Hopefully basic studies, such as discussed here, of the behavior of

* Chemistry Department, Brookhaven National Laboratory, Upton, NY 11973, USA.
E-mail: holroyd@bnl.gov, rholroyd@suffolk.lib.ny.us

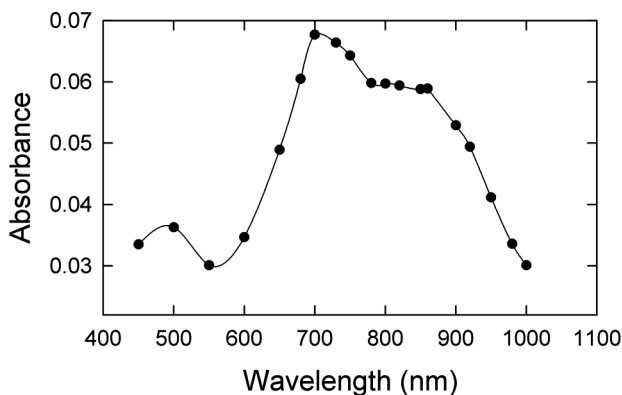
charged species in supercritical gases will provide information useful for the utilization of these solvents in industrial applications.

These studies require special cells to withstand the pressures involved, as well as radiation sources like high energy electrons or X-rays that will penetrate the necessarily thick windows or walls of the cell. Rare gases have the additional feature of high free ion yields that facilitate the study of ionic reactions. The high yield is a consequence of the long time required to thermalize the electron^{4,5}; several nanoseconds are required since only elastic collisions are available for energy loss. During this time the electron travels well beyond the Onsager escape distance from the cation. The escape probability is therefore nearly 100%. The free ion yield, G , is around 5 ion-pairs/100 eV in xenon.^{6,7} The yield is 5.4 in liquid krypton⁸ and 4.1 for krypton gas.⁹ Dense krypton and xenon fluids have not often been used as solvents for the study of reactions by pulse radiolysis. In the case of xenon this may be due in part to the high cost. However, since rare gases are radiation stable, they can be reused if additives from previous studies are removed.

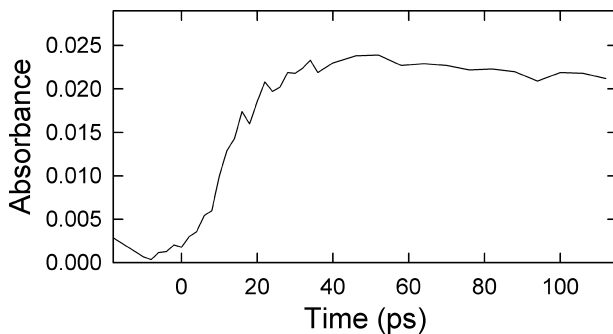
This chapter focuses on the properties and reactions of charged species, electrons and ions in supercritical rare gases, as studied by pulse radiolysis. Intermediates have been detected either by their optical absorption or by conductivity. The transparency of the rare gases throughout the IR, visible and UV parts of the spectrum facilitates optical detection of intermediates, and the dielectric properties also permit DC conductivity measurements. Studies have been done in both xenon and krypton with picosecond resolution, which elucidate the early processes involving electron-ion recombination and excimer formation. Electron properties such as mobility and conduction band energy are reviewed because of their significance in the understanding of electron reactions. Partial molar volumes have been determined from studies of electron attachment reactions as a function of pressure. The properties and reactions of ions are also discussed. Mobility measurements have shown that ions have lower mobility than would be expected, which is attributed to clustering around the ions due to electrostriction. The clustering is also shown to affect the rate of charge transfer reactions in supercritical rare gases.

2. Early Processes

Pulse-probe studies using the Laser Electron Accelerator Facility (LEAF)¹⁰ at Brookhaven National Laboratory have revealed changes in optical absorption occurring on the picosecond time scale in rare gas fluids. In xenon, excimers are formed which absorb in the visible and near infra-red as shown in Fig. 1a. The absorption grows in during the first 50 picoseconds [see Fig. 1(b)].¹¹ This growth is concomitant with ion recombination that leads first to excited atoms, reaction 1(a), which immediately form excimers, Xe_2^* , because of the high density of xenon.

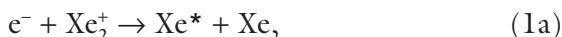


(a)



(b)

Fig. 1. (a) Spectra of excimers in xenon at 79 bar; (b) Growth of excimer spectra at 800 nm in xenon at 67 bar.



The observed fast formation of excimers in supercritical xenon, occurring in the first 50 ps, corresponds to a second order rate constant for reaction (1a) of $7.5 \times 10^{16} \text{ M}^{-1}\text{s}^{-1}$ at a pressure of 67 bar. The density in this case was 1.33 g/cc and the ion concentration $1.5 \mu\text{M}^{11}$; the pulse width was 7 ps.¹⁰ This measured rate can be compared to the theoretical rate for electron-ion recombination as given by the reduced Debye equation:

$$k_r = 4\pi e (\mu_+ + \mu_-)/\epsilon = 1.09 \times 10^{15} (\mu_+ + \mu_-)/\epsilon \text{ M}^{-1} \text{ s}^{-1}, \quad (2)$$

where μ_+ and μ_- are the mobilities of the positive ion and electron, respectively, in units of cm^2/Vs , and ϵ is the dielectric constant of the fluid. The mobility of the electron is many orders of magnitude larger than that of the ion, thus μ_+ can be ignored. The usual low-field mobility of the electron cannot be used in this case because the electrons are still “hot” at picosecond times. The mobility of electrons at high electric fields, where the electrons are also “hot”, is between 60 to 100 cm^2/Vs .¹² The use of these values in Eq. (2) leads to a range for k_r from 5.0 to $8.4 \times 10^{16} \text{ M}^{-1}\text{s}^{-1}$, consistent with the experimental value.

Two species of excimers are formed in xenon. One decays with a half-life of 5.4 ns, independent of pressure. This was identified as the singlet excimer. The other component is longer lived and the lifetime increases with decreasing pressure; this was identified as the triplet excimer.¹¹

In supercritical krypton the formation of excimers has also been time resolved but the results contrast with those for xenon.¹³ As in xenon, electron-ion recombination should occur rapidly. Again, electrons remain hot for many nanoseconds in krypton^{4,5,14} and the mobility of hot electrons is in the range of 150 to 400 cm^2/Vs . This leads to a theoretical range for k_r of 1.4 to $3.6 \times 10^{17} \text{ m}^{-1}\text{s}^{-1}$ at a density of 0.48 g/cm^3 . In pulse radiolysis studies using optical detection, the concentration of intermediates is around 0.5 to 1 μM , thus the first half-life for recombination of electrons with ions is less than 10 ps in krypton. What has been observed is that an excimer species (A), the

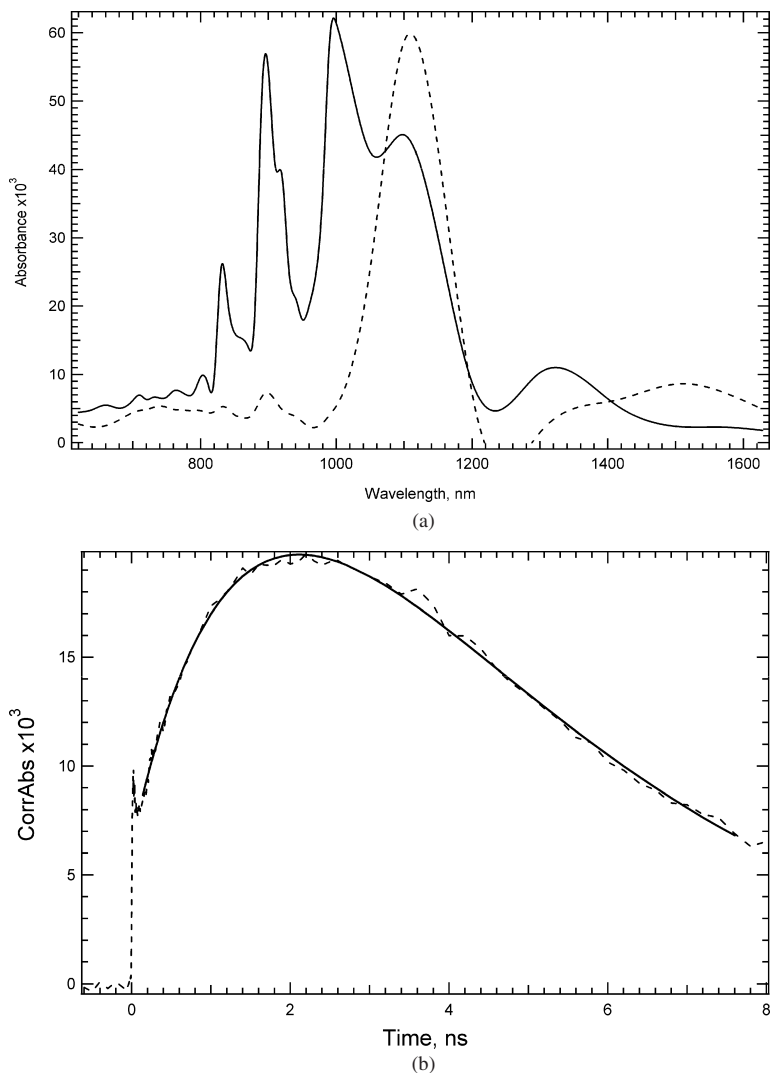


Fig. 2. (a) Spectra of excimers in krypton at 110 bar; — Spectra at 1 ns after pulse; --- spectra at 9 ns; (b) Growth and decay of an excimer species in krypton at 113 bar recorded at 920 nm. Solid line is fit.

spectrum of which is shown in Fig. 2(a) with peaks at 830, 890 and 990 nm, grows in over a period of a few nanoseconds [see Fig. 2(b)].

Thus some of the excimers are formed after a delay. Recombination leads to a precursor, which then relaxes to this excimer

species. At 113 bar the observed lifetime for relaxation is 1.9 ns. As is shown in Fig. 2(b), there is significant absorption present immediately following the pulse. This could be due to the precursor but may be due to excimers formed via the fast relaxation of vibrationally excited excimers. Further mechanistic details can be found elsewhere.^{13,15} At a pressure of 109 bar the excimer species (A) decays with a lifetime of 3.4 ns and a new excimer species (B) is formed which absorbs at 1100 nm [see Fig. 2(a)] with a lifetime of 9 ns. The lifetimes of both excimer species A and B increase as the pressure decreases.

2.1. *Excitation transfer*

The rare gas excimers readily transfer energy to various additives. Rates for transfer to nitrogen and hydrogen in krypton are known at 1 atm.¹⁶ Because excimer species have strong absorptions in the visible region, it is necessary to quench them when studying reactions of other intermediates by absorption spectroscopy. Ethane has been shown to be convenient for this purpose. The rate constant for excitation transfer from excimers to ethane in xenon was measured by the pulse-probe technique to be 3.4×10^{10} molal⁻¹s⁻¹ at pressures near 50 bar.¹¹ Thus, addition of a small concentration of ethane can be used to reduce the absorption due to excimers to a small level at nanosecond times.

3. Ionic Properties

3.1. *Theory of electrostriction*

It is important to be aware of clustering caused by electrostriction in order to understand reactions of ions in supercritical rare gases. If a classical continuum model is used to calculate clustering, the magnitude of the volume change due to electrostriction would be overestimated because such a model ignores the density build-up around the ion. Because of this density augmentation, the compressibility of the fluid near the ion is less and, since electrostriction is proportional to compressibility, the actual electrostriction will be less

than predicted by a continuum model. A compressible continuum model (CC) was developed that takes clustering around the ion into account.^{17,18} In this model the attraction between the ion and induced dipoles of solvent molecules is considered as a pressure. The local density is then calculated from the pressure at each point using an equation of state. The local dielectric constant is calculated from this density. This process is iterated until the results converge. The volume change due to electrostriction, V_{el} , is then obtained by integrating over all space in the presence and absence of the ion.

In a similar way the polarization energy, $P^-(CC)$, by the ions in a supercritical fluid can be calculated with this model taking into account the density dependence of the dielectric constant, which is enhanced as far out as 1 nm from the ion. Again integration over all space is involved and $P^-(CC)$ is obtained from the difference of the calculated energy of the ion in the supercritical fluid and the energy in vacuum. The magnitude of $P^-(CC)$ calculated this way is generally larger than if the polarization energy is calculated using the Born continuum model. The compressible continuum model is used for estimation of the energetics of electron reactions (see below).

3.2. *Experimental evidence of clustering*

Evidence that clustering of rare gas atoms occurs around ions comes from: (a) ion mobility measurements, and (b) volume changes occurring on electron attachment to solutes. The mobility of positive ions in xenon decreases with increasing pressure and at pressures near 100 bar is $1.3 \times 10^{-3} \text{ cm}^2/\text{Vs}$ [see Fig. 3(a)] near room temperature.¹² An estimate of the size of the cluster moving with the ion may be obtained from such data using the Stokes equation,

$$R_{ion} = e/6\pi\eta\mu, \quad (3)$$

where η is the bulk value of the viscosity. This equation indicated clusters of about 0.6 nm at high pressure and much larger clusters in regions of high compressibility [see Fig. 3(b)]. Equation (3) is only an approximation since the high viscosity near an ion should be

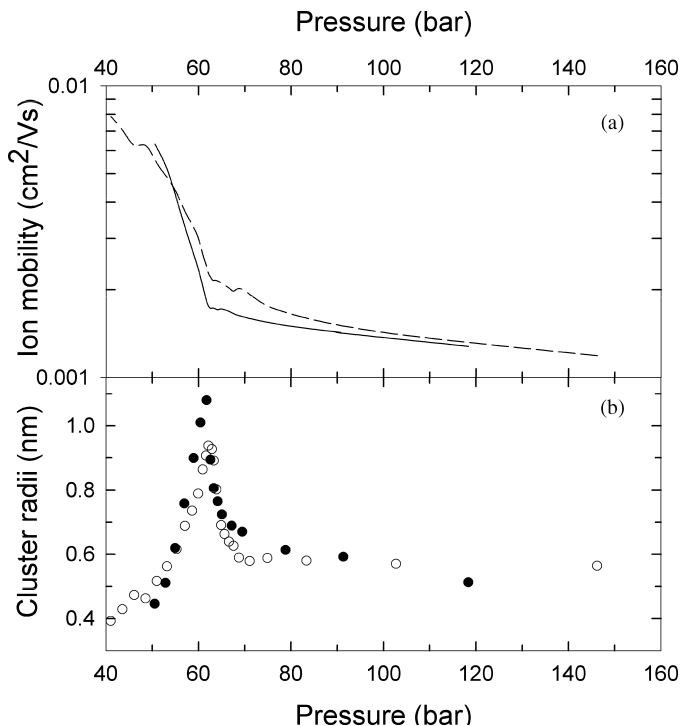


Fig. 3. (a) Mobility of ions in Xe versus pressure: — Xe₂⁺, --- C₆F₆⁻. (b) Radii of ions in Xe versus pressure calculated using the Stokes' Eq. (3): ● Xe₂⁺, ○ C₆F₆⁻.

considered. This effect was taken into account in the hydrodynamic compressible continuum model (HCC).¹² The HCC model also indicates the size of moving clusters to be 0.6 nm, or one complete solvation shell, in xenon at pressures above 75 bar, and nearer to 1 nm in regions of high compressibility.

Several studies have shown that clustering also occurs around negative ions in supercritical fluids. The mobility data for C₆F₆⁻ in xenon [see Fig. 3(a)] indicate that the clusters around C₆F₆⁻ are slightly smaller [see Fig. 3(b)] than those around the positive ion but the pressure dependence is similar.¹¹ Measurements of the mobility of O₂⁻ in argon at a temperature just above the critical temperature indicated the O₂⁻ ion also moves with a large solvation shell.¹⁹

Evidence of clustering is also obtained from studies of electron attachment reactions. These reactions occur in supercritical gases with large volume changes due to electrostriction around the negative ion formed. In supercritical ethane, it has been shown that the compressible continuum model accurately predicts volume changes for reactions of electrons with CO_2 ,¹⁸ pyrimidine²⁰ and pyrazine.²¹ In xenon volume changes are smaller because of the significant clustering that occurs around neutrals, as discussed in the electron attachment/detachment section below.

4. Electron Properties

4.1. Mobility

In order to understand the high rate of reaction of electrons in supercritical fluids, one needs to know the electron mobility and how it changes with pressure. The electron mobility provides information on the diffusion constant since $D_e = \mu_e k_B T / e$ and values of D_e are necessary to calculate the rate of electron-ion recombination (see Sec. 2) and other diffusion-controlled reactions (see Sec. 5). For supercritical xenon and krypton, the electron mobility in the pressure range of interest is shown in Fig. 4. The mobility is generally high, from which it can be concluded that electrons are in a quasi-free state; that is, there are no trapped states. However, in xenon the mobility at 20°C becomes unusually low near 60 bar as shown in Fig. 4. To explain this behavior of quasifree electrons, a modification of the Basak-Cohen model²² has been invoked.²³ In this model the scattering of the electron is the result of density fluctuations resulting in a deformation potential. This potential is a function of derivatives of V_0 , the conduction band energy, which is discussed in the next section. The model leads to Eq. (4) for the mobility:

$$\mu_e = \frac{2e\hbar^4 \sqrt{2\pi}}{3m^{*5/2} (k_B T)^{1/2} n^2 [V_0'^2 k_B T \chi + (\text{terms involving } V_0'', V_0''')]} \quad (4)$$

where m^* is the reduced mass of the electron and n is the density. The mobility also depends on the compressibility, χ . In the original

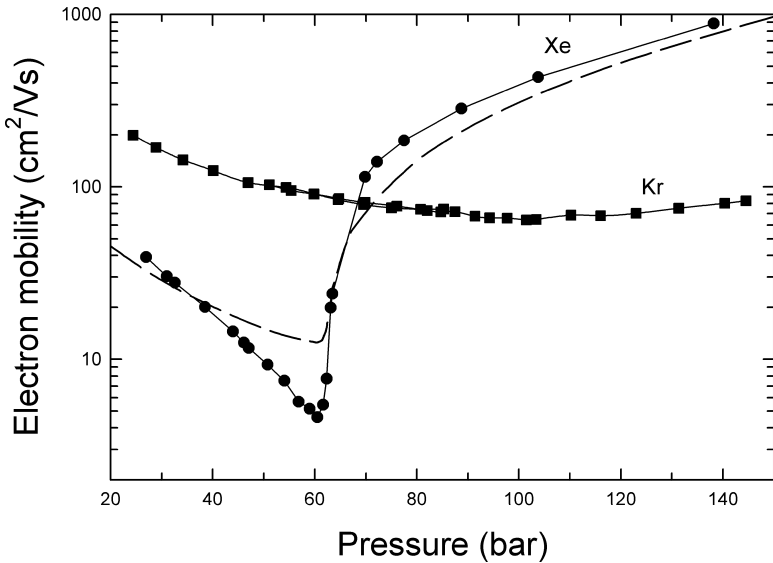


Fig. 4. Electron mobility in ● Xe and ■ Kr at 293 K versus pressure. Dashed line is theory for Xe, Eq. (4), using the adiabatic compressibility.

theory the isothermal compressibility was used, however it diverges near critical densities because density fluctuations become quite large. This results in a predicted near zero mobility in the vicinity of the critical density. It was suggested by many that electrons do not interact with large density fluctuations^{24,25} and it was more appropriate to use the adiabatic compressibility. When the adiabatic compressibility (which changes smoothly with density) is used, Eq. (4) accounts for the pressure dependence of the mobility in xenon remarkably well as shown by the dashed line in Fig. 4.

The mobility in krypton is quite high at all pressures and there is only a shallow minimum in this case. The data shown in Fig. 4 are for 20°C, which is well above the critical temperature. The minimum becomes lower at lower temperatures but not as low as in xenon. The electron mobility in krypton is also reasonably well represented by Eq. (4) when the adiabatic compressibility is used.¹⁴

4.2. Conduction band energy

The energy of the electron in the conduction band in these fluids, measured from the vacuum level, is designated V_0 . This energy term is important for several reasons. As shown in the previous section the electron mobility is a function of the derivatives of V_0 . To first order the electron mobility depends inversely on $(dV_0/dn)^2$. Thus where the slope of the V_0 curve is steep as for xenon around 62 bar (see Fig. 5) the mobility is quite low (see Fig. 4). For krypton the slope of the V_0 curve is not as steep, as shown in Fig. 5, and consequently the mobility is higher in this pressure region. Also V_0 is important because the energy change for electron attachment/detachment reactions is a function of V_0 (see next section). V_0 is negative at all pressures in both krypton and xenon because the interaction between electrons and atoms is positive. V_0 is quite low at higher pressures, which is consistent with the high values of the electron mobility observed. Generally trapping is unimportant for fluids with low V_0 .

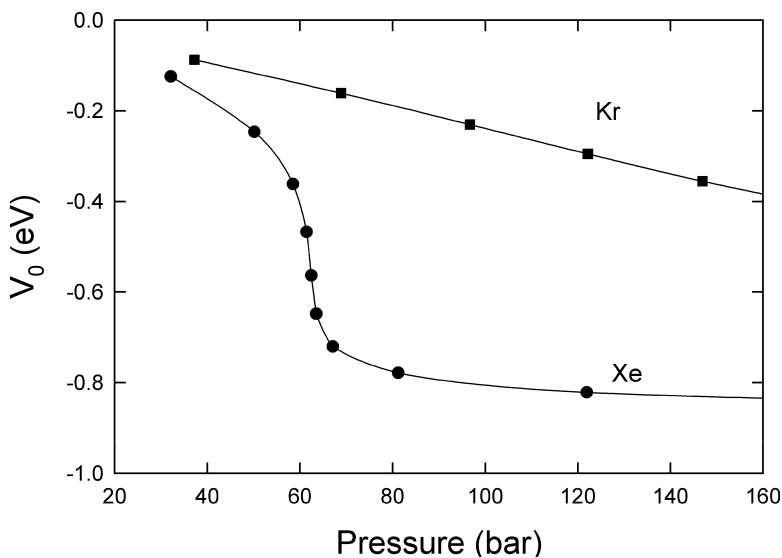


Fig. 5. Conduction band energy in ● Xe and ■ Kr versus pressure at 293 K (data from Refs. 28 and 29).

An early theoretical approach to calculate V_0 utilized the Wigner–Seitz model.²⁶ This model considered both the attractive polarization potential, including screening, and the repulsive kinetic energy of the impenetrable hard cores. There have been several modifications to the theory over the years using various techniques. A modification of the Wigner–Seitz model by Pleniewicz *et al.*²⁷ using an accurate pseudopotential gave reasonably good fits to experimental values of V_0 as a function of density. Recently Evans and Findley²⁸ reproduced their measurements of V_0 in krypton and argon to high precision using this model with an adjustable phase shift parameter.

The first measurements of V_0 in liquids utilized the change in work function of a metal when immersed in the liquid. Other techniques like photoionization have also been used. Recently a method utilizing the field ionization of a Rydberg state of an added solute has been applied to xenon and krypton.^{28,29} The results for krypton shown in Fig. 5 were obtained by this method. Synchrotron radiation is used in this technique to excite the solute in the presence of an electric field. Photocurrents are measured at both high and low electric field. The field ionization spectrum is obtained by subtracting the spectrum at low field from one at high field. Such spectra show a peak near threshold due to the high-lying states that ionize at the high voltage but not at the low. The position of these peaks, E_{th} , shifts as the density or pressure changes depending on the value of V_0 and the polarization energy, P^+ , of the positive ion of the solute according to:

$$E_{\text{th}} = \text{IP} + P^+ + V_0. \quad (5)$$

In this technique, determination of V_0 also requires calculation of the polarization energy of the positive core, P^+ . The data in Fig. 5 are best fits to the experimental results obtained in recent studies.

5. Electron Reactions

5.1. *Electron attachment*

The reaction of electrons with a few solutes has been studied in xenon



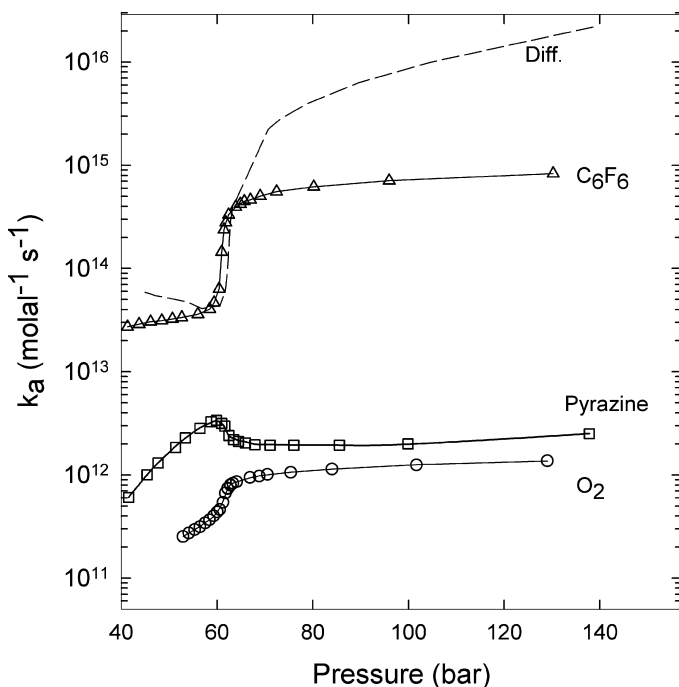


Fig. 6. Rate constants for electron attachment versus pressure. \circ O_2 ; \square pyrazine; \triangle C_6F_6 ; --- calculated rate of diffusion.

In the case of oxygen the rate of attachment, k_a , is 2×10^{11} molal $^{-1}$ s $^{-1}$ at low pressure (see Fig. 6) and increases with increasing pressure overall by a factor of five.³⁰ Most of the increase occurs in the region of high compressibility around 62 bar. Electron attachment to O_2 is a resonance process and the rate will depend on the energy level of the electron in the fluid, V_0 , and the polarization energy of the fluid by O_2^- . This reaction is quite exothermic; the free energy change is -1.8 eV at 100 bar in xenon [see Eq. (13)]. This mismatch in energy accounts for the slow rate.

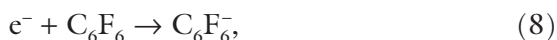
The activation volume, V_a^* , for electron attachment to O_2 is calculated using Eq. (7):

$$V_a^* = -RT \partial(\ln k_1) / \partial P. \quad (7)$$

Values of V_a^* are generally small except near 62 bar where V_a^* reaches a minimum value of -9 L/mol. This is approximately one-third of that expected theoretically for electrostriction by O_2^- . Clearly there is a volume decrease in the reaction but the lack of agreement with theory indicates either that the full volume change is not obtained until the reaction is complete, or that O_2 has a significant cluster around it; i.e. the partial molar volume of neutral O_2 in xenon is negative.

The results for electron attachment to pyrazine as shown in Fig. 6 are similar to those for O_2 at low and high pressures; that is, the rate increases at low pressure and is fairly constant at high pressure. However around 62 bar, where the O_2 rate is increasing, the rate of attachment to pyrazine actually decreases slightly. The values of V_a^* derived from the data are negative at low pressures and generally quite small, but in contrast to O_2 exhibit a maximum of 3 L/mol at intermediate pressures. The explanation for this behavior lies in the significant role of clustering around the neutral pyrazine as explained under the electron attachment/detachment section below.

The rate constant for electron attachment to C_6F_6 in xenon,



is much larger than that of the other two solutes as shown in Fig. 6. The rate increases monotonically with pressure and shows a sharp increase at 62 bar.¹¹ The change in rate with pressure was originally interpreted as an activation volume, calculated using Eq. (7). That analysis showed that V_a^* is small and negative except near 62 bar where a value of -28 L/mol was reported.¹¹ The value of -28 L/mol is coincidentally close to the value expected for electrostriction calculated by the compressible continuum model, which is discussed above. However, the change in rate with pressure should not have been attributed to a volume change because, as is shown in Fig. 6, the rate is clearly diffusion limited, at least at low and intermediate pressures. The diffusion rate is calculated from the mobility of the electron, μ_e , using:

$$k_D = 4\pi R\mu_e k_B T \rho N / e 1000 \text{ molal}^{-1} \text{ s}^{-1}. \quad (9)$$

The value of the radius, R , used is 1 nm, ρ is the density in g/cm^3 . The value of the rate constant at high pressure is below the theoretical diffusion rate, however it is actually at or above the maximum value expected for electron attachment rates. Warman predicted that electron attachment rate constants are not expected to exceed $3 \times 10^{14} \text{ M}^{-1} \text{ s}^{-1}$.³¹ That rate constant corresponds, in the units used in Fig. 6, to a value of $6 \times 10^{14} \text{ molal}^{-1} \text{ s}^{-1}$ at the highest pressure; the observed rate is actually above this. Therefore deriving activation volumes from the C_6F_6 rate data is questionable.

5.2. Electron attachment/detachment

The reaction of the electron with pyrazine is reversible and the rate of electron detachment, k_d , from the pyrazine anion has been measured in supercritical xenon³²



When the values of k_d are combined with values of k_a (see Fig. 6), the free energy of reaction is obtained from: $\Delta G_r = -RT \ln(k_a/k_d)$. The change in ΔG_r with pressure provides information on the volume change in the reaction, since $\Delta V_r = (\partial \Delta G_r / \partial P)_T$. In xenon the free energy of reaction changes slowly with pressure and the derived volume changes are small, less than a few liters per mole. This is in contrast to the results obtained for electron attachment to pyrazine and methylpyrazine in supercritical ethane where ΔG_r decreases rapidly over very narrow pressure ranges which leads to volume changes ranging from -1 to -45 L/mol , depending on pressure and temperature.²¹ Those volume changes were adequately accounted for by electrostriction of the ethane fluid around the pyrazine anion. Calculations of this effect using the compressible continuum model were in good agreement with the experimental values of ΔV_r . It was also concluded that in supercritical ethane the partial molar volumes of the neutral pyrazine and methylpyrazine are small in magnitude, at least in comparison to that of the ions.

To explain the small volume changes observed for electron attachment to pyrazine in supercritical xenon, it was proposed that clustering around the neutral pyrazine is comparable to that around the ion.³² The volume change in this reaction is given by:

$$\Delta V_r = \bar{V}(\text{Pyz}^-) - \bar{V}(\text{Pyz}), \quad (11)$$

where the partial molar volume of the electron is presumed small. The partial molar volume of the neutral, $\bar{V}(\text{Pyz})$, was calculated from experimental volume changes, ΔV_r , using this equation and $\bar{V}(\text{Pyz}^-)$, taken as the volume of electrostriction calculated by the compressible continuum model. At higher pressures $\bar{V}(\text{Pyz})$ and $\bar{V}(\text{Pyz}^-)$ were comparable. Values of $\bar{V}(\text{Pyz})$ thus obtained ranged from 0 to -9 L/mol and were proportional to the compressibility as expected according to Eq. (12), where the coefficient a is negative.

$$\bar{V}(\text{Pyz}) = a(T)\chi_T + b(T). \quad (12)$$

Thus in xenon reaction (10) should be considered as electron attachment to a pyrazine molecule that already has a cluster of xenon atoms around it.

5.3. Energetics

In liquids the free energy change in electron attachment reactions is given by^{33,34}:

$$\Delta G_r(\text{liq}) = \Delta G_r(\text{gas}) + P^- - \Delta G_s(e^-), \quad (13)$$

where the polarization energy P^- is often approximated by the Born equation. However, in supercritical fluids the Born equation does not work since it is a continuum model. In supercritical fluids there is considerable build-up of density around ions that affects this energy. The compressible continuum (CC) model works well and accounted for the free energy changes when reaction (10) was studied in supercritical ethane.²¹ The CC model was also used to calculate the polarization

energy for pyrazine ions in supercritical xenon. $\Delta G_s(e^-)$ is the free energy of solution of the electron and is approximated by V_0 , which changes considerably with pressure as is shown in Fig. 5. If $\Delta G_r(\text{gas})$ is approximated by $-E.A.$, where $E.A.$ is the electron affinity, Eq. (13) becomes:

$$\Delta G_r(\text{liq}) = -E.A. + P_{CC}^- - V_0. \quad (13a)$$

The electron affinity normally used is that of the molecule in the gas phase. But in this case the volume change information shows that the electron reacts with a clustered pyrazine molecule, PyzXe_m , and the electron affinity of the clustered species should be used. Since there was evidence that the electron affinity of the analogous species in argon, PyzAr_m , increased with m by a few tenths of an electron volt,³⁵ the measured values of $\Delta G_r(\text{liq})$ were used with Eq. (13a) along with calculated values of P_{CC}^- and V_0 to evaluate $E.A.$ The results showed that the electron affinity of PyzXe_m also increases by a few tenths of an electron volt as m increases.

6. Charge Transfer Reactions

Some electron transfer reactions have been studied in supercritical xenon. Two of them have been shown to be diffusion controlled and two are energy controlled. These reactions have been followed by changes in the optical absorption after the pulse. To carry out these studies requires that the rate of electron attachment to the solute be sufficiently fast to compete with ion recombination, which occurs on the picosecond time scale in pulse radiolysis. The solute hexafluorobenzene satisfies this criterion; the rate constant is sufficiently large (see Fig. 6) that millimolar concentrations will allow formation of anions. The rate constant for attachment to 4,4'-bipyridine (bipy) is also sufficiently large to satisfy this need.³⁰ Another requirement for making these studies is to quench the excimers whose optical absorptions are strong and can interfere with detection of ions. As mentioned under Sec. 2, a small concentration of ethane (0.4%) is sufficient for this purpose.

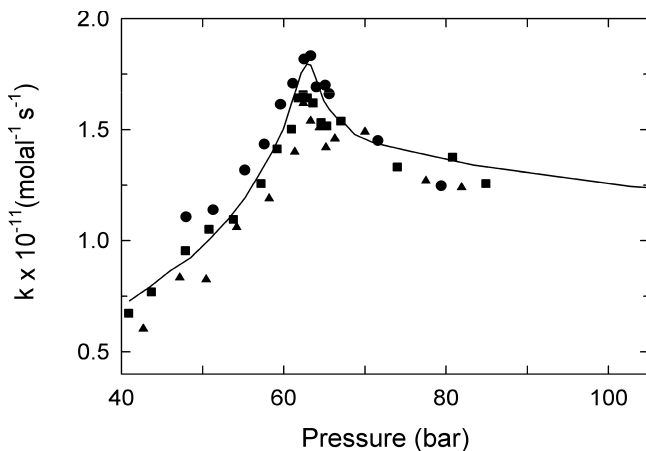


Fig. 7. Rate constant for electron transfer from $C_6F_6^-$ to benzoquinone versus pressure. Points are experimental; the solid line is from Eq. (15) using the cluster radii for $C_6F_6^-$ calculated with Stokes' Eq. (3).

The rate constant for electron transfer from $C_6F_6^-$ to benzoquinone (BQ),



shown by the points in Fig. 7, was determined by the rate of decay of the 550 nm absorption of the hexafluorobenzene anion in the presence of benzoquinone.¹¹ The diffusion rate, shown by the solid line, was calculated from:

$$k_D = 4\pi(R_{ion} + R_{BQ})(D_{ion} + D_{BQ})\rho N/1000 \text{ m}^{-1} \text{ s}^{-1}. \quad (15)$$

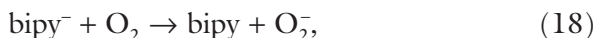
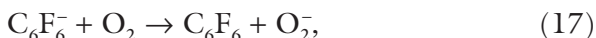
The values of R_{ion} and D_{ion} used in Eq. (15) were obtained from the mobility of the clustered anions. D_{ion} , calculated by the Einstein relation: $D_{ion} = \mu_{ion} k_B T/e$, follows the mobility of the ion, which is shown in Fig. 3(a). For R_{BQ} the radius derived from the molar volume was used. D_{BQ} was derived from the radius using the Stokes–Einstein relation: $D_{BQ} = k_B T/6\pi\eta R_{BQ}$. The good agreement of the calculated line

with the experimental results indicates the reaction is diffusion controlled. The peak in rate near 62 bar can be attributed to the peak in R_{ion} observed at this pressure, [see Fig. 3(b)] where the compressibility is a maximum. Very similar results were obtained for the reaction³⁰:



This rate also shows a maximum in the same pressure region and is also diffusion limited.

Two other electron transfer reactions have been studied in xenon:



The rate constants for these reactions vary little with pressure and are well below the calculated rate of diffusion. Both reactions are exothermic as can be demonstrated by taking the difference of the constituent half reactions. That is, for reaction (17) the free energy change is the difference between the free energy for attachment to O_2 , reaction (6) and that for attachment to C_6F_6 , reaction (8). Thus ΔG_r for reaction (17) should be given by:

$$\Delta G_r(17) = \text{E.A.}(\text{C}_6\text{F}_6) - \text{E.A.}(\text{O}_2) + P^-(\text{O}_2^-) - P^-(\text{C}_6\text{F}_6^-). \quad (19)$$

A similar equation applies to reaction (18). Estimated values of ΔG_r for these reactions are given in Table 1.

Table 1. Energies and rates of charge transfer.

Reaction	Pressure (bar)	ΔG_r (eV)	Rate constant (molal ⁻¹ s ⁻¹)
17	52	-0.68	1.0×10^{10}
17	75	-0.68	1.4×10^{10}
18	52	-0.86	1.6×10^{10}
18	75	-0.85	3.3×10^{10}

Both reactions are exothermic. Transfer from bipy^- to O_2 is more favorable than transfer from C_6F_6^- to O_2 and the rate is faster for the former reaction (18) which is in agreement with the energy gap law of electron transfer.³⁶ Also the free energy does not change with pressure for these two reactions, which implies that there are no overall volume changes in the reactions. This is as expected since clustering around the products should be very similar to that around the reactants.

7. Conclusion

Supercritical xenon and krypton are interesting solvents for the study of electron and ion reactions. The high free ion yields facilitate such studies. Clustering around ionic species must be recognized as it affects the mobility and diffusion of these species. The formation of excimers following ion-recombination has been elucidated by picosecond pulse-probe studies. The excimers readily transfer energy to added solutes like ethane. Electron attachment reactions can be fast because of the high mobility of electrons. Studies of the reversible electron attachment to pyrazine in xenon have shown that significant clustering occurs around neutral species. The electron mobility is shown to be a function of the derivatives of the conduction band energy. The conduction band energy also is important in understanding the energetics of electron reactions.

Acknowledgment

This research was carried out at Brookhaven National Laboratory under contract DE-AC02-98-CH10886 with U.S. Department of Energy and supported by its Division of Chemical Sciences, Biosciences and Geosciences, Office of Basic Energy Sciences. The author would like to thank Jack Preses for assistance in the preparation of this chapter.

References

1. Eckert CA, Knutson BL, Debenedetti PG. (1996) Supercritical fluids as solvents for chemical and materials processing. *Nature* **383**: 313–318.

2. Savage PE, Gopalan S, Mizan TI, Martino CJ, Brock EE. (1995) Reactions at supercritical conditions: Applications and fundamentals. *AIChE Journal* **41**: 1723–1778.
3. Kern W. (1993) *Handbook of Semiconductor Wafer Cleaning Technology*. William Andrew Publishing, NY.
4. Sowada U, Warman JM, de Hass MP. (1982) The density dependence of hot-electron thermalization in liquid argon, krypton and xenon. *Chem Phys Lett* **90**: 239.
5. Sowada U, Warman JM, de Haas MP. (1982) Hot-electron thermalization in solid and liquid argon, krypton and xenon. *Phys Rev B* **25**: 3434–3437.
6. Bolotnikov A, Ramsey B. (1997) The spectroscopic properties of high-pressure xenon. *NIM A* **396**: 360–370.
7. Srdoc D, Inokuti M, Krajcar-Bronic I. (1995) Yields of ionization and excitation in irradiated matter. In *Atomic and Molecular Data for Radiotherapy and Radiation Research*, pp. 547–633. IAEA, Vienna.
8. Aprile E, Bolotnikov A, Chen D, Mukherjee R. (1993) W value in liquid krypton. *Phys Rev A* **48**: 1313–1318.
9. Combecher D. (1980) Measurement of W values of low energy electrons in several gases. *Radiation Research* **84**: 189–218.
10. Wishart JF, Cook AR, Miller JR. (2004) The LEAF picosecond pulse radiolysis facility at Brookhaven National Laboratory. *Rev Sci Instr* **75**: 4359–4366.
11. Holroyd RA, Wishart JF, Nishikawa M, Itoh K. (2003) Reactions of charged species in supercritical xenon as studied by pulse radiolysis. *J Phys Chem B* **107**: 7281–7287.
12. Itoh K, Holroyd RA, Nishikawa M. (2001) Ion mobilities in supercritical ethane, xenon, and carbon dioxide. *J Phys Chem A* **105**: 703–709.
13. Holroyd RA, Preses JM. pulse radiolysis of krypton using picosecond electron pulses (to be submitted).
14. Nishikawa M, Holroyd RA. (2007) Mobility of electrons in supercritical Kr; role of density fluctuations. *J Chem Phys* **127**: 014504.
15. Janssens H, Vanmarcke M, Desoppere E, Lenaerts J, Boucique R, Wieme W. (1987) A general consistent model for formation and decay of rare gas excimers in the 10^{-2} – 10^{+5} mbar pressure range, with application to krypton. *J Chem Phys* **86**: 4925–4934.
16. Ito Y, Arai S. (1984) Kinetic study of excited diatomic molecules of krypton and xenon. *Bull Chem Soc Jpn* **57**: 3062–3065.
17. Nishikawa M, Holroyd R, Itoh K. (1998) Electron attachment to NO in supercritical ethane. *J Phys Chem B* **102**: 4189–4192.
18. Nishikawa M, Itoh K, Holroyd RA. (1999) Electron attachment to CO₂ in supercritical ethane. *J Phys Chem A* **103**: 550–556.
19. Borghesani AF, Neri D, Barbarotto A. (1997) Mobility of O₂⁻ ions in near critical Ar gas. *Chem Phys Lett* **267**: 116–122.

20. Holroyd RA, Nishikawa M, Itoh K. (1999) Thermodynamics of electron attachment to pyrimidine and styrene in supercritical ethane. *J Phys Chem B* **103**: 9205–9210.
21. Holroyd RA, Nishikawa M, Itoh K. (2000) Solvent clustering around pyrazine ions in the high-compressibility region of supercritical ethane. *J Phys Chem B* **104**: 11585–11590.
22. Basak S, Cohen MH. (1979) Deformation-potential theory for the mobility of excess electrons in liquid argon. *Phys Rev B* **20**: 3404–3414.
23. Holroyd RA, Itoh K, Nishikawa M. (2003) Density inhomogeneities and electron mobility in supercritical xenon. *J Chem Phys* **118**: 706–710.
24. Steinberger IT, Zeitak R. (1986) Estimation of electron mobilities near the critical point in simple nonpolar fluids. *Phys Rev B* **34**: 3471–3474.
25. Nishikawa M. (1985) Electron mobility in fluid argon: Application of a deformation potential theory. *Chem Phys Lett* **114**: 271–273.
26. Springett BE, Jortner J, Cohen MH. (1968) Stability criterion for the localization of an excess electron in a nonpolar fluid. *J Chem Phys* **48**: 2720–2731.
27. Plenkiewicz B, Frongillo Y, Lopez-Castillo J-M, Jay-Gerin J-P. (1996) A simple but accurate “core-tail” pseudopotential approach to the calculation of the conduction-band energy V_0 of quasifree excess electrons and positrons in nonpolar fluids. *J Chem Phys* **104**: 9053–9057.
28. Evans CM, Findley GL. (2005) Energy of the quasifree electron in argon and krypton. *Phys Rev A* **72**: 022717.
29. Altmann KN, Reininger R. (1997) Density dependence of the conduction-band minimum in fluid krypton and xenon from field ionization of $(\text{CH}_3)_2\text{S}$. *J Chem Phys* **107**: 1759–1764.
30. Holroyd RA, Nishikawa M, Itoh K. (2005) Rates and energy of reactions of charged species in supercritical xenon. *Radiat Phys Chem* **74**: 146–151.
31. Warman JM. (1982) The dynamics of electrons and ions in nonpolar liquids. In: Baxendale JH, Busi F. (eds.), *The Study of Fast Processes and Transient Species by Electron Pulse Radiolysis*, 433ff. Reidel, Dordrecht, Holland.
32. Holroyd RA, Preses JM, Nishikawa M, Itoh K. (2007) Energetics and volume changes in electron attachment to pyrazine in supercritical xenon. *J Phys Chem*.
33. Holroyd RA, Nishikawa M. (2002) Pressure effects on electron reactions and mobility in nonpolar liquids. *Radiat Phys Chem* **64**: 19–28.
34. Holroyd R, Itoh K, Nishikawa M. (1997) Studies of $e^- + \text{CO}_2 = \text{CO}_2^-$ equilibria in hexamethyldisiloxane and bis(trimethylsilyl)methane. *Chem Phys Lett* **266**: 227–232.
35. Song JK, Lee NK, Kim SK. (2002) Photoelectron spectroscopy of pyrazine anion clusters. *J Chem Phys* **117**: 1589–1594.
36. Tachiya, M. (1993) Generalization of the Marcus equation for the electron-transfer rate. *J Phys Chem* **97**: 5911–5916.

Chapter 11

Radiation-Induced Processes at Solid–Liquid Interfaces

*Mats Jonsson**

1. Introduction

Radiation-induced processes at solid–liquid interfaces are of significant importance in many applications of nuclear technology. In water-cooled nuclear reactors, ionizing radiation induces reactions in the water as well as in the interface between the coolant and various system surfaces such as the reactor vessel and the fuel cladding. These processes will directly or indirectly influence the performance as well as the safety of the reactor. In nuclear fuel reprocessing, the significance of radiation-induced interfacial processes is even more obvious. Many countries plan to store spent nuclear fuel in deep geological repositories.

The political decision to build and take into use a deep geological repository for long term storage of spent nuclear fuel will largely depend on the outcome of thorough scientifically-based safety assessments. Given the very long operational time span for the repository, the

* Nuclear Chemistry, Department of Chemistry, Royal Institute of Technology, SE 10044 Stockholm, Sweden. E-mail: matsj@kth.se

safety assessments must be performed on the basis of extreme extrapolation of a number of fairly complicated processes. Consequently, the quality demands on the experimental results as well as the models underlying these extrapolations must be very high.

One of the key processes here is the dissolution of the spent nuclear fuel matrix in groundwater liberating radioactive fission products and actinides. Without this process no radioactivity will be released to the biosphere.

Despite their importance, the interfacial processes are often poorly understood both qualitatively and quantitatively.

The chemistry of heterogeneous systems is far from restricted to nuclear technological applications. In heterogeneous catalysis, corrosion science, surface polymerization, biochemistry and many industrial applications such as liquid–liquid extraction, interfacial processes are of vital importance. In nuclear technological applications, the presence of ionizing radiation increases the complexity further.

To fully understand radiation-induced processes at solid–liquid interfaces, a number of different parameters and processes must be known:

- Geometrical dose distribution.
- Mechanism and kinetics of reactions between radiolysis products in solution and the solid surface.
- Sorption and dissolution reactions.
- Effects of energy deposition in the solid phase.

One of the most extensively studied systems, due to its high importance, is dissolution of spent nuclear fuel in aqueous solution. For this reason, many of the examples used in this chapter originate from this field of studies.

2. Geometrical Dose Distribution

Roughly, two relevant types of systems can be identified: (1) Systems irradiated by an external source and (2) Systems where the solid material

contains radionuclides and acts as an internal source. Nuclear reactors mainly belong to the first category while dissolution of spent nuclear fuel during reprocessing or in a deep geological repository belongs to the second category. In general, the type of radiation of relevance in systems irradiated by an external source is mainly γ while all types of radiation could be of relevance in systems where the solid phase contains radionuclides. For systems irradiated by an external γ -source the dose can often be assumed to be more or less homogeneously distributed in the system. However, for systems belonging to the second category, the dose is far from uniformly distributed. The dose in the liquid phase will be highest in close proximity to the surface and decrease, depending on geometry, energy and type of radiation, with increasing distance from the surface. This is particularly emphasized in systems containing α -emitting solids, e.g. spent nuclear fuel.

A prerequisite for quantitative description of the interfacial chemistry is quantitative knowledge about the concentrations of radiolysis products. For systems where the dose is homogeneously distributed, the radiolytical production rate can be easily calculated from the dose rate, but for systems where the dose is not homogeneously distributed, we have to determine the geometrical dose distribution, i.e. the dose rate as a function of distance from the solid surface. Using radionuclide inventory data (specific activity and decay energy for each radionuclide present), taking self shielding in the solid and absorption in the surrounding liquid phase into account, the geometrical dose distribution has been calculated in a fairly simple manner.¹ The geometrical α - and β -dose distribution for spent nuclear fuel (100 years after discharge) is illustrated in Fig. 1.

As can be seen, the dose rate decreases significantly with distance from the surface within the maximum range for α -radiation. It is also obvious that, in this particular case, the contribution from β -radiation within the α -volume is insignificant. As can be seen, radiolysis due to radiation from the spent nuclear fuel inherently introduces a concentration gradient in the surrounding aqueous phase. Hence, diffusion of radiolysis products will also be of significant importance.

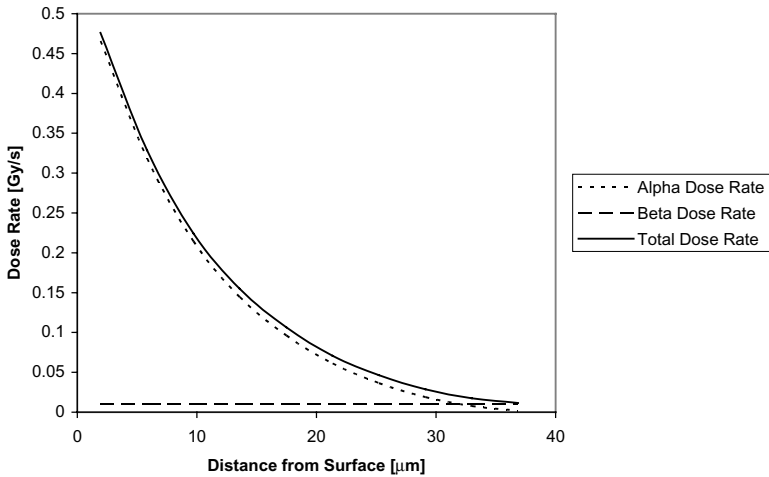


Fig. 1. Geometrical α - and β -dose rate distribution for spent nuclear fuel 100 years after discharge.

This will be discussed further in the section on the steady-state approach.

3. Effects of Solid–Liquid Interfaces on the Radiation Chemical Yield

One of the most important questions when studying radiation chemistry in heterogeneous systems is whether the radiation chemical yield is influenced by the presence of solid–liquid interfaces. In a series of papers, LaVerne and co-workers have studied the influence of oxide surfaces on the radiation chemical yield of hydrogen.^{2–5} Some of these studies were performed on thin films of water while others were performed on suspensions and slurries. In general, the G-value for H_2 increases with decreasing number of water layers on the oxide surface. The maximum increase in the G-value for H_2 is in the order of a factor of 10. It is also clear that the effect depends on the type of oxide and on the surface morphology. ZrO_2 gives a significantly higher G-value than CeO_2 and UO_2 in γ -irradiated systems.² In He-ion irradiated systems ZrO_2

gives the same G-value as the other oxides and the general trend is the same as for γ -radiolysis.²

The origin of the surface-enhanced G-value for H_2 is probably that radiation energy originally deposited in the solid phase is transferred to the liquid phase. Several mechanisms for this process have been proposed. The radiation chemical yield of H_2O_2 does not appear to be affected by the presence of oxide surfaces to the same extent.² Experiments performed on slurries and suspensions show that very high solid surface area to solution volume ratios are required to significantly increase the G-value for H_2 above that for water.³ For SiO_2 in water a surface area to solution volume ratio of 1.6×10^7 is required to observe an effect on the G-value.³ This corresponds to a water layer with a thickness of ca 60 nm. For a solid material containing an α -emitting radionuclide, the irradiated water layer (i.e. the maximum range of the α -particles) has a thickness of 30–40 μm . Consequently, the oxide surface-enhanced production of H_2 can be of significance for dry storage of spent nuclear fuel and other radioactive materials but not for dissolution of spent nuclear fuel in aqueous solution, where the solid surface area to solution volume ratio is considerably lower than 1.6×10^7 .

4. Kinetics of Interfacial Reactions

As for bimolecular reactions, collision theory can also be used to describe the kinetics of interfacial reactions between a solid surface and solutes in the liquid phase. Astumian and Schelly have described the theory for the kinetics of interfacial reactions in detail.⁶ The complete rate expression, derived by Astumian and Schelly, for solutes reacting with suspended solid spherical particles is given by Eq. (1)

$$\frac{d[\text{Solute}]}{dt} = -\frac{2k_B T}{3\pi\eta} \frac{R_{\text{SolidMol}}^2}{R_{\text{Solute}} R_P} \left(e^{-\frac{E_a}{RT}} \right) [\text{Solute}] \frac{N_{\text{SolidMol}}}{V}, \quad (1)$$

where k_B denotes the Boltzmann constant, η is the viscosity of the solvent, R_{SolidMol} is the molecular radius of the solid material, R_{Solute} is

the molecular radius of the reacting solute, R_p is the radius of the solid particle, N_{SolidMol} is the amount of solid molecules on the surface being exposed to the solution of volume V . From this expression it can clearly be seen that with increasing particle size, the diffusion-controlled rate constant (collision frequency) decreases. As a consequence, the maximum rate constant decreases with increasing size of the solid particle.

In practice, the amount of solid molecules on the surface being exposed to the solution is difficult or even impossible to quantify. Instead, the solid surface area to solution volume ratio is often used to quantify the amount of solid reactant. Therefore, experimentally determined second-order rate constants for interfacial reactions have the unit m s^{-1} . As the true surface area of the solid is very difficult to determine, the BET (Brunauer–Emmett–Teller) surface area is frequently used. The maximum diffusion-controlled rate constant for a particle suspension containing μm -sized particles is ca 10^{-3} m s^{-1} and for mm-sized particle suspensions the corresponding value is 10^{-6} m s^{-1} . Unfortunately, the discrepancy between the true surface area and the BET surface area and the non-spherical geometry of the solid particles makes it impossible to exactly determine the theoretical diffusion-controlled rate constant.

Rate constants for interfacial reactions have mainly been determined from experiments using particle suspensions where the concentration of reactive solute is monitored as a function of time.⁷ In these experiments, the solid surface is in large excess and the consumption of reactive solute follows first order kinetics. By plotting the pseudo-first-order rate constant against the solid surface area to solution volume ratio, the second-order rate constant can be obtained (from the slope). The main limitation here is that only relatively stable solutes can be studied experimentally. It is not possible to study the reactivity of short-lived species such as radicals using this approach.

The rate of reactive solute consumption is given by Eq. (2) while the rate of surface reaction is given by Eq. (3).

$$-\frac{d[\text{Solute}]}{dt} = k_1 \left(\frac{SA}{V} \right) [\text{Solute}], \quad (2)$$

$$-\frac{dn_{\text{surface}}}{dt} = k_1(SA)[\text{Solute}]. \quad (3)$$

SA denotes the solid surface area and V is the solution volume.

Experimentally determined rate constants can only be converted to other geometries if the activation energy is independent of the particle size. For nanosized materials it is well known that the activation energy will depend on the particle radius.⁸ This is not obvious for larger particles. In a recent work, the activation energy of the reaction between MnO_4^- and $\text{UO}_2(\text{s})$ as a function of particle size (7–40 μm) was studied.⁹ The results are shown in Fig. 2.

As can be seen, the activation energy decreases with increasing size also in this size range. The change in activation energy can be described by Eq. (4)

$$-\Delta E_a = k_B T \ln \frac{n_s}{n_b}, \quad (4)$$

where n_s and n_b denote the number of molecules on the surface and the total molecule content of the particle, respectively. The origin of this equation is discussed in Refs. 9 and 10. Interestingly, the size

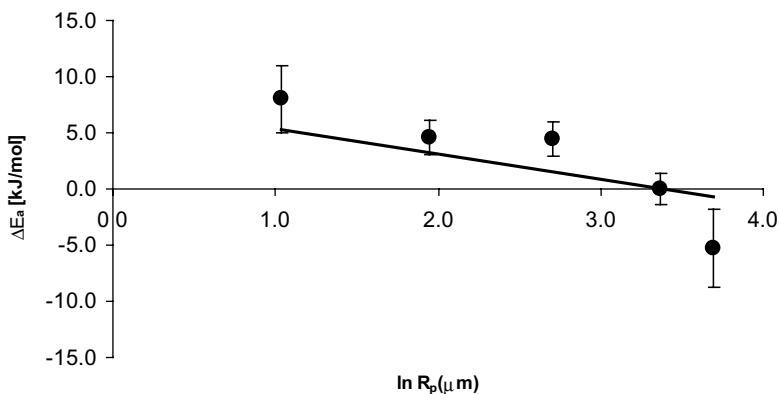


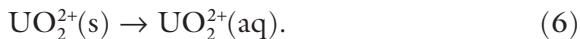
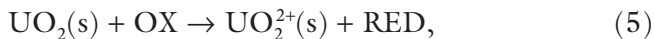
Fig. 2. Relative activation energy for the reaction between MnO_4^- and UO_2 as function of the UO_2 particle size. The trendline was calculated using Eq. (4).

effect on the activation energy counteracts the size effect on the collision frequency.

By combining Eqs. (1) and (4) it can be concluded that the rate constant for activation-controlled reactions between solutes and solid particles is completely independent of particle size, i.e. the increase in collision frequency for decreasing particle size is completely compensated by the increase in activation energy. A prerequisite for this is however that the particles are perfectly spherical, which is rarely the case. Experimental studies show that the rate constant is in fact depending on the particle size.⁹ However, the effect is smaller than would be expected from the size effect on the collision frequency. Given the effect of particle size on the diffusion-controlled rate constant as well as on the activation energy, it can be noted that the difference between diffusion-controlled rate constants and activation-controlled rate constants will decrease with increasing particle size (i.e. the activation-controlled rate constant will remain constant while the diffusion-controlled rate constant will decrease with increasing particle size). Hence, the relative reactivity of solutes will depend on the geometry of the system. This is often not accounted for which results in an overestimation of the relative reactivity of the most reactive species, i.e. the radicals.

5. Kinetics and Mechanism of $\text{UO}_2(\text{s})$ Oxidation

As mentioned in the introduction, dissolution of spent nuclear fuel in aqueous solution is one of the most extensively studied systems in this category.¹¹ Most fuels used in commercial reactors are based on UO_2 and, for this reason, the spent fuel contains >95% UO_2 . Consequently, the stability of UO_2 determines the stability of the spent nuclear fuel. The mechanism for oxidative dissolution of $\text{UO}_2(\text{s})$ is given by reaction (5) and (6)



Numerous studies on the dynamics of oxidative dissolution of UO_2 have been carried out. In most cases the rates of dissolution have been the

primary data obtained and rate constants for the reactions involved have not been presented. For this reason, it has been difficult to quantitatively compare data from different studies. A large number of electrochemical studies on UO_2 corrosion have also been performed.¹¹

In a series of experiments the kinetics of $\text{UO}_2(\text{s})$ oxidation by different oxidants was studied.⁷ The results clearly showed that the logarithm of the rate constant for oxidation of $\text{UO}_2(\text{s})$ is linearly dependent on the one-electron reduction potential of the oxidant.⁷ The correlation was also in excellent agreement with previous kinetic studies on different radiolytic oxidants.¹¹ On the basis of the correlation it was possible to estimate the rate constants for the more reactive (less stable) radiolytical oxidants of relevance (i.e. OH^\bullet and $\text{CO}_3^{\bullet-}$). The rate constants for these species were estimated to be limited by diffusion in particle suspensions of μm -sized particles.

Studies on reactions between different oxidants and Fe_3O_4 , Fe_2CoO_4 and Fe_2NiO_4 reveal similar trends in reactivity for the oxidants. An important exception is observed for H_2O_2 where the reactivity is markedly lower than expected from the trend for the other oxidants.¹² The rationale for this is probably that H_2O_2 is consumed by catalytic decomposition (as will be discussed below) on the surface while the other (stronger) oxidants are capable of oxidizing the metal oxides used in this study.

It should be noted that it is only possible to correctly determine the rate constant for oxidation if the reaction is not affected by the kinetics of dissolution of the oxidized product.¹³ If the oxidized product on the solid surface is not rapidly dissolved, the surface accessible to the solute oxidants will decrease with time. This will slow down the surface reaction. For the UO_2 -system, HCO_3^- and other potential ligands enhance the dissolution due to the formation of strong water soluble complexes with UO_2^{2+} . The effect of HCO_3^- on the kinetics of UO_2 oxidation has also been studied quantitatively enabling a more correct determination of the rate constant for UO_2 oxidation.¹³

6. Relative Impact of Radiolysis Products

Given the complexity of heterogeneous systems, it is necessary to elucidate the relative importance of the different radiolysis products.

The impact of an oxidant in the process of oxidative dissolution depends on the rate constant for the surface reaction as well as the oxidant concentration (at the surface). In some previous studies the impact of radical species has been argued to be high.¹⁴ These studies were however not based on kinetics. The total rate of oxidation is given by Eq. (7)

$$\text{rate} = \frac{dn_{\text{U(VI)}}}{dt} = A_{\text{UO}_2} \sum_{\text{ox}=1}^n k_{\text{ox}} [\text{Ox}] \frac{n_e^-}{2}, \quad (7)$$

where A_{UO_2} is the surface area of the solid (UO_2 in this particular case) and n_e^- is the number of electrons involved in the redox process (two for H_2O_2 and O_2 and one for the radicals).

Experimental studies of γ -irradiated aqueous solutions containing UO_2 pellets and powder combined with numerical simulations of homogeneous radiolysis of the aqueous solution revealed that the molecular oxidants have the largest impact on the oxidative dissolution even in γ -irradiated systems (where production of radicals is favoured).¹⁵ Under anoxic conditions, H_2O_2 is the most important oxidant. For shorter irradiation times (seconds to minutes) the radicals do have a significant impact. In Fig. 3, the amounts of dissolved U(VI) at different irradiation times determined from experiments (where aqueous UO_2 powder suspensions were exposed to γ -irradiation) and calculated using Eq. (7) on the basis of numerically simulated concentrations of the oxidants are plotted against each other.

As can be seen, the agreement between the experiments and the calculations is excellent. It is also interesting to note that the surface reactions at the solid surface area to solution volume ratios used here do not influence the bulk concentrations of aqueous radiolysis products significantly. However, this is only valid when the dose is uniformly distributed in the whole volume. Under deep repository conditions, i.e. in systems dominated by α -radiolysis, the relative impact of H_2O_2 has been shown to be >99.9%.¹⁵ Consequently, H_2O_2 is the only radiolytical oxidant needed to be accounted for when

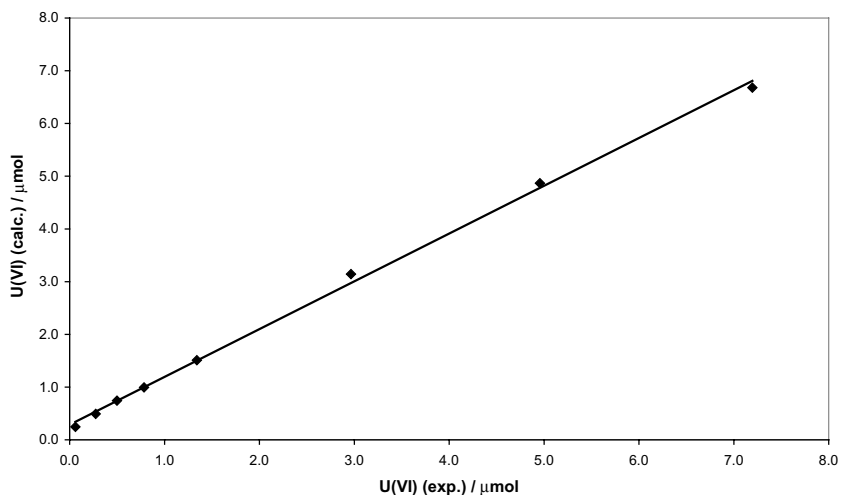


Fig. 3. Calculated amount of dissolved U(VI) plotted against experimentally determined amount of dissolved U(VI) for γ -irradiated suspensions of UO_2 .

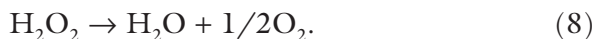
exploring the rate of spent nuclear fuel dissolution. These findings simplify the analysis of radiation-induced processes at solid-liquid interfaces considerably.

Indeed, radiolytically produced reductants should also be accounted for in some cases. In the system described above the UO_2 surface is kept free from oxidized UO_2 and the fraction of the surface area available for reductants is very small. On the other hand, in systems not containing HCO_3^- or any other species capable of facilitating removal of the oxidized UO_2 , the impact of radiolytical reductants could become significant. The solvated electron and the hydrogen atom are expected to react with the oxidized surface. The rate constants for these reactions are probably diffusion limited. However, the steady-state concentrations of these species will be very low. The concentration of H_2 will be many orders of magnitude higher but the reactivity is low and the reduction by H_2 often requires a catalyst. Previous studies of the uncatalyzed reduction of UO_2^{2+} by H_2 in aqueous solution reveal that the activation energy for this reaction is 130 kJ mol^{-1} .¹⁶

7. Reactions Between H_2O_2 and Metal Oxides

As shown above, the most important radiolytical oxidant in view of interfacial reactions in aqueous systems is H_2O_2 . For this reason, rate constants for reactions between H_2O_2 and solid surfaces are of crucial importance. The reactivity of H_2O_2 towards a number of different solid oxide materials has been studied.^{7,10,13,17} All these studies were performed using particle suspensions. In Table 1, activation energies for some of these solid materials are presented.

Interestingly, the activation energy does not vary much between most of the oxide materials presented in the table. The only exception is UO_2 for which the activation energy is somewhat lower. UO_2 is also the only oxide capable of reducing H_2O_2 . The main reaction responsible for the decomposition of H_2O_2 in the other systems is most probably a general surface-catalyzed decomposition of H_2O_2 producing O_2 .



Hence, this process does not change the surface. For UO_2 , about 80% of the H_2O_2 consumption leads to surface oxidation.¹⁸ The remaining 20% is catalytically decomposed by the UO_2 surface. This indicates

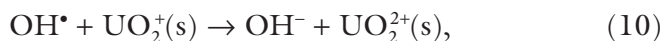
Table 1. Activation energies for reactions between H_2O_2 and metal oxides.

Metal oxide	E_a (kJ mol ⁻¹)
UO_2	24.5 [Ref. 9]
Fe_3O_4	52 ± 4 [Ref. 10]
Fe_2CoO_4	44 ± 5 [Ref. 10]
Fe_2NiO_4	57 ± 7 [Ref. 10]
SiO_2	48 [Ref. 17]
Al_2O_3	38 [Ref. 17]
TiO_2	36 [Ref. 17]
CeO_2	40 [Ref. 17]
ZrO_2	42 [Ref. 17]
Pyrex	41 [Ref. 17]

that, provided the same surface sites are involved in both reactions, the activation energy for surface-catalyzed decomposition of H_2O_2 on UO_2 is about 3–4 kJ mol^{-1} higher than the activation energy for reduction of H_2O_2 . This would correspond to an activation energy close to 30 kJ mol^{-1} which is somewhat lower than for the other oxides in Table 1.

It is also evident that the collision frequency (or pre-exponential factor) differs between different metal oxides for comparable surface areas. Hence, the active site density depends on the type of metal oxide and most likely also on pre-treatment and manufacturing of the oxide particles. In practice, determining the active site density is very difficult or even impossible since it is based on BET measurements of the specific surface area. The BET surface area can give a measure of the sorption site density which deviates significantly from the actual specific surface area.¹⁹ Again, this demonstrates the difficulties encountered when trying to compare the reactivity of different solid materials at a given temperature on the basis of the specific surface area.

The mechanism for UO_2 oxidation by H_2O_2 is given by reaction (9) and (10):



where the first reaction is rate limiting. It has sometimes been argued that the hydroxyl radical produced in reaction (9) would escape the surface.²⁰ However, considering the high reactivity of the hydroxyl radical, this is very unlikely to occur since the radical is produced at the readily oxidized surface. It has also been argued that, in aqueous solutions containing HCO_3^- , the oxidant responsible for oxidizing UO_2 is HCO_4^- rather than H_2O_2 .⁷ Both oxidants have similar redox properties. Recent studies on the ionic strength effect on UO_2 oxidation by H_2O_2 in HCO_3^- -containing solutions clearly show that the active oxidant is not charged.²¹ Hence, the active oxidant must be H_2O_2 , also in systems containing significant amounts of HCO_3^- .

8. Radiation-Enhanced Reactivity of the Solid Interface

It has been shown that irradiation of metal-oxide-semiconductor structures can alter the semi-conducting properties of the material.²² In stoichiometrically pure UO_2 electric conductivity would require promotion of electrons from the U 5f level to the conduction band. The energy gap is ~ 1.1 eV and at room temperature the probability for electrons to be transferred to the conduction band is extremely low.²³ Furthermore, it is reasonable to believe that the energy deposition in the material due to irradiation could induce such a transfer. Increased electrical conductivity is also gained by hyperstoichiometry as well as by impurities, which can give the material p-type semiconducting properties.²⁴ Upon irradiation it is also likely that the energy deposit in the material gives rise to structural changes (i.e. effects on grain size, etc.) which might affect the reactivity.

In earlier studies, e.g. by Gromov²⁵ and Matzke,²⁶ it has been observed that the dissolution rate of UO_2 increases as a result of irradiation (or simulated radiation damage). From these observations it is however difficult to draw any conclusions regarding the cause for the increased solubility.

In a series of experiments, the influence of γ and electron irradiation on the reactivity of UO_2 towards MnO_4^- during and after irradiation was studied.²⁷ γ -irradiated UO_2 did not display any difference in reactivity. However, electron irradiation of UO_2 at doses >40 kGy increases the reactivity of the material. The effect seems to be limited to ~ 1.3 times the reactivity of unirradiated UO_2 and appears to be due to permanent changes in the material. It should be pointed out that the doses used γ -irradiating UO_2 were much lower than 40 kGy. Indeed, further studies are required in order to understand this effect.

9. The Steady-State Approach

As shown above, consumption of radiolysis products through surface reactions will not influence the bulk concentrations significantly

in γ -irradiated systems or in any other homogeneously irradiated system for that matter. As previously stated, for systems where the source of radiation is the solid material itself and where α and β are the dominating types of radiation the dose will not be uniformly distributed in the whole volume. For such systems it is not straightforward to calculate the surface concentrations of radiolysis products.

Since H_2O_2 has been shown to be by far the most important oxidant, we focus our attention on this species.

On the basis of the geometrical dose distribution for spent nuclear fuel described above, a function describing the rate of H_2O_2 production as a function of distance can be derived. In order to simulate the evolution of the H_2O_2 concentration profile, a simple model where the total volume is divided into incremental volume elements has been developed.²⁸ The model takes into account the distance-dependent H_2O_2 production rate, consumption of H_2O_2 via a surface reaction as well as diffusion of H_2O_2 under the assumption that reaction products are not accumulated on the surface (i.e. the surface area accessible to H_2O_2 is constant throughout the simulation). The surface reaction is accounted for in the first volume element using the rate expression previously derived [Eq. (11)].

$$r = k_{\text{H}_2\text{O}_2} [\text{H}_2\text{O}_2], \quad (11)$$

where $k_{\text{H}_2\text{O}_2}$ is the rate constant for the surface reaction consuming H_2O_2 and r is the reaction rate in $\text{mol m}^{-2} \text{s}^{-1}$. Diffusion between the volume elements is determined by the concentration gradient between two adjacent elements using Fick's first law [Eq. (12)]

$$J = -D \frac{\partial C}{\partial x}. \quad (12)$$

The diffusion coefficient used for H_2O_2 was $10^{-9} \text{ m}^2 \text{ s}^{-1}$. The contributions from the above processes are added together and applied to the concentration vector to determine a new concentration vector for each time-step in an iterative process. In Fig. 4 the evolution of the H_2O_2 concentration profile is illustrated.²⁹

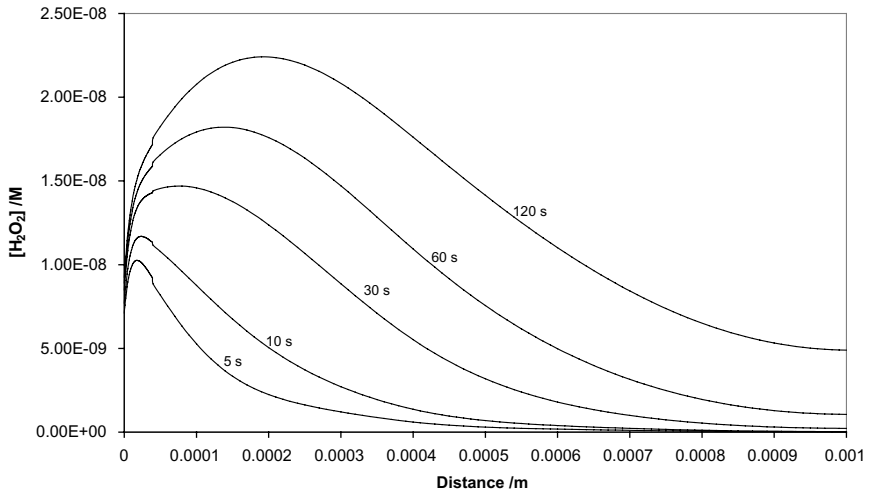


Fig. 4. H_2O_2 concentration as a function of distance from the spent nuclear fuel surface for different times.

As can be seen, the surface concentration approaches a constant value fairly rapidly. This value corresponds to the steady-state concentration of the system, i.e. the surface concentration at which the rate of radiolytic H_2O_2 production is balanced by the rate of H_2O_2 consumption through the surface reaction. This is hardly unexpected since any system being continuously irradiated will reach a steady-state. What is more surprising is the fact that the surface concentration approaches the steady-state level fairly rapidly also in systems of large liquid volumes. Reaching the steady-state concentration in the whole liquid volume would take substantially longer time. The time required to reach the steady-state surface concentration depends on the rate constant for the surface reaction. A higher rate constant corresponds to a lower steady-state concentration. Consequently, the steady-state concentration is approached more rapidly with increasing reactivity of the surface. For irradiation times longer than one hour the time to approach steady-state is insignificant and we can simply use the steady-state conditions when calculating the rate of H_2O_2 consumption even for fairly low surface reaction rate constants.

Under realistic conditions, other processes than the surface reaction will also consume H_2O_2 and thereby reduce the surface steady-state concentration.

Quantitative elucidation of the impact of solutes capable of reducing H_2O_2 in solution is not straightforward for a system with inhomogeneous production of H_2O_2 . For this reason, simulations taking into account solutes consuming H_2O_2 have also been conducted.²⁹

In Table 2, the relative steady-state surface concentration (with respect to the maximum steady-state concentration defined by the lowest surface reaction rate constant used in the study) as a function of surface reaction rate constant and pseudo-first-order rate constant for the bulk reaction is given.

As can be seen, the steady-state surface concentration decreases with increasing pseudo-first-order rate constant for the bulk reaction. The decrease is however not linearly related to the rate constant for the process. The main reason for the non-linearity is the inhomogeneous production of H_2O_2 giving rise to concentration gradients. For higher homogeneous rate constants the bulk concentration of H_2O_2 approaches zero and the actual volume containing H_2O_2 decreases. As can also be seen, the steady-state surface concentration is mainly determined by the homogeneous pseudo-first-order rate constant. For high surface reaction rate constants the steady-state surface concentrations are significantly lower for the lowest homogeneous

Table 2. Relative steady-state H_2O_2 surface concentration as a function of surface rate constant and homogeneous pseudo-first-order rate constant.

Surface rate constant (ms^{-1})	Homogeneous pseudo-first-order rate constant (s^{-1})						
	0	0.01	0.1	1	10	100	1000
7.33×10^{-8}	1	0.021	0.0059	0.0015	3.2×10^{-4}	4.8×10^{-5}	n.d.
7.33×10^{-7}	0.1	n.d.	0.0056	0.0015	n.d.	n.d.	n.d.
7.33×10^{-6}	0.01	n.d.	n.d.	0.0012	3.0×10^{-4}	4.5×10^{-5}	n.d.
7.33×10^{-5}	0.001	n.d.	7.2×10^{-4}	4.7×10^{-4}	1.9×10^{-4}	4.0×10^{-5}	5.3×10^{-6}

pseudo-first-order rate constants. Hence, the system is governed by the surface reaction in these extreme cases. Consequently, even for the low homogeneous pseudo-first-order rate constant, the steady-state surface concentration and thereby the rate of the surface reaction will be governed by the bulk reaction. For this system, the relative steady-state surface concentration ($[\text{H}_2\text{O}_2]_{s-s}^*/[\text{H}_2\text{O}_2]_{s-s}$) as a function of the homogeneous pseudo-first-order rate constant can be approximated by Eq. (13). ($[\text{H}_2\text{O}_2]_{s-s}^*$ is the surface concentration taking the bulk reaction into account and $[\text{H}_2\text{O}_2]_{s-s}$ is the surface concentration in the absence of bulk reactions consuming H_2O_2).

$$\log \frac{[\text{H}_2\text{O}_2]_{s-s}^*}{[\text{H}_2\text{O}_2]_{s-s}} = -0.66 \log k^* - 2.9. \quad (13)$$

It should be noted that Eq. (13) is independent of the average dose rate. The rate of the surface reaction can then be calculated from Eq. (14)

$$r_{\text{surf}} = r_{\text{surf}}^{\circ} 10^{-0.66 \log k^* - 2.9}, \quad (14)$$

where r_{surf}° is the rate of the surface reaction in the absence of solutes consuming H_2O_2 .

10. Dissolution of Spent Nuclear Fuel

To demonstrate the use of the findings presented above the focus will now be turned to the process of spent nuclear fuel dissolution under deep geological repository conditions.

In a repository of the type planned to be used in Sweden and Finland, the spent nuclear fuel elements will be placed in copper canisters with an iron insert. The canisters will be embedded in bentonite clay in the bedrock at a depth of about 500 m. In the event of a complete barrier failure, groundwater can enter the canister. At this depth groundwater (containing approximately 2 mM HCO_3^-)

is reducing but water will corrode the iron in the canister producing H_2 and Fe_3O_4 . The water will eventually also come in contact with the spent fuel itself.

Upon contact between the spent nuclear fuel and the groundwater, radiolysis of water will begin. From the point of view of a safety assessment it is relevant to define the worst-case, but still realistic, scenario. Hence, the maximum possible dissolution rate for the UO_2 fuel matrix (assuming congruent dissolution) must be defined. As shown above, oxidation of U(IV) to U(VI) is required for dissolution to occur. Consequently, the rate of dissolution can never exceed the rate of oxidation and the rate of oxidation can be used to estimate the maximum dissolution rate. It has also been shown that, for longer irradiation times, the only oxidant that must be taken into account is H_2O_2 and that the surface concentration of H_2O_2 approaches the steady-state concentration fairly rapidly. The concentration will never exceed the steady-state concentration and therefore we can use the steady-state approach to make a realistic estimate of the maximum dissolution rate.

Using the previously elaborated approach to calculate the geometrical dose distribution for spent nuclear fuel on the basis of the radionuclide inventory, the steady-state concentration of H_2O_2 and thereby the maximum dissolution rate can be calculated in a very simple fashion. The dissolution rate for 15-years-old spent nuclear fuel, for which experimental leaching data are also available,³⁰ has been estimated. The leaching experiments were performed in aqueous solution containing 10 mM HCO_3^- , i.e. oxidation rather than dissolution of the oxidized product is expected to be the rate limiting process. The estimated and average experimental dissolution rates agree within a factor of two.³¹ This is a remarkably good agreement given the fact that the experimental rate of dissolution varies by more than a factor of two. It is also important to note that all experimental values are lower than the estimated value.

Some of the fission products (e.g. Pd) in spent nuclear fuel form metallic nanoparticles having catalytic properties. Electrochemical studies on synthetic spent nuclear fuel containing metallic nanoparticles

show that the corrosion potential is significantly lowered in the presence of H_2 (likely to be produced from corrosion of the canister).³² This effect is not observed for pure UO_2 which indicates that the nanoparticles are galvanically coupled to the UO_2 matrix. On the basis

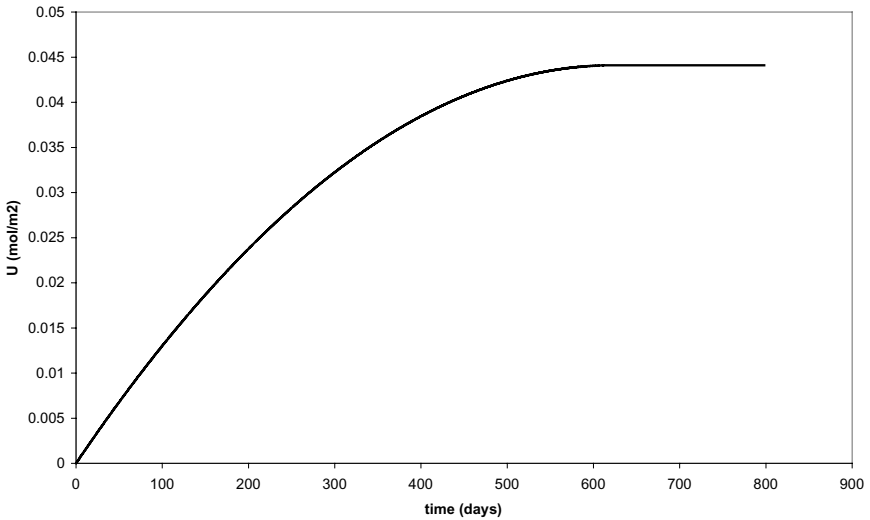
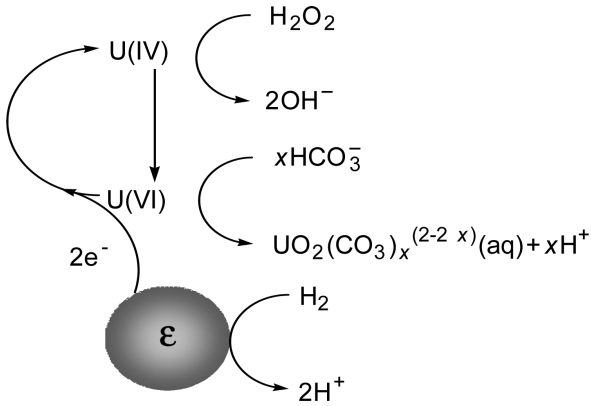


Fig. 5. Dynamics of spent nuclear fuel dissolution taking into account UO_2 oxidation by H_2O_2 , H_2 production and noble metal particle catalyzed reduction of $UO_2^{2+}(s)$ by H_2 .

of this observation one can expect that H_2 will inhibit oxidation of the spent nuclear fuel matrix. In order to elucidate this effect, further experiments using UO_2 pellets containing Pd particles have been performed.³³ When exposing these pellets to H_2O_2 solutions in the presence of H_2 , the oxidative dissolution of UO_2 was effectively inhibited. Interestingly, the oxidation process also appears to be catalyzed by the presence of noble metal particles as observed in experiments in the absence of H_2 . The processes responsible for oxidation, dissolution and reduction (inhibition) are illustrated in Scheme 1.

The dissolution is completely inhibited when the rate of reduction by H_2 is equal to the rate of dissolution of oxidized UO_2 .

Long term spent nuclear fuel dissolution experiments show that the rate of dissolution decreases with time and eventually the process appears to stop.³⁴ The inhibition is strongly connected to the radiolytical production of H_2 in the system. The dynamics of such a system is illustrated in Fig. 5.

Judging from this, the concept of deep geological storage of spent nuclear fuel in copper coated steel canisters would appear to be an inherently safe solution where the canister material as well as the spent nuclear fuel itself provide conditions for self-healing upon canister failure.

References

1. Nielsen F, Jonsson M. (2006) Geometrical α - and β -dose distributions and production rates of radiolysis products in water in contact with spent nuclear fuel. *J Nucl Mater* **359**: 1–7.
2. LaVerne JA, Tandon L. (2002) H_2 production in the radiolysis of water on CeO_2 and ZrO_2 . *J Phys Chem B* **106**: 380–386.
3. LaVerne JA, Tonnie SE. (2003) H_2 production in the radiolysis of aqueous SiO_2 suspensions and slurries. *J Phys Chem B* **107**: 7277–7280.
4. LaVerne JA, Tandon L. (2003) H_2 production in the radiolysis of water on UO_2 and other oxides. *J Phys Chem B* **107**: 13623–13628.
5. LaVerne JA. (2005) H_2 formation from the radiolysis of liquid water with zirconia. *J Phys Chem B* **109**: 5395–5397.
6. Astumian RD, Schelly ZA. (1984) Geometric effects of reduction of dimensionality in interfacial reactions. *J Am Chem Soc* **106**: 304–308.

7. Ekeroth E, Jonsson M. (2003) Oxidation of UO_2 by radiolytic oxidants. *J Nucl Mater* **322**: 242–248.
8. Belloni J, Mostafavi M. (2001) Radiation chemistry of nanocolloids and clusters. In: Jonah CD, Rao BSM (eds.), *Radiation Chemistry — Present Status and Future Trends*, pp. 411–452. Elsevier, Amsterdam.
9. Roth O, Bönemark T, Jonsson M. (2006) The influence of particle size on the kinetics of UO_2 oxidation in aqueous powder suspensions. *J Nucl Mater* **353**: 75–79.
10. Nejad MA, Jonsson M. (2004) Reactivity of hydrogen peroxide towards Fe_3O_4 , Fe_2CoO_4 and Fe_2NiO_4 . *J Nucl Mater* **334**: 28–34.
11. Shoemith DW. (2000) Fuel corrosion processes under waste disposal conditions. *J Nucl Mater* **282**: 1–31.
12. Nejad MA, Jonsson M. (2005) Dynamics for oxidation of Fe_3O_4 , Fe_2CoO_4 and Fe_2NiO_4 . *J Nucl Mater* **345**: 219–224.
13. Hossain MM, Ekeroth E, Jonsson M. (2006) Effects of HCO_3^- on the kinetics of UO_2 oxidation by H_2O_2 . *J Nucl Mater* **358**: 202–208.
14. Christensen H, Sunder S. (2000) Current state of knowledge of water radiolysis effects on spent nuclear fuel. *Nucl Technol* **131**: 102–123.
15. Ekeroth E, Roth O, Jonsson M. (2006) The relative impact of radiolysis products in radiation induced oxidative dissolution of UO_2 . *J Nucl Mater* **355**: 38–46.
16. Ekeroth E, Jonsson M, Eriksen TE, Ljungqvist K, Kovács S, Puigdomenech I. (2004) Reduction of UO_2^{2+} by H_2 . *J Nucl Mater* **334**: 35–39.
17. Hiroki A, LaVerne JA. (2005) Decomposition of hydrogen peroxide at water–ceramic oxide interfaces. *J Phys Chem B* **109**: 3364–3370.
18. Jonsson M, Ekeroth E, Roth O. (2004) Dissolution of UO_2 by one- and two-electron oxidants. *Mater Res Soc Symp Proc* **807**: 77–82.
19. Hossain MM, Jonsson M. (2008) UO_2 oxidation site densities determined by one- and two-electron oxidants. *J Nucl Mater* **373**: 186–189.
20. De Pablo J, Casas I, Clarens F, El Aamrani F, Rovira M. (2001) The effect of hydrogen peroxide concentration on the oxidative dissolution of unirradiated uranium dioxide. *Mater Res Soc Symp Proc* **663**: 409–416.
21. Hossain MM, Jonsson M. (2008) Effects of ionic strength on the kinetics for UO_2 oxidation. *J Nucl Mater* **373**: 190–193.
22. Tugluoglu N, Altindal S, Tataroglu A, Karadeniz S. (2004) Dielectric properties in $\text{Au}/\text{SnO}_2/\text{n-Si}$ (MOS) structures irradiated under ^{60}Co - γ rays. *Microelectron J* **35**: 731–738.
23. Shoemith DW, Sunder S, Hocking WH. (1994) Electrochemistry of UO_2 nuclear fuel. In: Lipkowski J, Ross PN (eds.), *The Electrochemistry of Novel Materials*, pp. 297–338. VCH Publishers Inc New York.
24. Hocking WH, Shoemith DW, Betteridge JS. (1992) Reactivity effects in the oxidative dissolution of UO_2 nuclear fuel. *J Nucl Mater* **190**: 36–45.

25. Gromov V. (1981) Dissolution of uranium oxides in the gamma-radiation field. *Radiat Phys Chem* **18**: 135–146.
26. Matzke H. (1992) Radiation damage-enhanced dissolution of UO_2 in water. *J Nucl Mater* **190**: 101–106.
27. Roth O, Nilsson S, Jonsson M. (2006) Radiation enhanced reactivity of UO_2 . *J Nucl Mater* **354**: 131–136.
28. Nielsen F, Lundahl K, Jonsson M. (2008) Simulations of H_2O_2 concentration profiles in the water surrounding spent nuclear fuel. *J Nucl Mater* **372**: 32–35.
29. Nielsen F, Jonsson M. (2008) Simulations of H_2O_2 concentration profiles in the water surrounding spent nuclear fuel taking mixed radiation fields and bulk reactions into account. *J Nucl Mater* **374**: 281–285.
30. Bruno J, Cera E, Grivé M, Eklund U-B, Eriksen T. (1999) Experimental determination and chemical modelling of radiolytic processes at the spent fuel/water interface. Swedish Nuclear Fuel and Waste Management Co, TR-99-26.
31. Nielsen F, Ekeröth E, Eriksen TE, Jonsson M. (2008) Simulation of radiation induced dissolution of spent nuclear fuel using the steady-state approach. A comparison to experimental data. *J Nucl Mater* **374**: 286–289.
32. Broczkowski ME, Noël JJ, Shoesmith DW. (2005) The inhibiting effects of hydrogen on the corrosion of uranium dioxide under nuclear waste disposal conditions. *J Nucl Mater* **346**: 16–23.
- 33 Trummer M, Nilsson S, Jonsson M. (2008) On the effects of fission product noble metal inclusions on the kinetics of radiation induced dissolution of spent nuclear fuel. *J Nucl Mater* **378**: 55–59.
34. Cera E, Bruno J, Duro L, Eriksen T. (2006) Experimental determination and chemical modelling of radiolytic processes at the spent fuel/water interface. Long contact time experiments. Swedish Nuclear Fuel and Waste Management Co, TR-06-07.

Chapter 12

Radiolysis of Water Confined in Nanoporous Materials

*Raluca Musat[†], Mohammad Shahdo Alam[†]
and Jean Philippe Renault ^{*†,‡}*

1. Introduction

Radiolysis of water in nanoporous media has raised a lot of interest and involved research in the recent years, with respect to concerns arising from the storage of nuclear waste. In the civil nuclear industry, storing of nuclear wastes for a long time requires safety evaluations in order to test the durability of the materials involved. Among these materials, concrete and clays are a complex heterogeneous material that traps important quantities of interstitial water. Irradiation that arises from the nuclear wastes stored in these materials may lead to the radiolysis of the interstitial water, and the formation of radiolytic products. These products, such as H_2 , O_2 or H_2O_2 , may cause the breaking or the corrosion of the confining matrix. Despite its importance in the development of nuclear waste storing means, the study of

* jprenault@cea.fr

[†] CEA, IRAMIS, SIS2M, Laboratoire de Radiolyse, F-91191 Gif-sur-Yvette Cedex, France

[‡] CNRS, Laboratoire Claude Fréjacques, F-91191 Gif-sur-Yvette Cedex, France

the radiolysis in confined media has long been neglected. In this paper, we will only be concerned with radiolysis of water confined in nanostructured inorganic materials.

2. The Questions Raised by Radiolysis of Confined Water

Standard description of radiolytic events distinguishes three main steps in water radiolysis:

- (1) the physical stage, comprising the energy transfer from ionizing particles to water, fast processes such as molecular dissociation and ionization in the track of the ionizing particle;
- (2) the physico-chemical stage, comprising the reorganization and recombination of the species produced in the previous step and their intra track reactions; and
- (3) the chemical stage, comprising intertrack reactions and reactions of the radiolytic species in the bulk solution.

The characteristic time scales and length scales of these different steps are presented in Fig. 1.

In a nanoporous network, the radiolytic species cannot migrate in all directions as in the case of bulk water, and there is no occurrence of a homogeneous kinetics regime: confinement suppresses the as-defined chemical stage. For nanoporous systems the alternative characteristic time scale is the one for which the radiolysis species escape from their original pore. This time scale may separate a stage for which reactions occur mainly between species coming from different pores (an interpore regime) from a stage for which reactions occur mainly between species produced in the same pore (an intrapore regime).

Figure 1 shows that the physicochemical stage is purely “intrapore,” the characteristic diffusion length of radiolytic species being in the nanometer range. Confinement in nanopores will impact this physicochemical step by limiting the diffusion of primary species out of their

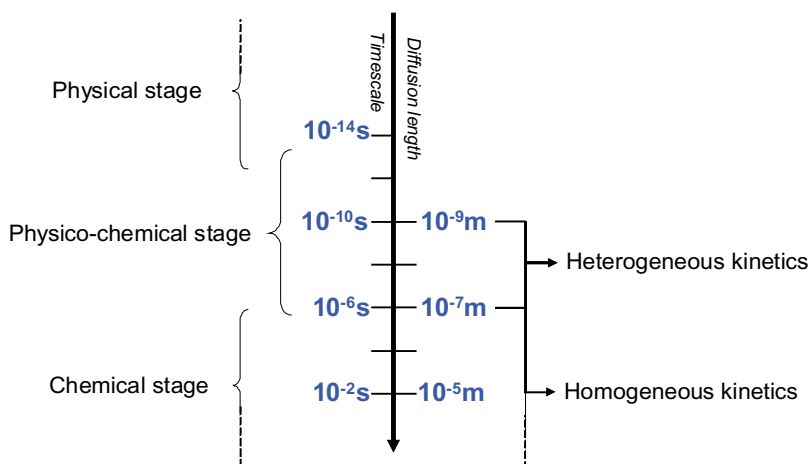


Fig. 1. Characteristic time scale and associated diffusion length of radiolytic species of the major stages of water radiolysis.

production sites. It may favor the meeting of the reactive species and therefore their recombination, provided the interface between water and material behaves like a perfectly reflective one. Confinement will also render the reaction kinetics in this stage even more complex than those in bulk water.

One should also consider that various energy transfer processes can occur between the initial interaction of a highly energetic particle with the medium and the final conversion of the deposited energy in a chemical event in water. This implies that, in heterogeneous systems, the initial energy deposition can occur in one phase, and the final chemical event in another, resulting in a net energy transfer between the two phases. Depending on the nature of the transfer process, this will correspond formally to a change in the dose (secondary electron transfer during the physical step) or to a change in initial radiolytic yields (thermalized particles or excitations transfer during the physical stage). These latter phenomena may be especially important in nanoporous materials owing to the very high contact surface (usually more than $100 \text{ m}^2/\text{g}$) between the mineral and aqueous phases in such highly divided materials.

Therefore, a detailed understanding of radiolysis in nanoconfined media would require:

- a good description of the properties of nanoconfined water,
- an extensive knowledge of the real dose received by water,
- a knowledge on how the reaction kinetics is modified by confinement,
- the measurement of radiolytic yields as a function of confinement and time.

3. Confining Materials and Confined Water

In order to have a better understanding of the influence of confinement upon radiolysis, we need to have a global view of the confinement-induced modifications of water properties and of the perturbation of diffusion processes inside pores.

Numerous studies have been performed in order to elucidate the structure and the dynamics of confined water using a variety of experimental techniques — NMR,¹ quasi-electron neutron diffraction,^{2,3} IR absorption spectroscopy,⁴ or molecular dynamics simulation.^{5,6} Most of these studies use model porous media such as clays,⁷ polymer membranes,⁸ different types of silica⁹ and zeolites.¹⁰ Some of these systems (cf. Fig. 2) may be used to study water radiolysis in nanoporous media.

3.1. *Confining materials*

The micro-porosity of clay is due to the stacking of aluminosilica platelets. The typical platelet thickness is about 7 Å and its long dimension is within several microns. The inter-platelet distance can vary from a few to several tens of angstroms depending on the water content. The stacking of platelets, which also depends on the hydration level of the material, gives particles between which a mesoporous network develops. Therefore, clays do not have a rigid porous network with well-defined pore size. This explains why, despite their large interest in nuclear waste disposal, clays have been largely understudied in radiation chemistry.

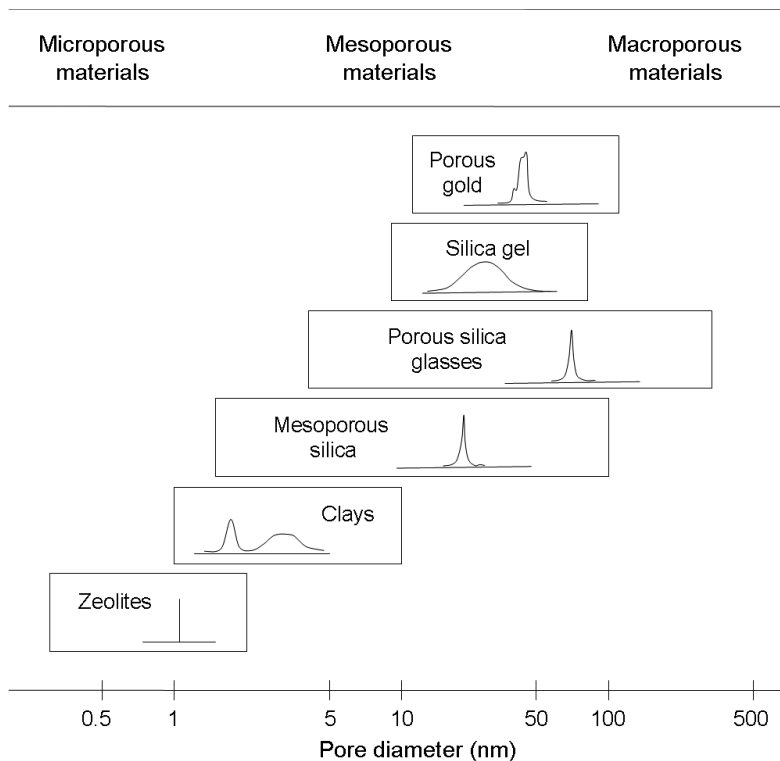


Fig. 2. Pore size distribution of model materials discussed in the text and their classification according to International Union of Pure and Applied Chemistry.

Much more attention has been given to zeolites. Zeolites are crystalline microporous materials whose structure is based on a three-dimensional tetrahedral network of AlO_4 and SiO_4 (the Al/Si ratio can be varied from 1 to 0). The excess negative charges carried by AlO_4 units are compensated by cations (Na^+ , H^+) which ensure the high hydrophilicity of the aluminated zeolites. The crystallinity of zeolites ensures also a very precise pore size. Typically, the size of zeolite pores ranges from 3 to 8 Å, and the inner diameter of the interior spaces from 5 to 13 Å.

For larger pores with a narrow diameter distribution, mesoporous silica of the M41S family can be used. Since their discovery by scientists

of the Mobil Corporation in 1992, these ordered silica-based mesoporous materials have attracted enormous interest. These materials show ordered arrangements of channels and cavities of different geometry. Their preparation is based on the utilization of organic species capable of self-structuration (tensioactives micelles). The pore size is variable and can be controlled and modified, in a reasonable range, using *in situ* and *ex situ* synthetic strategies. The major members of the M41S family are the MCM-41, which shows a 2D hexagonal structure with pores around 2 to 10 nm, MCM-48 family with a cubic structure with pore size between 2 to 4 nm and MCM-50 family with a lamellar structure.

The possibility of obtaining different pore sizes and geometries allows studying the specific role of the pore diameter and interconnection in confinement effects. However, the main problem in the use of MCM materials in radiolysis is the poor definition of the silica-based walls. The presence of micropores and a high content in non-condensed silica (silanols groups) has been evidenced in some cases.

For even larger pores, silica gels may be of interest. They are cheap and can be obtained in large amounts. Silica gels consist of large porous particles (usually more than 5 μm) obtained by sol-gel processes. They have amorphous structure, with average pore radii ranging from 5 to 50 nm. However, their pore size distribution is ill defined, and for large pore, the use of Vycors or controlled pore glasses (CPGs) is usually preferred. Vycor and CPGs have a high porosity, a well-characterized pore size and excellent mechanical and thermal properties. CPGs can also be prepared with a wide range of porosities and average pore sizes (the pore size can be controlled in the fabrication process to provide a diameter ranging from 5 to 300 nm).

Even though zeolites and porous glasses are materials that allow covering two orders of magnitude in pore diameter, they remain silica based. A complete description of the role of the confining material in radiolysis would require the access to alternative porous materials. The development of metallic porous frameworks has been studied for catalysis (Raney Nickel), electrochemistry and heat dissipation.

Among these materials, porous gold is the most intensely studied nowadays¹¹ due to its stability under atmospheric conditions and its monolithic character.

It has an open sponge-like morphology of interconnected Au ligaments with a narrow pore size distribution. The pore size can be controlled during the manufacturing process, ranging from 10 to 1000 nm. This medium may be an interesting alternative to silica-based materials for radiolysis studies.

3.2. *Confined water*

When water is confined in a porous medium, its liquid structure is affected by the interaction with the substrate molecules and by the geometrical confinement itself. Surface tends to control the behavior of nearby water molecules: water near hydrophilic surfaces shows a strongly reduced mobility,¹² whereas interactions with the substrate induce distortions in the H-bond network.¹³ These two phenomena are expected to induce large variation in the water density (layering) near the pore wall. Recent studies estimate for the layer with modified properties (distorted hydrogen bond, modified dynamics upon confinement) a thickness of about 10 Å.^{13,14} Farther from the surface, one would expect a water behavior similar to that of the bulk. However, even for mesoporous matrix (pore size larger than 20 Å), neutron scattering experiments have shown a global modification (slowing down) of the dynamics due to the confinement.¹⁵ The rotational dynamics has been found to be three to five times slower than its bulk value. Still, this modification is smaller than in the case of the translational dynamics¹⁶ with an effective slowing down by a factor of four to five.

As a consequence, solvent viscosity is also modified by confinement. Molecular dynamics simulations show that the average viscosity in the pore is greater than that in a bulk liquid at the same temperature by more than 50% for the smaller pores.¹⁷ The local viscosity varies across the pore, showing oscillations as the pore wall is approached; for the smaller pores these oscillations persist across the entire width of the pore. Indeed, studies on the diffusion of liquids

inside pores (intrapore regime) have shown a pore-size dependence of the diffusion coefficient.

In smaller pores where the majority of the molecules are in the proximity of the walls, the presence of an immobile superficial layer limits even more the diffusion coefficient by reducing the effective pore diameter: as a result in saturated Vycor (pore size 29 Å) the movement of particles is about two times slower than the one in bulk phase, while in MCM-41-S (pore diameter 25 Å) and MCM-48-S (pore diameter 22 Å) the movement of particles is about four to ten times slower.¹⁸ The limit case is an in-file diffusion process, where particles are unable to pass each other in a channel.¹⁹

These descriptions apply to diffusion processes inside a pore, but on a longer time scale (interpore regime), the diffusion of solutes will be controlled by the shape of the porous network itself (which can be treated as a Knudsen diffusion regime). The description of Knudsen diffusion is beyond the scope of this paper, but we can recollect that the tortuosity of the medium, besides the pore diameter, is an important parameter that can slow down interpore diffusion and hence diffusion-controlled reactions.^{20,21}

4. Dosimetry in Nanoporous Media

Performing an accurate dosimetry is a prerequisite of any radiolysis study. However, all standard chemical dosimetry methods cannot be used in nanoporous media, as they all rely on known radiolytic yields that are expected to be modified by confinement. An alternative would be to use Monte Carlo particle transport code (i.e. MNCP, EGS4, Geant, Penelope) that allows a calculation of the deposited dose. PENELOPE (Penetration and Energy Loss of Positrons and Electrons) has especially proven to be efficient in microdosimetric calculations.^{22,23} This code can treat electron propagation down to 100 eV, for any material. Therefore, these simulations cannot handle sub-nanometric pore and do not take into account the fact that for certain materials pore diameter is smaller than spurs and/or track size. For nanometric to micrometric pores, the approximation usually proposed is to correct the dose by the mean density of the system

(for example 1.4 for water-filled porous glasses). However, the dose received by water confined in silica was calculated to be very similar to the dose received by bulk water.²⁴ These similarities arise from the fact that, in this system, the confining material and water have comparable behavior with respect to the production and absorption of secondary particle. Whenever the confining material has a very different stopping power from water, the repartition of the energy between water and material will be geometry dependant, crude approximations will not stand and more detailed calculations should be performed.

5. Radiolytic Yields Modification by Confinement

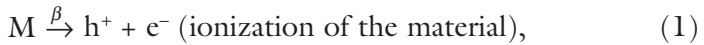
5.1. Dihydrogen

Dihydrogen production of confined water has been studied in CPG glasses, MCM-41,^{24,25} and Zeolites.²⁶ These studies have shown that H₂ production came both from the confined water and from the confining material, the latter contribution being the major one (Fig. 3 summarizes the measured yields for dry and wet CPGs). Such production is not specific to porous materials and has been observed in the radiolysis of other heterogeneous systems. The high yields measured (20×10^{-7} and 155×10^{-7} mol J⁻¹ for one to two water layers on CeO₂ and ZrO₂,²⁷ from 40×10^{-7} ,²⁸ upto 85×10^{-7} mol J⁻¹,²⁹ on silica gels for sub-monolayer coverage) have been explained by an energy transfer from the solid to the molecules chemisorbed or physisorbed at the interface.^a

H₂ production on solid materials is indeed a particular case of energy redistribution in a multiphase system, which is sometimes also referred to as radiation catalysis: the energy of ionising radiation absorbed in one phase can be delivered to the interface and can induce physical and chemical processes in the other phase.

^a These radiation-chemical yields have no meaning *per se* and should rather be calculated with respect to the energy absorbed by the molecules both directly and indirectly (i.e. delivered from the adsorbent).

Hydrogen production from the material is currently described as a three-step process:



In the first step radiation induces electron–hole pairs in the materials which can rapidly recombine, giving an exciton [reactions (1) and (2)]. In the second step, excitons diffuse in the material until they are trapped by a defect site; an example of such a trap being surface hydroxyl groups of the material (silanol groups, chemisorbed or physisorbed water). This surface trapping of excitons induces the homolytic rupture of O–H bonds [reaction (3)]. In the third step the produced H^\bullet atoms may then recombine with their parent radical which dimerize to give dihydrogen [reaction (4)]. H^\bullet atoms production has indeed been observed upon radiolysis of MCM-41 or Vycor glasses.^{30,31}

This scheme may be modified for other systems (alumina, zeolites³²) where the surface chemistry reflects a more ionic situation than on silica. In such cases, H^\bullet atoms (and subsequently H_2) may arise from dissociative attachment of the electrons produced by ionization of the solid to the OH groups near the surface.



There are several parameters which can contribute collectively to enhanced radiolysis at the interfaces and finally affect the hydrogen yield at the surface: the material band-gap (the band gap determines energy of excitons and therefore their ability to break OH groups³³), the surface density of hydroxyl groups²⁵ and the exciton migration distance.^{24,25,33} Nanoporous materials have very high surface/volume ratio and small mineral domains that obviously favor exciton surface

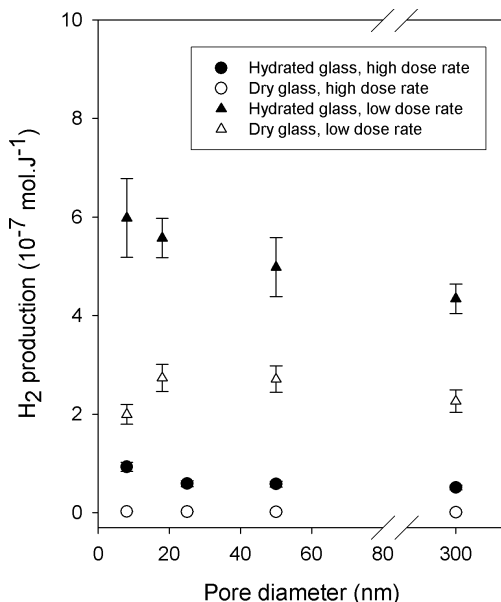


Fig. 3. Dihydrogen production in controlled pore glasses. The data are gathered from Refs. 24 and 25.

trapping. Studies on silica glasses at moderate dose rates (Fig. 3) have indeed shown that the energy transfer process decreases when pore size increases.

This decrease, observed in CPGs, is somewhat limited even for material domains as big as 100 nm. However, it must be noted that most studies on radiolytic hydrogen production at the surface of nanoporous material have been conducted on silica-based systems, and the exact role of substrate chemistry has still to be deciphered.

Hydrogen production on surfaces is indeed a fast-growing research subject. However, in hydrated nanoporous materials, a significant part of the H_2 is also produced through direct energy capture by water, and understanding this “in pore” production requires a deconvolution of the surface production.

One possible way to do this is to switch off the energy transfer from the material to the confined water. This is possible by taking

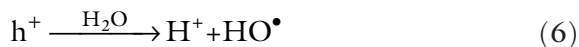
advantage of the very high dose rates upon irradiation by fast electrons. At such dose rates, excitons in the solid annihilate (the H_2 yields measured in the dried solid are almost zero), leaving apparently only the H_2 production from confined water. Indeed, in such conditions, the H_2 yields are not drastically different from the one obtained in bulk water, considering that solvated electrons are not scavenged in these studies.

An important observation is that there is a production of H_2 even without HO^\bullet scavengers (in bulk water only neglectable amounts of H_2 are produced in the absence of such scavengers). This indicates that the chain reaction which controls the back reaction of H_2 and H_2O_2 in pure bulk water does not occur in confined water. In confined water the diffusion of the radiolytic species is limited, thereby reducing the interpore encounter of HO^\bullet and H_2 . Confinement, besides early radiolytic events, may also impact the long-term behavior of radiolytic species and their accumulation.

A second observation is the (limited) increase of H_2 yield when the pore size decreases. This behavior may reveal an increased radical recombination of the reductive radical species, H^\bullet and e_{aq}^- . This may be the mark of a cage effect inside small pores.

5.2. Hydroxyl radical

The production of hydroxyl radical in water confined in zeolites has been proved by Thomas and co-workers by trapping of organic compounds.³⁴ The high values of the G measured (about $6 \times 10^{-7} \text{ mol J}^{-1}$) evidence a hole transfer from the material to the water, following Eqs. (1) and (6).



Hydroxyl radical production has also been proven in controlled pore glasses via selective capture by coumarin.³⁵ In these systems, the contribution of energy transfer to HO^\bullet production is more limited than in zeolites, being at the most of 30% for the smaller pore sizes and neglectable for large pores. Therefore, the HO^\bullet yields

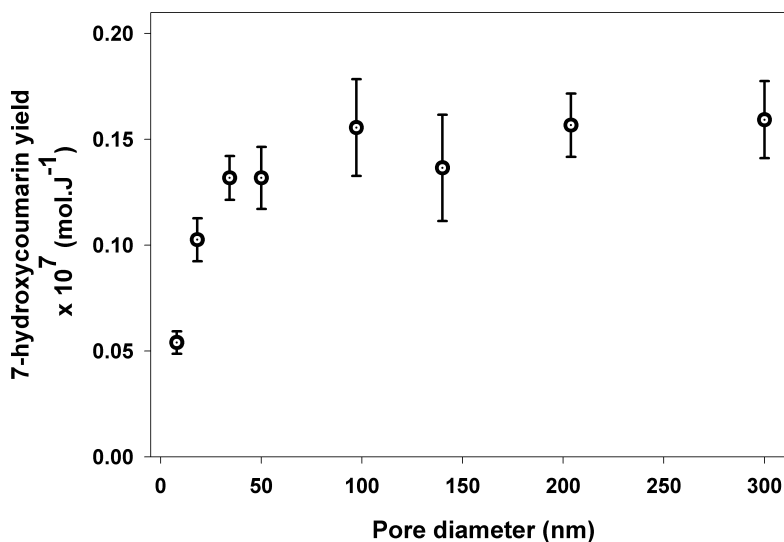


Fig. 4. Effect of pore size on the yield of 7-hydroxy-coumarin produced in CPG glasses. Data taken from Ref. 35.

are connected to the radiation chemistry occurring inside confined water pools.

As shown in Fig. 4, for pore diameter larger than 150 nm, the HO[•] production in confined solutions is similar to that obtained in homogenous solutions, whereas below 100 nm, the HO[•] yields decrease with the pore size. The amount of HO[•] available for reaction with coumarin is decreased by almost a factor of 6 for 8 nm pores compared to bulk water and by a factor of 1.5 for a pore as large as 50 nm. For such large pores, this decrease cannot be explained by a pore-cage effect, but rather by an interpore decreased diffusion that limits the amount of radicals that escape their production site.

5.3. Aqueous electron

Contrary to other type of radiolysis studies, the solvated electron has not been the workhorse used to understand radiation chemistry in confined environment. Whereas in bulk solution the solvated electron

yield can be directly measured by pulse radiolysis, such methods are difficult in confined environment. Most of these materials are obtained as micronic powders that strongly diffuse light. However, in a few cases, the materials are transparent enough to allow pulse radiolysis studies, like the one conducted by J. K. Thomas on zeolites.³⁴

The formation of hydrated electrons (in the water-saturated zeolites X and Y) has been identified through their absorption spectra, their short lifetimes distinct from the long-lived cation cluster-trapped electrons, and their reactivity towards typical hydrated electron quenchers such as methylviologen. Based on these spectra (Fig. 5), yields between $4 \times 10^{-7} \text{ mol J}^{-1}$ and $6 \times 10^{-7} \text{ mol J}^{-1}$ were measured for electrons in fully hydrated NaY. These high radiolytic yields were also explained by electron transfer from the ionized zeolitic skeleton to the water clusters [Eqs. (1) and (7)].



However, the electron spectrum in nanometer cavity depends strongly on the water loading. The red spectral shift with decreasing size of the confined water clusters presumably demonstrates a decreased solvation of the electron and an increased delocalization. This interpretation was confirmed by recent mixed quantum-classical simulations³⁶ that predict larger electron gyration radius for low water loading. The chemical implications of this decreased solvation of the electron are still to be investigated.

A proper study of electron behavior in alternative nanoporous systems will rely on the development of easily accessible monolytic porous materials. This will give a straightforward access to the kinetics behavior of radiolytic species in porous media.

5.4. *Hydrogen peroxide*

Hydrogen peroxide is absent in most descriptions of heterogeneous radiolysis. Indeed, silica materials used in the studies are expected to accelerate the decomposition of H_2O_2 in a surface-dependent

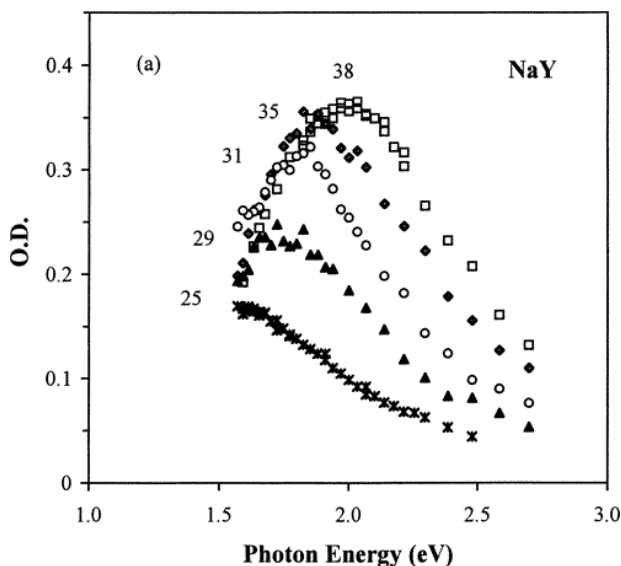
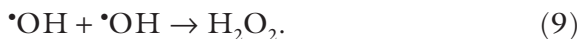


Fig. 5. Transient absorption spectra of hydrated electron in zeolites NaY recorded at 20 ns after the electron pulse. The water contents are denoted by the number of water molecules per pseudo-cell (a sodalite cage plus a supercage). [Reprinted with permission from Ref. 34 Copyright 1997, American Chemical Society].

process.³⁷ However, in CPGs, no oxygen production under irradiation was observed by gas chromatography, neither were peroxospecies by solid state O^{17} NMR.³⁸ We have been able only recently³⁹ to quantify H_2O_2 production in these materials. Hydrogen peroxide production is the exact counterpart of H_2 production, both at high-dose rate and low-dose rate. Most of the H_2O_2 production arises from an energy transfer from the material to the water, and the hydrogen peroxide production was explained using reactions (6), (8) and (9):



Even though most radiolytic species have been identified in confined media, the literature available fails to give a global picture of their

production mechanisms. Certain radiolytic yields are dominated by phenomena occurring at interfaces, others by phenomena connected to the bulk. However, it seems that, once subtracted the surface contributions, the measured yields are not drastically different from the ones measured in bulk water for pore sizes in the 100–300 nm range, and that the differences observed in the 10–50 nm range may be simply interpreted in terms of “in pore” increased radical recombination.

6. Kinetics Modification by Confinement

When people consider confinement effects, they consider mainly an increase in the encounter probability inside a single pore and therefore, expect an acceleration of the reaction. Such in-pore acceleration has been quantified by Tachiya and co-workers for diffusion-limited reactions through the so-called confinement factor [see Eq. (11.58) in Ref. 40]. From this treatment, confinement effects are expected to disappear when the reaction radius is less than one tenth of the confinement radius. Considering the reaction radii of radiolytic species, no acceleration by confinement should be expected for pore diameter larger than 10 nm. For smaller pore size, acceleration of the recombination reactions within spurs would be critical in the determination of radiolytic yields in the nanosecond time range. However, the existence of such an acceleration of radiolytic reactions has not been suggested in the nanosecond pulse radiolysis of zeolites and has still to be assessed using picosecond pulse radiolysis.

Barzykin and Tachiya have also developed a kinetics model⁴¹ to predict the behavior of bimolecular reactions in interconnected pore networks (Fig. 6). This effective model medium, where diffusion between pores is modeled by a potential barrier, shows an acceleration of diffusion-limited reactions on short time scale. However, if the diffusion between pores is small, only a long time scale slowing down becomes apparent, the apparent interpore kinetics constant being strongly time dependent.

Pulse radiolysis in zeolites indeed showed a decrease of the reaction speed of the solvated electron or of the hydroxyl radical with

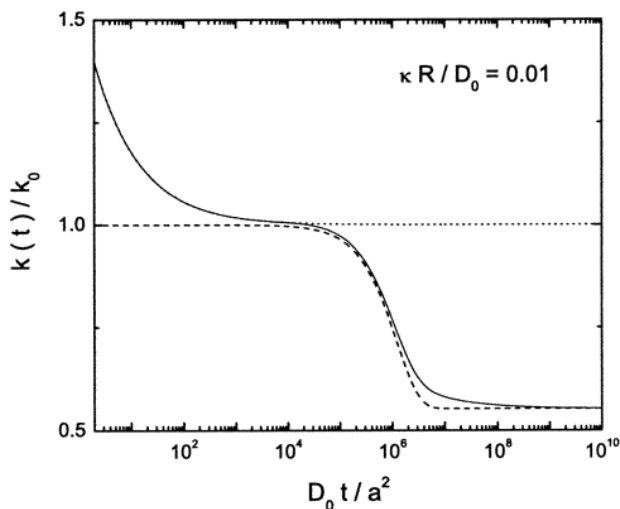


Fig. 6. Normalized time-dependent rate coefficient. Solid line corresponds to Effective Medium Approximation, and dotted line shows the usual Smoluchowski kinetics (without any obstruction). [Reproduced with permission from Ref. 41, Copyright 2003 American Chemical Society].

organic molecules of one to two orders of magnitude.³⁴ In such cases, compartmentalization effects on diffusion-limited reactions can be simply approximated by a decrease in the interpore diffusion coefficients of the reactive species.

However, this slowing down may not be observed for reactions with a significant activation energy: simulations conducted by Lopez-Quintela^{42,43} and co-workers show that partially diffusion-controlled reactions are more favored in media with a higher degree of compartmentalization because of an increase in the recollision probability.

One must also consider that these models assume a perfectly reflective surface for the pore wall and do not allow a prediction of the impact on the kinetics of a charged or partially absorbent⁴³ wall. The effect of an anisotropic distribution of reactant may also have to be investigated, especially for high LET radiations. Theoretical and experimental considerations^{44,45} show that the kinetic behavior in tubular-like environments strongly depends on the initial distribution

of the species. The variety of kinetic behavior is considerable⁴⁶ and up to now, most of these regimes have not been observed.

7. Conclusions and Perspectives

Hopefully, the ongoing work will enable us to complete our knowledge of radiolytic yields in confined media. But their proper interpretation relies on a profound understanding of the energy transfer phenomena occurring between phases and of the kinetic perturbation induced by confinement. Simulations already allow to make assumptions on these perturbations, but only time-resolved experiments can determine the dominant ones and put numbers on the time scale involved.

The more demanding research topic will be the description of the radiolytic species' surface chemistry. Owing to the very high specific surface of nanostructured materials (up to $1000 \text{ m}^2 \text{ g}^{-1}$), even moderate reaction rates between radiolytic species and surface may have a profound impact on the radiolytic schemes. The few studies available deal only with the surface reactivity of hydroxyl radical in gas phase^{47,48} and suggest a HO^\bullet capture by silica and alumina. This shows that surfaces that are usually considered as inert may become active under irradiation, once more demonstrating the exceptional reactivity of radiolytic species.

References

1. Findenegg GH, Jahnert S, Akcakayiran D, Schreiber A. (2008) Freezing and melting of water confined in silica nanopores. *Chemphyschem* **9**: 2651–2659.
2. Steytler DC, Dore JC. (1985) Neutron diffraction studies of water in porous silica II: Temperature variation in the super cooled regime. *Mol Phys* **56**: 1001–1015.
3. Bruni F, Ricci MA, Soper AK. (1998) Water confined in Vycor glass. I. A neutron diffraction study. *J Chem Phys* **109**: 1478–1485.
4. Musat R, Renault JP, Candelaresi M, Palmer DJ, Le Caer S, Righini R, Pommeret S. (2008) Finite size effects on hydrogen bonds in confined water. *Angew Chem Int Edit* **47**: 8033–8035.
5. Zhang L, Davis HT, Kroll DM, White HS. (1995) Molecular dynamics simulations of water in a spherical cavity. *J Phys Chem* **99**: 2878.

6. Rovere M, Ricci MA, Vellati D, Bruni F. (1998) A molecular dynamics simulation of water confined in a cylindrical SiO₂ pore. *J Chem Phys* **108**: 9859–9867.
7. Delville A. (1993) Structure and properties of confined liquids: A molecular model of the clay-water interface. *J Phys Chem* **97**: 9703–9712.
8. Wiggins PM. (1988) Water-structure in polymer membranes. *Prog Polym Sci* **13**: 1–35.
9. Crupi V, Majolino D, Migliardo P, Venuti V. (2002) Neutron scattering study and dynamic properties of hydrogen-bonded liquids in mesoscopic confinement. 1. The water case. *J Phys Chem B* **106**: 10884–10894.
10. Crupi V, Majolino D, Migliardo P, Venuti V, Wanderlingh U, Mizota T, Telling M. (2004) Neutron scattering study and dynamic properties of hydrogen-bonded liquids in mesoscopic confinement. 2. The zeolitic water case. *J Phys Chem B* **8**: 4314–4323.
11. Erlebacher J, Aziz MJ, Karma A, Dimitrov N, Sieradzki K. (2001) Evolution of nanoporosity in dealloying. *Nature* **410**: 450–453.
12. Gallo P, Ricci MA, Rovere M. (2002) Layer analysis of the structure of water confined in vycor glass. *J Chem Phys* **116**: 342–346.
13. Steytler DC, Dore JC, Wright CJ. (1983) *Neutron Diffraction Studies of Water in Meso- and Micro-Pores*. Taylor & Francis, pp. 1031–1051.
14. Bellissent-Funel M-C. (2001) Structure of confined water. *J Phys-Condens Matter* **13**: 9165–9177.
15. Faraone A, Liu L, Mou CY, Shih PC, Copley JRD, Chen SH. (2003) Translational and rotational dynamics of water in mesoporous silica materials: MCM-41-S and MCM-48-S. *J Chem Phys* **119**: 3963.
16. Takahara S, Sumiyama N, Kittaka S, Yamaguchi T, Bellissent-Funel M-C. (2005) Neutron scattering study on dynamics of water molecules in MCM-41. 2. Determination of translational diffusion coefficient. *J Phys Chem B* **109**: 11231–11239.
17. Akhmatskaya E, Todd BD, Davis PJ, Evans DJ, Gubbins KE, Pozhar LA. (1997) A study of viscosity inhomogeneity in porous media. *J Chem Phys* **106**: 4684–4695.
18. Koone N, Shao Z, Zerda TW. (1995) Diffusion of simple liquids in porous sol-gel glass. *J Phys Chem* **99**: 16976–16981.
19. Barzykin AV, Hashimoto S. (2000) Reaction kinetics in zeolites as a random walk problem: Theory vs. experiment. *J Chem Phys* **113**: 2841–2845.
20. Kainourgiakis ME, Kikkinides ES, Stubos AK, Kanellopoulos NK. (1999) Simulation of self-diffusion of point-like and finite-size tracers in stochastically reconstructed Vycor porous glasses. *J Chem Phys* **111**: 2735–2743.
21. Burganos VN. (1998) Gas diffusion in random binary media. *J Chem Phys* **109**: 6772–6779.
22. Stewart RD, Wilson WE, McDonald JC, Strom DJ. (2002) Microdosimetric properties of ionizing electrons in water: A test of the PENELOPE code system. *Phys Med Biol* **47**: 79–88.

23. Mainardi E, Donahue RJ, Wilson WE, Blakely EA. (2004) Comparison of microdosimetric simulations using PENELOPE and PITS for a 25 keV electron microbeam in water. *Radia Res* **162**: 326–331.
24. Rotureau P, Renault JP, Lebeau B, Patarin J, Mialocq JC. (2005) Radiolysis of confined water: Molecular hydrogen formation. *Chemphyschem* **6**: 1316–1323.
25. Le Caer S, Rotureau P, Brunet F, Charpentier T, Blain G, Renault JP, Mialocq JC. (2005) Radiolysis of confined water: Hydrogen production at a high dose rate. *Chemphyschem* **6**: 2585–2596.
26. Nakashima M, Masaki NM. (1996) Radiolytic hydrogen gas formation from water adsorbed on type Y zeolites. *Radiat Phys Chem* **47**: 241–245.
27. LaVerne JA, Tandon L. (2002) H₂ production in the radiolysis of water on CeO₂ and ZrO₂. *J Phys Chem B* **106**: 380–386.
28. Nakashima M, Tachikawa E. (1983) Hydrogen evolution from tritiated water on silica gel by gamma-irradiation. *Radiochim Acta* **33**: 217–222.
29. Garibov AA, Gezalov KB, Velibekova GZ, Ramazanov MK, Kasumov RD, Agaev TN, Gasanov AM. (1987) Heterogeneous radiolysis of water: Effect of the concentration of water in the adsorbed phase on the hydrogen yield. *High Energy Chem* **21**: 416–420.
30. Chemirsov SC, Werst DW, Trifunac AD. (2001) Formation, trapping and kinetics of H atoms in wet zeolites and mesoporous silica. *Radiat Phys Chem* **60**: 405–410.
31. Tarasov VF, Chemirsov SD, Trifunac AD. (2003) H-atom electron-spin polarization in irradiated water and ice confined in the nanopores of Vycor glass. *J Phys Chem B* **107**: 1293–1301.
32. Thomas JK. (2005) Physical aspects of radiation-induced processes on SiO₂, gamma-Al₂O₃, zeolites, and clays. *Chem Rev* **105**: 1683–1734.
33. Petrik NG, Alexandrov AB, Vall AI. (2001) Interfacial energy transfer during gamma radiolysis of water on the surface of ZrO₂ and some other oxides. *J Phys Chem B* **105**: 5935–5944.
34. Liu X, Zhang G, Thomas JK. (1997) Spectroscopic studies of electron and hole trapping in zeolites: Formation of hydrated electrons and hydroxyl radicals. *J Phys Chem B* **101**: 2182–2194.
35. Foley S, Rotureau P, Pin S, Baldacchino G, Renault JP, Mialocq J-C. (2004) Production and reactivity of hydroxyl radical in nano-confined water.
36. Coudert FX, Boutin A. (2006) Confinement effect on the hydrated electron behaviour. *Chem Phys Lett* **428**: 68–72.
37. Hiroki A, LaVerne JA. (2005) Decomposition of hydrogen peroxide at water-ceramic oxide interfaces. *J Phys Chem B* **109**: 3364–3370.
38. Brunet F, Charpentier T, Le Caer S, Renault JP. (2008) Solid-state NMR characterization of a controlled-pore glass and of the effects of electron irradiation. *Solid State Nucl Magn Reson* **33**: 1–11.

39. Le Caer S, Renault JP, Mialocq JC. (2007) Hydrogen peroxide formation in the radiolysis of hydrated nanoporous glasses: A low and high dose rate study. *Chem Phys Lett* **450**: 91–95.
40. Tachiya M. (1987) Stochastic and diffusion models of reactions in micelles and vesicles. In *Kinetics of Nonhomogeneous Processes. A Practical Introduction for Chemists, Biologists, Physicists, and Material Scientists*, (ed.) Freeman GR, Wiley, New York, pp. 575–650.
41. Barzykin AV, Tachiya M. (2003) Diffusion of probe molecules in polymer gels as observed by fluorescence quenching techniques. *J Phys Chem B* **107**: 2953–2957.
42. Bujan-Nunez MC, Lopez-Quintela MA. (2004) Enhancement of the recollision rate in diffusion-influenced reactions in an inhomogeneous medium. *J Chem Phys* **121**: 886–889.
43. Bujan-Nunez MC, Lopez-Quintela MA. (2005) Diffusion of a Brownian walker in a bidimensional disordered medium constituted by adsorbing spheres suspended in a solvent. *Mol Phys* **103**: 1221–1229.
44. Lindenberg K, Romero AH, Sancho JM. (1998) Nonclassical kinetics in constrained geometries: Initial distribution effects. *International Journal of Bifurcation and Chaos* **8**: 853–868.
45. Monson E, Kopelman R. (2000) Observation of laser speckle effects and nonclassical kinetics in an elementary chemical reaction. *Phys Rev Lett* **85**: 666–669.
46. Ahn J, Kopelman R, Argyrakis P. (1999) Hierarchies of nonclassical reaction kinetics due to anisotropic confinements. *J Chem Phys* **110**: 2116–2121.
47. Suh M, Bagus PS, Pak S, Rosynek MP, Lunsford JH. (2000) Reactions of hydroxyl radicals on titania, silica, alumina, and gold surfaces. *J Phys Chem B* **104**: 2736–2742.
48. Konecny R. (2001) Reactivity of hydroxyl radicals on hydroxylated quartz surface. I. Cluster model calculations. *J Phys Chem B* **105**: 6221–6226.

Chapter 13

Metal Clusters and Nanomaterials: Contribution of Radiation Chemistry

Hynd Remita[†] and Samy Remita[‡]*

1. Introduction

In the last few decades, metal clusters and nanomaterials have attracted increasing attention due to their unique properties which differ from those of the bulk.¹⁻¹² Metal nano-objects are of great interest in the field of nanosciences. They are the ideal structures for fundamental research and applications. Indeed, from the confinement of the charge carriers in such limited objects,¹ one expects a shift of the plasmon resonance absorption,² non-linear optical effects,^{3,4} non-metallic conductivity,⁵ and nanocatalytic effects.⁶ Nanomaterials can have important applications in several fields such as catalysis, electrocatalysis, electronics, optical limitation, biology, etc.

* Corresponding author.

[†] Laboratoire de Chimie Physique, UMR 8000-CNRS, Université Paris-Sud, 91405 Orsay, France. E-mail : hynd.remita@lcp.u-psud.fr

[‡] Chaire de Génie Analytique, EA 4131, Pôle Sciences et Techniques Industrielles STI, Conservatoire National des Arts et Métiers, 292 rue Saint Martin, 75141 Paris Cedex 03, France.

Many physical and chemical routes have been used to obtain metal clusters and nanoparticles either in ultra high vacuum,⁷ gas phase⁸ or liquid phase.^{2,9,10} The method of preparation of nanoparticles in aqueous medium involves reduction of metal precursor salt by a suitable reducing agent (such as sodium borohydride, ascorbic acid, formaldehyde and hydrazine). The reduction of metal precursor salt may also be carried out using UV-irradiation,¹³ microwave radiation¹⁴ and ionizing radiations like γ , X-rays or electron beams.^{11,12} Among these methods, radiolytic synthesis in solution presents the advantage of simple physicochemical conditions (room temperature, atmospheric pressure, absence of contaminants) and leads to homogeneous reduction and nucleation in the bulk.^{9,12}

While steady-state radiolysis of metal ions solutions is a powerful method to generate small and monodisperse metal clusters and to synthesize metal nano-objects with controlled size, shape and structure,^{9,11,12,16} pulse radiolysis technique enables to follow, in particular by time-resolved spectroscopy, the nucleation steps and the growth kinetics of the nanoparticles.^{9,11,12,17}

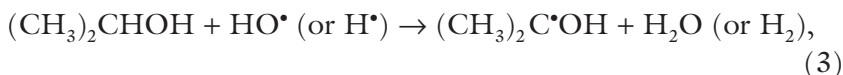
2. Radiation Induced Formation of Metal Clusters and Dose Effect

High-energy irradiation (γ -rays, X-rays, electrons or ions beams, etc.) of deoxygenated water at neutral pH leads to the formation of free radicals such as hydrated electrons (e_{aq}^-) and hydrogen atoms (H^\bullet) which are strong reducing agents with the respective redox potentials: $E^\circ(H_2O/e_{aq}^-) = -2.87 V_{NHE}$ and $E^\circ(H^+/H^\bullet) = -2.3 V_{NHE}$. Energy deposition throughout the solution ensures an initial homogeneous distribution of the radiolytic radicals. These free radicals can reduce dissolved metal ions down to the zero-valent state. In the case of a free or complexed monovalent metal ion M^+ , the reduction proceeds through:

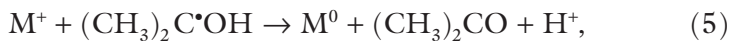


In contrast, multivalent ions are reduced down to the zero-valent state according to a multi-step reaction mechanism involving intermediate valencies by disproportionation. These redox reactions, which are often diffusion-controlled, have extensively been studied by pulse radiolysis in the case of several free or complexed metal ions.

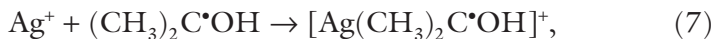
During the irradiation of deoxygenated water, hydroxyl radicals (HO^\bullet), which are very strong oxidative species ($E^0(\text{HO}^\bullet/\text{H}_2\text{O}) = +2.8 \text{ V}_{\text{NHE}}$), are also formed. To avoid competitive oxidation reactions which may limit or even prevent metal reduction, hydroxyl scavengers must be added in solution prior to irradiation. Among these scavengers, primary or secondary alcohols (such as propan-2-ol) molecules or formate ions, which also react with hydrogen atoms, are generally used^{9,12,15}:



Due to their redox potentials [$E^0((\text{CH}_3)_2\text{CO}/(\text{CH}_3)_2\text{C}^\bullet\text{OH}) = -1.8 \text{ V}_{\text{NHE}}$ at pH7,¹⁸ and $E^0(\text{CO}_2/\text{COO}^{\bullet-}) = -1.9 \text{ V}_{\text{NHE}}$],¹⁹ the radicals formed by reactions (3) and (4) are almost as powerful reducing agents as H^\bullet atoms. Thus, in some cases, these radicals are able to directly reduce metal ions into lower valencies and even into a zero-valence state. In the case of monovalent cations:



The reduction down to the zero-valence state can also proceed *via* the formation of a complex involving the metal ion and the alcohol radical as a ligand, as it has been observed in the case of silver²⁰:



Due to the quasi-uniform energy deposition into the irradiated medium, the metal atoms are formed with a homogeneous distribution throughout the solution. Since the binding energy between two metal atoms is stronger than the atom-solvent or atom-ligand interaction energies, the atoms dimerize or associate with excess metal ions after a fast diffusion step. Finally, according to a multi-step coalescence process, metal clusters are formed with a remarkable monodispersity:



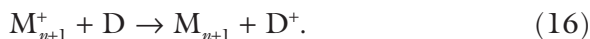
m , n , p and $q = m + p$ represent the clusters nuclearity (number of reduced atoms), while x , y and $z = x + y$ correspond to the number of the respective associated ions.

Increasing the dose (the deposited energy into the irradiated medium, expressed in Grays, $1 \text{ Gy} = 1 \text{ J.kg}^{-1}$) leads to more reduced metal ions and then to more clusters with higher nuclearities.

During the coalescence process, the reducing radicals e_{aq}^- , $(\text{CH}_3)_2\text{C}\cdot\text{OH}$ or $\text{COO}\cdot^-$ which reduce metal ions [reactions (1), (2), (5) and (6)] are also able to reduce metal clusters according to reaction (13). The competition between reduction of free metal ions [reactions (1), (2), (5), (6)] and reduction of adsorbed ions [reaction (13)] is controlled by the formation rate of the reducing radicals. At a high dose rate (expressed in Gy.s^{-1}) and therefore at a high concentration in reducing species, cluster formation proceeds predominantly according to steps (1), (2), (5) and (6). As a consequence, the dose rate has also an effect on the particle size. At high dose rates, the metal ions reduction is faster and a large number of seeds are formed in the bulk. Thus, small particles are radio-synthesized with a narrow distribution in size. In the pulsed regime (at high dose rates), all

reducing species are produced and scavenged within a short time. These reactions are followed by the coalescence of atoms separately created.²¹ In contrast, in the continuous irradiation regime (at lower dose rates), the association of M^+ ions with atoms (forming charged dimers M_2^+ and clusters M_{n+1}^+) and the subsequent coalescence processes are faster than the production rate of the reducing radicals. Therefore, the reduction of M^+ ions occurs mostly *in situ* on charged clusters M_{n+1}^+ already formed. As a consequence, the newly formed atoms are not isolated in the bulk but contribute to the growth of preformed seeds. Thus, the final nuclearity n and the cluster radius, which are proportional to $n^{1/3}$, are found to be systematically larger in the case of steady-state radiolysis.

When a chemical agent generally chosen as an electron donor D is added to the medium, its redox potential ($E^0(D^+/D)$) is in general not negative enough to reduce directly isolated metal ions into atoms. Thus, it essentially reduces ions adsorbed on the nuclei generated by radiolysis which act as seeds [reactions (14)–(16)]. Then a development process occurs which results in still larger clusters^{22,23}:



While steady-state radiolysis enables the synthesis of stable metal clusters in view of their characterization and the study of their physicochemical properties, pulse radiolysis allows the real-time kinetic and spectral study of transient clusters during the aggregation mechanism. For instance, the first steps of silver clusters nucleation have been studied by the teams of A. Henglein,^{24,25} E. Janata²⁶ and J. Belloni^{27,28} using pulse radiolysis, and some of the corresponding rate constants in water have been determined:





Coupling pulse radiolysis with time-resolved spectroscopy also allowed the determination of the transient absorption spectra of hydrated silver atom and of the first silver clusters showing that the absorption properties of silver atoms and metal aggregates in solution are different from that of bare clusters in gas phase. Silver atom presents an absorption maximum at 360 nm in water,²⁰ while it absorbs at substantially shorter wavelengths in argon (292–310 nm) or in xenon (322–333 nm) atmosphere.²⁹

Pulse radiolysis experiments also allowed the study of the reactivity and the redox properties of transient species such as silver atoms and silver clusters. Ag^0 reacts faster than Ag_2^+ and both species act as strong electron donors since their respective redox potentials are $E^0(\text{Ag}^+/\text{Ag}^0) = -1.8 \text{ V}_{\text{NHE}}$,^{30,31} and $E^0(2 \text{ Ag}/\text{Ag}_2^+) = -1.2 \text{ V}_{\text{NHE}}$.¹¹

Radiolysis has been used successfully in order to synthesize various noble (such as silver, gold and platinum) and non-noble (such as nickel and iron) metal nanoparticles in aqueous solution and also in other solvents such as alcohols.^{9,12,15,32} Due to their relatively low redox potential compared to that of the bulk, metal clusters can be oxygen-sensitive. However, the deoxygenation (by bubbling with an inert gas such as argon or nitrogen) of the solutions prior to irradiation and their study under inert atmosphere prevent their oxidation. Moreover, since water radiolysis leads to the formation of protons in addition to that of hydrated electrons, radio-induced acidification of the medium may lead to non-noble metal clusters corrosion. Therefore, to avoid the oxidation by protons, the solutions can be prepared in slightly basic medium.

3. Ligand Effect and Size Control of Metal Nanoparticles

In order to control the size of metal nanoparticles and to avoid cluster coalescence into large colloids, which eventually precipitate, stabilizing

agents can be added to the medium prior to irradiation. Polymers [poly(vinyl)alcohol PVA, polyacrylate PA, poly(acrylamide) PAM, poly(vinyl)pyrrolidone PVP...] or surfactants (sodium dodecyl sulphate SDS, cetyl-trimethylammonium bromide CTAB...) were often used. In these conditions, small metal clusters of a few atoms were successfully stabilized. For instance, PA enabled the synthesis of Pt_{5-7} platinum clusters³³ as well as very stable Ag_7^{3+} silver oligomers as observed by Scanning Tunneling Microscopy (STM) after deposition on highly oriented pyrolytic graphite (HOPG) substrate [Fig. 1(a)].^{34,35} These oligomers are characterized by an unusual absorption maximum at 800 nm.³⁶ As a consequence of the initial homogeneous distribution of metal atoms in solution, the size distribution of the radio-synthesized nanoparticles is often notably narrow in the presence of polymers or surfactants as observed by Atomic Force Microscopy (AFM) [Figs. 1(b) and 1(c)]. Phase imaging in tapping mode AFM is a powerful tool for characterization of clusters stabilized by polymer matrices.³⁷ In the presence of PVA, gold nanoparticles with a remarkable monodispersity in size were synthesized [Fig. 1(c)]. When deposited onto a mica substrate, these

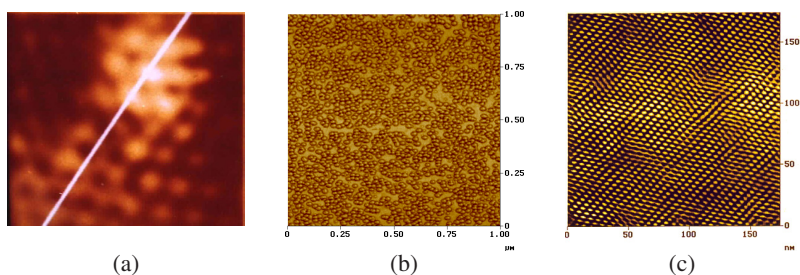


Fig. 1. Examples of metal clusters and nanoparticles synthesized by radiolysis. (a) STM image of a silver oligomer (Ag_7^{3+}) in the presence of PA [reproduced with permission from Ref. 34, copyright 1994 Elsevier]. (b) AFM image of silver nanoparticles stabilized by PVA and deposited onto mica [reproduced with permission from Ref. 12, copyright 2006 Elsevier]. (c) AFM image of gold nanoparticles stabilized by PVA and self-assembled onto mica in a 2D network. [reproduced with permission from Ref. 12, copyright 2006 Elsevier].

nanoparticles self-assemble in two-dimensional (2D) array as shown in [Fig. 1(c)].

When the irradiation is carried out in the presence of ligands such as CO³⁸ or PPh₃,³⁹ metal ion reduction, ligation and aggregation reactions are in competition, leading initially to reduced metal complexes and finally to molecular clusters. Carbonyl metal clusters of different nuclearities were radio-synthesized in alcohols in the case of various metals: Fe₃(CO)₁₂, Co₂(CO)₈, Ru₃(CO)₁₂, H₂Ru₆(CO)₁₈, Rh₆(CO)₁₆, [Rh₁₂(CO)₃₀]²⁻, [Os₅(CO)₁₅]²⁻, Fe₃(CO)₁₂, RuOs₂(CO)₁₂, Ru₂Os(CO)₁₂,... Platinum metal clusters [Pt₃(CO)₆]_{*n*}²⁻ (*n* = 2–10) were synthesized by irradiation of Pt^{II} or Pt^{IV} complexes in 2-propanol or in an equivolumic water/alcohol mixture under CO atmosphere.⁴⁰ Under these conditions, an additional reducing effect of CO exists. The synthesis is very selective and the nuclearity *n* is controlled by the dose and by the metal-to-ligand ratio. These molecular clusters exhibit two very intense UV–visible absorption bands (their positions depend on the nuclearity). Pulse radiolysis study indicated that these species are very efficient electron scavengers.^{41,42}

The growth kinetics as well as the thermodynamic and spectral properties of metal clusters depend not only on the solvent, but also on the chemical nature of the anionic ligands present in the irradiated solutions. In the case of silver ions reduction, ligand effect was studied by pulse radiolysis.^{43–45} It was demonstrated that the optical properties of silver atom and of Ag₂⁺ cation depend on the ligand present in the medium (CN⁻, EDTA or NH₃). The absorption bands of the complexed Ag⁰ and Ag₂⁺ species are markedly shifted compared to those of the non-coordinated ones.⁴⁵ Also, it was shown that the redox potentials of complexed silver clusters are more negative than that of free ones.^{45,46} While pulse radiolysis experiments showed that complexation of silver ions by anionic ligands decreases the formation rate of silver atoms⁴⁴ and slows down the aggregation process, steady-state radiolysis demonstrated that chelating ligands such as EDTA lead to nanoparticles of controlled shapes. The latter are spherical or anisotropic depending on the pH conditions.⁴⁶

4. Size-Dependent Properties

There is a considerable amount of interest in nanoparticles as a distinct state of matter, with particular attention paid to their structure and reactivity. The unique properties of very small metal nanoparticles originate from the size-dependent distribution of the electron energy levels and in quantum-size effects. In particular, silver nanoparticles are of great interest because of their optical properties, their application in photographic process and also for their usage as substrates for surface-enhanced Raman spectroscopy.⁴⁷ Gold nanoparticles^{23,48,49} have attracted much attention because of their application in catalysis^{50,51} as well as in imaging, cancer diagnostic and therapy.⁵² A large attention is also paid to the magnetic nanoparticles, such as those containing iron, because of their industrial application in the field of magnetic data storage.⁵³

Nano-objects made out of noble metal atoms have proved to present specific physicochemical properties linked to their dimensions. In metal nanoparticles, collective modes of motion of the electron gas can be excited. They are referred to as surface plasmons. Metal nanoparticles exhibit surface plasmon spectra which depend not only on the metal itself and on its environment, but also on the size and the shape of the particles.^{54,55} Pulse radiolysis experiments enabled to follow the evolution of the absorption spectrum during the growth process of metal clusters.^{9,11,56} Inversely, this spectral signature made it possible to estimate the metal nanoparticles size and shape as a function of the dose in steady-state radiolysis.

Baxendale *et al.* observed, by pulse radiolysis, that Ag^0 as well as Ag_2^+ , produced by the scavenging of hydrated electrons e_{aq}^- and H^\bullet radicals, were easily oxidized by oxygen back to Ag^+ .⁵⁷ This observation demonstrated that the silver atom and the first oligomers deviate from the known noble character of bulk silver. In the case of Cu^+ irradiated in liquid ammonia, no stable copper clusters were formed. However, molecular hydrogen was instead produced, as a consequence of copper corrosion in its nascent state.⁵⁸ Therefore it was

postulated that metal clusters of a few atoms present a redox potential lower than the bulk metal, making them easily oxidizable by oxygen or by solvents. Besides, Walker *et al.* determined, by photoionization of transient zerovalent silver clusters, that their redox potential was lower than that of the bulk metal.⁵⁹ The redox potential of silver atoms in water was then derived by Henglein *et al.* from a thermodynamical cycle: it was found to be equal to $E^\circ(\text{Ag}^+/\text{Ag}^0) = -1.8 \text{ V}_{\text{NHE}}$ [2.6 V lower than that of the bulk metal $E^\circ(\text{Ag}^+/\text{Ag}_{\text{met}}) = 0.79 \text{ V}_{\text{NHE}}$].⁶⁰

Evidently, the redox potential values of clusters must be comprised between the limit values of the atom and the bulk metal. As the other physicochemical properties, redox potentials of clusters depend on their nuclearity, mostly at low n (Fig. 2).^{12,17} Kinetic studies, through time-resolved techniques, allowed to derive redox properties of transient clusters M_n . For this purpose, a redox couple D^+/D (D being an electron donor) with a known and appropriate redox

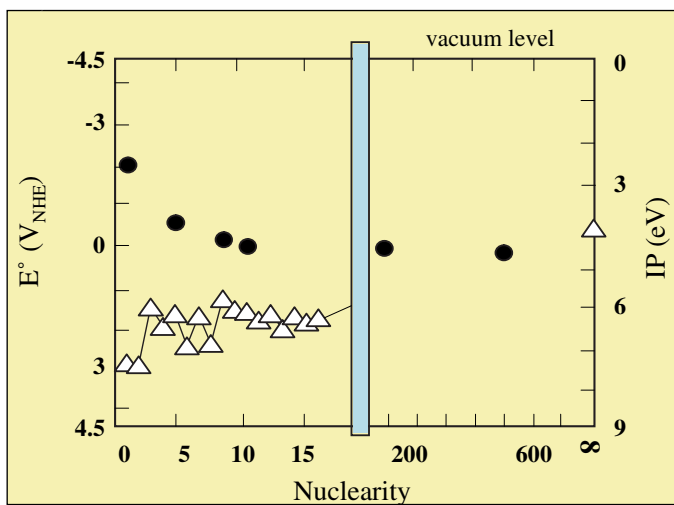


Fig. 2. Size-dependence of the redox potential of silver clusters in water (\bullet)^{24,61–63} and of the ionization potential of silver clusters in the gas phase (Δ) [modified with permission from Ref. 12, copyright 2006 Elsevier].^{64,65} The redox potentials refer to the normal hydrogen electrode (NHE) which is at 4.5 eV above vacuum.

potential was used in real time to estimate the redox potential of M_n^+/M_n . The electron donor D (chosen as reference) was generated during pulse radiolysis. During the cluster coalescence the redox potential $E^0(M_n^+/M_n)$ increases and the effective electron transfer from D to M_n^+ was observed after a critical time t_c , when the size-dependent cluster potential becomes higher than the threshold potential imposed by the reference. The process was followed by the kinetic evolution of the system D^+/D , which was also selected for its intense optical absorption properties. The critical size n_c was derived from t_c and from the aggregation kinetics. As far as $n < n_c$, the cluster growth is observed and the absorbance of D remains constant. However, when $n > n_c$, D starts to decay due to an electron transfer from D to M_n^+ [reactions (14)–(16)].

By changing the reference potential in a series of redox monitors, it is then possible to determine the dependence of the cluster potential on the nuclearity. The general trend of increasing redox potential with nuclearity is the same for all metals in solution as it is illustrated in Fig. 2 in the case of $E^0(\text{Ag}_n^+/\text{Ag}_n)_{\text{aq}}$. However, in gas phase, the variation of the ionization potential $\text{IP}_g(\text{Ag}_n)$ exhibits the opposite trend versus the nuclearity n . Indeed, since the Fermi potential of the normal hydrogen electrode (NHE) in water is 4.5 eV, and since the solvation free energy of Ag_n^+ decreases with size as deduced from the Born model, one can explain the two opposite variations with size of $E^0(\text{Ag}_n^+/\text{Ag}_n)_{\text{aq}}$ and $\text{IP}_g(\text{Ag}_n)$ as illustrated in Fig. 2.

Important consequences result from the increase of the redox potential of metal clusters with their nuclearity. Indeed, independently of the metal, the smaller clusters are more sensitive to oxidation and can undergo corrosion even by mild oxidizing agents. Moreover, size-dependent redox properties explain the catalytic efficiency of colloidal particles during electron transfer processes. Their redox potentials control their role as electron relays: the required potential being intermediate between the thresholds of the potentials of the donor (more negative) and of the acceptor (more positive). Catalytic properties of the nanoparticles are thus size-dependent. Haruta and co-workers^{66,67} reported that gold nanoparticles smaller than 5 nm have potential applications in catalysis as they are very active in

CO oxidation when deposited on Co_3O_4 , Fe_2O_3 , or TiO_2 . Electrocatalytic properties can also be related to the particle size. It was shown for example that Pt nanoparticles synthesized by radiolysis and supported on graphite powder exhibit different activities toward the hydrogen evolution reaction (HER) depending on their size and their surface morphology.⁶⁸

5. Bimetallic Nanoparticles Synthesis and Dose Rate Effect

Nanoscale materials such as multimetallic nanoparticles, particularly when alloyed, are of great importance due to their diverse range of electrical, optical, and catalytic properties. Bimetallic nanoparticles often exhibit enhanced catalytic reaction rates and better selectivity compared to the monometallic compounds. Such mixed nanoparticles were successfully synthesized by irradiating a solution containing a mixture of two (and even more) metal ions M^{x+} and M^{y+} precursors. Different bimetallic systems were studied, such as Ag/Pd, Au/Pd and Ag/Au nanoparticles. However, depending on the experimental conditions, both situations of alloyed or, more often, core-shell nanoparticles can be obtained.

5.1. *Ag/Pd system*

Synthesis of alloyed silver–palladium bimetallic nanoparticles was achieved by γ -irradiation of aqueous solutions containing a mixture of Ag^{I} and Pd^{II} metal ions using different Ag/Pd ratios.⁶⁹ The synthesis of alloys implies the simultaneous radio-induced reduction of silver and palladium ions. The nanoparticles were characterized by UV–visible spectroscopy, transmission electron microscopy (TEM) and energy dispersive X-ray spectroscopy (EDS). The Ag–Pd nanoparticles display a face-centered cubic (fcc) crystalline structure. The lattice parameter was measured for several Ag/Pd ratios and was found to closely follow Vegard's law, which indicates the formation of homogeneous alloys.⁷⁰ In order to avoid the simultaneous reduction of silver and palladium ions which leads to alloyed bimetallic nanoparticles,

the synthesis of bilayered $\text{Ag}_{\text{core}}-\text{Pd}_{\text{shell}}$ nanoparticles was achieved by the radio-induced reduction of Pd^{II} ions onto pre-formed silver clusters.⁷¹

5.2. Au/Ag system

Synthesis of gold–silver bimetallic nanoparticles was achieved by γ -irradiation of aqueous solutions containing an equimolar mixture of Au^{III} and Ag^{I} metal ions (the precursors being KAuCl_4 and Ag_2SO_4) in the presence of PVA at a dose rate of $3.8 \text{ kGy}\cdot\text{h}^{-1}$.⁷² Figure 3(a) displays the evolution of the corresponding optical absorption spectra with increasing γ -irradiation doses. At low doses (up to 2 kGy), the optical absorption spectrum is identical to that of pure gold clusters, displaying a plasmon band at a maximum wavelength of 520 nm. Moreover, EDAX (Energy Dispersive X-Ray Analysis) analysis of the corresponding nanoparticles clearly indicates the predominance of gold within the clusters. At higher doses, the absorption intensity still increases but the absorption maximum progressively shifts to a wavelength of 430 nm, which corresponds to the plasmon absorption band of silver, the colloidal solution turning from pink to yellow. This shift indicates that the surface composition of the nanoparticles changes with the dose. At low doses, gold nanoparticles are obtained, whereas at higher doses $\text{Au}_{\text{core}}-\text{Ag}_{\text{shell}}$ nanoparticles are formed with increasing silver thickness.⁷² This core–shell structure is confirmed by EDAX analysis. The reduction of gold ions is thus more efficient than that of silver. In this case, the reduction process is controlled by the redox potentials of both silver and gold systems. The initially reduced silver atoms are reoxidized in a further step through an electron transfer to gold ions as far as gold ions are present in solution. Then, when gold is completely reduced, the silver reduction must occur efficiently, in particular at the surface of gold clusters where silver ions are adsorbed, leading to core–shell nanoparticles.

At the same dose rate, when the metal ionic precursors are gold and silver cyanides, bimetallic nanoparticles are still formed. However, $\text{Ag}_{\text{core}}-\text{Au}_{\text{shell}}$ nanoparticles with a different chemical structure are obtained, indicating the more efficient silver reduction in these

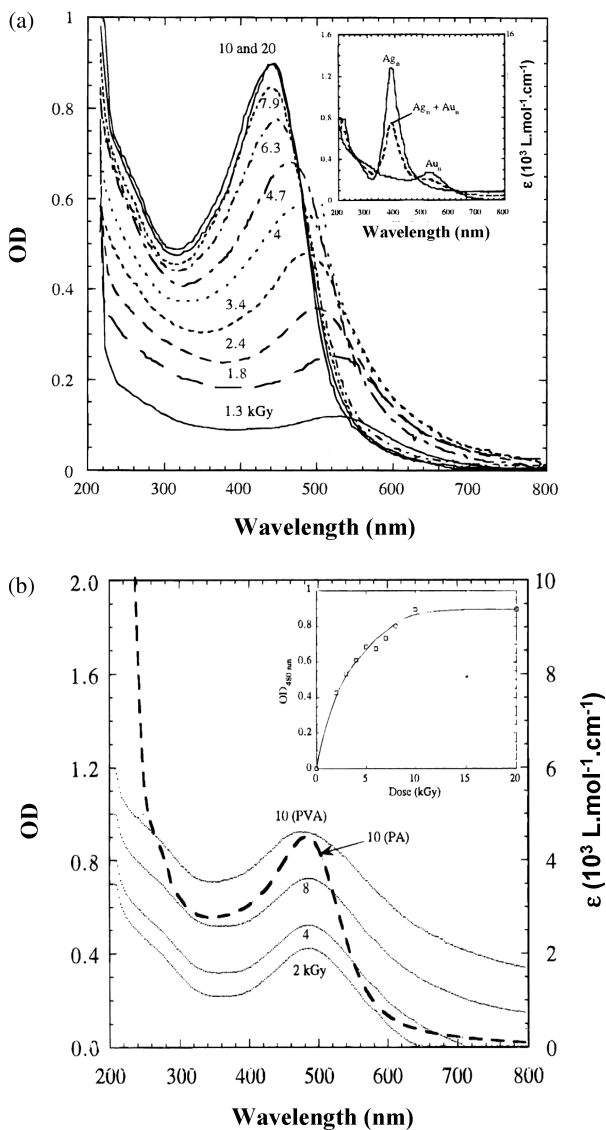


Fig. 3. Evolution with increasing γ -dose of the absorption spectra of an aqueous solution containing: $[\text{Au}^{\text{III}}] = [\text{Ag}^{\text{I}}] = 5 \times 10^{-4} \text{ mol L}^{-1}$, $[\text{PVA}] = 0.1 \text{ mol L}^{-1}$, $[\text{propan-2-ol}] = 0.2 \text{ mol L}^{-1}$, at pH10. Optical length = 2 mm [modified with permission from Ref. 72, copyright 1998 American Chemical Society]. (a) Dose rate of 3.8 kGy.h⁻¹. Inset: plasmon absorption spectra of pure silver and pure gold nanoparticles. (b): Dose rate of 35 kGy.h⁻¹. Inset: Evolution with the dose of the absorbance at $\lambda = 480$ nm.

experimental conditions.⁷³ This can be understood in terms of metal complexation by the cyanide ligands which displace the redox potentials of gold and silver systems, gold behaving in this case as the less noble metal. A pulse-radiolysis study of this mixed $\text{Au}^{\text{I}}/\text{Ag}^{\text{I}}$ system provided the first time-resolved observation of an intermetallic electron transfer. At short time, both types of metal atoms are formed. However, at the scale of seconds, the intensity of the silver plasmon band increases slowly concomitantly with the decay of the plasmon band of gold. This is due to the electron transfer from gold atoms to silver ions in the presence of cyanide ligands.

When aqueous solutions containing an equimolar mixture of Au^{III} and Ag^{I} (the precursors being KAuCl_4 and Ag_2SO_4) are irradiated at a higher dose rate ($35 \text{ kGy}\cdot\text{h}^{-1}$), the absorption spectrum, characterizing the radio-synthesized nanoparticles, does not shift with the dose while its intensity progressively increases [Fig. 3(b)]. The absorption spectrum displays a constant maximal wavelength of 480 nm, which is an intermediate value between the absorption maxima of pure silver and pure gold [Fig. 3(b)]. This spectral evolution, which differs from the one obtained at lower dose rate, indicates that the surface composition of the nanoparticles does not change with the dose. In addition, the local X-ray analysis shows that the ratio gold to silver is 1:1 and that it is homogeneous along the diameters of the nanoparticles.⁷⁴ Thus, at high dose rate, the radio-induced reduction of metal ions is faster than the inter-metallic electron transfer leading, in these experimental conditions, to alloyed nanoparticles.

5.3. *Au/Pd system*

Due to a kinetic competition between inter-metallic electron transfer and radiation-induced reduction of mixed metal ions, it was shown, thanks to radiolysis, that the core-shell or alloyed structure of a bimetallic nanoparticle depends not only on the redox potentials of the mixed systems but also on the metal ions reduction rate which is controlled by the dose rate.

While γ -radiolysis at relatively low dose rates enabled the synthesis of a few alloyed clusters such as Ag–Pd nanoparticles (also chemically synthesized), radiolysis at very high dose rates (by electron beams) led to the synthesis, at room temperature, of a lot of new alloys such as Au–Pd bimetallic nanoparticles.⁷⁵ Like in the case of Ag–Au system, at low dose rate (γ -irradiation), bilayered $\text{Au}_{\text{core}}\text{-Pd}_{\text{shell}}$ nanoparticles were obtained. However, at high dose rates (electron beams), the reduction is faster than the possible inter-metal electron transfer, then alloyed clusters were prepared. Moreover, since the radio-induced reduction of metal ions is faster at high dose rates, the synthesized particles are, in these conditions, always smaller with a narrow distribution in size.

6. Linear Energy Transfer (LET) Effect

There are only very few studies concerning the effect of LET on the formation yield, as well as on the size and the structure of metal nanoparticles.⁷⁶ However, monometallic silver and bimetallic gold–platinum nanoparticles were successfully synthesized, in aqueous solution, using a C^{6+} -ion-beam irradiation at high dose rate, at Grand Accélérateur National d'Ions Lourds (GANIL, Caen, France). The results were compared to those obtained in the case of γ -rays and electron beam irradiations. This work gave further evidence of the effect of the irradiation dose rate on the mean size and on the structure of the radio-synthesized nanoparticles. As the dose rate increases, the particles become smaller and less dispersed in size (Fig. 4). In addition, in the case of bimetallic systems, such as Au–Pt, alloyed structures were obtained using C^{6+} ion beam, while at low dose rate, bilayered $\text{Au}_{\text{core}}\text{-Pt}_{\text{shell}}$ nanoparticles had been formed. Moreover it was shown that the LET seems to have an influence on the shape of the particles which appear less spherical. Nevertheless, the most important effect of the LET concerns the formation yield of the metal nanoparticles since the radiolytic reduction yield decreases at high LET.⁷⁶

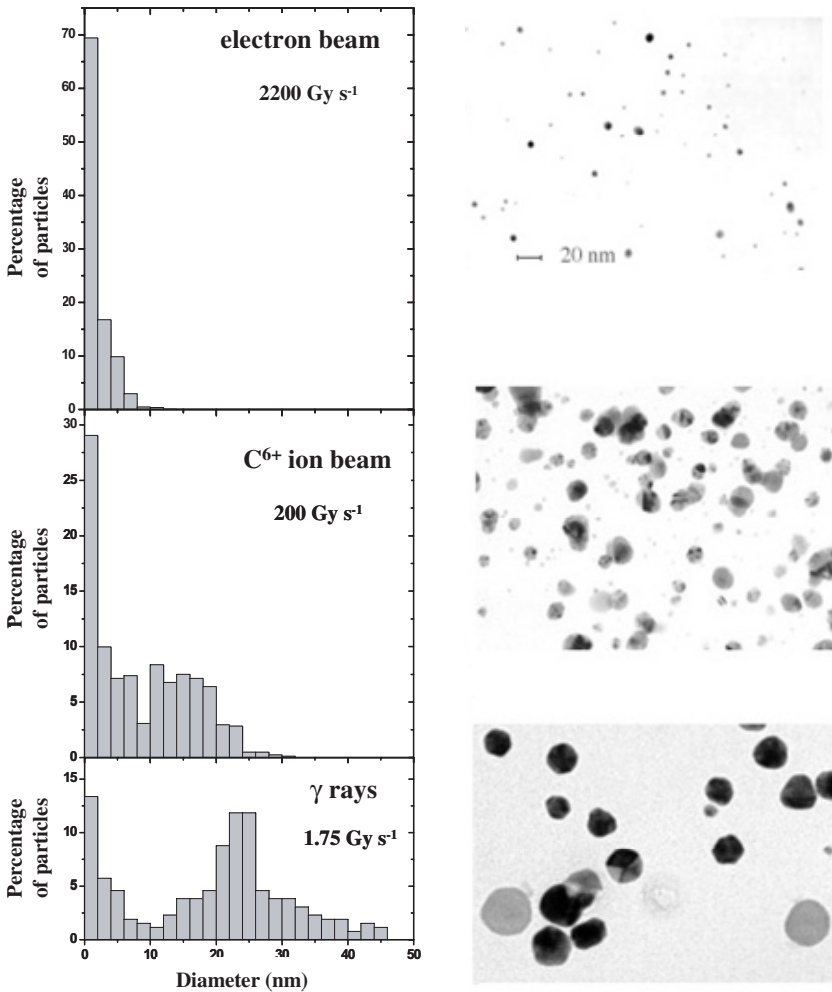


Fig. 4. TEM micrographs and size distribution of silver nanoparticles obtained by reduction of solutions containing 2×10^{-3} -M AgClO_4 , 0.1-M PVA and 2-M propan-2-ol at different dose rates: γ -irradiation (dose rate: 1.75 Gy s^{-1} , dose: 4200 Gy), electron beam irradiation (dose rate: 2200 Gy s^{-1} , dose: 3500 Gy), C^{6+} ion beam irradiation (flux: $1.35 \times 10^9 \text{ ions.cm}^{-2}.\text{s}^{-1}$, fluence: $27 \times 10^{10} \text{ ions.cm}^{-2}$). The scale is the same for the three micrographs [modified with permission from Ref. 76, copyright 2006 Elsevier].

7. Some Applications of Metallic and Bimetallic Nanoparticles

7.1. *Silver photography*

A growth mechanism similar to that established for silver clusters in solutions was proposed for Ag nucleation in silver halides.^{77,78} During light exposure, a few silver atoms (0 to 10) are produced by the photoelectrons in silver halide microcrystals leading to small clusters. This latent image is revealed by a further chemical reduction of silver ions on the seeds, this process being called development. This step results in a huge amplification ($\times 10^7$ to 10^8) together with a specific discrimination preventing the unexposed parts of the latent image, which is finally dissolved during the fixing step. Pulse radiolysis experiments showed that this chemical development only occurs for a critical size of silver oligomers n_c which depends on the reduction potential of the developer. The discrimination induced by the developer is the consequence of a quantum-size effect on the silver nuclei redox potential which, at the aqueous interface, increases with n . The critical size n_c is determined by the threshold imposed by the first one-electron reduction potential of the developer ($n_c = 3$ to 5 for the usual developers). Only supercritical oligomers Ag_n , with $n > n_c$, having a potential higher than that of the developer, act as seeds. Most of the commercial emulsions are sensitized by ions of more noble metals such as gold. In this case, the nuclearity-dependent potential scale of the initial alloyed clusters, acting as further development nuclei, is somewhat shifted to more positive values. This results in a decrease of the critical size n_c from five (for primary emulsions) to three in the case of sensitization by gold.⁷⁹

Another important contribution of radiation chemistry in photography was the enhancement of the sensitivity of photographic emulsions. The primary effect of photon absorption by silver halides is the formation of an electron-hole pair. However, because of the very fast and efficient electron-hole recombination and oxidation by hole of the newly formed silver atoms, the conversion yield of light is very low. The analogy with HO^\bullet oxidation processes occurring in irradiated solutions led to the use of the same scavenging method to inhibit the electron-hole pair recombination and the oxidation by the

holes.⁸⁰ Doping silver halides with formate ions ($\text{HCOO}^-/\text{Ag}^+ = 10^{-6}$) resulted in a huge enhancement of the conversion light quantum yield from 0.2 to 2. The holes produced by light, simultaneously with electrons, are immediately and very efficiently scavenged by the formate ions to produce formyl radicals. Then a supplementary reduction of Ag^+ occurs by the strong reducing formyl radicals. This remarkable enhancement in sensitivity is applicable to all the processes based on silver imaging such as black-and-white photography, radiography and holography.⁸⁰

7.2. Raman scattering

The observation of the Raman spectra of single molecules by Surface Enhanced Raman Scattering (SERS) initially reported by Kneipp's and Nie's groups generated considerable renewal of interest in SERS.^{81,82} The need for substrates enabling detection and study of adsorbed molecules by SERS promoted a great deal of interest in metal nanoparticles. In particular, silver and gold nanoparticles are widely exploited as solid substrates to study *in situ* the molecular chemisorption or physisorption through highly sensitive SERS.⁸³ Pulse radiolysis allowed the SERS observation of *p*-benzosemiquinone radical anion produced by one-electron reduction of *p*-benzoquinone on aqueous silver nanoparticles.⁸⁴ Giant enhancement factor of Raman signals was reported on faceted silver nanoparticles synthesized by gamma-radiolysis followed by a chemical development by ethylenediaminetetraacetic acid (EDTA).^{46,85} On these faceted particles, when Ag^+ ions are reduced, SERS enhancement is much lower. The hot spots exhibiting giant signals seem to be located on adsorbed Ag^+ . This photo-oxidative character of the sites that exhibit giant enhancement of Raman signal could be an important factor in SERS signals.⁸⁵

7.3. Optical limitation

At low light fluence, metal nanoparticles behave like other molecules, and their optical absorbance is independent of the exciting light fluence because of their fast relaxation. However at high light fluence

($\geq 0.9 \text{ J.cm}^{-2}$) delivered by a picosecond laser, the absorbance of gold nanoparticles, for instance, increases suddenly, particularly for large nanoparticles (15 nm mean radius), indicating a non-linear optical behavior. The metal nanoparticles behave then as ultra-fast optical limiters or shutters, indicating their ability to be used as a shielding against powerful lasers.^{86,87}

7.4. *Catalysis*

Actually, one of the most important applications of metal nanoparticles is in the field of catalysis. Catalysts should offer large specific area in order to accelerate the access of reactants to the active sites. Nanoparticles, such as those synthesized by radiolysis, are thus particularly efficient in a number of reactions. However, catalyzed reactions are controlled not only by the kinetics, but also by the thermodynamics. Thus, due to their redox properties, nanoparticles with small sizes and low polydispersities are able to play a role as intermediate electron relays in an overall electron transfer between a donor and an acceptor.

Radiation-induced nanoparticles and supported catalysts exhibit particularly high efficiency and selectivity, assigned to their small and monodisperse size and possibly to tight bounding to the support. Highly dispersed nickel clusters and intermetallic phases NiCe and Ni₂Ce were obtained by irradiation of Ni(NH₃)₆²⁺ adsorbed on CeO₂.⁸⁸ Their catalytic activity in the benzene hydrogenation reaction is remarkably high and the total conversion into cyclohexane was achieved at a particularly low temperature range.⁸⁸ Ni/ α -Al₂O₃ catalysts synthesized by radiolysis were studied for methane conversion in the vapo-cracking reaction.⁸⁹ The catalytic test showed that the reaction starts at low temperature with a very high selectivity. It was also shown that radiolytically prepared Pt nanoparticles on glass support were active for CO oxidation at temperatures higher than 150°C.⁹⁰

Bimetallic nanoparticles constitute suitable model systems for studying alloying effects in catalysis. In particular, palladium-based bimetallic systems were developed in order to increase the selectivity

of the hydrogenation of but-1,3-diene which is the main impurity in olefin C4's cut. The activity and selectivity of Au/Pd and Ag/Pd bimetallic nanoparticles, synthesized by γ -radiolysis or by electron beam irradiation and deposited on alumina for selective hydrogenation of the buta-1,3-diene, were recently studied.⁷¹ The effect of the structure (core-shell or alloyed) was analyzed. Au/Pd bimetallic system exhibited different activities depending on the nanoparticles structure and composition. Ag/Pd bimetallic nanoparticles, radio-synthesized by electron-beams, exhibited a high selectivity compared to conventional bimetallic catalysts prepared by chemical methods.⁷¹

7.5. *Electrocatalysis and fuel cells*

Radiolysis was also used to graft metal nanoparticles onto anodes or cathodes involved in the electrochemical chlorine-soda process.⁹¹ Bimetallic nanoparticles Pt-Ru and Ni-Ru grafted onto bulk metal electrodes (Ti or Ni) displayed a remarkable electro-catalytic efficiency for this reaction and a drastic decreasing of the overpotential was observed for Pt-Ru alloys (2:1 atomic ratio).

Pt-based electrocatalysts are usually employed in proton exchange membrane fuel cells (PEMFC) and direct methanol fuel cells (DMFC).⁹² In direct-methanol fuel cells (DMFCs), aqueous methanol is electro-oxidized to produce CO₂ and electrical current. To achieve enhanced DMFC performance, it is important to develop electro-catalysts with higher activity for methanol oxidation. Pt-based catalysts are currently favored for methanol electro-oxidation. In particular, Pt-Ru catalysts, which gave the best results, seem to be very promising catalysts for this application. Indeed, since Pt activates the C-H bonds of methanol (producing a Pt-CO and other surface species which induces platinum poisoning), an oxophilic metal, such as Ru, associated to platinum activates water to accelerate oxidation of surface-adsorbed CO to CO₂.⁹³

Highly monodispersed platinum-based nanoparticles Pt, Pt-Ru, Pt-Ru-Sn^{9,40,94} were synthesized by γ - or electron beam-radiolysis and then deposited onto Vulcan carbon powder with high loadings (up to

40 wt.% Pt) without noticeable increase in particle sizes (1–4 nm). It was shown that these platinum-based catalysts are very efficient for methanol electro-oxidation. The bi- and tri-metallic clusters synthesized by electron-beams are more electro-active than the ones prepared by γ -radiolysis, probably because of their alloyed structure. The optimized atomic compositions are $\text{Pt}_{0.70}\text{Ru}_{0.15}\text{Sn}_{0.15}$ and $\text{Pt}_{0.70}\text{Ru}_{0.20}\text{Sn}_{0.10}$ which exhibit higher current densities.⁹

Besides, it has been shown that palladium is promising for direct alcohol fuel cells applications as it is very active for ethanol electro-oxidation in basic media and that its electroactivity is even higher than that of platinum.⁹⁵ Recently, Pd nanoballs and nanowires synthesized by radiolysis in hexagonal mesophases have shown an important electrocatalytic activity for ethanol electro-oxidation.^{98,99}

In the field of electrocatalysis, there is now an increasing interest in synthesizing carbon nanotubes (CNT)-metal nanocomposites.^{100–102} Indeed, because of their large surface areas and their high electric conductivity, the CNT are very promising supporting materials for metal nanoparticles-based catalysts, such as Pt and Pd. Well dispersed and uniform Pt nanoparticles supported on multi-walled carbon nanotubes (MWNTs) were obtained by radiolysis.¹⁰³ Test runs on a single stack proton exchange membrane fuel cell showed that these electro-catalysts are very promising for fuel cell applications. Functionalization of multi-walled carbon nanotubes, by surfactants which self-assemble on MWNTs into rings,¹⁰⁴ allowed more effective and more homogeneous deposition of nanoparticles by γ - and electron beam-radiolysis, as it was shown with Pd and Pt for example.¹⁰⁵

8. Shape Effect and Shape Control Metal Nano-Objects

Synthesis of metal nanostructures with tunable properties (optical, magnetic, electronic, catalytic, etc.), in specific physicochemical environments, is today of great importance from a fundamental as well as an applied point of view. Since the physicochemical properties of nanostructures are strongly dependent not only on the size but also on the shape, controlling the architecture of metal nanoparticles

(nanospheres, nanowires, nanotubes, nanoshells, nanocups, nanofilms, etc.) becomes a fascinating challenge.¹⁰⁶ The aspect ratio of the nanoparticles is not only controlled by the environment (polymers or surfactants, nature of the counterions, ions and polymers concentrations), but also by the reduction kinetics. The first nucleation steps are thus evidently very important in the further growth process and must determine the final shape of the nanoparticles.¹⁰⁷ As an example, it was shown that trimeric clusters Ag_3^+ or Ag_3 , present in aqueous AgNO_3 solutions, can serve as nuclei for the addition of newly formed silver atoms and may lead to the formation of triangular nanoplates. It was also demonstrated that slow generation of silver atoms in solution with a kinetically controlled process can lead to the formation of platelike nanostructures.

Metal nanoparticles with high aspect ratios are usually produced in the presence of ligands⁴⁶ or surfactants,¹⁰⁸ sometimes with the aid of preformed seeds and more often by wet chemistry. Steady-state radiolysis allowed the synthesis of very anisotropic silver nanoparticles in the presence of ligands such as EDTA, as observed by Transmission Electron Microscopy (TEM)⁴⁶ [Fig. 5(a)]. Surfactants (such as CTAB) can adsorb on specific faces favoring the growth of metal nanoparticles in one preferential direction.¹⁰⁸ Particle shape anisotropy can improve the outstanding properties of a metal such as platinum in catalysis and in CO chemisorption. For example, the high catalytic activity of Pt nanowires for water-gas shift reactions has been established by Ichikawa and co-workers.¹⁰⁹ However, there are very few reports dealing with the synthesis of platinum nanorods. Some of these studies were carried out using hard templates like mesoporous silica or carbon nanotubes.^{110,111} Monodisperse single-crystalline platinum nanorods were synthesized by radiolysis through a simple process at room temperature, in CTAB solutions. The complexation of CTA^+ surfactant ions with tetrachloroplatinate anions, in the presence of hexanol, led to the formation of a precipitate with a lamellar crystalline structure. The reduction of Pt(II) metal ions to Pt(0) was carried out using γ -radiolysis. TEM observations of the nanoparticles extracted from the solution, a few days after radiolysis, revealed single-crystalline Pt nanorods, monodisperse in diameter (3–4 nm)

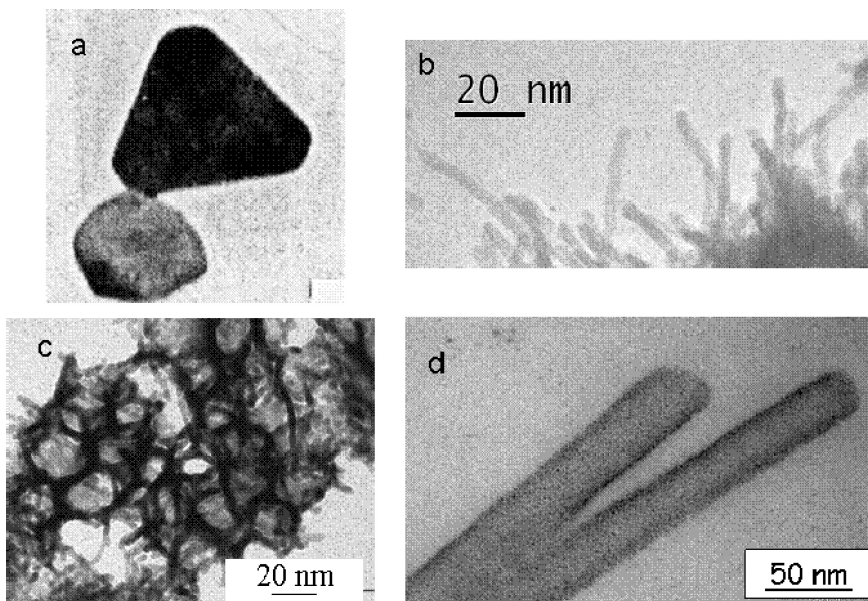


Fig. 5. Metal nanostructures synthesized by radiolysis. (a) Ag triangles stabilized by EDTA [reproduced with permission from Ref. 46, copyright 1994 RSC]. (b) Pt monocrystalline nanorods synthesized by irradiation of the Pt^{II}-CTAB complex [reproduced with permission from Ref. 112, copyright 2006 Wiley-VCH Verlag GmbH & Co. KGaA]. (c) Pt porous nanoballs synthesized in hexagonal mesophases containing CTAB as surfactant [reproduced with permission from Ref. 113, copyright 2007 American Chemical Society]. (d) Pt nanotubes synthesized in hexagonal mesophases containing CPCI (cetylpyridinium chloride) as surfactant.¹³⁸

and 20 to 60 nm long. Shape variation of the nanorods during the nanomaterial growth indicated that the single-crystalline nanorods grow by coalescence of spherical seeds 3–4 nm in diameter [Fig. 5(b)].¹¹²

Palladium nanostructures formed by nanowires, nanoplates or having a flower-like shape were synthesized using γ -radiolysis, by the slow reduction of palladium acetylacetonate in propan-2-ol under CO atmosphere.¹¹⁴ By a fast radiolytic reduction, at much higher dose rate with electron beams, 2-nm nanoparticles were obtained, showing that the dose rate, which determines the reduction kinetics, has an influence

on the nanostructure growth. In these experiments, the presence of CO and the use of low irradiation dose rate favored the formation of anisotropic nanostructures. Like other face-centered cubic (fcc) noble metals, the thermodynamically favorable shapes of Pd nanocrystals are cubooctahedra and multiple twinned particles. The synthesis of Pd nanoplates or nanofoils requires the control of the reduction kinetics, particularly at the seeding stage, as formation of these anisotropic structures becomes favorable in a slow reduction process.^{114–116} When the reduction becomes slow, one can obtain nanoparticles with shapes deviated from the thermodynamic ones.

Anisotropic bimetallic nanoparticles can also be synthesized by radiolysis. Indeed, γ -irradiation of an aqueous solution containing silver and platinum metal ions and a polymer (PVA), at dose rates lower than $0.5 \text{ kGy}\cdot\text{h}^{-1}$, led to the synthesis of wire-like Ag-Pt structures with lengths up to $3.5 \text{ }\mu\text{m}$ and diameters between 3 and 20 nm.¹¹⁷

9. Metal Nanoparticles in Confined Media

An important application of metal nanoparticles is their use as catalysts on solid supports or in confined media. When the solution containing metal ions is in contact with a solid support, the ions can diffuse in the pores and adsorb on the surface. Therefore, the penetration of the ionizing radiation enables the *in situ* reduction of metal ions and then the further coalescence of metal atoms inside the confined volumes of porous materials, such as zeolites, alumino-silica-gels, colloidal oxides such as TiO_2 or polymeric membranes.

Zeolites are attractive host materials as they present regular channel systems, providing crystallographic defined locations for metal clusters. Hence, the size of the clusters inside the zeolites can be limited by the dimensions of their channels and cages. Zeolite-supported noble metal catalysts were extensively studied due to their wide application as catalysts in petroleum industry.¹¹⁸ Reduction of silver in zeolite hosts has been carried out by γ -irradiation.¹¹⁹ The intermediate paramagnetic (charged) silver clusters formed in γ -irradiated silver-exchanged zeolites have been studied by electron spin resonance (ESR)

spectroscopy and diffuse reflectance spectroscopy.¹²⁰ Nanosized zeolites, in water suspensions, were used as host matrix for the stabilization of copper clusters,^{121,122} and platinum nanoparticles were prepared by radiolysis in sodium zeolites A.¹²³

Silver nanoparticles were also synthesized inside mesoporous silica by γ -irradiation.¹²⁴ These hard templates can also be used as nanoreactors to obtain nanomaterials of controlled shapes such as metal nanowires. Ichikawa and co-workers synthesized platinum and palladium nanowires in mesoporous silica FSM-16.^{109,125} However, one drawback of using hard templates lies in the requirement to apply strong chemical treatment such as hydrofluoric acid to get rid of the silica template for extraction of the nanomaterials synthesized within.

Soft templates, as lyotropic liquid crystals, offer a good alternative since they can be easily removed. Hence, mesophases resulting from surfactant self-assembly provide a class of useful and versatile templates for generating 1D, 2D or 3D nanostructures in relatively large quantities. Attard and co-workers demonstrated that liquid crystalline phases made by a ternary mixture (a non-ionic surfactant, hexachloroplatinic acid, H_2PtCl_6 , and water) can be used as “soft” templates for the preparation of nanostructured metals.^{126,127} A large range of nanomaterials were synthesized in reverse hexagonal liquid crystals such as crystalline silver fibers,¹²⁸ platinum and palladium nanorods,¹²⁹ polyaniline nanowires¹³⁰ and semiconductors.^{131–135} Recent studies showed that direct hexagonal mesophases made of a quaternary system (water, surfactant, co-surfactant and oil)^{136–138} can be used as nanoreactors to synthesize nanostructured materials both in the aqueous and in the oil phases such as Pd nanowires, Pd and Pt porous nanoballs made of connected nanowires [Fig. 5(c)], as well as Pt nanotubes [Fig. 5(d)].^{98,99,113,129,139,140} For sensing and catalysis, such materials with three-dimensions open-porosity are favored because they allow the unlimited transport of molecules.¹⁴¹ Compared to chemical reducing processes that follow a diffusion front, radiolysis induces a homogenous nucleation and growth in the whole

volume. As these mesophases can be doped by high concentrations of metal salts (up to 0.2 M), relatively large quantities of metal nanostructures can be obtained.

10. Composite Nanomaterials and “Metal-Organic” Hybrid Nanostructures

Recently, there has been a great interest in the controlled fabrication of composite materials consisting of organic molecules (such as polymers) and metal particles. Such hybrid materials represent a new class of nanomaterials that may combine desirable physical properties characteristic of both organic and metallic components within a single composite. The metallic part offers the potential for a wide range of electrical and optical properties, substantial mechanical hardness and thermal stability; while the organic part can provide high fluorescence efficiency, large polarizability and plastic mechanical properties. Thus, such hybrid nanostructures present unique electronic, photonic, magnetic and catalytic properties. In particular, such composite materials are more attractive to pursue their wide potential applications in the areas of advanced nanoelectronic devices, organic light-emitting diodes, field-effect transistors, non-linear optics, electrochemical sensors and bio-analysis.¹⁴² They may also find a wide range of applications as catalysts, shape-selective adsorbents and capsules for controlled release of therapeutic agents.¹⁴³

PVA was widely used as a matrix for preparation of nanocomposites due to its easy processability, high clarity¹⁴⁴ and biocompatibility.¹⁴⁵ Ag-PVA nanocomposites were prepared by reduction of Ag⁺ ions in PVA aqueous solutions using gamma irradiation followed by solvent evaporation.¹⁴⁶ Ag-PVA hydrogel nanocomposite was obtained by simultaneous reduction of Ag⁺ and cross-linking of PVA by γ -irradiation.¹⁴⁷

Among conductive plastics, polyaniline has attracted much interest because of its environmental stability and its tunable electrical properties. Composite materials consisting of polyaniline nanofibers

decorated with Ag or Au nanoparticles were synthesized by γ -radiolysis.¹⁴⁸ Exposure of the solution to γ -rays in the presence of an oxidant (such as benzoyl peroxide) induced both polymerization of aniline as very thin fibers and formation of metal nanoparticles (decorating the nanofibers). The shape and size of the metal particles can be changed from nanometer-sized spheres to micron-sized dendrites by varying the ratio of aniline to the metal precursor. The electrical conductivity of the composites is up to 50 times higher than that of pure polyaniline nanofibers. In other respects, entrapped silver and gold clusters were successfully formed in a silica aerogel matrix by γ -irradiation of hydrogel precursors loaded with aqueous solutions containing silver and gold metal ions.¹⁴⁹

Recently, radiolysis was used to synthesize metal-organic interfaces using self-assembled surfactant systems dispersed in aqueous solutions (spherical micelles)^{150,151} or self-assembled at the air–water interface (Langmuir monolayers)¹⁵² as templates. Indeed, due to the electrostatic interaction between the polar head-groups of anionic (or cationic) surfactant molecules and cationic (or anionic) metal ions, the radiolysis method provides an atom coalescence localized onto the surface of a direct surfactant self-assembly. Owing to the diversity in surfactant phase diagrams, this approach presents a considerable potential toward the synthesis of metal-organic interfaces with numerous controlled shapes. In a tri-dimensional geometry, irradiating an aqueous solution containing silver ions and spherical linoleate micelles led to the formation of silver nanoshells around the spherical organic cores (Fig. 6).^{150,151} The formation of nanoshells was evidenced by Small Angle X-ray Scattering and cryoelectron microscopy. In a bi-dimensional geometry called “surface radiolysis,” a Langmuir monolayer deposited onto a silver ions containing sub-phase and irradiated by an incident X-ray synchrotron beam impinging below the critical angle for total reflection, induced the formation of a stable nanostructured metal-organic ultra-thin film at the air–water interface (Fig. 7).¹⁵² The formation of the metal layer was *in situ* monitored by X-ray scattering during the radio-induced synthesis process, and the metal film was characterized by AFM after transfer onto a silicon substrate.

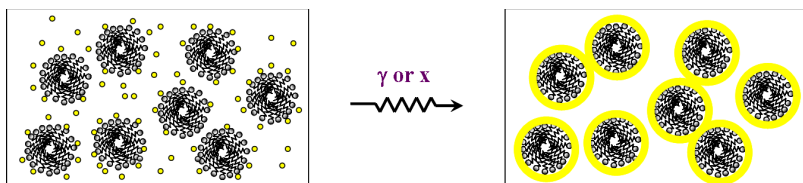


Fig. 6. Schematic view of the formation process of metallic nanoshells around organic micelles in aqueous solution.^{150,151}

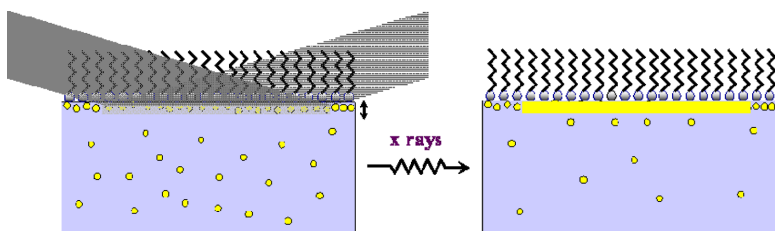


Fig. 7. Schematic view of the formation process of a metal nanofilm at the air–water interface.¹⁵²

11. Electron Beam Lithography

The miniaturization of optical and electronic devices for application in information technology requires a capability to generate nanopatterns on surfaces. Because of their specific conductance^{153,154} and their optical properties,^{155–157} these nanopatterns have promising applications in industry. Tunable metallization by assembly of palladium nanoparticles in poly(methyl methacrylate) (PMMA) thin films were obtained by photo- or electron beam-lithography.¹⁵⁸ Electron beam techniques have considerable potential for formation of small features compared to conventional techniques such as photolithography. Patterned arrays of gold nanoparticles (2 to 4.5 nm in diameter) were prepared by electron beam reduction and subsequent thermolysis of Au(I)-thiolate complexes on silicon surfaces.¹⁵⁹ Variation of electron dose allowed the control of the interparticle distances. High-resolution transmission electron microscopy (HRTEM) results suggested that small gold nuclei are formed during the electron beam reduction step

of Au(I)-thiolates, while the nanoparticles growth occurs during the thermolysis step.

12. Conclusion

Radiation chemistry methods are of high potentiality not only in generating small clusters and metal nanoparticles of homogenous size and shape, but also in studying the nucleation steps and clusters growth. Pulse radiolysis is a powerful tool to study the first nucleation reactions, which are the key parameters to better control the shape and size of nanoparticles. It also provides the means to directly observe, by time-resolved techniques, their nuclearity-dependent properties during the clusters growth, such as the optical absorption spectra and the redox potentials. The dose rate, which determines the number of seeds and the reduction rate, has a large effect on nanoparticles size, structure and shape. In particular, irradiation at high dose rate generates small and homogeneous nanoparticles. Formation of anisotropic shapes needs in general slow reduction on seeds which is achieved at low dose rate in the presence of ligands or surfactants. Irradiation of mixed solutions containing two salts of different metals leads to the formation of bimetallic nanoparticles of controlled structure (core-shell or alloyed), depending on the dose rate. As ionizing rays are highly penetrating, composite materials can also be obtained by radiolytic synthesis. These nanoparticles and nanomaterials can have important applications in several fields: catalysis, electrocatalysis, sensors, electronics, optical limitation, and SERS.

References

1. Porath R, Ohms T, Scharte M, Beesley J, Wessendorf M, Andreyev O, Wiemann C, Aeschlimann M. (2003) In *Low Dimensional Systems: Theory, Preparation and Some Applications*, Liz-Marzan LM, Gierring M. (eds.), p. 227. Kluwer Academic Publishers, Dordrecht, Netherland.
2. Liang HP, Wang LJ, Bai CL, Jiang L. (2005) *J Phys Chem B* **109**: 7795.
3. Brudny VL, Mendoza BS, Mochan WL. (2000) *Phys Rev B* **62**: 11152.
4. Abid JP, Nappa J, Girault HH, Brevet PFJ. (2004) *Chem Phys* **121**: 12577.
5. Henzler M, Lürer T, Burdach A. (1998) *Phys Rev B* **58**: 10048.

6. Narayanan R, El-Sayed MA. (2005) *J Phys Chem B* **109**: 18460.
7. Renaud G, Lazzari R, Revenant C *et al.* (2003) *Science* **300**: 1416.
8. Nepijko SA, Levlev DN, Schulze W, Urban J, Ertl G. (2000) *Chem Phys Chem* **3**: 140.
9. Belloni J, Mostafavi M, Remita H, Marignier JL, Delcourt MO. (1998) *New J Chem* **1239**.
10. Anderson M, Pedersen JS, Palmqvist AEC. (2005) *Langmuir* **21**: 11387; Wang W, Chen X, Efrima S. (1999) *J Phys Chem B* **103**: 7238.
11. Henglein A. (1989) *Chem Rev* **89**: 1861.
12. Belloni J. (2006) *Catal Today* **113**: 141.
13. Henglein A. (1998) *Chem Mater* **10**: 444.
14. Patel K, Kapoor S, Dave DP, Mukherjee T. (2005) *J Chem Soc* **117**: 53.
15. Marignier JL, Belloni J, Delcourt M-O, Chevalier JP. (1985) *Nature* **317**: 344.
16. Remita S, Fontaine P, Lacaze E, Borenzstein Y, Sellame H, Farha R, Rochas C, Goldmann M. (2007) *Nucl Instr Meth B* **263**: 436.
17. Henglein A. (1995) *Ber Bunsenges Phys Chem* **99**: 903.
18. Elliott J, Simon AS. (1984) *Radiat Phys Chem* **24**: 229.
19. Schwarz HA, Dodson RW. (1989) *J Phys Chem* **93**: 409.
20. Tausch-Treml R, Henglein A, Lilie J. (1978) *Ber Bunsenges Phys Chem* **82**: 1335.
21. Belloni J, Mostafavi M. (2001) Metal and semiconductor clusters. In *Studies in Physical and Theoretical Chemistry 87. Radiation Chemistry: Present Status and Future Trends*, Jonah CD, Rao M. (eds.), p. 411, Elsevier.
22. Mostafavi M, Marignier JL, Amblard J, Belloni J. (1989) *Radiat Phys Chem* **34**: 605; Belloni J, Amblard J, Marignier JL, Mostafavi M, La photographie révélée (1990) *La Recherche* **48**: 212; Belloni J, Amblard J, Marignier JL, Mostafavi M. (1991) The principles of photographic development, *Endeavour* **2**: 59.
23. Gachard E, Remita H, Khatouri J, Keita B, Nadjo L, Belloni J. (1998) *New J Chem* **1257**.
24. Ershov BG, Janata E, Henglein A, Fotjtk A. (1993) *J Phys Chem* **97**: 4589.
25. Janata E, Henglein A, Ershov BG. (1994) *J Phys Chem* **98**: 10888.
26. Janata E. (2003) *J Phys Chem* **107**: 7334.
27. Platzer O, Amblard J, Marignier JL, Belloni J. (1992) *J Phys Chem B* **96**: 2334.
28. Amblard J, Platzer O, Ridard J, Belloni J. (1992) *J Phys Chem B* **96**: 2341.
29. Kolb DM, Forstmann F. (1981) In *Matrix Isolation Spectroscopy*, Barnes AJ, Orville-Thomas WJ, Müller A, Gaufres R. (eds.), p. 347. Reidel. Dordrecht.
30. Henglein A. (1977) *Ber Bunsenges Phys Chem* **81**: 556.
31. Dubois V, Archirel P, Boutin A. (2001) *J Phys Chem B* **105**: 9363.

32. Dey GR, Remita H, Mostafavi M. (2006) *Chem Phys Lett* **83**: 431.
33. Keita B, Nadjo L, de Cointet C, Amblard J, Belloni J. (1994) *Chem Phys Lett* **115**: 218.
34. Remita S, Orts JM, Feliu JM, Mostafavi M, Delcourt MO. (1994) *Chem Phys Lett* **218**: 115.
35. Mostafavi M, Keghouche N, Delcourt MO, Belloni J. (1990) *Chem Phys Lett* **167**: 193.
36. Mostafavi M, Keghouche N, Delcourt MO. (1990) *Chem Phys Lett* **169**: 81.
37. Keita B, Nadjo L, Gachard E, Remita H, Khatouri J, Belloni J. (1997) *New J Chem* **21**: 851.
38. Remita H, Derai R, Delcourt MO. (1991) *Radiat Phys Chem* **37**: 221.
39. Derai R, Remita H, Delcourt MO. (1991) *J Chim Phys* **88**: 845.
40. Le Gratiet B, Remita H, Picq G, Delcourt MO. (1996) *Radiat Phys Chem* **47**: 263.
41. Treguer M, Remita H, Pernot P, Khatouri J, Belloni J. (2001) *J Phys Chem A* **105**: 6102.
42. Treguer M, Remita H, Belloni J, de Keyzer R. (2002) *J Imag Sc Tech* **46**: 193.
43. Remita S, Archirel P, Mostafavi M. (1995) *J Phys Chem* **99**: 13198.
44. Remita S, Mostafavi M, Delcourt MO. (1996) *J Phys Chem* **100**: 10187.
45. Mostafavi M, Remita S, Delcourt MO, Belloni J. (1996) *J Chim Phys* **93**: 1828.
46. Remita S, Mostafavi M, Delcourt MO. (1994) *New J Chem* **18**: 581.
47. Tsang JC, Demuth JE, Sanda PN, Kirtley JR. (1980) *Chem Phys Lett* **76**: 54; Freeman RG, Grabar KC, Allison KJ, Bright RM, Davis JA, Guthrie AP, Hommer MB, Jackson MA, Simth PC, Walter DG, Natan MJ. (1995) *Science* **267**: 1629; Stöckle RM, Deckert V, Fokas C, Zenobi R. (2000) *Appl Spectrosc* **54**: 1577; Kobayashi Y, Salgueiriño-Maceira V, Liz-Marzán L. (2001) *Chem Matter* **13**: 1630; Saito Y, Wang JJ, Smith DA, Batchelder DN. (2002) *Langmuir* **18**: 2959.
48. Henglein A, Meisel D. (1998) *Langmuir* **14**: 7392.
49. Daniel MC, Astruc D. (2004) *Chem Rev* **104**: 293.
50. Thompson DT. (2007) *Nanotoday* **2**: 40.
51. Hvolbæka B, Janssensb TVW, Clausenb BS, Falsigc H, Christensenc CH, Nørskov JK. (2007) *Nanotoday* **2**: 14.
52. Huang X, El-Sayed IH, Qian W, El-Sayed MA. (2006) *Abstracts of Papers, 232nd ACS National Meeting*, San Francisco, CA, United States, September 10–14.
53. Huber DL. (2005) *Small* **1**: 482.
54. Mulvaney P. (1996) *Langmuir* **12**: 788.
55. Hodak JH, Henglein A, Hartland GV. (2000) *Pure Appl Chem* **72**: 189.
56. Henglein A. (1989) *Chem Phys Lett* **154**: 473.

57. Baxendale JH, Fielden EM, Keene JP, Ebert M. (1965) In *Pulse Radiolysis*, Keene JP, Swallow AJ, Baxendale JH. (eds.), p. 207. Academic Press, London.
58. Delcourt MO, Belloni J. (1973) *Radiochem Radioanal Lett* **13**: 329.
59. Basco N, Vidyarathi SK, Walker DC. (1973) *Can J Chem* **51**: 2497.
60. von Pukies J, Roebke W, Henglein A. (1968) *Ber Bunsenges Phys Chem* **72**: 842.
61. Khatouri J, Mostafavi M, Amblard J, Belloni J. (1993) *Z Phys D* **26**: 82.
62. Khatouri J, Mostafavi M, Ridard J, Amblard J, Belloni J. (1993) *Z Phys D* **34**: 47.
63. Belloni J, Khatouri J, Mostafavi M, Amblard J. (1993) In *Ultrafast Reactions Dynamics and Solvent Effects*, Rossky PJ, Gauduel Y. (eds.), p. 541. American Institute of Physics.
64. Jackschath C, Rabin I, Schulze W. (1992) *Z Phys D* **22**: 517.
65. Alameddin G, Hunter J, Cameron D, Kappes MM. (1992) *Chem Phys Lett* **192**: 122.
66. Haruta M, Kobayashi T, Sano H, Yamada N. (1987) *Chem Lett* 405.
67. Haruta M, Yamada N, Kobayashi T, Ijima S. (1989) *J Catal* **115**: 301.
68. Remita H, Siril PF, Mbomekalle IM, Keita B, Nadjo L. (2006) *J Sol State Electrochem* **10**: 506.
69. Remita H, Khatouri J, Tréguer M, Amblard J, Belloni J. (1997) *Z Phys D* **40**: 127.
70. Doudna CM, Bertino MF, Tokuhiko AT. (2002) *Langmuir* **18**: 2434.
71. Redjala T, Remita H, Apostolescu G, Mostafavi M, Thomazeau C, Uzio D. (2006) *Oil Gas Sci Technol* **61**: 789.
72. Tréguer M, de Cointet C, Remita H, Khatouri J, Mostafavi M, Amblard J, Belloni J, De Keyser R. (1998) *J Phys Chem B* **102**: 4310.
73. de Cointet C, Mostafavi M, Khatouri J, Belloni J. (1997) *J Phys Chem* **101**: 3512.
74. De Vyt A, Gijbels R, Davock H, Van Roost C, Geuens I. (1999) *J Anal Atom Spectrom* **14**: 499.
75. Remita H, Etchebery A, Belloni J. (2003) *J Phys Chem B* **107**: 31.
76. Remita H, Lampre I, Mostafavi M, Balanzat E, Bouffard S. (2005) *Radiat Phys Chem* **72**: 575.
77. Mostafavi M, Marignier JL, Amblard J, Belloni J. (1989) *Radiat Phys Chem* **34**: 605.
78. Belloni J. (1997) In *Homogeneous Photocatalysis*, Chanon M. (ed.), John Wiley, p. 169.
79. de Cointet C, Mostafavi M, Khatouri J, Belloni J. (1997) *J Phys Chem* **101**: 3512.
80. Belloni J, Tréguer M, Remita H, De Keyser R. (1999) *Nature* **402**: 865.

81. Kneipp K, Wang Y, Kneipp H, Perelman LT, Itzkan I, Dasari RR, Feld MS. (1997) *Phys Rev Lett* **78**: 1667.
82. Nie S, Emory SR. (1997) *Science* **275**: 1102.
83. Tsang JC, Demuth JE, Sanda PN, Kirtley JR. (1980) *Chem Phys Lett* **76**: 54; Freeman RG, Grabar KC, Allison KJ, Bright RM, Davis JA, Guthrie AP, Hommer MB, Jackson MA, Simth PC, Walter DG, Natan MJ. (1995) *Science* **267**: 1629; Stöckle RM, Deckert V, Fokas C, Zenobi R. (2000) *Appl Spectrosc* **54**: 1577; Kobayashi Y, Salgueiriño-Maceira V, Liz-Marzán L. (2001) *Chem Matter* **13**: 1630; Saito Y, Wang JJ, Smith DA, Batchelder DN. (2002) *Langmuir* **18**: 2959.
84. Tripathi GNR. (2003) *J Am Chem Soc* **125**: 1178.
85. Débarre A, Jaffiol R, Julien C, Tchénié P, Mostafavi M. (2004) *Chem Phys Lett* **386**: 244.
86. Francois L, Mostafavi M, Belloni J, Delouis J-F, Delaire J, Feneyrou P. (2000) *J Phys Chem B* **104**: 6133.
87. Francois L, Mostafavi M, Belloni J, Delaire J. (2001) *Phys Chem Chem Phys* **3**: 4965.
88. Chettibi S, Keghouche N, Wojcieszak R, Boudjennad EH, Belloni J, Bettahar MM. (2006) *Catal Today* **114**: 157.
89. Keghouche N, Chettibi S, Latreche F, Bettahar MM, Belloni J, Marignier JL. (2005) *Radiat Phys Chem* **74**: 185.
90. Kapoor S, Belapurkar AD, Mittal JP, Mukherjee T. (2005) *Mat Res Bull* **40**: 1654.
91. Amblard J, Belloni J, Platzer O. (1991) *J Chim Phys* **88**: 835.
92. Hogarth MP, Ralph TR. (2002) *Platinum Metal Rev* **46**: 117.
93. Hogarth MP, Ralph TR. (2002) *Platinum Metals Rev* **46**: 146.
94. Le Gratiet B, Remita H, Picq G, Delcourt MO. (1996) *J Catal* **164**: 36.
95. Gupta SS, Datta J. (2005) *J Power Sources* **145**: 124.
96. Liu J, Ye J, Xu C, Jiang SP, Tong Y. (2007) *Electrochem Commun* **9**: 2334.
97. Xu C, Wang H, Shen PK, Jiang SP. (2007) *Adv Mater* **19**: 4256.
98. Ksar F, Surendran G, Ramos L, Keita B, Nadjo L, Prouzet E, Beaunier P, Hagège A, Audonnet F, Remita H. (2009) *Chem Mater* **21**: 1612.
99. Surendran G, Ksar F, Ramos L, Keita B, Nadjo L, Prouzet E, Beaunier P, Dieudonné P, Audonnet F, Remita H. (2008) *J Phys Chem C* **112**: 10740.
100. Wildgoose GG, Banks CE, Compton RG. (2006) *Small* **2**: 182.
101. Lee Y, Song HJ, Shin H, Shin HJ, Choi HC. (2005) *Small* **1**: 975.
102. Liao S, Holmes KA, Tsapailis H, Birss V. (2006) *J Am Chem Soc* **128**: 3504.
103. Wang H, Sun X, Ye Y, Qiu S. (2006) *J Power Sources* **161**: 839.
104. Mioskowski C. (2003) *Science* **300**: 775.
105. Mackiewicz N, Surendran G, Remita H, Keita B, Zhang G, Nadjo L, Hagège A, Doris E, Mioskowski C. (2008) *J Am Chem Soc* **130**: 8110.

106. Pilleni MP. (2007) *J Phys Chem* **111**: 9019.
107. Xiong Y, Washio I, Chen J, Sadilek M, Xia Y. (2007) *Angew Chem Int Ed* **45**: 4917.
108. Pilleni MP. (2003) *Nat Mater* **2**: 145.
109. Fukuoka A, Higashimoto N, Sakamoto Y, Sasaki M, Sugimoto N, Inagaki S, Fukushima Y, Ichikawa M. (2001) *Catal Today* **66**: 23.
110. Sakamoto Y, Fukuoka A, Higuchi T, Shimomura N, Inagaki S, Ichikawa M. (2004) *J Phys Chem B* **108**: 853.
111. Govindraj A, Satishkumar BC, Nath M, Rao CNR. (2000) *Chem Mater* **12**: 202.
112. Krishnaswamy R, Remita H, Imperor-Clerc M, Even C, Davidson P, Pansu B. (2006) *Chem Phys Chem* **7**: 1510.
113. Surendran G, Ramos L, Pansu B, Prouzet E, Beaunier P, Audonnet F, Remita H. (2007) *Chem Mat* **19**: 5045.
114. Redjala T, Apostolecu G, Beaunier P, Mostafavi M, Etcheberry A, Thomazeau C, Uzio D, Remita H. (2008) *New J Chem* **32**: 1403.
115. Mullin JW. (1961) *Crystallization*. Butterworth, London.
116. Xiong Y, McLellan JM, Chen J, Yin Y, Li ZY, Xia Y. (2005) *J Am Chem Soc* **127**: 17118.
117. Doudna CM, Bertino MF, Blum FD, Tokuhiko AT, Lahiri-Dey D, Chattopadhyay S, Terry J. (2003) *J Phys Chem B* **107**: 2966.
118. Ichikawa M. (1992) *Adv Catal* **38**: 283.
119. Michalik J, Kevan L. (1986) *J Am Chem Soc* **108**: 4247.
120. Michalik J, Sadlo J, Kodaira T, Shimomura S, Yamada HJ. (1998) *Radioanal Nucl Chem* **232**: 135.
121. Kecht J, Tahri Z, De Waele V, Mostafavi M, Mintova S, Bein T. (2006) *Chem Mater* **18**: 3373.
122. De Waele V, Kecht J, Tahri Z, Mostafavi M, Bein T, Mintova S. (2007) *Sensors Actuators, B: Chem* **126**: 338.
123. Vijayalakshmi R, Kapoor D, Kulshreshtha SK. (2002) *Solid State Sciences* **4**: 489.
124. Hornebecq V, Antonietti M, Cardinal Y, Tréguer-Delapierre M. (2003) *Chem Mater* **15**: 1993.
125. Fukuoka A, Hidenobu A, Sakamoto Y, Inagaki S, Fukushima Y, Ichikawa M. (2003) *Inorg Chim Acta* **371**: 350.
126. Attard GS, Göltner CG, Corker JM, Henke S, Templer RH. (1997) *Angew Chem Int Ed Engl* **36**: 1315.
127. Attard GS, Barlett PN, Coleman NRB, Elliott JM, Owen JR, Wang JH. (1997) *Science* **278**: 838.
128. Andersson M, Alfredsson V, Kjellin P, Palmqvist AEC. (2002) *Nano Lett* **2**: 1403.

129. Surendran G, Pena dos Santos E, Tokumoto MS, Remita H, Ramos L, Kooyman PJ, Santilly CS, Bourgaux C, Dieudonné P, Prouzet E. (2005) *Chem Mater* **17**: 1505.
130. Huang L, Wang Z, Wang H, Cheng X, Mitra A, Yan Y. (2002) *J Mater Chem* **12**: 388.
131. Jiang X, Xie Y, Lu J, Zhu L, He W, Qian Y. (2001) *Chem Mater* **13**: 1213.
132. Li Y, Wan J, Gu Z. (2000) *Mater Sci Eng A* **286**: 106.
133. Braun PV, Osenar P, Stupp SI. (1996) *Nature* **380**: 325.
134. Braun PV, Osenar P, Tohver V, Kennedy S, Stupp SI. (1999) *J Am Chem Soc* **121**: 7302.
135. Braun PV, Stupp SI. (1999) *Mater Res Bull* **34**: 463.
136. Ramos L, Fabre P. (1997) *Langmuir* **13**: 682.
137. Ramos L, Fabre P, Ober R. (1998) *Eur Phys B I*: 319.
138. Surendran G, Ramos L, Prouzet E, Remita H. (2006) *NSTI Nanotech* **1**: 38.
139. Pena dos Santos E, Tokumoto MS, Surendran G, Remita H, Bourgaux C, Dieudonné P, Prouzet E, Ramos L. (2005) *Langmuir* **21**: 4362.
140. Surendran G, Apostolescu G, Tokumoto M, Prouzet E, Ramos L, Beaunier P, Kooyman PJ, Etcheberry A, Remita H. (2005) *Small* **1**: 964.
141. Rolison DR. (2003) *Science* **299**: 1698.
142. Lu C, Wu N, Jiao X, Luo C, Cao W. (2003) *Chem Commun* **1056**.
143. Caruso F. (2000) *Chem Eur J* **6**: 413.
144. Tadd E, Zeno A, Zubris M, Dan N, Tannenbaum R. (2003) *Macromol* **36**: 6497.
145. Li Y, Neoh KG, Kang ET. (2004) *Polymer* **45**: 8779.
146. Krkljes AN, Marinovic-Cincovic MT, Kacarevic-Popovic ZM, Nedeljkovic JM. (2007) *Eur Polym J* **43**: 2171.
147. Krklješ A, Nedeljković JM, Kačarević-Popović ZM. (2007) *Polymer Bull* **58**: 271.
148. Pillalamarri SK, Blum FD, Tokuhiko AT, Bertino MF. (2005) *Chem Mat* **17**: 5941.
149. Hund JF, Bertino MF, Zhang G, Sotiriou-Leventis C, Leventis N, Tokuhiko AT, Farmer A. (2003) *J Phys Chem B* **107**: 465.
150. Remita S, Fontaine P, Rochas C, Muller F, Goldmann M. (2005) *Eur Phys JD: Atomic, Molecular and Optical Physics* **34**: 231.
151. Attia J, Remita S, Jonic S, Lacaze E, Faure MC, Larquet E, Goldmann M. (2007) *Langmuir* **23**: 9523.
152. Muller F, Fontaine P, Remita S, Fauré MC, Lacaze E, Goldmann M. (2004) *Langmuir* **20**: 4791.
153. Li CZ, Sha H, Tao NJ. (1998) *Phys Rev B* **58**: 6775.
154. Bietsch A, Schneider MA, Welland ME, Michel B. (2000) *J Vac Sci Technol B* **18**: 1160.

155. Maier SA, Kik PG, Atwater HA, Meltzer S, Harel E, Koel BE, Requicha AAG. (2003) *Nat Mater* **291**: 125, and references therein.
156. Bruzzone S, Arrighini GP, Guidotti C. (2003) *Chem Phys* **291**: 125.
157. Schider G, Krenn JR, Hohenau A, Ditlbacher H, Leitner A, Aussenegg FR, Schaich, WL Puscasu L, Monacelli B, Boreman G. (2003) *Phys Rev B* **68**: 155427.
158. Yin D, Horiuchi S, Morita M, Takahara A. (2005) *Langmuir* **21**: 9352.
159. Corbierre MK, Beerens J, Lennox RB. (2005) *Chem Mater* **17**: 5774.

Chapter 14

Radiation-Induced Oxidation of Substituted Benzenes: Structure–Reactivity Relationship

*B. S. M. Rao**

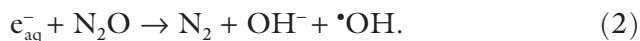
1. Introduction

Radiation-induced oxidation of benzene and its derivatives in aqueous solution has been extensively studied and well documented (see Ref. 1 for a collection of rate constants and visit www.ndrl.edu for an update). However, it still continues to be a fascinating area of research for several reasons. Radiation chemical methods are ideal for generation of the $\cdot\text{OH}$ or one-electron oxidizing radicals in known yields and therefore the evaluation of the kinetics and the stoichiometry becomes easy. Low solute concentrations (≤ 1 mM) — the usual solubility limit of an aromatic compound in water — can be easily employed. The electrophilic nature of the $\cdot\text{OH}$ /oxidizing radical and the availability of a large number of aromatic systems containing electron-donating substituents and/or electron-withdrawing substituents make them particularly suitable for investigating the

* National Centre for Free Radical Research, Department of Chemistry, University of Pune, Pune 411007, India. E-mail: bsmr@chem.unipune.ernet.in

structure–reactivity relationship. This chapter is not a comprehensive review of the published work on radiation-induced chemical oxidation of benzene derivatives, nor does it cover redox properties and energetics of radical cations of substituted benzenes. The latter aspects have already been reviewed by Jonsson^{2(a)} earlier. In a series of papers,^{2(b)–2(d)} Jonsson and co-workers have clearly shown correlations between substituent pattern and redox properties of radical cations of substituted benzenes. Further, it has been shown by them that the product pattern is governed by the charge distribution on the radical cation and the electron density distribution on the corresponding substituted benzene. This chapter is an overview of the work carried out on radiation-induced oxidation of substituted benzenes with emphasis on the contribution to the area from our research group.

The $\bullet\text{OH}$ radical can be easily produced by radiolysis of aqueous solutions saturated with N_2O to scavenge e^-_{aq} [reactions (1) and (2)]:



The one-electron oxidant reactive species $\text{SO}_4^{\bullet-}$ ($E^\circ = 2.5 \text{ V}$) is another radical commonly employed by radiation chemists to mimic the direct effect of radiolysis in dilute aqueous solutions.

2. Experimental Methodology

The experimental methodology in radiation-induced oxidation of benzene systems involved the measurement of rate constants and the transient absorption spectra by pulse radiolysis and the determination of yields of hydroxylated products on oxidation of the hydroxycyclohexadienyl radicals under steady-state conditions. The two commonly used oxidants — $\text{K}_3\text{Fe}(\text{CN})_6^{3-}$ and IrCl_6^{2-} — convert quantitatively the OH adducts to the corresponding phenolic products. Thus, the pulse radiolysis technique in combination with product analysis using analytical techniques such as UV–VIS spectroscopy, HPLC, GC–MS, etc. under steady state conditions has provided valuable information in the understanding of the oxidation reaction mechanism of aromatics in

aqueous solution (see Ref. 3 for a review of elucidation of peroxy radical reactions).

The transient absorption spectrum reported recently⁴ in the reaction of $\cdot\text{OH}$ radical with benzene in aqueous solutions is given in Fig. 1. The weakly electrophilic $\cdot\text{OH}$ radical generally reacts by addition⁴⁻¹¹ to the aromatic ring, forming the corresponding hydroxycyclohexadienyl radical. The first step in the addition of $\cdot\text{OH}$ is the formation of the π complex, which immediately rearranges to σ complex, leading to the formation of the different isomeric OH adducts. For example, the $\cdot\text{OH}$ addition to $\text{C}_6\text{H}_5\text{X}$ ($\text{X} = -\text{OH}, -\text{NH}_2$, etc) preferentially occurs to the *para* position of the electron-donating group (Scheme 1).

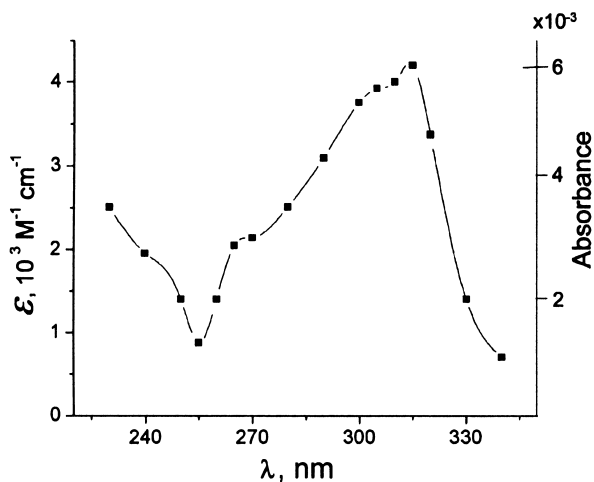
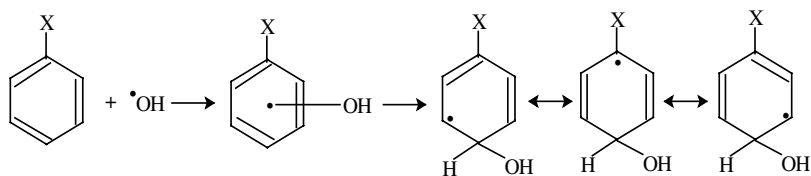


Fig. 1. The transient spectrum of the benzene OH adduct radical monitored at 10 μs after the pulse. [Reprinted with permission from Ref. 4. Copyright 2006, American Chemical Society.]



Scheme 1. The addition of $\cdot\text{OH}$ radical to monosubstituted benzene system.

A fine example of the use of pulse radiolysis technique in combination with steady-state product distribution is the recent study by Schuler and co-workers¹² to probe charge distribution in aromatics. Their initial studies on biphenyl¹³ which were extended recently to phenol¹² have been concerned with the determination of relative yields at *o*-, *m*- and *p*-positions to examine the substituent effects on charge distribution. For example, Fig. 2 shows the contour plot of HPLC chromatographic data obtained in the $\bullet\text{OH}$ radical reaction following the irradiation of phenol in the presence of the oxidant ferricyanide. Figure 3 shows the transient absorption spectra recorded in the reactions of $\bullet\text{OH}$ and $\bullet\text{N}_3$ radicals with phenol. The absorption

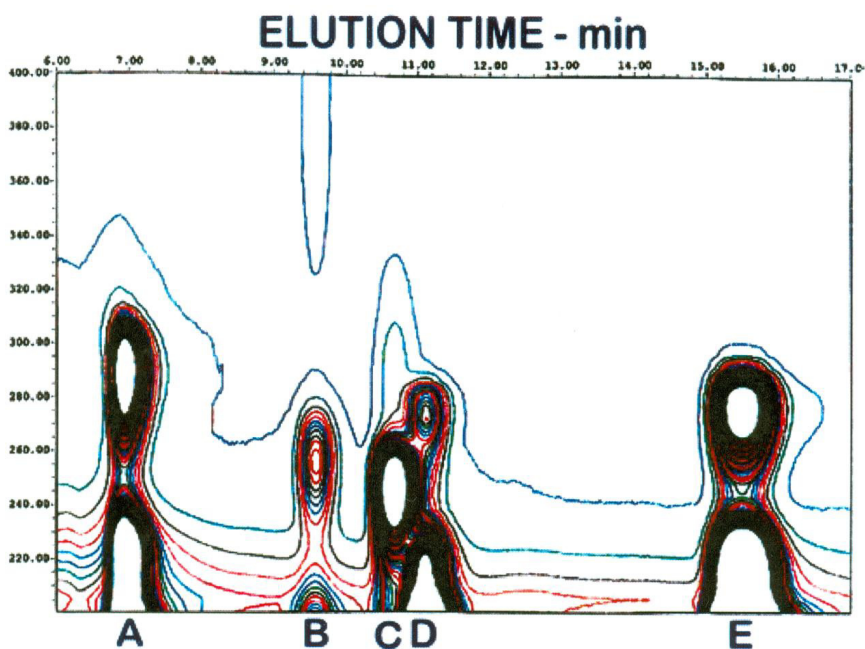


Fig. 2. Contour plot (50 contours from 0 to 0.1 mAU) of a 5-mM solution of phenol containing 2.7-mM ferricyanide irradiated to a dose of 834 Gy: (A) hydroquinone, (B) hydroxyquinone, (C) quinone, (D) resorcinol, (E) catechol. [Reprinted with permission from Ref. 12. Copyright 2007, American Chemical Society.]

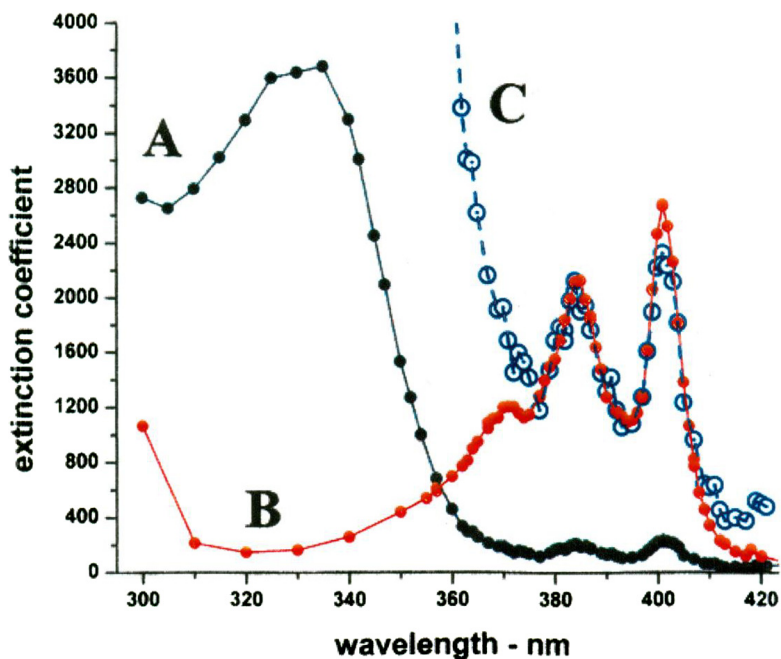


Fig. 3. Absorption spectra observed in the pulse radiolysis of (A) 5×10^{-3} mol dm $^{-3}$ phenol solution at pH7 and (B) also containing 20×10^{-3} mol dm $^{-3}$ sodium azide. (C) Spectrum A magnified by a factor of 10. (A) was recorded 250–750 ns and (B) 2.5–7.5 μ s after the pulse at which time oxidation was complete. [Reprinted with permission from Ref. 12. Copyright 2007, American Chemical Society.]

band measured in the $\cdot\text{OH}$ reaction at 335 nm is a mixture of isomeric phenol- $\cdot\text{OH}$ adducts and the weak absorption in the 370–410 nm region was attributed to the phenoxyl radical formation based on its spectrum obtained in the $\cdot\text{N}_3$ reaction. Further, it has been shown that the relative yields for $\cdot\text{OH}$ addition to each of the *ortho*, *meta*, *para* and *ipso* positions are in the ratio of 0.25: 0.04: 0.34: 0.08, respectively, and the phenoxyl radicals were formed from the adducts at diffusion controlled rates ($t_{1/2} \sim 20$ ns).

Studies have been reported by our group^{14,15} in the case of chlorotoluenes and cresols, where relative yields of phenolic products were determined to obtain information on the sites of $\cdot\text{OH}$ attack. (*vide infra*).

Another important aspect that has been well addressed^{3,16-21} is on the radiation-induced degradation of benzene and its derivatives in aqueous solution. The *Advanced Oxidation Processes* (e.g. O₃-H₂O₂, H₂O₂-UV, electron beam) make use of the highly reactive •OH radical in the degradation of water pollutants. Radiation chemical methods are superior to other methods (Fenton or photolysis) in the generation of peroxy radicals from the reaction of OH adducts.



$$k_{\text{obs}} = k_f[\text{O}_2] + k_r. \quad (4)$$

The addition of molecular oxygen to carbon-centered radicals in aqueous solutions is usually fast, with rates close to those of diffusion-controlled mechanisms. The cyclohexadienyl radical, for example, reacts very rapidly, which is followed by rapid elimination of HO₂ with other competing processes (e.g. bimolecular decay by disproportionation). On the other hand, its addition to OH adducts of benzene and its derivatives was reported to be slower and reversible [reaction (3)]. By monitoring the decay of absorption of OH adducts in the presence of oxygen at lower doses, Fang *et al.*¹⁸ determined the rate constants using Eq. (4). It has been further shown by them that the forward (k_f) and backward (k_r) rates depend on the nature of the substituent, with k_f values lying between 8×10^8 for anisole and $1.6 \times 10^7 \text{ dm}^3 \text{ mol}^{-1} \text{ s}^{-1}$ for terephthalate ion and the corresponding values of k_r are between 7.5×10^4 and $0.35 \times 10^4 \text{ s}^{-1}$. This was further extended to halotoluenes by us¹⁴ and Fig. 4(A) depicts the spectrum recorded in oxygenated solutions of 3-chlorotoluene where the formation of the peroxy radical can be clearly seen.

The decay of absorption at 325 nm in the presence of oxygen [Fig. 4(B)] and plots of k_{obs} determined from such traces as a function of $[\text{O}_2]$ for chlorotoluenes and cresols are shown in Fig. 4(C).

Recently, Al-Sheikhly *et al.*⁴ studied the radiation-induced destruction of benzene and dienes. Their pulse radiolysis work gave a rate constant $k = 7.8 \times 10^9 \text{ dm}^3 \text{ mol}^{-1} \text{ s}^{-1}$ to form the hydroxycyclohexadienyl radical, absorbing at 315 nm with a molar extinction coefficient of $4.2 \times 10^3 \text{ dm}^3 \text{ mol}^{-1} \text{ cm}^{-1}$ (Fig. 1). The OH adduct

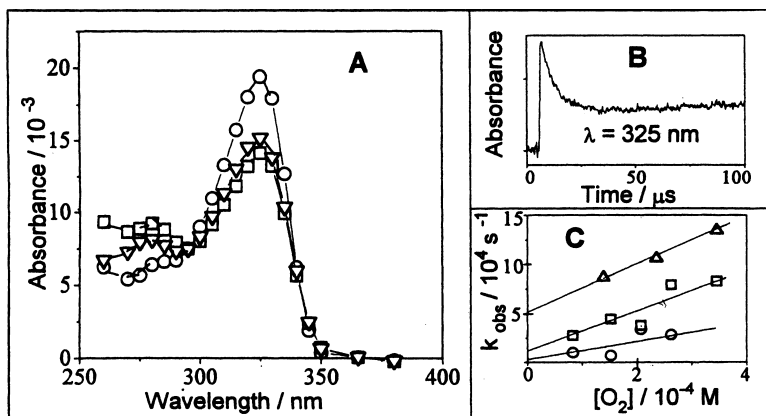


Fig. 4. (A) Time-resolved absorption spectra obtained from pulse radiolysis of $\text{N}_2\text{O}/\text{O}_2$ (4:1 v/v) saturated solutions of 3-chlorotoluene at 3 (O), 40 (V), and 90 μs (\square). Dose per pulse = 600–700 rad. (B) Decay trace at 325 nm in the presence of oxygen in 3-cresol. (C) Plot of k_{obs} as a function of $[\text{O}_2]$ in (O) 2- and (Δ) 3-chlorotoluenes and (\square) 3-cresol. [Reprinted with permission from Ref. 14. Copyright 1997, American Chemical Society.]

radical decays by second-order self reactions, but the decay is accelerated and increases linearly with $[\text{O}_2]$ and reacts with a rate constant of $3 \times 10^8 \text{ dm}^3 \text{ mol}^{-1} \text{ s}^{-1}$ in a reversible fashion. The authors proposed, in addition to O_2^- elimination, a chain reaction involving peroxy radical with benzene at low doses under gamma radiolysis. These studies have provided a basis for understanding the mechanism of degradation of volatile organic compounds such as benzene in waste and drinking-water treatment streams.

3. Kinetics: Hammett Correlation

The rates of the reaction of the $\cdot\text{OH}$ radical with benzene derivatives are generally studied from the build-up of the transient species (OH adducts) at the absorption maxima under pseudounimolecular reaction conditions at concentrations $\leq 10^{-3} \text{ mol dm}^{-3}$ and the second-order rate constants were evaluated from the plots of k_{obs} versus [solute]. The $\cdot\text{OH}$ radical is reactive towards arenes with diffusion-controlled

Table 1. k ($10^9 \text{ dm}^3 \text{ mol}^{-1} \text{ s}^{-1}$), λ_{max} (nm), and ϵ ($\text{mol dm}^{-3} \text{ cm}^{-1}$) obtained in the reactions of $\bullet\text{OH}$ and $\text{SO}_4^{\bullet-}$ with some selected substituted benzenes. Data taken from Refs. 14 and 15.

Compound	k		$\lambda_{\text{max}}(\bullet\text{OH})$	ϵ	$\lambda_{\text{max}}(\text{SO}_4^{\bullet-})$
	$\bullet\text{OH}$	$\text{SO}_4^{\bullet-}$			
Bromobenzene	4.4	1.8			320, 400
Chlorobenzene	5.5	1.5	325	4600	325, 400
1-bromo-2-chlorobenzene	2.0	0.7	330	3800	325, 425
1,2-Dibromobenzene	2.3	0.4	330	3200	330, 435
1,3-Dibromobenzene	1.9	0.5	330	4800	330
1,2-Dichlorobenzene	2.5	0.6	325	3800	320
1,3-Dichlorobenzene	2.2	1.1	330	5300	330
2-Bromotoluene	1.7	2.3	330	3450	315, 435
3-Bromotoluene	4.9	1.7	330	5200	320
4-Bromotoluene	2.9	1.0	315	3700	275, 325
2-Chlorotoluene	6.5	1.7	325	3600	320
3-Chlorotoluene	3.5	0.9	330	4200	325
4-Chlorotoluene	5.5	1.1	310	4000	270, 315
2-Cresol	12.0	3.4	295	3060	290, 380–400
3-Cresol	10.0	3.8	325	4970	290, 390
4-Cresol	9.2	6.1	305	4210	290, 390

rates having k values between 10^9 to $10^{10} \text{ dm}^3 \text{ mol}^{-1} \text{ s}^{-1}$ depending on the substituent. The rate constants measured in the reaction of the $\bullet\text{OH}$ and $\text{SO}_4^{\bullet-}$ radicals with some selected benzene systems reported by us²²⁻²⁴ are tabulated in Table 1.

The earlier work on the reaction of the $\bullet\text{OH}$ radical with substituted benzenes has shown the correlation of second-order rate constants with the Hammett parameter (ρ^+).²⁵ The Hammett treatment [Eq. (5)] involves the relation between the rate constants and the electronic parameters (σ and ρ^+).

$$\log k = \sigma\rho^+ + A, \quad (5)$$

where k and k_0 are the rate constants for the substituted and the unsubstituted compounds respectively, σ is a constant, characteristic

of the substituted group, ρ^+ is a constant for a given reaction under a given set of conditions and $A = \log k_0$.

For the compounds obeying the Hammett equation, the distribution pattern for the $\bullet\text{OH}$ attack can be estimated by assuming that the position on the ring with the maximum σ value has the least probability, while the one with the minimum has the greatest probability. In our recent work^{26,27} on cinnamate derivatives where the addition of the $\bullet\text{OH}$ radical to the olefinic double bond is an additional pathway, a ρ^+ value of -0.3 was estimated from the Hammett plot (Fig. 5). This value is in agreement with those reported earlier^{23,25} for several substituted benzenes ($\rho^+ = -0.52$ to -0.4). However, the Hammett treatment for reactions with rate constants close to diffusion-controlled ones may not be satisfactory due to limited variation in kinetic data and large experimental uncertainty. In contrast, better correlation is expected in the corresponding gas phase reactions.

Among the various radiation chemical studies, our work^{14,15,22-24,26-33} has been concerned with reactions of oxidizing radicals ($\bullet\text{OH}$, $\text{SO}_4^{\bullet-}$, $\text{X}_2^{\bullet-}$

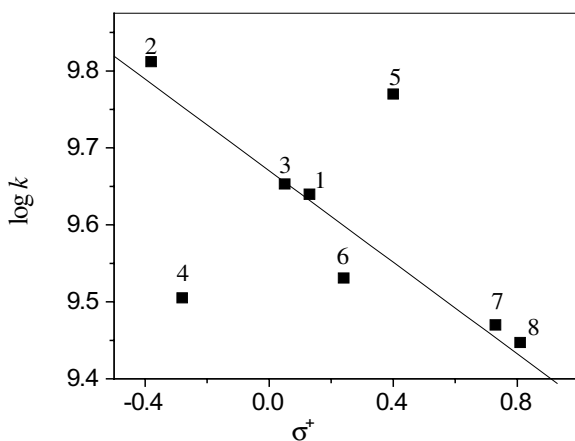


Fig. 5. Hammett plot for the reaction of $\bullet\text{OH}$ radical with cinnamate derivatives: (1) *m*-hydroxycinnamate, (2) *p*-hydroxycinnamate, (3) *m*-methoxycinnamate, (4) *p*-methoxycinnamate, (5) *m*-chlorocinnamate, (6) *p*-chlorocinnamate, (7) *m*-nitrocinnamate, and (8) *p*-nitrocinnamate; pH 7, Dose/pulse ~ 15 Gy. [Taken from P. Yadav, Ph.D. Thesis, University of Pune, 2006.]

($X = \text{Br}^-$ or Cl^-) with substituted benzenes of the type $\text{C}_6\text{H}_{5-n}\text{X}_n\text{Y}$, where $X =$ halogen and $Y = \text{NH}_2, \text{Cl}, \text{Br}, \text{CH}_3, \text{CH}_2\text{Cl}$ or OCH_3 and results from some individual systems are discussed here.

4. Halobenzenes and Halotoluenes

Among benzene derivatives, halogen-substituted compounds have been extensively studied and in the structure–reactivity studies^{15,22–24} carried out on the reaction of $\bullet\text{OH}$ and $\text{SO}_4^{\bullet-}$ with the *ortho* and *meta* isomers of dichloro and dibromobenzenes and mono-bromotoluenes, the formation of substituted hydroxycyclohexadienyl radical was observed to be the major reaction channel. The bimolecular rate constants obtained for the reaction of $\bullet\text{OH}$ with substituted halobenzenes are in the range $(1.7 \text{ to } 9.3) \times 10^9 \text{ dm}^3\text{mol}^{-1}\text{s}^{-1}$. The rate constants obtained are found to follow the Hammett relationship for the reaction of $\bullet\text{OH}$ with substituted halobenzenes²⁴ and the ρ^+ was found to be -0.5 , indicating that $\bullet\text{OH}$ radicals react by addition to the benzene ring.

In the reaction of $\text{SO}_4^{\bullet-}$ with halobenzenes the correlation of the rate constants with the Hammett parameters gave ρ^+ values of -1.2 and -1.6 with halotoluenes. Studies on product distribution in substituted toluenes¹⁴ have shown that H atom abstraction from $-\text{CH}_3$ group is an additional reaction pathway, especially in toluenes containing substituent at *para*-positions (e.g. 4-chlorotoluene and 3,4-dichlorotoluene).

The spectra of the intermediate transients formed in the reaction of $\bullet\text{OH}$ with dichloro- and dibromo-benzenes and chloro- and bromo-toluenes exhibited absorption maxima around 325–330 nm¹⁵ with both *ortho*- and *meta*-isomers of dichlorobenzenes, dibromobenzenes, and bromotoluenes (Fig. 6). The transients were assigned to the isomeric OH adducts formed from the addition of $\bullet\text{OH}$ to the benzene ring. A blue shift was observed in the absorption maximum of *p*-bromotoluene (315 nm) when compared to its *ortho*- and *meta*-isomers which have maxima at 330 nm. Such a behavior was also seen¹⁵ in the absorption spectra of OH adducts of *o*- and *m*-chlorotoluenes (325–330 nm) and *m*-xylenes (326–328 nm) as compared to their

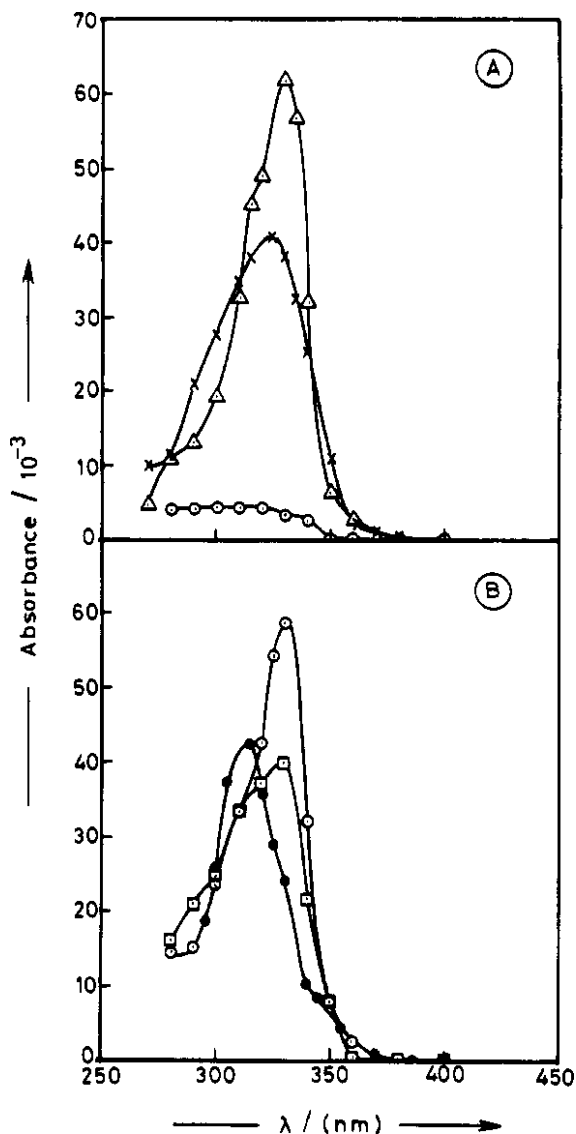


Fig. 6. Transient absorption spectra recorded 2 μ s after the pulse obtained in the reaction of $\cdot\text{OH}$ with (A) 1,2-dichlorobenzene (\times), 1,3-dichlorobenzene without (Δ) and with 0.2 M tert-butyl alcohol (\circ), (B) 2-bromotoluene (\square), 3-bromotoluene (\circ) and 4-bromotoluene (\bullet). Dose per pulse = 2 krad; pH = 7; [solute] = 10^{-3} mol dm^{-3} . [Reprinted with permission from Ref. 15. Copyright 1994, American Chemical Society.]

para-isomers (310 nm). This is also reflected in the more intense absorption observed in the spectra of their *meta*-isomers.

The extinction coefficient for the OH adducts of *m*-bromotoluene ($5200 \text{ dm}^3 \text{ mol}^{-1} \text{ cm}^{-1}$) is higher than that observed for its *para*-isomer ($3700 \text{ dm}^3 \text{ mol}^{-1} \text{ cm}^{-1}$). The red shift in *ortho*- and *meta*-substituted isomeric OH adducts was attributed to the stabilization of their excited states because the unpaired spin, especially in the OH adducts of *meta*-isomers, is delocalized on both $-\text{Cl}$ and $-\text{CH}_3$ substituents and they are therefore, relatively more stable than the *para*-isomers.¹⁵

The stabilization of hydroxycyclohexadienyl radicals by $-\text{CH}_3$ and halogen groups is apparent from the bathochromic shifts in the spectra of OH adducts of chloro- and bromo-benzenes (325 nm) and toluene (317 nm) relative to benzene (313 nm). This is in accordance with the work of Chen and Schuler¹³ where the phenyl substituent leading to a more intense and a strong red shift in the transient absorption spectra was seen in the reaction of $\bullet\text{OH}$ radical with biphenyl.

The transient absorption spectra maxima of substituted benzenes are usually in the range 310–330 nm. This is evident from the spectra reported in the case of halobenzenes and halotoluenes (Fig. 6) and for benzene (Fig. 1).

5. Cresols

Reactions of $\bullet\text{OH}$, $\text{O}\bullet^-$ and $\text{SO}_4\bullet^-$ radicals with cresols were studied in detail by pulse radiolysis and laser flash photolysis techniques combined with product analysis.¹⁴ The rate constants of the $\bullet\text{OH}$ reaction with cresols are very high ($k \sim 1 \times 10^{10} \text{ dm}^3 \text{ mol}^{-1} \text{ s}^{-1}$) whereas $\text{O}\bullet^-$ was found to be less reactive ($k \sim 2.4 \times 10^9 \text{ dm}^3 \text{ mol}^{-1} \text{ s}^{-1}$). The second-order rate constants of the reaction for $\text{SO}_4\bullet^-$ reaction with cresols are in the range of $(3 \text{ to } 6) \times 10^9 \text{ dm}^3 \text{ mol}^{-1} \text{ s}^{-1}$. The transient absorption spectra obtained in the reaction of $\bullet\text{OH}$ with isomers of cresols have peaks in the region 295–325 nm. Merga *et al.*¹⁵ and Choure *et al.*¹⁴ carried out a detailed product analysis by HPLC on radiolysis of chlorotoluenes and cresols. Table 2 lists the products obtained in deoxygenated and oxygenated solutions of these systems.

Table 2. Product distribution obtained in γ -radiolysis of deoxygenated and oxygenated solutions of chlorotoluenes and cresols. Taken from Ref. 14 [The numbers are the G values of the individual phenolic products formed in deoxygenated (given in parantheses) and oxygenated solutions of chlorotoluenes (X = Cl) and cresols (X = OH). The total yields are based on $G(\cdot\text{OH}) = 5.6$ per 100 eV. n.f. = not formed].

Isomer	Products			Total Yield : %OH
<i>Ortho</i>				
	X = Cl	0.20 (1.1)	0.70 (2.4)	
X = OH	1.4 (1.4)	n.f. (1.4)	n.f.	1.40 : 25% (2.80 : 50%)
<i>Meta</i>				
	X = Cl	0.4 (2.1)	0.2 (2.3)	
X = OH	1.2 (1.2)	n.f.	1.1 (1.1)	2.3 : 41% (2.3 : 41%)
<i>Para</i>				
	X = Cl	0.3 (2.5)	0.2 (2.2)	
X = OH	2.0 (3.6)	n.f. (1.3)		2.0 : 36% (4.9 : 87%)

5.1. Substituent effects in $\bullet\text{OH}$ reaction

The partial rate constants for the attack of $\bullet\text{OH}$ at different positions of isomers of monochlorotoluenes were determined from the observed yields and rate constants (Fig. 7).¹⁵ The relative rate constants of 1.18 and 1.39 at positions 3 and 6 of 2-chlorotoluene have shown the effects of activation of the *ortho*-positions and the deactivation of the *meta*-positions by $-\text{CH}_3$ and $-\text{Cl}$ groups. A similar trend was found for 4-chlorotoluene where the relative rate constants at positions 2 (*ortho* to $-\text{CH}_3$ and *meta* to $-\text{Cl}$) and 3 (*ortho* to $-\text{Cl}$ and *meta* to $-\text{CH}_3$) are comparable. Further, the deactivation of the *meta*-position by the methyl and phenyl groups in toluene and biphenyl (the respective relative rate constant values being 0.61 and 0.63) is compensated by the *ortho*-directing $-\text{Cl}$ group. The relative rate constant values of 2.25 and 2.47 at positions 4 and 6 of 3-chlorotoluene which are either *ortho* or *para* to the $-\text{CH}_3$ and $-\text{Cl}$ groups revealed that both positions are activated to the same extent. A comparison of these values with those observed at the *ortho*- (1.28) and *para*- (1.34) positions of toluene show the cumulative effect of activation by $-\text{CH}_3$ and $-\text{Cl}$ groups. Further, this total activation is

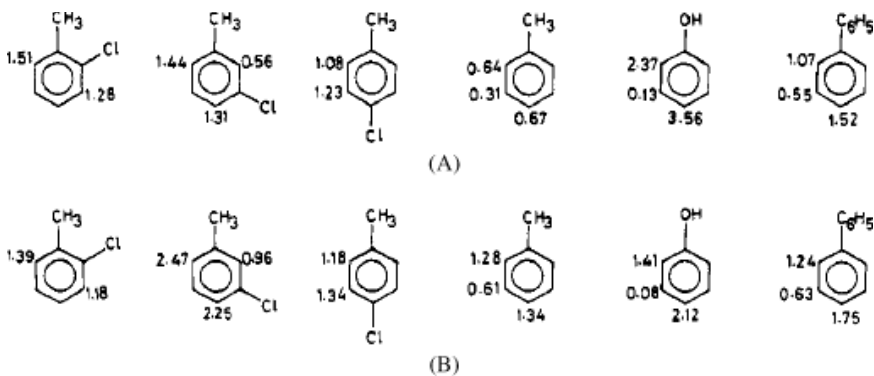


Fig. 7. (A) Partial $10^9 \text{ dm}^3 \text{ mol}^{-1} \text{ s}^{-1}$ and (B) relative rate constants for the reaction of $\bullet\text{OH}$ with 2-, 3-, and 4-chlorotoluenes. Values in (B) are given relative to benzene. [Reprinted with permission from Ref. 15. Copyright 1994, American Chemical Society.]

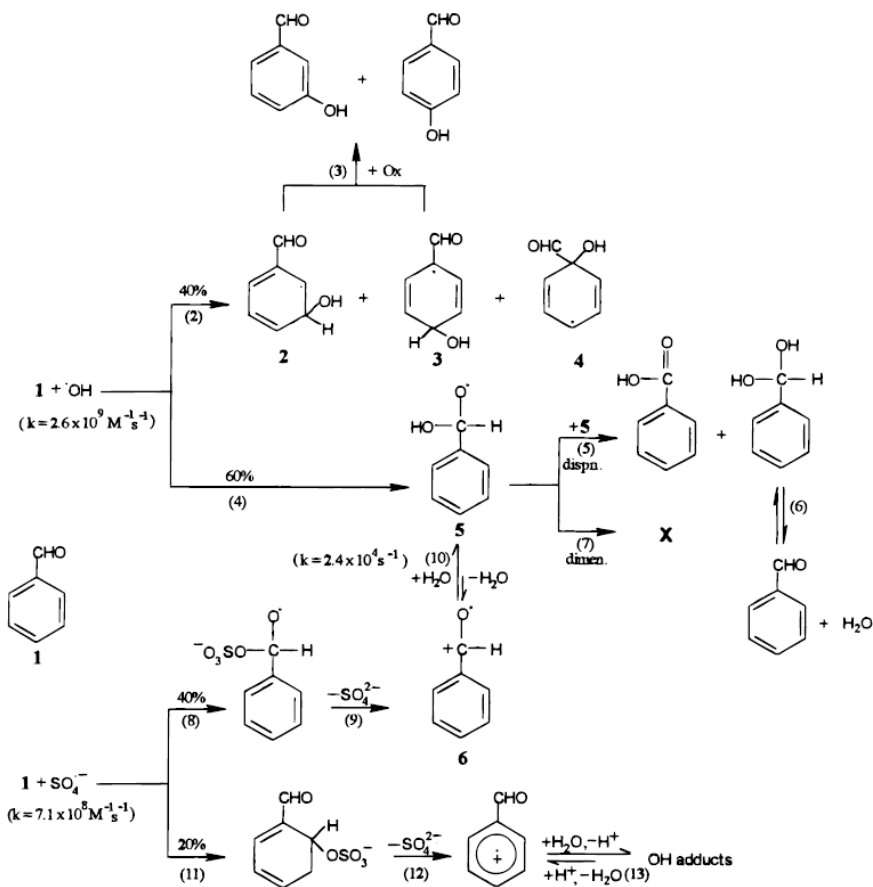
nearly equal to the *para*-directing effect of the highly electron-donating-OH group in phenol, having a relative rate constant of 2.12.

Similarly, the deactivation of both $-\text{CH}_3$ and $-\text{Cl}$ groups for the *meta*-attack is evident from the complete inactivation of position 5 of 3-chlorotoluene. On the other hand, position 2, though *ortho* to both substituents, has a value close to that of benzene which is lower than one would expect and may be due to the steric hindrance. The similarity in the magnitude of the activating effects of the $-\text{CH}_3$ and $-\text{Cl}$ groups is in line with the expected behavior of the free radical aromatic substitution where all substituents enhance reactivity at *ortho*- and *para*-positions over that of benzene. This is because the $\bullet\text{OH}$ radical, though slightly electrophilic, is predominantly neutral in nature. In the case of cresols, the analysis was limited to the *para*-isomer and the results are in accordance with the strong activation of *ortho*- and deactivation of *meta*-positions by the $-\text{OH}$ group.

6. Benzaldehyde, Acetophenone, Aniline and Their Derivatives

The k values for the reaction of $\bullet\text{OH}$ with benzaldehyde, acetophenone and benzophenone are between $(2.6 \text{ to } 7.7) \times 10^9 \text{ dm}^3 \text{ mol}^{-1} \text{ s}^{-1}$.^{28,29} The increase in the values on going from benzaldehyde to benzophenone agrees with the increase in electron density due to the replacement of $-\text{H}$ by $-\text{CH}_3$ or $-\text{C}_6\text{H}_5$ in the functional group. Studies carried out on hydroxylation of benzaldehyde and acetophenone revealed that the $\bullet\text{OH}$ addition to the functional group of benzaldehyde predominates over the addition to the benzene ring while addition to the ring is predominant in the case of acetophenone.³³ The reaction mechanism involved the addition of the $\bullet\text{OH}$ radical to the $-\text{CHO}$ group of benzaldehyde followed by disproportionation of the exocyclic OH adduct as its addition to the benzene ring is considerably reduced due to its deactivation by the $-\text{CHO}$ group. The reaction mechanism for the $\bullet\text{OH}$ and $\text{SO}_4^{\bullet-}$ reactions with *p*-hydroxybenzaldehyde is shown in Scheme 2.

In a theoretical study of the $\bullet\text{OH}$ radical reaction with a series of halogenated acetaldehydes, Rayez *et al.*³⁴ have shown that the



Scheme 2. Reaction pathways for $\bullet\text{OH}$ radical attack on benzaldehyde. [Taken from Ref. 33].

H abstraction from the functional $-\text{CHO}$ group is more probable than the addition/elimination reaction.

The second-order rate constants for the reaction of $\bullet\text{OH}$ radical with *meta*- and *para*-isomers of hydroxy-, methoxy-, chloro- and nitro-benzaldehydes are in the range $(2.8 \text{ to } 12) \times 10^9 \text{ dm}^3 \text{ mol}^{-1} \text{ s}^{-1}$. The higher rate in methoxybenzaldehyde is attributed to the activation of the ring by the electron-donating $-\text{OCH}_3$ group.

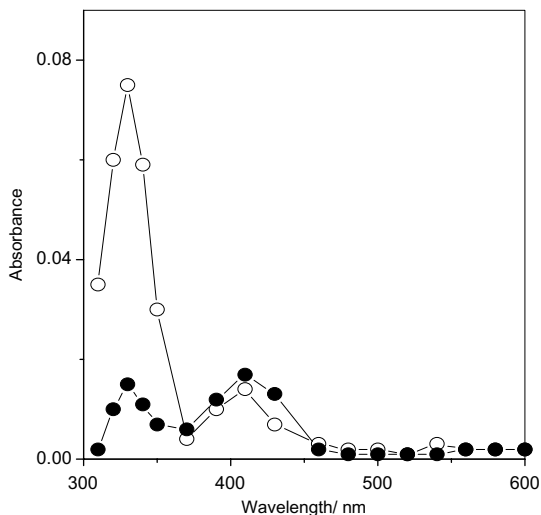


Fig. 8. Time-resolved transient absorption spectra obtained in the reaction of $\bullet\text{OH}$ with *p*-hydroxybenzaldehyde $1 \times 10^{-3} \text{ mol dm}^{-3}$ at 1.5 (○) and 10 (●) μs after the pulse; dose/pulse = 1.5 krad. [Reprinted with permission from Ref. 28. Copyright 2001, Elsevier.]

The spectral nature for the transients formed in the $\bullet\text{OH}$ reaction with *p*-hydroxybenzaldehyde (Fig. 8) was found to be different from those recorded with its *ortho*- and *meta*-isomers. In addition to a single peak around 370–410 nm observed with the latter, a more intense peak at 325 nm by four folds was seen. Furthermore, this peak decayed faster with a first-order rate constant $k = 5.5 \times 10^5 \text{ s}^{-1}$. This decay was found to be acid-catalyzed. In the reaction of $\bullet\text{OH}$ radical with hydroxybenzaldehydes,²⁸ the time resolved spectral changes are interpreted in terms of the formation of phenoxyl radical *via* intermediate radical cation in the case of *ortho*- and *para*-isomers whereas phenoxyl radical formation by dehydration seems to be the predominant reaction pathway for the *meta*-isomer.

The charge distribution at different carbon atoms of the ring and the aldehyde group for isomers of hydroxybenzaldehyde and hydroxyacetophenone was determined using semiempirical quantum chemical

calculations. The analysis revealed that the electron density distribution is in accordance with the activation and deactivation effects of the $-OH$ and $-CHO$ groups. The probable positions for the $\bullet OH$ attack are, thus, different for the three isomers. Furthermore, there is no single unique site for the exclusive attack of $\bullet OH$, implying the formation of different isomeric OH adducts.

A general feature of this analysis is that the electron density at the carbon attached to $-CHO$ group is significant whereas it is minimum at the exocyclic carbon. The order of the charge distribution at the carbon attached to $-CHO$, among the three isomers, is *ortho* > *para* > *meta*. The absorption maxima of transients formed with *o*-, *m*- and *p*-hydroxyacetophenones were reported to be similar to those obtained with the corresponding isomers of hydroxybenzaldehydes.

The reaction mechanism reported in the reaction of $\bullet OH$ with benzaldehydes is shown in Scheme 2. The $\bullet OH$ radical attacks the ring [reaction (2)] and the $-CHO$ group [reaction (4)]. The attack of $\bullet OH$ on the *ortho*-position of benzaldehyde was considered negligible because of the lack of formation of salicylaldehyde under steady-state conditions. The two hydroxycyclohexadienyl radicals (structures 2 and 3) were oxidized to the corresponding phenols in the presence of an oxidant [reaction (3)], while the ipso OH adduct (structure 4) was not.

Since the measured yields of the phenolic products corresponded to 30% $\bullet OH$ yield, the ipso adduct formation is limited to 10% $\bullet OH$ yield. Since the combined *G* value of *m*- and *p*-hydroxybenzaldehydes in N_2O -saturated solutions in the presence of $IrCl_6^{2-}$ is 1.7, only 30% $\bullet OH$ seems to add to the ring. The reason for low phenolic yields in the case of benzaldehyde is the possibility of another reaction channel leading to the formation of the exocyclic OH adduct (structure 5) from the addition of $\bullet OH$ to the carbonyl group of benzaldehyde [reaction (4)].

Radiation chemical oxidation of benzaldehyde to benzoic acid is interpreted in terms of the disproportionation of the exocyclic OH adduct (structure 5) to give benzoic acid [reaction (5)], which can account for the complete consumption of $\bullet OH$. Dimerization of this adduct seems to be a minor process.

$\bullet\text{OH}$, $\text{O}^{\bullet-}$ and N_3^{\bullet} radicals were reported³⁰ to react with chloro- and hydroxy-derivatives of aniline at diffusion-controlled rates with $k > 10^9 \text{ dm}^3 \text{ mol}^{-1} \text{ s}^{-1}$ and the rates are nearly identical for all isomers of chloroaniline. The $\bullet\text{OH}$ radical reaction involves both addition and direct H abstraction and the extent of the two reactions is determined by the position of the substituent. The initially formed OH adduct then undergoes dehydration to give the anilino radical. The attack of the $\bullet\text{OH}$ radical at the carbon bonded to Cl is a minor pathway (not more than 15%) as was confirmed by the detection of Cl^- ions.

7. Cinnamic Acid/Cinnamate Derivatives

There is a growing interest in naturally occurring phenolic compounds that display biological antioxidant properties such as *p*-hydroxycinnamic acid,³⁵ ferulic acid,³⁶ caffeic acid,^{37,38} and curcumin³⁹⁻⁴¹ which are ubiquitous in plant food. It has been demonstrated^{38,42,43} that the interaction of the oxidizing OH adduct of DNA, poly-A and poly-G with hydroxycinnamic acid derivatives proceed via electron transfer. Cinnamic acid derivatives have been shown to be able to scavenge superoxide, peroxy, and hydroxyl radicals.^{38,44,45}

The $\bullet\text{OH}$ radical, in benzene derivatives with a substituent having a double bond, can add either to the benzene ring or to the side chain. Bobrowski and Raghavan⁴⁵ have performed experiments on the cinnamic acid and shown that the $\bullet\text{OH}$ radical adds to both the ring and the olefinic group, the relative extent being 3:7 respectively.

The pulse radiolysis technique combined with quantum chemical calculations have been carried out by our group²⁷ to examine the effect of substituent and its position on the reactivity of both oxidizing and reducing radicals with derivatives of cinnamic acid containing either an electron-donating ($-\text{OH}$ or $-\text{OCH}_3$) or electron-withdrawing substituent ($-\text{Cl}$ or $-\text{NO}_2$). The reactions were studied both at pH3 and pH7 in order to examine their nature in undissociated and dissociated forms ($\text{pK}_a \sim 4$). The absorption spectrum recorded in the reaction of $\bullet\text{OH}$ radical with cinnamate at pH7 exhibited two peaks centered at 310 and 365 nm (Fig. 9). This spectrum is in agreement with that reported earlier.⁴⁵ The two peaks at 310 and 365 nm are

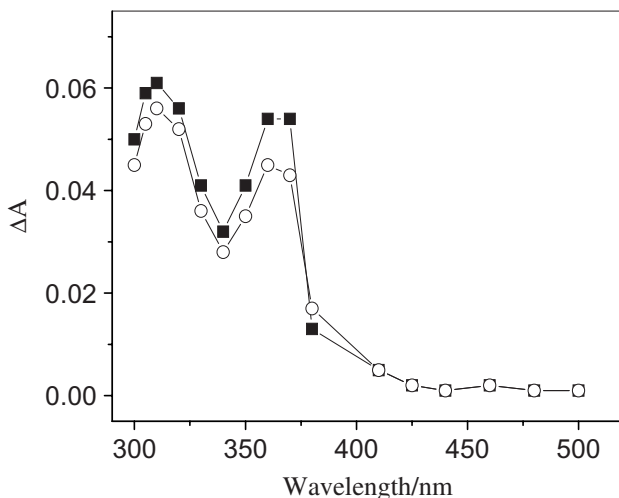


Fig. 9. Transient absorption spectra obtained in the reaction of $\bullet\text{OH}$ with cinnamate at pH 7, at (■) 2.5 and (○) 40 μs . [cinnamate] = 1×10^{-3} mol dm^{-3} , Dose/pulse = 14 Gy. [Reprinted with permission from Ref. 27. Copyright 2008, Elsevier.]

assigned to the benzylic and hydroxycyclohexadienyl radicals following the addition to the double bond of the substituent and the ring respectively. The molar extinction coefficients for the former radical determined by the two groups are in the range 9700–9900 $\text{dm}^3 \text{mol}^{-1} \text{cm}^{-1}$.

The extent of the $\bullet\text{OH}$ radical attack at the side chain in cinnamate derivatives was estimated to be significant (60–80% $\bullet\text{OH}$ yield), which is in accordance with the theoretical calculations. Among the addition products of *o*-, *m*-, and *p*-methoxycinnamic acids, the DFT calculations have shown that the addition of $\bullet\text{OH}$ to the olefinic carbon atom C8 is the most stable followed by C7 while the product obtained from $\bullet\text{OH}$ addition to the ring carbon atom C1 (ipso with respect to the acid functional group) is the least stable. The most stable structure among the ring addition products is the (C4OH) \bullet adduct. The relative stabilities of the addition products of *o*-, *m*- and *p*-methoxycinnamic acids with respect to (C8OH) \bullet adduct is shown in Fig. 10.

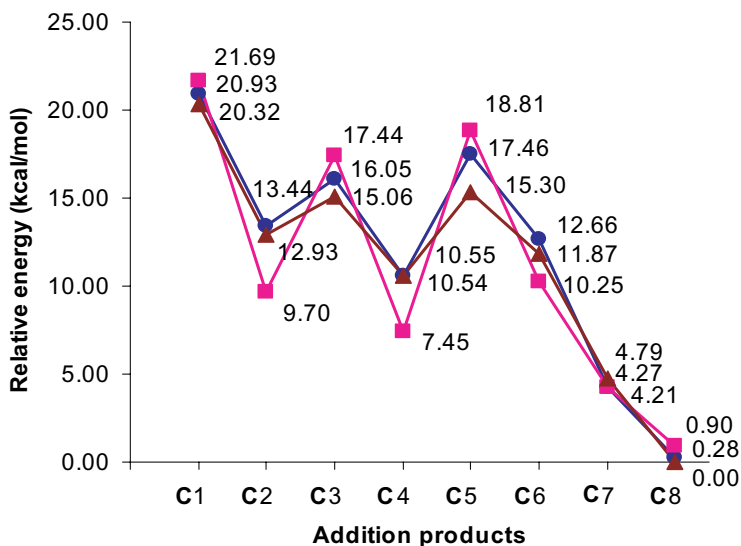


Fig. 10. Relative energy (E_r) values of $\cdot\text{OH}$ addition products: *ortho*- (●), *meta*- (■) and *para*- (▲) methoxycinnamic acid derivatives. On the X-axis, C1–C8 corresponds to the products obtained by the addition of $\cdot\text{OH}$ to C1–C8 atoms, respectively. [Reprinted with permission from Ref. 27. Copyright 2008, Elsevier.]

The higher stability of addition products on olefinic carbon atoms C8 and C7 was explained based on loss of aromaticity because addition to the ring breaks the cyclic delocalization leading to the loss of accounting to around 30 kcal/mol of destabilization of the system. Further excellent linear correlation between the relative stabilities of the OH adducts (after accounting for the aromatic stabilization in olefinic adducts) and the maximum spin density values was also obtained.

8. Summary

The radiation chemical reactions of oxidizing radicals with substituted benzenes of the type $\text{C}_6\text{H}_{5-n}\text{X}_n\text{Y}$, where X = halogen and Y = NH_2 , Cl, Br, CH_3 , CH_2Cl or OCH_3 are discussed. They form an interesting class of compounds for structure–reactivity studies as they contain

both electron-donating/electron-withdrawing groups, and radiation chemical methods are suitable as known amounts of oxidizing radicals can be generated selectively. The methodology involves both pulse radiolysis and product analysis under steady-state conditions in combination with theoretical calculations. Despite extensive work carried out on pulse radiolysis of substituted benzenes since its advent more than four decades ago, product distribution data are still limited for the quantitative estimation of the extent of the radical attack at different sites in several systems.

Acknowledgments

I acknowledge with gratitude the contribution of my former graduate students Drs. Mohan Mudaliar, C. T. Aravinda Kumar, Sujata Shinde, Getahun Merga, Sumit Sharma, Geeta Sharma, Avinash Singh and Pooja Yadav whose work is reviewed in this chapter. I thank the DAE-BRNS for the award of the Raja Ramanna Fellowship.

References

- (a) Buxton GV, Greenstock CL, Helman WP, Ross AB. (1988) Critical review of rate constants for reactions of hydrated electrons, hydrogen atoms and hydroxyl radicals (OH/O) in aqueous solution. *J Phys Chem Ref Data* **17**: 513–817.

(b) Neta P, Huie RE, Ross AB. (1988) Rate constants for reactions of inorganic radicals in aqueous solutions. *J Phys Chem Ref Data* **17**: 1027–1284.
- (a) Jonsson M. (2001) Redox chemistry and energetics of radical cations of substituted benzenes. In *Radiation Chemistry: Present Status and Future Trends*, Jonah CD, Rao BSM (eds.), pp. 319–340, Elsevier, Amsterdam.

(b) Jonsson M, Lind J, Eriksen TE, Merenyi G. (1994) Redox and acidity properties of 4-substituted aniline radical cations in water. *J Am Chem Soc* **116**: 1423–1427.

(c) Jonsson M, Lind J, Eriksen TE, Merenyi G. (1995) N–H bond dissociation energies, reduction potentials and pK_as of multisubstituted anilines and aniline radical cations. *J Chem Soc Perkin Trans* **2**: 61–65.

(d) Jonsson M, Lind J, Eriksen TE, Merenyi G. (1995) Redox properties of 4-substituted aryl methyl chalcogenides in water. *J Chem Soc Perkin Trans* **2**: 67–70.

3. von Sonntag C, Schuchmann H-P. (1991) The elucidation of peroxy radical reactions in aqueous solution with the help of radiation-chemical techniques. *Angew Chem Int Ed Engl* **30**: 1229–1253.
4. Al-Sheikhly M, Poster DL, An J-C, Neta P, Silverman J, Huie RE. (2006) Ionizing radiation-induced destruction of benzene and dienes in aqueous media. *Environ Sci Technol* **40**: 3082–3088.
5. Solar S, Getoff N. (1995) Radical anions of chlorinated benzaldehydes in aqueous solution. *J Phys Chem* **99**: 9425–9429.
6. Solar S, Solar W, Getoff N. (1986) Resolved multisite OH-attack on aqueous aniline studied by pulse radiolysis. *Radiat Phys Chem* **28**: 229–234.
7. Eberhardt MK. (1977) Radiation induced homolytic aromatic substitution. 6. The effect of metal ions on the hydroxylation of benzonitrile, anisole, and fluorobenzene. *J Phys Chem* **81**: 1051–1057.
8. Eberhardt MK. (1975) Radiation induced homolytic aromatic substitution. III. Hydroxylation and nitration of benzene. *J Phys Chem* **79**: 1067–1069.
9. Sehested K, Corfitzen H, Christensen HC, Hart EJ. (1975) Rates of reaction of oxygen(1-) ions, hydroxyl radicals, and atomic hydrogen with methylated benzenes in aqueous solution. Optical spectra of radicals. *J Phys Chem* **79**: 310–315.
10. Eberhardt MK, Martinez MI. (1975) Radiation induced homolytic aromatic substitution. V. Effect of metal ions on the hydroxylation of toluene. *J Phys Chem* **79**: 1917–1920.
11. Bhatia K, Schuler RH. (1974) Oxidation of hydroxycyclohexadienyl radical by metal ions. *J Phys Chem* **78**: 2335–2338.
12. Albarran G, Schuler RH. (2007) Hydroxyl radical as a probe of the charge distribution in aromatics. *J Phys Chem A* **111**: 2507–2510.
13. Chen X, Schuler RH. (1993) Directing effects of phenyl substitution in the reaction of hydroxyl radical with aromatics: The radiolytic hydroxylation of biphenyl. *J Phys Chem* **97**: 421–425.
14. Choure SC, Bamatraf MMM, Rao BSM, Das R, Mittal JP. (1997) Aromatic hydroxylation of chlorotoluenes and cresols: A pulse radiolysis, flash photolysis and product analysis study. *J Phys Chem A* **101**: 9837–9846.
15. Merga G, Rao BSM, Mohan H, Mittal JP. (1994) Reactions of OH and $\text{SO}_4^{\cdot-}$ with some halobenzenes and halotoluenes: A radiation chemical study. *J Phys Chem* **98**: 9158–9164.
16. Pan X-M, Schuchmann MN, von Sonntag C. (1993) Oxidation of benzene by the OH radical. A product and pulse radiolysis study in oxygenated aqueous solution. *J Chem Soc Perkin Trans* **2**: 289.
17. Pan X-M, Schuchmann MN, von Sonntag C. (1993) Hydroxyl-radical-induced oxidation of cyclohexa-1,4-diene by O_2 in aqueous solution. A pulse radiolysis and product study. *J Chem Soc Perkin Trans* **2**: 1021–1028.

18. Fang X, Pan X, Rahmann A, Schuchmann H-P, von Sonntag C. (1995) Reversibility in the reaction of cyclohexadienyl radicals with oxygen in aqueous solution. *Chem Eur J* **1**: 423–429.
19. Legrini O, Oliveros E, Braun AM. (1993) Photochemical processes for water treatment. *Chem Rev* **93**: 671–698.
20. von Sonntag C, Mark G, Mertens R, Schuchmann MN, Schuchmann H-P. (1993) UV-radiation and/or oxidants in water pollution control. *Water Supply Res Technol-Aqua* **42**: 201–211.
21. von Sonntag C. (1996) Degradation of aromatics by advanced oxidation processes in water remediation: Some basic considerations. *Water Supply Res Technol-Aqua* **45**: 84–91.
22. Mohan H, Mudaliar M, Aravindakumar CT, Rao BSM, Mittal JP. (1991) Studies on structure-reactivity in reaction of OH radicals with substituted halobenzenes in aqueous solutions. *J Chem Soc Perkin Trans 2*: 1387–1392.
23. Mohan H, Mudaliar M, Rao BSM, Mittal JP. (1992) Reactions of hydrated electron with substituted benzenes. *Radiat Phys Chem* **40**: 513–517.
24. Merga G, Aravindakumar CT, Mohan H, Rao BSM, Mittal JP. (1994) Pulse radiolysis study of the reactions of $\text{SO}_4^{\bullet-}$ with some substituted benzenes in aqueous solution. *J Chem Soc Faraday Trans 90*: 597–604.
25. Anbar M, Meyerstein D, Neta P. (1966) The reactivity of aromatic compounds toward hydroxyl radicals. *J Phys Chem* **70**: 2660–2662.
26. Yadav P, Mohan H, Rao BSM, Mittal JP. (2002) Redox Chemistry of *o*- and *m*-hydroxycinnamic acids: A pulse radiolysis study. *Proc Ind Acad Sci* **114**: 721–730.
27. Yadav P, Mohan H, Maity DK, Suresh CH, Rao BSM. (2008) Oxidation of cinnamic acid derivatives: A pulse radiolysis and theoretical study. *Chem Phys* **351**: 57–64.
28. Geeta S, Sharma SB, Rao BSM, Mohan H, Dhanya S, Mittal JP. (2001) Kinetics and spectra of OH adducts of hydroxy derivatives of benzaldehyde and acetophenone. *Photochem Photobiol Chemistry A* **140**: 99–103.
29. Geeta S, Rao BSM, Mohan H, Mittal JP. (2004) Radiation induced oxidation of substituted benzaldehydes: A pulse radiolysis study. *J Phys Org Chem* **17**: 194–198.
30. Singh TS, Gejji SP, Rao BSM, Mohan H, Mittal JP. (2001) Radiation chemical oxidation of aniline derivatives. *J Chem Soc Perkin Trans 2*: 1205–1211.
31. Merga G, Schuchmann H-P, Rao BSM, von Sonntag C. (1996) Oxidation of benzyl radicals by $\text{K}_3\text{Fe}(\text{CN})_6$. *J Chem Soc Perkin Trans 2*: 551–556.
32. Merga G, Schuchmann H-P, Rao BSM, von Sonntag C. (1996) OH radical induced oxidation of chlorobenzene in aqueous solution in the absence and presence of oxygen. *J Chem Soc Perkin Trans 2*: 1097–1103.

33. Sharma SB, Mudaliar M, Rao BSM, Mohan H, Mittal JP. (1997) Radiation chemical oxidation of benzaldehyde, acetophenone and benzophenone. *J Phys Chem* **101**: 8402–8408.
34. Rayez MT, Rayez JC, Berces T, Lendvay G. (1993) Theoretical study of the reactions of hydroxyl radicals with substituted acetaldehydes. *J Phys Chem A* **97**: 5570–5576.
35. Bobrowski K. (1984) *J Chem Soc Faraday Trans* **80**: 1377.
36. Khopade SM, Priyadarshini KI, Guha SN, Mukherjee T. (2001) Hydroxyl radical induced oxidation of 4-hydroxy 3-methoxy cinnamic acid (ferulic acid). *Res Chem Intermed* **27**: 519–527.
37. Lin W, Navaratnam S, Yao S, Lin N. (1998) Antioxidative properties of hydroxycinnamic acid derivatives and a phenylpropanoid glycoside. A pulse radiolysis study. *Radiat Phys Chem* **53**: 425–430.
38. Li X, Cai Z, Katsumura Y, Wu G, Muroya Y. (2001) Reactions of reducing and oxidizing radicals with caffeic acid: A pulse radiolysis and theoretical study. *Radiat Phys Chem* **60**: 345–350.
39. Jovanovic SV, Steenken S, Boone CW, Simic MG. (1999) H-atom transfer is a preferred antioxidant mechanism of curcumin. *J Am Chem Soc* **121**: 9677–9781.
40. Priyadarsini KI. (1999) Free radical reactions of curcumin in model membranes. *Free Radical Biol Med* **23**: 838–844.
41. Sreejayan N, Rao MNA, Priyadarsini KI, Devasagayam TPA. (1997) Hydroxyl radical induced lipid peroxidation in rat liver microsomes: Inhibition by curcumin. *Int J Pharm* **151**: 127–130.
42. Jiang Y, Lin W, Yao S, Lin N, Zhu D. (1999) Fast repair of oxidizing OH adducts of DNA by hydroxycinnamic acid derivatives. A pulse radiolytic study. *Radiat Phys Chem* **54**: 355–359.
43. Jiang S, Yao N, Lin N. (1997) Fast repair of oxidizing OH radical adduct of dGMP by hydroxycinnamic acid derivatives: A pulse radiolytic study. *Radiat Phys Chem* **49**: 447–450.
44. Wang WF, Luo J, Yao SD, Lian ZR, Zhang JS, Lin NY. (1993) Interaction of phenolic antioxidants and hydroxyl radicals. *Radiat Phys Chem* **42**: 985–987.
45. Bobrowski K, Raghavan NV. (1982) Pulse radiolytic and product analysis studies of the reaction of hydroxyl radicals with cinnamic acid: The relative extent of addition to the ring and side chain. *J Phys Chem* **86**: 4432–4435.

Chapter 15

Femtosecond Events in Bimolecular Free Electron Transfer

Ortwin Brede[†] and Sergej Naumov[‡]*

1. Introduction

In recent years, much work has been done on the electron transfer phenomenon called free electron transfer (FET).¹ FET stands for an electron transfer process where the molecule oscillations of the donor are reflected in a bimolecular reaction. This is reasoned by an unhindered electron jump proceeding in the first encounter of the reactants. So “free” means *unhindered* and concerns the *transfer*, not the electron.

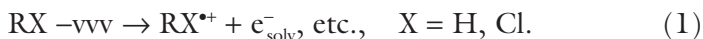
In non-polar solvents such as alkanes and alkyl chlorides (RX), ionizing irradiation produces metastable parent radical cations^{2,3} of high reactivity [Eq. (1)]. Usually, these species decay by neutralization, deprotonation and fragmentation. At room temperature such parent radical cations exhibit lifetimes up to 200 nanoseconds. In the presence

* Corresponding author.

[†] University of Leipzig, Interdisciplinary Group Time-Resolved Spectroscopy, Permoserstr. 15, 04303 Leipzig, Germany. E-mail: brede@uni-leipzig.de

[‡] Leibniz Institute for Surface Modification, Permoserstr. 15, 04303 Leipzig, Germany. E-mail: sergej.naumov@iom-leipzig.de

of additives (S) of lower ionization potential as the solvents, a rapid electron transfer in the sense of an ion–molecule reaction³ takes place [see Eq. (2)].



This reaction represents a universal tool for the generation of scavenger radical cations also in such cases where these species have rather low pK values under polar conditions.⁵

Investigating the electron transfer very thoroughly, it has been found that for some substituted aromatics (S), a parallel generation of two products was observed such as the expected S^{•+} and unexpected S-derived radicals. First discovered for phenols⁶ as electron donors, cf. Eq. (3), this phenomenon appeared to be a general one for electron donors consisting of an aromatic moiety substituted with larger polarizing groups.¹



Here, this special kinetic behavior named “free electron transfer” (FET) should be discussed in more detail in this chapter.

2. Properties of Solvated Parent Ions

Parent radical cations derived from alkanes and alkyl chlorides can be directly observed in the nanosecond time domain by time-resolved spectroscopy such as laser flash photolysis and electron pulse radiolysis. Especially the latter one enables the direct ionization of the solvents independently on the optical properties of the sample and a well-defined electron transfer regime according to Eq. (2) or (3). Representative examples of the radiolytic generation of solvent radical cations are given in Eqs. (4) and (5a) for the cases of 1-chlorobutane⁷ and *n*-decane.⁸

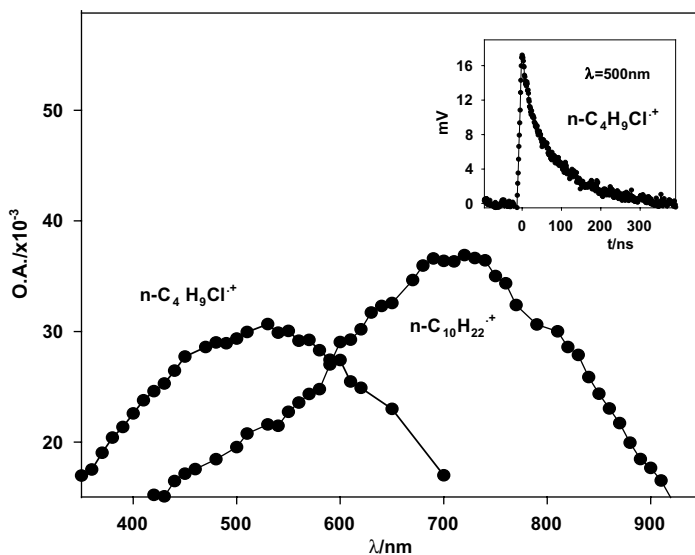


Fig. 1. Optical absorption spectra of parent radical cations taken in the pulse radiolysis of the pure solvents *n*-decane or 1-chlorobutane. The inset shows a time profile of the 1-chlorobutane radical cation at a characteristic wavelength.

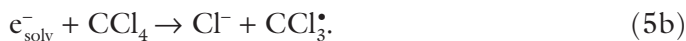
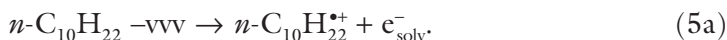
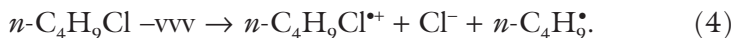


Figure 1 shows the corresponding optical absorption spectra of these radical cations as taken in the pulse radiolysis of the pure solvents. To avoid the influence of solvated electrons, in the case of alkanes, an electron scavenger such as tetrachloromethane is usually added [see Eq. (5b)]. Alkyl chlorides are internal electron scavengers and do not need further additives. In most of the cases, for the study of electron transfer reactions of type 2 or 3, the solvent derived radicals do not disturb because of their much lower reactivity compared with those of the ions.

Because of the non-polarity of the media, the mentioned solvent parent ions have no real solvation shell. They represent

pure sigma-bonded systems where spin and charge are equally distributed over the whole molecule.⁹ This is shown in Fig. 2 for the example of the 1-chlorobutane radical cation.

The rate of the electron transfer 2 depends on the free energy of the reaction which can be approximately expressed by the difference of the ionization potentials (ΔIP) of the reaction partners. Using a diversity of additives, reaction (2) has been found to be reaction-controlled up to $\Delta I \approx 0.8$ eV. At higher values the diffusion-controlled rate limit is reached.¹⁰ This can be seen from Fig. 3 where the

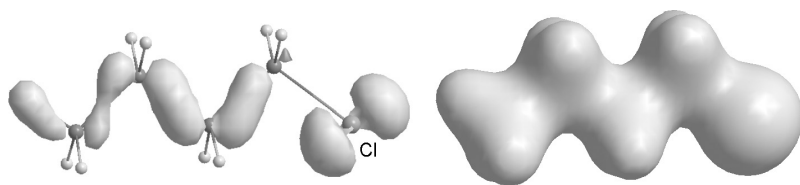


Fig. 2. Spin density (left) and charge distribution (right) of the radical cation derived from 1-chlorobutane calculated by DFT method.⁹

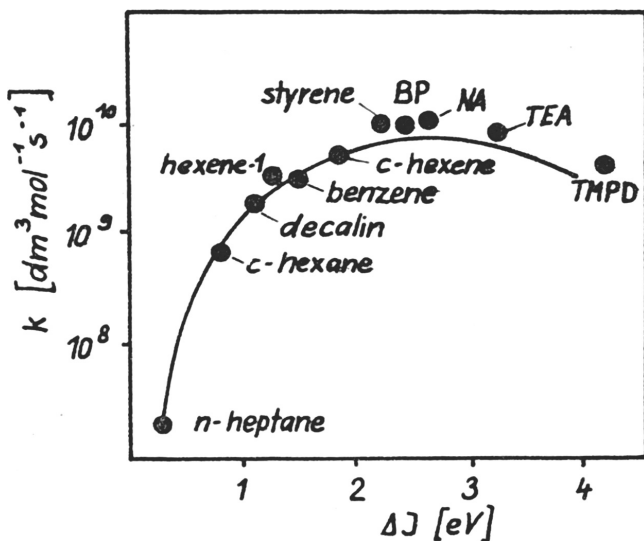


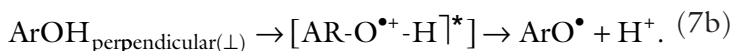
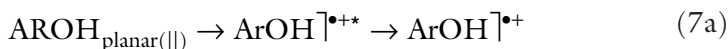
Fig. 3. Plot of the rate constant k_3 vs. ΔI for the electron transfer of Eq. (6). The scavengers used are named in the figure. Abbreviations mean: BP — benzophenone, NA — naphthalene, TEA — triethylamine, TMPD — dimethyl-p-phenylenedi-amine. [From Ref. 11, with permission of the editors.]

dependence of the rate constant of the electron transfer from various scavengers to the 1-chlorobutane radical cation is demonstrated; see also Eq. (6).



3. Products of the Electron Transfer Involving Phenols

As already mentioned, the electron transfer [Eq. (3)] shows an unusual product pattern. Therefore from here we are using the term free electron transfer (FET) indicating peculiarities of this reaction type elucidated later on. Taking phenols (ArOH) as electron donors, a 1:1 product ratio of radical cations $\text{ArOH}^{\bullet+}$ and phenoxyl radicals ArO^\bullet has been observed. These species were produced in a parallel manner as shown in the reaction sequence given in Eqs. (7).



As a representative example, Fig. 4(a) gives the results of pulse radiolysis experiments with 4-chlorophenol as electron donor, which was chosen because of the good separation of the optical transient absorption.¹² Starting 10 ns after the electron pulse, the products of FET exhibit three marked absorption maxima at $\lambda_{\text{max}} = 310, 420$ and 460 nm. The different time behavior indicates that at least two transients are involved. Focusing the interest on the absorptions in the visible range, the 420-nm peak is caused by the phenoxyl radical ArO^\bullet whereas the 460 nm one is due to the phenol radical cation $\text{ArOH}^{\bullet+}$. Although the optical absorptions are superimposed, looking into the time profiles taken in these maxima and considering a different

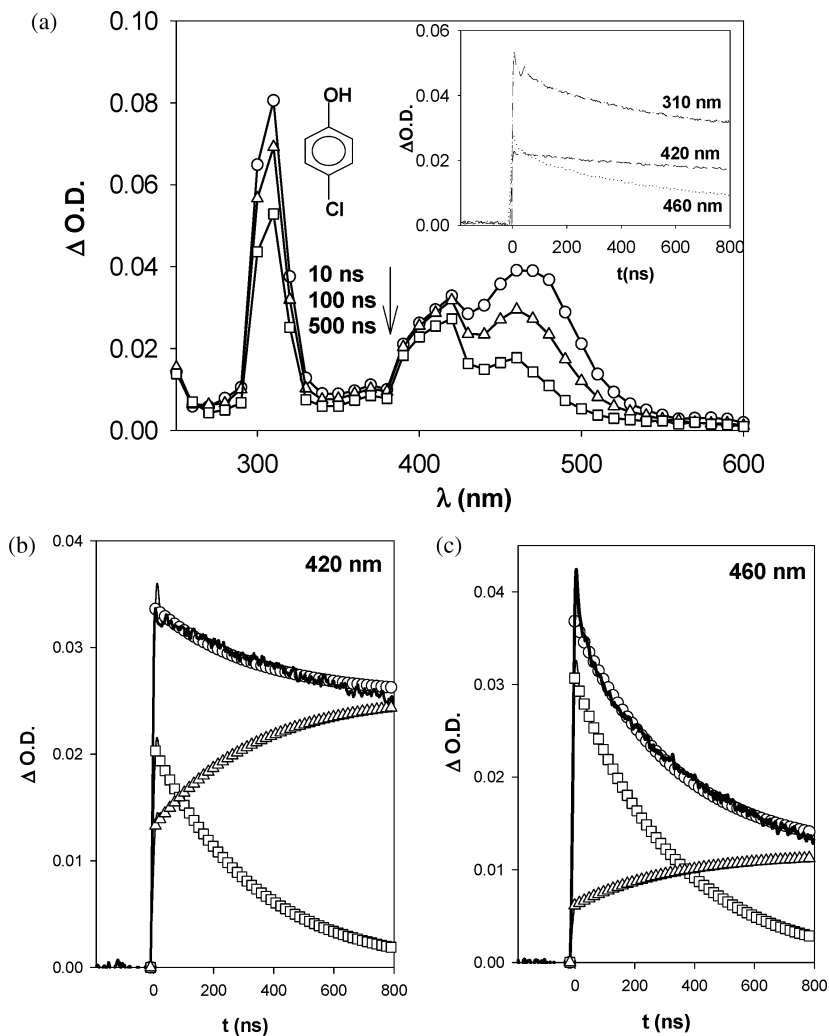


Fig. 4. (a) Transient optical absorption spectra obtained in the pulse radiolysis of nitrogen saturated solution of 0.01 mol dm^{-3} 4-Cl-ArOH in $n\text{-C}_4\text{H}_9\text{Cl}$ after (—) 10 ns, (— Δ) 100 ns and (— \square) 500 ns. The inset shows the time profiles of nitrogen saturated solution of 0.01 mol dm^{-3} 4-Cl-ArOH in $n\text{-C}_4\text{H}_9\text{Cl}$ at different wavelengths. The simulations of the time profiles (o) obtained using the ACUCHEM program^{12a,12b} are as shown at 420 nm (b) and at 460 nm (c) with the solid line being the original measurement curve. The additional curves represent the results of simulation for the formation of the phenoxyl radicals (Δ) and the decay of the radical cations (\square), cf. Ref. 12.

chemical behavior of radicals and radical cations, the time profiles of Figs. 4(b) and 4(c) are clearly different, which means that one of the species is dominating.

However, with a mathematical fit procedure¹² the kinetic connections can be visualized: both absorptions are formed within 10 ns, i.e. with the rate of the diffusion-controlled FET of $k_7 \approx 10^{10} \text{ dm}^3 \text{ mol}^{-1} \text{ s}^{-1}$. They are direct products of FET. $\text{ArOH}^{*\bullet}$ decays in the nanosecond range whereas ArO^\bullet lives at least tenths of microseconds. The fit curves describe the single transient behavior and indicate that half of the radicals exist from the very beginning. The other half is formed in a time-resolved manner by the decay of the radical cations. So the fit of the radical kinetics enables the conclusion that $\text{ArOH}^{*\bullet}$ and ArO^\bullet are primarily generated with an estimated ratio 1:1.

Exactly this kinetic behavior has also been observed for a large variety of phenols, independent of the characteristics of substituents and also of deuteration of the polar group. Thiophenols¹³ and selenols¹⁴ show an analogous effect, however, with other product ratios. This is concluded in Table 1.

4. Mechanism of FET

To understand the reason of the unusual product distribution of FET, some general considerations about reaction dynamics should be undertaken. The donor molecules consist of aromatic moieties substituted with hetero-atom containing groups such as $-\text{OH}$, $-\text{SH}$ and $-\text{SeH}$. In the ground state, of the intramolecular oscillations of those molecules, the deformations caused by bending motions (torsion, wagging etc., simplified treated as rotation) of the substituent are connected with electron fluctuation of the electrons in the HOMO and n -orbitals. As a result of a quantum-chemical calculation, this is shown in Fig. 5 for the n -orbital of phenol depending on the angle of rotation of the hetero-group around the arrow-marked bond $\text{Ar}-\text{C}-\text{OH}$.^{6,15}

From the dynamic point of view, the motion (rotation) of the substituent takes place in the femtosecond range with a frequency of $\geq 10^{13} \text{ Hz}$. If any chemical reaction is faster than this motion, the

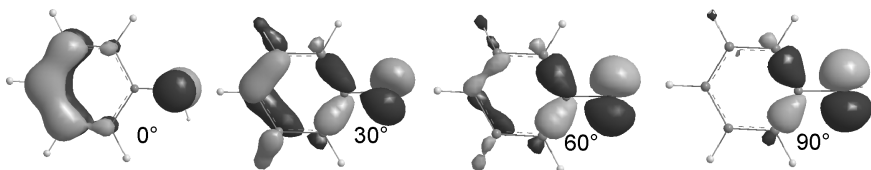
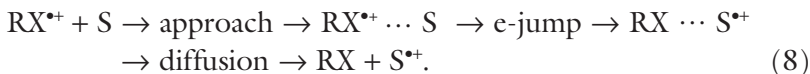


Fig. 5. Phenol: quantum-chemically calculated (B3LYP/6-31G(d)) distribution of n -electrons of the oxygen atom depending on the rotation angle of the OH-group.

permanent changing electron distribution could be detected by it, and this seems to be the case in FET.

Although it looks like an elementary reaction, Eq. (2) stands for FET as a sum of single reaction steps. In the classical understanding,¹⁶ such reaction steps can be written as a sequence given in Eq. (8). Diffusion brings the reactants together to something like an encounter situation. Then the electron jump can happen resulting in a successor situation. Subsequently diffusion separates the products.



In the description of diffusion-controlled reactions, the reactants interact by several collisions (up to 100) before the successor situation can be reached. However, if each collision results directly in products, in the case of a rapid electron transfer, such an efficient process takes place in times ≤ 1 fs. This is at least one hundred times faster than the mentioned rotation of the substituent in the donor molecule and, therefore, the variety of rotation states, i.e. of electron distributions, might be recognized. For the example of phenol, it means that different ionization products would be formed¹:

- one derived from the planar state of the molecule where the electrons of the n -orbital are equally distributed over the molecule

(Fig. 5, 0° , structure on the left) which in FET results in a metastable product radical cation, and

- and one derived from a twisted (deformed) state where the electron density is shifted more to the hetero-atom (Fig. 5, 90° , right hand side) which in the prompt ionization should result in an extremely unstable and dissociative radical cation with high charge density at the hetero-atom.

In the reactions shown in Eqs. 7(a) and 7(b), we tried to symbolize this dynamic behavior in a simplified manner. Certainly, the rotation motion around the Ar-OH axis generates a diversity of momentary electron distributions and thus very *mixed conformer states*. This diversity can hardly be introduced into an all-comprising chemical model. Hence, for simplification we define and further consider only two borderline states: the *planar state* stands for the donor molecules with low angle of twist, whereas the *perpendicular state* includes the molecules with higher deformation angle.

At least two points should be especially emphasized. (i) From the solvent part, the parent radical cations exist in a non-polar surrounding. Hence, the cations have practically no solvation shell which makes the electron jump easier in respect to more polar solvents.¹⁷ In a rough approximation the kinetic conditions of FET stand between those of gas phase and liquid state reactions, exhibiting critical properties such as collision kinetics, no solvation shell, relaxed species, etc. (ii) The primary species derived from the donor molecules are two types of radical cations with very different spin and charge distribution. One of the donor radical cations is dissociative, i.e. it dissociates within some femtoseconds, before relaxing to a stable species. The other one is metastable and overcomes to the nanosecond time range. This is the typical behavior needed for (macroscopic) identification of FET.^{6,18}

5. Energetics of the Cation Dissociation

In most of the cases the electron transfer² from functional donors to parent radical cations of alkanes and alkyl chlorides is highly exergonic. Taking phenol as electron donor and 1-chlorobutane radical

cations as acceptor, based on the ionization potential difference, an excess energy of $\Delta H = -2$ eV results; see Eq. (9).



This amount of energy can be splitted into two parts: 1.3 eV for the electron transfer and 0.7 eV as relaxation (reorganization) energy.⁶

The energetics of the postulated prompt deprotonation of the unstable part of the donor radical cations [existing in the perpendicular conformation, cf. Eq. 7(b)] can be explained by the proton affinity of the solvent as well as of the different level and the depth of the potential curves. This situation is illustrated in Fig. 6. The potential curve of the rotating ground state $\text{Ar}-\text{O}^{\ominus}-\text{OH}$ is rather flat whereas that of the phenol radical cation is considerably deeper, which also means that rotation of the substituent is non-probable because of the rigidity of the critical bond. Here it can be seen that a substantial energy difference between the metastable cation state and the perpendicular one exists. The dissociation (vibration) potentials of the phenol radical cations given on the right hand side of Fig. 6 show that the perpendicular radical cation crosses the level of the proton affinity of the solvent at a distance of $L > 1.3 \text{ \AA}$. This critical length is easily reached during the first vibration motion of the bond $\text{ArO}^{\bullet}-\text{H}^+$ and, as a consequence, dissociation (deprotonation) takes place.

6. Generalization of the FET Phenomenon

The concept of the free electron transfer is based on the hypotheses that molecule-deformation motions happening in the time range ≥ 100 femtoseconds are directly connected with electron shifts in the HOMO- π - and n -orbitals of the donor molecules. Hence, free and non-hindered electron jumps visualize this dynamic situation by formation of different primary product radical cations, which can be experimentally distinguished if one of the product cations is stable and the other one is dissociative, forming a radical and a solvent-stabilized proton.

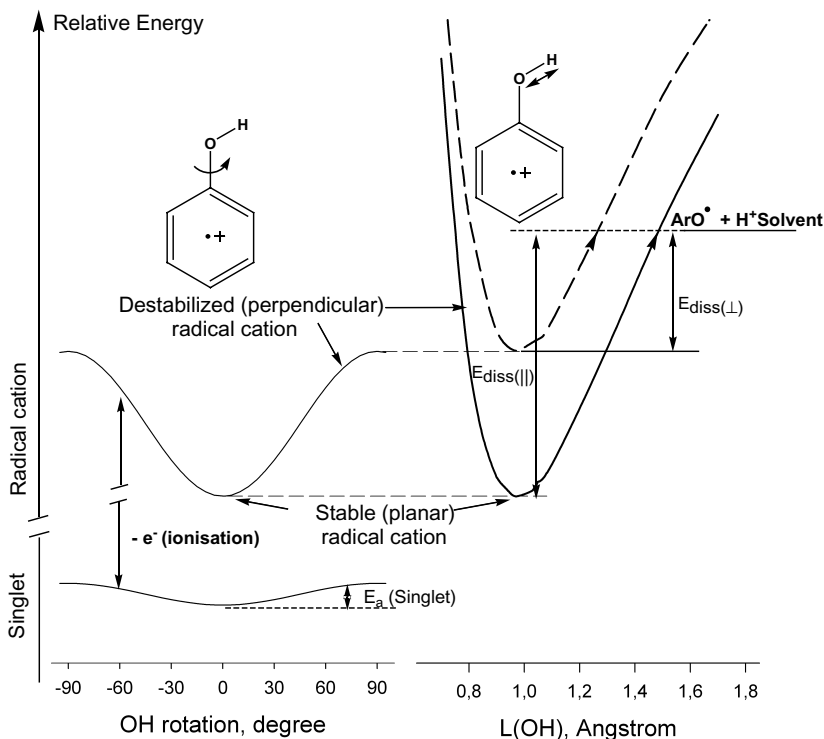
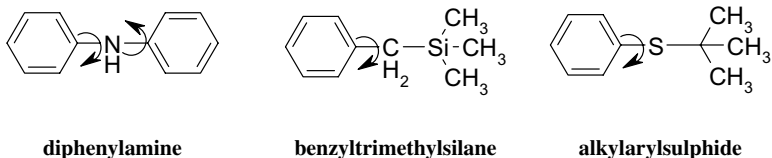


Fig. 6. Potential diagrams describing the energetic situation of phenol as donor in the ground state and for the different conformer radical cations. The left part shows the potentials dependent on the rotation angle, and the right part demonstrates energy changes dependent on the bond length (L) of Ar-OH.

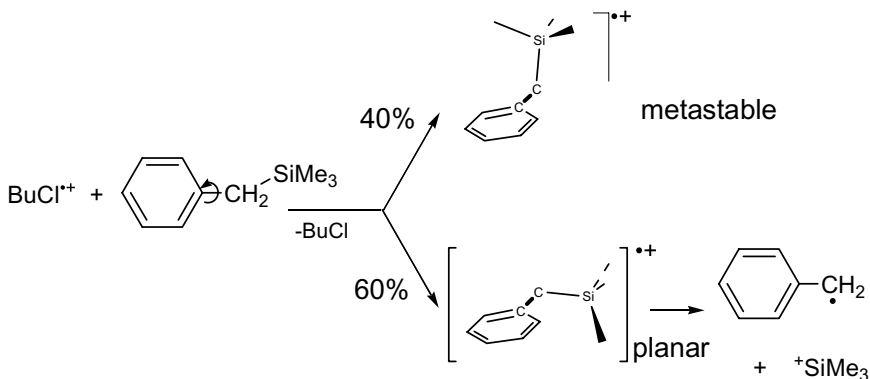
This concept has been proofed for other compounds than phenols such as thiophenols,¹³ selenols¹⁴ and also secondary aromatic amines.^{19,20} And indeed, an analogous reaction behavior has been found. FET ionization resulted in two products: metastable radical cations and radicals corresponding to the dissociative cation structure. Furthermore, the concept is also working for compounds where instead of protons, another leaving group has been used as symbolized for the following structures:^{21-23,a}

^a Structure formulae, with rotating arrow indicating the characteristic bending motion. Instead of the methyl substituents, phenyl can also be written.



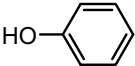
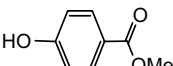
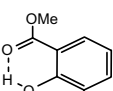
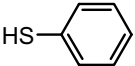
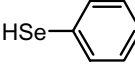
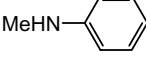
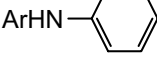
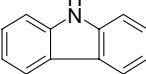
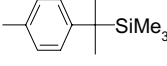
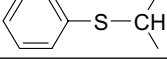
So a variety of molecules following the same reaction principle has been investigated. Table 1 gives a survey about the substance groups indicating also product yields and dynamic parameters quantum-chemically calculated with DFT B3LYP/6-31G(d).¹ As an example demonstrating the common validity of the FET concept, the ionization of trimethylarylsilanes is shown.^{21,22} In contrast to phenols and amines where the n -electrons are shifted towards the aromatic moiety, in such silanes, π -electrons of the aromatic ring are shifted towards the hetero-group (Scheme 1). Therefore, the plane structure is the dissociative one, and the twisted radical cation is metastable up to microseconds.

As an experimental proof of the interpretation of the observed product control by femtosecond dynamics, the ionization of those molecules has been studied, which contain hetero-atom groups that are immobile because of structural restrictions such as hydrogen bonding (*o*-salicylate)²⁴ or real chemical bonding



Scheme 1. FET with trimethylbenzylsilanes.

Table 1. Calculated time of one motion of bending (wagging) and valence (stretching) oscillations (B3LYP/6-31G(d)). T_{exp} gives the experimental lifetime of the part of the metastable cations. E_a denotes the energy barrier of rotation along the Ar-X axis for the singlet ground state, as well as for the radical cation (in brackets).

Electron donor molecules (S)	T_{exp} observed S^+ [ns]	t_{bending} rotation [fs]	$t_{\text{stretching}}$ vibration [fs]	E_a singlet (cation) [kJ/mol]	product ratio [%] ($\bullet+$):(\bullet)	Ref.
	280	97	9.3	12.6 (62)	50:50	5, 15
	250	89	9.3	17	50:50	24
	400*	294	12.8	61	100:0	24
	150	294	12.8	1.7 (89)	35:65	13, 27
	100	347	14.8	2.9 (82)	10:90	14
	400*	334	9.3	25 (112)	50:50	19
	450*	608 (torsion)	9.2	13	50:50	19
	500*	—	9.1	—	100:0	20
	150 ns –2 μ s	1–2 μ s	37	14–24 (60–90)	40:60	21
	≤ 100 ns	850	55	5(39)	70:30	23

(carbazol, fluorenylsilanes, etc.).^{20,22} As expected, in these cases only one product was found, i.e. only the metastable donor radical cation has been formed. Corresponding examples are given in Table 1.

7. Quantum-Chemical Justifications

As already shown for phenol (see Fig. 2), the effect of the electron shift in the ground state molecules depending on the angle of the rotating substituent can be well illustrated by electron distributions obtained by quantum-chemical calculations. Today the dynamic parameters are also available using DFT methods.^{25,26} Hence for all examples investigated, the relevant data of oscillations have been obtained such as stretching and rotation frequencies, activation barriers, etc. These data help to judge the mobility of the hetero-atom containing substituent and, therefore, to estimate the product ratio. The data are given in Table 1. Here most of the donor structures stand for a variety of similar molecules with slightly modified substitution pattern. To gain more insight into the experimental details, the second column provides the experimental lifetime of the part of the metastable donor radical cations. The columns belonging to bending and stretching motions provide the time needed for one cycle, i.e. the reciprocals of frequencies. The activation energies of the bending motions show clearly that in the ground state the barrier is low whereas in the radical cation state the critical bond is rigid. The last column gives the estimated ratios for the relation of both the reaction channels. Certainly, because of technical difficulties (spectral superpositions) these values are determined only semi-quantitatively. But they allow us to draw some conclusions:

- (1) For all phenol type compounds, a 50:50 ratio between $\text{ArOH}^{+\bullet}$ and ArO^\bullet has been found, independent of the nature of further substituents at the aromatic ring, neither of sterical nor of electronical character. This holds also for deuteration at the phenoxy group. Changing the hetero-atom (substituting oxygen by sulphur or selenium), the product ratio of FET changes on costs of the yield of the donor radical cations. These facts speak for the major influence of the bending motions and certainly also for the role of the preferred stable configuration (plane or twisted) in the ground state.¹ Concerning the latter point, phenols prefer

the planar state whereas for thiophenols and much more for selenols the twisted state is favored.

- (2) Also the product ratio observed for donor molecules with other leaving groups than protons can be understood under the above mentioned aspects. So for the compounds of trimethylbenzylsilane and of sulphide type, the product distribution of FET depends on the mobility of the critical bond (bending frequency and activation barrier of this motion). Details of these observations should be taken from the publications cited in the last column of Table 1.

8. Time Regime of the Single Steps of FET

The reaction steps of FET are governed by physical and chemical processes. Already indicated in Eq. (8) are the following processes: diffusional approach of the reactants, electron jump, and separation of the products. The fate of the gross reaction, however, will be decided in the encounter situation of the reactants. If any primary encounter is directly connected with a prompt electron jump, then it leads to a donor radical cation being in the momentary rotation conformation of the ground state molecule. Here it is decided whether or not the product radical cation is metastable or unstable (dissociative). This “one collision — one product” scenario is typical for the free electron transfer. It would mean that no defined encounter complex exists and ionization products are formed in a non-delayed way. Then the dissociation of the unstable donor radical cations is assumed to happen during the first stretching motion of the critical bond. This would mean that the dissociation is faster than the relaxation (reorganization) of the product cations.

Figure 7 gives an idea of the time regimes of the physical and chemical steps of an electron transfer reaction. Above the time axis common knowledge about the time range of some principal processes is given.²⁷ More specifically, below the axis you will find the processes which are in particular involved in the free electron transfer. It can be seen

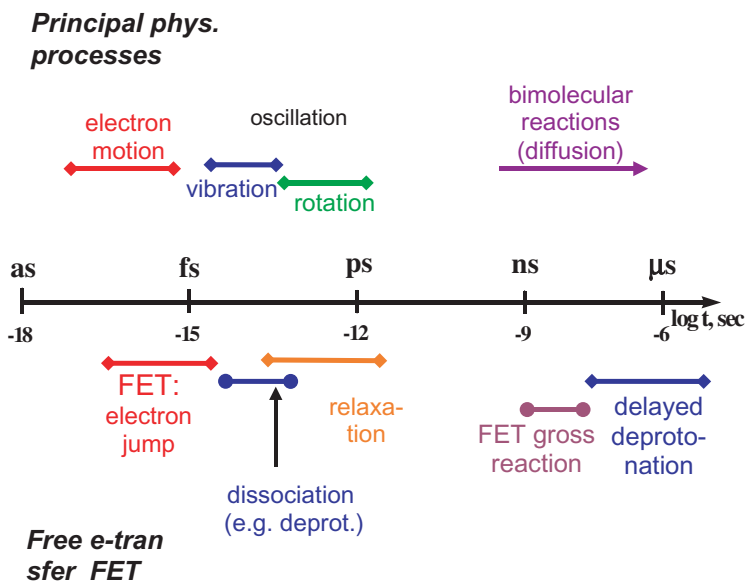


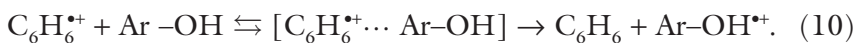
Fig. 7. Time range of processes relevant to the free electron transfer. Rotation (torsion) stands also for other similar motions such as necking, wagging, bending, etc.

that the electron jump is faster than any molecular motion. This is also the necessary condition for identifying the actual rotation (conformer) state of the molecules. Dissociation of the unstable conformer part of the radical cations takes place before relaxation of the electron transfer products. The slowest process is the approaching of the reactants by diffusion which then is identical with the observed gross reaction of FET, described by the common rate constant of the diffusion (here around $10^{10} \text{ dm}^3 \text{ mol}^{-1} \text{ s}^{-1}$). The delayed deprotonation of the metastable cation part happens in most of the cases in times slower than those of the FET gross reaction.

9. FET at Low Excess Energies, Change in the Mechanism

As mentioned in the very beginning, at low free energies of the electron transfer reaction ($\Delta H \leq 0.6 \text{ eV}$), activation-controlled rate constants

were measured. Recently it has also been found that the product pattern of FET changes from the typical two product situation (donor radical cation and donor derived radical) to a uniform product such as the donor radical cation. This observation is of importance for the interpretation of the mechanism of FET. As a consequence of the low energy excess, the electrons are not jumping at each collision of the reactants. The reactants approach and interact in the form of an encounter complex. During this interaction and within the encounter complex, an energetic optimization takes place resulting in the stable donor conformer state (planar for phenols) combined with the electron accepting solvent radical cation. The electron transfer in this complex did not proceed as a prompt jump. It is a more smooth transfer from the donor part to the acceptor which requires times defined by the lifetime of the encounter complex, which is typically in the range of tenths of femtoseconds. The deciding point, however, is the optimization of the energy of the donor molecule and its structural fixation. In the course of the slightly delayed electron transition, the originally rotating bond becomes more and more rigid. In the consequence only one (metastable) product radical cation is formed. From the experimental side this effect has been observed for the electron transfer from phenol to benzene radical cations¹⁵ as shown in Eq. (10).



Because of the low excess energy, a multi-collision interaction leads to an encounter situation combined with structural optimization to something like an asymmetric charge transfer complex which here is identical with an encounter complex. Then the delayed electron transfer takes place, as mentioned above. This can be well illustrated in terms of the quantum-chemically calculated electron and charge distributions of the involved orbitals as shown in Fig. 8.

A similar observation has been made in the study of the energy-dependent transfer from aromatic sulfides to various acceptor radical cations as derived from benzene, alkylbenzenes and biphenyl.²³ Whereas the reaction in the case of the first two cations

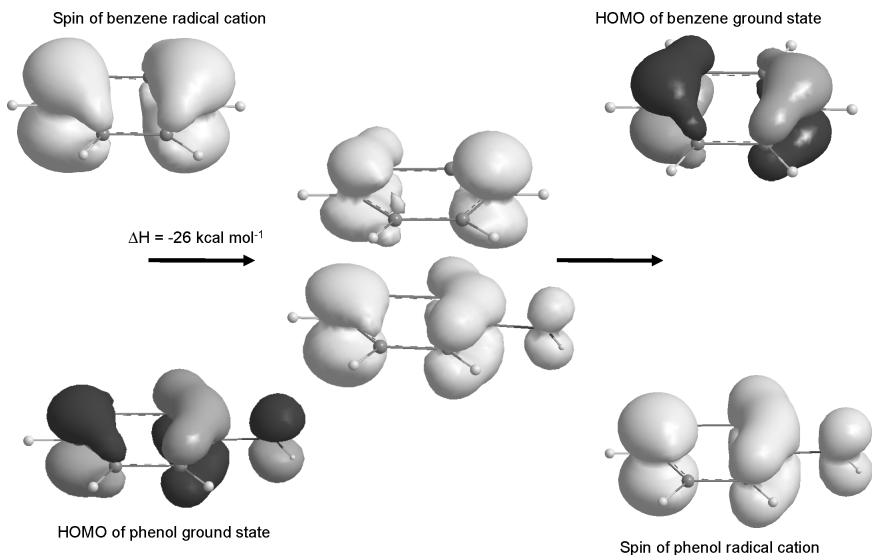


Fig. 8. Electron transfer from ground state phenol to benzene radical cation via a sandwich-like charge transfer complex [calculated at B3LYP/6-31G(d) level].

is exergonic by more than 0.8 eV and the typical two product situation is found, in the latter case only one reaction channel has been observed ($\Delta H = -0.4 \text{ eV}$).

The mentioned effect seems to be of general importance for the detailed interpretation of the kinetics of electron transfer reactions. In the present case we have two reaction lines:

- one governed by the intramolecular motions (bending, rotation, ... , FET) of the donor molecule which are indicated by the *prompt electron transfer*. Then two products are formed standing for the different kinds of rotation (conformer) states, and
- another one where an *encounter complex* causes energetic optimization and delays the electron transition to a more smooth process.

Such clear change in the elementary steps of a bimolecular chemical reaction seems to be seldom and is unknown to the authors of this

article. In the common understanding of a diffusion-controlled reaction, more than one encounter is assumed, up to ten or more. In the case of the discussed free electron however, the one collision situation can be clearly distinguished from a mechanism where more encounters and also encounter complexes exist.

10. Conclusion

The unrestricted and free electron transfer (FET) from donor molecules to solvent radical cations of alkanes and alkyl chlorides has been studied by electron pulse radiolysis in the nanosecond time range. In the presence of arenes with hetero-atom-centered substituents, such as phenols, aromatic amines, benzylsilanes, and aromatic sulfides as electron donors, this electron transfer leads to the practically simultaneous formation of two distinguishable products, namely donor radical cations and fragment radicals, in comparable amounts.

This unusual behavior is interpreted as a reflection of the femtosecond dynamics of the donor molecules and an extremely rapid electron jump within the FET. Because this jump is much faster than the rotation and bending motions of the substituents, the donor presents himself as a dynamic mixture of the conformers. Ionization of these conformers results in the formation of two types of radical cations, one of which is metastable whereas the other one dissociates immediately into radicals and cations. In line with this interpretation, donor molecules with restricted bending motions as well as rigid structures form only one ionization product, which is normally the metastable radical cation.

At low free energy of the electron transfer reaction, the mechanism changes. Instead of prompt electron jumps in each collision (see above), an encounter complex appears which delays the electron transition and controls the energetics of the process. This results in the formation of only one uniform and metastable donor radical cation.

References

1. Warman JM. (1982) The dynamics of electrons and ions in non-polar liquids. In *The Study of Fast Processes and Transient Species by Electron Pulse Radiolysis*, Baxendale JH, Busi F. (eds.), pp. 433–527. D. Reidel Publ. Company, Dordrecht.
2. Mehnert R. (1991) Radical cations in pulse radiolysis. In *Radical Ionic Systems*, Lund A, Shiotani M. (eds.), pp. 231–284. Kluwer Academic Publ., Dordrecht.
3. Brede O, Mehnert R, Naumann W. (1987) Kinetics of excitation and charge transfer reactions in non-polar media. *Chem Phys* **115**: 279–296.
4. Hamill WH. (1968) Ionic processes in γ -irradiated organic solids at -196° . In *Radical Ions*, Kaiser ET, Kevan L. (eds.), pp. 321–416. Interscience Publ., New York.
5. Mahalaxmi GR, Hermann R, Naumov S, Brede O. (2000) Free electron transfer from several phenols to radical cations of non-polar solvents. *Phys Chem Chem Phys* **2**: 4947–4955.
6. Brede O, Naumov S. (2006) Femtodynamics reflected in nanoseconds: Bimolecular free electron transfer in nonpolar media. *J Phys Chem A* **110**: 11906–11918.
7. Mehnert R, Brede O, Naumann W. (1982) Charge transfer from solvent radical cations to solutes in pulse-irradiated liquid *n*-butylchloride. *Ber Bunsenges Phys Chem* **86**: 525–529.
8. Mehnert R, Brede O, Naumann W. (1984) spectral properties and kinetics of cationic transients generated in electron pulse irradiated C_7 - to C_{16} -alkanes. *Ber Bunsenges Phys Chem* **88**: 71–78.
9. Brede O, Ganapathi MR, Naumov S, Naumann W, Hermann R. (2001) Localized electron transfer in nonpolar solution: Reaction of phenols and thiophenols with free solvent radical cations. *J Phys Chem A* **105**: 3757–3764.
10. Brede O. (2001) Peculiarities in free electron transfer. *Res Chem Intermed* **27**: 709–715.
11. Brede O, Mehnert R, Naumann W. (1986) Kinetics of excitation and charge transfer reactions. *ZfI-Mitt (Leipzig)* **122**: 5–38.
- 12a. Brown W, Herron JT, Kahaner DK. (1988) Kinetic simulation by ACUCHEM. *Int J Chem Kin* **20**: 51–58.
- 12b. Brede O, Hermann R, Naumann W, Naumov S. (2002) Monitoring of the hetero-group twisting dynamics in phenol-type molecules via different characteristic free-electron-transfer products. *J Phys Chem A* **106**: 1398–1405.
13. Hermann R, Dey GR, Naumov S, Brede O. (2000) Thiol radical cations and thiyl radicals as direct products of the free electron transfer from aromatic thiols to *n*-butyl chloride radical cations. *Phys Chem Chem Phys* **2**: 1213–1220.

14. Brede O, Hermann R, Naumov S, Mahal HS. (2001) Discrete ionization of two rotation-conditioned selenophenol conformers by rapid electron transfer to solvent parent radical cations. *Chem Phys Lett* **350**: 165–172.
15. Brede O, Naumov S, Hermann R. (2003) Monitoring molecule dynamics by free electron transfer. *Radiat Phys Chem* **67**: 225–230.
16. Strehlow H. (1992) *Rapid Reactions in Solution*. VCH Verlag, Weinheim, p. 249.
17. Kavarnos GJ. (1993) *Fundamentals of Photoinduced Electron Transfer*. VCH, New York, p. 53.
18. Brede O. (2001) Peculiarities in free electron transfer. *Res Chem Intermed* **27**: 709–715.
19. Maroz A, Hermann R, Naumov S, Brede O. (2005) Ionization of aniline and its N-methyl and N-phenyl substituted derivatives by (free) electron transfer to n-butyl chloride parent radical cations. *J Phys Chem A* **109**: 4690–4696.
20. Brede O, Maroz A, Hermann R, Naumov S. (2005) Ionization of cyclic aromatic amines by free electron transfer: Products are governed by molecule flexibility. *J Phys Chem A* **109**: 8081–8087.
21. Brede O, Hermann R, Naumov S, Perdikomatis GP, Zarkadis AK, Siskos MG. (2004) Free electron transfer mirrors rotational conformers of substituted aromatics: Reaction of benzyltrimethylsilanes with n-butyl chloride radical cations. *Phys Chem Chem Phys* **6**: 2267–2275.
22. Karakostas N, Naumov S, Siskos MG, Zarkadis AK, Hermann R, Brede O. (2005) Free electron transfer from xanthenyl and fluorenylsilanes (Me-3 or Ph-3) to parent solvent radical cations: Effect of molecule dynamics. *J Phys Chem A* **109**: 11679–11686.
23. Karakostas N, Naumov S, Brede O. (2007) Ionization of aromatic sulfides in non-polar media: Free vs reaction-controlled electron transfer. *J Phys Chem A* **111**: 71–78.
24. Brede O, Hermann R, Karakostas N, Naumov S. (2004) Ionization of the three isomeric hydroxybenzoates by free electron transfer: Product distribution depends on the mobility of the phenoxyl group. *Phys Chem Chem Phys* **6**: 5184–5188.
25. Becke AD. (1993) Density-functional thermochemistry. III. The role of exact exchange. *J Chem Phys* **98**: 5648–5652.
26. Becke AD. (1996) Density-functional thermochemistry. IV. A new dynamical correlation functional and implications for exact-exchange mixing. *J Chem Phys* **104**: 1040–1046.
27. Dey GR, Hermann R, Naumov S, Brede O. (1999) Encounter geometry determines product characteristics of the electron transfer from 4-hydroxythiophenol to n-butyl chloride radical cations. *Chem Phys Lett* **310**: 173–184.
28. Klessinger M, Michl J. (1995) *Excited States and Photochemistry of Organic Molecules*. VCH Publishers, New York.

Chapter 16

Chemistry of Sulfur-Centered Radicals

*Krzysztof Bobrowski**

In the past few years, unprecedented progress has been made in the recognition and understanding of the role and structure, and reaction mechanisms of sulfur-centered radicals. Relevant examples include radical processes connected with repairing and protective mechanisms, oxidative stress, aging, and various diseases.

1. Introduction

Radiation chemistry, and pulse radiolysis in particular, is now a mature subject that is available as a very valuable and a powerful tool by which fundamental problems in free radical reaction mechanisms can be addressed. This chapter is restricted to studies concerning sulfur-centered radicals and radical-ions performed by radiation chemistry techniques in the first eight years of XXI century (2001–2008). Sulfur-centered radicals represent a very interesting class of radicals since they exhibit very interesting redox chemistry, including biological redox processes, and different spectral and kinetic properties as

* Institute of Nuclear Chemistry and Technology, 03-195 Warszawa, Poland
E-mail: kris@ichtj.waw.pl

compared to carbon-centered radicals. This is due to the fact that the lone electron pairs present in sulfur atom influenced the overall electronic structure of radicals.

Moreover, sulfur-centered radicals and radical ions often represent a special class of radicals with odd-electron bonds and they can serve as convenient models for the evaluation of the characteristic features of such bonds.

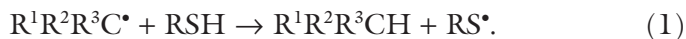
In the past few years, unprecedented progress has been made in the recognition and understanding of the structure and reaction mechanisms of sulfur-centered radicals. Research on these transients flourished particularly in systems that are relevant in biology, biochemistry, and medicine. Relevant examples include radical processes connected with repairing and protective mechanisms, a damage of biological material, oxidative stress, aging, inflammation processes, and various diseases including cancer and neurodegenerative diseases.

The chapter is divided into four main parts: Sec. 2 “Thiols”, Sec. 3 “Thioethers”, Sec. 4 “Disulfides”, and Sec. 5 “Sulfoxides and Sulfonyls”. They describe how sophisticated radiation-chemical techniques have been applied to address the role of sulfur-free radicals derived from these three classes of sulfur-containing compounds, in particular, in the biological environment. Important outputs from these studies are new directions for improving our knowledge of how sulfur-centered radicals interact with major cellular targets during oxidative stress, i.e. proteins, DNA, and lipids.

This chapter highlights only the very recent achievements emerging from radiation chemical studies. There are several excellent and comprehensive reviews and books which present and discuss the topic of sulfur-centered free-radical chemistry in a more general and detailed manner; see Refs. 1–7.

2. Thiols

The most well-known function of thiols (RSH) in free-radical biology is the repair of damage by donating a hydrogen atom, e.g. in “repairing” a carbon-centered radical [reaction (1)]



Hydrogen-atom donation from thiols to carbon-centered radicals was too often assumed to be the only property of thiols that is important in free radical processes in biology. Moreover, it was a common presumption that reaction (1) was the end of the biological pathway in which thiols “repair” radicals. Equilibria turned out to be much more important in sulfur radical chemistry than was first thought. For instance, the hydrogen-donation reaction was found to be a reversible equilibrium over 30 years after it was first observed.^{8,9}

2.1. Thiols as repairing agents

Much research has been carried out towards the identification of DNA-derived radicals formed after reaction with $\bullet\text{OH}$ radicals or other one-electron oxidants. The main features of DNA free radical chemistry have been reasonably well established from studies performed on DNA itself as well as on model systems including nucleobases, sugars, nucleosides and nucleotides, poly-U, poly-A, and DNA oligomers.¹⁰

Knowledge of the interaction of thiols with DNA-derived radicals is much less extensive. Moreover, one function of endogenous thiols is to repair radical damage in nucleic acids. Surprisingly, little was known about the rate constants for the thiol-repair reactions with pyrimidine-derived radicals having well-defined structures ($\text{Pyr}\bullet$) [reaction (2)]:



The rate constants of repair reactions of pyrimidinyl radicals of various structures ($\text{Pyr}\bullet$) by different thiols — RSH = cysteamine (CysAmSH), 2-mercaptoethanol (MerSH), cysteine (CysSH) and penicillamine (PenSH) — were determined by means of pulse radiolysis in aqueous and alcohol-containing solutions.¹¹

2.1.1. Repair reactions of hydroxyl radical adducts to the pyrimidine C5–C6 double bonds

The following $\bullet\text{OH}$ radical adducts to the pyrimidine C5–C6 double bonds ($\text{Pyr}\bullet\text{OH}$) were selected, $\text{U}\bullet(\text{C5OH})$, $\text{U}\bullet(\text{C6OH})$, $\text{T}\bullet(\text{C5OH})$,

T*(C6OH), C*(C5OH), C*(C6OH) (see Chart 1), to monitor their repair reactions [reaction (3)]:



The rate constants are shown in Table 1.

The repair rate constants do not differ significantly between the various thiols used and they are in the range from $1.6 \times 10^6 \text{ dm}^3\text{mol}^{-1}\text{s}^{-1}$ to $3.4 \times 10^6 \text{ dm}^3\text{mol}^{-1}\text{s}^{-1}$. Only cysteine (CysSH) seems to react slightly slower than the other thiols.

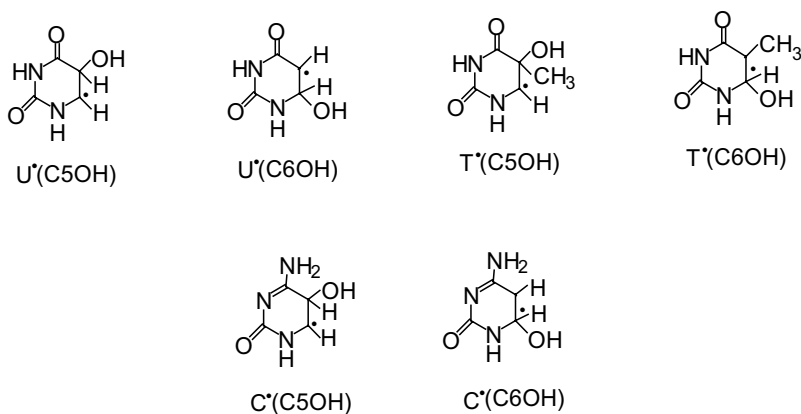


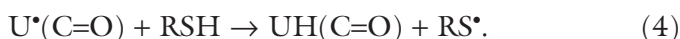
Chart 1. Structures of the *OH adducts to the pyrimidine C5–C6 double bonds.

Table 1. Repair rate constants of OH adducts to the pyrimidine C5–C6 double bonds.

Radical (Pyr*OH)	CyAmSH $k_3 \times 10^{-6}$ $\text{dm}^3\text{mol}^{-1}\text{s}^{-1}$	MerSH $k_3 \times 10^{-6}$ $\text{dm}^3\text{mol}^{-1}\text{s}^{-1}$	CysSH $k_3 \times 10^{-6}$ $\text{dm}^3\text{mol}^{-1}\text{s}^{-1}$	PenSH $k_3 \times 10^{-6}$ $\text{dm}^3\text{mol}^{-1}\text{s}^{-1}$
U*OH	2.6	2.6	2.1	2.5
T*OH	2.8	2.2	1.6	2.5
C*OH	2.7	3.4	2.5	3.2

2.1.2. Repair reactions of C6-uracilyl radical with carbonyl group at the C5 position

The repair reactions of C6-uracilyl radical, $U^*(C=O)$ (Chart 2), with carbonyl group at the C5 position [reaction (4)] were monitored at two wavelengths: $\lambda = 320$ and 400 nm, close to the wavelengths where $U^*(C=O)$ exhibits optical absorption maxima ($\lambda_{\max} = 330$ nm and the spectral region 400–425 nm:



The rate constants are shown in Table 2. The repair rate constants do not differ significantly between the various thiols used and they are in the range from $1.4 \times 10^7 \text{ dm}^3\text{mol}^{-1}\text{s}^{-1}$ to $4.8 \times 10^7 \text{ dm}^3\text{mol}^{-1}\text{s}^{-1}$.

Only penicillamine (PenSH) seems to react slightly slower than the other thiols. A limiting value of k_4 was estimated for PenSH ($k_4 \leq 1 \times 10^7 \text{ dm}^3\text{mol}^{-1}\text{s}^{-1}$).

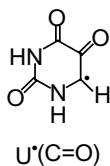


Chart 2. The structure of C6-uracilyl radical.

Table 2. Repair rate constants of C6-uracilyl radical with carbonyl group at C5 position.

Radical	Lambda	pH	CyAmSH $k_4 \times 10^{-7}$ $\text{dm}^3\text{mol}^{-1}\text{s}^{-1}$	MerSH $k_4 \times 10^{-7}$ $\text{dm}^3\text{mol}^{-1}\text{s}^{-1}$	CysSH $k_4 \times 10^{-7}$ $\text{dm}^3\text{mol}^{-1}\text{s}^{-1}$
$U^*(C=O)$	320	2.8–3.0	2.8	3.0	1.7
			2.8	2.2	1.4
	400	5.0–5.5	4.4	4.1	1.8
			4.8	3.2	1.8

2.1.3. Repair reactions of pyrimidine radical anions protonated at the C6 position

The following pyrimidine radical anions protonated at the C6 position were studied, $U^*(C6H)$, $T^*(C6H)$, and $C^*(C6H)$ (Chart 3), to monitor their repair reactions [reaction (5)]:



The rate constants measured at pH2.5 and 100 Gy/pulse dose are shown in Table 3.

The rate constants for the repair of $U^*(C6H)$ radicals were found to be smaller than those for the repair of $C^*(C6H)$ radicals. However, the repair rate constants for the particular $Pyr^*(C6H)$ do not differ significantly between the various thiols used and they are in the range from $0.5 \times 10^7 \text{ dm}^3\text{mol}^{-1}\text{s}^{-1}$ to $1.6 \times 10^7 \text{ dm}^3\text{mol}^{-1}\text{s}^{-1}$ for $U^*(C6H)$ and from $3.8 \times 10^7 \text{ dm}^3\text{mol}^{-1}\text{s}^{-1}$ to $5.7 \times 10^7 \text{ dm}^3\text{mol}^{-1}\text{s}^{-1}$ for $C^*(C6H)$.

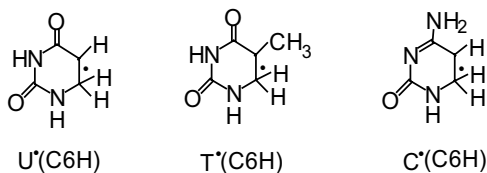


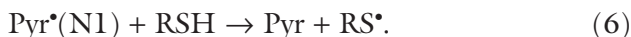
Chart 3. Structures of pyrimidine radical anions protonated at the C6 position.

Table 3. Repair rate constants of C6H radical anions protonated at C6 position.

Radical	CyAmSH $k_5 \times 10^{-7}$ $\text{dm}^3\text{mol}^{-1}\text{s}^{-1}$	MerSH $k_5 \times 10^{-7}$ $\text{dm}^3\text{mol}^{-1}\text{s}^{-1}$	CysSH $k_5 \times 10^{-7}$ $\text{dm}^3\text{mol}^{-1}\text{s}^{-1}$	PenSH $k_5 \times 10^{-7}$ $\text{dm}^3\text{mol}^{-1}\text{s}^{-1}$
$U^*(C6H)$	0.5	1.3	1.1	1.6
$C^*(C6H)$	4.8	5.7	5.0	3.8

2.1.4. Repair reactions of uracil- and thymine-derived N1-centered radicals

The following uracil- and thymine-derived N1-centered radicals, $U^*(N1)$ and $T^*(N1)$ (Chart 4), were studied to monitor their repair reactions [reaction (6)]:



The rate constants measured at pH 3.0–3.5 and 100 Gy/pulse dose are shown in Table 4.

In the measured pH range, pH variation does not affect the rate constants. The rate constants of the repair reactions are very similar for both the $U^*(N1)$ and $T^*(N1)$ radicals, with the exception of the repair of the $U^*(N1)$ radicals by MerSH.

The differences in the rate constants of repair were rationalized by the combined effects of the energy gap between the interacting molecular orbitals, the charge distribution within the radicals being

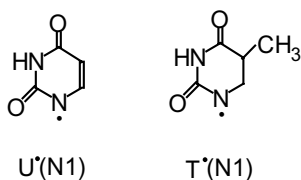


Chart 4. Structures of uracil- and thymine-derived N1-centered radicals.

Table 4. Repair rate constants of $\text{Pyr}^*(N1)$ radicals.

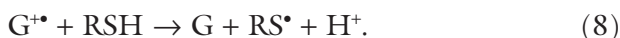
Radical	CyAmSH $k_6 \times 10^{-6}$ $\text{dm}^3\text{mol}^{-1}\text{s}^{-1}$	MerSH $k_6 \times 10^{-6}$ $\text{dm}^3\text{mol}^{-1}\text{s}^{-1}$	CysSH $k_6 \times 10^{-6}$ $\text{dm}^3\text{mol}^{-1}\text{s}^{-1}$	PenSH $k_6 \times 10^{-6}$ $\text{dm}^3\text{mol}^{-1}\text{s}^{-1}$
$U^*(N1)$	1.5	31.0 ^a	2.4	2.5
$T^*(N1)$	2.9	3.9	2.0	1.2

^a Measured at $\lambda = 540$ nm.

repaired, and the coefficients of the atomic orbitals using quantum chemical calculations, at the B3LYP/6-31g(d,p) and SCRFPCM level.

2.1.5. *Influence of dithiothreitol and cysteamine on the protection and repair of radiation-induced damage to DNA*

The effect of dithiothreitol (DTT) on DNA radiolysis at cryogenic temperatures was investigated by the EPR technique in order to elucidate its properties as a radioprotector and to establish which DNA radicals can be repaired.¹² The DTT, even at concentrations up to 1 M, does not repair more than 30% of DNA radicals. However, the ability of DTT to donate hydrogen atoms to damaged DNA in frozen aqueous solutions is limited to the allyl radical of thymine [reaction (7)] and guanine radical cation [reaction (8)]:



If the concentration of DTT is high enough to provide a sufficient amount of disulfide radical anions $(\text{RSSR})^{\bullet-}$, reaction (9) becomes important:



Contrary to the system containing DTT, the protective effect of cysteamine (CyaSH) on DNA was observed at 77 K.¹³ These differences in protection and repairing efficiency between DTT and CyaSH illustrate the distribution of both thiols in the vicinity of DNA helix. The cysteamine ($\text{H}_3\text{N}^+\text{CH}_2\text{CH}_2\text{SH}$) positive charge (+1) at physiological pH facilitates condensation in the vicinity of the polyanionic DNA helix and thus allows efficient hole transfer from DNA. In the case of DTT, the increase in the local concentration of the $-\text{SH}$ groups around the strands during freezing is not sufficient to protect DNA at 77 K. The positively charged thiols seem to be more effective in this regard.

2.2. Chemistry of thiyl radicals

For a long time, thiyl radicals (RS^\bullet) have been considered as rather unreactive species. They were formed as a result of a hydrogen atom donation from thiols (RSH) to carbon-centered radicals, in a process responsible for the “repair” of damage in biological environment. However, the H-atom donation or “repair” reaction is now known to involve a reversible equilibrium: the RS^\bullet radicals are able to abstract H-atoms. Hence, the common presumption that H-atom donation by RSH is the end of the biological pathway in which RSH repairs radicals is incorrect.

The RS^\bullet radicals are able to abstract H-atoms, though in a thermodynamically unfavorable process. The equilibrium constant involving penicillamine (PenSH) and the 2-propanol radical was estimated to be around 10^4 [reaction (10)]:



The consequences of such equilibria are profound since alternate reaction pathways involving other reactants may pull the equilibrium in either direction.

More recently, several reactions of RS^\bullet radicals generated chemically have been characterized and kinetically described, such as H-atom abstraction from the $^\alpha\text{C-H}$ bonds¹⁴ and from amino acid side chain C-H bonds¹⁵ in model peptides, and from bisallylic methylene groups in polyunsaturated fatty acids (PUFA).¹⁶

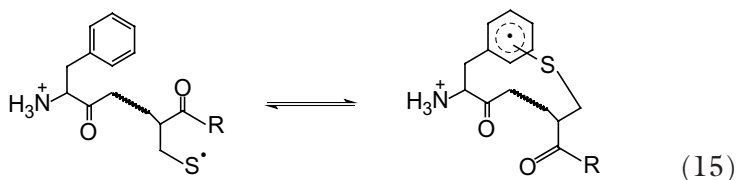
2.2.1 Intramolecular addition to aromatic rings

The intramolecular addition of cysteine thiyl radicals (CysS^\bullet) to phenylalanine yielding alkylthio-substituted cyclohexadienyl radicals was observed in Cys-Phe and Phe-Gly-Cys-Gly peptides.¹⁷ CysS^\bullet radicals were generated by pulse irradiation of aqueous solution containing the respective disulfide-linked peptide [reactions (11)–(14)]:





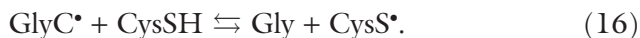
Formation of the intramolecular $\text{CyS}\cdot$ adduct to Phe [reaction (15)] is accompanied by a build-up of an absorbance with $\lambda_{\text{max}} = 324 \text{ nm}$ and a shoulder around 315 nm with $t_{1/2} \approx 0.5 \mu\text{s}$.



This process occurs when Phe and Cys are separated by a Gly residue and might be of great biological significance since it presents a possible free radical pathway to thioether-containing peptide and protein cross-links.

2.2.2. Reversible intramolecular hydrogen transfer in peptides

The reversible H-transfer reactions between αC -centered radicals in glycine ($\text{GlyC}\cdot$) and cysteine (CysSH) play an important role in various enzymatic processes [reaction (16)].¹⁸

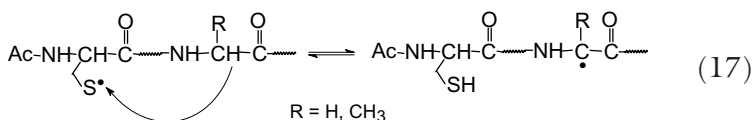


The extent to which equilibrium (16) is located on either side depends predominantly on the local environment around the Gly residue.¹⁸

Experimental data on the rate constants of equilibrium 16 and the intramolecular reaction of $\text{CysS}\cdot$ radicals with amino acids are rather sparse. An intramolecular H-transfer reaction between $\text{CysS}\cdot$ radicals and the N-terminal γ -glutamic acid was quantified for glutathione ($\gamma\text{-Glu-Cys-Gly}$).¹⁹

However, the rate constants for intramolecular H-transfer reaction between CysS• radicals and amino acids within a peptide chain were unknown.

The absolute rate constants for these reversible H-atom transfer reactions [reaction (17)] in three model peptides (N-Ac-Cys-Gly₆, N-Ac-Cys-Gly₂-Asp-Gly₃ and N-Ac-Cys-Ala₂-Asp-Ala₃) were measured by means of pulse radiolysis.²⁰

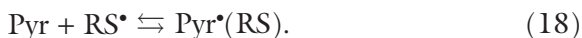


For the first two peptides, CysS• radicals abstract hydrogen atoms from the α -carbon of glycine with $k_{17} = (1.0 \text{ to } 1.1) \times 10^5 \text{ s}^{-1}$, while the reverse reaction proceeds with $k_{-17} = (8.0 \text{ to } 8.9) \times 10^5 \text{ s}^{-1}$. For the latter peptide, CysS• radicals abstract hydrogen atoms from the α -carbon of alanine with $k_{17} = (0.9 \text{ to } 1.0) \times 10^4 \text{ s}^{-1}$ while the reverse reaction proceeds with $k_{-17} = 1.0 \times 10^5 \text{ s}^{-1}$. The order of reactivity, Gly > Ala, is in accordance with previous studies on intermolecular reactions of thiyl radicals with these amino acids. The fact that $k_{17} < k_{-17}$ suggests that some secondary structure prevents the adoption of extended conformations for which calculations of homolytic bond dissociation energies would have predicted $k_{17} > k_{-17}$.

2.2.3. Addition to the C5–C6 double bond in pyrimidines

Knowledge of the mechanism of interaction between RS• radicals and the double bond C5–C6 in pyrimidines (Pyr) was rather scarce. There was, however, chemical evidence that RS• radicals add to the C6 position of the pyrimidine ring on the basis of steady-state product analysis.²¹ The phenyl-cyclopropyl substituent at the C5 position was used to leave the “fingerprint” of the RS• radical addition. This kind of addition is probably coupled with the elimination reaction

via the equilibrium [reaction (18)] which is strongly shifted to the left-hand side,

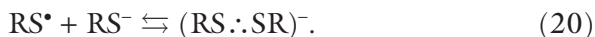


Addition and elimination reactions of RS^\bullet radicals derived from cysteamine and 2-mercaptoethanol involving C5–C6 double bond in various pyrimidines (thymine, uracil, and cytosine) were studied by the pulse radiolysis technique in aqueous solutions.²² For this purpose the kinetic parameters, i.e. the rate constants of the addition and elimination reactions, were determined using two chemical-monitoring systems.

The first system was based on the $(\text{RS}:\cdot\text{SR})^-$ absorption at $\lambda_{\text{max}} = 420$ nm for various Pyr concentration. The RS^\bullet radicals formed in reaction (19):



react subsequently in a competitive mode with RS^- [reaction (20)] and Pyr [reaction (18)] *vide supra*:



The second monitoring system was based on the pentadienyl radical (LA^\bullet) absorption at $\lambda_{\text{max}} = 275$ nm derived from PUFA, for various Pyr concentrations. The RS^\bullet radicals once generated via reaction (19), react subsequently in a competitive mode with PUFA [reaction (21)]:



The rate constants for addition and elimination of RS^\bullet radicals were determined by applying the modified version of ACUCHEM for simulations of the experimentally observed kinetic traces in $(\text{RS}:\cdot\text{SR})^-$ and LA^\bullet systems (Table 5), at the specified wavelengths:

Aliphatic RS^\bullet radicals react with the pyrimidine C5–C6 double bond by adding reversibly to the C6 position in the ring. Addition

Table 5. Addition (reaction 18) and elimination (reaction -18a) obtained in the (RS·:SR)⁻ and LA· (in parentheses) monitoring systems.

	Addition $k_{18} \times 10^{-7}$ $\text{dm}^3\text{mol}^{-1}\text{s}^{-1}$		Elimination $k_{-18} \times 10^{-5} \text{ s}^{-1}$	
	CystSH	MerSH	CystSH	MerSH
Thymine	1.0 (3.0)	1.2 (1.0)	1.5 (1.0)	1.6 (1.0)
Uracil	1.0 (1.0)	1.2 (3.0)	1.5 (1.0)	2.0 (0.7)
Cytosine	2.5 (3.0)	1.8 (1.0)	1.5 (0.9)	1.2 (1.0)

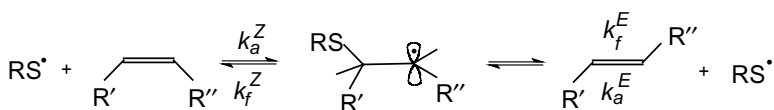
occurs with $k_{18} = (1.0\text{--}3.0) \times 10^7 \text{ dm}^3\text{mol}^{-1}\text{s}^{-1}$ and elimination with $k_{-18} = (0.7\text{--}2.0) \times 10^5 \text{ s}^{-1}$.

The addition occurs at the C6 position of the pyrimidine ring. The energy of interaction of RS· radicals and the pyrimidine C5–C6 double bond is weak as shown by quantum mechanical calculations at the B3LYP/6-31G(d)/PCM level.

2.2.4. Catalyzed *cis/trans* isomerization of lipid double bonds in monounsaturated fatty acids

In the previous decade, RS·-initiated *cis/trans* isomerization of the double bonds in membrane phospholipids, producing *trans*-isomers of unsaturated fatty acid moieties, had been demonstrated (Scheme 1). RS· radicals derived from biologically relevant thiols such as glutathione (GSH) and cysteine (CysH) initiate the isomerization process that results in the incorporation of *trans*-isomers into membranes to give more rigid packing of the bilayer.

There was little information on the rate constants of the individual reactions of Scheme 1 which could help to model biological processes.



Scheme 1.

Table 6. Rate constants for the isomerization of MUFA methyl esters catalyzed by RS• radicals at RT (symbols as in the Scheme 1).

	$k_f^E \times 10^{-8} \text{ s}^{-1}$	$k_f^Z \times 10^{-7} \text{ s}^{-1}$	$k_a^E \times 10^{-5} \text{ dm}^3 \text{ mol}^{-1} \text{ s}^{-1}$	$k_a^Z \times 10^{-5} \text{ dm}^3 \text{ mol}^{-1} \text{ s}^{-1}$
Z → E	1.6 ± 0.3	2.2 ± 0.9	2.0 ± 0.8	1.5 ± 0.3
E → Z	1.4 ± 0.4	2.2 ± 0.6	1.4 ± 0.5	1.1 ± 0.4

Therefore, the kinetics and the product yields of isomerization and thiol adduct formation for a variety of *Z*- and *E*-monounsaturated fatty acid (MUFA) esters were studied.²³ The reactions were initiated by continuous ⁶⁰Co γ -irradiation of N₂O-saturated *tert*-butanol solutions containing β -mercaptoethanol and MUFA esters. The time-dependent isomerizations and thiol additions were analyzed on the basis of the radiation chemical yields of radicals and established rate data. The rate constants for the reversible RS• addition, within experimental error, do not depend on the double bond position in the alkyl chains (*vide* Table 6).

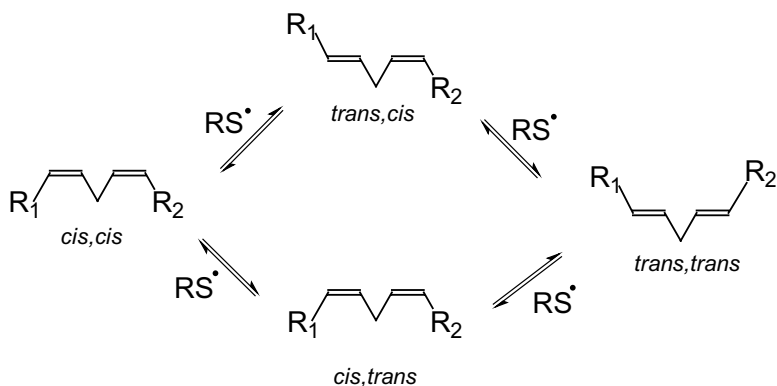
The rate of β -elimination of RS• radical to the *E*-isomer k_f^E is larger than the β -elimination of RS• radical to the *Z*-isomer k_f^Z . This fact indicates that the barrier for the fragmentation to the more stable *E*-isomer is smaller than that to the less stable *Z*-isomer. Different energies required for the formation of the transition states from the equilibrium structure of the intermediate radical MUFA(RS)• (Scheme 1) might explain this phenomenon. A faster addition of RS• radicals to *E*- than to *Z*-isomers was observed ($k_a^E/k_a^Z = 1.3$) similarly as for C-centered radicals.²⁴

2.2.5. Catalyzed *cis/trans* isomerization of lipid double bonds in polyunsaturated fatty acids

Radical processes involving membrane phospholipids are mainly referring to the peroxidation of polyunsaturated fatty acids (PUFA). In the previous decade, reactions of PUFA with a variety of RS• radicals were studied.¹⁶ Pentadienyl-type radicals (Chart 5, left structure) and radical



Chart 5. Structures of pentadienyl-type radicals and radical adducts.



Scheme 2.

adducts (Chart 5, right structure) to the double bonds were identified among transient products.

The RS^\bullet -induced *cis-trans* isomerization in PUFA was reported, however, it was rationalized in terms of reactions between pentadienyl radicals and thiols.²⁵

Therefore, the *cis-trans* isomerization mechanism in PUFA was revisited.²⁶ The reactions were initiated by continuous ^{60}Co γ -irradiation of N_2O -saturated *tert*-butanol solutions containing β -mercaptoethanol or benzenethiol and PUFA esters. Product studies led to a proposed detailed mechanistic scheme (Scheme 2).

The initial disappearance of the *cis,cis* isomer is replaced by the two mono-*trans* isomers, which in their turn are the precursors of the *trans,trans* isomer, i.e. a step-by-step isomerization.

Arachidonic acid residue (5c,8c,11c,14c-20:4) was studied in order to assess whether the *cis-trans* isomerization induced by RS^\bullet radicals depends on location of a *cis* double bond.²⁷ Thiyl radicals

were generated by γ -radiolysis in homogeneous i-PrOH solutions and in unilamellar vesicles in aqueous solutions containing phospholipids. The *cis-trans* isomerization was found to be a random process in homogeneous solutions. However, in the case of vesicles, the supramolecular organization of lipids produced a regioselective *cis-trans* isomerization. This effect indicates that RS^{\bullet} radicals entering the hydrophobic region of the membrane bilayer start to isomerize PUFA residues having the double bonds nearest to the membrane surfaces.

The *cis-trans* lipid isomerization induced by thiols was tested in human monocytic leukemia cells, where free radical stress was induced by γ -irradiation.²⁸ These results offer the first evidence that *trans* lipids can be formed in eukaryotic cells and confirm the damaging role of RS^{\bullet} radicals to the integrity of *cis* lipid geometry.

Two excellent and comprehensive reviews which present and discuss these problems in a more detailed manner have been published recently.^{29,30}

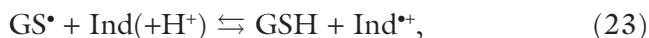
2.3. Reduction potential of GS^{\bullet} radicals

Glutathione (GSH) is the most abundant low-molecular-weight thiol protectant and antioxidant present in intracellular concentrations of several millimoles. This concentration affords protection against oxidative free radical damage by H-transfer or redox reactions. The glutathione thiyl radicals (GS^{\bullet}) are produced when GSH either donates a H-atom or electron to “repair” free radicals and are themselves oxidizing.³¹ Therefore, the reduction potential for reduction of GS^{\bullet} to GSH, represented by the mid-point electrode potential $E_m = (GS^{\bullet}, H^+/GSH)$, is a key property. Because of the relevance of GS^{\bullet} radicals in chemical biology, it was desirable to obtain experimental values of the reduction potential of the GS^{\bullet} radicals around physiological pH and thus avoid extrapolation from other pHs. The dependence of reduction potential upon pH was expected to reflect the ionization of the RSH to thiolate ion (RS^-) [reaction (22)]:



with $pK_a \sim 9$, with the electrode potential $E_m = (\text{GS}^\bullet, \text{H}^+/\text{GSH})$ expected to increase by ~ 0.06 V per pH unit with decreasing pH.

The method involved measuring the equilibrium constants for the electron transfer reactions of the type [reaction (23)]:



where Ind = a redox indicator (aniline or phenothiazine) of known or measurable reduction potential $E(\text{Ind}^{*\bullet}/\text{Ind})$. GS^\bullet and $\text{Ind}^{*\bullet}$ were generated by pulse radiolysis, and the position of redox equilibrium or the kinetics of the approach to an apparent equilibrium were measured by fast kinetic spectrophotometry.³² The electrode potential $E_m = (\text{GS}^\bullet, \text{H}^+/\text{GSH})$ varied with pH, with the expected decrease of $\Delta E_m \sim 0.06$ V per pH unit as pH was increased from ~ 6 to 8, reflecting GSH/GS^- dissociation, and permitting interpolation of a value of $E_m = 0.92 \pm 0.03$ V vs. NHE at pH 7.4. However, the oxidizing power (reduction potential) of GS^\bullet radicals did not appear to increase with decreasing pH in the region ~ 6 to 3 as expected. Apparently almost invariant potentials between pH ~ 3 and 6, with potentials significantly lower were measured using a similar approach by applying both anilines and phenothiazines as redox indicators. Deviations in reduction potential E_m were assigned in part to errors arising from radical decay during the approach to the redox equilibrium or slow electron transfer of thiol (GSH) compared to thiolate (GS^-).

2.4. Aromatic thiols

Free electron transfer (FET) from thiophenols (ArSH) to molecular radical cations of some selected nonpolar solvents was studied using the pulse radiolysis technique [reaction (24)]³³⁻³⁵



For thiophenols, along with the expected radical cations $[\text{ArSH}]^{*\bullet}$, a comparable amount of thiyl radicals (ArS^\bullet) was observed

Table 7. Average product ratio (in percent) of the ET reaction (25) in organic solvents.

Donor (ArSH)	[ArSH] ^{•+}	ArS [•]	ArO [•]
Thiophenol (PhSH)	34	66	
4-methylthiophenol (4-CH ₃ -PhSH)	34	66	
4-methoxythiophenol (4-CH ₃ O-PhSH)	44	56	
4-hydroxythiophenol (4-OH-PhSH)	20	40	40

(see Table 7), which arises in a parallel reaction channel of the type shown in the reaction (25):



The appearance of [ArSH]^{•+} and ArS[•] was attributed to two alternative, locally different pathways for FET resulting from the existence of two different types of short-living solute radical cation intermediates, which either relax to a relatively stable state [ArSH]^{•+} or promptly deprotonate to the ArS[•]. A femtoseconds dynamics of the donor molecules and an extremely rapid electron jump within the FET is responsible for this unusual behavior.³⁶ The donor is present as a dynamic mixture of conformers because this electron jump is much faster than the rotation and bending motions of the substituents. Ionization of this dynamic conformer mixture results in the formation of two types of radical cations, one which is metastable whereas the other is dissociative. Rotation and bending motions (especially around the Ar–SH axis) cause maximal changes of the molecular geometry and lead to substantial changes of the electron distribution, especially of the *n*-electrons of the sulfur in thiophenols.³⁵ In the planar structure, due to the strong resonance with the π -electrons of the aromatic ring, the *n*-electrons are shifted from the heteroatom (S) to the aromatic ring. Rotation around Ar–SH axis disturbs this coupling, and the molecular orbital in the perpendicular structure assumes *n*-symmetry and is almost localized at the heteroatom. A detailed survey of aspects and consequences emerging from these observations is presented in an excellent original feature article, i.e. Ref. 36.

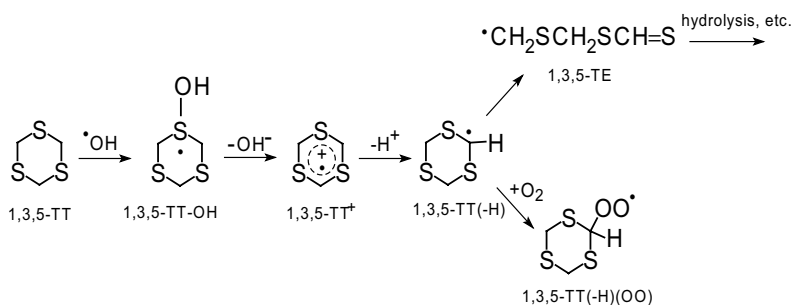
3. Thioethers

One-electron oxidation of organic sulfides (thioethers) leads primarily to a sulfur-centered radical cation, $R_2S^{\bullet+}$, which is stabilized either by resonance (e.g. if R = Aryl) or interaction with a free electron pair provided by a second sulfur atom (typically in the case of aliphatic sulfides). The latter stabilization occurs *inter-* or *intra-*molecularly with the former depending on the sulfide concentration, while the intramolecular process requires a geometry of the two interacting *p* orbitals which is favorable for overlap. This concept has been verified in numerous experiments and supported by theoretical calculations.³

3.1. Multi-sulfur-centered molecules

3.1.1. OH-induced oxidation

An interesting extension occurs for molecules containing more than two not-directly-connected sulfur atoms in the same molecule, the simplest example being 1,3,5-trithiane (1,3,5-TT). The one-electron oxidation product, namely, the **1,3,5-TT^{•+}** has been reported to absorb in the visible range with $\lambda_{\max} = 610$ nm.³⁷ The position of the maximum does not differ much from the radical cation derived from 1,3-dithiane (1,3-DT) where $\lambda_{\max} = 600$ nm. This observation indicates that the sulphur-sulfur interaction in **1,3,5-TT^{•+}** involves mainly two S atoms, thus resembling the situation in **1,3-DT^{•+}**. The contribution of the third S atom is revealed in a significant broadening of the absorption band of **1,3,5-TT^{•+}** as compared with **1,3-DT^{•+}**, which might indicate electronic participation. The recent radical chemistry studies on 1,3,5-TT performed by radiation chemical techniques, have provided further insight into the one-electron oxidation of this compound by $\bullet\text{OH}$ radicals in aqueous solutions.³⁸ Of particular interest are consecutive reactions of **1,3,5-TT^{•+}**. The most characteristic feature in the oxidation of 1,3,5-TT is the formation of the C-centered radical with a dithioester function **$\bullet\text{CH}_2\text{SCH}_2\text{SCH}=\text{S}$ (1,3,5-TE)[•]** (reactions in Scheme 3).



Scheme 3.

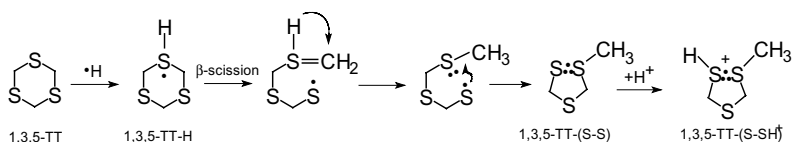
The oxidation leads, via a short-lived hydroxysulfuranyl radical (**1,3,5-TT-OH**)[•], to the radical cation **1,3,5-TT**^{•+} [$\lambda_{\text{max}} = 610 \text{ nm}$, $\epsilon_{610} = (1000 \pm 150) \text{ dm}^3\text{mol}^{-1}\text{cm}^{-1}$]. A defined pathway of the decay of **1,3,5-TT**^{•+} is proton elimination which yields the cyclic C-centered radical **1,3,5-TT(-H)**[•]. The latter radical decays via ring opening (β -scission) with an estimated rate constant of 10^5 s^{-1} to the (**1,3,5-TE**)[•] ($\lambda_{\text{max}} = 310 \text{ nm}$).

The disappearance of the (**1,3,5-TE**)[•] radical is mainly associated with the hydrolysis of the dithioester functionality and the loss of the chromophore (reactions in Scheme 3).

The formation of (**1,3,5-TE**)[•] can be suppressed in the presence of oxygen, the rationale for this being that reaction of the **1,3,5-TT(-H)**[•] with O_2 leads to **1,3,5-TT(-H)(OO)**[•].

3.1.2. •H-atom induced degradation

H atoms ($\text{H}\cdot$) tend to abstract hydrogen atoms from C–H bonds, particularly if these are activated by neighboring functionalities such as sulfur atoms. The sulfur atom in thioethers was not usually considered as the primary target of $\text{H}\cdot$ atom despite some, mostly recent, reports showing that bimolecular homolytic substitutions with $\text{H}\cdot$ atom might occur with thioethers. Because these sulfur atoms are hypervalent, they can form adducts with $\text{H}\cdot$ atoms. Radical chemistry studies on 1,3,5-trithiane (**1,3,5-TT**), performed by pulse radiolysis,



Scheme 4.

have provided further insight into the role of sulfur atom as a potential target of H^\bullet atom attack. This reaction yields a strongly absorbing, three-electron-bonded $2\sigma/1\sigma^*$ radical cation $[1,3,5\text{-TT}(\text{S}:\cdot\text{S})\text{-H}]^+$ [$\lambda_{\text{max}} = 400 \text{ nm}$, $\epsilon_{400} = (4700 \pm 500) \text{ dm}^3\text{mol}^{-1}\text{cm}^{-1}$].³⁸

Its formation is based on an addition of H^\bullet atom to one of the sulfur atoms, followed by β -scission, intramolecular sulfur-sulfur coupling (constituting a ring contraction), and further stabilization of the $\text{S}:\cdot\text{S}$ -bond thus formed by protonation (Scheme 4).

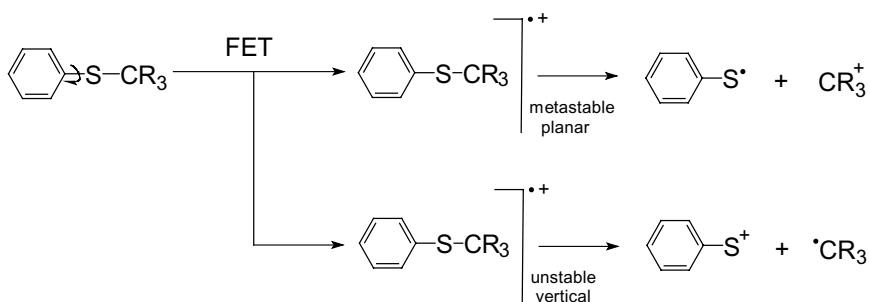
$[1,3,5\text{-TT}(\text{S}:\cdot\text{S})\text{-H}]^+$ formation can be suppressed by the addition of oxygen which scavenges the H^\bullet atoms prior to their reaction with 1,3,5-TT.

3.2. Aromatic sulfides

3.2.1. Free vs. reaction-controlled electron transfer

Aromatic sulfides analogous to thiophenols constitute a group of molecules that fulfils the structural conditions necessary for the observation of FET (Sec. 2.4), i.e. they exhibit a low barrier to rotation about the $\text{C}_{\text{sp}2}\text{-S}$ bond. Thus, the torsion motions of the substituents can be accompanied by considerable fluctuation of the electrons in the highest molecular orbitals with two extreme examples of conformers, planar and vertical. The presence of two radical cation conformers was deduced as primary products of the bimolecular free electron transfer (FET) from aromatic sulfides PhSCH_2Ph , PhSCHPh_2 , and PhSCPh_3 to *n*-butyl chloride radical based on the nanosecond pulse radiolysis experiments.³⁹

The FET products observed in the nanosecond time scale such as the metastable radical cations $(\text{Ar-S-CR}_3)^{\bullet+}$, the dissociation products



Scheme 5.

R_3C^+ and $\text{R}_3\text{C}^\bullet$, and their experimentally nondetectable respective counterparts ArS^\bullet and ArS^+ can be rationalized by the existence of two distinct channels for the dissociation of the C–S bond of the radical cations (Scheme 5). These radical cations are characterized by the same configuration but different spin distribution.

The variation of the free energy of the FET by stepwise electron transfer using mediator radical cations (benzene, butylbenzene, biphenyl) allows the energetic distinction between the diffusion-controlled (free) and the reaction-controlled electron transfer process.

3.2.2. Redox properties of organic sulfides

The one-electron reduction potentials of the radical cations of thioanisole, benzyl methyl sulphide, and 2-hydroxyethyl benzyl sulfide in water and several organic solvents were investigated by cyclic voltammetry. For comparison, the one-electron oxidations in water were also measured using pulse radiolysis.⁴⁰ The two methods are complementary and the reversible potentials determined by pulse radiolysis are fairly close to the peak potentials determined by cyclic voltammetry (Table 8) indicating that the peak potentials do correspond to the formation of sulfur radical cations for all three sulfides.

Table 8. One-electron reduction potentials (in V vs. Fe⁺/Fe) for radical cations measured by cyclic voltammetry and pulse radiolysis.

Method of generation	Thioanisole	Benzyl methyl sulfide	2-hydroxyethyl benzyl sulfide
Pulse radiolysis ^a	0.83	0.86	0.86
Cyclovoltammetry ^b	0.906	0.982	0.932

^a Uncertainty ± 20 mV; ^b Uncertainty ± 5 mV.

3.2.3. Radiation-induced radicals in polycrystalline aromatic carboxylic acids containing a thioether group

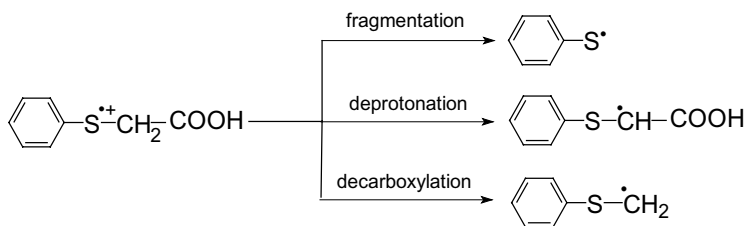
Radicals and radical ions, formed on γ -radiolysis of several polycrystalline aromatic carboxylic acids containing a thioether group in various positions with respect to the aromatic ring and to the carboxylic function, were identified using the electron spin resonance technique at 77 K and on subsequent warming over the temperature range of 95–293 K.⁴¹

The sulfur monomeric radical cations (X-S⁺–Y–COOH) were formed from direct ionization of the sulfur atom in parental aromatic carboxylic acids. These X-S⁺–Y–COOH were found to decay by three competitive pathways: (i) fragmentation via the cleavage of the C–S bond producing thiyl-type radicals XS[•], (ii) deprotonation from the methyl/methylene groups adjacent to the sulfur producing α -(alkylthio)alkyl radicals, and (iii) decarboxylation producing C-centered radicals (for phenylthioacetic acid, *vide* Scheme 6). The efficiency of each pathway is dependent on the structure of the aromatic carboxylic acid studied.

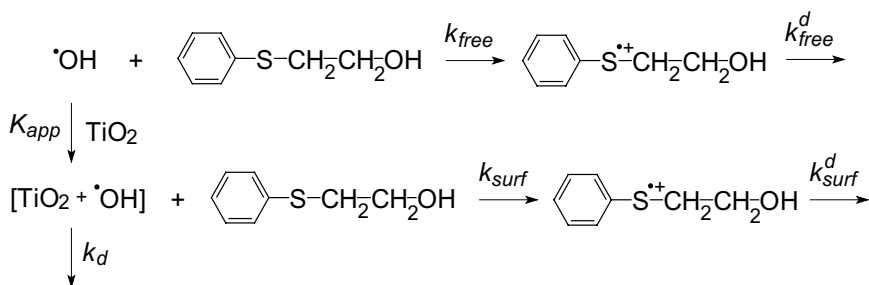
3.2.4. Oxidation processes of aromatic sulfides in colloidal solutions

The oxidation mechanism of 4-methylthiophenylmethanol (MTPM) and 2-phenyl-thioethanol (PTE) (*vide* Scheme 7) in colloidal TiO₂ aqueous solution at pH2 was studied by pulse radiolysis.⁴²

The [•]OH radicals generated during pulse radiolysis of the colloidal TiO₂ aqueous solution are strongly adsorbed on the TiO₂



Scheme 6.



Scheme 7.

Table 9. Kinetic parameters for the formation of sulfur radical cations in TiO_2 colloidal solutions containing MTPM and PTE at room temperature.

Sulfide	$k_{\text{free}} \times 10^{-9}$ $\text{dm}^3\text{mol}^{-1}\text{s}^{-1}$	$k_{\text{surf}} \times 10^{-9}$ $\text{dm}^3\text{mol}^{-1}\text{s}^{-1}$	$k_{\text{free}}^{\text{d}} \times 10^{-4}\text{s}^{-1}$	$k_{\text{surf}}^{\text{d}} \times 10^{-5}\text{s}^{-1}$
MTPM	7.0 ± 1.2	2.3 ± 0.5	3.4 ± 0.5	2.6 ± 0.4
PTE	9.5 ± 1.8	2.8 ± 0.5	8.0 ± 0.9	3.2 ± 0.5

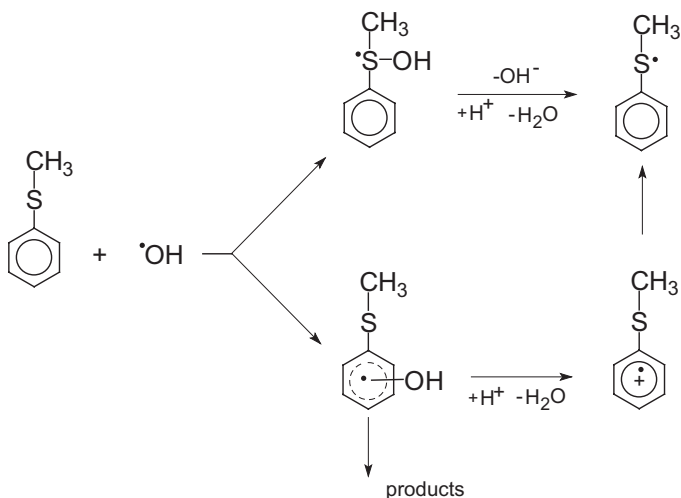
particles with an apparent association constant K_{app} of $10^6 \text{ dm}^3 \text{ mol}^{-1}$. The obtained k_{surf} values are small compared to the k_{free} values (see Table 9), suggesting that the oxidation ability of the surface-bound $\bullet\text{OH}$ radical is lower than the free $\bullet\text{OH}$ radical.

The reduction potential of the surface-bound $\bullet\text{OH}$ radical was estimated as $\geq 1.6 \text{ V}$ vs. NHE. The $k_{\text{surf}}^{\text{d}}$ values are roughly 5–10-fold faster than $k_{\text{free}}^{\text{d}}$, which was attributable to the random-walk on two- or three-dimensional lattices of the TiO_2 surface.

3.2.5. Sulfur monomeric radical cations derived from aromatic thioethers

Sulfur-centered radical cations derived from aromatic thioethers (Ar-S-Ar) have been investigated much less extensively. An important feature of one-electron oxidation of aromatic thioethers is the lack of dimeric radical sulfur radical cations (ArS \cdot :S-Ar)⁺ because of the spin delocalization onto the aromatic ring.⁴³ Oxidation of thioanisole (Ar-S-CH₃) by \cdot OH radicals was studied using pulse radiolysis.⁴⁴ At neutral pH, \cdot OH addition led to the prompt formation of monomeric sulfur radical cations and hydroxycyclohexadienyl radicals (see Scheme 8).

The latter radicals decay into products which do not include the corresponding radical cations with the delocalized positive charge on the aromatic ring. At low pH, \cdot OH addition, both to the thioether functionality and to the aromatic ring, led promptly only to the monomeric sulfur radical cations. These observations were rationalized in terms of the highly unstable nature of Ph⁺-S-CH₃ radical



Scheme 8.

cations and their rapid conversion into $\text{Ph-S}^+\text{-CH}_3$, and were supported by quantum mechanical calculations using DFT.

Monomeric sulfur radical cations derived from various carboxylic acids containing thioether functionality were generated in aqueous solutions using $\bullet\text{OH}$ radicals.^{44–47} Three decay pathways (decarboxylation, deprotonation, and β -fragmentation), similar to those presented for phenylthioacetic acid (*vide supra*, Scheme 6), were identified and found to be dependent upon the structure of sulfur radical cations.

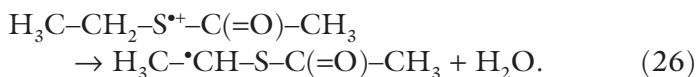
3.3. Substituted aliphatic sulfides

3.3.1. $\bullet\text{OH}$ -induced reactions

Neighboring group participation is an important concept for understanding how the oxidation of organic sulfides is controlled. These neighboring groups can provide a lone pair of electrons which can be shared with the sulfur radical cation center, $>\text{S}^+$, forming a three-electron-bonded species which effectively stabilizes the radical. The same applies to the $\bullet\text{OH}$ -induced oxidation of organic sulfides where the $\bullet\text{OH}$ radicals directly attack the sulfur, forming hydroxysulfuranyl radicals ($>\text{S}^+\text{-OH}$), but their subsequent reactions are strongly influenced by the presence of neighboring groups.

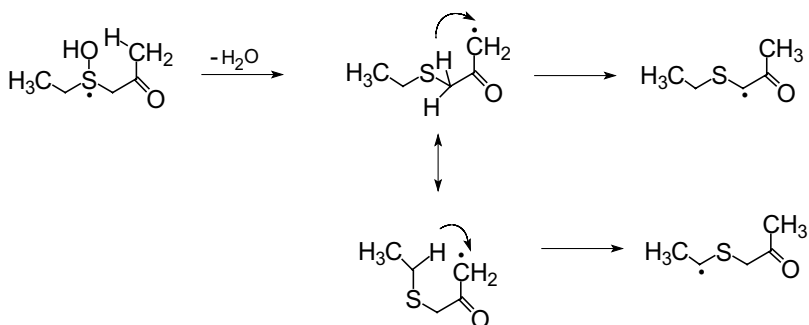
The reactions of the $\bullet\text{OH}$ radicals with two model thioether compounds, S-ethylthioacetate (SETAc) ($\text{H}_3\text{C-CH}_2\text{-S-C(=O)-CH}_3$) and S-ethylthioacetone (SETA) ($\text{H}_3\text{C-CH}_2\text{-S-CH}_2\text{-C(=O)-CH}_3$), containing electron withdrawing acetyl groups in the α and β positions, with respect to the sulfur atom have been studied by pulse radiolysis.⁴⁸ The α -positioned acetyl group in SETAc destabilizes $>\text{S}^+\text{-OH}$ radicals within the five-membered structure that leads to the formation of alkyl-substituted radicals $\text{H}_2\text{C}^+\text{-CH}_2\text{-S-C(=O)-CH}_3$ and $\text{H}_3\text{C-CH}_2\text{-S-C(-O)-}\bullet\text{CH}_2$. At high proton and SETAc concentration, the $\bullet\text{OH}$ -induced oxidation does not lead to intermolecularly three-electron-bonded dimeric radical cations $\text{SETAc(S}\cdot\text{:S)}^+$, only the α -(alkylthio)alkyl radicals $\text{H}_3\text{C-}\bullet\text{CH-S-C(=O)-CH}_3$ were observed ($\lambda_{\text{max}} = 420 \text{ nm}$). These observations are rationalized in terms of the

rapid deprotonation of sulfur monomeric radical cations SETAc($>S^+$) [reaction (26)]:



A different picture was observed for SETA, which contains a β -positioned acetyl group. The main pathway involves the formation of hydroxysulfuranyl radicals SETA($>S^{\bullet}-\text{OH}$) ($\lambda_{\text{max}} = 340 \text{ nm}$), and highly stabilized through captodative effect α -(alkylthio)alkyl radicals $\text{H}_3\text{C}-\text{CH}_2-\text{S}^{\bullet}\text{CH}-\text{C}(=\text{O})-\text{CH}_3$ ($\lambda_{\text{max}} = 380 \text{ nm}$). At low pH, SETA ($>S^{\bullet}-\text{OH}$) radicals undergo efficient conversion to intermolecularly three-electron-bonded dimeric radical cations SETA($\text{S}:\text{S}^+$) ($\lambda_{\text{max}} = 500 \text{ nm}$), especially for high SETA concentrations. In contrast, at low proton concentrations, SETA($>S^{\bullet}-\text{OH}$) radicals, even at high concentrations of SETA, decompose via elimination of water, formed through intramolecular H-transfer within the six-membered structure that leads to the formation of C-centered radicals which further undergo a 1,3-H shift and/or intra-molecular H-abstraction within the six-membered structure leading to the α -(alkylthio)alkyl radicals (Scheme 9).

Quantum mechanical calculations using *ab initio* method (Møller-Plesset perturbation theory MP2) and DFT-B3LYP method

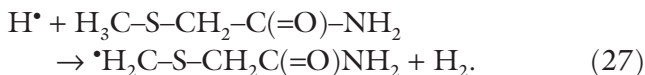


Scheme 9.

were performed for optimizations and energy calculations of the parent molecules and radicals and radical cations derived from them. The low activation energies of the transition states pointed toward the efficient direct conversion of the hydroxysulfuranyl radicals derived from SETAC and SETA into the repective C-centered radicals.⁴⁹

3.3.2. *H-atom induced reactions*

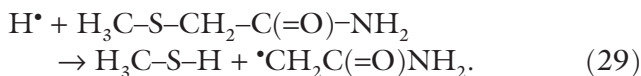
A convenient way to study the kinetics and the mechanisms of $\bullet\text{H}$ atom reactions in solution is to generate them by the pulse radiolysis of aqueous solutions at a low pH. Acetamide radicals, $\bullet\text{CH}_2\text{C}(=\text{O})\text{NH}_2$, were identified in the pulse radiolysis of aqueous solutions of α -(methylthioacetamide), $\text{H}_3\text{C-S-CH}_2\text{C}(=\text{O})\text{NH}_2$, by time-resolved electron spin resonance (TRESR) spectroscopy.⁵⁰ Only three mechanisms seemed plausible for such an observation. The first possibility is a two-step mechanism with an H-abstraction [reaction (27)]:



followed by a β -scission [reaction (28)]:



The energetics of the H abstraction reaction [reaction (27)], $\Delta G = -11.4 \text{ kcal mol}^{-1}$, and the β -scission [reaction (28)], $\Delta G = +8.1 \text{ kcal mol}^{-1}$, are from DFT calculations. The two-step mechanism was excluded because of the endothermic step in reaction (28). However, a concerted reaction [combining reactions (27) and (28)] would be spontaneous, but with only a small exothermicity, $\Delta G_{\text{concerted}} = -3.3 \text{ kcal mol}^{-1}$. Therefore, the source of these radicals appears to be a bimolecular homolytic substitution ($\text{S}_{\text{H}2}$) of the acetamide, by hydrogen atoms [reaction (29)]:



This reaction is exothermic by a significant amount and is driven by the strong S–H bond formation while only breaking a relatively weak C–S bond. From DFT calculations, $\Delta G = -29.7 \text{ kcal mol}^{-1}$.

Similar $S_{\text{H}}2$ mechanism takes place when $\bullet\text{H}$ atoms react with two other thioethers, each containing either carbonyl or carboxyl groups.⁵¹ The pulse radiolysis of acidic aqueous solutions of 2-(methylthio)ethanoic acid and S-ethylthioacetone yielded carboxymethyl radicals, $\bullet\text{CH}_2\text{COOH}$, and acetylmethyl radicals, $\bullet\text{CH}_2\text{-C(=O)-CH}_3$, respectively. Support for this assignment was given by DFT calculations and radical scavenging experiments with *tert*-butanol. DFT calculations indicated that the thermochemistry of the $S_{\text{H}}2$ reactions should be feasible with ΔG between -29 and $-33 \text{ kcal mol}^{-1}$ in both cases.

3.4. Methionine and its derivatives

3.4.1. $\bullet\text{OH}$ -induced oxidation of methionine derivatives

One-electron oxidation mechanism of methionine methyl ester (MME),⁵² N-acetylmethionine (NAM),⁵³ N-acetylmethionine amide (NAMA),⁵⁴ and N-acetylmethionine methyl ester (NAMME)⁵⁵ employing $\bullet\text{OH}$ radicals were studied by means of pulse radiolysis in aqueous solutions.

The transient observed in neutral solution containing MME by optical absorption with $\lambda_{\text{max}} = 380 \text{ nm}$ was assigned to a monomeric radical cation characterized by a three-electron-bond between sulfur and nitrogen atoms in a five-membered ring configuration and confirmed by quantum chemical calculations (Chart 6).

At low pH and higher concentration of MME, a dimeric radical cation with intermolecular three-electron bond between sulfur atoms

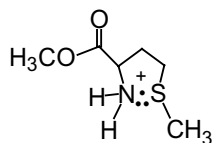


Chart 6. The structure of the S...N-bonded radical cation.

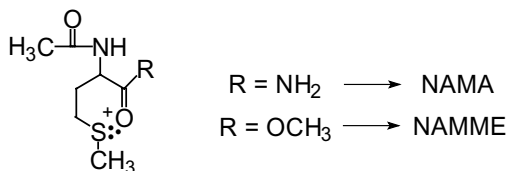


Chart 7. The structure of the S...O-bonded radical cation.

was observed by optical absorption with $\lambda_{\text{max}} = 480$ nm, resembling the optical absorption features in methionine.⁵²

The effect of N-acetyl substitution in methionine on the nature of transients formed after one-electron oxidation was studied as a function of pH and NAM concentration. The observed absorption bands with $\lambda_{\text{max}} = 290$ nm, 360 nm, and 490 nm were respectively assigned to α -(alkylthio)alkyl, hydroxysulfuranyl and dimeric radical cations with intermolecular three-electron bond between sulfur atoms.⁵³

N-acetylmethionine amide (NAMA) (Chart 7) represents a simple chemical model for the methionine residue incorporated in a peptide. Pulse radiolysis studies coupled to time-resolved UV-Vis spectroscopy and conductivity detection of N-acetyl methionine amide delivered the first experimental evidence that a sulfur radical cation can associate with the oxygen of an amide function (*vide infra*).^{54,55}

In a neutral amide $-\text{C}(=\text{O})-\text{NH}_2$, the carbonyl oxygen atom represents the better nucleophile compared to nitrogen atom. This fact is corroborated by pulse radiolysis studies of N-acetylmethionine methyl ester (NAMME) (Chart 7) showing similar kinetic and spectral features to NAMA.⁵⁵ The theoretical parameters calculated by DFT (including TD-DFT) methods support to a large extent the experimentally identified one-electron oxidation mechanism of NAMA.⁵⁶

3.4.2. Reactions of dimeric radical cations with S-S three electron bonds with selected compounds

The electron transfer reactions between sulfur-sulfur three-electron-bonded complexes derived from methionine and four hydroxycinnamic acid (HCA) derivatives (caffeic acid, ferulic acid, sinapic acid, and chlorogenic acid) were studied by pulse radiolysis with spectrophotometric detection.⁵⁷ These HCA derivatives are widely distributed

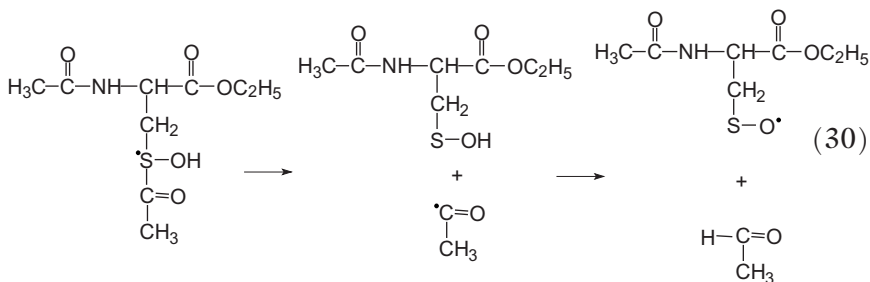
Table 10. Rate constants for the reaction of HCA derivatives with dimeric $\text{Met}(\text{S}:\text{S})^+$ radical cations.

Compound	$k_{\text{decay}}(\text{Met}(\text{S}:\text{S})^+) \times 10^{-8}$ $\text{dm}^3\text{mol}^{-1}\text{s}^{-1}$	$k_{\text{form}}(\text{HCA}^{**}) \times$ $10^{-8} \text{dm}^3\text{mol}^{-1}\text{s}^{-1}$
Caffeic acid	8.3	9.5
Ferulic acid	6.9	8.1
Sinapic acid	8.1	9.2
Chlorogenic acid	9.7	11.0

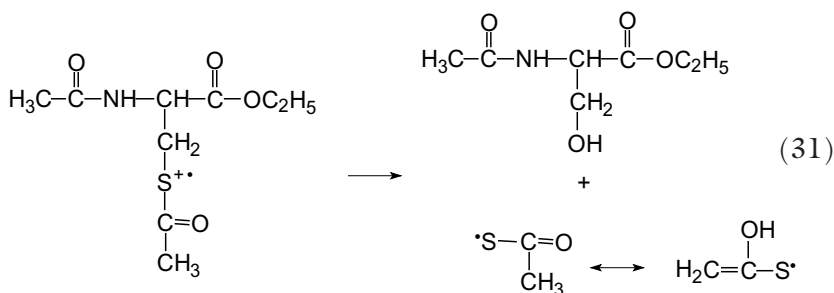
phenolic acids in fruits and vegetables and were identified as good antioxidants. The high reaction rate constants between HCA derivatives and dimeric sulfur-sulfur three-electron-bonded radical cations (see Table 10) imply that oxidized methionine residues present in the form of dimeric radical cations can be efficiently repaired by HCA derivatives via electron transfer mechanism.

3.4.3. Oxidation processes in the *S*-acetylated *L*-cysteine ester derivative

The mechanism of the $\cdot\text{OH}$ -induced oxidation of *N,S*-diacetyl-*L*-cysteine ethyl ester (SNACET) was investigated in aqueous solution using pulse radiolysis and steady-state γ -radiolysis.⁵⁸ The adjacent electron-withdrawing acetyl group destabilizes hydroxysulfuranyl radical because of a very fast fragmentation ($k_{\text{fragm}} \geq 7.9 \times 10^7 \text{ s}^{-1}$) into acyl radicals and the respective sulfenic acid. Subsequently, these intermediates react via a hydrogen-abstraction reaction that yields acetaldehyde and the respective sulfinyl radical ($\text{RSO}\cdot$) [reaction (30)].



The efficiency of that process depends on the extent to which hydroxysulfuranyl radicals undergo OH^- elimination by external proton catalysis, leading to the formation of monomeric sulfur radical cations ($\lambda_{\text{max}} = 420 \text{ nm}$). The latter species, in contrast, is stabilized by the adjacent acetyl group because of spin delocalization in the carbonyl group. The monomeric sulfur radical cation decays by two pathways: cleavage of the C–S bond producing acetyl thiyl radical [reaction (31)], and deprotonation producing a carbon-centered [$(\alpha\text{-alkylthio})\text{alkyl}$ type] radical.



3.5. Peptides

3.5.1. Oxidation of methionine in β -amyloid peptide

The first experimental evidence that Met^{35} in $\beta\text{-AP1-42}$ is more easily oxidized than in other peptides and proteins comes from one-electron oxidation of $\beta\text{AP1-40}$ using azide radicals (N_3^\bullet) produced by pulse radiolysis.⁵⁹ Thermodynamic considerations indicate that N_3^\bullet should not oxidize Met residues unless the one-electron reduction potential of Met is lowered because of favorable environment. It was shown that Met^{35} is the target in $\beta\text{-AP(1-40)}$ oxidation. Conversely the oxidation of $\beta\text{-AP(40-1)}$ with a reversed sequence of amino acids has shown that Tyr^{10} is the target of N_3^\bullet radicals. These observations are the first experimental evidences that: (i) Met^{35} in $\beta\text{-AP(1-40)}$ is more easily oxidized than in other peptides or proteins, and (ii) a change in a primary sequence drastically affects the one-electron reduction potential of Met, even in a small peptides.

Recent molecular modeling studies showed that $\beta\text{AP26-40}$ (a representative fragment of the native $\beta\text{AP1-42}$) has a high

probability of forming S–O bonds between Ile³¹C=O and Met³⁵S due to the specific structural properties of the polypeptide fragment (an α -helical motif).⁶⁰ Such a stabilization could drive the Cu^{II}-catalyzed oxidation of Met³⁵ in native β AP1-42 leading to the formation of β AP Met radical cations, Met(S⁺).

3.5.2. Stabilization of sulfide radical cations with N- and O-atoms of peptide bonds

As it has been already mentioned (*vide* Sec. 3.3), neighboring groups containing electron-rich heteroatoms play a significant role during the one-electron oxidation since they stabilize the forming sulfide radical cations. In oligopeptides, very often heteroatoms in peptide bonds are the only nucleophiles present in the vicinity of the sulfide radical cation site Met(S⁺).

In this regard, pulse radiolysis studies with UV/Vis spectrophotometrical and conductometric detection were performed in model peptides containing a single methionine residue, N-Ac-Gly-(Gly)_{n-1}-Met-(Gly)_n.⁵⁵ They show for the first time that:

- (i) MetS⁺ in peptides can be stabilized intramolecularly through bond formation with either the oxygen or the nitrogen atoms of adjacent peptide bonds (Chart 8);
- (ii) the formation of transients with S⁺:O-bonds ($\lambda_{\max} = 400$ nm; $\epsilon_{400} = 3250$ dm³mol⁻¹cm⁻¹) is kinetically preferred, but on longer

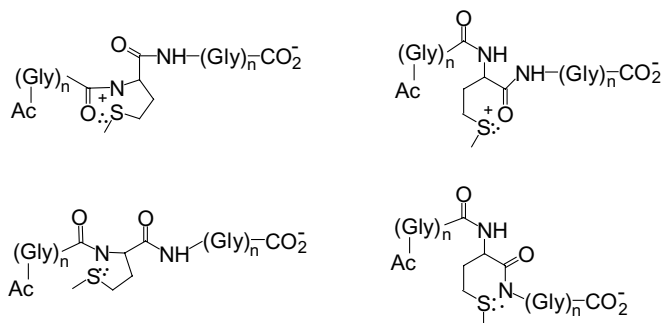


Chart 8. Structures of the S⁺:N-bonded radicals and S⁺:O-bonded radical cations in peptides.

time scales transients with S:O-bonds convert into transients with S:N-bonds ($\lambda_{\max} = 390$ nm; $\epsilon_{390} = 4500$ dm³mol⁻¹cm⁻¹) in a pH-dependent manner;

- (iii) the ratio of intramolecularly S:N-bonded species vs. intermolecularly S:S-bonded species increases with increasing peptide size suggesting that in a peptide as large as β -amyloid peptide the intramolecularly S:N-bonded species will be the dominant form of sulfur-centered radicals present; and
- (iv) ultimately transients with sulfur-nitrogen bonds transform intramolecularly into C-centered radicals ($\lambda_{\max} = 350$ nm; $\epsilon_{350} = 3700$ dm³mol⁻¹cm⁻¹) located on the C $_{\alpha}$ moiety of the peptide backbone. Another type of C-centered radical, located in the side chain of Met residue, is formed via deprotonation of MetS⁺. Carbon-centered radicals are precursors for peroxy radicals that might be involved in chain reactions of peptide and/or protein oxidation. Support for spectra assignments was additionally given by DFT calculations.⁶¹

Neighboring group participation was investigated in the •OH-induced oxidation of *S*-methylglutathione (γ -Glu-*S*-Me-Cys-Gly) in aqueous solutions by means of nanosecond pulse radiolysis.⁶² The following sulfur-centered radicals and radical cations were identified: an intramolecularly bonded [$>S:NH_2$]⁺ intermediate, an intermolecularly S:S-bonded radical cation, and an intramolecularly (S:O)⁺-bonded intermediate (Chart 9).

The latter radical is of particular note in that it supports recent observations of sulfur radical cations complexed with the oxygen

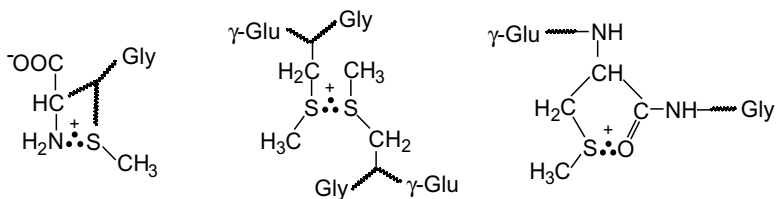


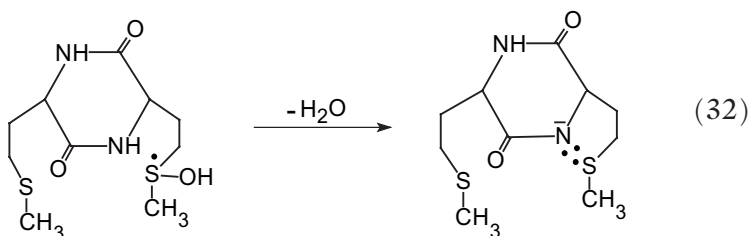
Chart 9. Structures of the S:N-, S:S-, and S:O-bonded radical cations in *S*-methylglutathione.

atoms of peptide bonds, and thus has biological and medical implications. This $(S\cdot O)^+$ -bonded intermediate had an absorption maximum at $\lambda_{\max} = 390$ nm, is formed with the rate $k \geq 6 \times 10^7$ s⁻¹, and exists in an equilibrium with the intermolecularly $S\cdot S$ -bonded radical cation. The $S\cdot S$ -bonded radical cation is formed from the monomeric sulfur radical cation ($>S^{*\cdot}$) and an unoxidized *S*-methylglutathione molecule with the rate constant of 1.0×10^9 dm³mol⁻¹s⁻¹. The short-lived $[>S\cdot NH_2]^+$ intermediate is a precursor of decarboxylation, absorbs at $\lambda_{\max} \sim 390$ nm, and decays on the time scale of hundreds of nanoseconds.

Additional insight into the details of a sulfur radical cation association with the oxygen atom of a peptide bond was gained by comparing the behavior of the *S*-methylglutathione ($S\cdot O^+$ -bonded five-membered ring) with the peptide γ -Glu–Met–Gly ($S\cdot O^+$ -bonded six-membered ring). Methionine is the homologue of *S*-methylcysteine (*S*-Me–Cys), and contrasting the behavior of these two residues provides insight into the kinetic and thermodynamic preference for six- versus five-membered ring configurations, respectively, in the formation of intramolecularly $(S\cdot O)^+$ -bonded species.

In order to define the potential reactions of $Met(S^{*\cdot})$ in long oligopeptides and proteins containing multiple and adjacent *Met* residues (e.g. prion proteins PrP, calmodulin CaM), an attempt was made to isolate some of the mechanistic steps during $\cdot OH$ -induced oxidation of a cyclic dipeptide (*L*-Met–*L*-Met). Cyclic dipeptides are suitable model compounds for the study of peptide free-radical chemistry. While appearing very small to be models for proteins, they have the unique feature of having no terminal groups. This makes them invaluable for studying interactions between side chains and peptide bonds. A small model cyclic dipeptide, *c*-(*L*-Met–*L*-Met), was oxidized by $\cdot OH$ radicals generated *via* pulse radiolysis, and the ensuing reactive intermediates were monitored by time-resolved UV/Vis spectroscopic and conductometric techniques.⁶³ An efficient formation of the $Met(S\cdot N)$ radicals was observed, in spite of the close proximity of two sulfur atoms, located in the side chains of methionine residues, and in spite of the close proximity of

sulfur atoms and oxygen atoms, located in the peptide bonds. Moreover, the formation of Met(S \cdot :N) radicals can proceed directly, via H $^+$ -transfer, with the involvement of hydrogen from the peptide bond to an intermediary hydroxysulfuranyl radical [see reaction (32)].



Ultimately, the Met(S \cdot :N) radicals decayed *via* two different pH-dependent reaction pathways, (i) conversion into sulfur–sulfur, intramolecular, three-electron-bonded radical cations, Met(S \cdot :S)⁺, and (ii) a proposed hydrolytic cleavage of the protonated form of the intramolecular, three-electron-bonded radicals {Met(S \cdot :N)/Met(S \cdot :NH)⁺}, followed by electron transfer and decarboxylation. Surprisingly, α -(alkylthio)alkyl radicals also enter the latter mechanism in a pH-dependent manner.

In order to look more closely at the conditions under which sulfur radical cations in Met can be stabilized by lone pairs of electrons from neighboring sulfur atoms, two other cyclic model dipeptides, *c*-(D-Met–L-Met) and *c*-(Gly–L-Met), were studied with combined optical and conductometric detection following radiolytic oxidation.⁶⁴ Little or no intramolecular stabilization by the unoxidized sulfur in the neighboring Met was observed in *c*-(D-Met–L-Met) (Fig. 1, right) in contrast to the previously observed intramolecular sulfur stabilization of the sulfur radical cation in the isomer *c*-(L-Met–L-Met) (Fig. 1, left).⁶³ This oxidation pattern observed in *c*-(D-Met–L-Met) was confirmed using the oxidation of *c*-(Gly–L-Met) which has no chance for intramolecular stabilization of sulfur radical cation.

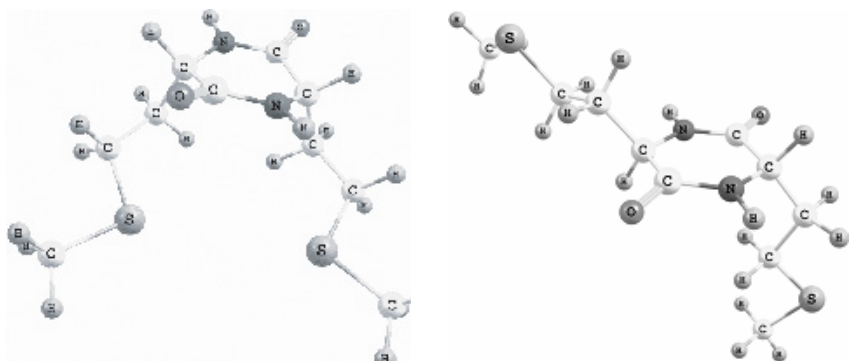


Fig. 1. Native configurations of the two optical isomers *c*-(Met-Met) (L,L on the left and D,L on the right).

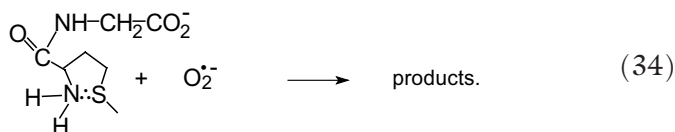
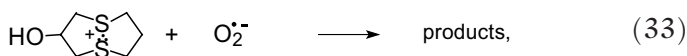
This contrasting behavior between the two cyclic Met-Met dipeptide isomers was shown to be due to the structural differences between the two isomers as computed by molecular modeling (*vide infra*).

The most important recent results obtained by means of time-resolved techniques (pulse radiolysis and laser flash photolysis) on model peptides containing single or multiple Met-residues and in selected naturally occurring peptides (Met-enkephalin and β -amyloid peptide) and proteins (thioredoxin and calmodulin) have been recently reviewed.⁶⁵

3.5.3. Reactions of sulfide radical cation complexes with $O_2^{\bullet-}$

The reactions of superoxide radical anions ($O_2^{\bullet-}$) with sulfide radical cation complexes might represent an important and efficient reaction pathway for the formation of sulfoxides in peptides and proteins containing methionine residues. Absolute rate constants for two sulfide radical cation complexes ($S\cdot:S^+$) from 1,5-dithia-3-hydroxycyclooctane and ($S\cdot:N^+$) from Met-Gly dipeptide with $O_2^{\bullet-}$ were measured using pulse radiolysis.⁶⁶ The rate constant for the

reaction of $O_2^{\bullet-}$ with the $(S\cdot:N)^+$ complex ($k_{34} = 5.3 \times 10^9 \text{ dm}^3\text{mol}^{-1}\text{s}^{-1}$) was found to be ca. 3-fold slower as compared to that of the reaction with the $(S\cdot:S)^+$ complex ($k_{33} = 1.6 \times 10^{10} \text{ dm}^3\text{mol}^{-1}\text{s}^{-1}$),



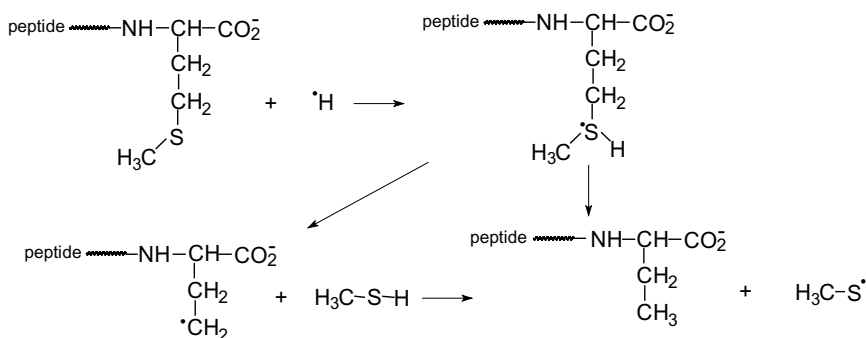
This drop in reactivity may, in part, reflect the lower probability of $O_2^{\bullet-}$ to encounter S atom in the $(S\cdot:N)^+$ complex as compared to the symmetrical $(S\cdot:S)^+$ complex. It is important to note that the reactions of $O_2^{\bullet-}$ with the sulfide radical cation complexes proceed 2.5- to 8-fold faster than the reaction of $O_2^{\bullet-}$ with superoxide dismutase ($k \approx 2 \times 10^9 \text{ dm}^3\text{mol}^{-1}\text{s}^{-1}$). From a biological point of view, it means that sulfide radical cation- $O_2^{\bullet-}$ reactions might represent a potential source for sulfoxide formation when the system is exposed to high concentrations of reactive oxygen species.

3.5.4. Reactions of H-atoms with peptides containing methionine

The role of H^\bullet atoms in biology has not yet been completely assessed. Their involvement is not limited to the effect of ionizing radiation in water but can be placed in the context of biological tandem protein-lipid damage. This is due to the fact that H^\bullet atoms are formed efficiently in the reaction of electrons with dihydrogen phosphate anion ($H_2PO_4^-$) present in biological environment.⁶⁷ The reductive attack of H^\bullet atoms on Met causes degradation, with formation of α -aminobutyric acid and CH_3S^\bullet (Scheme 10).

The sulfur-centered radicals involved in such degradation have been recently connected with a type of tandem peptide-lipid damage, based on the reaction of RS^\bullet radicals with unsaturated fatty acids.^{68,69}

The reactions of the H^\bullet atoms with Met-enkephalin (Tyr-Gly-Gly-Phe-Met) and related peptides containing methionine (Gly-Met,



Tyr–Met, Trp–Met and Met–Met) have been studied by pulse radiolysis and steady-state γ -radiolysis in aqueous and lipid vesicle suspensions.⁶⁸ In Met-enkephalin, the attack of the H^\bullet atoms occurs to $\sim 50\%$ on Met with formation of methanethiyl radicals ($\text{CH}_3\text{S}^\bullet$) (Scheme 10; peptide = Tyr–Gly–Gly–Phe–). The remaining percentage is divided roughly evenly between Tyr and Phe. The formation of diffusible $\text{CH}_3\text{S}^\bullet$ derived from the reaction presented in Scheme 10 was monitored using *trans* lipids as a biomarker in the peptide–liposome (1-palmitoyl-2-oleoyl phosphatidyl-choline (POPC) vesicles) system. The *cis-trans* isomerization of phospholipids was detected due to the catalytic action of thiyl radicals (*vide supra*, Scheme 1).

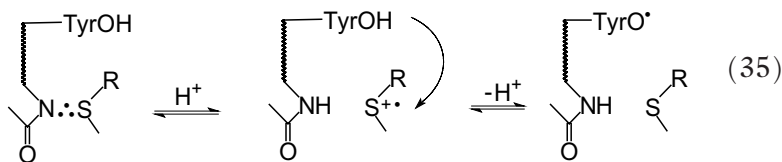
The same approach was used to study the reductive modification of a methionine residue (Met³⁵) in the amyloid- β peptide [$\text{A}\beta(1-40)$] and its reversed sequence [$\text{A}\beta(40-1)$].⁶⁹ The $\text{A}\beta$ peptide suffers the highly selective attack of H^\bullet atoms on the Met³⁵ residue, with the formation of a modified peptide containing an α -amino-butyric acid residue. Formation of *trans*-lipids in POPC system as a marker of radical damage to $\text{A}\beta$ peptide clearly shows the transfer of radical damage from the peptide to the lipid domain.

These phenomena suggest a link between lipidomics and proteomics, due to the known interaction of the Met-enkephalins and $\text{A}\beta$ peptide with cell membranes.⁷⁰

3.6. Proteins

3.6.1. Stabilization of sulfur-centered radical cations

The nine Met residues in calmodulin (a regulatory “Ca-sensor protein”) find themselves in a variety of local environments, so the stabilization of $\text{Met}(\text{S}^{\bullet+})$ can be realized in various ways depending upon local structure. For example, two pairs of Met residues are adjacent (i.e. $\text{Met}^{71}/\text{Met}^{72}$ and $\text{Met}^{144}/\text{Met}^{145}$). On the other hand, the individual Met residues have proximity to different nucleophilic groups located either in peptide bonds or in side groups of amino acid residues. The one-electron oxidation of calmodulin (CaM-Ca_4 , wild type) using pulse radiolytically generated $\bullet\text{OH}$ radicals has led to the first experimental evidence for the formation of $\text{Met}(\text{S}^{\bullet+})$ which complexes to amide groups in adjacent peptide bonds.⁷¹ The transient optical absorption spectrum recorded 0.6–1.1 μs after the pulse is broad with $\lambda_{\text{max}} \approx 390$ nm and shows a close similarity to that characteristic for (S: \cdot N)-bonded sulfide radicals. At longer times, 5–5.5 μs after the pulse, the absorption maximum is shifted to $\lambda_{\text{max}} = 405\text{--}415$ nm and shows characteristic features of the tyrosyl radical (TyrO^\bullet) spectrum. This observation is rationalized in terms of the conversion of (S: \cdot N)-bonded sulfide radicals into TyrO^\bullet radicals via intramolecular electron transfer from Tyr to Met radical cation complex [reaction (35)].



Importantly, pulse irradiation of mutants lacking Met^{144} and/or Met^{145} residues did not generate TyrO^\bullet radicals, suggesting that (S: \cdot N)-bonded sulfide radicals are precursors of TyrO^\bullet radicals.

Thioredoxin Ch1 (Trx) from *Chlamydomonas reinhardtii* contains two Met residues: Met^{41} and Met^{79} . The one-electron oxidation of W35A mutant of Trx by pulse-radiolytically generated azide

radicals N_3^\bullet leads to the transient absorption spectrum with three absorption maxima located at $\lambda = 390, 420, \text{ and } 480 \text{ nm}$.⁷² The peak at 420 nm indicated formation of tyrosyl radicals (TyrO $^\bullet$). On the other hand the bands with absorption maxima at $\lambda = 390 \text{ and } 480 \text{ nm}$ indicated the formation of sulfur-centered radicals probably either complexed to an oxygen atom of the carbonyl function of Phe³¹ or with the sulfur atom of Cys³⁹, respectively. However, at the end of the process, no oxidized products derived from methionine were detected. An intramolecular electron migration from a Tyr residue to Met-derived radicals might be responsible for the latter observation.

3.6.2. Reactions of H-atoms with proteins containing methionine

The reaction of H $^\bullet$ atoms with bovine pancreatic ribonuclease A (RNase A) has been studied by steady-state γ -radiolysis of lipid vesicle suspensions containing RNase A.⁷³ The inactivation of RNase A caused by interaction of H atoms with protein involved selective attack on methionine residues and was connected with release of diffusible thyl radicals [reaction (36)]:



RS $^\bullet$ radicals enter the bilayer, then reach and isomerize the lipid double bonds from *cis* to *trans* (*vide supra*, Scheme 1). The conclusion that Met residues in RNase A are the major source was further confirmed by monitoring of vesicle γ -irradiation containing RNase T1 (two S–S bridges, no Met residues) where the formation of the *trans* isomer was found only to 0.6% after 1 kGy.

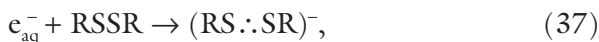
4. Disulfides

4.1. S–S bond mesolysis in aromatic sulfides

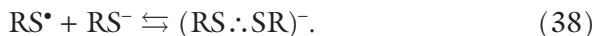
The sulfur–sulfur bond plays an important role in the tertiary structure of polypeptides and proteins. Moreover, dialkyl (RS–SR) and diaryl

(ArS–SAr) disulfides behave as radiation protection agents in biological systems. A large number of steady-state and pulse-radiolysis studies have been performed on the formation and decay of the disulfide radical anions $(\text{RS}\cdot\text{SR})^-$ in cystine and related compounds.³

Depending on the nature of R, absorption maxima range from 380–430 nm and molar absorption coefficients are about $(8 \text{ to } 9) \times 10^3 \text{ dm}^3\text{mol}^{-1}\text{cm}^{-1}$. These species are generally formed either by an attachment of hydrated electrons (e_{aq}^-), generated from water radiolysis [reaction (37)], which occurs with rate constants at the diffusion controlled limit.



or from the oxidation of thiols (RSH) and/or thiolate anions (RS^-) by $\cdot\text{OH}$ radicals, yielding thiyl radicals ($\text{RS}\cdot$), which are involved in the equilibrium [reaction (38)]:

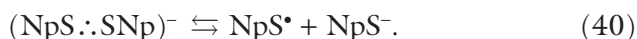


The inherent lifetime of the $(\text{RS}\cdot\text{SR})^-$ radical anion (i.e. in the absence of RS^-) is generally very short (typically $\tau_{1/2} = 200 \text{ ns}$ to $2 \mu\text{s}$) that corresponds to first-order rate constants that range from 10^5 – 10^6 s^{-1} . This species undergoes rupture of the disulfide linkage, [reaction (39)]:



Most of the studies concerning the formation and decay mechanisms of $(\text{RS}\cdot\text{SR})^-$ radical anions have been performed on aliphatic disulfides in aqueous solutions. Since the solubility of aromatic disulfides (ArS–SAr) is very poor in water, their radical anions $(\text{ArS}\cdot\text{SAr})^-$ can be easily investigated in organic solvents. A dissociation mechanism of the S–S bond in the α, α' -dinaphthyl disulfide radical anion $(\text{NpS}\cdot\text{SNp})^-$ in dimethylformamide (DMF) solutions was investigated by pulse radiolysis and in methyltetrahydrofuran (MTHF) rigid glasses by γ -radiolysis.⁷⁴

The $(\text{NpS}:\cdot\text{SNp})^-$ radical anion generated in MTHF glasses at 77 K showed an absorption band with $\lambda_{\text{max}} = 430$ nm which, upon an increase of the ambient temperature to 273 K, shifted to $\lambda_{\text{max}} = 560$ nm. This shift was interpreted with the aid of DFT calculations in terms of molecular conformational changes of $(\text{NpS}:\cdot\text{SNp})^-$ radical anion due to the elongation of the S–S bond from 0.213 nm in a rigid matrix at 77 K up to 0.290 nm in fluid phase at 273 K. The $(\text{NpS}:\cdot\text{SNp})^-$ radical anion dissociates into naphthylthiyl radical and thionaphtholate anion [reaction (38)] in DMF solution at 293 K with a first-order rate constant $k \cong 10^6 \text{ s}^{-1}$.



The activation energy, ΔE_a for the S–S bond cleavage in $(\text{NpS}:\cdot\text{SNp})^-$ radical anion was determined to be 1.8 kcal mol⁻¹, along with a frequency factor of $3.4 \times 10^7 \text{ s}^{-1}$. Assuming that the stretching between the S–S bond promotes the S–S bond cleavage in the radical anions and considering that the force constant of the $(\text{NpS}:\cdot\text{SNp})^-$ radical anion is much larger than those of the smaller $(\text{RS}:\cdot\text{SR})^-$, the naphthyl groups of the $(\text{NpS}:\cdot\text{SNp})^-$ radical anion due to their steric hindrance upon the S–S bond stretching motion may prevent a fast separation of the $(\text{NpS}:\cdot\text{SNp})^-$ radical into NpS^\bullet and NpS^- due to the viscosity of the surrounding solvent.

The stabilization of a disulfide anion through formation of a sandwich-type structure involving heterocyclic substituents providing the possibility for π interaction was observed in bis-[1-(2',3',5'-tri-*O*-acetylribosyl)uracilyl-4-yl] disulfide (USSU) (Chart 10) by means of pulse radiolysis.⁷⁵

The $(\text{US}:\cdot\text{SU})^-$ radical anion was generated via the one-electron reduction of USSU, initiated by hydrated electrons [analogous to reaction (37)], and is characterized by a broad optical absorption band with $\lambda_{\text{max}} = 450$ nm, $\epsilon_{450} = 6000 \text{ M}^{-1}\text{cm}^{-1}$, and a half-width of 1.0 eV. It exists in equilibrium with the conjugated thiyl radical (US^\bullet) and the corresponding thiolate ion (US^-) [reaction (41)]



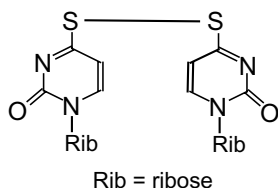


Chart 10. Structure of the bis-(1-substituted-uracilyl) disulfide.

The rate determining step for the disappearance of that remarkably stable $(\text{US}::\text{SU})^-$ radical anion is the protonation of both radical anion [reaction (42)] and the free thiolate [reaction (43)] by reaction with H^+ .



Absolute rate constants have been measured for these protonation processes which are in the range of $(0.85 \text{ to } 4.15) \times 10^4 \text{ s}^{-1}$ at pH range 8.1–4.9, respectively, and for the electron transfer between the $(\text{US}::\text{SU})^-$ radical anion and molecular oxygen ($k_{44} = 3.7 \times 10^7 \text{ M}^{-1}\text{s}^{-1}$).



The elongation of the disulfide bond after electron attachment from 2.02 to 2.73 Å in $(\text{US}::\text{SU})^-$ radical anion seems to facilitate the interaction of the heterocycles and leads to an increase in stabilization energy of 100–140 kJ mol⁻¹ as evaluated by theoretical *ab initio* calculations.⁷⁵

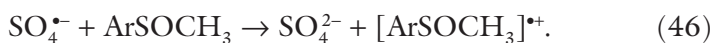
The relatively long lifetime of the $(\text{US}::\text{SU})^-$ radical anion implicates the redox properties of the equilibrium 41 which, in contrast to aliphatic systems, reveal a much higher reducing capacity.

5. Sulfoxides and Sulfonyls

5.1. Aryl sulfoxides radical cations

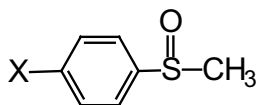
Aromatic sulfoxide radical cations have been generated by pulse radiolysis from the parent sulfoxides (Chart 11).⁷⁶

The radical cations were produced in argon-saturated aqueous solution by reaction with the strongly oxidizing sulphate radical anion ($\text{SO}_4^{\bullet-}$) via the sequence of the following reactions:



They are characterized by an intense absorption band in the UV region (≈ 300 nm) and a broad, less-intense band in the visible region (from 500 to 1000 nm) whose position depends on the nature of the ring substituents: H/550 nm, OCH_3 /900 nm, CH_3 /670 nm, Br/660 nm, and CN/560 nm. At low radiation doses the radical cations decayed by first-order kinetics with the decay rate increasing with pH. The decay involves a nucleophilic attack of H_2O or OH^- on the positively charged sulfur atom resulting in the formation of $[\text{ArSO}(\text{OH})\text{CH}_3]^{\bullet+}$, as suggested earlier for dialkyl sulfoxide radical cations.⁷⁷

DFT calculations were carried out for aromatic sulfoxide radical cations showing that in the lowest energy conformers the S–O bond is almost coplanar with the aromatic ring. In all radical cations the major fraction of charge and spin density is localized on the $-\text{S}(=\text{O})-\text{Me}$



X = H, OCH_3 , CH_3 , Br, CN

Chart 11. Structures of aromatic sulfoxides.

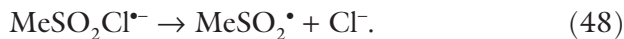
group and on the ring (~50% for OCH₃ derivative and ~30% for the other radical cations). This suggests some conjugative interaction between the -S(=O)-Me group and the aromatic group.

5.2. Sulfonyls

Unambiguous evidence was provided for a relatively long-lived electron adduct to methylsulfonyl chloride formed in reaction (47) ($k_{47} = (3.3 \pm 0.3) \times 10^{10} \text{ M}^{-1}\text{s}^{-1}$ and involving pulse radiolytically generated hydrated electron⁷⁸):



In the absence of a suitable redox partner, it eliminates chloride ion (Cl⁻) forming the sulfonyl radical (MeSO₂[•]) [reaction (48)] with $k_{48} = 1.5 \times 10^6 \text{ M}^{-1}\text{s}^{-1}$.



In the presence of oxygen, MeSO₂Cl^{•-} establishes equilibrium with superoxide radical anion [reaction (49)]:



The rate constant for the forward reaction (k_{49}) was measured to $4.1 \times 10^9 \text{ M}^{-1}\text{s}^{-1}$, while for the back reaction only an interval of $1.7 \times 10^5 \text{ s}^{-1}$ to $1.7 \times 10^6 \text{ s}^{-1}$ for k_{-49} was estimated. These data together with reference value of the reduction potential $E^0(\text{O}_2/\text{O}_2^{\bullet-}) = -155 \text{ mV}$ enable the calculation of the reduction potential of the sulfonyl chloride couple, which is equal to $E^0(\text{MeSO}_2\text{Cl}/\text{MeSO}_2\text{Cl}^{\bullet-}) = -355$ and -414 mV (vs. NHE).

The MeSO₂[•] radical reacts with oxygen [reaction (50)] with a rate constant $k_{50} = 1.1 \times 10^9 \text{ M}^{-1}\text{s}^{-1}$, however, the back reaction is very slow with $k_{-50} \ll 10^5 \text{ s}^{-1}$.



MeSO₂[•] radicals also act as the catalyst for the *cis-trans* isomerization of several *Z*- and *E*-monounsaturated fatty acid methyl esters (see Sec. 2.2.4) in homogeneous solutions.

References

1. Asmus KD. (2001) Heteroatom-centered free radicals. Some selected contributions by radiation chemistry. In *Radiation Chemistry: Present Status and Future Prospects*, Jonah C, Rao BSM. (eds.), pp. 341–393. Elsevier Science, Amsterdam.
2. Asmus KD, Bonifačić M. (2000) Free radical chemistry. In *Handbook of Oxidants and Antioxidants in Exercise*, Sen CK, Packer L, Hanninen O. (eds.), pp. 3–54. Elsevier Science B.V. Amsterdam.
3. Asmus KD, Bonifačić M. (1999) Sulfur-centered reactive intermediates as studied by radiation chemical and complementary techniques. In *S-Centered Radicals*, Alfassi ZB. (ed.), pp. 141–191. John Wiley & Sons Ltd., Chichester.
4. Glass RS. (1999) Sulfur radical cations. *Topics in Current Chemistry* **205**: 1–87.
5. Alfassi ZB. (ed.). (1999) *S-Centered radicals*. John Wiley & Sons, Chichester.
6. Packer LE, Cadenas E. (eds.) (1995) *Biothiols in Health and Disease*. Marcel Dekker, Inc., New York.
7. Asmus KD. (1990) Sulfur-centered three-electron bonded radical species. In *Sulfur-Centered Reactive Intermediates in Chemistry and Biology*, Chatgililoglu C, Asmus KD. (eds.), pp. 155–172. Plenum Press, New York.
8. Schöneich C, Bonifačić M, Asmus KD. (1989) Reversible H-atom abstraction from alcohol by thiyl radicals: Determination of absolute rate constants by pulse radiolysis. *Free Rad Res Comms* **6**: 393–405.
9. Akhlaq MS, Schuchmann HP, von Sonntag C. (1987) The reverse of the ‘repair’ reaction of thiols: H-abstraction at carbon by thiyl radicals. *Int J Radiat Biol* **51**: 91–102.
10. von Sonntag C. (2006) *Free-Radical-Induced DNA Damage and Its Repair*. Springer-Verlag, Berlin, Heidelberg, New York.
11. Wojcik A, Naumov S, Marciniak B, Brede O. (2006) Repair reactions of pyrimidine-derived radicals by aliphatic thiols. *J Phys Chem B* **110**: 12738–12748.
12. Ambroz HB, Kemp TJ, Kornacka E, Przybytniak G. (2002) The influence of dithiothreitol on DNA radiolysis in frozen aqueous solution: An EPR study. *Radiat Phys Chem* **64**: 107–113.
13. Ambroz H, Kornacka EM, Przybytniak GK. (2004) Influence of cysteamine on the protection and repair of radiatio-induced damage to DNA. *Radiat Phys Chem* **70**: 677–686.
14. Nauser T, Schöneich C. (2003) Thiyl radicals abstract hydrogen atoms from the αC-H bonds in model peptides: Absolute rate constants and effect of amino acid structure. *J Am Chem Soc* **125**: 2042–2043.

15. Nauser T, Pelling J, Schöneich C. (2004) Thiyl radical reaction with amino acid side chains: Rate constants for hydrogen transfer and relevance for posttranslational protein modification. *Chem Res Toxicol* **17**: 1323–1328.
16. Schöneich C, Dillinger U, von Bruchhausen F, Asmus KD. (1992). *Arch Biochem Biophys* **292**: 456–467.
17. Nauser T, Casi G, Koppenol WH, Schöneich C. (2005) Intramolecular addition of cysteine thiyl radicals to phenylalanine in peptides: Formation of cyclohexadienyl type radicals. *Chem Comm* 3400–3402.
18. Himo F, Siegbahn PEM. (2003) Quantum chemical studies of radical-containing enzymes. *Chem Rev* **103**: 2421–2456.
19. Zhao R, Lind J, Merenyi G, Eriksen TE. (1997) Significance of the intramolecular transformation of glutathione thiyl radicals to α -aminoalkyl radicals. Thermochemical and biological implications. *J Chem Soc Perkin Trans II*: 569–574
20. Nauser T, Casi G, Koppenol W, Schöneich C. (2008) Reversible intramolecular hydrogen transfer between cysteine thiyl radicals and glycine and alanine in model peptides: Absolute rate constants derived from pulse radiolysis and laser flash photolysis. *J Phys Chem B* **112**: 15034–15044.
21. Carter KN, Taverner T, Schiesser CH, Greenberg MM. (2000) Chemical evidence for thiylradical addition to the C-6-position of a pyrimidine nucleoside and its possible relevance to DNA damage amplification. *J Org Chem* **65**: 8375–8378.
22. Wojcik A, Naumov S, Marciniak B, Hermann R, Brede O. (2005) Thiyl radical interaction with pyrimidine C5–C6 double bond. *J Phys Chem B* **109**: 15135–15144.
23. Chatgililoglu C, Alltieri A, Fisher H. (2002) The kinetics of thiyl radical-induced reactions of monounsaturated fatty acid esters. *J Am Chem Soc* **124**: 12816–12823.
24. Fischer H, Radom L. (2001) Factors controlling the addition of carbon-centered radicals to alkenes-an experimental and theoretical perspective. *Angew Chem Int Ed* **40**: 1340–1371.
25. Schwinn J, Sprinz H, Drossler K, Leistner S, Brede O. (1998) Thiyl radical-induced *cis/trans*-isomerization of methyl linoleate in methanol and of linoleic acid residues in liposomes. *Int J Radiat Biol* **74**: 359–365.
26. Ferreri C, Costantino C, Perrotta L, Landi L, Mulazzani QG, Chatgililoglu C. (2001) Cis-trans isomerization of polyunsaturated fatty acid residues in phospholipids catalyzed by thiyl radicals. *J Am Chem Soc* **123**: 4459–4468.
27. Ferreri C, Samadi A, Sassatelli F, Landi L, Chatgililoglu C. (2004) Regioselective cis-trans isomerization of arachidonic double bonds by thiyl radicals: The influence of phospholipid supramolecular organization. *J Am Chem Soc* **126**: 1063–1072.
28. Ferreri C, Kratzsch S, Brede O, Marciniak B, Chatgililoglu C. (2005) *Trans* lipid formation induced by thiols in human monocytic leukemia cells. *Free Radic Biol Med* **38**: 1180–1187.

29. Ferreri C, Chatgililoglu C. (2005) Geometrical *trans* lipid isomers: A new target for lipidomics. *Chem Bio Chem* **6**: 1722–1734.
30. Chatgililoglu C, Ferreri C. (2005) Trans lipids: The free radical path. *Acc Chem Res* **38**: 441–448.
31. Wardman P. (1995) Reactions of thyl radicals. In *Biothiols in Health and Disease*, Packer L, Cadenas E. (eds.), pp. 1–19. Marcel Dekker, Inc., New York.
32. Madej E, Wardman P. (2007) The oxidizing power of the glutathione thyl radical as measured by its electrode potential at physiological pH. *Arch Biochem Biophys* **462**: 94–102.
33. Brede O, Hermann R, Naumann W, Naumov S. (2002) Monitoring of the heterogroup twisting dynamics in phenol type molecules via different characteristic free-electron-transfer products. *J Phys Chem A* **106**: 1398–1405.
34. Brede O, Ganapathi MR, Naumov S, Naumann W, Hermann R. (2001) Localized electron transfer in nonpolar solution: Reaction of phenols and thiophenols with free solvent radical cations. *J Phys Chem A* **105**: 3757–3764.
35. Hermann R, Dey GR, Naumov S, Brede O. (2000) Thiol radical cations and thyl radicals as direct products of the free electron transfer from aromatic thiols to *n*-butyl chloride radical cations. *Phys Chem Chem Phys* **2**: 1213–1220.
36. Brede O, Naumov S. (2006) Femtodynamics reflected in nanoseconds: Bimolecular free electron transfer in nonpolar media. *J Phys Chem A* **110**: 11906–11918.
37. Asmus KD, Bahnemann D, Bonifačić M, Gillis GA (1978) Free radical oxidation of organic sulphur compounds in aqueous solution. *Faraday Discuss Chem Soc* **63**: 213–225.
38. Asmus KD, Hug GL, Bobrowski K, Mulazzani QG, Marciniak B. (2006) Transients in the oxidative and H-atom-induced degradation of 1,3,5-trithiane. Time-resolved studies in aqueous solution. *J Phys Chem A* **110**: 9292–9300.
39. Karakostas N, Naumov S, Brede O. (2007) Ionization of aromatic sulfides in nonpolar media: Free vs reaction-controlled electron transfer. *J Phys Chem A* **111**: 71–78.
40. Taras-Goslinska K, Jonsson M. (2006) Solvent effects on the redox properties of thioethers. *J Phys Chem A* **110**: 9513–9517.
41. Strzelczak G, Korzeniowska-Sobczuk A, Bobrowski K. (2005) Electron spin resonance study of radiation-induced radicals in polycrystalline aromatic carboxylic acids containing a thioether group. *Radiat Phys Chem* **72**: 135–141.
42. Tojo S, Tachikawa T, Fujitsuka M, Majima T. (2004) Oxidation processes of aromatic sulfides by hydroxyl radicals in colloidal solution of TiO₂ during pulse radiolysis. *Chem Phys Lett* **384**: 312–316.
43. Baciocchi E, Gerini MF. (2004) Rotational barriers, charges, and spin densities in alkyl aryl sulfide radical cations: Density functional study. *J Phys Chem A* **108**: 2332–2338
44. Korzeniowska-Sobczuk A, Hug GL, Carmichael I, Bobrowski K. (2002) Spectral, kinetics, and theoretical studies of radical cations derived from thioanisole and its carboxylic derivative. *J Phys Chem A* **106**: 9251–9260.

45. Filipiak P, Hug GL, Carmichael I, Korzeniowska-Sobczuk A, Bobrowski K, Marciniak B. (2004) Lifetimes and modes of decay of sulfur-centered radical zwitterions containing carboxylate and phenyl groups. *J Phys Chem A* **108**: 6503–6512.
46. Gawandi VB, Mohan H, Mittal JP. (2003) Investigations on the nature of the transient species formed on pulse radiolysis of a aqueous solution of 4-(methylthio)benzoic acid. *Res Chem Intermed* **29**: 51–62.
47. Mohan H, Mittal JP. (2002) Different channels of hydroxyl radical reaction with aryl sulfides: Effect of the substituents. *J Phys Chem A* **106**: 6574–6580.
48. Varmenot N, Bergès J, Abedinzadeh Z, Scemama A, Strzelczak G, Bobrowski K. (2004) Spectral, kinetics, and theoretical studies of sulfur-centered reactive intermediates derived from thioethers containing an acetyl group. *J Phys Chem A* **108**: 6331–6346.
49. Bergès J, Varmenot N, Scemama A, Abedinzadeh Z, Bobrowski K. (2008) Energies, stability and structure properties of radicals derived from organic sulfides containing an acetyl group after the $\bullet\text{OH}$ attack: Ab initio and DFT calculations vs experiment. *J Phys Chem B* **112**: 7015–7026
50. Wisniowski PB, Bobrowski K, Carmichael I, Hug GL. (2004) Bimolecular homolytic substitution (S_{H_2}) reaction with hydrogen atoms. Time resolved ESR detection in the pulse radiolysis of α -(methylthioacetamide). *J Am Chem Soc* **126**: 14668–14474.
51. Wisniowski P, Bobrowski K, Filipiak P, Carmichael I, Hug GL. (2005) Reactions of hydrogen atoms with α -(alkylthio)carbonyl compounds. Time-resolved ESR detection and DFT calculations. *Res Chem Intermed* **31**: 633–641.
52. Shirdhonkar M, Maity DK, Mohan H, Rao BSM. (2006) Oxidation of methionine methyl ester in aqueous solution: A combined pulse radiolysis and quantum chemical study. *Chem Phys Lett* **417**: 116–123.
53. Mishra B, Priyadarsini KI, Mohan H. (2005) Pulse radiolysis studies on reaction of OH radical with N-acetyl methionine in aqueous solution. *Res Chem Intermed* **31**: 625–632.
54. Schöneich C, Pogocki D, Wisniowski P, Hug GL, Bobrowski K. (2000) Intramolecular sulfur-oxygen bond formation in radical cations of N-acetylmethionine amide. *J Am Chem Soc* **122**: 10224–10225.
55. Schöneich C, Pogocki D, Hug GL, Bobrowski K. (2003) Free radical reactions of methionine in peptides: Mechanisms relevant to β -amyloid oxidation and Alzheimer's disease. *J Am Chem Soc* **125**: 13700–13713.
56. Ji WF, Li ZL, Shen L, Kong DX, Zhang HY. (2007) Density Functional Theory methods as powerful tools to elucidate amino acid oxidation mechanisms: A case study on methionine model peptide. *J Phys Chem B* **111**: 485–489.
57. Lu C, Yao S, Lin N. (2001) Studies on reactions of oxidizing sulfur-sulfur three-electron-bond complexes and reducing α -amino radicals derived from OH

- reaction with methionine in aqueous solution. *Biochim Biophys Acta* **1525**: 89–96.
58. Varmenot N, Remita S, Abedinzadeh Z, Wisniowski P, Strzelczak G, Bobrowski K. (2001) Oxidation processes of N,S-diacetyl-L-cysteine ethyl ester: Influence of S-acetylation. *J Phys Chem A* **105**: 6867–6875.
59. Kadlčík V, Sicard-Roselli C, Mattioli TA, Kodiček M, Houée-Levin C. (2004) One-electron oxidation of β -amyloid peptide: Sequence modulation of reactivity. *Free Radic Biol Med* **37**: 881–891.
60. Pogocki D, Schöneich C. (2002) Redox properties of Met35 in neurotoxic β -amyloid peptide. A molecular modeling study. *Chem Res Toxicol* **15**: 408–418.
61. Brunelle P, Schöneich C, Rauk A. (2006) One-electron oxidation of methionine peptides — Stability of the three-electron S-N(amide) bond. *Can J Chem* **84**: 893–904.
62. Bobrowski K, Hug GL, Pogocki D, Marciniak B, Schöneich C. (2007) Sulfur radical cation peptide bond complex in the one-electron oxidation of S-methylglutathione. *J Am Chem Soc* **129**: 9236–9245.
63. Bobrowski K, Hug GL, Pogocki D, Marciniak B, Schöneich C. (2007) Stabilization of sulfide radical cations through complexation with the peptide bond: Mechanisms relevant to oxidation of proteins containing multiple methionine residues. *J Phys Chem B* **111**: 9608–9620.
64. Hug GL, Bobrowski K, Pogocki D, Hörner G, Marciniak B. (2007) Conformational influence on the type of stabilization of sulfide radical cations in cyclic peptides. *Chem Phys Chem* **8**: 2202–2210.
65. Bobrowski K, Houée-Levin C, Marciniak B. (2008) Stabilization and reactions of sulfur radical cations: Relevance to one-electron oxidation of methionine in peptides and proteins. *Chimia* **62**: 728–734.
66. Bonifačić M, Hug GL, Schöneich C. (2000) Kinetics of the reactions between sulfide radical cation complexes, $[S\cdot:S]^+$ and $[S\cdot:N]^+$, and superoxide or carbon dioxide radical anions. *J Phys Chem A* **104**: 1240–1245.
67. Ferreri C, Manco I, Faraone-Minella MR, Torregiani A, Tamba M, Manara C, Chatgililoglu C. (2006) The reaction of hydrogen atoms with methionine residues: A model of reductive radical stress causing tandem protein-lipid damage. *Chem Bio Chem* **7**: 1738–1744.
68. Mozziconacci O, Bobrowski K, Ferreri C, Chatgililoglu C. (2007) Reactions of H atoms with Met-enkephalin and related peptides. *Chem Eur J* **13**: 2029–2033.
69. Kadlčík V, Sicard-Roselli C, Houée-Levin C, Kodiček M, Ferreri C, Chatgililoglu C. (2006) Reductive modification of a methionine residue in the amyloid- β peptide. *Angew Chem Int Ed* **45**: 2595–2598.
70. Atrian S, Bobrowski K, Capdevilla M, Chatgililoglu C, Ferreri C, Houée-Levin C, Salzano AM, Scaloni A, Torregiani A. (2008) Biomimetic chemistry on tandem protein/lipid damages under reductive radical stress. *Chimia* **62**: 721–727.

71. Nauser T, Jacoby M, Koppenol WH, Squier TC, Schöneich C. (2005) Calmodulin methionine residues are targets for one-electron oxidation by hydroxyl radicals: Formation of S.:N three-electron bonded radical complexes. *Chem Commun* 587–589.
72. Sicard-Roselli C, Lemaire S, Jacqout JP, Favaudon V, Marchand C, Houée-Levin C. (2004) Thioredoxin Ch1 of *Chlamydomonas reinhardtii* displays an unusual resistance toward one-electron oxidation. *Eur J Biochem* 271: 3481–3487.
73. Ferreri C, Manco I, Faraone-Menella MR, Torreggiani A, Tamba M, Chatgililoglu C. (2004) A biomimetic model of tandem radical damage involving sulfur-containing proteins and unsaturated lipids. *Chem Bio Chem* 5: 1710–1712.
74. Yamaji N, Tojo S, Takehira K, Tobita S, Fujitsuka M, Majima T. (2006) S-S Bond mesolysis in α,α' -dinaphthyl disulfide radical anion generated during γ -radiolysis and pulse radiolysis in organic solution. *J Phys Chem A* 110: 13487–13491.
75. Wenska G, Filipiak P, Asmus KD, Bobrowski K, Koput J, Marciniak B. (2008) Formation of a sandwich-structure assisted, relatively long-lived sulphur-centered three-electron bonded radical anion in the reduction of a bis(1-substituted-uracilyl) disulfide in aqueous solution. *J Phys Chem B* 112: 10045–10053.
76. Bacciochi E, Del Giacco T, Gerini MF, Lanzalunga O. (2006) Aryl sulfoxide radical cations. Generation, spectral properties, and theoretical calculations. *J Phys Chem A* 110: 9940–9948.
77. Kishore K, Asmus KD. (1989) Radical cations from one-electron oxidation of aliphatic sulphoxides in aqueous solution. A radiation chemical study. *J Chem Soc Perkin Trans II* 2079–2084.
78. Tamba M, Dajka K, Ferreri C, Asmus KD, Chatgililoglu C. (2007) One-electron reduction of methanesulfonyl chloride. The fate of $\text{MeSO}_2\text{Cl}^\bullet$ and MeSO_2^\bullet intermediates in oxygenated solutions and their role in the cis-trans isomerization of mono-unsaturated fatty acids. *J Am Chem Soc* 129: 8716–8723.

Chapter 17

Radiolysis of Metalloproteins

*Diane E. Cabelli**

1. Introduction

This review covers the interaction of radicals generated from low LET radiation in water with protein components, proteins and, finally, the metallocenters themselves. It commences with a discussion of the experimental techniques that have been the most amenable to these studies, those of gamma and pulse radiolysis. It then addresses, very generally, the radiolysis of the building blocks of proteins, amino acids, and follows with the radiolysis of the proteins themselves. In both cases, the discussion is limited to radiolysis of dilute solute in water, where the initial radiation is absorbed totally by water and does not directly interact with the amino acids/proteins.

The final part of the review describes two instances where radiation chemistry has been used to probe enzymatic systems with metals at the active sites. The first case involves use of a radical formed in the radiolysis of water, in this instance the strongly reducing carbon dioxide anion radical, to shift the oxidation state of redox active metal center(s) of the enzyme and thus probe the nature of long distance

* Chemistry Department, Brookhaven National Laboratory, Upton, New York, 11973-5000, USA. E-mail: cabelli@bnl.gov

electron transfer in a protein. This has been demonstrated very nicely in classic pulse radiolysis studies of copper proteins: very elegantly and simply in azurin. The second case is that where the radical generated in the radiolysis process is actually the substrate of the enzyme and thus enzymatic activity can be probed directly via pulse radiolysis. This is best illustrated with superoxide dismutases, where the superoxide radical is both the substrate and a radiolytically generated secondary radical.

2. Experimental Techniques

The use of radiation chemistry to study proteins in water can be accomplished through slow or fast techniques: gamma radiolysis and pulse radiolysis, respectively. The difference between these two applications of radiation chemistry is that, in the former case, a continual irradiation of the water produces a steady-state flux of radicals and usually involves a gamma-ray generator such as a ^{60}Co source to produce the radicals. In the latter case, an electron accelerator is used to deliver short bursts of electrons to water in the nanosecond (10^{-9} s) to picosecond (10^{-12} s) time scale.

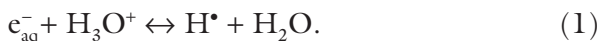
2.1. Gamma radiolysis

Gamma radiolysis involves the use of a radiation source such as ^{60}Co or ^{137}Cs that produces gamma rays as they are energetic enough to ionize water.^{1,2} Upon irradiation of water with gamma rays (or pulses of electrons, as will be described in Sec. 2.2), water is ionized and then cleaved, yielding the following species:

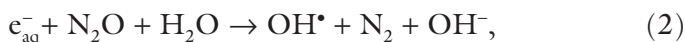


The primary radicals formed in greatest yield are e_{aq}^- (2.8) and OH (2.8) radicals, the former a strong reductant (-2.87V)³ and the latter a strong oxidant ($E_o(\text{OH}/\text{OH}^-) = 1.89\text{V}$)^{3,4} where the values in brackets are G values, that is the number of species formed per 100 eV energy dissipated in solution. The other primary radical, the H atom (0.6), is

produced in far lower yield and is interconnected in aqueous solution with the hydrated electron via a pH-dependent equilibrium with water:



The judicious choice of scavenging chemicals for the primary radicals can lead to the production of solely oxidizing or solely reducing conditions as shown below:



where $\text{CO}_2^{\bullet-}$, produced in a deoxygenated, N_2O saturated solution containing formate, is a strongly reducing radical [$E_o(\text{CO}_2/\text{CO}_2^{\bullet-}) = -1.9\text{V}$].⁵ In contrast, an oxidizing radical that has been used with increasing frequency lately, in large part because of the recognition of the increasingly important role of bicarbonate/ CO_2 in *in vivo* systems, is the carbonate anion radical, $\text{CO}_3^{\bullet-}$, produced in a deoxygenated, N_2O saturated solution containing bicarbonate/carbonate.



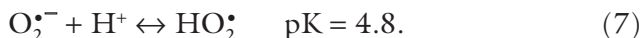
Finally, one of the most highly studied acid–base radical pairs is the superoxide/perhydroxyl ($\text{HO}_2^\bullet/\text{O}_2^{\bullet-}$) radical.⁶ In the presence of oxygen, the electron is scavenged in a diffusion-controlled reaction:



The addition of formate allows reaction (3) to occur and that is then followed by the very fast reaction between the carbon dioxide anion radical and oxygen to yield, again, $\text{O}_2^{\bullet-}$:



where superoxide is in equilibrium with its conjugate acid, HO₂[•]:



As gamma irradiation produces a steady-state source of radicals upon radiolysis, it is a very powerful tool when a low steady concentration of radical is desired to limit any secondary bimolecular reactions that, of course, occur at faster rates as the radical concentrations increase.

A system for the detection of the changes resulting from gamma radiolysis is the greatest challenge in these studies. As gamma radiolysis affords a production of radical that can be generated homogeneously in aqueous solution, product analysis has been a very sensitive and much used methodology. As will be discussed later, changes in enzymatic activity and determination of sites of protein modification are well-established measures of changes upon protein radiolysis. Observing an optical change, where the protein has an observable chromophore, upon gamma radiolysis is also a well-established detection system that has been used very successfully with metalloproteins.^{2,7}

2.2. *Pulse radiolysis*

Pulse radiolysis, in contrast to gamma radiolysis, involves the rapid production of radicals via a pulse of electrons deposited into an aqueous solution, usually delivered by a van de Graaff or electron accelerator.⁸ The production and distribution of radicals are identical to that described in gamma radiolysis, but here the radicals are generally produced in sub-microsecond pulses with current fast limits of picosecond pulses. This affords the advantage of following reaction kinetics and not just looking at overall yields.

Again, the challenge involves a suitable detection system. As illustrated in Fig. 1, many radicals produced upon pulse irradiation of an aqueous system have UV/Vis absorption bands that can be monitored. Clearly, it is suitable to directly follow absorbance changes in the hydrated electron and the carbonate radical anion, with absorption maxima of 715 nm and 600 nm respectively, through the use of an UV/vis spectrophotometer with fast response time. The OH radical,

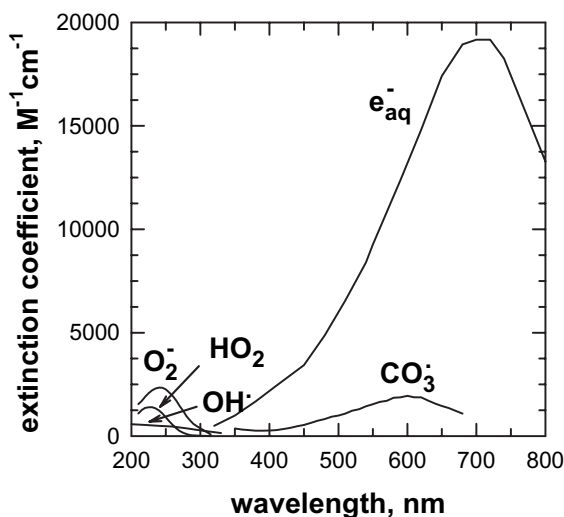


Fig. 1. Radicals formed upon radiolysis of water. OH^\bullet and e_{aq}^- are primary radicals. $\text{O}_2^{\bullet-}/\text{HO}_2^\bullet$ and $\text{CO}_3^{\bullet-}$ are secondary radicals formed in the presence of various $\text{OH}^\bullet/e_{\text{aq}}^-$ scavengers (see Sec. 2.1).

H atom, carbon dioxide radical anion and even HO_2^\bullet and $\text{O}_2^{\bullet-}$ have low molar absorptivities and absorption bands in the region where the protein itself has a large absorbance, making optical detection a challenge. Competition kinetics has proven very useful, using a competitor with a well-defined chromophore. Both direct observation and competition kinetics have been used with great success to understand the chemistry that ensues upon radiolysis of proteins in water.

3. Radical Reactions with Amino Acids

As discussed previously, the radicals produced upon irradiation of water [Eq. (I)] have very different characteristics. Primary radicals (OH^\bullet , H^\bullet and e_{aq}^-) and their interactions with amino acids will be addressed first.⁹⁻¹⁵ The two secondary radicals that will be discussed here are superoxide radical and carbonate radical ($\text{O}_2^{\bullet-}$, $\text{CO}_3^{\bullet-}$), in large part because oxygen is omnipresent when discussing cellular

systems and bicarbonate/carbon dioxide concentration is known to be very high in mammalian cells.

3.1. *Amino acids and primary radicals*

The oxidation of amino acids by hydroxyl radical has received much attention.^{9,11,12} In water, hydroxyl radical is a strong oxidant that can abstract hydrogen atoms. Amino acids can have many sites of attack depending upon the particular functional group. The reactivity of OH radicals with glycine has received the most attention because it is the template for all amino acids, having only the amino and the carboxylate groups with one carbon linker. Here, the zwitterion was shown to react rather more slowly than the anion.⁹⁻¹¹ Initial OH radical attack involves both abstraction of the alpha hydrogen and electron abstraction from the nitrogen. Rate constants for OH radical reaction with amino acids can be found in the compendium compiled by Buxton *et al.*³

Once the amino acid has some functionality in the group bridging the amino and the carboxylate moieties, the scenario becomes more complicated. The reaction between OH radical and an aromatic group on an amino acid occurs primarily via OH radical addition to the ring, initially forming a hydroxycyclohexadienyl radical.¹² This reaction is extremely rapid, of the order of $10^{10} \text{ M}^{-1}\text{s}^{-1}$. The subsequent reactions can be very complicated, depending upon the particular amino acid. The other class of amino acid with specific reactivity is sulfur-containing amino acids (methionine and cysteine).¹⁴ Here, the OH radical is again an H atom abstractor.

The reaction of amino acids with the hydrated electron occurs at a range of different rates depending upon the side chain. Aliphatic amino acids tend to react very slowly with e_{aq}^- whereas aromatic amino acids react at a somewhat more rapid rate and cysteine has a very facile reaction to lose HS^- ; see Table 1. The caveat in these systems is that reaction (5), the reaction of e_{aq}^- with oxygen, is diffusion controlled and oxygen is omnipresent in most systems at a relatively high concentration (250 μM in air and 1.2 mM in O_2 -saturated water).

Table 1. Rate constants for the reaction of some amino acids with e_{aq}^- .

Amino Acid	k , $M^{-1}s^{-1}$ (pH) ^a	Amino Acid	k , $M^{-1}s^{-1}$ (pH) ^a
Cysteine	8×10^9 (5–7) ^b	Serine	$< 3 \times 10^7$ (6.1)
Cystine	1.0×10^{10} (5–7) ^b	Valine	$< 5 \times 10^6$ (6.4)
Histidine	9×10^8 (6.5)	Leucine	$< 1 \times 10^7$ (6.5)
	6.7×10^7 (8.0) ^c		
Tryptophan	$(2.2\text{--}3) \times 10^8$ (6–8)	Glycine	8.0×10^6 (6.2–6.4)
			1.7×10^6 (pH11.8)
Tyrosine	2.8×10^8 (<9.1) ^d	Alanine	1.2×10^7 (7.4)
			6×10^6 (6.4)
Phenylalanine	$(1.1\text{--}1.6) \times 10^8$ (6.3–7)	Aspartate	1.8×10^7 (7.0) ^f
Asparagine	1.5×10^8	Glutamate	2×10^7 (5.7)
	2.4×10^7 (11.7)		
Arginine	1.5×10^8 (6.1)	Lysine	2.0×10^7 (7.4)
	5×10^7 (11) ^e		
Methionine	$(3.5\text{--}4.5) \times 10^7$ (6–7.3)	Threonine	2.0×10^7 (7.0)
		Valine	2.0×10^7 (6.7)

^a All values from Ref. 3 unless otherwise specified.

^b Rate constant dropping off at higher pH, Ref. 14.

^c Strong pH dependence with rapid reaction only for protonated histidine (pKs generally in the pH 6–7 range in proteins), Refs. 15 and 16.

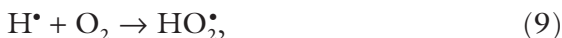
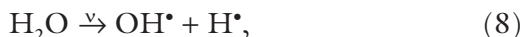
^d Below the pK of 9.1 for tyrosine OH and slows down after that, Ref. 17.

^e Rate constant falls off rapidly for anion, Ref. 18.

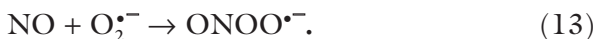
^f No observed reaction for the dianion and higher rate constant for the acid ($6 \times 10^8 M^{-1}s^{-1}$), Ref. 3.

3.2. Amino acids and secondary radicals

A very comprehensive study of superoxide radical with all amino acids was carried out by taking advantage of a technology where $O_2^{\bullet-}$ could be produced by photolyzing water at 157 nm in a Xenon plasma.¹⁹ The photolytic water cleavage to H^\bullet and OH^\bullet in the presence of ethanol or formate and oxygen was combined with stopped flow technology to allow rapid mixing of the resultant $O_2^{\bullet-}$ with the amino acid substrate. In these studies, carried out at near molar amino acid, no reactions were observed for the reaction of $O_2^{\bullet-}/HO_2^\bullet$ with amino acids, leading to upper limits of $0.1 M^{-1}s^{-1}$ at pH > 10 and $10 M^{-1}s^{-1}$ at pH ~ 2.¹⁹



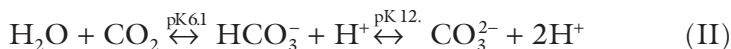
The carbonate anion radical has received a great deal of attention recently, as it has been shown to be produced upon the decay of peroxynitrite in the presence of CO_2 . NO, also known as the endothelium-derived relaxing factor (EDRF), was shown to react very rapidly with superoxide to yield peroxynitrite.^{20,21}



In the presence of CO_2 , an adduct is formed and the adduct then rapidly decomposes to form both $\text{NO}_2\cdot$ and $\text{CO}_3^{\cdot-}$.^{22,23}



The acid–base equilibria between carbonate/bicarbonate/carbon dioxide clearly show that *in vivo* systems sufficient amounts of CO_2 will be present such as to allow reactions to occur and point out the relevance of the reactivity of $\text{CO}_3^{\cdot-}$ with biologically significant compounds. The carbonate radical anion is a strong oxidant that reacts by either H-atom abstraction or electron transfer ($E_0(\text{CO}_3^{\cdot-}, \text{H}^+/\text{HCO}_3^-) = 1.78\text{V}$,²⁴ where the former is generally slower than the latter.



The reactivity of carbonate radical anion, $\text{CO}_3^{\cdot-}$, with amino acids in neutral aqueous solution is not high²⁵ with $k = 10^5\text{M}^{-1}\text{s}^{-1}$ for amino acids with aliphatic side chains and somewhat higher for amino acids with sulfur moieties, $k = (10^6\text{--}10^7)\text{M}^{-1}\text{s}^{-1}$. The reactivity of aromatic moieties vary considerably but indole rings tend to react most rapidly with $k \approx 10^8\text{M}^{-1}\text{s}^{-1}$.²⁶ Hydrogen abstraction likely occurs through an

Table 2. Rate constants for the reaction of some amino acids with $\text{CO}_3^{\bullet-}$.

Amino acid	k , $\text{M}^{-1}\text{s}^{-1}$ (pH)		
d/l Histidine	8.5×10^6 (10) ^a	1×10^6 (5) ^a	
d/l phenylalanine	5×10^4 (7) ^c		
d/l methionine	2×10^7 (7) ^a	5×10^7 (11) ^a	1.2×10^8 (11.4) ^c
tyrosine	1.4×10^8 (11) ^a	2.9×10^8 (11.2) ^d	
d/l tryptophan	6.2×10^8 (9) ^c	4.4×10^8 (11.2) ^d	4.9×10^8 (11.4) ^c
d/l tryptophan			4.3×10^8 (12) ^c
Arginine	9×10^4 (7) ^b		
Aspartate	1×10^4 (7) ^b		
Glycine	$<1 \times 10^3$ (7) ^b		
Cysteine	4.6×10^7 (7) ^b	3.5×10^8 (10) ^a	1.8×10^8 (11.4) ^c
		2.7×10^8 (11.2) ^d	2.5×10^8 (12) ^a
Cystine	1.2×10^7 (11.4) ^c		

^a Ref. 28; ^b Ref. 26; ^c Ref. 27; ^d Ref. 29; ^e Ref. 30.

initial adduct formation with cystine and methionine, such that CO_3^- addition to the sulfur produces the corresponding perthyl radical and thyl radical cation, respectively²⁷; see Table 2 for a compilation of the kinetics data for various amino acids.

4. Radical Reactions with Proteins

One great strength of protein radiolysis as a tool for exploration of protein structure/function is that radiolysis is a very “clean” technique, offering exquisite control over physical parameters such as pH, temperature, pressure, etc. The other great strength of radiolysis is that it can be carried out both as a continuous process, allowing for quantitative product analysis, as well as a fast kinetic technique, allowing the actual observation of reaction mechanisms under pre-steady-state conditions.

4.1. Radiation targeting

Extensive studies were carried out by Garrison *et al.*³¹ in the early stages of development of radiation chemical techniques for the study of proteins. Amino acids combine to form peptides and these ultimately

fold into proteins. It is this folding that renders amino acids in the interior of the protein, inaccessible to radiation induced radical attack. In the early days of radiation biology, this inaccessibility allowed links to be made between radiation damage of proteins and protein size. Empirical rules were devised to describe this phenomenon, and it was called “radiation targeting.”³²

Radiation targeting involved exposing proteins to $(\text{OH}/e_{\text{aq}}^-)$ or exclusively OH radical attack and then correlating activity loss with radiation dose. This correlation, using a set of empirically designed relationships, allowed a determination of protein size.³³ It was, however, dependent upon a number of parameters such as temperature and protein concentration. Recent research carried out by Houee-Levin and co-workers^{33–37} as well as other groups have shown this technique to be dependent upon the judicious choice of protein and the empirical correlations fail in a wide number of systems.

4.2. Radiation footprinting

More recently, studies have been carried out linking OH radical attack with various analytical techniques to determine protein modification, allowing a definitive assignment of exposed areas on a folded protein or protein–substrate complex. This is becoming known as “radiation footprinting.”^{38–43} The concept behind this technique is that OH radicals are quite energetic and relatively promiscuous and will attack many surface exposed amino acid residues. If the protein is examined by mass spectrometry after OH radical attack, inferences can be made about the relationship between the site of attack and the surface exposure. This allows some sense of where one protein might be docking on the surface of another protein or how a protein is folding in the absence of a crystal structure. This technique elicits complementary information to that obtained in studies of hydrogen/deuterium exchange in a protein to determine surface exposed protonation sites.^{38,39}

There are a few important points to make with the concept behind this technique. The first is that the most effective method involves OH radical attack on the protein surface. The OH radical can

be generated chemically, for example using a Fenton-type system involving the reaction of a reduced metal with hydrogen peroxide ($M^{(n-1)+} + H_2O_2 \rightarrow M^{n+} + OH^\bullet + OH^-$), radiolytically as described above or taking advantage of the radiation produced in a synchrotron light source. The significant advantage in the latter method is the rapid deposition of energy, thus allowing rapid OH radical attack. The other important point is that the reactivity of the modified residue and the products that are formed lead to characteristic mass spectral signatures.^{42,43} Understanding that reactivity allows the unambiguous assignment of modification using mass spectral tools.

This has been illustrated in some recent studies carried out by the Chance group.^{38,39} Here, a protein–substrate complex was allowed to form. The complex was then irradiated. After allowing a substantial portion of OH radical attack, the enzymes were treated to a cleaving/digestion system and the modified amino acid residues were determined. The crucial information here involves understanding which residues are likely to be exposed on the surface and which are buried because the surface amino acids that are modified are contrasted with those surface amino acids that are covered by the substrate and thus inaccessible to attack. This allows structural information on large systems that are not amenable to conventional crystallography and solution information instead of rigid crystal information.

5. Radical Reactions with Metalloproteins

Metalloproteins, where the active site includes one or more metals, represent a very different class of proteins than those discussed above. The particular kinds of metalloproteins discussed here are those where the metal is redox active and represents a functional and not structural component of the system. Many mechanistic studies of metalloproteins have been carried out using radiation chemistry in the past 50 years. Two different ways of using radiation chemistry to query mechanisms will be illustrated here. The first, as described in the earliest of these studies using blue copper proteins such as azurin, involves using pulse radiolysis to change an oxidation state and thus

allows intramolecular electron transfer between the metal site and other redox active sites in a protein to be interrogated. The second, described in studies of superoxide dismutases, involves using radiation chemistry to actually generate the substrate and then following the subsequent reactions mechanism in detail. Another use of pulse radiolysis, that will not be discussed here, to collect mechanistic data in metalloproteins involves changing the oxidation state of the active site in the presence of the substrate and then monitoring change on a fast, pre-steady-state timescale. Studies of the mechanism of various catalases have been addressed very effectively this way.

5.1. *Enzymes with type (1)/type (2) copper centers: Azurin*

Some of the first protein systems where pulse radiolysis was used to help determine mechanism were those of blue copper proteins.^{44,45} These are proteins that are blue in solution and contain what are known as type (1) and type (2) copper centers. Two of the most well-known and well-characterized examples of these are azurin and cytochrome c. It was the studies of these systems that opened up the field of long-distance electron transfer in proteins and, by using the protein structure as a framework for electron transfer through space and through bonds, allowed for the development of a broad theoretical basis and many fascinating experiments on long-range electron transfer. Here, I will limit the discussion to electron transfer studies in azurin as illuminated by pulse radiolysis studies.⁴⁶

Azurin is a protein that functions as an electron transfer mediator and has a single copper center possessing a strong absorption band at 600 nm, hence the inclusion as a “blue copper protein.” The copper binding ligands are a cysteine, two histidines and a methionine, and the copper redox potential is 260–300 mV (vs. NHE) for azurins isolated thus far. The intense blue color results from a sulfur (cysteine) to Cu^{2+} ligand-to-metal charge transfer band. In addition, a single disulfide exists approximately 26 angstroms (2.6 nm) from the copper center. This disulfide is not thought to have a functional role in the electron transfer of the protein mediates. However, upon reduction of the disulfide, it is expected that electrons will flow from the reduced

disulfide to the oxidized copper center. This has led to its use in studying the protein influence on intramolecular electron transfer.

Both the Cu^{II} (absorbing at *ca* 620 nm) and the disulfide (RSSR) can be reduced easily with $\text{CO}_2^{\bullet-}$ (generated as described in Sec. 2), producing Cu^{I} or $(\text{RSSR})^{\bullet-}$ (absorbing at 410 nm). The initial loss of Cu^{II} or formation of $(\text{RSSR})^{\bullet-}$ by $\text{CO}_2^{\bullet-}$ can be followed by monitoring the disappearance in absorbance at 600 nm or concomitant growth at 410 nm on a very rapid time scale and the subsequent intramolecular electron transfer can then be monitored by following the disappearance in 410 nm or concomitant disappearance at 600 nm) on a somewhat slower time scale. Studies of the observed rates as a function of Azurin concentration serve to distinguish between the initial reduction (concentration-dependent) process [reactions (15) and (16)] and the intramolecular electron transfer (concentration-independent) process [reaction (17)].^{47,48} These studies have shown that the bimolecular rate constants for reactions (15) and (16) are virtually diffusion-controlled whereas the rate constant for reaction (17) is relatively slow, with a half life of tens of milliseconds, depending upon the particular species of enzyme origin.

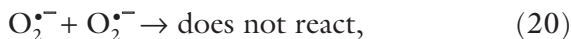
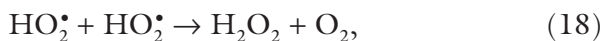


The coupling of fast kinetic resolution using pulse radiolysis with site-directed mutagenesis of specific protein residues allowed resolution of many structure–function questions in azurin as well as allowed the discussion to be broadened to questions of electron transfer over distances. The way the rate is modulated upon specific changes in the copper binding ligands and protein between the redox centers, as well as physical parameters such as temperature and pressure, have been used to test theories developed to describe long-range electron transfer and address issues such as solvent reorganization,⁵⁰ nature of the protein (e.g. beta sheet) spacers,⁴⁶ ligands around the redox center and the effect on the redox potentials of the redox-active

centers,⁴⁹ tunneling and proton involvement in the electron transfer process.⁵¹

5.2. Copper, zinc superoxide dismutase

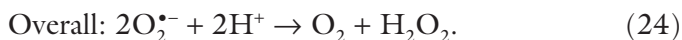
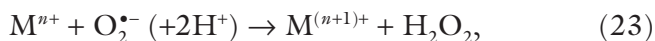
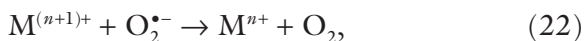
Excess electrons in cellular systems may occur as a consequence of oxidative phosphorylation in the mitochondria, where estimates suggest that 1–2% of all electrons required for phosphorylation leak into solution. As oxygen is the most prevalent and reactive molecule in aerobic cells, superoxide radical ($O_2^{\bullet-}$) is easily formed, as described in Sec. 2.1. The superoxide radical does disproportionate but in a highly pH-dependent process that slows down significantly as the pH is increased above 5.⁷



The superoxide radical itself, as described earlier,⁷ is not particularly reactive with amino acids and proteins but it does react with redox-active metals, particularly copper, iron and manganese.

Superoxide dismutases (SODs), enzymes that convert superoxide radical to oxygen and peroxide,⁵² are found in the majority of aerobic organisms. The redox-active metal has an oxidation potential sufficient to both oxidize and reduce the superoxide so they are capable of carrying out the catalytic process without any need for an exogenous electron donor. Superoxide dismutases represent the rare group of enzymes where radiation chemical techniques are able to generate the substrate for enzyme function. This was recognized immediately upon assignment of SOD function to the blue copper protein, erythrocyuprein, by McCord and Fridovich in 1969⁵³ and the first pulse radiolysis papers defining the details of the mechanism appeared in 1972.^{54,55}

Superoxide dismutases^{56,57} come in four “flavors”: (1) copper, zinc superoxide dismutase with redox active $\text{Cu}^+/\text{Cu}^{2+}$ at the center, (2) manganese superoxide dismutase with $\text{Mn}^{2+}/\text{Mn}^{3+}$ as the redox active center, (3) iron superoxide dismutases with $\text{Fe}^{2+}/\text{Fe}^{3+}$ as the redox center, and (4) nickel superoxide dismutases, where a combination of $\text{Ni}^{2+}/\text{Ni}^{3+}$ and liganded sulfur gives redox activity.^{58,59} In all cases, the higher oxidation state metal (also the resting state of the enzyme) accepts an electron for the superoxide [reaction (22)] while the lower oxidation state metal gives up an electron to the superoxide [reaction (23)] in what has become known as a “ping-pong” mechanism leading to overall dismutation.^{56,57}



The overall advantage of enzymatic dismutation of superoxide is illustrated in Fig. 2, where the rate constants for dismutation for three of the enzyme classes are plotted as a function of pH on a graph that also has the self-dismutation rate constants for superoxide/perhydroxyl radical plotted as a function of pH. It should be noted, though, that the enzymatic rate constants are catalytic and therefore only depend upon the enzyme concentration whereas the self-dismutation is bimolecular in superoxide. This leads to very important ramifications with regards to the enzyme–substrate concentrations. Figure 3 illustrates three different scenarios and shows the relative rate constants at different extremes of $[\text{SOD}]:[\text{O}_2^{\bullet-}]$. The *in vivo* implications of this are profound.

As stated above, there was a rapid realization among different groups that pulse radiolysis was an ideal method to examine the details of the enzyme function. This is because the natural substrate, superoxide, is one of the secondary radicals that can be formed rapidly and efficiently upon the radiolysis of water, as discussed in Sec. 2, over a very wide pH range. The classic method for superoxide generation, using the xanthine/xanthine oxidase system, has pH range

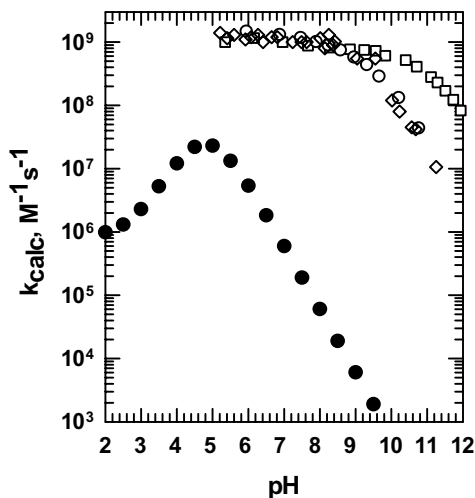


Fig. 2. Rate constants for dismutation of superoxide in the absence (closed circles) and presence of superoxide dismutases [NiSOD (open circle), *E. coli* MnSOD (open diamond), bovine CuZnSOD (open square)] as a function of pH.

<p style="text-align: center;">pH 7.0 1 micromole (10^{-6}M) O_2^- 1 nanomole (10^{-9} M) SOD</p> <p>$t_{1/2}(O_2^-)$ spontaneous rxn is 5 sec (30x slower) $t_{1/2}(O_2^-)$ SOD-catalyzed rxn is 175 msec</p>
<p style="text-align: center;">pH 7.0 1 nanomole (10^{-9}M) O_2^- 1 nanomole (10^{-9} M) SOD</p> <p>$t_{1/2}(O_2^-)$ spont. rxn is 80+ hours (10^5–10^6x slower) $t_{1/2}(O_2^-)$ SOD-catalyzed rxn is 175 msec</p>
<p style="text-align: center;">pH 7.0 1 nanomole (10^{-9}M) O_2^- 1 micromole (10^{-6} M) SOD</p> <p>$t_{1/2}(O_2^-)$ spont. rxn is 80+ hours (10^8–10^9x slower) $t_{1/2}(O_2^-)$ SOD-catalyzed rxn is 175 μsec</p>

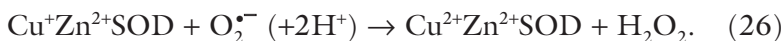
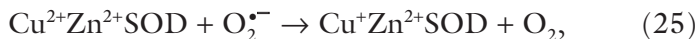
Fig. 3. A comparison of the half-lives for superoxide disappearance at different enzyme/substrate ratios.

limitations as generation of superoxide comes from reaction of an enzyme and substrate(s).

The very well established chemical technique of using potassium superoxide or ammonium superoxide suffers from the pH instability described in reactions (15) to (17): the superoxide is only stable at very high pH, or the use of an organic solvent, most often dimethylsulfoxide (DMSO).^{60,61} Still a great number of very impressive studies were carried out using stopped flow technique combined with potassium superoxide in dimethylsulfoxide, particularly by Fee and co-workers⁶¹ and then by Silverman and co-workers.^{62,63}

The discussion here is limited to CuZnSOD for a number of reasons. First, in this system the “ping-pong” mechanism described in reactions (22) and (23) is operative as written whereas both MnSOD⁶²⁻⁶⁵ and FeSOD^{66,67} carry out catalysis by mechanisms that involve observable enzyme–substrate complexes under certain conditions. Secondly, this enzymatic system has been studied as a model to look at such factors as electrostatic guidance of substrate (see below). Finally, the link that was demonstrated between over 100 point mutations in CuZnSOD and the inherited version of amyotrophic lateral sclerosis (Lou Gehrig’s Disease) has made underscored the importance in understanding details of enzyme function.^{68,69}

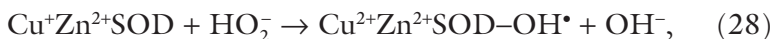
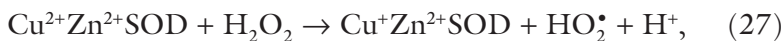
CuZnSOD is a function dimer with each monomer containing one copper and one zinc in the active site bridged by the imidazole group of a histidine. The copper is also bound by three histidines and, in the oxidized state, a water molecule. In addition to the bridging histidines, the zinc is also bound by two histidines and an aspartate. Both oxidized and reduced enzymes are structurally similar except for a loss of the bond to the bridging histidines and a shift in position for the reduced copper. Copper is the only redox active metal; zinc plays a structural role only.



The initial pulse radiolysis studies established that enzymatic catalysis was pH-independent (pH 5–9.5) and occurred with virtually

diffusion-controlled rate constants; $k_{22} = k_{23} \approx 2 \times 10^9 \text{ M}^{-1}\text{s}^{-1}$.^{54,55} It was suggested that the very rapid rate constant between $\text{O}_2^{\bullet-}$ and CuZnSOD, in light of the roughly two order of magnitude size differential between the enzyme and substrate, was a result of electrostatic funneling of the superoxide anion to the copper center.⁷⁰⁻⁷² Pulse radiolysis studies⁷³ measuring the catalytic rate constant for a number of CuSODs where various residues near the active site were modified by site-directed mutagenesis have shown that the arginine situated at the top of the active site channel is responsible for much of the electrostatic guidance. In these studies, the arginine was selectively mutated to a lysine (reflecting the same positive charge but with a different pH for protonation of the amine) with no reflected change in the rate constant for catalysis, an isoleucine/alanine (neutral charge) with a resultant catalytic rate constant of $10^8 \text{ M}^{-1}\text{s}^{-1}$ and to a glutamate/aspartate (negatively charged residues at $\text{pH} > 7$) with a resultant catalytic rate constant of $10^7 \text{ M}^{-1}\text{s}^{-1}$. In another study, an enzyme that was, startlingly, faster than the naturally occurring enzyme was produced by modifying a negatively charged glutamate residue near the active site to a glutamine. Pulse radiolysis studies of activity as a function of ionic strength and pH allowed a careful characterization of this modified enzyme.⁷⁴

Another catalytic cycle in this enzyme is a peroxidative cycle, described by reactions of peroxide with both the reduced and oxidized enzyme.⁷⁵⁻⁷⁸



The significant point here is that reaction (28) is a Fenton-type reaction where a reduced metal reacts with H_2O_2 to yield the OH radical (see Sec. 4.2 on radiation footprinting). Reactions (27) and (28), when combined with reactions (25) and (26) that remove the $\text{HO}_2^{\bullet-}$ produced in reaction (27), lead to catalytic generation of O_2 and OH^{\bullet} with regeneration of 1/4 of the H_2O_2 . The OH^{\bullet} generated in reaction (27)

can react with and deactivate the CuZnSOD, or react with an external substrate. That this peroxidative cycle occurs in the wild-type enzyme is well documented. This mechanism describes a method for converting the more benign superoxide radical into the much more reactive OH radical, albeit at a very slow rate in the wild-type enzyme. Oxidative damage resulting from this cycle has been addressed with regards to the connection between Lou Gehrig's Disease and mutant CuSODs.^{79,80}

6. Conclusion

As has been discussed here, the reactions that occur upon radiolysis of dilute solutions of proteins in water are very much dependent upon the amino acid composition of the protein, protein folding (i.e. residues that are surface exposed), the presence of metal catalytic centers and the particular radicals that are generated in solution. As has been illustrated in the last two examples, radiation chemistry can serve as a probe of the redox processes that occur upon catalysis and, under very specific systems, can also serve to generate the substrate for enzyme catalysis.

References

1. Buxton GV. (1987) Aqueous solutions. In *Radiation Chemistry*, Farhataziz, Rodgers MA. (eds.), pp. 321–349, VCH Publishers Inc.
2. Bonnefont-Rousselot D. (2004) Gamma radiolysis as a tool to study lipoprotein oxidation mechanisms. *Biochimie* **86**: 903–911.
3. Buxton GV, Greenstock CL, Helman WP, Ross AB. (1988) Critical review of rate constants for reactions of hydrated electrons, hydrogen atoms and hydroxyl radicals in aqueous solution. *J Phys Chem Ref Data* **17**: 513–886.
4. Schwarz HA, Dodson RW. (1984) Equilibrium between hydroxyl radicals and thallium(II) and the oxidation potential of OH(aq). *J Phys Chem* **88**: 3643–3647.
5. Schwarz HA, Creutz C, Sutin N. (1985) Homogeneous catalysis of the photoreduction of water by visible light. 4. Cobalt(I) polypyridine complexes. Redox and substitutional kinetics and thermodynamics in the aqueous 2,2'-bipyridine and 4,4'-dimethyl-2,2'-bipyridine series studied by the pulse-radiolysis technique. *Inorg Chem* **24**: 433–439.

6. Bielski BHJ, Cabelli DE, Arudi RL, Ross AB. (1985) Reactivity of HO_2/O_2^- radicals in aqueous solution. *J Phys Chem Ref Data* **14**: 1041–1082.
7. Von Sonntag C. (1987) *The Chemical Basis of Radiation Biology*. Taylor & Francis, London.
8. Patterson LK. (1987) Instrumentation for measurement of transient behavior in radiation chemistry. In *Radiation Chemistry*, Farhataziz, Rodgers MA. (eds.), pp. 65–96, VCH Publishers Inc.
9. Monig J, Chapman R, Asmus KD. (1985) Effect of the protonation state of the amino group on the OH radical induced decarboxylation of amino acids in aqueous solution. *J Phys Chem* **89**: 3139–3144.
10. Armstrong DA, Asmus K-D, Bonifacic MJ. (2004) Oxide radical anion reactivity with aliphatic amino compounds in aqueous solution: Comparison of H-atom abstraction from C-H and N-H groups by $\cdot\text{O}^-$ and $\cdot\text{OH}$ Radicals. *J Phys Chem A* **108**: 2238–2246.
11. Bonifacic M, Stefanic I, Hug GL, Armstrong DA, Asmus K-D. (1998) Glycine decarboxylation: The free radical mechanism. *J Am Chem Soc* **120**: 9930–9940.
12. Neta P, Simic M, Hayon E. (1970) Pulse radiolysis of aliphatic acids in aqueous solution. Simple amino acids. *J Phys Chem* **74**: 1214–1220.
13. Getoff N. (1992) Pulse radiolysis of aromatic amino acids — State of the art. *Amino Acids* **2**: 195–214.
14. Mezyk SP. (1995) Rate constant determination for the reaction of sulfhydryl species with the hydrated electron in aqueous solution. *J Phys Chem* **99**: 13970–13975.
15. Faraggi M, Bettelheim A. (1977) The reaction of the hydrated electron with amino acids, peptides, and proteins in aqueous solutions: III. Histidyl peptides. *Radiat Res* **71**: 311–324.
16. Tilly V, Pin S, Hickel B, Alpert B. (1997) Pulse radiolysis reduction of myoglobin: Hydrated electrons diffusion inside the protein matrix. *J Am Chem Soc* **119**: 10810–10814.
17. Feitelson J, Hayon E. (1973) Electron ejection and electron capture by phenolic compounds. *J Phys Chem* **77**: 10–15.
18. Braams R. (1966) Rate constants of hydrated electron reactions with amino acids. *Radiat Res* **27**: 319–329.
19. Bielski BHJ, Shiue G. (1979) Reaction rates of superoxide with essential amino acids in oxygen free radicals and tissue damage. *Ciba Foundation Symposium 65 Excerpta Medica* 43–56.
20. Padmaja S, Huie RE. (1993) Reaction of nitric oxide with peroxy radicals. *Biochem Biophys Res Comm* **195**: 539.
21. Goldstein S, Czapski G. (1995) The reaction of NO with O_2^- and HO_2^- : A pulse radiolysis study. *J Free Rad Biol Med* **19**: 505–510.

22. Lymar SV, Hurst JK. (1995) Rapid reaction between peroxyxynitrite ion and carbon dioxide: Implications for biological activity. *J Am Chem Soc* **117**: 8867–8868.
23. Lymar SV, Hurst JK. (1998) CO₂-catalyzed one-electron oxidations by peroxyxynitrite: Properties of the reactive intermediate. *Inorg Chem* **37**: 294–301.
24. Augusto O, Bonini MG, Amanso AM, Linares E, Santos CCX, DeMenzes SL. (2002) Nitrogen dioxide and carbonate radical anion: Two emerging radicals in biology. *Free Rad Biol Med* **32**: 841–859.
25. Neta P, Huie RE, Ross AB. (1988) Rate constants for reactions of inorganic radicals in aqueous solution. *J Phys Chem Ref Data* **17**: 1027–1284.
26. Chen SN, Hoffman MZ. (1973) Rate constants for the reaction of the carbonate radical with compounds of biochemical interest in neutral aqueous solution. *Radiat Res* **56**: 40–47.
27. Huie RE, Shoute LCT, Neta P. (1991) Temperature dependence of the rate constants for the reactions of the carbonate radical with organic and inorganic reactants. *Int J Chem Kinet* **23**: 541–552.
28. Chen S-N, Hoffman MZ. (1975) Effect of pH on the reactivity of the carbonate radical in aqueous solution. *Radiat Res* **62**: 18–27.
29. Adams GE, Aldrich JE, Bisby RH, Cundall RB, Redpath JL, Willson RL. (1972) Selective free radical reactions with proteins and enzymes: Reactions of inorganic radical anions with amino acids. *Radiat Res* **49**: 278–289.
30. Chen S-N, Hoffman MZ. (1974) Reactivity of the carbonate radical in aqueous solution. Tryptophan and its derivatives. *J Phys Chem* **78**: 2099–2102.
31. Garrison WM. (1987) Reaction mechanisms in the radiolysis of peptides, polypeptides, and proteins. *Chem Rev* **87**: 381–398.
32. Kempner ES. (1999) Advances in radiation target analysis. *Anal Biochem* **113**–123.
33. Schussler H, Navaratnam S, Distel L. (2001) Pulse radiolysis studies on histones and serum albumin under different ionic conditions. *Radiat Phys Chem* **61**: 123–128.
34. Bataillea C, Baldacchinoa G, Cosson RP, Coppoc M, Trehenc C, Vignerona G, Renaulta JP, Pina S. (2005) Effect of pressure on pulse radiolysis reduction of proteins. *Biochim Biophys Acta* **1724**: 432–439.
35. Audette M, Blouquit Y, Houee-Levin C. (2000) Oxidative dimerization of proteins: Role of tyrosine accessibility. *Arch Biochem Biophys* **376**: 217–220.
36. Audette-Stuart M, Houee-Levin C, Potier M. (2005) Radiation-induced protein fragmentation and inactivation in liquid and solid aqueous solutions. Role of OH and electrons. *Radiat Phys Chem* **72**: 301–306.
37. Terryn H, Deridder V, Sicard-Roselli C, Tilquin B, Houee-Levin C. (2005) Radiolysis of proteins in the solid state: An approach by EPR and product analysis. *J Synchrotron Rad* **12**: 292–298.

38. Xu G, Chance MR. (2007) Hydroxyl radical-mediated modification of proteins as probes for structural proteomics. *Chem Rev* **107**: 3514–3543.
39. Takamoto K, Chance MR. (2006) Radiolytic protein footprinting with mass spectrometry to probe the structure of macromolecular complexes. *Annual Review of Biophysics and Biomolecular Structure* **35**: 251–276.
40. Maleknia SD, Wong KWH, Downard KM. (2004) Photochemical and electrophysical production of radicals on millisecond timescales to probe the structure, dynamics and interactions of proteins. *Photochem Photobiol Sci* **3**: 741–748.
41. Adilakshmi T, Lease RA, Woodson SA. (2006) Hydroxyl radical footprinting *in vivo*: Mapping macromolecular structures with synchrotron radiation. *Nucleic Acids Res* **34**: e64.
42. Xu G, Chance MR. (2005) Radiolytic modification and reactivity of amino acid residues serving as structural probes for protein footprinting. *Anal Chem* **77**: 4549–4555.
43. Xu G, Takamoto K, Chance MR. (2003) Radiolytic modification of basic amino acid residues in peptides: Probes for examining protein–protein interactions. *Anal Chem* **75**: 6995–7007.
44. Dennis D. (2005) Investigating the structure and function of cupredoxins. *Coord Chem Rev* **249**: 3025–3054.
45. Gray HB, Malmstrom BG, Williams RJP. (2000) Copper coordination in blue proteins. *J Biol Inorg Chem* **5**: 551–559.
46. Farver O, Pecht I. (1999) Copper proteins as model systems for investigating intramolecular electron transfer processes. In *Advances in Chemical Physics: Electron Transfer — from Isolated Molecules to Biomolecules*. Part 2, Prigogine I, Rice SA. (eds.), Vol. 107, John Wiley and Sons.
47. Farver O, Pecht I. (1989). Long-range intramolecular electron transfer in azurins. *Proc Nat Acad Sci USA* **86**: 6968–6972.
48. Farver O, Canters GW, van Amsterdam I, Pecht I. (2003) Intramolecular electron transfer in a covalently linked mutated azurin dimer. *J Phys Chem A* **107**: 6757–6760.
49. Farver O, Jeuken LJC, Canters GW, Pecht I. (2000) Role of ligand substitution on long-range electron transfer in azurins. *Eur J Biochem* **267**: 3123–3129.
50. Farver O, Hwang HJ, Lu Y, Pecht I. (2007) Reorganization energy of the Cu_A center in purple azurin: Impact of the mixed valence-to-trapped valence state transition. *J Phys Chem B* **111**: 6690–6694.
51. Farver O, Bonander N, Skow LK, Pecht I. (1996) The pH dependence of intramolecular electron transfer in azurins. *Inorg Chim Acta* **243**: 127–133.
52. Fridovich I. (1995) Superoxide radical and superoxide dismutases. *Ann Rev Biochem* **64**: 97–112.
53. McCord JM, Fridovich I. (1969) Superoxide dismutase. An enzymatic function for erythrocyte hemocuprein (hemocuprein) *J Biol Chem* **244**: 6049–6060.

54. Klug-Roth D, Fridovich I, Rabani J. (1973) Pulse radiolytic investigations of superoxide catalyzed disproportionation. Mechanism for bovine superoxide dismutase. *J Am Chem Soc* **95**: 2786–2790.
55. Rotilio G, Bray RC, Fielden EM. (1972) A pulse radiolysis study of superoxide dismutase. *Biochim Biophys Acta* **268**: 605–609.
56. Bertini I, Magnani S, Viezzoli M-S. (1998) Structure and properties of copper-zinc superoxide dismutases. In *Advances in Inorganic Chemistry*, Sykes AG. (ed.), pp. 127–250, Academic Press: New York.
57. Cabelli DE, Riley D, Rodriguez JA, Valentine JS, Zhu H. (2002) Models of superoxide dismutases. In *Biomimetic Chemistry*, Meunier B. (ed.), pp. 461–508, Imperial College Press: London.
58. Choudhury BS, Lee J-W, Davidson G, Yim Y-I, Bose K, Sharma ML, Kang S-O, Cabelli DE, Maroney MJ. (1999) Examination of the nickel site structure in *Streptomyces seoulensis* superoxide dismutase reveals a sulfur-rich coordination environment. *Biochem* **38**: 3744–3752.
59. Bryngelson PA, Arobo SE, Pinkerton JL, Cabelli DE, Maroney MJ. (2004) Expression, reconstitution and mutation of recombinant streptomyces coelicolor NiSOD. *J Am Chem Soc* **126**: 460–461.
60. Valentine JS, Miksztal AR, Sawyer DT. (1984) Methods for the study of superoxide chemistry in nonaqueous solutions. *Methods Enzymol* **105**: 71–81.
61. Fee JA, Bull C. (1982) Steady-state kinetic studies of superoxide dismutases. Saturative behavior of the copper- and zinc-containing protein. *J Biol Chem* **261**: 13000–13005.
62. Hearn AS, Stroupe ME, Cabelli DE, Lepock JR, Tainer JA, Nick HS, Silverman DN. (2001) Kinetic analysis of product inhibition in human manganese superoxide dismutase. *Biochem* **40**: 12051–12058.
63. Cabelli DE, Guan Y, Leveque V, Hearn AS, Tainer JA, Nick HS, Silverman DN. (1999) Role of tryptophan 161 in catalysis by human manganese superoxide dismutase. *Biochem* **38**: 11686–11692.
64. McAdam ME, Lavelle F, Fox RA, Fielden EM. (1977) A pulse-radiolysis study of the manganese-containing superoxide dismutase from bacillus stearothermophilus. *Biochem J* **165**: 81–87.
65. Pick M, Rabani J, Yost F, Fridovich I. (1974) Catalytic mechanism of the manganese-containing superoxide dismutase of *Escherichia coli* studied by pulse radiolysis. *J Am Chem Soc* **96**: 7329–7333.
66. Lavelle F, McAdam ME, Fielden EM, Roberts PB. (1977) A pulse-radiolysis study of the catalytic mechanism of the iron-containing superoxide dismutase from *Photobacterium leiognathi*. *Biochem J* **161**: 3–11.
67. Nettleton CJ, Bull C, Baldwin TO, Fee JA. (1984). Isolation of the *Escherichia coli* iron superoxide dismutase gene: Evidence that intracellular superoxide concentration does not regulate oxygen-dependent synthesis of the manganese superoxide dismutase. *Proc Nat Acad Sci USA* **81**: 4970–4973.

68. Cabelli DE. (2003) Oxidative stress in familial amyotrophic lateral sclerosis. In *Redox Genome Interactions in Health and Disease*, Packer L, Fuchs J, Podda M (eds.), Marcel Dekker, Inc., New York; and references therein.
69. Hayward LJ, Rodriguez JA, Jang G, Tiwari A, Goto JJ, Cabelli DE, Valentine JS, Brown Jr RH. (2002) Decreased metallation and activity in subsets of mutant superoxide dismutases associated with familial ALS. *J Biol Chem* **277**: 15923–15931.
70. Koppenol WH. (1981) The physiological role of the charge distribution on superoxide dismutase. In *Oxygen and Oxy-Radicals in Chemistry and Biology*, Rodgers MA, Powers EL. (eds.), pp. 671–674, Academic Press, New York.
71. Cudd A, Fridovich I. (1982) Electrostatic interactions in the reaction mechanism of bovine erythrocyte superoxide dismutase. *J Biol Chem* **257**: 11443–11447.
72. Getzoff ED, Tainer JA, Weiner PK, Kollman PA, Richardson JS, and Richardson DC. (1983) Electrostatic recognition between superoxide and copper, zinc superoxide dismutase. *Nature* **306**: 287–290.
73. Fisher CL, Cabelli DE, Tainer JA, Hallewell RA, Getzoff ED. (1994) The role of arginine 143 in the electrostatics and mechanism of Cu, Zn superoxide dismutase: Computational and experimental evaluation by mutational analysis. *Proteins* **19**: 24–34.
74. Getzoff ED, Cabelli DE, Fisher CL, Parge HE, Viezzoli M-S, Banci L, Hallewell RA. (1992) Faster superoxide dismutase mutants designed by enhancing electrostatic guidance. *Nature* **358**: 347–351.
75. Bray RC, Cockle SA, Fielden EM, Roberts PB, Rotilio G, Calabrese L. (1974) Reduction and inactivation of superoxide dismutase by hydrogen peroxide. *Biochem J* **139**: 43–48.
76. Hodgson EK, Fridovich I. (1975) The interaction of bovine erythrocyte superoxide dismutase with hydrogen peroxide. Inactivation of the enzyme. *Biochemistry* **14**: 5294–5303.
77. Fuchs H, Borders C. (1983) Affinity inactivation of bovine Cu, Zn superoxide dismutase by hydroperoxide anion, HO₂⁻. *Biochem Biophys Res Commun* **116**: 1107–1113.
78. Cabelli DE, Allen D, Bielski BHJ, Holcman J. (1989) The interaction between Cu(I) superoxide dismutase and hydrogen peroxide. *J Biol Chem* **264**: 9967–9971.
79. Stine-Elam J, Malek K, Rodriguez JA, Doucette PA, Taylor AB, Hayward LW, Cabelli DE, Valentine JS, Hart PJ. (2003) Mechanism of bicarbonate-mediated peroxidation by copper-zinc superoxide dismutases. *J Biol Chem* **278**: 21032–21039.
80. Goto JJ, Gralla EB, Valentine JS, Cabelli DE. (1998) Reactions of hydrogen peroxide with FALS mutant human copper-zinc superoxide dismutases studied by pulse radiolysis. *J Biol Chem* **273**: 30104–30109.

Chapter 18

Mechanisms of Radiation-Induced DNA Damage: Direct Effects

*David Becker[†], Amitava Adhikary[†]
and Michael D. Sevilla^{*†}*

1. Introduction

DNA is recognized as the principal cellular target for all forms of ionizing radiation such as γ -radiation, X-rays, and ion-beams.¹⁻⁴ Effects such as mutagenesis, oncogenesis, transformations and cell death can originate with damage to the cellular DNA.⁵⁻⁷ Of the variety of DNA damage induced by ionizing radiation, strand breaks are known to be among the most biologically significant, with the double strand break being a potentially lethal lesion.^{6,7} Free radicals on the deoxyribose moiety of DNA are the immediate precursors to DNA strand breaks.¹⁻⁸ As a consequence, the focus of this review will be the chemical origins of DNA irradiation damage, especially the damage that originates with radicals produced by the direct and quasi-direct effects of ionizing radiation and that leads to strand breaks.

* E-mail: sevilla@oakland.edu

[†] Department of Chemistry, Oakland University, Rochester, MI 48309, USA

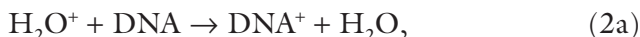
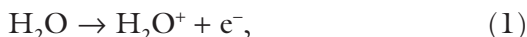
High-energy radiation traversing a solvated DNA molecule results in ionizations and excitations,^{1-5,8-10} in approximate proportion to the number of electrons present at any specific site. Low linear energy transfer (LET) electromagnetic radiations such as γ -radiation and X-rays, which ionize molecules via direct absorption and the Compton effect, are relatively sparsely ionizing. Higher LET charged particles, such as alpha particles, protons and ion beams, produce a dense trail of ionizations.^{5,8-12} The different spatial characteristics of the energy deposition from these different radiations (high LET vs. low LET) have significant effects on the resulting damage.^{5,8-17}

After the initial ionization from impinging radiation, high-energy electrons are ejected. These high-energy electrons produce further ionizations, resulting in a cascade of medium and lower-energy electrons that cause still further ionizations as well as numerous excited states.^{1-5,8-23} The resulting DNA radicals (cationic, anionic and neutral) and excited states are responsible for most of the subsequent damage to the DNA. In addition, low-energy electrons with energies below the ionization threshold (LEE) can also directly damage DNA through a dissociative electron attachment process,¹⁸⁻²³ causing sugar-phosphate bond cleavage leading to strand break formation.²³ Recently, it has been discovered that purine cation-radical excited states also lead to free radical damage to the DNA-sugar-phosphate backbone.^{20,22} Free radicals, although highly reactive, can be stabilized at low temperatures and studied using ESR spectroscopy.^{1,3,9,14-20}

Since there are many charge transfer and spin transfer processes that occur after an initial ionization, the specific location of the chemical damage and, consequently, the ultimate biological damage from DNA irradiation may be removed from the initial ionization site.²⁰ The pertinent charge and spin transfer processes have recently been reviewed.²⁰

DNA waters of solvation play a significant role in the DNA damage process from ionizing radiation.²⁴⁻³¹ In fully hydrated DNA, approximately 8-10 water molecules per nucleotide ($\Gamma = 8-10 \text{ H}_2\text{O}/\text{nucleotide}$) form a primary solvation shell of molecules directly in contact with the DNA and its counterion. When these molecules are ionized, hole transfer to the DNA molecule is faster than deprotonation

of the $\text{H}_2\text{O}^{\bullet+}$ formed and these molecules act as antennae, funneling damage into the DNA itself. In addition, DNA is a good electron scavenger and the electrons ejected from these water molecules by ionization are largely scavenged by the DNA.^{8,18–20,24–28} The primary solvation shell increases the damage to the DNA from ionizing radiation by about 50% (based on valence electron count).²⁰ Reactions (1) and (2) show the pertinent reactions.



This review focuses primarily on results from recent efforts in our laboratory and from the laboratories of other investigators that have amplified and elucidated the mechanisms of action described above. Several other reviews should be consulted for a more complete background to these efforts.^{8,18–20,24}

We note that the acid–base properties (pK_a value) of the one-electron-oxidized guanine moiety suggest an equilibrium between the protonated ($\text{G}^{\bullet+}$) and deprotonated forms ($\text{G}(-\text{H})^\bullet$).^{3,8} Steenken originally pointed out that in the GC cation radical, the equilibrium between the N1 hydrogen on G and N3 position on C will slightly favor $\text{G}(-\text{H})^\bullet$ (i.e. $\text{G}(-\text{H})^\bullet\text{-C}(\text{N3})\text{H}^+$), by *ca.* -0.6 kcal/mol.^{3b–d} Numerous theoretical calculations also show evidence for proton transfer in GC cation radical but predict that it is endothermic by *ca.* $+1$ kcal/mol thereby slightly favoring $\text{G}^{\bullet+}$.^{22,38b,c} Readers are requested to keep in mind that in double stranded DNA, one-electron oxidized guanine has been shown to be the deprotonated species $\text{G}(-\text{H})^\bullet\text{:C}(\text{+H}^+)$.^{38d}

2. Electron-Loss (Oxidative) Pathways

2.1. Introduction

As mentioned earlier, the initial ionizing radiation results in a cascade of electrons that, through inelastic collisions, cause ionization of

DNA. For high-energy electrons, the probability of ionization is proportional to the local electron density. As the energy degrades to medium and low-energy electrons, the probability of ionization at a specific locale becomes proportional to the number of valence electrons present. Since the numerous moderate and low-energy electrons vastly overwhelm the few initial high-energy electrons, overall ionization is related mainly to valence electron count. For DNA, about 43% of the ionizations occur at the bases, which have an average of 48 valence electrons and 57% at the sugar phosphate backbone, which contains 63 valence electrons.²⁰

However, the location and concentration of the radicals stabilized at 77 K in γ -irradiated DNA indicate that considerable charge and spin transfer occurs after the original ionizations.^{8,18–20,24} Because there is substantial evidence that electron-loss radicals are a significant source of strand breaks,^{8,18–20,22} the processes that lead to these radicals at 77 K must be understood if the origins of radiation-induced strand breaks are to be elucidated. In addition, even in those circumstances in which strand breaks do not result from an electron-loss damage site, the site may be part of a localized multiply damaged site (MDS),⁴ for which normal cellular DNA repair mechanisms are impaired.

2.2. Radical trapping and hole transfer at 77 K

Figure 1(A) shows the ESR spectrum, at 77 K, that results from hydrated DNA ($\Gamma = 12 \pm 2$), γ -irradiated, at 77 K, to a dose of 8.8 kGy; the spectrum is a composite resulting from a number of radicals stabilized and trapped at 77 K. An analysis of the composition of the underlying radicals is done by a least-square fitting of the appropriate individual radical benchmark spectra to the composite spectrum. An error parameter is calculated for each spectrum fit and a visual comparison of the computer simulated composite spectrum is done with the experimental spectrum to assure that deconvolutions are properly performed.^{19,20,24,32}

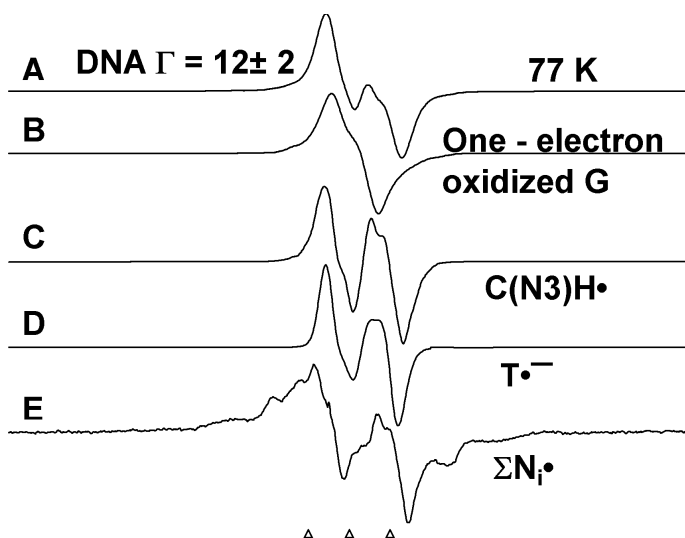
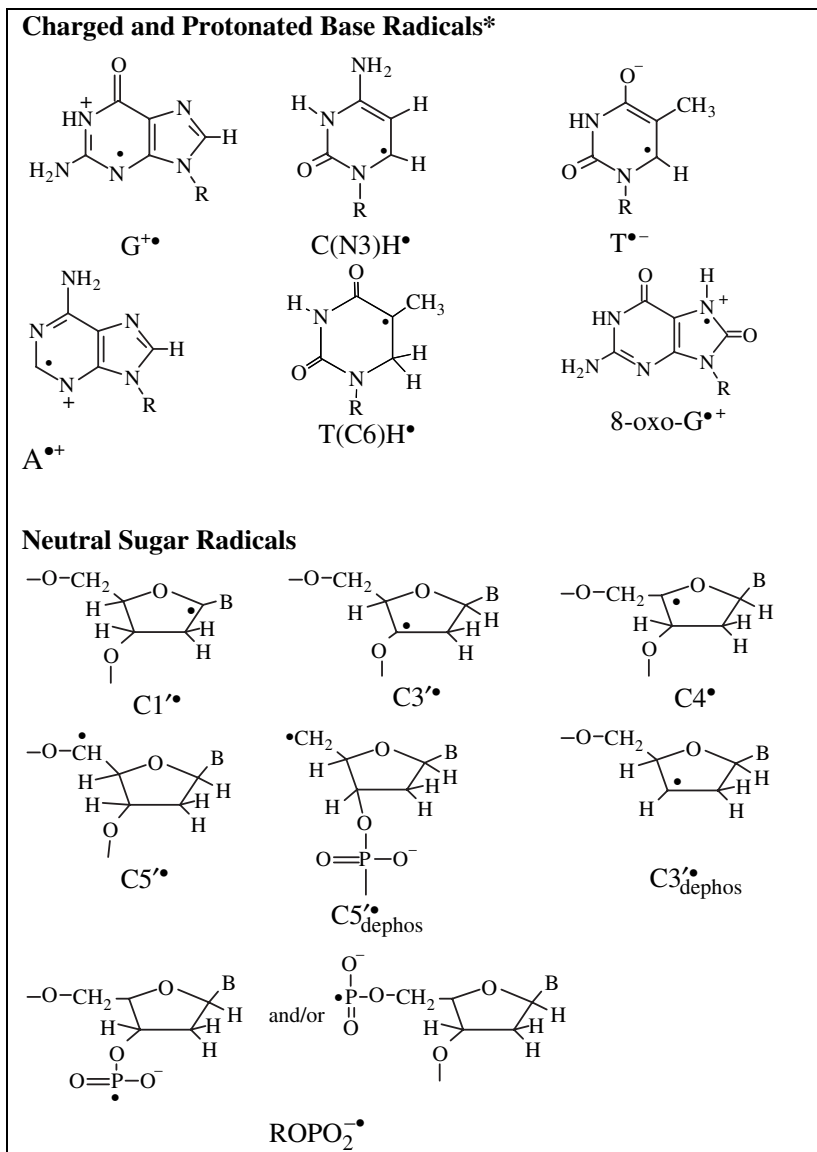


Fig. 1. (A) ESR spectrum of hydrated DNA at 77 K after 8.8 kGy γ -irradiation at 77 K. The three markers at the bottom are the positions of the Fremy Salt resonances, with $g = 2.0056$ and $A_N = 2.0056$. (B) to (E) are spectra used as benchmarks for deconvolution of the DNA spectrum. (B) One-electron oxidized guanine. (C) One-electron reduced cytosine (i.e. the protonated anion radical). (D) Thymine anion radical. (E) Composite spectrum of neutral sugar radicals.

The benchmark spectra used to analyze composite γ -irradiated DNA spectra are shown in Figs. 1(B) to 1(E). By determining the low-dose yield [G value ($\mu\text{mol}/\text{J}$)] of each radical using dose-response curves, the low-dose composition of the free radical cohort is determined to be: $\text{G}^{\bullet+}$ ($35 \pm 5\%$), $\text{T}^{\bullet-}$ ($25 \pm 5\%$), $\text{C}^{\bullet-}$ [$\text{C}(\text{N}3)\text{H}^{\bullet}$] ($25 \pm 5\%$), $\Sigma\text{N}_i^{\bullet}$ ($15 \pm 5\%$). Scheme 1 presents the structures of the first three radicals. $\Sigma\text{N}_i^{\bullet}$ represents a composite spectrum of neutral radicals, which is assumed to originate mostly with the sugar-phosphate backbone ($\text{C}1^{\bullet}$, $\text{C}3^{\bullet}$, $\text{C}5^{\bullet}$, $\text{C}3^{\bullet}_{\text{dephos}}$). A semi-quantitative analysis indicates that, of the 15% of assumed backbone radicals, about 11% originate with electron loss and about 4% with low-energy electrons (Sec. 3.3). Thus, about 46% of the stabilized radicals at 77 K are electron-loss



*C(N3)H• is reversibly protonated C^{-•}; T(C6)H• is irreversibly protonated T^{-•}.

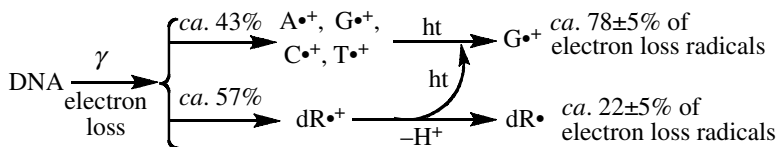
Scheme 1. Structures of radicals discussed.

radicals, with 35% of these identified as $G^{\bullet+}$ and 11% as sugar radicals. Thus, *ca.* 78% of the electron-loss radicals are $G^{\bullet+}$ and *ca.* 22% sugar radicals.

These analyses indicate that 78% of holes that are trapped end up on the bases even though less than half of the original ionizations occurred there. Since the sites of hole stabilization are different from the locations of the original ionizations, ESR results provide strong evidence that charge and spin transfer occurs in irradiated DNA at 77 K.²⁰ In addition, rapid short time-scale charge migration results in extensive recombination of electrons and holes so that only 25% to 50% of the initial ionizations are trapped as radicals.^{19,20,25,26,32} For the electron-loss path, this is shown in Scheme 2.

2.3. Electron and hole transfer in DNA

In a series of papers, Cai and co-workers presented an explication of electron and hole transfer in γ -irradiated DNA that clarified some confusion and some inconsistencies that existed in the literature at the time.³³⁻⁴⁰ Using ESR at 77 K, Cai co-workers analyzed hole and excess electron transfer by observing, simultaneously, the concentration of both the electron/hole donor and the electron/hole acceptor as a function of time, thereby verifying that the underlying transfer occurs in the specific manner assumed for the mathematical analysis used. Because the analysis for excess electrons is identical to that for holes, we present both analyses here.



Scheme 2. Hole and spin transfer (ht) in the electron-loss path after γ -irradiation of DNA. It should be noted that extensive recombination occurs after the initial ionizations. This scheme assumes that fast recombination is equally efficient for all cationic radicals. Net hole transfer occurs from the adenine, cytosine and thymidine base cation radicals to guanine and from the sugar phosphate backbone to the bases.^{19,20,25,26,32}

In the relevant experiment to determine electron transfer, the DNA intercalator mitoxantrone (MX) is used.³⁴ MX binds well to DNA and has a high electron affinity.³⁴ MX appears to intercalate randomly if used at an intercalator:base-pair ratio of 1/20 or less. In a 7-M LiBr glass at 77 K, γ -irradiation produces electrons that attach randomly onto the DNA and MX, and the holes are sequestered as $\text{Br}_2^{\bullet-}$.^{33,34} The electrons are trapped on the DNA bases in the form of $\text{T}^{\bullet-}$ and $\text{C}(\text{N3})\text{H}^{\bullet}$ (Scheme 1). Over time, the electron transfers from $\text{T}^{\bullet-}$ and $\text{C}(\text{N3})\text{H}^{\bullet}$ to MX to form $\text{MX}^{\bullet-}$. The ESR spectrum of $\text{MX}^{\bullet-}$ can be distinguished from those of $\text{T}^{\bullet-}$ and $\text{C}(\text{N3})\text{H}^{\bullet}$,^{33,34-38,40} so the transfer can be experimentally monitored. For hole transfer studies, hydrated DNA is used, so after irradiation, many of the holes are trapped on the DNA as G^+ , and the transfer of holes from G^+ to MX can be monitored. This involves the analysis of composite ESR spectra for individual radical contributions and the original work by Cai *et al.* should be consulted for details.^{34-38,40} The transfer distance with time, D_p , and the value of the tunneling decay constant, β were determined in the rate constant expression for tunneling, $k = k_0 e^{-\beta D_p}$. Table 1 shows the results for these studies for both hole and electron transfer with MX as both the electron and the hole acceptor.

Table 1. Transfer distance and distance decay constant for hole/electron transfer.^a

Ploynucleotide	Medium	Donor	$D_1(1')$ (bp)	β (\AA^{-1})	Ref.
Electron Transfer					
(polydAdT) ₂	D ₂ O glass	$\text{T}^{\bullet-}$	9.4 ± 0.5	0.75 ± 0.1	38
(polydIdC) ₂	D ₂ O glass	$\text{C}(\text{N3})\text{D}^{\bullet}$	5.9 ± 0.5	1.4 ± 0.1	38
DNA	D ₂ O glass	$\text{T}^{\bullet-} + \text{C}(\text{N3})\text{D}^{\bullet}$	9.5 ± 1.0	0.9 ± 0.1	41
Hole Transfer					
polyA-poly U	D ₂ O ice	$\text{A}^{+\bullet}$	13 ^b	0.7 ^c	38
polyC-polyG	D ₂ O ice	$\text{G}^{+\bullet}$	8 ^b	1.1 ^c	38
DNA	D ₂ O ice	$\text{G}^{+\bullet}$	8 ^b	1.1 ^c	42

^a Distances transferred in one minute at 77 K.

^b In ices, transfer in three-dimensions is observed.

^c Estimated assuming $k_0 = 1 \times 10^{11} \text{ s}^{-1}$.

For hole transfer at 4–77 K, the value of β obtained in DNA (*ca.* 1.1 \AA^{-1}) is consistent with transfer over distances of *ca.* eight bases in one minute. The low temperature of the transfer and the fact that the kinetics follows the relationships predicted from tunneling are reasonable assurances that the transfer occurs through tunneling rather than through an activated process.^{33,43}

In this body of work,^{33–38,40} it was also shown that: (1) Electron transfer occurs over longer ranges with intercalators of higher electron affinity. (2) As DNA duplexes are separated from each other using waters of hydration or complexing agents, the rate of interduplex electron and hole transfer decreases. (3) There is no significant deuterium isotope effect associated with the transfer rate. (4) The base sequence in polynucleotides markedly affects the transfer rates (Table 1). For example, the difference between (polydAdT)₂ and (polydIdC)₂ was explained by invoking a rapid proton transfer process that greatly slows electron transfer in (polydIdC)₂, whereas for (polydAdT)₂ no such transfer occurs.^{38a–c} The proton transfer from base-paired I to C^{•-} forming C(N3)H[•] was actually shown by theory to be essentially barrierless and be quite exothermic (–9 kcal/mole).^{22,38b,c} In GC^{•-}, proton transfer between N1 on G and N3 on C is predicted to have a small barrier and be only slightly exothermic (–3 kcal/mol).^{22,38b,c} Since at low temperatures, a difference in activation energies will be especially significant, proton transfer in IC^{•-} results in a far lower rate of electron transfer than proton transfer in GC^{•-}. For hole transfer, a similar proton transfer process occurs between the GC base pair cation radical (G^{•+}C) forming [•]G(–H)CH⁺ and this tends to limit the rate of transfer as evidenced by a relatively high value of β (1.1 \AA^{-1}). For electron transfer in polyGpolyC, Cai *et al.* also showed that at temperatures below 130 K tunneling dominated, whereas above 130 K, electron transfer occurs through an activated process.^{19,20,33–38,40}

Finally, we should note that there is a vast literature regarding the study of hole and electron transfer in DNA using a variety of experimental methods other than ESR spectroscopy of irradiated samples. Recent reviews^{33,43} regarding these other methods should be consulted for further information.

2.4. *Electron loss mechanism for production of strand breaks*

As the significance of radiation damage to DNA via direct effects became understood,^{1-5,8,14,15,18-22,24} it became important to understand the origin of strand breaks from direct type effects (i.e. direct and quasi-direct effects).^{3a} It was well understood that free radicals on the sugar-phosphate backbone were responsible for strand breaks,^{1-3,5,14,15} but it was unclear whether these radicals originated from direct ionizations of the backbone or whether base radical damage might transfer to the sugar moiety to form the radical precursors leading to strand breaks. In two papers involving product analyses, Swarts *et al.* showed that the base release in γ -irradiated DNA could be quantitatively accounted for through ionization of the sugar moiety alone.^{25,26}

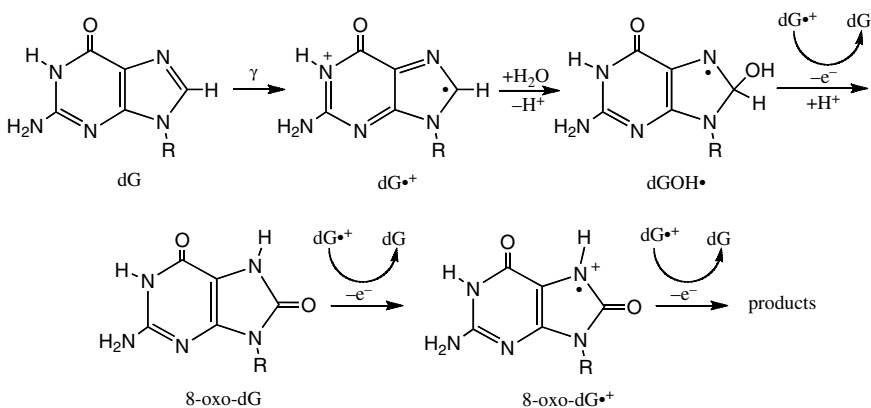
This was accomplished by estimating the percentage of ionizations that occur at the bases as well as at the sugar-phosphate backbone, and then tracking the fate of these ionizations to endpoints as damaged bases or as base release. It was assumed that approximately 56% of the original ionizations occur on the sugar-phosphate backbone and 44% on the bases (for salmon sperm DNA).^{25,26} Using the model proposed, 37% of the ionizations on the backbone ended up as released bases and 18% transferred to the bases to eventually track to base damage ($37\% + 18\% = 55\%$).²⁴⁻²⁶ Since there is thought to be a close correlation between base release and strand breaks,^{1-5,8} this work was significant in showing that there is no need to invoke a mechanism through which strand breaks form through the reactions of damaged bases. It is possible to account for all base release (as a surrogate for strand breaks) by the initial ionizations that occur at the sugar-phosphate backbone. Recently, it has become clear that low-energy electron damage to the deoxyribose-phosphate backbone is also a contributor to strand cleavage processes (Sec. 3). Work regarding the identification of specific radicals associated with LEE-induced damage suggests that it contributes about 4% of all radicals. This small yield was not included in our calculations shown above, since these calculations assumed that only electron-loss processes were a source of strand breaks.

2.5. Reactions of dG^{*+} as a possible radioprotective process

The guanine moiety has the lowest ionization potential of any of the DNA bases or of the sugar-phosphate backbone.^{1,3,8} As a result, radiation-produced holes are stabilized as dG^{*+} for hydrated DNA irradiated at 77 K. There is an extensive literature describing the role of dG^{*+} in the radiation chemistry of DNA as studied by pulse radiolysis, flash photolysis, and product analysis.^{8,33,43,44} In order to explicate the oxidative reaction sequence in irradiated DNA and to more firmly identify the relevant radical intermediates, ESR spectroscopy was employed to investigate γ -irradiated hydrated DNA ($\Gamma = 12 \pm 2$). Some experiments were also performed on hydrated ($\Gamma = 12 \pm 2$) DNA in which an electron scavenger [thallium(III) (Tl^{3+})] was employed to isolate the oxidative path.⁴⁴ Oxygen-17 isotopically enriched water was also used to confirm a proposed water addition step to G^{*+} and the subsequent transformations that follow.⁴⁴ These experiments were run in oxygen-free samples under conditions for which indirect effects were unimportant.

ESR spectra of these γ -irradiated samples were recorded as the temperature was increased from 77 K to 258 K in steps.⁴⁴ Computer analyses of the spectra were performed using benchmark spectra for the radicals involved, dG^{*+} , $T^{\bullet-}$, $dC(N3)H^{\bullet}$, $dGOH^{\bullet}$, 8-oxo- dG^{*+} , $T(C6)H^{\bullet}$, $T(C6)D^{\bullet}$, and various sugar radicals (as a group).⁴⁴ $dGOH^{\bullet}$ and 8-oxo- dG^{*+} were detected in irradiated DNA after annealing to *ca.* 200 K. As the temperature was increased to 273 K for 30 minutes (in samples with Tl^{3+}), the ESR spectrum obtained corresponded to almost pure 8-oxo- dG^{*+} .⁴⁴ Scheme 3 shows the proposed reaction sequence that best fits the observed ESR spectra as samples undergo step-wise annealing.

The reaction sequence in Scheme 3 has implications for radiation damage mechanisms in DNA. Since the electron-loss path is a major source of DNA damage, the transfer of multiple holes to a single guanine site would act as a radioprotective mechanism.⁴⁴ For doses that would be biologically relevant (a few Gray), electron-loss sites may be thought to be too sparse for this mechanism to be effective from inter-track reactions because the transfer distance required for a mobile hole to encounter a $dGOH^{\bullet}$, 8-oxo- dG or 8-oxo- dG^{*+} would be too large. However, even low LET radiation often deposits energy as multiple proximate ionizations.



Scheme 3. A single guanine, once ionized by radiation, becomes a sink for three or more other holes, here presumed to be $\text{dG}^{\bullet+}$. Holes on other bases or sugars will serve equally well for the reactions shown. The reduction potentials for the three subsequent oxidations are highly favorable.⁴⁴

Thus, a single track may form a multiply damaged site (MDS)⁴ and such a site can result in a biologically unreparable strand break on DNA. However, if, in such a cluster, several holes were to be funneled into a single guanine base (Scheme 3), a protective effect would result because only one damaged base would form from four proximate potential damage sites. Thus, the reactions in Scheme 3 may be operative as a radiation protective process even at low doses.

This work involving DNA at low temperatures⁴⁴ shows that formation of 8-oxo-G readily occurs at temperatures as low as 250 K. From this, it is clear that the activation barriers for these multiple one-electron oxidative processes (shown in Scheme 3) are small and the corresponding one-electron oxidations will be fast at biologically relevant temperatures.

2.6. Ion-beam irradiation of DNA

2.6.1. Ion-beam irradiation of DNA and high LET processes

In γ -irradiated samples, radiation damage is predominantly caused by the cascade of electrons that result from the interaction of the γ -ray

photons with matter. The (weighted) average linear energy transfer (LET) of these electrons is $0.43 \text{ keV}/\mu\text{m}$.^{5,20,24} Current models propose that energy from such low LET radiation is deposited in widely separated spurs, occasional blobs and rare short tracks. On the other hand, ion-beams, which have high LET, generally deposit energy in a much more heterogeneous fashion.^{3,5,8-15,18-20} The nature of the radical cohort stabilized in DNA samples at 77 K changes substantially with the LET and the associated track structure of the ionizing particles. In fact, in recent work,^{16,17} new radiation chemical processes not found with X- or γ -radiations are proposed for ion-beam radiations.

In a continuing study of ion-beam irradiation of hydrated DNA, both oxygen and argon ion-beams were used to investigate the radical yields and composition of the stabilized radical cohort in hydrated DNA at 77 K. For the argon ion-beam irradiated experiments, computer analysis of the DNA composite ESR spectra allowed quantification of the yields of G^+ , T^- , $\text{C}(\text{N3})\text{H}^\bullet$ and a mix of neutral (presumed) sugar radicals ΣS^\bullet .^{16,17} Qualitatively it is evident that ΣS^\bullet includes radicals formed by hydrogen atom loss from each of the three carbon atoms on the sugar ring, i.e. $\text{C1}'$, $\text{C3}'$, and $\text{C5}'$, and a radical formed by C–O bond cleavage at $\text{C3}'$ (Sec. 3).¹⁶ We note that the mixture of sugar radicals connoted by ΣS^\bullet is similar but not identical to that earlier called ΣN^\bullet for γ -irradiated samples. A full quantitative analysis of the composite spectrum of ΣS^\bullet for each of these species has not yet been accomplished. It was found that the overall yield of radicals in argon ion-irradiated samples was substantially lower than that in comparable γ -irradiated samples (Table 2).¹⁶ However, the neutral sugar radical yield $\text{G}(\Sigma\text{S}^\bullet)$ was higher as a percentage of overall yield, relative to estimated yields of sugar radicals from γ -irradiated samples (Table 2).¹⁶

The dose response of the neutral sugar radical cohort was also quite different from that of the three base radicals. The base radical yield departed from linearity at *ca.* 20–30 kGy and reached a firm plateau by *ca.* 250 kGy. However, the neutral radical mixture dose response was linear up to the highest dose used, 500 kGy.¹⁶

These results were interpreted to be a direct result of the ion-beam track structure, in which the high-energy ion-beam produces a

Table 2. Yields of radicals in argon ion-beam irradiated and γ -irradiated hydrated DNA.^a

Γ (H ₂ O/ nucleotide)	LET (keV/ μ m)	G_{Ar} (total) ^b	G_{γ} (total) ^b	$G_{\text{Ar}}(\Sigma\text{S}^{\bullet})/G_{\text{Ar}}(\text{total})^{\text{b,c}}$
7	600	0.049	0.156	0.20
9	650	0.106	0.172	0.20
12	350	0.148	0.207	0.22
12	600	0.136	0.207	0.24
12	800	0.063	0.207	0.24
14	400	0.139	0.234	0.27
16	500	0.211	0.267	0.29

^a Adapted with permission from Ref. 16.

^b All G values in $\mu\text{mol}/\text{J}$.

^c For γ -irradiated samples the yields of sugar radicals are *ca.* 10% to 15% of the total yield, i.e. $G_{\gamma}(\Sigma\text{S}^{\bullet})/G_{\gamma}(\text{total}) = 0.10$ to 0.15 .

densely ionized core, and energetic electrons emitted from the core (“delta rays”) produce dispersed spurs in much the same manner that the energetic electron cascade does in low LET irradiated samples (Fig. 2).^{3,5,8-17,45}

The relatively low overall yields of radicals were attributed to the high recombination rate of closely spaced base ion radicals in the densely ionized track core. The proximity of these radicals coupled with Coulomb attractions facilitates fast core ion radical-ion radical recombination. However, neutral sugar radicals in the core are not affected by Coulomb attractions, thus they do not recombine as readily. Therefore, most of the neutral sugar radicals stabilized at 77 K are presumed to form in the core. On the other hand, most of the base radicals that are stabilized at 77 K are assumed to form in the isolated, low LET-like spurs formed by delta-rays.⁴⁵ The similarity in the behavior of the base radicals in argon ion-beam irradiated samples and in γ -irradiated samples lends support to this picture.¹⁶ In this model $\text{C}(\text{N3})\text{H}^{\bullet}$ is in equilibrium with $\text{C}^{\bullet-}$ and is found to act as an ion-radical.^{16,45}

Based on this model, it was estimated in five samples ($16 \geq \Gamma \geq 9$ D₂O/nucleotide, $\text{LET} \leq 650$ keV/ μm) that *ca.* 50% of the energy of the argon ion-beam was deposited in the core and *ca.* 50% in low LET

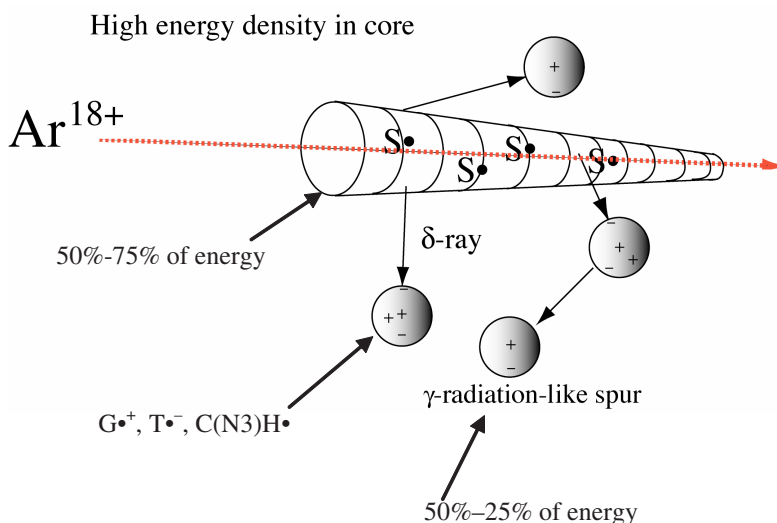


Fig. 2. Schematic of track of an Argon ion-beam in DNA. A high-energy density core is generated by deposition of *ca.* 50% of the energy of the ion in a relatively small volume. At 77 K, neutral sugar radicals are stabilized largely in the core. A much larger region of space formed by delta rays from the core is characterized by low LET-like spurs. Ion base radicals are stabilized in the spurs, with one-electron-reduced cytosine actually existing as a protonated species.

like spurs and for the remaining two samples (Table 2), *ca.* 75% of the energy appears to be deposited in the core and 25% elsewhere.¹⁶ These values are in good agreement with the track structure models of Chatterjee and his co-workers.⁹⁻¹¹

An investigation into the spatial orientation of the trapped radicals in argon ion-beam irradiated hydrated DNA provided a further remarkable confirmation of previously published track structure model predictions. Pulsed Electron Double Resonance (PELDOR) experiments analyzed using the theoretical construct of Tsvetkov and co-workers⁴⁵ concluded that the stabilized radical concentration (77 K) in the track core was higher than the average radical concentration, leading to the conclusion that multiply damaged sites existed in the DNA.⁴⁵ The mathematical model available did not allow treatment of a cylindrical track, so the parameters of a spherical cluster were evaluated

(Table 3). Based on the experimental design (neutral sugar radicals were probed), the sphere modeled is best thought of as a section of the track core.⁴⁵ The diameter of the core thus determined is, again, in good agreement with predictions from theoretical track structure models.^{9–11} Thus, these experiments provided the first quantitative experimental confirmation of the track structure models proposed by Chatterjee and his co-workers.^{9–11}

In a recent study of strand-break yields in He²⁺ irradiated hydrated (*ca.* $\Gamma = 31$ H₂O/nucleotide) pUC18 plasmid DNA at 5.6°C, it was found that the yield of prompt single-strand breaks does not significantly change as LET increases from 18 keV/μm to 95 keV/μm, but the yield of double-strand breaks does increase (Table 4).³¹

The same group found yields for similarly hydrated γ -irradiated pUC18 plasmid DNA samples to be $(7.2 \pm 0.5) \times 10^{-11}$ ssb/Gy/Da and $(0.72 \pm 0.07) \times 10^{-11}$ dsb/Gy/Da.³⁰ These yields for γ -irradiated samples are not very different from those obtained from He²⁺ ion-irradiated samples (Table 4). Therefore, as noted by these authors,^{30,31} with an

Table 3. MDS track parameters from argon ion-beam irradiated hydrated DNA.^a

Track parameter	Average (3 doses, 1.7–50 kGy)
N_R (Radicals per MDS)	17.7 ± 0.7
Spherical cluster radius (nm)	6.79
$[R^*]$ in cluster (10^{18} cm^{-1})	13.5 ± 0.5

^a Adapted with permission from Ref. 45.

Table 4. Yield of prompt strand breaks in hydrated, He²⁺ irradiated pUC18.^a

LET (keV/μm)	ssb/Gy/Da ($\times 10^{-11}$)	dsb/Gy/Da ($\times 10^{-11}$)	ssb/dsb
19	6.85	0.37	18.3
63	7.21	0.75	9.6
95	6.74	1.09	6.2

^a Adapted with permission from Ref. 31.

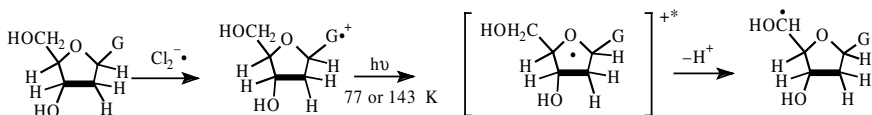
increase in LET, more clustered lesions are formed and a higher yield of double-strand breaks induced. In addition, the number of base lesions susceptible to enzymatic cleavage to form single-strand breaks by Nth and/or Fpg decreases as the LET increases.^{30,31} This, again, is tentatively interpreted to be a result of the clustering of damage, with the base lesions being less readily cleaved by the enzymes when they are part of a clustered damage site.^{30,31}

2.6.2. New mechanisms for radiation damage in ion-beam irradiated DNA

A comparison of the nature of the DNA-radicals produced with γ -radiation relative to those produced by ion-beams shows that some radical species which are found in low amounts using γ -radiation (low LET) increase by an order of magnitude in absolute yield with ion-beam (high LET) irradiation. For example, work using oxygen ion-beams found evidence for a phosphoryl radical (ROPO_2^{\bullet} , Scheme 1) in DNA. This radical, formed by dissociative electron attachment (Sec. 3), is clear evidence for a prompt strand break.¹⁶ In addition, formation of sugar radicals via excited states was proposed (Sec. 2.7).

2.7. Role of excited states in DNA damage: experimental and theoretical results

As described earlier, formation of substantially increased amounts of DNA-backbone-sugar and -phosphate radicals are observed in argon and oxygen ion-beam irradiated hydrated DNA samples relative to those found with low LET γ -irradiation.^{16,17} The usual mechanism suggested for formation of sugar radicals, i.e. hole deprotonation from direct ionization of the sugar^{3,4,8,14,15,18–20,24,46a} cannot explain the higher yield of such radicals observed in high LET irradiated samples. This led to the proposal that excited states, formed in the densely ionized ion-beam track core, may be responsible for their formation.^{16,20,22} One proposed mechanism for sugar radical formation hypothesizes that excitation of a base cation radical leads to charge and spin transfer to the adjoining sugar group. Deprotonation of



Scheme 4. Proposed mechanism of sugar radical formation (using C5[•] as an example) *via* photo-excitation of one-electron oxidized Guanine in dGuo. Reprinted with permission from Ref. 47, *Nucleic Acid Research* © (2005), Oxford University Press.

the resulting sugar cationic radical, results in a neutral sugar radical.^{20,22,46a,47–50} This hypothesized mechanism is illustrated in Scheme 4, using excited-state guanine cation radical (G^{•+}).

For verification of the proposed hypothesis, photo-excitation of the one-electron oxidized guanine in guanine deoxynucleosides and deoxynucleotides in aqueous (D₂O) glassy systems was performed. In agreement with the hypothesis, photo-excitation produces sugar radicals in abundant yields (80 to 90%).⁴⁷ For example, in dGuo, primarily C5[•] and C3[•] are found, for 3'-dGMP C5[•] and C1[•] are found, and for 5'-dGMP only C1[•] is produced.⁴⁷ Photo-excitation of one-electron oxidized adenine in deoxynucleosides and deoxynucleotides also led to sugar radical formation (*ca.* 80–100%).^{48a} The identification of the specific sugar radicals was achieved by employing dGuo derivatives with selective isotopic substitution (e.g. deuteration⁴⁷ and ¹³C substitution^{48a} in the sugar moiety). From the ESR of C3[•] in 5'-¹³C-dAdo, the first instance of a β-¹³C coupling (*ca.* 16 G) in the literature was reported.^{48a}

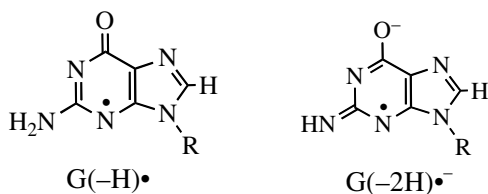
The specific site of deprotonation at the deoxyribose sugar varied with the site of phosphate substitution (either 3' or 5'), with deprotonation less likely when a phosphate group is present.^{20,22,47,48a,52} However, this was not the only determining factor in the mechanism of action. As is shown below pH/pD, excitation energy and oligo length all affect which sugar radical(s) forms as well as its yield.^{46a,49}

The pH (or pD in D₂O) was found to have a great effect on sugar radical formation from excited states of one-electron oxidized guanine (in dGuo) but not for one electron oxidized dAdo and its

derivatives.^{47,48a} The N1 hydrogen in $G^{\bullet+}$ has a pK_a of *ca.* 5 to 6 in glassy D_2O at low temperatures,⁵¹ so at $pD \geq 7$ the N1 proton is largely dissociated.⁵¹ Since the native pD of aqueous (D_2O) 7–7.5-M LiCl glassy systems is *ca.* 5, the proton at N1 in the guanine cation radical ($G^{\bullet+}$) is about 50% retained. Thus about half the radicals in one-electron oxidized guanine are in the deprotonated form, $G(-H)^{\bullet}$.⁵¹ In aqueous (D_2O) 7-M LiCl glassy systems, sugar radical formation via photo-excitation of one-electron oxidized guanine was found to occur from pD 2 to 6, but is suppressed for pDs above 7. In summary, the photo-conversion of one-electron oxidized guanine to sugar radicals was effective for its cation radical ($G^{\bullet+}$) in dGuo,⁴⁷ in dinucleoside phosphates, DNA oligomers and presumably in DNA,^{46a,47,49} but not for its N1-deprotonated state [$G(-H)^{\bullet}$] (Scheme 5).⁴⁷

In $G(-2H)^{\bullet-}$ (Scheme 5), both the N1 hydrogen and one of the hydrogens at the exocyclic nitrogen deprotonate.⁵¹ At pDs for which $G(-2H)^{\bullet-}$ exist, no significant photo-conversion is found.⁴⁷

A recent study employing ESR spectroscopy and density functional theory calculations has shown that the adenine cation radical ($A^{\bullet+}$) in aqueous glassy solutions of dAdo and of the DNA oligomer $(dA)_6$ is stabilized by base stacking interactions.^{48b} The pK_a of the adenine cation radical in isolated dAdo in aqueous solutions is *ca.* 1 and, therefore, $A^{\bullet+}$ readily deprotonates from its exocyclic amine group,^{3a,3b,8} nevertheless, these researchers find that the pK_a of the adenine cation radical in stacked systems to be *ca.* 8 at 150 K. It appears that the hole delocalizes over several bases, which stabilize it by charge resonance interactions. Calculations show that in the



Scheme 5. The structures of $G(-H)^{\bullet}$ and $G(-2H)^{\bullet-}$ [Ref. 51 and references therein for details].

adenine dimer cation radical, $A_2^{\bullet+}$, full delocalization of the hole over both bases occurs and, also, that the dimer cation radical is stabilized by *ca.* 12–16 kcal/mol relative to the monomers, $A^{\bullet+}$ and A. As found for $G^{\bullet+}$ in dGuo and its derivatives, sugar radicals ($C1^{\bullet}$, $C3^{\bullet}$ and $C5^{\bullet}$) are formed on excitation of $A^{\bullet+}$ in dAdo and its derivatives.^{48a} However, photo-excitation of $G(-H)^{\bullet}$ shows no appreciable sugar radical formation, whereas photo-excitation of $A(-H)^{\bullet}$ results in complete conversion to $C3^{\bullet}$.^{48a}

In model compounds i.e. in deoxynucleosides, deoxynucleotides and even in the DNA-oligomer TGGT, wavelengths of light from 320 nm to 650 nm are found to be highly effective in the formation of sugar radicals from one-electron oxidized guanine excited states.^{46a} On the other hand, sugar radical formation from photo-excitation of one-electron oxidized guanine in γ -irradiated, hydrated ($\Gamma = 12 \pm 2$ D₂O/nucleotide) DNA is wavelength dependent.⁴⁷ In the 310–480 nm range, conversion of one-electron oxidized guanine to $C1^{\bullet}$ in substantial yields occurs from 77 K to 180 K.^{46a,47} However, above 500 nm, no observable sugar radical formation occurs.⁴⁷ The extent of photo-conversion of one-electron oxidized guanine to sugar radicals, as well as its initial rate of conversion, decreases with increasing size of the oligonucleotides, although it still remains substantial (50%) even for high molecular weight salmon testes DNA.^{46a} As might be expected from the above, for the oligo TTGGTTGGTT, there is a relative increase in the formation of $C1^{\bullet}$ compared with shorter oligos, as well as a decline in the overall extent of sugar radical formation via photo-excitation of one-electron oxidized guanine at wavelengths >500 nm.^{46a}

A general observation is that light with wavelengths >500 nm becomes less effective at forming sugar radicals from one-electron oxidized guanine ($G^{\bullet+}$) as the oligomer length increases.^{46a} This is thought to result from an increase in the relative effectiveness of base-to-base hole transfer for the larger oligomers. At longer wavelengths, base-to-base hole transfers compete effectively with base-to-sugar hole transfer.^{46a}

Theoretical studies using time-dependent density functional theory (TD-DFT) of one-electron oxidized guanine in dGuo and $A(-H)^{\bullet}$ in

dAdo^{47,48a} showed that all the electronic transitions in the near-UV/visible range originate from the inner shell (core) molecular orbitals (MOs) and many of these involved hole transfer to the sugar ring. Therefore, from the TD-DFT studies and experimental results, it was established that excitation of one-electron oxidized purine base radicals results in delocalization of a significant fraction of the spin and charge onto the sugar moiety.^{20,22} Subsequent deprotonations leads to the formation of a neutral sugar radical as shown in Scheme 4.^{20,22} TD-DFT studies in TpdG^{•+}⁴⁹ and also in other one electron oxidized dinucleoside phosphates (TpdG, dGpdG, dApdA, dApdT, TpdA, and dGpdT)⁵⁰ show that the lower energy (i.e. longer wavelength) transitions in all these systems involve base-to-base π - π^* hole transfers. Thus, theoretical calculations for dinucleoside phosphates provide some support for the hypothesis that the excitation process induces base-to-base hole transfer at long wavelengths and low excitation energies in stacked DNA base systems, whereas shorter wavelengths induce base-to-sugar hole transfer.^{20,22,49,50} Also, sugar radical formation has been observed via photo-excitation of G^{•+} in Guo, as well as in RNA-oligomers.^{46b}

2.8. *The role of trapped free radicals in strand break formation*

It is a standing proposition of the free radical chemistry of DNA that radiation-induced strand breaks originate with sugar radicals.^{1-5,8} In recent work investigating the connection between sugar free radicals and strand breaks, it was observed that, at the lowest hydrations (*ca.* $\Gamma \leq 10$), the yield of strand breaks (observed at room temperature) exceeded the yield of *trapped* sugar radicals (at 4.2 K) in the same samples for X-ray-irradiated pUC18 plasmid DNA films.⁵³ Polycrystalline samples of d(CGCGCG)₂ at $\Gamma = 2.5$ or 7.5⁵⁴ behaved similarly. These observations were interpreted as an indication that, even at 4.2 K, chemical reactions occur which result in a diamagnetic precursor to strand breaks.^{53,54}

Both single and double strand breaks were measured in X-ray-irradiated pUC18 plasmid DNA films at different doses as well as at

different levels of hydrations ($\Gamma = 2.5\text{--}34.5 \text{ H}_2\text{O/nucleotide}$) by gel electrophoresis and these data were correlated with the free radical yields in these samples obtained by Q-band ESR studies.⁵³ Employing DNA along with its solvation shell as the target mass, and neglecting the amount of the excess salt present, the yields of the trapped DNA-sugar radicals were found to be the same as the total yields of strand breaks for fully hydrated DNA ($\Gamma > 10$) but significantly smaller than the corresponding yields of single strand breaks at the lowest hydration, $\Gamma \text{ ca. } 2.5$ (Table 5).⁵³

On the basis of these data, it was proposed that precursors other than trapped sugar radicals are responsible for causing a significant fraction of strand breaks at low hydrations.⁵³ A new mechanism was proposed in which two one-electron oxidations of a sugar at the same site lead to a diamagnetic product (which cannot be detected by ESR).⁵³ Mechanistically, it was later proposed that the diamagnetic product is a carbocation formed by direct ionization followed by an oxidation by a mobile or nearby base cation radical.⁵⁴

The prompt strand breaks, the (prompt + heat labile) strand breaks, and the strand breaks due to abasic lesions were measured by Yokoya, O'Neill and co-workers³⁰ in γ -irradiated pUC18 films at very similar hydration levels ($\Gamma = 4.5\text{--}34.5 \text{ H}_2\text{O/nucleotide}$). They found that, in these samples, the maximum yield of base lesions (quantified

Table 5. Yields in X-irradiated pUC18 plasmid DNA.⁵³

Hydration ($\text{H}_2\text{O}/$ nucleotide) (Γ)	G (sugar free radicals) $\mu\text{mol/J}$ (4.2 K) ^a	G(ssb) $\mu\text{mol/J}$ (Room temperature)	
		G(ssb) Prompt	G(ssb) Prompt + G(ssb) Heat labile
2.5 ± 0.2	0.033 ± 0.005	0.069 ± 0.014	0.092 ± 0.016
7.5 ± 0.6	0.040 ± 0.006	0.058 ± 0.012	0.081 ± 0.014
11.5 ± 0.3	0.056 ± 0.008	0.060 ± 0.008	0.078 ± 0.008
15.0 ± 0.7	0.069 ± 0.010	0.063 ± 0.008	0.077 ± 0.009
22.5 ± 1.1	0.079 ± 0.012	0.054 ± 0.007	0.066 ± 0.008

^a G(sugar free radicals) have been obtained using a semi-empirical model which predicts that 89% of the total free radicals are trapped on the bases and 11% on the sugar phosphate backbone (Ref. 53).

Table 6. Yields in X-irradiated pUC18 plasmid DNA.³⁰

Hydration (H ₂ O/ nucleotide)	G(ssb) $\mu\text{mol}/\text{J}$ (Room temperature)		
	G(ssb) Prompt	G(ssb) Prompt + G(ssb) Heat labile	G(ssb) Prompt + G(ssb) Heat labile + G(ssb) Fpg
4 \pm 1.5	0.054 \pm 0.009	0.047 \pm 0.007	0.094 \pm 0.006
8 \pm 2.2	0.065 \pm 0.008	0.053 \pm 0.007	0.130 \pm 0.015
14.5 \pm 4.1	0.069 \pm 0.005	0.062 \pm 0.004	0.130 \pm 0.016
24.5 \pm 6.9	0.071 \pm 0.006	0.068 \pm 0.006	0.130 \pm 0.014
34.5 \pm 9.7	0.072 \pm 0.005	0.067 \pm 0.008	0.16 \pm 0.009

by enzymatically-induced ssbs) is almost identical to those of radiation-induced prompt ssbs (Table 6). They found a similar trend with dsbs as well (Table 1 in Ref. 30). Therefore, they suggested that radiation-induced clustered DNA-damage (i.e. two or more lesions, closely located, one on each DNA strand) in enzyme sensitive sites in these DNA samples is responsible for high yields of total strand breaks.³⁰ In this case the diamagnetic precursor would be the damaged bases rather than a carbocation. In Table 5, G(ssb) (either prompt or total) tends to decrease with increasing Γ whereas, in Table 6, the opposite effect is observed. However, the results in Tables 5 and 6 for G(ssb) are in agreement within error limits for all values except that at the lowest hydration. Given the experimental difficulty in measuring strand breaks, this is excellent agreement. For the two different explanations given for the observed data, i.e. double oxidation versus clustering of damage, damage clustering includes a variety of types of damage at different DNA moieties which could include double oxidations, whereas the double oxidation mechanism evokes a specific process.

3. Low-Energy Electron Pathways

3.1. Introduction

Early investigations of DNA irradiation damage from the indirect effect clearly indicated that hydrated electrons (e_{aq}^-), formed as a result

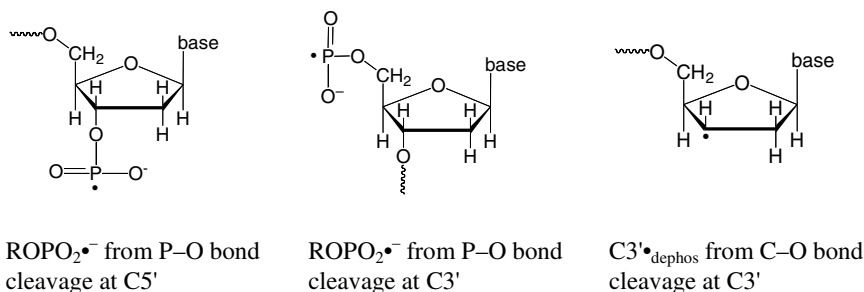
of the irradiation of water, add to the DNA bases and do not result in DNA strand breaks.^{1-5,8} Thus, it became a consensus model that the electron-loss path is the major source of strand breaks from the indirect effect, due primarily to hydroxyl radical ($\cdot\text{OH}$) attack.^{1-5,8}

For many years, this view was extrapolated to direct-type effects, and the role of the electron as a possible source of strand breaks was minimized. However, more recently, two disparate lines of investigation have shown that although aqueous electrons are ineffective in causing strand breaks, unsolvated electrons with residual kinetic energy, defined as low-energy electrons (LEE), can do so. In 1996 a phosphoryl radical ($\text{ROPO}_2^{\cdot-}$) in oxygen-16 ion-irradiated hydrated DNA was reported from a direct effect process.¹⁷ This radical is likely formed *via* dissociative electron attachment, and is indicative of a prompt strand break. This same phosphoryl radical was found in later work using argon-beam irradiated hydrated DNA. Thus, the reductive path was implicated in DNA strand break formation.

In a ground-breaking paper in 2000, it was shown by the Sanche group that sub-ionization low-energy electrons could cause DNA strand breaks.^{21,23} Later work (*vide infra*) confirmed and expanded this original finding to near thermal, but unsolvated, electrons. It is now well accepted that low-energy electrons can cause both single and double strand breaks in DNA.

3.2. Electron spin resonance experiments in ion-beam irradiated samples

Ion-beam irradiation (77 K) of DNA hydrated to $\Gamma = 18 \text{ D}_2\text{O}/\text{nucleotide}$ resulted in a DNA-phosphorus-centered radical.^{16,17} Samples were irradiated with 60 MeV/u, O^{8+17} or 100 MeV/u Ar^{18+} .¹⁶ The ESR results showed the presence of an axially symmetric spectrum with large phosphorus couplings ($A_{\parallel} = 77.5 \text{ mT}$ and $A_{\perp} = 61.0 \text{ mT}$, $g_{\parallel} = 2.000$, $g_{\perp} = 2.001$), from a radical that constituted *ca.* 0.1% to 0.2% of the total radical concentration. Earlier literature regarding the origin and ESR spectra of such radicals existed^{16-18,24} and it was concluded that the radical was a phosphoryl radical ($\text{ROPO}_2^{\cdot-}$, Scheme 6), formed from the electron gain path. In DNA, such a radical could result only from P-O bond cleavage at either the C3' or C5' of the deoxyribose sugar



Scheme 6.

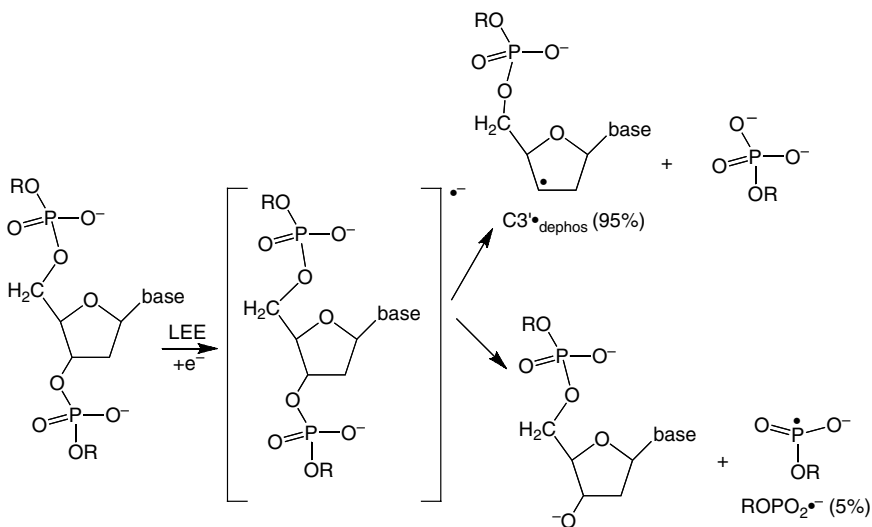
and a concomitant prompt strand break. The formation of this radical(s) is direct evidence that strand breaks originate with the direct effect-electron gain path.^{16,17}

In argon ion-beam irradiated hydrated DNA,¹⁶ a sugar radical formed by PO–C bond cleavage [C3'•_{dephos}] (Scheme 6), was found in substantially higher concentrations than the phosphoryl radical. This radical displays hyperfine coupling to four hydrogen atoms and, thereby, results in an ESR spectrum with a larger breadth than any other known DNA deoxyribose sugar radical. This radical can form only as the direct product of a prompt strand break.¹⁶ The overall picture of low-energy electron attack at the sugar group in hydrated, irradiated DNA as deduced by ESR investigation is shown in Scheme 7.

The set of reaction paths shown in Scheme 7 was deduced from results in ion-beam irradiated samples.^{16,17} However, both the phosphoryl radical and C3'•_{dephos} have been found in γ -irradiated samples at lower concentrations.⁵⁵ This mechanism might be expected to result in similar yields for both low and high LET radiation, but there is increasing evidence that along the track core, both electronic and vibrational excitations act jointly with LEE to cause the strand cleavage processes shown in Scheme 7.

3.3. Strand breaks in plasmid DNA via dissociative electron attachment (DEA)

The role of low-energy electrons in causing strand breaks was demonstrated unequivocally with experiments that measured strand breaks in



Scheme 7.

plasmid DNA. Boudaïffa *et al.* showed that low energy electrons (1–20 eV) caused single strand breaks in dry ($\Gamma = 2.5 \text{ H}_2\text{O}/\text{nucleotide}$) plasmid DNA [pGEM 3Zf(-)].^{21,23} Strand breaks are caused by electrons below the ionization limit (*ca.* 7.5 eV), thus their formation is consistent with a dissociative electron attachment (DEA) mechanism.^{21,23} In addition, a resonance phenomena was observed. This suggests that the damaging electrons add to a specific portion of the DNA structure as the initial step in the DEA process. At the *ca.* 7 eV peak, approximate yields of 8.2×10^{-4} single strand breaks per electron and 2×10^{-4} double strand breaks per electron were found.²³ Later work showed that even electrons close to 0 eV could induce single strand breaks.²¹

More recent study of the effect of LEE on the tetramers CGTA and GCAT resulted in the quantitative observation of products which enabled the authors to assign the distribution of bond cleavage caused by the electrons.^{56,57} The strand cleavage occurred at each phosphate sugar O–C bond. Later investigations of the tetramer GCAT and variants containing abasic sites in which the base is replaced by a hydrogen atom, (e.g. GCXT, XCAT), were carried out using 3–15 eV

electrons with no water present.^{56,57} For 6-eV electrons, the yield of strand breaks for XCAT and GCXT were significantly lower than for GCAT. This was interpreted to suggest that, for 6-eV electrons, the original electron attachment occurs at the base to form an excited transient anion, and that subsequent transfer of an electron to the corresponding phosphate group results in C–O bond cleavage and a concomitant strand break.^{56,57}

Recent studies by Illenberger and co-workers regarding the LEE induced decomposition of D-ribose,⁵⁸ phosphoric acid esters⁵⁹ and thymidine⁶⁰ have added more interesting results and complexity to this picture. These results show that direct electron attachment to the phosphate and sugars can result in fragmentations even at low energies. The authors suggest that migration of the excess electron from the π^* orbital of the anion of the nucleobase to the DNA-backbone is inhibited and, hence may not contribute to ssb as proposed by Simons *et al.*⁶¹ To account for ssb formation in DNA at subexcitation energy (<4 eV), it was proposed that the initial electron directly attached to the phosphate group.^{59,60}

3.4. Mechanisms of LEE action

The studies described here indicate that significant amounts of bond cleavage from LEE occur on the sugar–phosphate backbone. Although a mechanism in which the initial low-energy electron attachment is to a base is indicated by some experimental results, other experimental results suggest that direct attachment to the phosphate group is also a viable mechanism.²² These processes have been intensively modeled via theoretical calculations with some interesting insights.^{22,61–66a}

Simons and co-workers proposed the first theoretical model of LEE-induced strand break formation by modeling C5'–O sugar–phosphate bond dissociation in 5'-dTMP and 5'-dCMP.^{22,61} According to Simons *et al.*, the initial attachment of the electron occurs in a π^* valence molecular orbital (shape resonance) in the pyrimidine base.⁶¹ Electron transfer occurs from the base to a σ^* molecular orbital of the C5'–O bond as C–O bond elongation takes place, thereby leading to

sugar–phosphate bond cleavage and strand break formation.⁶¹ An alternative mechanism of direct attachment of the electron to the sugar–phosphate moiety leading to the C–O sugar–phosphate bond dissociation was also proposed on the basis of B3LYP/6-31+G(d) and ONIOM studies in a sugar–phosphate–sugar model without any base.⁶² Barrier heights for the C–O bond dissociations at both the 3'- and 5'- sites were calculated and were found to be similar at *ca.* 10.0 kcal/mol.⁶² Recent calculations by these authors regarding the spin and density distribution of the excess electron indicate that the electron is initially in a dipole bond state and that the attachment of the LEE occurs in a σ^* molecular orbital on bond elongation. This results in dissociation of the C–O bond in the sugar-phosphate moiety.^{22,63} Also, recent calculations using the B3LYP/DZP++ level of theory by the Leszczynski group on C5'–O5' bond dissociations at the 5'-end in 5'-dTMPH (5'-phosphate protonated at 5'-dTMP) and in 5'-dCMPH⁶⁴ and again on C3'–O3' bond dissociations at the 3' end in 3'-dTMPH and in 3'-dCMPH⁶⁵ supported the mechanism already proposed by Simons *et al.*⁶¹

Recently, DFT calculations of C5'^o–O cleavage by LEE using 6–31 G* and 6–31++G** basis sets were performed again for 5'^o-dTMPH anion radical.^{22,66a} In this set of calculations, the vertical potential energy surface was compared to the adiabatic surface for C5'^o–O5' bond elongation. Surprisingly, the vertical activation barrier is found to be no larger than the adiabatic barrier for bond dissociation (*ca.* 12 kcal/mol).^{66a} Furthermore, the electron transfer process occurs earlier on the vertical PES. An adiabatic calculation for electron-induced bond dissociation for 5'^o-dTMP with sodium ion and 11 molecules of water of hydration was also performed.^{66a} The barrier to bond cleavage (strand break) was increased several fold to *ca.* 30 kcal/mol. These results show that the adiabatic pathway is not a likely route for strand cleavage in aqueous DNA and they provide a clear explanation for why solvated electrons do not cause DNA strand breaks.^{66a}

Although the adiabatic pathway appears unlikely, we note that the “shape resonance” or “single particle resonance” at low energy (*ca.* 0–7 eV) have several interacting pathways, including vibrational,

rotational, and electronic excitation of the molecule as well as dissociative electron attachment (DEA).^{22,66a} It is clear that excitations induced by LEE are critical to the cleavage process²¹⁻²³ as shown in the recent theoretical calculations on the transient negative ions in 5'-dTMPH.^{66b}

4. Conclusion

The work described in this review reflects the current interest in the mechanistic aspects of direct effects of radiation on DNA. Evidence is presented for migration of holes and excess electrons through DNA by tunneling over only short ranges < 10 bp and by activated processes over longer distances.^{18-20,34-40} A variety of reactions such as protonations/deprotonations and reactions with water compete with charge transfer to produce the ultimate molecular damage in DNA molecules.²⁰ Apart from the plausible "direct ionization" pathway in the sugar-phosphate moiety,^{1-5,8,18-20,46a} this review points out that pathways involving one-electron-oxidized purines^{20,46a,47-50} and low-energy electrons,^{16-23,56-66a} in combination with excitations, are crucial in causing DNA damage induced by high LET radiations.

Acknowledgments

The authors thank the National Cancer Institute of the National Institutes of Health (Grant RO1CA45424) for support.

References

1. von Sonntag C. (1987) *The Chemical Basis of Radiation Biology*. Taylor & Francis, London.
2. Lett JT. (1990) Damage to DNA and chromatin structure from ionizing radiations, and the radiation sensitivities of mammalian cells. *Prog Nucl Acid Res Mol Biol* **39**: 305-352.
3. (a) Becker D, Sevilla MD. (1993) The chemical consequences of radiation-damage to DNA. *Adv Radiat Biol* **17**: 121-180. (b) Steenken S. (1989) Purine bases, nucleosides and nucleotides: Aqueous solution redox chemistry and transformation reactions of their radical cations and e⁻ and OH adducts. *Chem Rev*

- 89**: 503–520. (c) Steenken S. (1992) Electron-transfer-induced acidity/basicity and reactivity changes of purine and pyrimidine bases. Consequences of redox processes for DNA base pairs. *Free Radical Res Commun* **16**: 349–379.
- (d) Steenken S. (1997) Electron transfer in DNA? Competition by ultra-fast proton transfer? *Biol Chem* **378**: 1293–1297.
4. Ward JF. (2000) Complexity of damage produced by ionizing radiation. *Cold Spring Harb Symp Quant Biol* **65**: 377–382.
 5. Kiefer J. (1990) *Biological Radiation Effects*. Springer-Verlag, Berlin, Heidelberg, New York.
 6. Kanaar R, Hoelijmakers JH, van Gent DC. (1998) Molecular mechanisms of DNA double strand break repair. *Trends Cell Biol* **8**: 483–489.
 7. Frankenberg D, Frankenberg-Schwager M, Blöcher D, Harbich, R. (1981) Evidence for DNA double-strand breaks as the critical lesions in yeast cells irradiated with sparsely or densely ionizing radiation under oxic or anoxic conditions. *Radiat Res* **88**: 524–532.
 8. von Sonntag C. (2006) *Free-radical-induced DNA Damage and Its Repair*. Springer-Verlag, Berlin, Heidelberg, New York.
 9. Farhataziz, Rodgers MAJ. (eds.) (1987) *Radiation Chemistry: Principles and Applications*. Verlag Chemie, Weinheim.
 10. Mozumdar A. (1999) *Fundamentals of Radiation Chemistry*. Academic Press, San Diego.
 11. Chatterjee A, Holley WR. (1993) Computer-simulation of initial events in the biochemical-mechanisms of DNA-damage. *Adv Radiat Biol* **17**: 181–226.
 12. Goodhead DT, Leenhouts HP, Paretzke, HG, Terrisol M, Nikjoo H, Blaauboer R. (1994) Track structure approaches to the interpretation of radiation effects on DNA. *Radiat Prot Dosim* **52**: 217–223.
 13. Nikjoo H, Uehara S. (2004) Track structure studies of biological systems. In *Charged Particle and Photon Interactions with Matter Chemical, Physicochemical and Biological Consequences with Applications*, Mozumdar A, Hatano Y. (eds.), pp. 491–531, Marcel Dekkar, Inc., New York, Basel.
 14. Fuciarelli AF, Zimbrick JD. (eds.) (1995) *Radiation Damage in DNA: Structure/Function Relationships at Early Times*. Battelle Press, Columbus, Richmond.
 15. Fielden EM, O'Neill P. (eds.) *The Early Effects of Radiation on DNA*. Nato ASI Series H: volume 54, Springer-Verlag, Berlin, Heidelberg, New York.
 16. Becker D, Bryant-Friedrich A, Trzasko C, Sevilla MD. (2003) Electron spin resonance study of DNA irradiated with an argon-ion beam: Evidence for formation of sugar phosphate backbone radicals. *Radiat Res* **160**: 174–185.
 17. Becker D, Razskazovskii Y, Callaghan MU, Sevilla MD. (1996) Electron spin resonance of DNA irradiated with a heavy-ion beam ($^{16}\text{O}^{8+}$): Evidence for damage to the deoxyribose phosphate backbone. *Radiat Res* **146**: 361–368.

18. Bernhard WA, Close DM. (2004) DNA damage dictates the biological consequences of ionizing irradiation: The chemical pathways. In *Charged Particle and Photon Interactions with Matter Chemical, Physicochemical and Biological Consequences with Applications*, Mozumdar A, Hatano Y. (eds.), pp. 431–470, Marcel Dekkar Inc., New York, Basel.
19. Sevilla MD, Becker, D. (2004) ESR studies of radiation damage to DNA and related biomolecules. In *Royal Society of Chemistry Specialist Periodical Report*, Gilbert BC, Davies MJ, Murphy DM. (eds.), *Electron Spin Resonance* **19**: 243–278.
20. Becker D, Adhikary A, Sevilla MD. (2007) The role of charge and spin migration in DNA radiation damage. In *Charge Migration in DNA: Physics Chemistry and Biology Perspectives*, Chakraborty T. (ed.), pp. 139–175, Springer-Verlag, Berlin, Heidelberg.
21. Bass AD, Sanche L. (2004) Interactions of low-energy electrons with atomic and molecular solids. In *Charged Particle and Photon Interactions with Matter Chemical, Physicochemical and Biological Consequences with Applications*. Mozumdar A, Hatano Y. (eds.), pp. 207–257, Marcel Dekkar, Inc., New York, Basel.
22. Kumar A, Sevilla MD. (2008) Radiation effects on DNA: Theoretical investigations of electron, hole and excitation pathways to DNA damage. In *Radiation Induced Molecular Phenomena in Nucleic Acid: A Comprehensive Theoretical and Experimental Analysis*, Shukla MK, Leszczynski J. (eds.), pp. 577–617, Springer-Verlag, Berlin, Heidelberg, New York.
23. Boudaïffa B, Cloutier P, Hunting D, Huels MA, Sanche L. (2000) Resonant formation of DNA strand breaks by low-energy (3–20 eV) electrons. *Science* **287**: 1658–1660.
24. Sevilla MD, Becker D. (1998) Radiation damage to DNA and related biomolecules. In *Royal Society of Chemistry Specialist Periodical Report*, Gilbert BC, Davies MJ, Murphy DM. (eds.), *Electron Spin Resonance* **16**: 79–114.
25. Swarts SG, Sevilla MD, Becker D, Tokar CJ, Wheeler KT. (1992) Radiation-induced DNA damage as a function of hydration. I. Release of unaltered bases. *Radiat Res* **129**: 333–344.
26. Swarts SG, Becker D, Sevilla MD, Wheeler KT. (1996) Radiation-induced DNA damage as a function of hydration. II. Base damage from electron-loss centers. *Radiat Res* **145**: 304–314.
27. Mroccka N, Bernhard WA. (1993) Hydration effects on free radical yields in DNA X-irradiated at 4 K. *Radiat Res* **135**: 155–159.
28. Mroccka N, Bernhard WA. (1995) Electron paramagnetic resonance investigation of X-irradiated poly(U), poly(A) and poly(A):poly(U): Influence of hydration, packing and conformation on radical yield at 4 K. *Radiat Res* **144**: 251–257.

29. Hüttermann J, Röhrig M, Köhnlein W. (1992) Free radicals from irradiated lyophilized DNA: Influence of water of hydration. *Int J Radiat Biol* **61**: 299–313.
30. Yokoya A, Cunniffe SM, O'Neill P. (2002) Effect of hydration on the induction of strand breaks and base lesions in plasmid DNA films by γ -radiation. *J Am Chem Soc* **124**: 8859–8866.
31. Urushibara A, Shikazono N, Watanabe R, Fujii K, O'Neill P, Yokoya A. (2006) DNA damage induced by the direct effect of He ion particles. *Radiat Prot Dosim* **122**: 161–165.
32. Sevilla MD, Becker D, Yan M, Summerfield, SR. (1991) Relative abundances of primary ion radicals in γ -irradiated DNA: Cytosine vs thymine anions and guanine vs adenine cations. *J Phys Chem* **95**: 3409–3415.
33. Schuster GB. (ed.) (2004) Long range charge transfer in DNA. I and II in *Topics In Current Chemistry*. Springer, Berlin; and the references therein.
34. Messer A, Carpenter K, Forzley K, Buchanan J, Yang S, Razskazovkii Y, Cai Z, Sevilla MD. (2000) Electron spin resonance study of electron transfer rates in DNA: Determination of the tunneling constant beta for single-step excess electron transfer. *J Phys Chem B* **104**: 1128–1136.
35. Cai Z, Sevilla MD. (2000) Electron spin resonance study of electron transfer in DNA: Inter-double-strand tunneling processes. *J Phys Chem B* **104**: 6942–6949.
36. Cai Z, Gu Z, Sevilla MD. (2000) Electron spin resonance study of the temperature dependence of electron transfer in DNA: Competitive processes of tunneling, protonation at carbon, and hopping. *J Phys Chem B* **104**: 10406–10411.
37. Cai Z, Gu Z, Sevilla MD. (2001) Electron spin resonance study of electron and hole transfer in DNA: Effects of hydration, aliphatic amine cations, and histone proteins. *J Phys Chem B* **105**: 6031–6041.
38. (a) Cai Z, Li X, Sevilla MD. (2002) Excess electron transfer in DNA: Effect of base sequence and proton transfer. *J Phys Chem B* **106**: 2755–2762. (b) Li X, Cai Z, Sevilla MD. (2001) Investigation of proton transfer within DNA base pair anion and cation radicals by density functional theory (DFT). *J Phys Chem B* **105**: 10115–10123. (c) Li X, Sevilla MD. (2007) DFT treatment of radiation produced radicals in DNA model systems. *Advances in Quantum Chemistry* **52**: 59–87. (d) Adhikary A, Khanduri D, Sevilla MD. (2009) Direct observation of the hole protonation state and hole localization site in DNA-oligomers. *J Am Chem Soc* **131**: 8614–8619.
39. Pal C, Hüttermann J. (2006) Postirradiation electron transfer vs differential radical decay in X-irradiated DNA and its mixtures with additives. Electron spin resonance spectroscopy in LiBr glass at low temperatures. *J Phys Chem B* **110**: 14976–14987.
40. Sevilla MD. (2006) Comment on electron transfer vs differential decay in irradiated DNA. *J Phys Chem B* **110**: 25122–25123.
41. Yan M, Becker D, Summerfield SR, Renke P, Sevilla MD. (1992) Relative abundance and reactivity of primary ion radicals in γ -irradiated DNA at

- low-temperatures. 2. Single-stranded vs double-stranded DNA. *J Phys Chem* **96**: 1983–1989.
42. Wang W, Becker D, Sevilla MD. (1993) The influence of hydration on the absolute yields of primary ionic free-radicals in γ -irradiated DNA at 77-K. 1. Total radical yields. *Radiat Res* **135**: 146–154.
43. Wagenknecht H-A. (ed.) (2005) *Charge Transfer in DNA: From Mechanism to Application*. Willey-VCH, Weinheim; and the references therein.
44. Shukla LI, Adhikary A, Pazdro R, Becker D, Sevilla MD. (2004) Formation of 8-oxo-7,8-dihydroguanine-radicals in γ -irradiated DNA by multiple one-electron oxidations. *Nucleic Acids Res* **32**: 6565–6574.
45. Bowman MK, Becker D, Sevilla MD, Zimbrick JD. (2005) Track structure in DNA irradiated with heavy ions. *Radiat Res* **163**: 447–454.
46. (a) Adhikary A, Collins S, Khanduri D, Sevilla MD. (2007) Sugar radicals formed by photo-excitation of guanine cation radical in oligonucleotides. *J Phys Chem B* **111**: 7415–7421. (b) Khanduri D, Collins S, Kumar A, Adhikary A, Sevilla MD. (2008) Formation of sugar radicals in RNA model systems and oligomers *via* excitation of guanine cation radical. *J Phys Chem B* **112**: 2168–2178.
47. Adhikary A, Malkhasian AYS, Collins S, Koppen J, Becker D, Sevilla MD. (2005) UVA-visible photo-excitation of guanine radical cations produces sugar radicals in DNA and model structures. *Nucleic Acids Res* **33**: 5553–5564.
48. (a) Adhikary A, Becker D, Collins S, Koppen J, Sevilla MD. (2006) C5'- and C3'- sugar radicals produced via photo-excitation of one-electron oxidized adenine in 2'-deoxyadenosine and its derivatives. *Nucleic Acids Res* **34**: 1501–1511. (b) Adhikary A, Kumar A, Khanduri D, Sevilla MD. (2008) Effect of base stacking on the acid–base properties of the adenine cation radical [A^{•+}] in solution: ESR and DFT studies. *J Am Chem Soc* **130**: 10282–10292.
49. Adhikary A, Kumar A, Sevilla MD. (2006) Photo-induced hole transfer from base to sugar in DNA: Relationship to primary radiation damage. *Radiation Res* **165**: 479–484.
50. Kumar A, Sevilla MD. (2006) Photoexcitation of dinucleoside radical cations: A time-dependent density functional study. *J Phys Chem B* **110**: 24181–24188.
51. Adhikary A, Kumar A, Becker D, Sevilla MD. (2006) The guanine cation radical: Investigation of deprotonation states by ESR and DFT. *J Phys Chem B* **110**: 24171–24180.
52. Colson AO, Sevilla MD. (1995) Elucidation of primary radiation damage in DNA through application of *ab initio* molecular orbital theory. *Int J Radiat Biol* **67**: 627–645.
53. Purkayastha S, Milligan JR, Bernhard WA. (2006) An investigation into the mechanisms of DNA strand breakage by direct ionization of variably hydrated plasmid DNA. *J Phys Chem B* **110**: 26286–26291.
54. Sharma KK, Purkayastha S, Bernhard WA. (2007) Unaltered free base release from d(CGCGCG)₂ produced by the direct effect of ionizing radiation at 4 K and room temperature. *Radiat Res* **167**: 501–507.

55. Shukla LI, Pazdro R, Becker D, Sevilla MD. (2005) Sugar radicals in DNA: Isolation of neutral radicals in gamma-irradiated DNA by hole and electron scavenging. *Radiat Res* **167**: 501–507.
56. Ptasinska S, Sanche L. (2007) Dissociative electron attachment to abasic DNA. *Phys Chem Chem Phys* **9**: 1730–1735.
57. Zheng Y, Wagner JR, Sanche L. (2006) DNA damage induced by low-energy electrons: Electron transfer and diffraction. *Phys Rev Lett* **96**: 208101.
58. (a) Baccarelli I, Gianturco FA, Grandi A, Sanna N, Lucchese RR, Bald I, Kopyra J, Illenberger E. (2007) Selective bond breaking in beta-d-ribose by gas-phase electron attachment around 8 eV. *J Am Chem Soc* **129**: 6269–6277. (b) Bald I, Kopyra J, Illenberger E. (2006) Selective excision of C5 from D-ribose in the gas phase by low-energy electrons (0–1 eV): Implications for the mechanism of DNA damage. *Angew Chem Int Ed Engl* **45**: 4851–4855.
59. Konig C, Kopyra J, Bald I, Illenberger E. (2006) Dissociative electron attachment to phosphoric acid esters: The direct mechanism for single strand breaks in DNA. *Phys Rev Lett* **97**: 018105.
60. Ptasinska S, Denifl S, Gohlke S, Scheier P, Illenberger E, Mark TD. (2006) Decomposition of thymidine by low-energy electrons: Implications for the molecular mechanisms of single-strand breaks in DNA. *Angew Chem Int Ed Engl* **45**: 1893–1896.
61. (a) Simons J. (2006) How do low-energy (0.1–2 eV) electrons cause DNA-strand breaks? *Acc Chem Res* **39**: 772–779. (b) Berdys J, Anusiewicz I, Skurski P, Simons J. (2004) Damage to model DNA fragments from very low-energy (< 1 eV) electrons. *J Am Chem Soc* **126**: 6441–6447.
62. Li X, Sevilla MD, Sanche L. (2003) Density functional theory studies of electron interaction with DNA: Can zero eV electrons induce strand breaks? *J Am Chem Soc* **125**: 13668–13669.
63. Li X, Sanche L, Sevilla MD. (2006) Base release in nucleosides induced by low-energy electrons: A DFT study. *Radiat Res* **165**: 721–729.
64. Bao X, Wang J, Gu J, Leszczynski J. (2006) DNA strand breaks induced by near-zero-electron volt electron attachment to pyrimidine nucleotides. *Proc Natl Acad Sci USA* **103**: 5658–5663.
65. Gu J, Wang J, Leszczynski J. (2006) Electron attachment-induced DNA single strand breaks: C3'-O3' sigma-bond breaking of pyrimidine nucleotides predominates. *J Am Chem Soc* **125**: 13668–13669.
66. (a) Kumar A, Sevilla MD. (2007) Low-energy electron attachment to 5'-thymidine monophosphate: Modeling single strand breaks through dissociative electron attachment. *J Phys Chem B* **111**: 5464–5474. (b) Kumar A, Sevilla MD. (2008) The role of $\pi\sigma^*$ excited states in electron-induced DNA strand break formation: A time-dependent density functional theory study. *J Am Chem Soc* **130**: 2130–2131.

Chapter 19

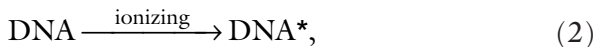
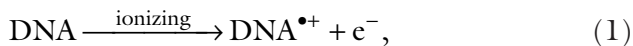
Radiation-Induced DNA Damage: Indirect Effects

*Clemens von Sonntag**

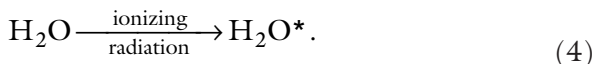
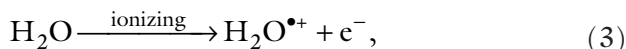
1. Introduction

In living cells, ionizing radiation may cause severe damage such as chromosomal aberrations and reproductive cell death. The target of these effects is largely the cell's DNA.^{1,2}

In the interaction of ionizing radiation with cellular DNA, two effects contribute: the *direct effect* [reactions (1) and (2)], where the energy of the ionizing radiation is absorbed by DNA itself; and the *indirect effect*, where the water that surrounds the DNA absorbs the energy of the ionizing radiation [reactions (3) and (4)].



* Max-Planck-Institut für Bioanorganische Chemie, Stiftstr, 34-36, 45413 Mülheim an der Ruhr, Germany. E-mail: clemens@vonsonntag.de



Both processes contribute to the observed DNA damage in cellular systems; for attempts to disentangle the individual contributions experimentally, see Ref. 2.

The electron produced in reactions (1) and (3) may still contain enough energy to cause further ionizations in the very near neighborhood. These areas, containing a number of ionization and occasionally also electronic-excitation events [reactions (2) and (4)], are called spurs. In the case of sparsely ionizing radiation, these spurs do not overlap. In densely ionizing radiation however, they form cylinders of spurs that are called tracks.

The water radical cation, produced in reaction (3), is a very strong acid and immediately loses a proton to neighboring water molecules thereby forming an $\cdot\text{OH}$ radical [reaction (5)]. The electron becomes hydrated by water [reaction (6)]. Electronically excited water can decompose into $\cdot\text{OH}$ and $\text{H}\cdot$ [reaction (7)]. Thus, three kinds of free radicals are formed side by side in the spurs, $\cdot\text{OH}$, e_{aq}^- , and $\text{H}\cdot$. To match the charge of the electrons, an equivalent amount of H^+ is also present.



A spur may contain more than one reactive intermediate, and they can interact with one another, e.g. $\cdot\text{OH} + \text{e}_{\text{aq}}^- \rightarrow \text{OH}^-$; $\text{H}^+ + \text{e}_{\text{aq}}^- \rightarrow \text{H}\cdot$; $\cdot\text{OH} + \text{H}\cdot \rightarrow \text{H}_2\text{O}$; $2\cdot\text{OH} \rightarrow \text{H}_2\text{O}_2$; $2\text{e}_{\text{aq}}^- + 2\text{H}^+ \rightarrow \text{H}_2$; $2\text{H}\cdot \rightarrow \text{H}_2$, in competition with a reaction with a neighboring solute such as DNA.

DNA has two main targets for the water-derived radicals, the nucleobases and the sugar-phosphate backbone (Fig. 1).

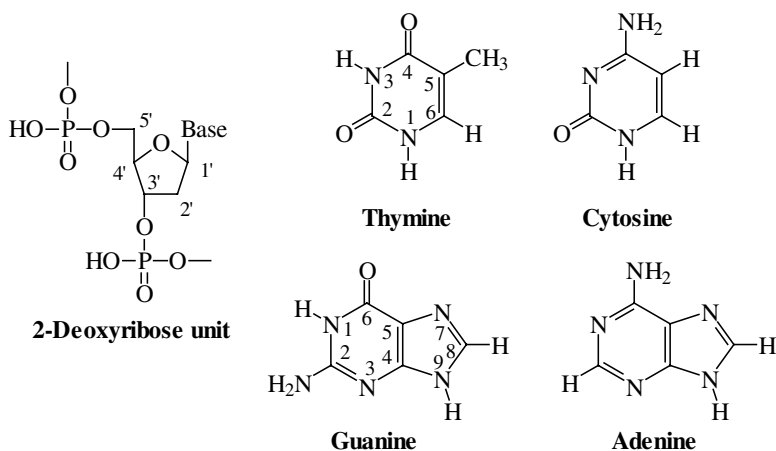


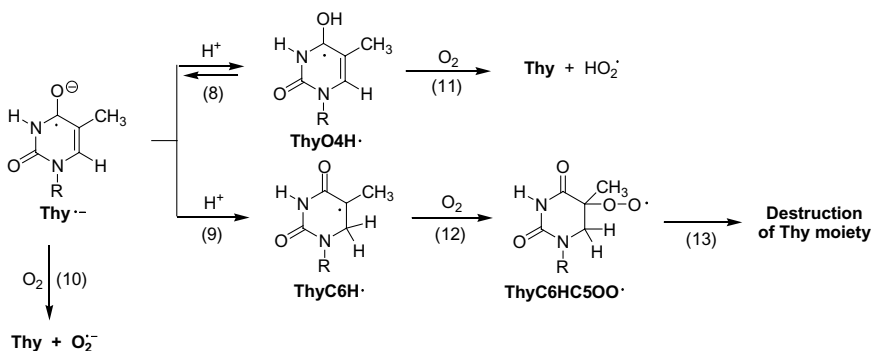
Fig. 1. Chemical structures of the DNA backbone (2-deoxyribose phosphate unit) and of the nucleobases thymine (Thy), cytosine (Cyt), guanine (Gua), and adenine (Ade).

In the following, a brief account will be given of what is known about the indirect effect of ionizing radiation on DNA (for the direct effects see Chap. 18 by Becker, Adhikary and Sevilla). Although most information has been obtained using radiation techniques, major insight in mechanistic details has been provided by experiments where specific radicals were generated by other means.³ As the present report can only be a brief and thus highly selective account, the interested reader is referred to a recent book that covers this subject in much more detail² and an earlier one that also discusses the very early literature.¹

2. The Reactions of the Solvated Electron

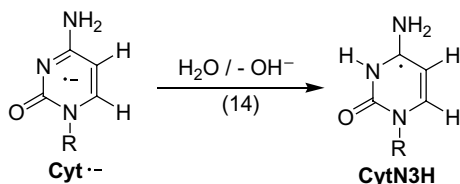
The solvated electron, e_{aq}^- , reacts with the nucleobases by electron attachment. The ensuing nucleobase radical anions are of considerably different basicity. The pK_a values of the conjugate acids of the uracil and Thy radical anions are near seven,⁴ while those of Cyt, Ade, Gua and their nucleosides react so fast with water that the pK_a values of their conjugate acids must be very high (>11 , see below). Protonation

occurs first at a heteroatom, preferably at the site of the highest electron density. For Thy, this is O₂ and O₄ [e.g. reaction (8)].

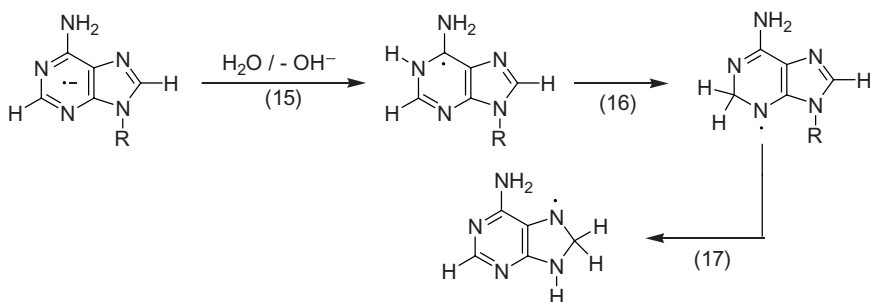


The pK_a value of **ThyO2H[•]** is very low (estimated at -2.3)⁵, and the species that is observed by pulse radiolysis is **ThyO4H[•]**. This species is not thermodynamically stable and rearranges into **ThyC6H[•]** [reaction (9)] whose pK_a value is much higher. The driving force for this rearrangement has been calculated at 49 kJ mol⁻¹, and from this value the pK_a value of **ThyC6H[•]** is estimated at 15.5.⁵ The transformation of **ThyO4H[•]** into **ThyC6H[•]** is accompanied by a marked change in the redox properties of the radicals. While **ThyO4H[•]** (like **Thy⁻**) has reducing properties, **ThyC6H[•]** is an oxidizing radical. This is also reflected in the reactions of these radicals with O₂. **Thy⁻** and **ThyO4H[•]** give rise to Thy and O₂⁻/HO₂[•] [reactions (10) and (11)], that is, with no resulting damage.⁶ Addition of O₂ to **ThyC6H[•]**, however, results in a destruction of the Thy moiety [reactions (12) and (13)]. The slowness of reaction (9) and the ready “repair” of **Thy⁻** and **ThyO4H[•]** by O₂ to Thy [reactions (10) and (11)] is of relevance for DNA, where damage by the solvated electron is minor as compared to [•]OH.

With **Cyt⁻**, rapid protonation occurs at N3 [reaction (14)].⁵ The pK_a value of **CytN3H[•]** must be higher than 13.^{7,8} A transformation to a carbon-protonated radical (**CytC6H[•]**) in analogy to reaction (9) does not occur here. According to quantum-chemical calculations, **CytC6H[•]** is higher in energy than **CytN3H[•]**.⁵



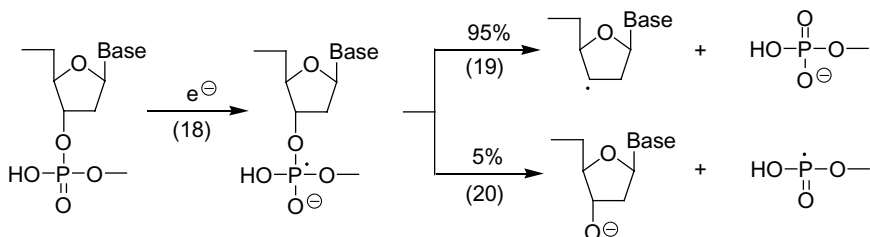
Similar to Cyt, the purine radical anions are also rapidly protonated by water [cf. reaction (15)].^{9,10} The primary H^{\bullet} adducts thus formed undergo a series of tautomerization reactions, eventually reaching thermodynamically more favorable H^{\bullet} adducts [cf. reactions (16) and (17)].¹¹



A re-oxidation of $\text{dAdo}^{\bullet-}$ yields, besides dAdo, a product that is characterized by a pK_a value of 8.8.¹² The nature of this product is as yet not known.

3. The Reactions of the Presolvated Electron with the 2-Deoxyribose Phosphate Moiety

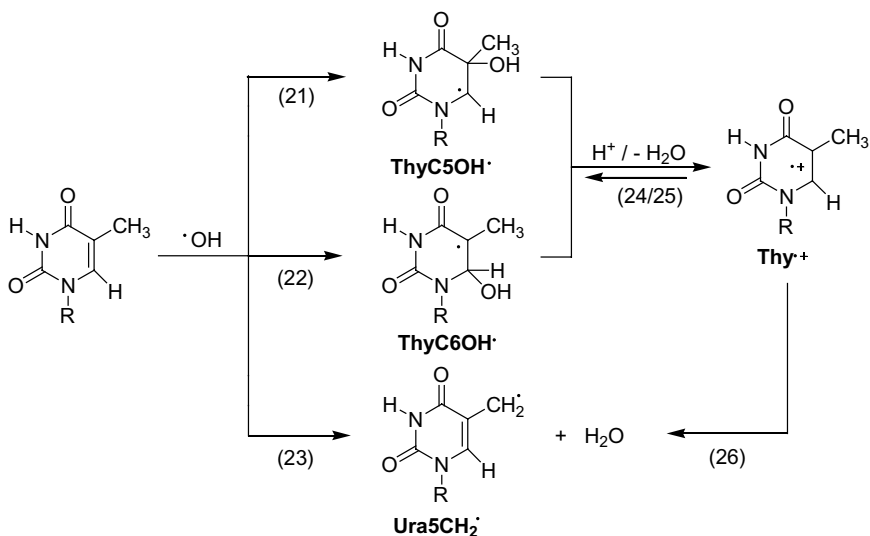
While e_{aq}^- does not react with the sugar-phosphate moiety, presolvated electrons that retain some excess energy may also undergo dissociative attachment to the phosphate group of DNA [reactions (18)–(20)].^{13,14}



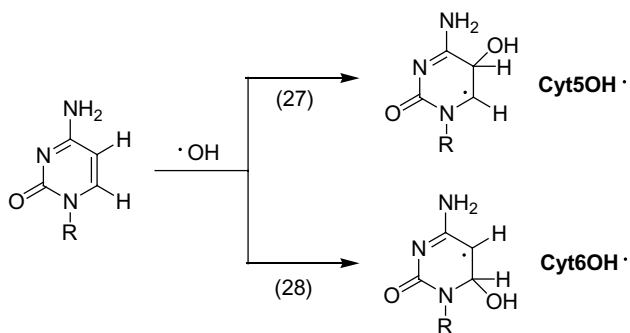
Both reactions lead to a DNA strand break. In the major pathway (95%), the O–C bond is broken, whereby the radical site is at C3' [reaction (19)]. To a much lower extent (5%), a cleavage of the O–P bond [reaction (20)] is observed. Here, the phosphate group is reduced.¹³

4. The Reactions of $\cdot\text{OH}$ with the Nucleobases

The $\cdot\text{OH}$ radical adds readily to C–C and C–N double bonds and undergoes H-abstraction reactions; for a recent review on $\cdot\text{OH}$ reactions, see Ref. 2. Based on its high reduction potential (2.3 V at pH 7),¹⁵ it could, in principle, one-electron-oxidize all four nucleobases, but electron transfer is typically a minor process unless the competing addition is hampered by a bulky substituent.¹⁶ Its rate of reaction with the nucleobases is close to diffusion controlled. Yet, a considerable regioselectivity as to the site of attack is observed.² This has been explained by the marked electrophilicity of $\cdot\text{OH}$, and in the pyrimidine bases, the pattern of $\cdot\text{OH}$ -addition is indeed reflected by the sites of highest electron density (frontier controlled). This simplified explanation breaks down for the purines, and it has been shown by quantum-chemical calculations of the distribution that here the effect of Mulliken charge now determines the regioselectivity (Naumov and von Sonntag, unpublished); for reviews on quantum-chemical calculations in DNA free-radical research, see Refs. 17 and 18. In Thy, the preferred site of attack is thus C5 [60%, reaction (21)], and addition to C6 is markedly lower [30%, reaction (22)]. H-Abstraction occurs to about 10% [reaction (23)].¹⁹

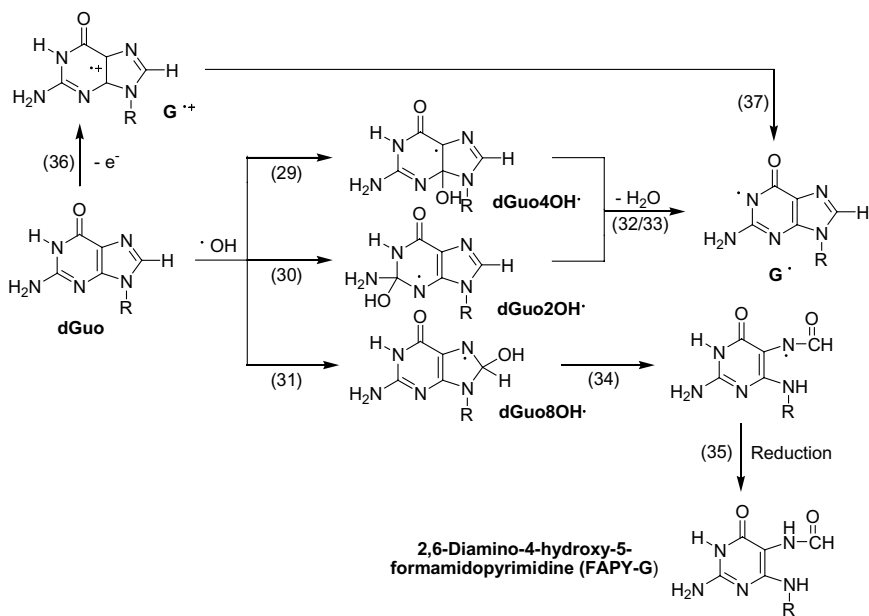


An even more pronounced regioselectivity has been observed for Cyt with 87% for reaction (27) and about 10% for reaction (28).²⁰



In the purines, there are more sites for $\cdot\text{OH}$ attack, and the situation as to where $\cdot\text{OH}$ adds preferentially is not as clear-cut as it is in the pyrimidines. On the basis of the oxidizing/reducing properties of the primary $\cdot\text{OH}$ adduct radicals, additions at C4 and C8 have been suggested to dominate dAdo: 50% at C4 (oxidizing), 37% at C8 (reducing);²¹⁻²³ dGuo: 60-70% at C4 (oxidizing), 17% at C8

(reducing).^{23,24} According to quantum-chemical calculations, $\cdot\text{OH}$ addition to C2 may also have to be considered in the contribution to the oxidizing radicals [reactions (29) and (30)] (Naumov and von Sonntag, unpublished).



5. Unimolecular Transformation of Nucleobase $\cdot\text{OH}$ Adduct Radicals

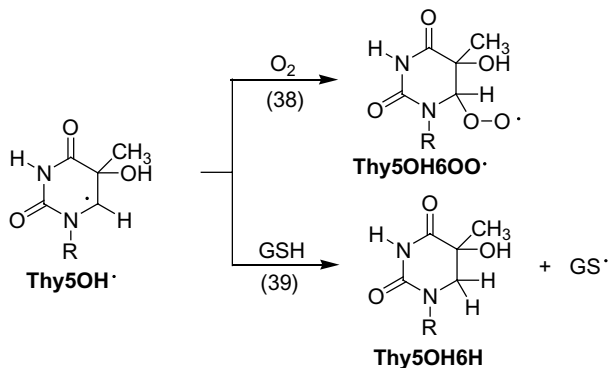
As the $\cdot\text{OH}$ addition reactions are controlled by kinetics rather than by thermodynamics, the primary $\cdot\text{OH}$ adduct radicals are not necessarily the thermodynamically most stable radicals. Thus, a number of rearrangement and water elimination reactions take place. For example, $\text{Thy6OH}\cdot$ is more stable than $\text{Thy5OH}\cdot$ by 42 kJ mol⁻¹,⁵ but $\text{Thy6OH}\cdot$ is formed preferentially.¹⁹ As has been shown in the case of 1,3-dimethyluracil in a detailed product study, acid catalysis converts the kinetically favored C6 $\cdot\text{OH}$ adduct into the

thermodynamically favored C5 $\cdot\text{OH}$ adduct.²⁵ Similar experiments are missing for the Thy system. Here, a water elimination reaction that gives rise to the **Ura5CH₂ \cdot** radical [reactions (24)–(26)] may be even thermodynamically more favorable if experiments with $\text{SO}_4^{\cdot-}$ are a good guide.²⁶ Quantum-chemical calculations put the exothermicity of the formation of **Thy6OH \cdot** and of **Ura5CH₂ \cdot** plus water at similar energies.⁵

In the purine series, water eliminations such as reactions (32) and (33) give rise to the guanyl **G \cdot** and adenylyl **A \cdot** radicals^{2,27} (for the structure of **G \cdot** see Refs. 28 and 29). The same radicals are formed upon one-electron oxidation followed by deprotonation [cf. reactions (36) and (37)]. The C8 $\cdot\text{OH}$ adducts undergo rapid ring opening. Among the various possibilities including a β -fragmentation,² only reaction (34) is exothermic.⁵ Upon reduction, the well-documented^{30,31} FAPY products are formed [cf. reaction (35)].

6. Reactions of Nucleobase Radicals with O₂, Oxidants/Reductants and Thiols

The $\cdot\text{OH}$ adduct radicals and the allyl type **Ura5CH₂ \cdot** radical react at about $2 \times 10^9 \text{ M}^{-1} \text{ s}^{-1}$ with O₂ [e.g. reaction (38)], but the heteroatom-centered radicals **G \cdot** and **A \cdot** do not react with O₂.³² In this respect, they behave like the structurally related phenoxyl radical.



The pyrimidine C5 $\cdot\text{OH}$ adducts have reducing properties (note the electron-donation by the α -nitrogen), while the C6 $\cdot\text{OH}$ adducts are oxidizing (note the spin density at the heteroatom). This property has been used to determine the yields in pulse radiolysis experiments using oxidants (e.g. tetranitromethane) and reductants (e.g. *N,N,N',N'*-tetramethyl-phenylenedimine) as probes.^{19,20} The adenylyl \mathbf{A}^\bullet ($E^7 = 1.56$ V) and guanylyl \mathbf{G}^\bullet ($E^7 = 1.29$ V) radicals are both oxidizing.³³

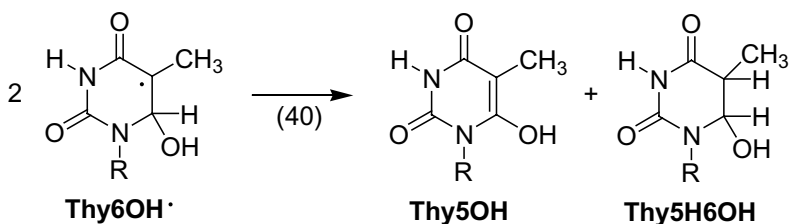
The reaction of nucleobase radicals with thiols is of importance in the context of “chemical repair” of DNA in cells that have been exposed to ionizing radiation. The thiol that is mainly responsible for this reaction is glutathione (GSH) that is present in cells at a concentration of 1–2 mM (unevenly distributed, average value).³⁴ The reaction of GSH with the nucleobase radicals is not very fast, in the order of $10^6 \text{ M}^{-1}\text{s}^{-1}$.² Moreover, this reaction rarely restitutes the nucleobase [e.g. reaction (39)]; for the mechanism of such H-transfer reactions see Refs. 35–37].

It has thus been concluded that the “chemical repair,” that is in competition with a reaction of the DNA radicals with O_2 , may reduce the severity of DNA damage by preventing damage amplification reactions induced by peroxy radicals (see below).³⁸

7. Bimolecular Decay of Nucleobase Radicals

In the absence of O_2 or GSH, the nucleobase radical will have to decay bimolecularly. On the model level, i.e. with nucleobases or nucleosides in aqueous solution, this reaction is close to diffusion controlled. In cells, the reaction may also be fast at sites where the free-radical density is high, a condition that may prevail when a spur overlaps with DNA. Otherwise, considerable segmental movements will be required to reach another DNA radical for bimolecular decay. Here, our knowledge is rather limited, but some information may be obtained from studies of simpler polymers.² In general, there are two reactions, dimerization and

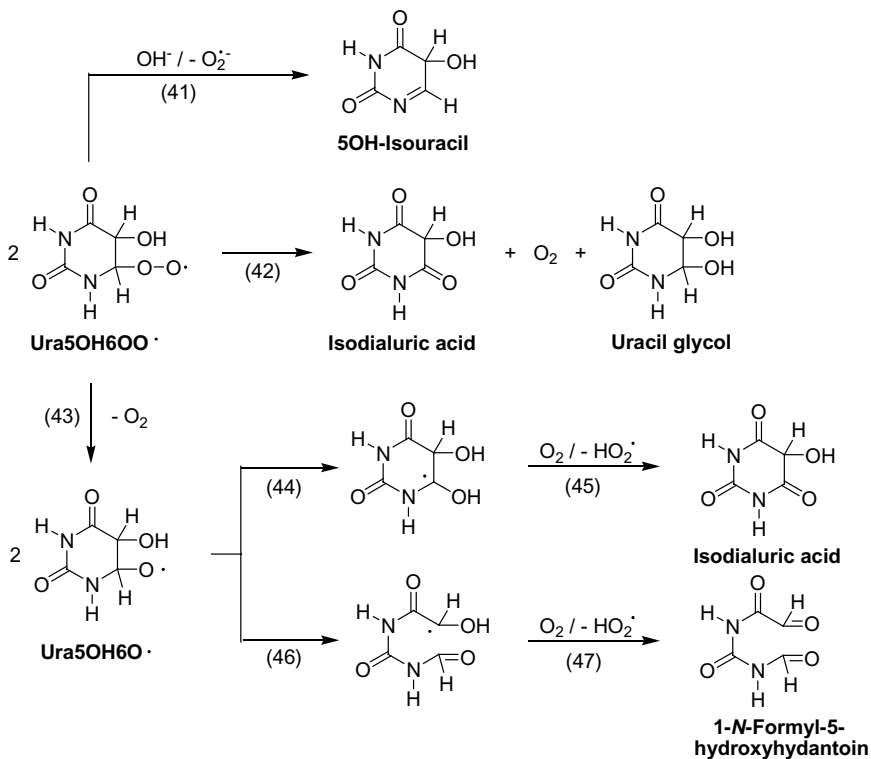
disproportionation. As to these reactions in nucleobase free-radical chemistry, the most complete material balance has been obtained with 1,3-dimethyluracil that also allowed the quantification of the dimers.²⁵ Disproportionation requires that a hydrogen is available in β -position [e.g. reaction (40)]; for the potentials of a dimer as an intermediate in a disproportionation reaction see Ref. 2].



Hydrogen atoms in β -position may not always be available, and thus for a number of nucleobase radicals (e.g. $\text{A}\cdot$ or $\text{G}\cdot$) disproportionation is not possible. The dimers that result from the recombination of two $\text{A}\cdot$ or two $\text{G}\cdot$ have not been detected as yet. This is one of the reasons why the purine free-radical chemistry is so poorly understood.

8. Bimolecular Decay of Nucleobase Peroxyl Radicals

In the bimolecular decay of peroxy radicals, a short-lived tetroxide is an intermediate. When a hydrogen is present in β -position to the peroxy function, a carbonyl compound plus an alcohol and O_2 [Russell mechanism, e.g. reaction (42)] or two carbonyl compound plus H_2O_2 (Bennett mechanism, not shown) may be formed in competition to a decay into two oxyl radicals plus O_2 [e.g. reaction (43)]; for details of peroxy radical chemistry in aqueous solution, see Refs. 2 and 39].



The most detailed information as to the decay of nucleobase peroxy radicals may be obtained from a study on uracil.⁴⁰ The limited space here does not allow for the discussion of details, but some aspects are shown in reactions (41)–(47). With the pyrimidine nucleobases, isopyrimidines are typical intermediates in these and other oxidation reactions cf. reaction (41). For their chemistry see Ref. 2.

Some peroxy radicals release $\text{HO}_2\cdot/\text{O}_2\cdot^-$ spontaneously and/or base-induced [OH^- and/or buffers; cf. reactions (41), (45) and (47)], and nearly all peroxy radicals give rise in one of their bimolecular routes (the oxyl radical pathway) to radicals that are capable of undergoing such reactions. For DNA free-radical chemistry, the formation of $\text{HO}_2\cdot/\text{O}_2\cdot^-$ is an interesting reaction insofar as $\text{O}_2\cdot^-$ that dominates at neutral pH [$\text{p}K_a(\text{HO}_2) = 4.8$] is a freely diffusing radical and may react with the much less mobile DNA radicals. $\text{O}_2\cdot^-$ is a rather long-lived radical, as in a cellular environment there are only few sinks

such as superoxide dismutase (SOD) and ascorbate.² Very little is known about the reaction of $O_2^{\bullet-}$ with other radicals. $O_2^{\bullet-}$ has a low reduction potential² and reacts fast with most strongly oxidizing radicals such as G^{\bullet} ³² or strongly oxidizing peroxy radicals such as the acetylperoxy radical,⁴¹ but markedly slower with less oxidizing peroxy radicals.² It is remarkable that with the oxidizing phenoxyl radical $O_2^{\bullet-}$ reacts by addition rather than by electron transfer, although the difference in the reduction potentials provides ample driving force for an electron transfer to occur.⁴² Whether or not addition is also the major route in the reactions of A^{\bullet} and G^{\bullet} with $O_2^{\bullet-}$ is not yet known. Electron transfer would result in a repair of the damaged Ade and Gua moieties, addition would not.

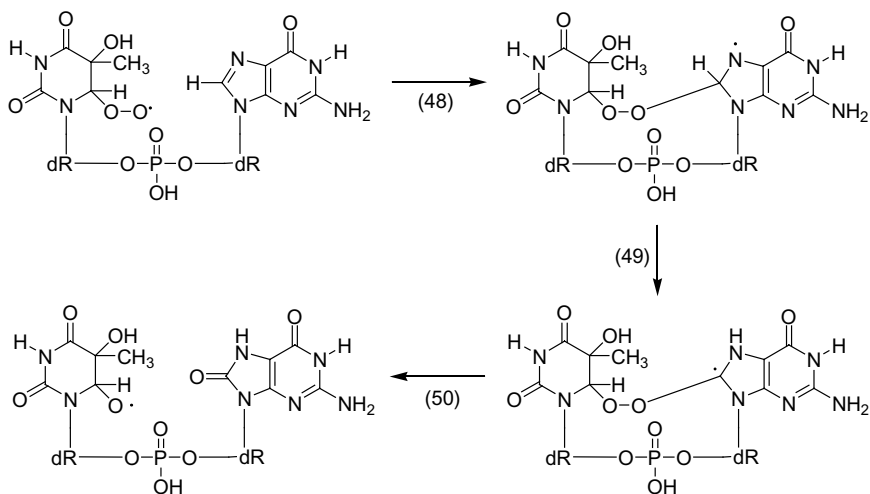
9. Reactions of Alkyl Radicals

In contrast to $\bullet OH$ and $\bullet H$ that are electrophilic radicals, alkyl radicals are nucleophilic and their preference of addition to the pyrimidines is reversed (preferred addition at C6).⁴³ The rate of reaction is several orders of magnitude lower than that of $\bullet OH$ and $\bullet H$.² In the case of purines that are more readily protonated than the pyrimidines, the effect of protonation could be studied. Protonation lowers the electron density, and thus the rate of reaction of the nucleophilic alkyl radicals goes up markedly upon protonation.⁴⁴

10. Damage Amplification Reactions

There are a number of damage enhancement reactions in the presence of O_2 , and these reactions are thought^{2,38} to contribute to or essentially cause the so-called "oxygen effect," that is, an increase in the cellular sensitivity in the presence of O_2 . In these reactions, a single $\bullet OH$ radical attacks the DNA. Oxygen adds to the DNA radical and the peroxy radical thus formed reacts with a neighboring DNA moiety, e.g. a nucleobase. For example, the reaction of $\bullet OH$ with Thy gives rise to **Thy6OH \bullet** [reaction (22)] that is subsequently converted into the corresponding peroxy radical which subsequently attacks a neighboring Gua moiety at C8 [reaction (48)]. The *N*-centered radical undergoes a 1,2 H-shift [reaction (49)] followed by a

β -fragmentation [reaction (50)]. The resulting oxyl radical can undergo a 1,2 H-shift or a β -fragmentation [cf. reactions (44) and (46)].



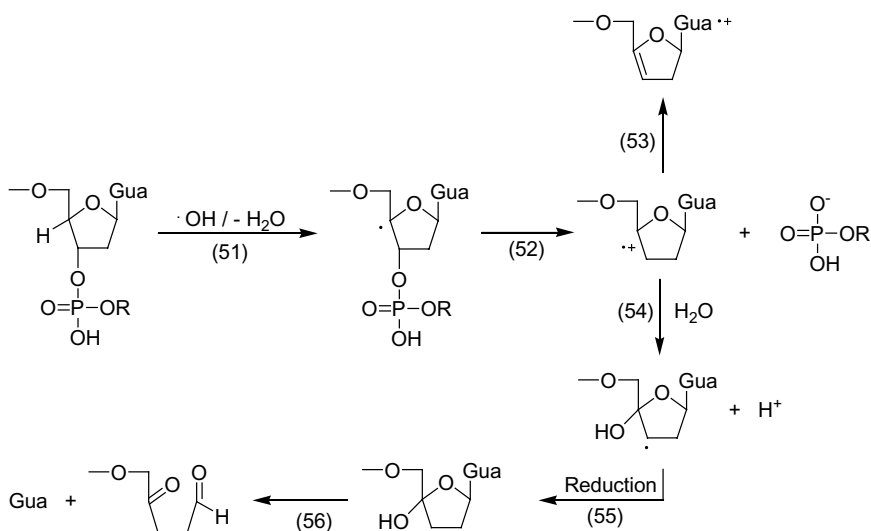
As a consequence, two damaged bases, a damaged Thy and a damaged Gua are formed by a single $\cdot\text{OH}$ as precursor. As at this point, the peroxy radical has not been terminated bimolecularly, so the peroxy radical chain could continue. So far there is no experimental information as to the formation of higher damaged sites, but they must occur, albeit with a lower probability than the vicinal lesion (tandem lesion) mentioned above. One prerequisite for such a damage amplification reaction is an adequate steric condition in this essentially topochemical reaction. Another prerequisite must be the rate of reaction. If this is too slow, other competing reactions may occur. For example, there is a marked oxidation of the sugar moiety by base radicals and base peroxy radicals in polyU,⁴⁵⁻⁴⁷ where the C2'H is only loosely bound. The analogous reaction has not yet been observed with DNA.

The tandem lesion discussed above is only one example; for other examples the reader is referred to the literature.⁴⁸⁻⁵³ For the vast literature on the formation of purine 8,5'-cyclonucleosides that also belong to that group of lesions see Ref. 2.

11. Strand Breakage and Base Release by $\cdot\text{OH}$ Radicals

For strand breakage and release of unaltered bases to be induced by $\cdot\text{OH}$, the sugar moiety must be attacked. For this reaction, the $\cdot\text{OH}$ radical has to pass largely through the major groove of DNA, and as its width depends strongly on the base sequence, there is a marked sequence dependence of $\cdot\text{OH}$ -induced reactions with the sugar moiety.⁵⁴

With respect to DNA strand breakage, the reactions that follow an abstraction of the C4'H [reaction (51)] are understood best.^{55,56}



The C4' radical releases a phosphate group in β -position either at C3' or at C5', whereby the phosphate release at C3' is preferred [cf. reaction (52)]. In this reaction an (oxidizing) radical cation is formed. If there is a Gua moiety in the close neighborhood, it may become oxidized [e.g. reaction (53)].^{57,58} In competition, the radical cation reacts with water. One possibility is shown in reaction (54). Upon reduction, a deoxy function is formed at the C3 position [reaction (55)] and subsequently the base is released [reaction (56)]. In the presence of O_2 , DNA stand breakage is also induced by

H-abstraction at C5' (and also, most likely, at C3'; experimental evidence missing). The space here does not allow discussing these reactions and the reader is referred to Ref. 2 where this and many other aspects are discussed in detail.

References

1. von Sonntag C. (1987) *The Chemical Basis of Radiation Biology*. Taylor and Francis, London.
2. von Sonntag C. (2006) *Free-Radical-Induced DNA Damage and Its Repair. A Chemical Perspective*. Springer Verlag, Berlin, Heidelberg.
3. Greenberg MM. (2007) Elucidating DNA damage and repair processes by independently generating reactive and metastable intermediates. *Org Biomol Chem* **5**: 18–30.
4. Hayon E. (1969) Optical-absorption spectra of ketyl radicals and radical anions of some pyrimidines. *J Chem Phys* **51**: 4881–4892.
5. Naumov S, von Sonntag C. (2008) The energetics of rearrangement and water elimination reactions in the radiolysis of the DNA bases in aqueous solution (e_{aq}^- and $\cdot OH$ attack). DFT calculations. *Radiat Res* **169**: 355–363.
6. Deeble DJ, von Sonntag C. (1987) Radioprotection of pyrimidines by oxygen and sensitization by phosphate: A feature of their electron adducts. *Int J Radiat Biol* **51**: 791–796.
7. Hissung A, von Sonntag C. (1979) The reaction of solvated electrons with cytosine, 5-methylcytosine and 2'-deoxycytidine in aqueous solution. The reaction of the electron adduct intermediates with water, p-nitroacetophenone and oxygen. A pulse spectroscopic and pulse conductometric study. *Int J Radiat Biol* **35**: 449–458.
8. Steenken S. (1992) Electron-transfer-induced acidity/basicity and reactivity changes of purine and pyrimidine bases. Consequences of redox processes for DNA base pairs. *Free Radical Res Commun* **16**: 349–379.
9. von Sonntag C. (1991) The chemistry of free-radical-mediated DNA damage. In *Physical and Chemical Mechanisms in Molecular Radiation Biology*, Glass WA, Varma MN. (eds.), pp. 287–321. Plenum Press, New York.
10. Candeias LP, Wolf P, O'Neill P, Steenken S. (1992) Reaction of hydrated electrons with guanine nucleosides: Fast protonation on carbon of the electron adduct. *J Phys Chem* **96**: 10302–10307.
11. Candeias LP, Steenken S (1992) Electron adducts of adenine nucleosides and nucleotides in aqueous solution: Protonation at two carbon sites (C2 and C8) and intra- and intermolecular catalysis by phosphate. *J Phys Chem* **96**: 937–944.
12. Hissung A, von Sonntag C, Veltwisch D, Asmus K-D. (1981) The reaction of the 2'-deoxyadenosine electron adduct in aqueous solution. The effects of the

- radiosensitizer p-nitroacetophenone. A pulse spectroscopic and pulse conductometric study. *Int J Radiat Biol* **39**: 63–71.
13. Becker D, Bryant-Friedrich A, Trzasko C-A, Sevilla MD. (2003) Electron spin resonance study of DNA irradiated with an argon-ion beam: Evidence for formation of sugar phosphate backbone radicals. *Radiat Res* **160**: 174–185.
 14. Li X, Sevilla MD, Sanche L. (2003) Density functional theory studies of electron interaction with DNA: Can zero eV electrons induce strand breaks? *J Am Chem Soc* **125**: 13668–13699.
 15. Wardman P. (1989) Reduction potentials of one-electron couples involving free radicals in aqueous solution. *J Phys Chem Ref Data* **18**: 1637–1755.
 16. Fang X, Schuchmann H-P, von Sonntag C. (2000) The reaction of the OH radical with pentafluoro-, pentachloro-, pentabromo- and 2,4,6-triiodophenol in water: Electron transfer *vs.* addition to the ring. *J Chem Soc, Perkin Trans 2*: 1391–1398.
 17. von Sonntag C. (2007) Free-radical-induced DNA damage as approached by quantum mechanics and Monte Carlo calculations: An overview from the standpoint of an experimentalist. *Adv Quantum Chem* **52**: 5–20.
 18. Li X, Sevilla MD. (2007) DFT treatment of radiation produced radicals in DNA model systems. *Adv Quantum Chem* **52**: 59–87.
 19. Fujita S, Steenken S. (1981) Pattern of OH radical addition to uracil and methyl- and carboxyl-substituted uracils. Electron transfer of OH adducts with *N,N,N',N'*-tetramethyl-p-phenylenediamine and tetranitromethane. *J Am Chem Soc* **103**: 2540–2545.
 20. Hazra DK, Steenken S. (1983) Pattern of OH radical addition to cytosine and 1-, 3-, 5- and 6-substituted cytosines. Electron transfer and dehydration reactions of the OH adducts. *J Am Chem Soc* **105**: 4380–4386.
 21. O'Neill P, Chapman PW, Papworth DG. (1985) Repair of hydroxyl radical damage of dA by antioxidants. *Life Sci Rep* **3**: 62–69.
 22. Vieira AJSC, Steenken S. (1990) Pattern of OH radical reaction with adenine and its nucleosides and nucleotides. Characterization of two types of isomeric OH adduct and their unimolecular transformation reactions. *J Am Chem Soc* **112**: 6986–6994.
 23. Vieira AJSC, Candeias LP, Steenken S. (1993) Hydroxyl radical induced damage to the purine bases of DNA: *In vitro* studies. *J Chim Phys* **90**: 881–897.
 24. Candeias LP, Steenken S. (2000) Reaction of HO• with guanine derivatives in aqueous solution: Formation of two different redox-active OH-adduct radicals and their unimolecular transformation reactions. Properties of G(-H)•. *Chem Eur J* **6**: 475–484.
 25. Al-Sheikhly M, von Sonntag C. (1983) γ -Radiolysis of 1,3-dimethyluracil in N₂O-saturated aqueous solutions. *Z Naturforsch* **38b**: 1622–1629.
 26. Deeble DJ, Schuchmann MN, Steenken S, von Sonntag C. (1990) Direct evidence for the formation of thymine radical cations from the reaction of SO₄⁻

- with thymine derivatives: A pulse radiolysis study with optical and conductance detection. *J Phys Chem* **94**: 8186–8192.
27. Steenken S. (1989) Purine bases, nucleosides and nucleotides: Aqueous solution redox chemistry and transformation reactions of their radical cations e^- and OH adducts. *Chem Rev* **89**: 503–520.
 28. Adhikary A, Kumar A, Becker D, Sevilla MD. (2006) The guanine cation radical: Investigation of deprotonation states by ESR and DFT. *J Phys Chem B* **110**: 24171–24180.
 29. Naumov S, von Sonntag C. (2008) Guanine-derived radicals: Dielectric constant-dependent stability and UV/Vis spectral properties: A DFT study. *Radiat Res* **169**: 364–372.
 30. Berger M, Cadet J. (1985) Isolation and characterization of the radiation-induced degradation products of 2'-deoxyguanosine in oxygen-free aqueous solutions. *Z Naturforsch* **40b**: 1519–1531.
 31. van Hemmen JJ, Bleichrodt JF. (1971) The decomposition of adenine by ionizing radiation. *Radiat Res* **46**: 444–456.
 32. von Sonntag C. (1994) Topics in free-radical-mediated DNA damage: Purines and damage amplification — superoxide reactions — bleomycin, the incomplete radiomimetic. *Int J Radiat Biol* **66**: 485–490.
 33. Steenken S, Jovanovic SV. (1997) How easily oxidizable is DNA? One-electron reduction potentials of adenosine and guanosine radicals in aqueous solution. *J Am Chem Soc* **119**: 617–618.
 34. Wardman P, von Sonntag C. (1995) Kinetic factors that control the fate of thiyl radicals in cells. *Meth Enzymol* **251**: 31–45.
 35. Reid DL, Shustov GV, Armstrong DA, Rauk A, Schuchmann MN, Akhlaq MS, von Sonntag C. (2002) H-Atom abstraction from thiols by C-centered radicals. An experimental and theoretical study. *Phys Chem Chem Phys* **4**: 2965–2974.
 36. Reid DL, Armstrong DA, Rauk A, Nese C, Schuchmann MN, Westhoff U, von Sonntag C. (2003) H-atom abstraction by C-centered radicals from cyclic and acyclic dipeptides. A theoretical and experimental study of reaction rates. *Phys Chem Chem Phys* **5**: 3278–3288.
 37. Reid DL, Armstrong DA, Rauk A, von Sonntag C. (2003) H-atom abstraction by thiyl radicals from peptides and cyclic dipeptides. A theoretical study of reaction rates. *Phys Chem Chem Phys* **5**: 3994–3999.
 38. von Sonntag C. (2007) DNA lesions induced by ionizing radiation. In *Chromosomal Alterations: Methods, Results and Importance in Human Health*, Obe, G, Vijayalaxmi (eds.), pp. 21–38. Springer.
 39. von Sonntag C, Schuchmann H-P. (1997) In *The Chemistry of Free Radicals: Peroxyl Radicals*, Alfassi ZB. (ed.), pp. 173–234. Wiley.
 40. Schuchmann MN, von Sonntag C. (1983) The radiolysis of uracil in oxygenated aqueous solutions. A study by product analysis and pulse radiolysis. *J Chem Soc, Perkin Trans 2*: 1525–1531.

41. Schuchmann MN, von Sonntag C. (1988) The rapid hydration of the acetyl radical. A pulse radiolysis study of acetaldehyde in aqueous solution. *J Am Chem Soc* **110**: 5698–5701.
42. Jin F, Leitich J, von Sonntag C. (1993) The superoxide radical reacts with tyrosine-derived phenoxyl radicals by addition rather than by electron transfer. *J Chem Soc, Perkin Trans 2*, 1583–1588.
43. Schuchmann H-P, Wagner R, von Sonntag C. (1986) The reactions of the hydroxymethyl radical with 1,3-dimethyluracil and 1,3-dimethylthymine. *Int J Radiat Biol* **50**: 1051–1068.
44. Aravindakumar CT, Mohan H, Mudaliar M, Rao BSM, Mittal JP, Schuchmann MN, von Sonntag C. (1994) Addition of e_{aq}^- and H atoms to hypoxanthine and inosine and the reactions of α -hydroxyalkyl radicals with purines. A pulse radiolysis and product study. *Int J Radiat Biol* **66**: 351–365.
45. Deeble DJ, von Sonntag C. (1984) γ -radiolysis of poly(U) in aqueous solution. The role of primary sugar and base radicals in the release of undamaged uracil. *Int J Radiat Biol* **46**: 247–260.
46. Deeble DJ, Schulz D, von Sonntag C. (1986) Reactions of OH radicals with poly(U) in deoxygenated solutions: Sites of OH radical attack and the kinetics of base release. *Int J Radiat Biol* **49**: 915–926.
47. Lemaire DGE, Bothe E, Schulte-Frohlinde D. (1984) Yields of radiation-induced main chain scission of poly U in aqueous solution: Strand break formation via base radicals. *Int J Radiat Biol* **45**: 351–358.
48. Box HC, Patrzyc HB, Dawidzik JB, Wallace JC, Freund HG, Iijima H, Budzinski EE. (2000) Double base lesions in X-irradiated DNA in the presence or absence of oxygen. *Radiat Res* **153**: 442–446.
49. Maccubbin AE, Iijima H, Ersing N, Dawidzik JB, Patrzyc HB, Wallace JC, Budzinski EE, Freund HG, Box HC. (2000) Double-base lesions are produced in DNA by free radicals. *Arch Biochem Biophys* **375**: 119–123.
50. Bourdat A-G, Douki T, Frelon S, Gasparutto D, Cadet J. (2000) Tandem base lesions are generated by hydroxyl radical within isolated DNA in aerated aqueous solution. *J Am Chem Soc* **122**: 4549–4556.
51. Cadet J, Bourdat A-G, D'Ham C, Duarte V, Gasparutto D, Romieu A, Ravanat J-L. (2000) Oxidative base damage to DNA: Specificity of base excision repair enzymes. *Mutation Res Rev Mutation Res* **462**: 121–128.
52. Cadet J, Bellon S, Berger M, Bourdat A-G, Douki T, Duarte V, Frelon S, Gasparutto D, Muller E, Ravanat J-L, Sauvaigo S. (2002) Recent aspects of oxidative DNA damage: Guanine lesions, measurements and substrate specificity of DNA glycosylases. *Biol Chem* **383**: 933–943.
53. Bellon S, Ravanat J-L, Gasparutto D, Cadet J. (2002) Cross-linked thymine-purine base tandem lesions: Synthesis, characterization, and measurement in γ -irradiated isolated DNA. *Chem Res Toxicol* **15**: 598–606.

54. Begusova M, Spothem-Maurizot M, Sy D, Michalik V, Charlier M. (2001) RADACK, a stochastic simulation of hydroxyl radical attack on DNA. *J Biomol Struct Dyn* **19**: 141–158.
55. Dizdaroglu M, von Sonntag C, Schulte-Frohlinde D. (1975) Strand breaks and sugar release by γ -irradiation of DNA in aqueous solution. *J Am Chem Soc* **97**: 2277–2278.
56. Beesk F, Dizdaroglu M, Schulte-Frohlinde D, von Sonntag C. (1979) Radiation-induced DNA strand breaks in deoxygenated aqueous solution. The formation of altered sugars as end groups. *Int J Radiat Biol* **36**: 565–576.
57. Giese B, Spichty M, Wessely S. (2001) Long-distance charge transport through DNA. An extended hopping model. *Pure Appl Chem* **73**: 449–453.
58. Giese B, Amaudrut J, Köhler A, Spormann M, Wessely S. (2001) Direct observation of hole transfer through DNA by hopping between adenine bases and by tunnelling. *Nature* **412**: 318–320.

Chapter 20

Radiation Chemistry Applied to Antioxidant Research

*K. Indira Priyadarsini**

1. Introduction

1.1. *Free radicals, oxidative stress and antioxidants*

In living cells, free radicals are regularly produced during normal cellular metabolism, and are known to contribute to healthy functions of eukaryotic cells.¹⁻⁸ Due to the presence of unpaired electron, free radicals are reactive and sometimes induce small chain reactions. In normal and healthy human beings, the free radical production is maintained in balance with the help of intracellular defense comprising of endogenous antioxidants like superoxide dismutase (SOD), catalase and glutathione peroxidase, glutathione, urate, etc. An *antioxidant* is defined as a compound, that when present in small quantities, prevents the oxidation of the bulk.^{1,3,6}

* Radiation and Photochemistry Division, BARC, Mumbai 400085, India.
E-mail: kindira@barc.gov.in

Under pathological conditions or during exposure to pollutants, stress, etc., this balance is disturbed and there is an excessive production of oxidizing free radicals, leading to a change in the redox environment of the cells. This condition of the shift from reducing status to oxidative status of the cells is known as oxidative stress.^{4,7,9} Free radicals or molecular species involved in oxidative stress are broadly classified into two types, known by two collective terms: reactive oxygen species (ROS) and reactive nitrogen species (RNS). These species, differing in their reactivity and oxidizing ability, participate in a variety of chemical reactions and their reactions with biomolecules can provoke irreversible chemical changes in cells.¹⁰⁻¹⁵

Change in the cellular redox environment can lead to several biological effects ranging from altered signal transduction pathways, gene expression, mutagenesis and cell death (apoptosis).^{7,9} Oxidative stress has now been implicated in many diseases such as atherosclerosis, Parkinson's disease, Alzheimer's disease, cancer, etc.^{1,8} For the protection of cells from oxidative stress, supplementation with exogenous antioxidants becomes necessary.

Antioxidants, depending on the chemical structures, have diverse mechanism of action. Preventive antioxidants, like desferrioximine or desferal, are compounds which form chelates with metals, thereby help in preventing the free radical production.^{1,8} Antioxidants showing free radical scavenging ability are some dietary compounds like vitamin E (α -tocopherol), and vitamin C (ascorbic acid). α -Tocopherol is a lipid-soluble chain-breaking antioxidant, which is often considered as a "Golden standard" in evaluating the antioxidant capacity of new compounds.^{6,16} Ascorbic acid is a water-soluble antioxidant and helps in recycling chain-breaking antioxidants like vitamin E. Some antioxidants in addition to scavenging free radicals also exhibit catalytic activity and thereby act as antioxidant enzyme mimics.

In the last two decades there has been a substantial progress in understanding the nature and reactions of biologically relevant free radicals, and the development of new antioxidants. Both biochemical methods and free radical scavenging techniques have been widely employed. Fast reaction kinetic techniques have been found to be very useful in directly probing the reactions of antioxidants with free

radicals with short lifetimes (few nanoseconds to seconds). Radiation chemical methods, including radiolysis of aqueous solutions and pulse radiolysis technique, had provided valuable information on such reactions.^{17,18}

Here in this chapter, some important and significant contributions from radiation chemical studies on the selective generation of biologically relevant ROS and RNS and their reactions with a few important antioxidants have been presented.

2. ROS and RNS: Precursors, Properties and Reactions

2.1. Precursors of ROS and RNS in living cells

Superoxide radicals ($O_2^{\bullet-}$) and nitric oxide ($\bullet NO$) are the two important precursors leading to the overall production of ROS and RNS in the body.¹⁰⁻¹⁵ Generation of both of these radicals is essential for normal physiological functioning and body defense. For example, during phagocytosis, macrophages and neutrophils produce large amount of $O_2^{\bullet-}$ (oxidative burst), thereby providing cellular defense from bacterial infection.¹ $\bullet NO$ is the most important signaling molecule that participates in vasodilation, neurotransmission and immune response.^{13,14}

Both $O_2^{\bullet-}$ and $\bullet NO$, if produced in excess, can be toxic and their excessive production has been implicated in several pathological conditions. The major source of $O_2^{\bullet-}$ radical in the cells is the electron-transport-chain reaction of mitochondria,⁵ wherein a single electron leakage takes place on oxygen producing $O_2^{\bullet-}$. Other sources of $O_2^{\bullet-}$ radicals are enzymatic reactions involving xanthine oxidase, peroxidase, autoxidation of biomolecules, and peroxy radical-induced reactions.¹ In cells, $\bullet NO$ is produced by the enzyme nitric oxide synthases (NOS), which catalyse the NADPH and oxygen-dependent oxidation of L-arginine to citrulline and $\bullet NO$.¹⁴

Interestingly, the redox potentials of both $O_2^{\bullet-}$ and $\bullet NO$ are such that they are not so reactive towards biomolecules. However, as both of them have long lifetimes (few seconds to minutes, sometimes a few hours) under physiological conditions, they participate in a number of

Table 1. Redox potential and absorption maximum of some important ROS and RNS.

Name of the radical	Symbol	E° (V versus NHE)*	Couple	Absorption Maximum, nm
Hydroxyl	$\bullet\text{OH}$	1.9	$\bullet\text{OH}/\text{OH}^-$	230
Superoxide radicals	$\text{O}_2^{\bullet-}$	-0.33 1.80	$(\text{O}_2/\text{O}_2^{\bullet-})$ $(\text{O}_2^{\bullet-}, 2\text{H}^+/\text{H}_2\text{O} + \text{O}_2)$	245
Singlet oxygen	$^1\text{O}_2$	0.65	$^1\text{O}_2/\text{O}_2^{\bullet-}$	1270**
Alkoxy radical	$\text{RO}\bullet$	1.0 to 1.6	$(\text{RO}\bullet, \text{H}^+/\text{ROH})$	<250
Alkyl peroxy radical	$\text{ROO}\bullet$	0.6 to 1.0	$\text{ROO}\bullet, \text{H}^+/\text{ROOH})$	<250
Nitric oxide	$\text{NO}\bullet$	1.21	NO^+/NO	253
		0.39	NO/NO^-	
Nitrogen dioxide	NO_2^{\bullet}	0.99	$\text{NO}_2/\text{NO}_2^-$	398
Peroxynitrite	ONOO^-			302
Carbonate	$\text{CO}_3^{\bullet-}$	1.78	$\text{CO}_3^{\bullet-}/\text{CO}_3^{2-}$	600

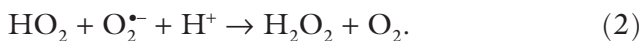
* References 1, 11, 12, 17, 18, 27, 28; ** Emission maximum.

catalyzed reactions, and are converted into new radicals, which can act as more powerful oxidants.¹⁰⁻¹⁵ Important properties of ROS and RNS that are critical to biological systems are given below along with their kinetic and thermodynamic properties. Table 1 lists the important physico-chemical properties of ROS and RNS.

2.2. Properties and inter-conversion reactions of ROS

The prototropic equilibrium constant (pKa) for the equilibrium between $\text{O}_2^{\bullet-}$ and HO_2^{\bullet} radicals is 4.7.^{11,17} Therefore at physiological pH, the superoxide radicals exist predominantly in the form of $\text{O}_2^{\bullet-}$ radicals. HO_2^{\bullet} radicals are more reactive than $\text{O}_2^{\bullet-}$ radicals, and react with substrates by hydrogen abstraction or by addition to the double bonds. $\text{O}_2^{\bullet-}$ radicals do not exhibit these reactions but participate in a number of redox reactions with metal ions and substrates like quinone, ascorbate, etc.^{10,11} The rate constants for these reactions are considerably lower than diffusion-controlled limits (10^4 to $10^7 \text{ M}^{-1} \text{ s}^{-1}$). $\text{O}_2^{\bullet-}$ radicals decay either by radical-radical dismutation reaction [Eq. (1)]

or by reaction of $O_2^{\bullet-}$ with HO_2^{\bullet} , [Eq. (2)] producing H_2O_2 . The respective rate constants for these reactions are 0.39 and $10^8 M^{-1} s^{-1}$.



H_2O_2 can be converted into $\bullet OH$ radicals in presence of transition metal ions like Fe^{2+} by Fenton reactions [Eq. (3)].^{1,10}



Hydroxyl radicals ($\bullet OH$) are powerful oxidants¹⁷⁻¹⁹ and participate in a number of reactions such as addition to the double bonds forming radical adducts, electron transfer reactions, and H-atom abstraction reaction. The rate constants for the reaction of $\bullet OH$ radicals with organic substrates are mostly diffusion controlled ($10^9-10^{10} M^{-1} s^{-1}$). When $\bullet OH$ radical reacts with cellular organic molecules (RH) either by hydrogen abstraction [Eq. (4)] or by addition reaction, it leaves a radical site on the molecule (R^{\bullet}) and sometimes these radicals can add to the oxygen present in the cells, to be converted to peroxy radicals [ROO^{\bullet} , Eqs. (4) and (5)]. Rate constants for these reactions vary between 10^5 to diffusion-controlled limits depending on the nature and substitution on RH.²⁰



Different types of peroxy radicals are produced in the cells. For example membrane lipids having unsaturated fatty acids are often converted to lipid peroxy radicals, which are implicated in lipid peroxidation.^{1,3,17,20} Other biologically important peroxy radicals are alkyl peroxy radicals, glutathione peroxy radicals, sugar peroxy radicals, peroxy radicals generated from the hydroxyl radical adducts of nucleic acids, etc.¹⁷ Some of the peroxy radicals are converted into $O_2^{\bullet-}$ radicals [Eq. (6)] and sometimes the tetroxides formed by the

bimolecular decay of peroxy radicals are converted into alkoxy radicals (RCO^\bullet), and singlet molecular oxygen ($^1\text{O}_2$ or $\text{O}_2^{\bullet-}$ radicals [Eq. (7)].



Both alkoxy and peroxy radicals react with substrates by a number of ways causing small chain reactions, and their reactivity depends on substitution and chemical structure of the radicals.^{17,20} In general, the alkoxy radicals are more oxidizing than the peroxy radicals, however, rates of reactions of alkoxy radicals have been found to be much slower than that of the peroxy radicals. Both alkoxy and peroxy radicals react with substrates either by hydrogen atom abstraction or by electron transfer. In general their rate constants with substrates vary between diffusion-controlled limits to several orders of magnitude less. $^1\text{O}_2$ is also a powerful oxidant and reacts with many organic and inorganic substrates by addition to double bonds, oxygen atoms transfer, and electron transfer.¹ In some of these reactions, $^1\text{O}_2$ is converted to $\text{O}_2^{\bullet-}$.

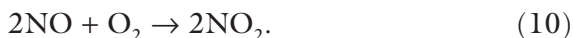
2.3. *Properties and inter-conversion reactions of RNS*

Important reactions of $^\bullet\text{NO}$ are binding to transition metals like heme iron as in hemoglobin to produce nitroso-hemoglobin, addition to thiols to produce nitrosothiols as given in Eqs. (8) and (9).^{14,21} The rate constants for the two reactions are reported by several groups and found to be in the range $(3-5) \times 10^7$ and $(1-3) \times 10^9 \text{ M}^{-1} \text{ s}^{-1}$.



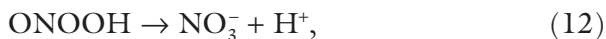
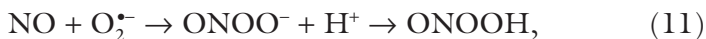
$^\bullet\text{NO}$ is converted into other powerful oxidants like NO_2 radical and peroxyxynitrite in the cells, which cause nitrosation reactions and these reactions are mainly responsible for the elevation of oxidative stress through the formation of RNS.^{12,15,21,22}

Alternatively, NO_2 radical is produced in the body by the reaction of $\bullet\text{NO}$ with oxygen [Eq. (10)] and also by peroxidase-catalyzed oxidation of nitrite salts.⁸



NO_2 radical is also one of the most important constituent free radicals of cigarette smoke and vehicular exhausts.¹⁵ NO_2 radical does not react with oxygen but reacts with $\bullet\text{NO}$ with rate constant of $1.1 \times 10^9 \text{ M}^{-1} \text{ s}^{-1}$ to form another oxidant N_2O_3 . However, this reaction may not be very significant at the low steady-state concentrations of NO and NO_2 produced in the cells. Unlike NO , the NO_2 radical can directly react with biomolecules such as polyunsaturated fatty acids, and participate in a number of reactions including addition, hydrogen-abstraction and one-electron oxidation.²¹⁻²⁶ The rate constants for the reaction of NO_2 radical with substrates can vary between diffusion-controlled limits to several orders of magnitude less. The reactions of NO_2 with substrates often lead to chain reactions causing lipid peroxidation, and so on.

Peroxynitrite (ONOO^-) is produced by the diffusion-controlled reaction [$\sim (4 \text{ to } 19) \times 10^9 \text{ M}^{-1} \text{ s}^{-1}$] of NO with $\text{O}_2^{\bullet-}$ radicals [Eq. (11)].²⁷ Peroxynitrite is converted to its protonated form, peroxynitrous acid (ONOOH) with a pK_a of 6.8. This acid form undergoes isomerization to form nitrate anion with a rate constant of 1.3 s^{-1} [Eq. (12)]. Peroxynitrite is a powerful oxidant and during oxidation reactions with substrates, it undergoes homolysis, generating two powerful oxidants $\bullet\text{OH}$ and NO_2 radicals ($\sim 28\%$) [Eq. (13)], which can mediate oxidation, nitration and nitrosation reactions leading to impaired function of biomolecules.^{12,15,22,27}



^a Reaction (13) occurs during oxidation and nitration reactions with substrates.

In the presence of physiological levels of carbon dioxide in the cells, peroxyxynitrite is converted to nitrosoperoxyxynitrite adduct (ONOOCO_2^-), which decays with a rate constant of $4.6 \times 10^4 \text{ M}^{-1} \text{ s}^{-1}$ to form two oxidants carbonate radicals ($\text{CO}_3^{\bullet-}$) and NO_2 radicals [Eq. (14)]. In biological systems, the decomposition of ONOO^- yields 30–35% of $\text{CO}_3^{\bullet-}$.^{15,28}



$\text{CO}_3^{\bullet-}$ radicals are one of the most powerful one-electron oxidants and they often react by electron transfer or hydrogen atom transfer, causing one-electron oxidation of the substrates and the rate constants with substrates vary from 10^6 to $10^9 \text{ M}^{-1} \text{ s}^{-1}$.¹⁶ The one-electron reduction potential for important ROS and RNS are listed in Table 1.

Peroxy radicals can also react with NO_2 , when present in enough concentrations, to produce peroxyxynitrites (ROONO_2) [Eq. (15)] with rate constants in the range of 10^8 to $10^9 \text{ M}^{-1} \text{ s}^{-1}$. These peroxyxynitrites are long-lived, in equilibrium with the parent radicals. Peroxy radicals can also react with NO to produce less reactive peroxyxynitrites [Eq. (16)], a reaction that is considered to be responsible for the antioxidant properties of $\bullet\text{NO}$. However, a small fraction of the peroxyxynitrites may decompose and undergo O–O bond cleavage [Eq. (17)] to produce NO_2 and alkoxy radicals.²⁹



Recently another radical, nitroxyl (HNO), which is a reduced form of NO , is attracting considerable attention. Its pharmacological properties are distinct from those of NO , and it is being considered to be significant in the treatment of heart failure.²¹ HNO is produced during the hydrolysis of some nitroso compounds.

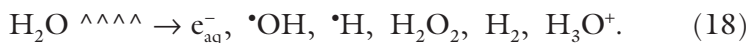
In addition to these commonly observed free radical inter-conversion reactions, the above radicals, when react with the cellular

organelles, may produce secondary radicals such as those obtained from DNA bases, amino acid radicals, thiyl radicals (RS^\bullet), and thiyl peroxy radicals. The possible damage induced by these radicals depends on the chemical structure of the radical and the site of their production as they often cause localized damage.¹⁷

3. Radiation Chemical Methods to Study Reactions of ROS and RNS

3.1. Generation of ROS and RNS

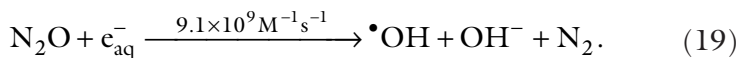
Irradiation of aqueous solutions by ionizing radiation has been found to be a very important and selective method for the generation of ROS and RNS. Interaction of ionizing radiation with dilute aqueous solutions causes excitation and ionization of water molecules which undergo subsequent changes, mainly due to ion–molecule reactions, dissociation reactions, and solvation reactions to produce a number of radical and molecular species [Eq. (18)].



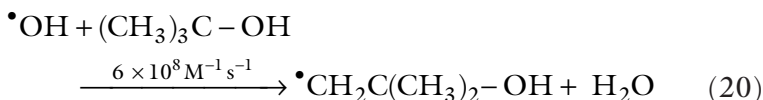
Out of these radical species, H^\bullet and e_{aq}^- are reducing in nature, while $\bullet OH$ radicals are oxidizing in nature. Employing suitable additives, such as inorganic salts and dissolved gases, it is possible to convert these primary radicals of water radiolysis to new radicals. The radiation chemical reactions leading to the conversion of these primary species into different ROS and RNS are given below.^{17–20,23,30}

3.1.1. $\bullet OH$ radicals

Radiolysis of N_2O -saturated aqueous solutions in the pH range from 3 to 10 produces predominantly $\bullet OH$ radicals [Eq. (19)]. The saturation solubility of N_2O in water is 25 mM.

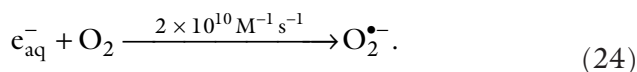
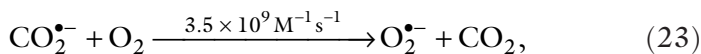
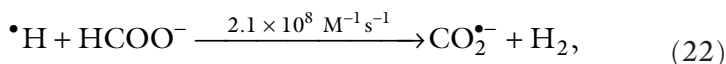
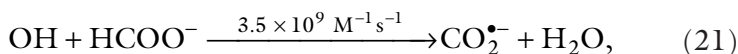


Wherever necessary, the $\bullet\text{OH}$ radical reactions can be eliminated by using tertiary butanol [Eq. (20)] as $\bullet\text{OH}$ radical scavenger, where the resultant tertiary butanol radicals are often not very reactive.



3.1.2. $\text{O}_2^{\bullet-}$ radicals

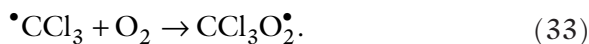
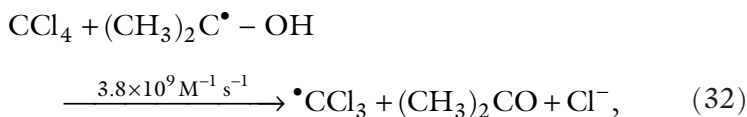
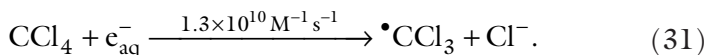
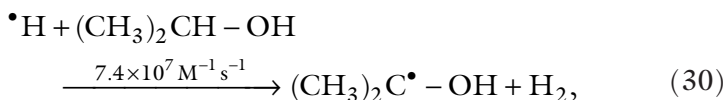
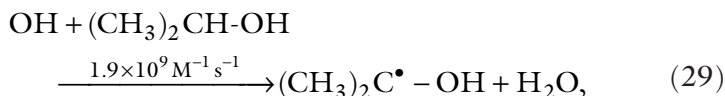
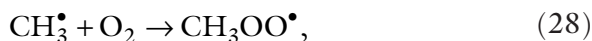
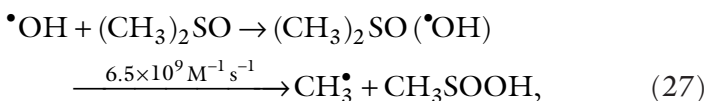
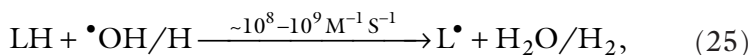
$\text{O}_2^{\bullet-}$ radicals are produced by the radiolysis of oxygen saturated aqueous solutions containing formate ion.²⁶ Under these conditions, formate ions (HCOO^-) react with both $\bullet\text{H}$ and $\bullet\text{OH}$ radicals to produce $\text{CO}_2^{\bullet-}$ radicals and these radicals in turn react with oxygen to give $\text{O}_2^{\bullet-}$ radicals [Eqs. (21)–(23)]. Alternatively, $\text{O}_2^{\bullet-}$ radicals can be generated by the direct reaction of e_{aq}^- with oxygen [Eq. (24)].



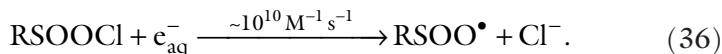
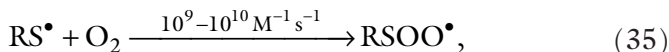
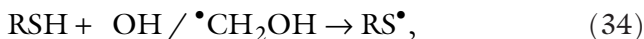
3.1.3. Peroxyl radicals

Although many different types of peroxyl radicals can be generated by radiation chemical methods,^{17,20,26,31} the most commonly used ones are linoleic acid peroxyl ($\text{LOO}\bullet$) radicals, methyl peroxyl ($\text{CH}_3\text{OO}\bullet$) radicals, trichloromethyl peroxyl radicals ($\text{CCl}_3\text{OO}\bullet$), and thiylperoxyl radicals ($\text{RSOO}\bullet$). $\text{LOO}\bullet$ radicals can be generated by the radiolysis of linoleic acid (LH) dissolved in aqueous solutions at alkaline pH

[Eqs. (25) and (26)], $\text{CH}_3\text{OO}\cdot$ radicals, by the reaction of $\cdot\text{OH}$ with dimethylsulfoxide [Eqs. (27) and (28)] and $\text{CCl}_3\text{OO}\cdot$ radicals by the radiolysis of aqueous solutions containing 48% 2-propanol, 4% CCl_4 according to [Eqs. (29) to (33)].

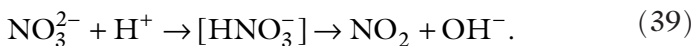
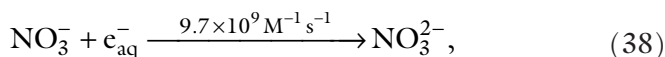
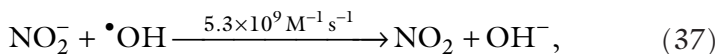


$\text{RSOO}\cdot$ are generated by the hydrogen abstraction from thiols by $\cdot\text{OH}$ radicals, alcohol radicals, etc.,^{17,26} producing thiyl radicals ($\text{RS}\cdot$) which on reaction with oxygen produce $\text{RSOO}\cdot$ [Eqs. (34) and (35)]. Alternatively, reaction of alkylsulfonyl chloride with e_{aq}^- produces alkyl sulfonyl peroxy radicals [Eq. (36)].



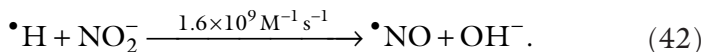
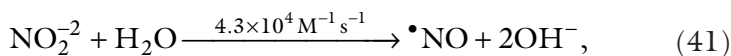
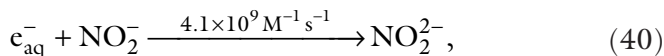
3.1.4. *NO₂ radicals*

These radicals are produced by the reaction of $\bullet\text{OH}$ radicals with nitrite anion in N_2O -saturated solutions or by e_{aq}^- reaction with nitrate in N_2 -saturated solutions under mild acidic conditions (pH 5).^{26,27} Due to limited solubility of N_2O gas and the competing reactions of e_{aq}^- with nitrite, often a mixture of nitrite (~ 10 mM) and nitrate solutions purged with N_2 gas is employed to generate high yields of NO_2 radicals [Eqs. (37)–(39)]:



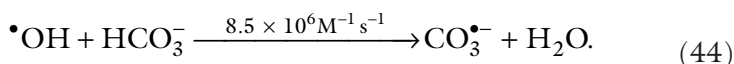
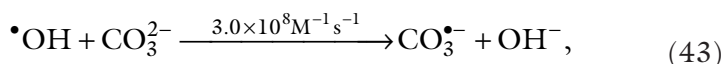
3.1.5. *Nitric oxide radicals*

Reaction of hydrated electrons and hydrogen atom with nitrite to produce NO_2^{2-} , which undergoes hydrolysis to produce NO .²⁷



3.1.6. Carbonate ($\text{CO}_3^{\bullet-}$) radicals

These radicals are produced by the reaction of $\bullet\text{OH}$ radicals with carbonate ions and bicarbonate ions [Eqs. (43) and (44)].



3.1.7. Peroxynitrite

Generation of peroxynitrite by pulse radiolysis involves very tricky adjustments of concentrations of additives and many other experimental conditions. Radiolysis of aerated aqueous solutions containing sodium formate and potassium nitrite in the pH range 3 to 10 produced peroxynitrite according to Eqs. (21) to (23), (40), (41) and (11). For this, initial concentrations of nitrite and formate have to be adjusted in such a way that the radiolytically produced concentration of the radicals of $[\text{O}_2^{\bullet-}] + [\text{HO}_2^{\bullet}] > \text{NO}$.²⁷ However, reactions of peroxynitrite with antioxidants are not generally studied by pulse radiolysis technique. Chemical methods such as ozonolysis of alkaline sodium azide solutions are commonly used to produce peroxynitrite in large quantities and its reactions studied by mixing techniques.¹²

3.1.8. Secondary radicals from proteins and DNA

It is necessary that an antioxidant protects cells at all stages of oxidative stress, and therefore an antioxidant should be able to scavenge the secondary radicals produced by the reaction of primary radicals with biomolecules. Radiation chemists designed methods to study reactions of secondary radicals from amino acids of proteins and base and sugar radicals of DNA with antioxidants.^{17,32-35} The most commonly employed aromatic amino acid radicals generated by radiation chemical experiments are the indolyl radicals of tryptophan (TRP^{\bullet}), the

tyrosine phenoxyl radicals (TYRO[•]), and sulfur-centered radicals from amino acids like histidine, methionine, glutathione, etc. These radicals are generated by the reaction of either the amino acids or the proteins containing these amino acids with [•]OH radicals and one-electron oxidants like Br₂^{•-}. When proteins containing both tryptophan and tyrosine react with one-electron oxidants, initial oxidation takes place on the tryptophan moiety producing TRP[•] radicals, which subsequently undergo electron transfer to tyrosine to give TYRO[•] radicals. Reactions of antioxidants with these radicals are used to evaluate their ability to protect proteins from oxidative damage, especially for hydrophobic antioxidants, which show preferential affinity towards proteins. Sulfur-centered amino acid radicals are generated by the reaction of these compounds with hydroxyl radicals and one-electron oxidants. To evaluate the ability of an antioxidant to protect DNA from oxidative damage, studies on the repair and electron transfer reactions of several antioxidants have been carried out with secondary DNA radicals. Using pulse radiolysis reactions of radicals such as hydroxyl radical adducts of deoxyguanosine monophosphate (dGMP-OH[•]), deoxyadenosine monophosphate (dAMP-OH[•]), polyadenylic acid (poly A-OH[•]), polyguanylic acid (poly G-OH[•]), single or double stranded DNA (DNA-OH[•]) and radical anions of thymine (T^{•-}) and thymidine monophosphate (TMP^{•-}), radical cations of dGMP and dAMP (dGMP^{•+} and dAMP^{•+}) have been studied with antioxidants. These radicals are generated by the reaction of [•]OH radicals, one-electron oxidants and hydrated electrons with monomeric and polymeric nucleotides.

3.2. Fast reaction techniques to monitor the reactions of ROS and RNS

As most of the free radicals are short-lived, direct monitoring of their reactions is not an easy task and powerful tools based on fast reaction techniques are required to follow such processes.^{17,18,36} Thus, fast reaction techniques utilize either short pulses of high-intensity flash of light or laser (in flash photolysis), or short pulses of charged particles and high-energy photons from accelerators (in pulse radiolysis).

These short pulses induce a non-equilibrium situation in a very short time scale, such that a sufficiently high concentration of transient free radical species is formed. These short-lived free radical species are detected in their lifetimes, by following the changes in their characteristic properties such as optical absorption, electrical conductivity, spin density, Raman spectroscopy, etc.³⁶ Pulse radiolysis has been found to be extremely useful in studying several of these free radical reactions. Although modern pulse radiolysis techniques are capable of producing much shorter pulses ($<10^{-12}$ seconds), most of the relevant studies with antioxidants have been performed in the time scale of nanoseconds to a few seconds. Alternatively, it is possible to exploit known chemical methods to produce stable radicals like ABTS^{•-} and non-radical species like peroxyxynitrite and follow their reactions by stopped-flow kinetic methods. Other techniques like electron spin resonance (ESR) spectroscopy can be employed for direct monitoring of free radicals.³⁷ This technique, although very selective, is limited to long-lived radicals. Other methods employed to overcome these problems are by using flow systems, freezing at low temperature and spin trapping. Pulse radiolysis and flash photolysis techniques coupled with ESR detection have been developed, but not many studies with antioxidants have been reported.³⁶

4. Pulse Radiolysis Studies of Antioxidants

Recently, many laboratories involved in radiation chemistry programmes have initiated antioxidant research and several papers are published on reactions of ROS and RNS with antioxidants using pulse radiolysis. The rate constants for the scavenging reactions of ROS and RNS by antioxidants were determined, at near physiological conditions. Studies on radical dynamics and their subsequent reactions with other additives have been found to be useful to quantify reaction kinetics and estimate the reactivity of antioxidant substances and measure the reduction potentials of the couples. Determining the transient spectra of radicals of antioxidants produced during these reactions has been useful in characterizing the nature of the radical species, and identifying the site of free radical attack on the antioxidant molecule.

4.1. *Different classes of antioxidants and vitamin E*

The antioxidants studied can be classified into two broad types: phenolic antioxidants and non-phenolic antioxidants. Phenolic antioxidants have been found to be more promising as they are obtained from dietary sources.^{3,16} Vitamin E (α -tocopherol), the first known chain-breaking antioxidant, is also an *o*-methoxy phenol. Pulse radiolysis studies of vitamin E and its water-soluble analogue, trolox C, have been reported several years ago.^{38,39} α -tocopherol reacts with almost all the oxidizing free radicals, and the phenoxyl radicals produced during oxidation reactions absorb at ~ 460 nm (Fig. 1). The regeneration reaction of α -tocopherol phenoxyl radicals back to α -tocopherol by water-soluble antioxidant ascorbic acid was also first reported by pulse radiolysis method.⁴⁰ The one-electron reduction potential of vitamin E is ~ 0.48 V vs. NHE.¹⁰ Both α -tocopherol and trolox C are used as standards for evaluating the antioxidant ability of new compounds.

Important phenolic antioxidants reported by pulse radiolysis in the recent past are hydroxy-flavonoids,⁴¹ catechins,⁴² methoxy phenols,^{43,44} tea polyphenols,⁴⁵ curcuminoids,⁴⁶ cinnamic acid derivatives,⁴⁷ hydroxystilbene,⁴⁸ ellagic acid,⁴⁹ sesamol,⁵⁰ tocopherol-glucosides,⁵¹ phenylpropanoid glycosides,⁵² tannins⁵³ and many other plant-derived polyphenols.^{43,54} In most of these oxidation reactions, the phenol reacts with the free radical either by hydrogen abstraction to produce a phenoxyl radical or by initial electron transfer to generate a radical cation, which subsequently undergoes fast proton loss to produce phenoxyl radicals. Some of the radicals like $\bullet\text{OH}$ radical, add to the aromatic ring of the phenol to produce a cyclohexadienyl-type radical, which undergoes loss of water or some other group to generate phenoxyl radicals. The phenoxyl radicals are resonance-stabilized and in general are not reactive enough to propagate the chain reactions induced by peroxy radicals.

Carotenoids,⁵⁵ cyclic nitroxides,⁵⁶ retinoids,⁵⁷ deferroxamine,²⁸ thiols, dithiols⁵⁸ are some of the well-known non-phenolic antioxidant systems recently studied.

A complete review of the application of radiation chemistry to the overall antioxidant research is beyond the scope of this chapter.

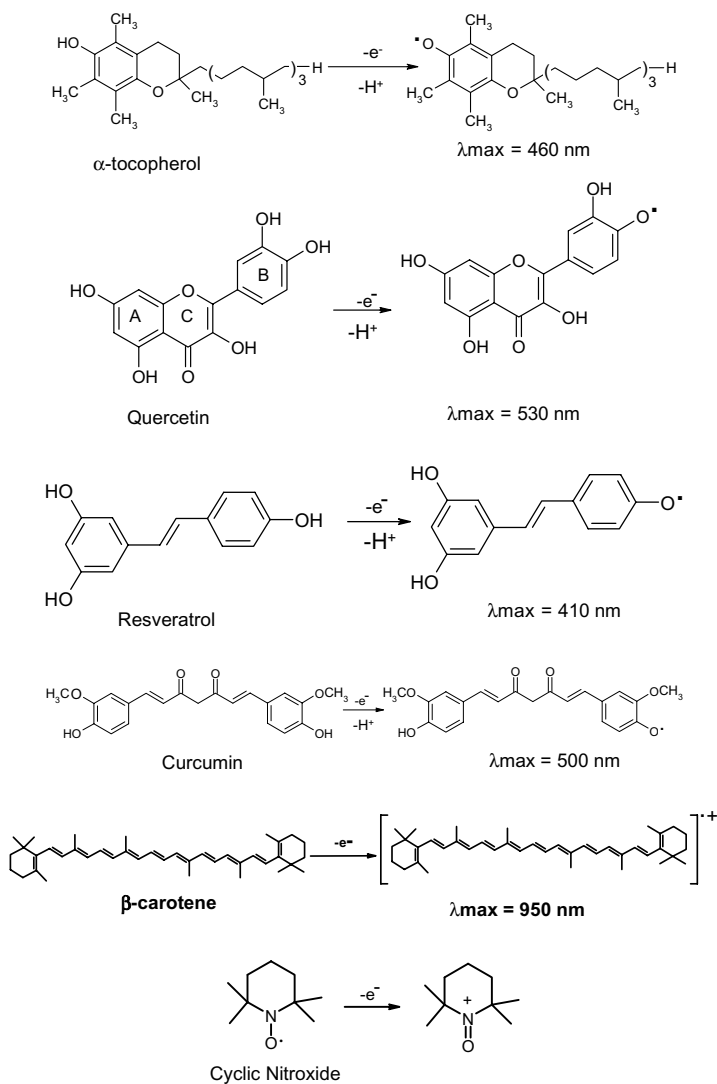


Fig. 1. Chemical structures of some important antioxidants and their transient radical species.

Therefore this present chapter is limited only to discussion on pulse radiolysis studies of promising compounds that exhibit potent biological activities; for example, hydroxyl-flavonoids, resveratrol, curcumin, β -carotene and cyclic nitroxides are reported here.

4.2. *Flavonoids*

Flavonoids are phenolic compounds present in many plant products.⁴¹ More than 2000 flavonoids are known with variations both in the nature of the chromane rings and substitutions. Hydroxy-substituted flavonoids mostly exhibit potent antioxidant ability. The chemical structure of flavonoids is denoted by the three rings A, B, and C (e.g. quercetin, in Fig. 1). Pulse radiolysis studies on reactions of oxidizing radicals with several structurally related hydroxy-flavonoids have been performed and the absorption spectra of the flavonoid phenoxyl radicals from compounds with different ring substitutions have been reported.⁵⁹⁻⁷¹ The absorption spectra of the phenoxyl radicals of flavonoids show distinct features. The phenoxyl radical spectra of hydroxy-flavonoids are closely related to catechol, or resorcinol, or 3,5-dihydroxy anisole, or 2,4-dihydroxyacetophenone.⁵⁹ This spectral similarity has been found to be useful in identifying the site of free radical attack on the flavonoid molecules, and also in characterizing different flavonoid phenoxyl radicals like if they are produced from the oxidation of the hydroxyl group from the A, B and C rings. Although hydroxyl substitution on the three rings makes them reactive towards peroxy radicals, the catechol hydroxyl group of the B-ring makes it a more effective scavenger of oxidizing radicals. The one-electron reduction potentials for a number of hydroxy flavonoids at the biologically relevant pH conditions have been reported.^{41,59} The reduction potential is significantly reduced when the 3-hydroxy group in the C ring is in conjugation with the catechol moiety. Accordingly, quercetin, a hydroxyl-substituted flavonol, is the best electron donor with reduction potential of $E_7 = 0.33$ V vs. NHE and its 3-rutinosylated derivative rutin has the reduction potential of $E_7 = 0.6$ V. Both quercetin and rutin are chain-breaking antioxidants and several biochemical studies confirmed that both of them exhibit potent biological activity. Reactions of radicals such as $\cdot\text{OH}$, N_3^{\cdot} , NO_2^{\cdot} , $\text{O}_2^{\cdot-}$, peroxy radicals, 1-hydroxyethyl radicals have been reported with quercetin. The transients have been characterized by absorption spectroscopy, conductivity measurements, and Raman spectroscopy.^{41,59,60} Based on such studies, the role of 2,3-double bond of the C ring and

the ring opening reactions⁶¹ on overall antioxidant activity under different oxidative stress-induced conditions has been reported.⁶²⁻⁶⁸ Quercetin could repair TRP• radicals produced during the oxidation of human serum albumin (HSA), and low density lipoprotein (LDL).⁶⁴ HSA-bound quercetin could repair urate radicals by electron transfer both in the presence and absence of copper (II). In the presence of oxygen the same reaction could not be observed, indicating that both copper (II) and oxygen modulate the antioxidant activity of quercetin.^{62,65} Rutin and quercetin could repair the deoxythymidine radical anion and dGMP-OH radical adduct,^{66,67} indicating their usefulness to the non-enzymatic DNA repair pathways. Other flavonoid compounds like catechins, epigallocatechin, proanthocyanidins, xanthenes, gallotanins, ellagotannis ginstein, etc. have also been reported by pulse radiolysis⁶⁹⁻⁷¹ and the phenoxyl radicals have been studied by transient spectra, decay kinetics, DFT calculations and also their reactions with other biomolecules. The antioxidant potential of these compounds was significantly influenced by the functional group substitutions, prototropic equilibria, O-H bond dissociation energies, etc.

4.3. *Trans resveratrol*

Trans-resveratrol (trans-3,5,4'-trihydroxystilbene) is a non-flavonoid polyphenol found in grapes, mulberries, and other food products.^{48,72,73} It is responsible for the antioxidant activity of red wine. Intake of moderate amount of red wine has been found to reduce the risk of cardiovascular diseases. In addition to antioxidant activity, resveratrol could inhibit platelet aggregation, and showed anticancer activity. The phenoxyl radicals of resveratrol produced during oxidation by hydroxyl radicals, one-electron oxidants, and peroxy radicals showed absorption maximum at 410 nm (Fig. 1). Reports indicate that trans-resveratrol is a better radical scavenger than vitamins E and C and its activity is similar to that of the flavonoids epicatechin and quercetin. From the comparison of the spectral and kinetic properties of the transients derived from trans-resveratrol and its analogues, it could be concluded that in the neutral and acidic solutions, the para-hydroxy

group of trans-resveratrol is more reactive than the meta-hydroxy groups. Resveratrol could repair the DNA and amino acid radicals with rate constants ranging from 10^9 to $10^8 \text{ M}^{-1} \text{ s}^{-1}$.⁷³

4.4. *Curcumin*

Curcumin is a major phenolic pigment derived from turmeric, which is commonly used as a spice and a household medicine in India. Recent scientific research has shown that curcumin is 10 times more effective as an antioxidant than vitamin E. It is also a potent anti-tumor agent and at present, several Phase I and Phase II clinical trials are going on for the treatment of different types of cancers. The greatest advantage of curcumin is the pharmacological safety to humans even at a dose of 8 g/day.^{74,75} Pulse radiolysis studies on reactions of superoxide radicals, $\text{CCl}_3\text{OO}^\bullet$ radicals, lipidperoxyl, methyl and methyl peroxyl radicals, glutathione radicals, tryptophan radicals, etc. with curcumin have been reported.^{35,76-79} The rate constants for the reactions of these radicals and several other oxidants have been reported in aqueous/aqueous-organic solutions. In all these reactions, a transient absorbance from 250 to 600 nm with maximum absorption at 500 nm was characterized as the phenoxyl radicals, which have resonance stabilization through the β -diketone structure. The lifetime of the phenoxyl radicals is of a few hundred microseconds. The phenoxyl radicals could be regenerated back to the parent curcumin by water-soluble antioxidants like ascorbic acid. Although there were some apprehensions on the actual site for free radical attack in curcumin such as the central methylenic (CH_2) group and the phenolic OH group, recent quantum chemical calculations confirmed that the O-H bond dissociation energy of the phenolic group of curcumin is 6.5 kcal/mol lower than the C-H bond dissociation energy of the central CH_2 group,⁷⁹ and therefore the phenolic-OH group should be involved in the free radical reactions in curcumin. Also several experimental studies comparing the antioxidant activity and free radical reactions of curcumin with many substituted analogues, confirmed that the phenolic OH is only responsible for both free radical scavenging activity and the antioxidant activity of curcumin.

Table 2. Rate constants for the reaction of different radicals with quercetin (QC) and curcumin (CR).

Radical reaction	Rate constant $M^{-1} s^{-1}$	Radical reaction	Rate constant $M^{-1} s^{-1}$
QC + N_3^{\bullet}	6.6×10^9	CR + N_3^{\bullet} (10% acetonitrile)	3.4×10^9
QC + LOO^{\bullet} (pH 11.5)	1.8×10^7	CR + $CCl_3O_2^{\bullet}$	1.2×10^8
QC + $O_2^{\bullet-}$ (pH 10)	4.7×10^4	CR + LOO^{\bullet} (pH 10.5)	7.3×10^5
QC + $(SCN)_2^{\bullet-}$	4×10^8	CR (Tx-100) + $O_2^{\bullet-}$	4.6×10^4
QC (CTAB) + urate radical	6×10^6	CR + GS^{\bullet}	1.0×10^8
QC + $TyrO^{\bullet}$ (LDL)	6.8×10^7	CR + TryO. (lysozymes)	5.0×10^8
QC + dGMP-OH $^{\bullet}$	3×10^8	CR + CH_3^{\bullet}	3.5×10^9
QC + dAMP $^{\bullet-}$	4.1×10^9	CR + t-butoxyl radical	7.5×10^9
QC + 1-hydroxyethyl radical	4.0×10^4	CR + 1O_2	1.3×10^6

The β -diketone moiety in conjugation with the phenolic groups contributes greatly to the anti-inflammatory and anti-tumor activity of curcumin.^{74,75} The rate constants for the reactions of several oxidizing free radicals with quercetin and curcumin are given in Table 2.

4.5. β -carotene

Carotenoids represent one large class of natural non-phenolic antioxidants present in many vegetables, fruits, and flowers. Several different types of carotenoids have been examined as antioxidants⁸⁰; important among these are all-trans- β -carotene, zeaxanthin, lycopene, canthaxanthin, lutein, etc. Most of the carotenoids exhibit very low solubility in water, but they are soluble in micellar solutions. β -carotene has been found to be an excellent scavenger of peroxy radicals and is a powerful chain-breaking antioxidant.⁸¹ Reaction of β -carotene with peroxy radicals produced β -carotene radical cation showing strong absorption at 950 nm. β -carotene could also neutralize thiyl, thiyl peroxy radicals, NO_2 radicals, peroxyxynitrite. It is a very efficient scavenger of singlet oxygen.^{26,81-84} The reaction of β -carotene with these different types of oxidizing radicals produced both radical cations absorbing at 950 nm and radical adducts absorbing in 300 to 500 nm

region. The one-electron reduction potential to form β -carotene radical cation from β -carotene in Tx-100 was reported to be 1.06 V vs. NHE.^{55,84} β -carotene radical cations are repaired by water-soluble vitamin C by a rate constant of $10^7 \text{ M}^{-1} \text{ s}^{-1}$. All these studies initially led to the assumption that the electron transfer reactions contribute to the antioxidant activity of β -carotene. However, a randomized double-blind study on the effect of β -carotene on the incidence of lung cancer suggested that male smokers who received β -carotene showed higher incidence of cancer, thus leading to the doubts on the antioxidant ability of β -carotene.⁸⁵ Later on a few other studies suggested that the radical adducts, which are formed by radical addition, may act as ROS inducers leading to the increased damage especially inside the lungs with very high oxygen levels and in the case of cigarette smokers, where the NO_2 levels are much higher.²⁴ These studies point out that the biological activity of β -carotene is mediated not only by free radical scavenging reactions, but also due to the involvement of more complex reactions.⁸²

4.6. Cyclic nitroxides

Cyclic nitroxides ($>\text{NO}^\bullet$) are stable free radicals, which are often used as biophysical markers for monitoring membrane fluidity, and contrast agents for *in vivo* MRI and ESR imaging. They have been found to reduce the oxidative stress in different cellular models and provide protection through oxidation of reduced transition metals, detoxification of semiquinones and scavenging of ROS and RNS.⁸⁶⁻⁹⁰ Unlike most low-molecular-weight antioxidants, which are depleted while attenuating oxidative damage, nitroxides can be recycled. The antioxidative activity of nitroxides is associated with electron transfer-induced switching between their oxidized and reduced forms. Pulse radiolysis studies on reactions of five- and six-member cyclic nitroxides with peroxy radicals, $^\bullet\text{OH}$, $\text{O}_2^\bullet-$, NO_2 and $\text{CO}_3^{\bullet-}$ radicals have been reported.^{56,86-90} Depending on the substitutions and types of radicals, the electron transfer rate constants vary between 10^7 to $10^8 \text{ M}^{-1} \text{ s}^{-1}$. The one-electron oxidation reactions formed oxoammonium cations ($>\text{N}=\text{O}^+$), with the reduction potentials for the

couple $>N=O^+ / >NO$, ranging from 0.7 to 0.9 V vs. NHE. The protective effect of nitroxides depends on the ring size and substitution. A clear correlation has been obtained between the kinetic and redox features of nitroxides and their biological antioxidant activities. Nitroxides with lower oxidation potential exhibit greater protection against cellular damage. The easy switching between the oxidized and reduced forms of cyclic nitroxides makes them potential candidates for antioxidant enzyme mimics^{89,90} such as superoxide dismutase (SOD), which is discussed under Sec. 4.8. The rate constants for the reactions of resveratrol, β -carotene and one representative cyclic nitroxide with oxidizing radicals are given in Table 3. The chemical structures of these compounds along with the corresponding oxidized species are given in Fig. 1.

4.7. Drugs and herbal formulations as antioxidants

Recently there is great interest in the development of therapeutic antioxidants from the existing allopathic drugs and formulations from traditional medicine. Some of the drugs evaluated for antioxidant

Table 3. Rate constants for the reaction of different radicals with β -carotene (β -C), resveratrol (RSV), and 2,2,6,6-tetramethylpiperidinoxyl (TPO).

Radical reaction	Rate constant $M^{-1} s^{-1}$	Radical reaction	Rate constant $M^{-1} s^{-1}$
RSV + $CCl_3O_2^*$ (pH 6)	9.6×10^7	β -C + $CCl_3OO^* Tx-100$ isopropanol-water	2.2×10^5 7.8×10^7
RSV + N_3 (pH 11)	4.0×10^9	β -C + NO_2^* (pH 10.5)	1.1×10^8
RSV + $O_2^{\cdot-}$	4.0×10^8	β -C + $HO(CH_2)_2S^*$	2.5×10^9
RSV + $\cdot OH$ (pH 6)	1.3×10^{10}	(t-butanol-water)	
TPO + HO_2	1.2×10^8	β -C + GS^*	2.2×10^8
TPO + $O_2^{\cdot-}$	$<10^3$	β -C + $C_2H_5SOO^*$	3.9×10^9
TPO $^{+}$ + $O_2^{\cdot-}$	3.4×10^9		
TPO + $CO_3^{\cdot-}$	4.0×10^8	β -C + $CysS^*$	2.6×10^8
TPO + Phenylalanine- HO^*	4.0×10^6	β -C + CH_3OO^*	4.8×10^8
TPO + $\cdot OH$	3.0×10^9		
TPO + $ONOO^-$	6.0×10^6	β -C + CBr_3OO^*	$\sim 10^9$
TPO + $\cdot NO_2$	7.0×10^8		

properties by radiation chemical methods are selective and non-selective β 1-adrenolytics with α 1-receptor blocking properties,⁹¹ anti-ulcer agents,⁹² e.g. sulfasalazine, 5-aminosalicylic acid, and an expectorant, ambroxol.⁹³ Several plant extracts and herbal formulations have been reported for antioxidant activity, and their free radical scavenging ability has been evaluated by pulse radiolysis.⁹⁴⁻⁹⁸ Most of the studies, when correlated with their biological activity, confirmed that free radical scavenging kinetics is one of the main factors controlling their antioxidant activity. Although these preliminary studies in this direction are very encouraging, due to the complexity of formulations and involvement of mixtures of components, these studies have remained only as screening techniques rather than for evaluating the reaction mechanisms.

4.8. Development of SOD mimics

Another important contribution of pulse radiolysis is in the evaluation of redox processes in native SODs and development of SOD mimics. SOD is an endogenous antioxidant enzyme which catalyzes the conversion of $O_2^{\bullet-}$ radicals to H_2O_2 . Different types of SODs are present in cells such as Mn-SOD in mitochondria and Cu, Zn-SOD in the cytosol and in extracellular surfaces.¹ Reactions of $O_2^{\bullet-}$ radicals with the active site of native SODs from bacterial and animal sources have been examined. In one recent study involving superoxide reductase (SOR) from *Desulfoarculus baarsii*, the precise step responsible for the catalytic action was examined.⁹⁹ Its active site contains an unusual mononuclear ferrous center. Since protonation processes are essential for the catalytic action, the pH dependence of the redox properties of the active site, both in the absence and in the presence of $O_2^{\bullet-}$ radicals, was studied using pulse radiolysis. The results confirmed that the reaction of SOR with $O_2^{\bullet-}$ radicals involves two reaction intermediates, an iron(III)-peroxo species and an iron(III)-hydroperoxo species. The protonation takes place in the second step, and therefore responsible for its catalytic activity.

Under oxidative stress conditions, such as ischemic reperfusion injury, the endogenous SODs are inadequate and need to be supplemented.

However, the native enzyme suffers from several disadvantages such as low shelf-life and non-availability, therefore new SOD mimics have been developed as alternatives. Although most of the antioxidants could scavenge $O_2^{\bullet-}$ radicals, not many showed SOD-like catalytic activity. Antioxidants having different functional groups that can undergo both oxidation and reduction showed SOD-mimicking activity. Flavonoids, curcumin, and cyclic nitroxides are some of the examples that have been found to act as SOD mimics, by participating in the reversible redox reactions with $O_2^{\bullet-}$ radicals.^{89,90,100,101} Several *in vitro* and *in vivo* studies confirmed their ability to protect the SOD levels under oxidative stress conditions.

Since the catalytic effects in the native enzymes are due to reversible redox reactions in metal centers, like copper, manganese and iron, transition metal complexes of natural antioxidants are being explored as new SOD mimics. Pulse radiolysis studies on reactions of superoxide radicals with such complexes and the determination of their one-electron redox potentials helped in the evaluation of such complexes as SOD mimics. Copper, manganese, iron, and vanadium complexes of hydroxy flavonoids, genistin, and curcumin were examined as SOD mimics and several *in vitro* and *in vivo* studies showed very encouraging results.¹⁰²⁻¹⁰⁵ Recently unique SOR activity has been reported from an adduct of a penta-coordinated ferrous iron complex $[Fe^{+2} (N-His)4(S-Cys)]$ and ferrocyanide. The adduct, while reducing $O_2^{\bullet-}$ radicals, did not generate H_2O_2 from this reaction. Since H_2O_2 formation could also contribute to oxidative stress, this particular adduct may be superior to the other conventional SOD mimics.¹⁰⁶

5. Future Scope

Radiation chemical methods and pulse radiolysis technique in particular, have been proved to be extremely useful in the selective generation of ROS and RNS and the direct monitoring of their reactions. Using these methods, a number of natural and synthetic products have been evaluated as new antioxidant molecules. Estimation of rate constants and one-electron reduction potentials in most of the promising cases confirmed the role of electron transfer

processes in the antioxidant activity. These studies also helped in the development of new synthetic derivatives with target specificity and efficacy better than that of the natural compounds.

Till now most of the scavenging studies have been carried out in homogeneous solutions. Since biological systems are much more complex and heterogeneous, extrapolating the existing results to real biological models would be difficult. It is therefore necessary to evaluate some of the parameters in experimental models in non-homogeneous systems, taking into consideration of the presence of other biomolecules like proteins and DNA, which can alter the activity of the compounds. Some recent pulse radiolysis studies reported with albumin, lysosomal, and LDL-bound antioxidants are indicative of such models.^{35,60,62} Future studies have to be directed to evaluate electron transfer reactions in cells and *in vivo* systems by using pulse radiolysis coupled with multiple detection systems like ESR, Raman, etc.

Physiological processes are very sensitive to small changes in the overall potential of the cell. For example, change in the half cell reduction potential of the cell from -240 mV to -200 mV can cause proliferating cells to undergo differentiation, and further change in potential can induce apoptosis.⁹ Till now the ratio of intracellular oxidized and reduced glutathione levels is used to correlate the redox status of the cells. Measuring transient electrochemical parameters would be very useful to understand the step-wise redox-controlled processes in cells. Hence pulse radiolysis facilities should be developed to measure the redox status of the cell under different stages of electron transfer process, which are responsible for the physiological changes.

It has been found that many antioxidants, when administered at large quantities, act as pro-oxidants and thereby increase oxidative stress. Hence it is necessary to understand the free radical kinetic reactions of antioxidants at concentrations that are close to their physiological concentrations. Verification of the bio-availability of the antioxidants at the target site is essential for this.

Radiation chemical studies of antioxidants and their products of radiolysis should be developed as markers for testing the irradiated foods and spices, which are known to contain many different types of

antioxidants. Although a recent report indicated monitoring changes in hydroxy chalcones as markers for irradiated vegetables and fruits,¹⁰⁷ many more such studies in this direction would be useful for evaluating the effect of antioxidant status in the irradiated food.

Thus, radiation chemistry and pulse radiolysis in particular have become crucial and unique tools, giving a different direction to the overall understanding and development of antioxidants. Proper coordination between the biochemists and the radiation chemists is therefore obligatory to exploit these studies to greater biological advantage.

Acknowledgments

The author would like to thank Drs. T. Mukherjee and S. K. Sarkar for the encouragement and support and Drs. B. Mishra and A. Kunwar for many useful suggestions.

References

1. Halliwell B, Gutteridge JMC. (1993) *Free Radicals in Biology and Medicine*. Clarendon Press, Oxford.
2. Finkel T, Holbrook NJ. (2000) Oxidants, oxidative stress and biology of ageing. *Nature* **408**: 239–247.
3. Fang Y-Z, Yang S, Wu G. (2002) Free radicals, antioxidants and nutrition. *Nutrition* **18**: 872–879.
4. Sies H. (1997) Oxidative stress: Oxidants and antioxidants. *Exp Physiol* **82**: 291–295.
5. Cadenas E, Davies KJA. (2000) Mitochondrial free radical generation, oxidative stress and ageing. *Free Radic Biol Med* **29**: 222–230.
6. Halliwell B. (1990) How to characterize a biological antioxidant. *Free Radic Res Commun* **9**: 1–32.
7. Mats JM, Segura JA, Alonso FJ, Marquez J. (2008) Intracellular redox status and oxidative stress: Implications for cell proliferation, apoptosis, and carcinogenesis. *Archives of Toxicology* **82**: 273–299.
8. Valko M, Rhodes CJ, Moncol J, Izakovic M, Mazur M. (2006) Free radicals, metals and antioxidants in oxidative stress induced cancer. *Chem-Biol Interact* **160**: 1–40.
9. Schafer FQ, Buettner GR. (2001) Redox environment of the cell as viewed through the redox state of the glutathione disulfide/glutathione couple. *Free Radic Biol Med* **30**: 1191–1212.

10. Buettner GR. (1993) The pecking order of free radicals and antioxidants: lipid peroxidation, α -tocopherol and ascorbate. *Arch Biochem Biophys* **300**: 535–543.
11. Beilski BHJ, Cabelli DE, Arudi R, Ross A. (1985) Reactivity of HO_2/O_2^- radicals in aqueous solutions. *J Phys Chem Ref Data* **14**: 1041–1100.
12. Koppenol WH. (1998) The basic chemistry of nitrogen monoxide and peroxy-nitrite. *Free Radic Biol Med* **25**: 385–391.
13. Priyadarsini KI. (2000) Characteristic chemical reactions of nitric oxide. *Proc Natl Acad Sci India* **LXX**: 339–352.
14. Fukuto JM, Ignarro LJ. (1997) *In vivo* aspects of nitric oxide chemistry: Does peroxynitrite play a major role in cytotoxicity. *Acc Chem Res* **30**: 149–152.
15. Goldstein S, Merčinyi G. (2008) The chemistry of peroxynitrite: Implications for biological activity. *Methods in Enzymology* **436**: 49–61.
16. Pryor WA. (1989) Vitamin E: The status of current research suggestions for future studies. *Ann New York Acad Sci* **570**: 400–405.
17. von Sonntag C. (1987) *The Chemical Basis of Radiation Biology*. Taylor & Francis, London.
18. Bensasson RV, Land EJ, Truscott TG. (1983) *Flash Photolysis and Pulse Radiolysis, Contributions to the Chemistry of Biology and Medicine*. Pergamon Press, London.
19. Wardman P. (1989) Reduction potentials of one-electron couples involving free radicals in aqueous solutions. *J Phys Chem Ref Data* **18**: 1637–1755.
20. Neta P, Huie RE, Ross A. (1990) Rate constants for reactions of peroxy radicals in fluid solutions. *J Phys Chem Ref Data* **19**: 413–513.
21. Hughes MN. (2008) Chemistry of nitric oxide and related species. *Methods in Enzymology* **436**: 3–19.
22. Goldstein S, Squadrito GL, Pryor WA, Czapski G. (1996) Direct and indirect oxidation by peroxynitrite neither involving the hydroxyl radicals, *Free Radic Biol Med* **21**: 965–974.
23. Neta P, Huie RE. (1988) Rate constants for reactions of inorganic radicals in aqueous solutions. *J Phys Chem Ref Data* **17**: 1027–1284.
24. Khopde SM, Priyadarsini KI, Mukherjee T, Kulkarni PB, Satav JG, Bhattacharya RK. (1998) Does β -carotene protect membrane lipids from peroxidation? *Free Radic Biol Med* **25**: 66–71.
25. Augusto O, Bonini MG, Amanso AM, Linares E, Santos CC, De Menezes SI. (2002) Nitrogen dioxide and carbonate radical anion: Two emerging radicals in biology. *Free Radic Biol Med* **32**: 841–859.
26. Everett SA, Dennis MF, Patel KB. (1996) Scavenging of nitrogen dioxide, thiol and sulfonyl radicals by nutritional antioxidant β -carotene. *J Biol Chem* **271**: 3983–3994.
27. Goldstein S, Czapski G. (1995) The reaction of NO with O_2^- and HO_2 : A pulse radiolysis study. *Free Radic Biol Med* **19**: 505–510.

28. Bartesaghi S, Trujillo M, Denicola A, Folkes L, Wardman P, Radi R. (2004) Reactions of desferrioxamine with peroxynitrite-derived carbonate and nitrogen dioxide radicals. *Free Radic Biol Med* **36**: 471–481.
29. Goldstein S, Lind J, Merenyi G. (2004) Reaction of organic peroxy radicals with NO₂ and NO in aqueous solution: Intermediacy of organic peroxynitrate and peroxynitrite species. *J Phys Chem A* **108**: 1719–1725.
30. Richter HW. (1998) Radiation chemistry: Principles and applications. In: Wishart JF, Nocera DG (eds.), *Photochemistry and Radiation chemistry*, pp. 5–33. Advances in Chemistry Series 254. Oxford University Press.
31. Schoneich C, Aced A, Asmus KD. (1991) Halogenated peroxy radicals as two-electron transfer agents. Oxidation of organic sulfides to sulfoxides. *J Am Chem Soc* **113**: 375–376.
32. O'Neill P, Chapman PW. (1985) Potential repair of free radical adducts of dGMP and dG by a series of reductants pulse radiolytic study. *Int J Rad Biol* **47**: 71–80.
33. Butler J, Land EJ, Swallow AJ, Prutz W. (1984) The azide radicals and its reaction with tryptophan and tyrosine. *Rad Phys Chem* **23**: 265–270.
34. Asmus K, Bonifacic M. (1999) Sulfur-centered reactive intermediates as studied by radiation chemical and complementary techniques. In: Alfassi ZB (ed.), *S-Centered Radicals*, p. 142. Wiley, New York.
35. Kapoor S, Priyadarsini KI. (2001) Protection of radiation-induced protein damage by curcumin. *Biophys Chem* **92**: 119–126.
36. NATO Advanced Study Institute. (1981) The study of fast processes and transient species by electron pulse radiolysis. In: Baxendale JH, Busi F (eds.), *Proceedings of the NATO Advanced Study Institute, Italy*. D. Reidel Publishing Company, USA.
37. Mason RP, Hanna PM, Burkitt MJ, Kadiiska MB. (1994) Detection of oxygen-derived radicals in biological systems using electron spin resonance. *Environ Health Perspect* **102**: 33–36.
38. Bisby RH. (1990) Interaction of vitamin E radicals and membrane. *Free Radical Res Com* **8**: 299–306.
39. Davies MJ, Forni LG, Wilson RL. (1988) Vitamin E analogue Trolox c. ESR and pulse radiolysis studies of free radical reactions. *Biochem J* **255**: 513–522.
40. Packer JE, Slater TF, Wilson RL. (1979) Direct observation of a free radical interaction between vitamin E and vitamin C. *Nature* **278**: 737–738.
41. Jovanovic SV, Steenken S, Tosic M, Morjanovic B, Simic MG. (1994) Flavonoids as antioxidants. *J Am Chem Soc* **116**: 4846–4851.
42. Li F, Fang X. (1998) Pulse radiolysis of epicatechin in aqueous solution. *Radiat Phys Chem* **52**: 405–408.
43. Bors W, Michel C, Stettmaier K. (2001) Structure-activity relationships governing antioxidant capacities of plant polyphenols. *Methods in Enzym* **335**: 166–180.

44. Mercero JM, Matxain JM, Lopez X, Fowler JE, Ugalde JM. (2002) Methoxyphenols-antioxidant principles in food plants and spices: Pulse radiolysis, EPR spectroscopy, and density functional theory calculations. *Int J Quantum Chem* **90**: 969–979.
45. Miao J-L, Wang W-F, Pan J-X, Lu C-Y, Li R-Q, Yao S-D. (2001) The scavenging reactions of nitrogen dioxide radical and carbonate radical by tea polyphenol derivatives: A pulse radiolysis study. *Rad Phys Chem* **60**: 163–168.
46. Priyadarsini KI. (1997) Free radical reactions of curcumin in membrane models. *Free Radic Biol Med* **23**: 838–843.
47. Bors W, Michel C, Stettmaier K, Lu Y, Yeap Foo L. (2003) Pulse radiolysis, electron paramagnetic resonance spectroscopy and theoretical calculations of caffeic acid oligomer radicals. *Biochim Biophys Acta* **1620**: 97–107.
48. Stojanovic S, Brede O. (2002) Elementary reactions of the antioxidant action of trans-stilbene derivatives: Resveratrol, pinosylvin and 4-hydroxystilbene. *Phys Chem Chem Phys* **4**: 757–764.
49. Priyadarsini KI, Khopde SM, Kumar SS, Mohan H. (2002) Free radical studies of ellagic acid, a natural phenolic antioxidant. *J Agr Food Chem* **50**: 2200–2206.
50. Joshi R, Kumar MS, Satyamoorthy K, Unnikrisnan MK, Mukherjee T. (2005) Free radical reactions and antioxidant activities of sesamol: Pulse radiolytic and biochemical studies. *J Agr Food Chem* **53**: 2696–2703.
51. Kapoor S, Mukherjee T, Kagiya TV, Nair CKK. (2002) Redox reactions of tocopherol monoglucoside in aqueous solutions: A pulse radiolysis study. *J Radiat Res* **43**: 99–106.
52. Bors W, Foo LY, Hertkorn N, Michel C, Stettmaier K. (2001) Chemical studies of proanthocyanidins and hydrolyzable tannins. *Antioxidants and Redox Signaling* **3**: 995–1008.
53. Bors W, Michel C. (1999) Antioxidant capacity of flavanols and gallate esters: Pulse radiolysis studies. *Free Radic Biol Med* **27**: 1413–1426.
54. Li Y-M, Han Z-H, Jiang S-H, Jiang Y, Yao S-D, Zhu D-Y. (2000) Fast repairing of oxidized OH radical adducts of dAMP and dGMP by phenylpropanoid glycosides from *Scrophularia ningpoensis* Hems. *Acta Pharm Sinica* **21**: 1125–1128.
55. Getoff NO. (2000) Pulse radiolysis studies of β -carotene in oxygenated DMSO solution, *Radiat Res* **154**: 692–696.
56. Samuni A, Goldstein S, Russo A, Mitchell JB, Krishna MC, Neta P. (2002) Kinetics and mechanism of OH-radical and OH-adduct radical reactions of nitroxides with their hydroxyl amines. *J Am Chem Soc* **124**: 8719–8724.
57. Lu C, Liu Y. (2002) Interactions of lipoic acid radical cations with vitamins C and E analogue and hydroxycinnamic acid derivatives. *Arch Biochem Biophys* **406**: 78–84.
58. Rozanowska M, Cantrell A, Edge R, Land EJ, Sarna T, Truscott TG. (2005) Pulse radiolysis study of the interaction of retinoids with peroxy radicals. *Free Radic Biol Med* **39**: 1399–1405.

59. Jovanovic SV, Steenken S, Hara Y, Simic MG. (1996) Reduction potentials of flavonoid and model phenoxyl radicals. Which ring in flavonoids is responsible for antioxidant activity? *J Chem Soc Perkin Trans 2* **11**: 2497–2504.
60. Torreggiani A, Trincherro A, Tamba M, Taddei P. (2005) Raman and pulse radiolysis studies of the antioxidant properties of quercetin: Cu(II) chelation and oxidizing radical scavenging. *J Raman Spectr* **36**: 380–388.
61. Marfak A, Trouillas P, Allais DP, Calliste CA, Cook-Moreau J, Duroux J-L. (2004) Reactivity of flavonoids with 1-hydroxyethyl radical: A γ -radiolysis study *Biochim Biophys Acta* **1670**: 28–39.
62. Filipe P, Morliere P, Patterson LK, Hug GL, Maziere J-C, Freitas JP, Fernandes A, Santos R. (2004) Oxygen-copper (II) interplay in the repair of semi-oxidized urate by quercetin bound to human serum albumin. *Free Radic Res* **38**: 295–301.
63. Zhao C, Shi Y, Wang W, Jia Z, Yao S, Fan B, Zheng R. (2003) Fast repair of deoxythymidine radical anions by two polyphenols: Rutin and quercetin. *Biochem Pharmacol* **65**: 1967–1971.
64. Filipe P, Morliere P, Patterson LK, Hug GL, Maziere J-C, Maziere C, Freitas JP, Fernandes A, Santos R. (2002) Repair of amino acid radicals of apolipoprotein B100 of low-density lipoproteins by flavonoids. A pulse radiolysis study with quercetin and rutin. *Biochemistry* **41**: 11057–11064.
65. Santos R, Patterson LK, Filipe P, Morliere P, Hug GL, Fernandes A, Maziere J-C. (2001) Redox reactions of the urate radical/urate couple with the superoxide radical anion, the tryptophan neutral radical and selected flavonoids in neutral aqueous solutions *Free Rad Res* **35**: 129–136.
66. Zhao C, Shi Y, Wang W, Lin W, Fan B, Jia Z, Yao S, Zheng R. (2002) Fast repair activities of quercetin and rutin toward dGMP hydroxyl radical adducts. *Radiat Phys Chem* **63**: 137–142.
67. Zhao C, Shi Y, Lin W, Wang W, Jia Z, Yao S, Fan B, Zheng R. (2001) Fast repair of the radical cations of dCMP and poly C by quercetin and rutin. *Mutagenesis* **16**: 271–275.
68. Miao J, Wang W, Pan J, Han Z, Yao S. (2001) Pulse radiolysis study on the mechanisms of reactions of CCl₃OO₂ radical with quercetin, rutin and epigallocatechin gallate. *Science in China, Series B: Chemistry* **44**: 353–359.
69. Mishra B, Priyadarsini KI, Sudheer Kumar M, Unnikrishnan MK, Mohan H. (2003) Effect of o-glycosilation on the antioxidant activity and free radical reactions of a plant flavonoid, chrysoeriol. *Bioorg & Med Chem* **11**: 2677–2685.
70. Mishra B, Priyadarsini KI, Sudheerkumar M, Unnikrishnan MK, Mohan H. (2006) Pulse radiolysis studies of mangiferin: A C-glycosyl xanthone isolated from *Mangifera indica*. *Rad Phys Chem* **75**: 70–77.
71. Zielonka J, Gebicki J, Gryniewicz G. (2003) Radical scavenging properties of genistein. *Free Radic Biol Med* **35**: 958–965.

72. Stojanovic S, Sprinz H, Brede O. (2001) Efficiency and mechanism of the antioxidant action of trans-resveratrol and its analogues in the radical liposome oxidation. *Arch Biochem Biophys* **391**: 79–89.
73. Mahal HS, Mukherjee T. (2006) Scavenging of reactive oxygen radicals by resveratrol: Antioxidant effect. *Res Chem Inter* **32**: 59–71.
74. Shishodia S, Sethi G, Aggarwal BB. (2005) Curcumin: Getting back to the roots. *Ann NY Acad Sci* **1056**: 206–217.
75. Lin C-L, Lin J-K. (2008) Curcumin: A potential cancer chemopreventive agent through suppressing NF- κ B signaling. *J Cancer Molecules* **4**: 11–16.
76. Gorman AA, Hamblett VS, Srinivasan VS, Wood PD. (1994) Curcumin derived transients: A pulsed laser and pulse radiolysis study. *Photochem Photobiol* **59**: 389–398.
77. Khopde SM, Priyadarsini KI, Venkatesan P, Rao MNA. (1999) Free radical scavenging ability and antioxidant efficiency of curcumin and its substituted analogue. *Biophys Chem* **80**: 85–91.
78. Jovanovic SV, Boone CW, Steenken S, Trinoga M, Kaskey RB. (2001) How curcumin works preferentially with water soluble antioxidants. *J Am Chem Soc* **123**: 3064–3068.
79. Priyadarsini KI, Maity DK, Naik GH, Sudheer Kumar M, Unnikrishan MK, Satav JG, Mohan H. (2003) Role of phenolic O-H and methylene hydrogen on the free radical reactions and antioxidant activity of curcumin. *Free Radic Biol Med* **35**: 475–484.
80. Pryor WA, Stahl W, Rock CL. (2000) Beta-carotene From biochemistry to clinical trials. *Nutrition Reviews* **58**: 59–53.
81. Hill TJ, Land EJ, McGarvey DJ, Schalch W, Tinkler JH, Truscott TG. (1995) Interactions between carotenoids and the CCl_3O_2 -radical. *J Amer Chem Soc*, **117**: 8322–8326.
82. El-Agamey A, Lowe GM, McGarvey DJ, Mortensen A, Phillip DM, Truscott TG, Young AJ. (2004) Carotenoid radical chemistry and oxidant/pro-oxidant properties. *Arch Biochem Biophys* **430**: 37–48.
83. Bohm F, Edge R, Mc Garvey DJ, Truscott TG. (1998) β -carotene with vitamin E and C offers synergistic cell protection against Nox. *FEBS Letters* **436**: 387–389.
84. Edge R, Land EJ, McGarvey J, Burke M, Truscott TG. (2000) The reduction potentials of β -carotene $^{*+}$ / β -carotene couple in an aqueous micro-heterogeneous environment. *FEBS Letters* **471**: 125–127.
85. Heinonen OP, Albanes D. (1994) The effect of vitamin E and beta carotene on the incidence of lung cancer and other cancers in male smokers. *New Eng J Med* **330**: 1029–1035.
86. Goldstein S, Samuni A, Russo A. (2003) Reaction of cyclic nitroxides with nitrogen dioxide: The intermediacy of oxoammonium cations. *J Am Chem Soc* **125**: 8364–8370.

87. Goldstein S, Samuni A, Hideg K, Merenyi G. (2006) Structure-activity relationship of cyclic nitroxides as SOD mimics and scavengers of nitrogendioxide and carbonate radicals. *J Phys Chem A* **110**: 3679–3685.
88. Goldstein S, Samuni A, Merenyi G. (2004) Reaction of NO, peroxyxynitrite and carbonate radicals with nitroxide and their oxonium cations. *Chem Res Toxicol* **17**: 250–257.
89. Goldstein S, Merenyi G, Russo A, Samuni A. (2003) The role of oxoammonium cation in the Sod-mimic activity of cyclic nitroxides. *J Am Chem Soc* **125**: 789–795.
90. Zhang R, Goldstein S, Samuni A. (1999) Kinetics of superoxide induced exchange and nitroxide antioxidant and their oxidized and reduced forms. *Free Radic Biol Med* **26**: 1245–1252.
91. Szajerski P, Zielonka J, Sikora A, Adamus J, Marcinek A, Gebicki J, Kozlovski VI, Drelicharz L, Chlopicki S. (2006) Radical scavenging and NO-releasing properties of selected beta-adrenoreceptor antagonists. *Free Radical Res* **40**: 741–752.
92. Joshi R, Kumar S, Unnikrishnan M, Mukherjee T. (2005) Free radical scavenging reactions of sulfasalazine, 5-aminosalicylic acid and sulfapyridine: Mechanistic aspects and antioxidant activity. *Free Rad Res* **39**: 1163–1172.
93. Tamba M, Torreggiani A. (2001) Physico-chemical and biological properties of ambroxol under irradiation. *Rad Phys Chem* **60**: 43–52.
94. Adhikari S, Priyadarsini KI, Mukherjee T. (2007) Physico-chemical studies on the evaluation of antioxidant activity of herbal extracts and active principles of some Indian medicinal plants. *J Clin Biochem Nutr* **40**: 173–184.
95. Dixit P, Ghaskadbi S, Mohan H, Devasagayam TPA. (2005) Antioxidant properties of germinated fenugreek seeds. *Phytotherapy Res* **19**: 977–983.
96. Prabhakar KR, Veerapur VP, Parihar KV, Priyadarsini KI, Rao BSS, Unnikrishnan MK. (2006) Evaluation and optimization of radioprotective activity of *Coronopus didymus* Linn. in γ -irradiated mice. *Int J Radiat Biol* **82**: 525–536.
97. Naik GH, Priyadarsini KI, Mohan H. (2006) Free radical scavenging reactions and phytochemical analysis of triphala, an ayurvedic formulation. *Curr Sci* **90**: 1100–1106.
98. Yaping Z, Suping Q, Wenli Y, Zheng X, Hong S, Side Y, Dapu W. (2002) Antioxidant activity of lycopene extracted from tomato paste towards trichloromethyl peroxy radical. *Food Chemistry* **77**: 209–212.
99. Niviere V, Asso M, Weill CO, Lombard M, Guigliarelli B, Favaudon V, Houee-Levin C. (2004) Superoxide Reductase from *Desulfoarculus baarsii*: Identification of protonation steps in the enzymatic mechanism. *Biochemistry* **43**: 808–818.
100. Singh D, Chander V, Chopra K. (2004) The effect of quercetin, a bioflavonoid on ischemia reperfusion induced renal injury in rats. *Arch Med Res* **35**: 484–494.

101. Mishra B, Priyadarsini KI, Bhide MK, Kadam RM, Mohan H. (2004) Reactions of superoxide radicals with curcumin: Probable mechanisms by optical spectroscopy and EPR. *Free Radic Re* **38**: 355–362.
102. Barik A, Mishra B, Shen L, Mohan H, Kadam RM, Dutta S, Zhang H-Y, Priyadarsini KI. (2005) Evaluation of a new copper (II)-curcumin complexes as superoxide dismutase mimic and its free radical reactions. *Free Radic Biol Med* **39**: 811–822.
103. Vajragupta O, Boonchoong P, Sumanont Y, Watanabe H, Wongkrajang Y, Kammasud N. (2003) Manganese-based complexes of radical scavengers as neuroprotective agents. *Bioorg Med Chem* **11**: 2329–2337.
104. Etcheverry SB, Ferrer EG, Naso L, Rivadencira J, Salinas, V, Williams PAM. (2008) Antioxidant effects of the VO(IV) hesperidin complex and its role in cancer chemoprevention. *J Biol Inorg Chemistry* **13**: 435–447.
105. Hirano T, Hirobe M, Kobayashi K, Odani A, Yamauchi O, Ohsawa M, Satow Y, Nagano T. (2000) Mechanism of superoxide dismutase-like activity of Fe(II) and Fe(III) complexes of tetrakis-N,N,N',N'(2-pyridylmethyl)ethylenediamine. *Chemical and Pharmaceutical Bulletin* **48**: 223–230.
106. Molina-Heredia FP, Houee-Levin C, Berthomieu C, Touati D, Tremey E, Favaudon V, Adam V, Niviere V. (2006) Detoxification of superoxide without production of H₂O₂: Antioxidant activity of superoxide reductase complexed with ferrocyanide. *Proc Natl Acad Sci USA* **103**: 14750–14755.
107. Mokrini R, Trouillas P, Kaouadji M, Champavier Y, Houee-Levin C, Calliste C-A, Duroux J-L. (2006) Radiolytic transformation of 2,2',4'-trihydroxychalcone. *Radiation Res* **165**: 730–740.

Index

- 1,2 H-shift 555
1,3,5-trithiane 451, 452
1,3-dimethyluracil 550, 553
1,3-dithiane 451
1,3-H shift 459
1,5-dithia-3-hydroxycyclooctane 469
2-deoxyribose 545, 547
2-hydroxyethyl sulfide 454, 455
2-methylthioethanoic acid 461
2-phenyl-thioethanol 455
2-propanol 441
4,4'-bipyridyl 260, 272
4-methylthiophenylmethanol 455
 ^{60}Co gamma radiolysis 486, 488
- α -(alkylthio)alkyl 464
 α -aminobutyric acid 470
 α -methylthioacetamide 460
 α , α' -dinaphthyl disulfide 474
 β -amyloid 464, 466, 469
 β -carotene 579, 583–585
 β -elimination 446, 464
 β -scission 452, 453, 460
 γ -irradiation 446–448, 473
 γ -radiolysis 448, 455, 463, 471, 473,
474
 π -interaction 475
- ab-initio calculations 476
absorbivity, molar 114, 115
absorption spectra 386, 388, 389,
391, 394–396, 401, 404
accelerator 122–124, 126, 128–135,
137, 141–143, 145–147, 149,
151–153
 double-decker accelerator 152
 Laser Linac Twin 123
 laser wakefield accelerator (LWA)
 134, 135
 photocathode electron gun
 126–129
 Van de Graaff 122
accelerator with FT-IR spectroscopy
213
acetaldehyde 463
acetophenone 399
acetyl thiol 464
action volume 291
activation energy 307, 308, 311–313
acyl 463
addition to the C5-C6 double bonds
443
adenine 545
 radical anion 545
 reaction with $\bullet\text{OH}$ 548

- adenyl radical 551, 552
advanced oxidation processes 390
alanine 443, 491, 502
alcohol 24, 28–30, 33, 34, 41, 44,
45, 50, 51
alcohol radiolysis 146
aliphatic disulfides 474
aliphatic sulfides 451, 458
aliphatic sulfoxide 484
alkali 22, 23, 25–28, 33, 37, 38, 40,
42
alkanes 28, 411–413, 419, 429
alkyl chlorides 411–413, 419, 429
alkyl radicals — reactions with
nucleobases 555
alkylthio-substituted cyclohexadienyl
441
alpha particles 2, 6
amine 22, 25, 38
amino acid 490, 491, 493–495, 503
ammonia 22–29, 40
amyotrophic lateral sclerosis (ALS)
501
anion clusters 59–61, 67, 68, 80, 81,
84, 87, 91
antioxidants 563–565, 575–580,
582–585, 587–589
Ar, Kr, Xe 170
arachidonic acid 447
arginine 491, 493, 502
aromatic carboxylic acids 455
aromatic disulfides 474
aromatic sulfides 453, 455, 473
aromatic sulfoxide 477
ascorbate ion 555
astrophysics/astrochemistry 206
auxiliary circuit 107
azide 464, 472
azurin 486, 495–497

back reactions 6, 8
base release 557

baseline compensation 108
bending 417, 421, 423–426, 428,
429
benzaldehyde 399, 400, 402
benzene 454
benzenethiol 447
benzyl methyl sulfide 454, 455
BET 306, 313
bimetallic nanoparticles 358, 359,
362, 364
bimolecular decay — nucleobase
radicals 552, 553
biopolymers 162, 172
biphenyl 454
bis-(1-substituted-uracilyl) disulfide
476
bond cleavage 475
butylbenzene 454

C60 176
C₆F₆ 168
C6-uracilyl 437
caffeic acid 462, 463
calmodulin 467, 469, 472
captodative effect 459
carbon nanotubes 368, 369
carbonate radical (CO₃^{•-}) 488, 489,
492
carbon-centered 434, 435, 441, 464,
466
Car–Parrinello calculations 61, 81
catalase 496
catalysis 347, 355, 357, 366, 369,
372, 376
catalytic decomposition 309
cavity 27, 30, 34, 40, 41, 44, 47
cavity electron 62, 63, 65, 73, 74,
76, 89
CCD camera 143, 144, 147–149
CCl₄ 164, 165, 170
CdS 174, 175
cell constant 112, 115

- cell, measuring 98, 100, 101, 103, 105, 106, 109, 110, 112, 115
- Cerenkov detector 109, 110
- Cerenkov light 123, 133, 135, 140, 143, 149, 151
- CH₃Br 168
- charge 23, 27, 33, 35, 38, 40
- charge per pulse 126, 128, 133, 134, 152
- charge transfer 295
- charge transfer to solvent 65
- chicane 124, 125, 132
- chloroaniline 403
- chlorogenic acid 462, 463
- cinnamate 392, 404
- cinnamic acid/cinnamate 403
- clusters 347, 348, 350–357, 359, 362, 364, 366, 368, 369, 371, 372, 374, 376
- CO₂ 166
- Co⁶⁰ 6, 7
- coaxial cable 108
- colloidal solutions 455, 456
- colloidal TiO₂ 455
- compressible continuum 285
- conductance 105, 106, 112, 115
- conduction band 62, 90
- conductivity 122, 137, 280
- confinement 326–328, 330–333, 336, 340, 342
- conformers 429
- conjugated polymers 162, 163, 173, 178–180, 182, 184, 185, 189
- controlled pore glass (CPG) 330, 332, 335, 337, 339
- cresols 389, 390, 396, 397, 399
- curcumin 579, 582, 583, 587
- current source 101, 105, 108
- cyclic dipeptides 467
- cyclic nitroxide 579, 585
- cyclic voltammetry 454, 455
- cyclohexadienyl 441
- cyclohexadienyl radical 390
- cyclohexane 168, 169
- cysteamine 435, 440, 444
- cysteine 435, 436, 441, 442, 445, 463
- cysteine thiol 441
- cystine 435, 436, 441, 442, 445, 463
- cytochrome c 496
- cytosine 444, 445, 545
- quantum chemical calculations 546, 548, 550, 551
- radical anion 545
- reaction with •OH 548
- data acquisition 110
- data retrieval 111, 112
- decarboxylation 455, 456, 458, 467, 468
- degradation 452, 470
- delta rays 522, 523
- density 260–263, 265, 267, 268, 270–273
- Density Functional Theory 527, 528
- deprotonation 455, 456, 458, 459, 464, 466
- detection 98–102, 104–108, 111, 116
- conductometric 104, 105
- optical 99–102
- DFT calculations 61, 81, 86, 88, 404, 460, 461, 466, 475, 477
- dialkyl 473, 477
- diamond films 152
- diaryl 473
- dielectric constant 257, 266, 267, 272, 273
- dielectric liquids 162, 163, 167, 184, 192
- diffusion theory 9
- discotic liquid crystals 162, 163, 173, 186
- dissociation 419, 420, 425, 426, 443, 449, 453, 454, 474

- dissociative electron attachment 72,
146, 510, 525, 532, 533, 534, 537
- disulfide 440, 441, 474–476, 496,
497
- disulfide linkage 474
- dithioester 451, 452
- dithiothreitol 440
- DNA 172, 173, 509–513, 515–525,
527–537, 543–548, 552,
554–557
- base release 518
 - base release by $\bullet\text{OH}$ 557
 - damage amplification
 - reactions 555
 - direct effect 509, 518, 519,
531, 532, 533, 537, 543,
545
 - double oxidation mechanism
531
 - electron loss pathways 515,
519, 532
 - electron transfer in 517
 - hole transfer in 515
 - indirect effect 543, 545
 - multiply damaged sites (MDS)
512, 520, 523, 524
 - phosphoryl radical 525, 532,
533
 - quasi-direct effect 518
 - radical cation at sugar moiety
557
 - radical cluster 523, 524
 - strand break 509, 510, 512,
518, 520, 524, 525,
529–536
 - strand breakage by $\bullet\text{OH}$ 557
 - strand breakage by
 - presolvated electron 547
 - strand break radical (prompt)
524, 525, 530, 532, 533
 - sugar radicals 513–515, 519,
521–530
 - water of solvation 510
- DNA Radicals 510, 525
- $\text{A}\bullet^+$ (dAdo \bullet^+), $\text{G}\bullet^+$ (dGuo \bullet^+)/
 $\text{G}(-\text{H})\bullet$ 527, 528
 - $\text{C}\bullet^-/\text{C}(\text{N3})\text{H}\bullet$ 513, 517, 522
 - $\text{C1}'\bullet$, $\text{C3}'\bullet$, $\text{C4}'\bullet$, $\text{C5}'\bullet$ 513,
514, 521, 526, 528
 - $\text{C3}'\bullet_{\text{dephos}}$, $\text{C5}'\bullet_{\text{dephos}}$ 513, 514,
533, 534
 - $\text{G}(-2\text{H})\bullet$ 527
 - $\text{H}_2\text{O}\bullet^+$ 511
 - $\bullet\text{OH}$ 532
 - 8-oxo- $\text{G}\bullet^+$ 514, 519, 520
 - $\text{ROPO}_2\bullet^-$ 532
 - sugar radical cohort 521
 - $\text{T}\bullet^-$ 513–516, 519, 521, 523
 - $\text{T}(\text{C6})\text{H}\bullet$ 514, 519
- donors 412, 415, 419, 429
- dose 125, 131, 142, 145, 147, 148,
152, 153
- dose monitor 112
- dose rate 350, 351, 358–363, 370,
371, 376
- dosimetry 112, 114, 115
- double probe pulse detection 143
- dry electron 13, 14, 69, 70, 90
- dynamics 417, 422, 429
- electrocatalysis 347, 367, 368, 376
- electrode 101, 105, 106, 107
- electron 2, 7, 9, 14–16, 280,
510–513, 515–520, 522, 523,
525–537
- hydrated 9–16, 22, 24, 25,
27, 28, 30, 35–38, 48, 49,
59, 60, 66, 74–78, 82–84,
90, 95, 241–243, 246,
258, 261, 264–266,
268, 270, 271, 474,
475, 510, 512, 513,
516, 519, 521, 522–525,
528, 530–533

- low energy 510, 512, 513, 531–536
- presolvated 547
- solvated 21, 22, 24–47, 49, 51, 59–63, 67, 71–74, 76–78, 80, 81, 88–91, 146, 148, 150, 336, 337, 340
- subexcitation 535
- unsolvated 532
- electron accelerator 281
- electron attachment 163, 164
- electron attachment reactions 280, 287, 294
- electron beam 348, 362, 363, 367, 368, 370, 375
- electron beam lithography 375
- electron density 386, 399, 402, 419
- electron energy 128
- electron gun 124, 126–130, 132, 133
- electron mobility 167, 168, 174, 175
- electron penetration 130
- electron pulse 122–125, 127, 130, 132, 134, 135, 137, 139, 140, 143, 144, 149, 151, 152
- electron reaction kinetics 167, 168
- electron scavenging 168
- electron spin echo envelope modulation (ESEEM) spectroscopy 60
- Electron Spin Resonance Spectroscopy 540
 - DNA benchmark spectra 513, 519
 - ^{13}C beta couplings 532
 - Q-band 530
- electron spin resonance 455, 460
- electron thermalization 165, 170
- electron transfer 122, 411–415, 417–420, 425–429, 449, 453, 454, 462, 463, 468, 472, 476, 496, 497
- electron tunneling 173, 186, 189, 190
- electron-donating 385, 387, 399, 400, 403
- electron-donating/electron-withdrawing 406
- electron-hole pair distance 146
- electron-ion recombination 146
- electrons in glasses 7
- electron-transfer reactions 12
- electron-withdrawing 385, 403
- electrophilic 385, 387, 399
- electrostatic 501, 502
- electrostriction 280
- emittance 125, 126, 128
- encounter complex 425, 427–429
- equivalent velocity spectroscopy 139
- ethane-1,2-diol (ethylene glycol, 12ED) 29, 30, 31, 45–49
- ethanol 29, 33, 40
- ether 40
- excimers 281
- excited states (DNA) 510, 525, 526, 528
- excited water 5, 6
- Faraday cup 133, 142
- fatty acids 441, 445, 446, 470
- femtosecond laser 123, 127, 134
- femtoseconds 419, 420, 427
- Fenton 495, 502
- ferulic acid 462, 463
- flash lamp 141, 149
- flavonoid 580, 581
- Fourier transform infrared (FT-IR) 205
- fragmentation 446, 455, 456, 458, 463
- free electron transfer 411, 412, 415, 420, 425, 426
- free energy 414, 429
- free ion yields 280

- free radicals 563, 564, 569,
576–578, 583, 584
Fricke 236, 237
Fricke dosimeter 5
fuel cells 367, 368
fused silica 101
- gases 162, 163, 165–167, 192
geminate recombination 34–36, 169
geometrical dose distribution 302,
303, 315, 319
glassy carbon 107
glutamate 491, 502
glutamic acid 442
glutamine 502
glutathione 442, 445, 448, 552
glycine 442, 443
gold 352, 353, 355, 357, 359–362,
364–366, 374, 375
group wavenumbers 202
guanine 440, 545
 radical anion 545
 reaction with $\cdot\text{OH}$ 548
guanyl radical 551, 552
G-values 256, 257, 263
- H_2 333–336, 339
 H_2O_2 315, 316, 325, 336, 339, 567,
571, 587
halobenzenes 394, 396
halotoluenes 390, 394, 396
Hammett Correlation 391
Hammett parameter 392, 394
Hammett plot 393
Hammett treatment 392, 393
H-atom abstraction 441
H-atom transfer reactions 443
H-atoms 441, 470, 473
heavy ion 231–235, 239–241, 243,
243, 245, 247–249
helium 165
heterogeneous systems 302, 304, 309
hexabenzocoronene 189–191
high pressure 285
high-LET 2, 8
hole mobility 168, 184, 188
hole reaction kinetics 168
homolytic substitution 452, 460
 $\text{HO}\cdot$ 336, 337, 342
hydrated electron *See* electron —
 hydrated
hydrocarbon 37
hydrogen 331, 334, 335, 338, 339
hydrogen bond 257, 271–273
hydrogen peroxide (H_2O_2) 3–5, 235,
241, 245, 247, 338, 339, 495
hydrolysis 452
hydrophobic 267, 268
hydroxycinnamic acid 462
hydroxycyclohexadienyl 457
hydroxycyclohexadienyl radicals 386,
387, 396, 402, 404
hydroxyl radical 12, 241, 243, 260,
261, 268–270, 336, 337, 340, 342,
386–388, 390–394, 396, 399–404,
435
 attack at sugar moiety of DNA
 557
 base release from DNA by 557
 DNA strand break formation by
 548, 557
 reaction with nucleobases 552
hydroxylation 399
hydroxysulfuranyl 452, 458, 459,
460, 462–464, 468
- ice 162, 171–173, 192, 207
infrared reflection-absorption
 spectroscopy (IR-RAS) 209
infrared spectrometer 204
inhibition 321
injector 126
instrumentation 97, 98, 113
interfaces 334, 340

- interfacial chemistry 303
- interfacial processes 301, 302
- interfacial reactions 305, 306, 312
- intramolecular hydrogen transfer 442
- ion beam irradiation (DNA) 520, 521, 532
 - argon beam 532
 - oxygen beam 521, 525
 - track core 522–525, 533
- ionic liquid radiolysis 147, 148
- ionic liquids 49, 50
- ionization 26, 34, 35, 41, 43, 46, 47
- ions 280
- isomerization cis/trans 445, 446
- isopyrimidine 554

- jitter 123, 129, 134, 137, 143, 144, 152

- kinetics 123, 137, 139, 147, 150, 153, 417, 419, 428

- laser 22, 24, 26, 37, 41
- laser flash photolysis 469
- laser-simulated radiation chemistry 15
- linear accelerator (linac) 123, 124
- linear energy transfer (LET) 233–241, 244–247, 249, 362, 510, 521
- long range electron transfer 496, 497
- lysine 491, 502

- macropulse 153
- magnetic compression 124, 125
- magnetic resonance 60, 75–77, 81
- MCM 330, 332, 334
- mechanism 36, 44–46, 48, 51
- mercaptoethanol 435, 444,
- mesolysis 473
- metal oxides 175, 309, 312, 313
- metalloprotein 485, 488, 495, 496
- Met-enkephalin 469–471

- methanol 29, 31, 33, 44, 45
- methionine 461–465, 467, 469–471, 473
- methionine methyl ester 461
- methyl sulfonyl chloride 478
- methyl viologen 260, 272
- methyltetrahydrofuran 474
- microsecond 122, 134
- microwave 124, 127, 129, 135, 144, 153
- microwave conductivity 161, 162, 165, 184, 185, 192
- mixed quantum-classical (MQC) calculations 61
- mobility 27, 28, 280
- modified prescribed diffusion 10
- molecular hydrogen 235, 241, 245
- molecular products 265
- monochromator 102
- monounsaturated 445, 446, 479
- Monte Carlo simulation 232, 240, 242, 245, 246
- Mulliken charge 548
- multichannel detector 104
- myoglobin 223

- N-acetylmethionine methyl ester 461, 462
- N-acetylmethionine 461, 462
- N-acetylmethionine amide 461, 462

- nanomaterials 218, 347, 372, 373
- nanoparticles 319, 320, 348, 352–355, 357–372, 374–376
- nanosecond 122, 123, 126, 153, 411, 412, 417, 419, 429
- n*-butyl chloride-derived 453
- near infrared (NIR) detector 140
- neighboring group 458, 465, 466
- NH₃ 167, 171
- nitrous oxide 163
- NO 565, 566, 568–570, 574, 584

- NO₂ 566, 568–570, 574, 580,
583–585
- noise 108, 110, 112, 116
- non-linear optical devices 142
- nuclear technology 301
- nucleobases — reaction with solvated
electron 545
- OH adducts 386, 387, 389, 390,
394, 396, 399, 402, 403, 405
- *OH radical *See* hydroxyl radical
- optical absorption 21, 24, 28–30, 32,
38, 39, 41, 122, 142, 145, 148,
152, 280
- optical cell 259
- optical delay 137, 142, 147
- optical density 108, 115
- optical emission 123
- optical fiber 104, 109, 142, 147,
148
- optical fiber single shot (OFSS) 138,
141, 147, 148, 153
- optical limitation 347, 365, 376
- optical parameter amplifier (OPA)
141
- optical path 138, 150
- organometallic chemistry 213
- oscilloscope 137, 142, 152
- oxidation 451, 452, 455–458,
461–468, 472, 474
- oxidative dissolution 308, 310, 321
- oxidative stress 563, 564, 568, 575,
581, 584, 586–588
- oxidizing radicals 385, 393, 405
- oxygen 452, 453, 462, 465–468,
470, 473, 476, 478
- oxyl radicals 553
- pair (cation–electron) 38, 40
- palladium 358, 366, 368, 370, 372,
375
- particle-in-a-box concept 61, 62, 73,
76, 80, 90
- p-state 65
- relaxation 60, 63, 65–69, 71,
87, 91
- s-state 65, 69
- stabilized multimer anion model
61
- in tetrahydrofuran 60
- transient hole burning
spectroscopy 79
- ultrafast pump-probe
spectroscopy 79
- vibrational features 87
- weakly bound 69, 70, 90
- PCBM 176
- Pd 319, 321
- penicillamine 435, 437, 441
- pentadienyl 444, 446, 447
- peptide bond 467, 468
- peptides 441–443, 464, 465, 469,
470
- peroxyl radical 386, 389–391, 567,
568, 570–573, 578, 580–584
of nucleobases 553–556
- peroxynitrite 566, 568–570, 575,
577, 583
- pH and sugar radicals 526
- phenolic products 386, 389, 397,
402
- phenols 415, 417, 421, 422, 424,
427, 429
- phenoxyl radical 401
- phenylalanine 441
- phenylthioacetic acid 455, 458
- photomultiplier tube (photocathode)
103, 126–130, 132, 134, 137, 141,
142, 149, 150, 152, 153
- photocathode-injected accelerators
14, 16
- photodetector 101–104, 107, 108,
137, 143
- photodiode 103, 104, 110, 137,
142
- photography 364, 365

- phthalocyanine 186, 189–191
picosecond (sub-nanosecond) pulse
 radiolysis 2, 10, 13, 14
plasmid DNA 524, 529, 530, 531,
 533, 534
platinum 352–354, 362, 367, 368,
 369, 371, 372
polarization energy 285
polarography 118
polydiacetylenes 177
polyethylene 176, 177, 182, 184
polymers 162, 163, 172, 173,
 176–180, 182, 184, 185, 189, 192,
 211, 212
polysilanes 182, 183
polystannane 183
polythiophene 184
polyunsaturated 441, 446
pores 326, 328–332, 336, 337,
 340
porphyrin 186, 189
PPV 180–182, 184, 185
pre-bunching 123, 124
preparation chamber 130, 133
presolvated electron 547
prion proteins 467
product ratio 415, 424, 425
propane-1,2,3-triol (glycerol, 123PT)
 29, 45, 47
propane-1,2-diol (12PD) 29–31, 47
propane-1,3-diol (13PD) 29–31, 47
proteins 434, 464, 467, 469, 472,
 473, 485, 486, 488, 489, 493–498,
 503
PR-TRMC 161–168, 170, 172–180,
 182–184, 186–189, 191, 192
pulse and probe detection 139, 140,
 146
pulse width 124, 126, 134, 135
pulsed electron double resonance
 (PELDOR) 523
pulse-pump-probe radiolysis 153
pyrimidine 435, 436, 438, 443–445
quantum chemical calculations
 cytosine 546, 548, 550, 551
 thymine 546, 548, 550, 551
quantum mechanical calculations
 445, 458, 459
quantum yield 129, 130, 152
quartz master oscillator 129
quercetin 579, 580, 581, 583
radiation biochemistry 221
radiation chemistry 433
radiation footprinting 494, 502
radiation targeting 493, 494
radical anion 401, 438, 440, 469,
 474, 475
 adenine 545
 cytosine 545
 guanine 545
 thymine 545
radical cation 386, 411–413,
 415–417, 419–421, 424–427, 429,
 449, 450, 453–460, 462–466, 468,
 472, 477, 478
radicals 6, 7, 10–12, 433–435,
 438–449, 451, 455, 457–461,
 463–468, 470–474
radioactivation 131
radiolytic yield 232–237, 240, 242,
 327, 328, 333, 338, 340, 342
Raman scattering 365
Raman spectroscopy 154
rapid scan 218
rare gases 279
rate constant 122, 257, 266, 267,
 269, 272, 435–439, 442–446, 463,
 469, 474, 476
reactivity 21, 22, 24, 34, 36
reactors 256, 268, 273
recombination 166, 167, 169, 175,
 176, 185, 189, 192
reduction 37, 40, 348–351, 354,
 358, 359, 361–365, 369–371, 373,
 375, 376

- reduction potential 448, 449,
454–456, 464, 478
- refractive index 138, 139
- regioselectivity 548, 549
- relaxation 40, 41, 44–48, 50
- repair reactions 435–439
- repetition rate 128, 129, 143, 150
- resveratrol 579, 581, 582, 585
- ribonuclease A 473
- ribonuclease T1 473
- RNS 564–566, 568, 570, 571, 576,
577, 584, 587
- ROS 564, 565, 566, 570, 571, 576,
577, 584, 587
- rotation 417–421, 423–426, 428, 429
- S-acetylated L-cysteine ester 463
- semiconductor 130, 149, 152, 162,
173
- S-ethylthioacetate 458, 461
- SF₆ 164, 166, 168
- shape resonance 535, 536
- shielding 126
- silicon 175
- silver 349, 351–356, 358–365, 369,
371, 372, 374
- simulation 30, 32, 38, 51, 112, 113
- sinapic acid 462, 463
- single shot electro-optic diagnostic 135
- single shot radiolysis 146
- S-methylglutathione 466, 467
- SOD *see* superoxide dismutase
- solvated electron *See* electron —
solvated
- absorption spectrum 71, 78,
80
 - s-p substructure 78
 - ammoniated 74, 76
 - anisotropy of 71
 - continuous blue shift in electron
salvation 67
 - encapsulated 89–91
 - “hot” states 65
 - in hydrocarbons 59
 - reaction with nucleobases 545
 - solvation dynamics 2, 4, 21, 26, 28
 - specific surface area 313
 - spectra 413, 416
 - spectral properties 257, 270, 272
 - spectral shifts 271, 272
 - spectrograph 149, 150
 - spent nuclear fuel 301–305, 308,
311, 315, 316, 318–321
 - spin distribution 454
 - spur 34, 258, 260, 273
 - steady-state 304, 311, 314, 316–319
 - step scan 218
 - strand breakage — of DNA by
presolvated electrons 547
 - streak camera 123, 135, 137, 138,
140, 143, 148–153
 - stroboscopic method 123
 - subpicosecond 134, 152
 - substituted aromatics 412
 - sugar radicals (DNA) 519, 521–530
 - dose response 513, 521
 - via photoexcitation 526–528 - sulfenic acid 463
 - sulfides 451, 453–455, 458, 473
 - sulfinyl 463
 - sulfonyl 434, 477, 478
 - sulfoxides 434, 469, 477
 - sulfur-centered 433, 434, 451, 457,
466, 470, 472, 473
 - sulphate 477
 - superconductor 173
 - supercritical fluids 255, 270, 273
 - supercritical krypton 279
 - supercritical water 255–257, 265,
273
 - supercritical xenon 146
 - superoxide (O₂⁻) 241, 244–246, 469,
470, 478, 498, 563, 565, 566, 582,
585–587

- superoxide dismutase (SOD) 470,
498–502, 555, 563, 585–587
- superoxide radical 561
- supersonic gas jet 134
- suspensions 304–306, 309–312
- swift heavy ions (SHI) 210
- synchronization 127, 129, 137
- tandem lesion 556
- temperature 129, 131
- tert*-butanol 446, 447, 461
- tetrahydrofuran (THF) 28, 29
- tetrahydrofuran radiolysis 144, 146
- thermionic cathode 124, 126, 143
- thioanisole 454, 455, 457
- thioethers 434, 451, 452, 457,
461
- thiolate anions 474
- thiols 434–438, 440, 441, 445,
447–449, 474
- thiophenols 449, 452, 453
- thioredoxin 469, 472
- thiyl 441, 443, 447–449, 455, 464,
471, 473–475
- three-electron-bond 461
- three-electron-bonded 453, 458,
459, 463, 468
- Three Mile Island 6
- thymine 439, 440, 444, 445, 545
quantum chemical calculations
546, 548, 550, 551
radical anion 545, 547
reaction with $\cdot\text{OH}$ 548
reactions of $\cdot\text{OH}$ -adduct radicals
550
- thymine-derived N1-centered 439
- time jitter compensation 143, 144
- time regime 425
- time resolution 122, 130, 131,
134, 135, 137, 139, 142–144, 146,
149, 150, 154
- time-of-flight 149
- time-resolved infrared spectroscopy
212
- TiO₂ 175
- track structure 232, 239, 240, 241,
244, 247, 249, 521, 523, 524
- trajectory 125
- transient absorption spectrum 144,
150
- transient species 122, 130, 138, 153,
257, 258, 260, 270–272
- trolox C 578
- tyrosyl 472, 473
- unsaturated 445, 470
- UO₂ 310
- uracil 439, 444, 445, 545, 554
- uracil-derived N1-centered 439
- vibrational spectroscopy 153
- vicinal lesion 556
- viscosity 28, 32, 46, 50
- vitamin E 564, 578, 582
- volume changes 279
- Vycor 330, 332, 334
- wakefield accelerators 16
- wastes 325
- water 325–328, 331, 333–340
- water radiolysis 257, 258, 266, 270
- water structure 257, 258
- white-light continuum 143
- xenon 279
- xenon lamp 110
- X-ray generator 4
- yield 129, 130, 146, 152, 153
- zeolites 328, 329, 330, 333, 334,
336, 338–340, 371, 372